Available online at www.sciencedirect.com

ScienceDirect

Aquatic Procedia 4 (2015) 1500 – 1507

Aquatic Procedia

www.elsevier.com/locate/procedia

INTERNATIONAL CONFERENCE ON WATER RESOURCES, COASTAL AND OCEAN ENGINEERING (ICWRCOE 2015)

Water Surface Profile Computation In Nonprismatic Compound Channels

B. Naik[a], K.K.Khatua[a]*

[a]*Department of Civil Engineering , N.I.T. Rourkela, INDIA.*

Abstract

A river generally exhibits a two stage geometry i.e. deeper main channel and shallow floodplain called compound section. In most of the compound channels, the floodplain geometry is found to be varying along the length of the flow called non-prismatic compound channel. The modelling of such flows is of primary importance when seeking to identify flooded areas and for flood risk management studies etc. The water surface profile is a series of transition curve from the normal depth line in one sub reach to the normal depth line in the adjacent sub reach. Water surface modeling help for the study of flood waves, water level calculation during flood, stage discharge relation, design of water work structures. All non-prismatic open channel flows are found to be unsteady and non-uniform. So these flows are difficult to analyse. In this paper experiments have been conducted to compute the water surface profile of non-prismatic compound channel for different converging angle and an attempt has been made to formulate mathematical models for predicting water surface profile by using the new experimental data of N.I.T, Rourkela and other standard data sets for different converging compound channels.

Peer-review under responsibility of organizing committee of ICWRCOE 2015

Keywords: water surface profile, compound channel, converging angle, flow depth

1. INTRODUCTION

A compound channel consists of a main channel and floodplains. The main river channel carries low flows and the flood plains transport overbank flows during flooding. The storage provided by floodplains in overbank flow reduces river channel that carries low flows flood stages. The interaction between the main channel and floodplain

* Corresponding author. Tel.:09861068249
E-mail address: kkkhatua@yahoo.co.in

Peer-review under responsibility of organizing committee of ICWRCOE 2015
doi:10.1016/j.aqpro.2015.02.194

flow is a complex one because of the momentum transfer at the interface. This phenomenon is more complex in non-prismatic compound channels with converging floodplains due to change in geometry. In converging compound channel the flow is forced to leave the flood plains and enter the main channel resulting in increased interactions and momentum exchange (Bousemer and Zech (1999), Bousemer et al. (2004), Proust et al. (2006), Rezai (2006)). This extra momentum exchange should also be taken into account in the flow modelling. Today more than half of the world's population live within 65km of a sea cost, and most of the major cities are also located on main river systems. So whenever flood occurs, this has lead to increase in the loss of life and economic cost (Knight and Shamseldin 2005). Water surface profile prediction is a vital issue in flood risk management and also in assessing ecological effects of bridge construction or changing the cross section geometry of channels. The effect of contraction on the water depth in a compound channel with converging compound channel is now investigated. In present work based on the experimental data of N.I.T Rourkela data and Rezai (2006) data an attempt has been made to develop a mathematical model for water surface calculation in converging compound channels. The method can be applied to the converging compound channels of different configurations and flow conditions.

Nomenclature

α	width ratio
δ	aspect ratio
β	relative depth
Xr	relative distance
θ	converging angle

2. EXPERIMENTAL WORK

2.1. Experimental Setup

Experiments had been conducted at the Hydraulics and Fluid mechanics Laboratory of Civil Engineering Department of National Institute of Technology, Rourkela, India. Three sets of non-prismatic compound channels with varying cross sections were built inside a concrete flume measuring 15m long × 0.90m width × 0.55m depth and flume with Perspex sheet of same dimensions. The width ratio of the channel was $\alpha = 1.8$ and the aspect ratio was $\delta = 5$. Keeping the geometry constant, the converging angles of the channels were varied as 12.38°, 9º and 50 respectively. Converging length of the channels fabricated were found to be 0.84m, 1.26m and 2.28m respectively. Longitudinal bed slope of the channel was 0.0011. Roughness of the floodplain and main channel were identical and the Manning's n was determined as 0.011 from the experimental runs in the channel. A re-circulating system of water supply was established with pumping of water from an underground sump to an overhead tank from where water flows under gravity to the experimental channel. Adjustable vertical gates along with flow strengtheners are provided in upstream section sufficiently ahead of rectangular notch to reduce turbulence and velocity of approach in the flow near the notch section. An adjustable tailgate at the downstream end of the flume helps to maintain uniform flow over the test reach. Water from the channel was collected in a volumetric tank that helps to measure the discharge rate. From the volumetric tank water runs back to the underground sump. Figure 1(a) shows the plan view of experimental setup. Figure 1(b) shows the plan view of experimental sections.

A movable bridge was provided across the flume for both span wise and stream wise movements over the channel area so that each location on the plan of compound channel could be accessed for taking measurements. The broad parameters of this channel are aspect ratio of main channel (δ), width-ratio (α).

A micro-Pitot tube of 4.77 mm external diameter in conjunction with suitable inclined manometer is used to measure velocity at these points of the flow-grid. The Pitot tube is physically rotated with respect to the main stream direction till it gives maximum deflection of the manometer reading. A flow direction finder having a least count of 0.1° is used to get the direction of maximum velocity with respect to the longitudinal flow direction. The angle of limb of Pitot tube with longitudinal direction of the channel is noted by the circular scale and pointer arrangement attached to the flow direction meter. The overall discharge obtained from integrating the longitudinal velocity plot

and from volumetric tank collection is found to be within ±3% of the observed values.

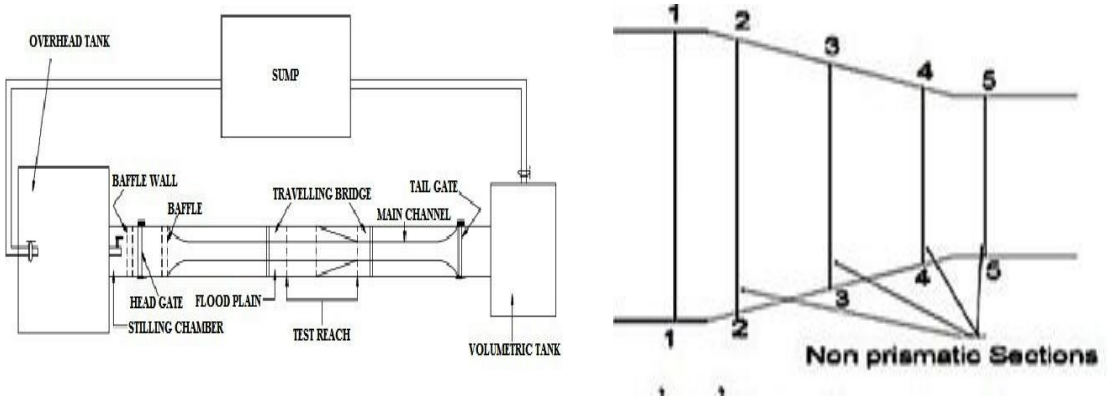

Fig.1 (a). Plan view of experimental Setup (b). Plan view of experimental Section

Table1.Hydraulic parameters for the experimental channel data set collected from literature experiments

Verified test channel	Types of channel	Angle of convergent (Θ)	Longitudinal slope (S)	Cross sectional geometry	Total channel width (B)	Main channel width (b)	Main channel depth (h)	Width ratio (sec-1) B/b (α)	Converging length (Xr)	Aspect Ratio b/h (δ)
					Meter	Meter	Meter		Meter	
Rezai (2006)	Convergent (CV2)	11.31°	0.002	Rectangular	1.2	0.398	0.05	3	2	7.96
Rezai (2006)	Convergent (CV6)	3.81°	0.002	Rectangular	1.2	0.398	0.05	3	6	7.96
Rezai (2006)	Convergent (CV6)	1.91°	0.002	Rectangular	1.2	0.398	0.05	3	6	7.96
N.I.T. Rkl	Convergent	5°	0.0011	Rectangular	0.9	0.5	0.1	1.8	2.28	5
N.I.T. Rkl	Convergent	9°	0.0011	Rectangular	0.9	0.5	0.1	1.8	1.26	5
N.I.T. Rkl	Convergent	12.38°	0.0011	Rectangular	0.9	0.5	0.1	1.8	0.84	5

3. EXPERIMENTAL RESULTS

The stage discharge relationship of different sections for the converging compound channel of angle 12.38° from in bank to over-bank flow conditions are shown in Fig.2 (a) and Fig.2 (b). A total 13 stage-discharge runs for are observed at the test reach.

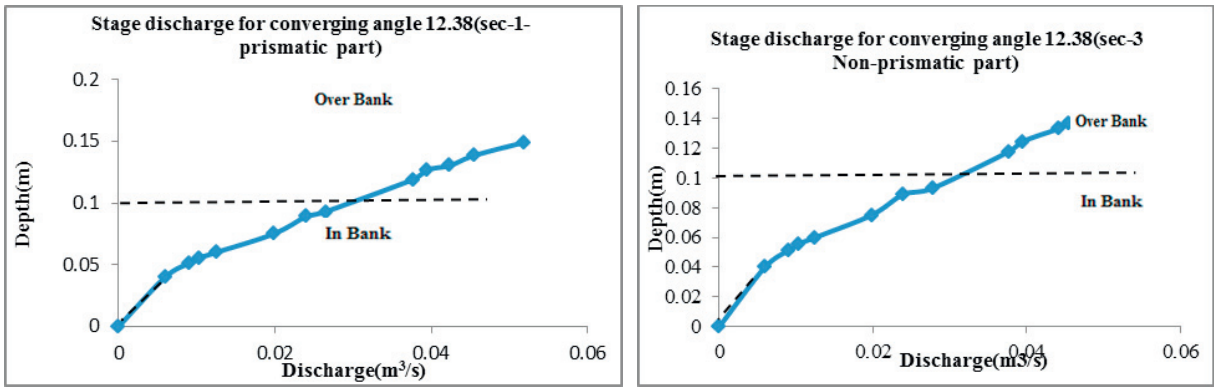

Fig. 2(a). Stage discharge relationship for the converging angle 12.38° (Sec-1 prismatic part) (b). Stage discharge relationship for the converging angle 12.38° (Sec-3- Non-prismatic part)

4. WATER SURFACE PROFILE COMPUTATION AND MODEL DEVELOPMENT

From the literature study, it is seen that water surface profile (*WP*) = F (α, β, δ) for prismatic compound channel, Where F is the functional symbol. But when all the equations are tested against non-prismatic compound channels of converging sections significant errors are found due variation of geometry. So an attempt has been made here to see the variation of Non prismatic water surface profile with respect to different independent parameters. Non prismatic water surface profile has been derived from a wide range of experimental data sets from three different types of converging compound channels of NIT, Rourkela, India along with three series of converging compound channels data of Rezai (2006) (details of the data sets are given in Table.1) These compound channels have homogeneous roughness both in the main channel and floodplain subsections. Manning's n values for all these smooth surfaces are taken as 0.01.A multiple-variable regression model is developed by taking five important dimensionless independent parameters. The dependency of Non dimensional water surface profile (*NWP* - Flow depth over floodplain divided by full main channel depth) and the best functional relationships of it have been found out from different plots described below. The relationships may be in the following form

$$NWP = F(\alpha, \beta, \delta, \theta, X_r) \quad (1)$$

The variation of *NWP* has been found out for six converging compound channels. The variation of *NWP* in terms of relative depth β and relative distance *Xr* are plotted for different converging angles θ in Fig 4, 5, 6, 7, 8, 9. From these figures it is seen that *NWP* increases with increase in relative depth.

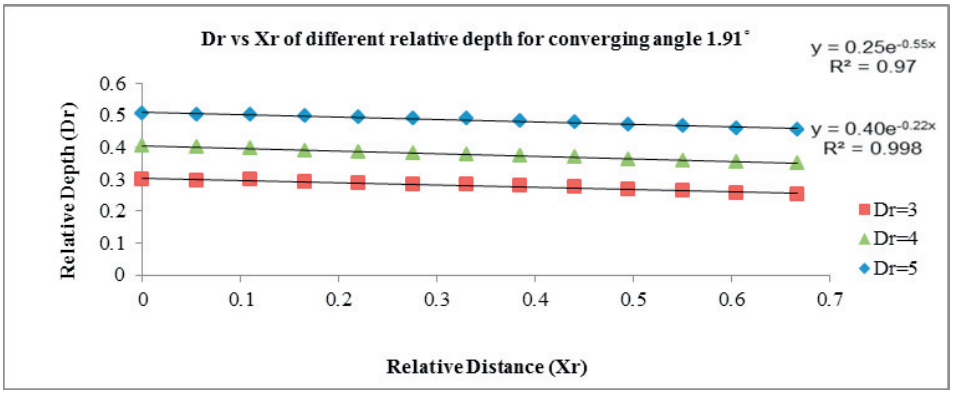

Fig.4. Variation of *NWP* along the Non prismatic length for converging angle 1.91˚

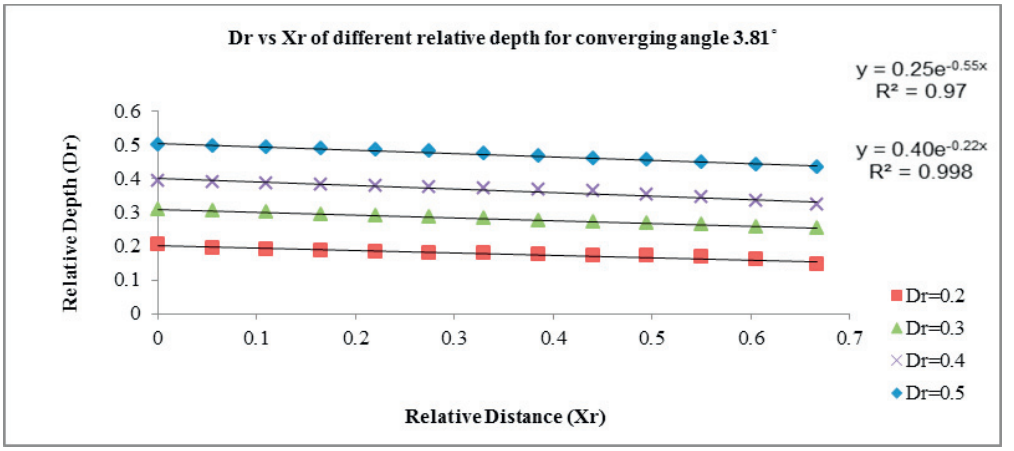

Fig.5. Variation of *NWP* along the Non prismatic length for converging angle 3.81˚

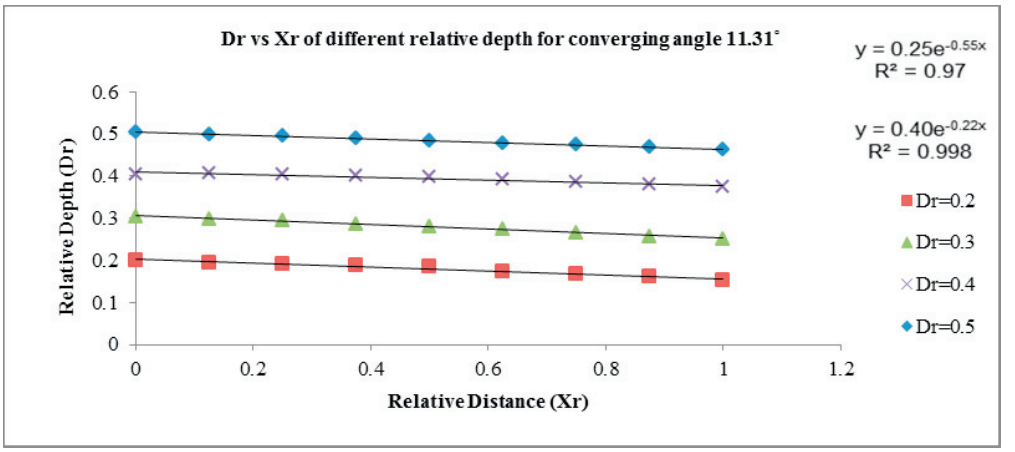

Fig.6. Variation of *NWP* along the Non prismatic length for converging angle 3.81˚

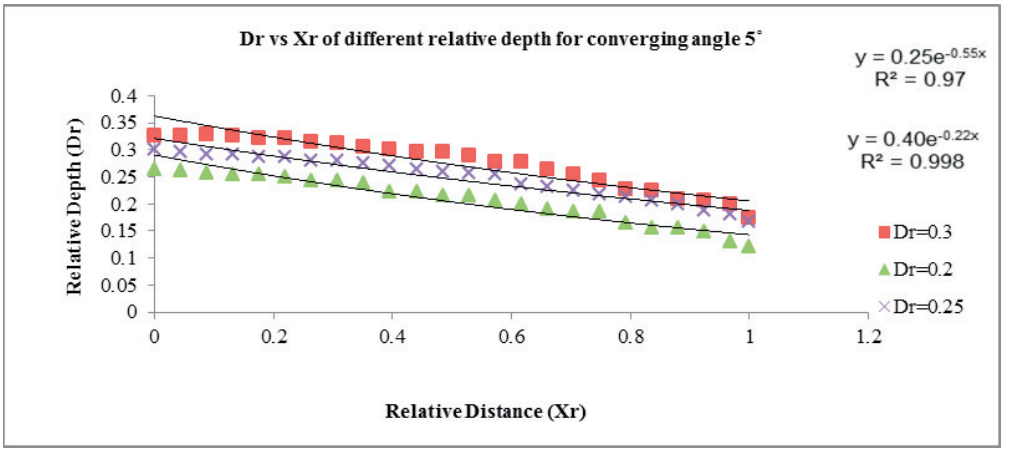

Fig.7. Variation of *NWP* along the Non prismatic length for converging angle 5˚

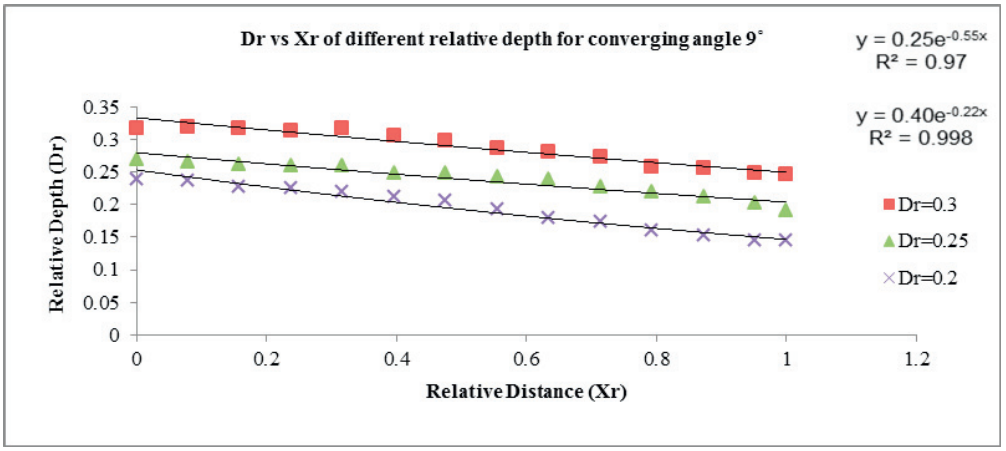

Fig.8. Variation of *NWP* along the Non prismatic length for converging angle 9˚

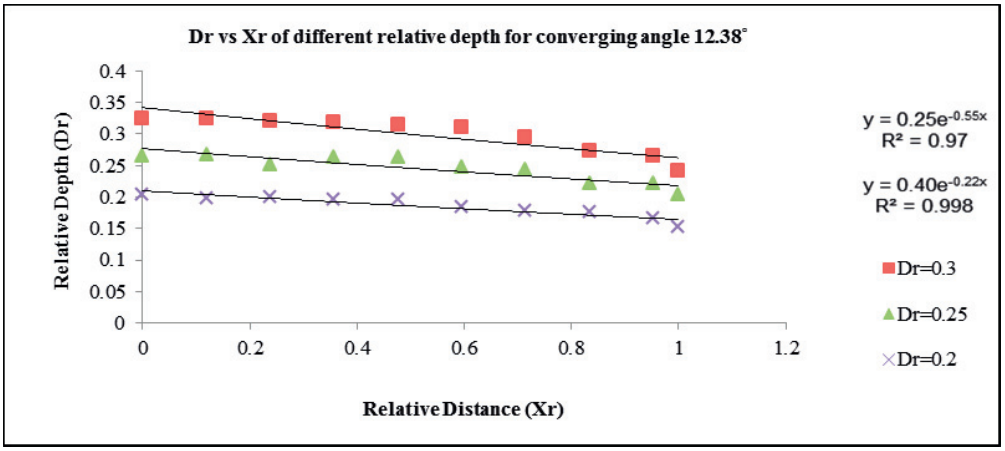

Fig.9. Variation of *NWP* along the Non prismatic length for converging angle 12.38˚

By analysing the above plots, the best functional relationships of *NWP* with different non-dimensional geometric and hydraulic parameters for the ranges of overbank flow depths are given by

$NWP = 0.25\, e^{-0.57 X_r}$ for lower Relative flow depth i.e D_r= 0.2, 0.25, 0.3 (2)

$NWP = 0.40\, e^{-0.22 X_r}$ for higher Relative flow depth i.e D_r= 0.4, 0.5 (3)

Here the R^2 value of the chosen functional relationship has been found to be very high and varies from 0.97 to 0.99 (please see the Fig. no. 4, 5, 6, 7, 8, 9). The equations (2) and (3) can be applied to compute the water surface profile of a converging compound channel flow for different converging angles and at different reaches in terms of relative distance from the starting part of non-prismatic reach i.e. X_r.

5. RESULTS AND DISCUSSION

The *NWP* for all the new non-prismatic compound channels and the data of Rezai (2006) has been computed using equation (2) and (3). The variation between the calculated values of *NWP* of equations (2) and (3) and the corresponding observed values for all the six types of channels are shown in Fig.10 for higher Relative depth and Fig.11 for lower Relative depth. The percentage error *NWP* is less for both Present experimental Channel as well as Rezai (2006) Channel proving the effectiveness of the equation (2) and (3).

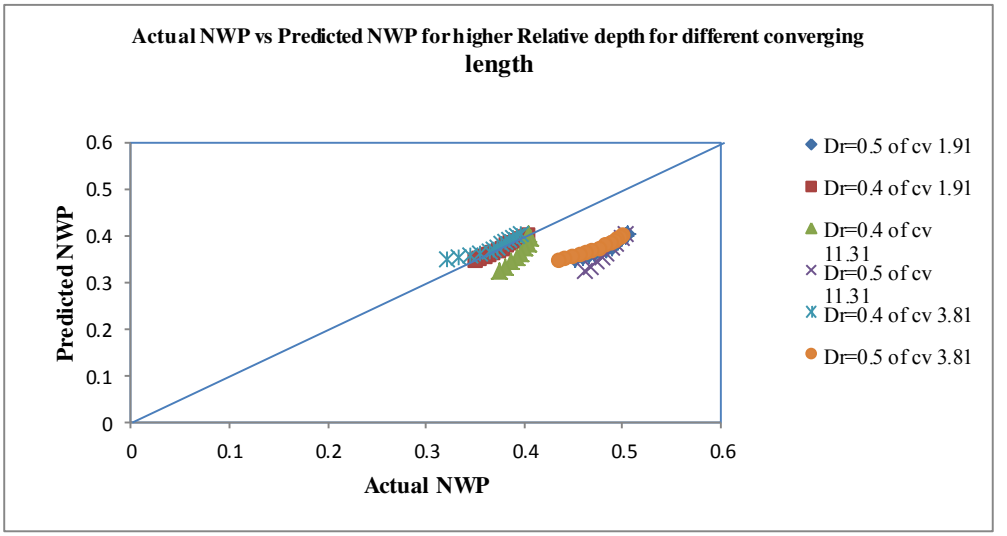

Fig.10. Scatter plot for observed and modelled value of *NWP* for higher D_r

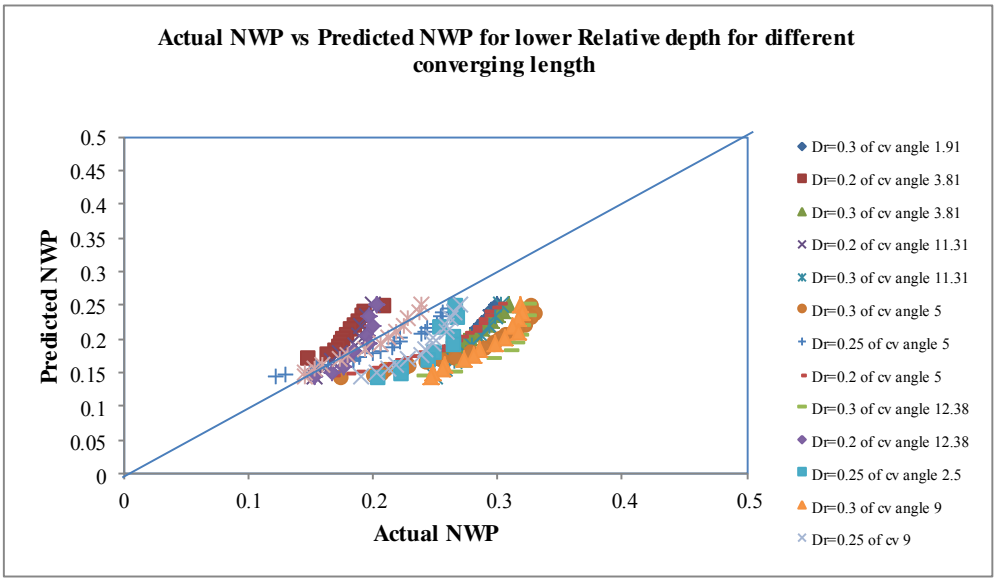

Fig.11. Scatter plot for observed and modelled value of *NWP* for lower D_r

6. CONCLUSIONS

The following conclusions can be derived from the above research presented in this work.

- From the experimental results on converging compound channels, the stage discharge of different sections of the converging compound channels is measured.
- The water surface profile along a non-prismatic compound channel are found to increase with increase of Relative depth for converging compound channels of different converging angles and decreases along the converging lengths of the channel under sub-critical flow conditions.
- The dependency of Non prismatic water surface profile is influenced by non-dimensional geometric and hydraulic parameters. The *NWP* in converging compound channel is found to be a non-linear function of all these non-dimensional parameters.
- The present mathematical model for a converging compound channel showing the dependency of *NWP* with relative distance for different flow depths are presented and modelled. The equations are found to provide good results when compared with the observed *NWP*.

7. ACKNOWLEDGEMENTS

The author wish to acknowledge thankfully the support from the Institute and the UGC UKIERI Research project (ref no UGC-2013 14/017) by the second authors for carrying out the research work in the Hydraulics laboratory at National Institute of Technology, Rourkela is thankfully acknowledged.

REFERENCES

Bousmar D and Zech Y (1999) Momentum transfer for practical flow computation in compound channel J. Hydraul. Eng., 125(7): 696-706

Bousmar D, Wilkin N, Jacquemart JH and Zech Y (2004) Overbank flow in symmetrically narrowing floodplains. J. Hydraul. Eng., ASCE, 130(4), 305-312

Proust S, Rivière N, Bousmar D, Paquier A, and Zech Y (2006) Flow in compound channel with abrupt floodplain contraction. J. Hydraul. Eng., 132(9), 958-970

Rezaei B(2006) Overbank flow in compound channels with prismatic and non-prismatic floodplains. PhD Thesis, Univ. of Birmingham, U.K..

Knight, D.W., and Shamseldin, A., (2005). "River basin modelling for flood risk mitigation",Taylor & Francis, the Nederlands.

Rezaei, B., and Knight, D.W., (2009). "Application of the Shiono and Knight Method in compound channel with non-prismatic floodplains" J.Hydraul. Research., 47(6), 716-726.

Rezaei, B., and Knight, D.W., (2011). "Overbank flow in compound channels with non prismatic floodplains" J. Hydraul. Eng.

Khatua KK, Patra KC, Mohanty PK (2012) Stage-Discharge prediction for straight and smooth compound channels with wide floodplains. J.Hydraulic. Eng., ASCE, 138(1): 93–99.

Bousmar, D., and Zech, Y., (2002). "Discussion of two-dimensional solution for straight and meandering overbank flows. " by D. A. Ervine, K. Babaeyan-Koopaei and Robert H. J. Sellin, J.H.E., 2000, 126(9). J. Hydraul. Eng., 128(5), 550-551.

Khiabani, M.H., and Kandasamy, J., (2005). "Friction factor for spatially varied flow with increasing discharge", J. Hydraul. Eng., 131(9), 792-799.

International Journal of Application or Innovation in Engineering & Management (IJAIEM)
Web Site: www.ijaiem.org Email: editor@ijaiem.org
Volume 4, Issue 7, July 2015 **ISSN 2319 - 4847**

Effectiveness of Time- Expansion of Consonants for the Benefit of Hearing Impaired Listeners

Dr N H SHOBHA

Department of Electronics & Communication Engineering, Methodist college of Engineering & Technology
Hyderabad, India

ABSTRACT

The current paper investigated the efficacy of consonant duration modification or consonant time- expansion on speech intelligibility for the impaired listeners. This work is an extension of author's previous papers and projects a comprehensive summary of the same along with the correlation of results with the current work. This paper highlights the importance of the lengthening an important acoustic attribute of clear speech - 'consonant-Duration'. A case for synthetic clear speech in the context of hearing impairment was argued for speech intelligibility. Consonant recognition in noise free and noisy situations using the non-sense syllable test (NST) was investigated upon (i) Hearing Impaired subjects, and (ii) Normal hearing subjects under simulated hearing impairment. Stops and Fricative consonants of English language with cardinal vowels were processed for time expansion. Non-uniform algorithm for waveform expansion involving selection and expansion of acoustic features was adopted. The Burst Duration, Voice Onset Time, Formant Transition Duration for Stops; and Fricative Noise Duration and Formant Transition Duration for Fricatives, were time-expanded by 50 - 100% of original duration. The speech perception in noise tests were quantified in terms of relative information transmission measures. The results reported that among the various segments selected for modifications, only Burst Duration of Stop-vowels has positive benefit on speech intelligibility improvement for the hearing impaired subject while the rest of them lead to perceptual errors.

Keywords- Burst Duration, Hearing impaired, Clear speech, Consonant Duration, Speech Intelligibility

1. INTRODUCTION

Good hearing is essential not only for communication and business, but also for many of the subtle joys that make life worth living. Persons with hearing impairment are less fortunate, as they often they have the greatest difficulty understanding speech in noisy environments. Sensorineural hearing losses (SNHL) are due to reduced sensitivity of the neural receptor that distorts the perception of sounds. The listeners with SNHL may suffer increased susceptibility to forward masking, making it more likely the vowels will mask energy in weaker adjacent consonants. SNHL are not amenable to medical intervention and patients need to use the hearing-aids for speech perception.

When confronted with difficult environments or when speaking to hearing-impaired person, humans instinctively change the way they speak and adopt a speaking style called clear speech. The acoustic analysis show that naturally produced clear speech typically involves a wide range of acoustic & articulatory adjustments referred as special attributes [1-3] such as decrease in speaking rate (longer segments), wider dynamic range, greater sound-pressure levels, more salient stop releases, greater rms intensity of non-silent portions (release burst, frication, and/or aspiration) of obstruent consonants.

Studies involving the difference between 'clear' and 'conversational' speech suggest that it may prove beneficial to attend to the temporal characteristics of speech for the benefit of SNHL hearing-impaired listeners. The clear speech modifications are aimed at providing the listener with more salient acoustic cues in the speech signal that may enhance their ability to access and comprehend the message. In this direction, the present paper focused on speech intelligibility enhancement based on Consonant Duration modifications (CDM).

2. EXPERIMENTATION

2.1 Speech Material

People suffering from hearing loss are often said to have greatest difficulty in identifying short speech sounds such as Stops and Fricative consonants. Hence nonsense syllables involving Stop consonants - /p, t, k, b, d, g/, and the Fricative consonants - /f, θ, s, v, ð, z/, with the accompanying cardinal vowels /a, ɛ, o/ and /a, i, u/ respectively were used as target stimuli.

The baseline stimuli were categorized as Stop-Vowel or /SV/ set and Fricative-Vowel or /FV/ set, with 18 syllables each grouped into two sub-sets, Voiceless sub-set and Voiced subset. The stimuli sets in /SV/ context were (i) Voiceless sub-set: /pa, p ɛ , po, ta, t ɛ , to, ka, k ɛ , ko/ / (ii) Voiced sub-set: /ba, b ɛ , bo, da, d ɛ, do, ga, g ɛ , go/ . Further in /FV/ context were , (i) Voiceless sub-set: / fa, fi, fu, θa, θi, θu, sa, si, su/and (ii) Voiced sub-set: /va, vi, vu, ða, ði, ðu, za, zi, zu/.

Stops are produced by first forming a complete closure in the vocal tract via a constriction at the place of constriction, during which there is a either silence or a low-frequency hum called 'voice bar'. The vocal tract is then opened suddenly releasing the pressure built up behind the constriction; this is characterized acoustically by a transient and /or a short duration noise Burst [4]. The period between the release of the stop and the beginning of voicing in the vowel is called the Voice Onset Time - VOT. During this period there is a silence and/or aspiration noise. The time interval between the onset of the following vowel and the instance when a formant frequency reaches its steady-state value is called the Formant Transition Duration- FTD. These temporal segments are visualized in the spectrograms shown in Figure 1.

Fricatives are produced when the turbulent air-flow occurs at a point of constriction in the vocal tract. Fricative consonants are characterized by a turbulent Noise, and may consist of the noise alone or may consist of the noise together with vocal cord vibration. The main acoustic cue that has been reported to affect perception of fricatives include-Noise Duration-ND, as well as adjacent Formant Transition Duration-FTD. The ND is said to extend from fricative onset time to offset time. The time interval between the onset of the following vowel and the instance when a formant frequency reaches its steady state value is called Formant transition.

Fricatives and plosives bursts are both characterized by high frequency random noise, which occurs on the opening of oral cavity. Plosives are characterized by highly transient cues, release burst very brief; whilst the noise spectrum of a fricative is quiet a great deal longer and rises to its target amplitude more gradually than a plosive does.

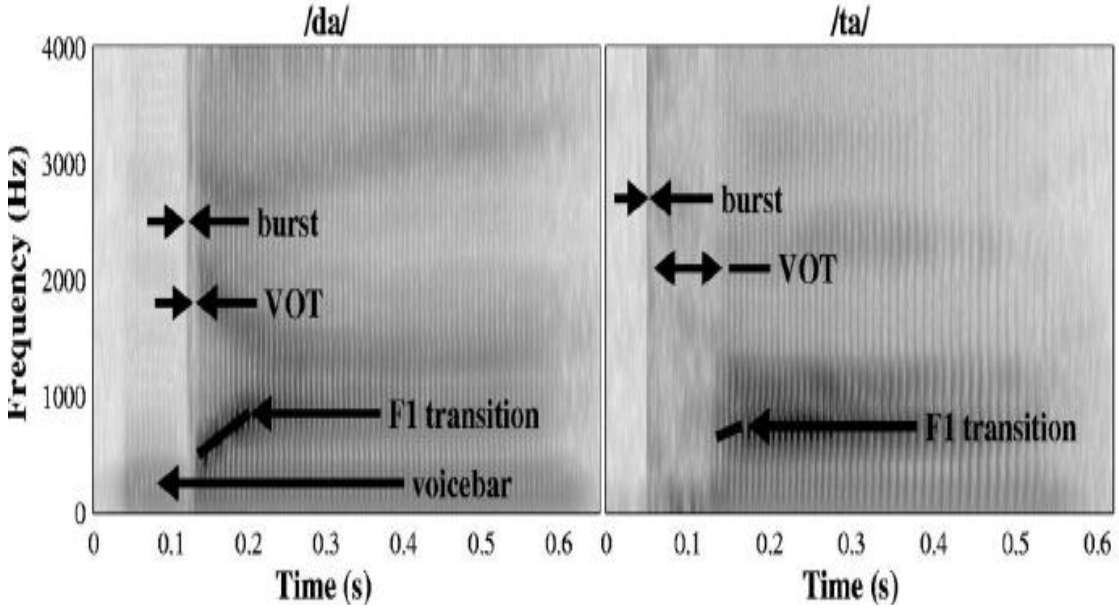

Figure 1. Spectrogram indicating acoustic segments of Voiced and Unvoiced Stops [5]

2.2 Listeners

The listeners were distinguished as Type 1 and Type 2 based on their hearing thresholds. Type 1 listeners were Hearing Impaired (HI) listeners whereas Type 2 were Normal Hearing (NH) listeners in simulated hearing impairment. Type 1 Listeners: One female and three male senior citizens in the age group of 58 to 62 yrs with hearing impairment ranging from moderate to severe loss (45 dB to 85 dB) in both ears, participated in the listening tests (as per PTA tests). Figure 2 displays the hearing thresholds for different stages of hearing loss. Type 2 Listeners: Two female and two male subjects with normal hearing with Pure Tone Audiometer (PTA) thresholds within 25dB of the normal hearing standards participated in the listening tests.

2.3 Speech Signal Processing

The experimentation spans into two phases, in the first phase the speech stimuli were processed for time-expansion using non-uniform algorithm for wave form expansion involving selection and modification of acoustic features. In the second phase the developed database was subjected to perception tests leading to the evaluation of speech intelligibility measures. A detailed explanation is as follows.

In the first phase, the recorded speech syllables were subjected to resynthesis using the procedure of LPC (linear prediction) analysis-synthesis as provided in PRAAT [7]. PRAAT (also the Dutch word for 'talk") is a free, multiplatform, scientific software program for the analysis of speech in phonetics. Resynthesis leads to synthetic copy rendering efficient and independent manipulation of the spectral, temporal and intensity characteristics. The LPC method is based upon the source-filter model; LPC analysis does it by estimating the vocal tract resonances from a signal's waveform, removing their effects from the speech signal (inverse filtering) in order to get the source signal (or residue). After the process of resynthesis, the synthesized tokens (baseline syllables) were normalized to 70 dB IL to avoid the signal clipping in subsequent processing stages.

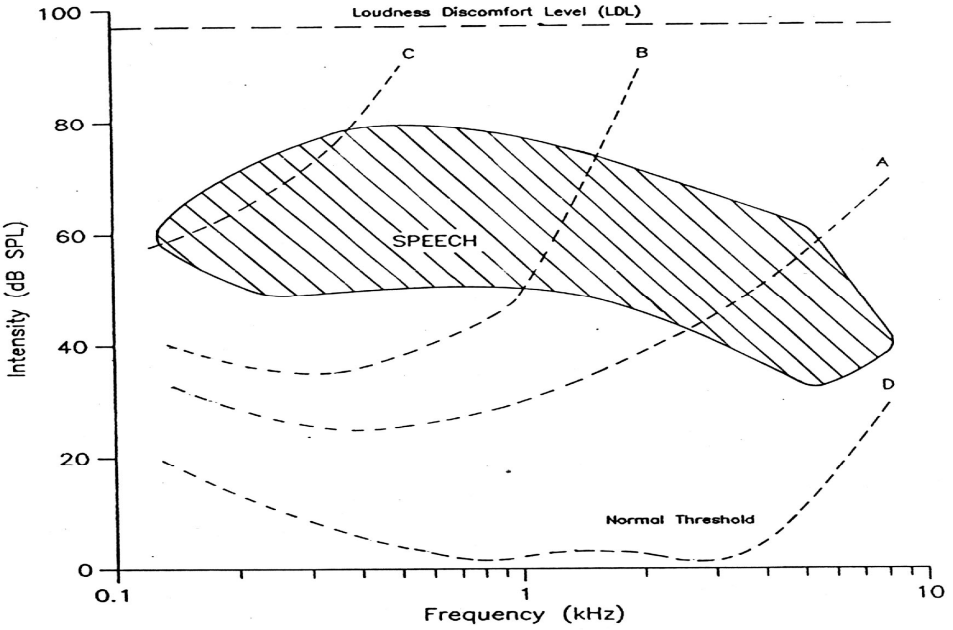

Figure 2. Sensorineural Hearing Thresholds: Hatched portion- Normal speech spectrum , Curve A-Mild to Moderate HL;B-Severe HL, C-Profound HL;D-Normal Hearing [6]

In the first stage of signal processing, baseline stimuli were temporally processed to generate stimuli sets at different levels of CD Modifications. The CD manipulations were based on PSOLA (Pitch-Synchronous Overlap and Add) algorithm using PRAAT. The basic PSOLA algorithm consists of three steps: analysis-modification-synthesis. The PSOLA analysis-modification-synthesis method belongs to the general class of STFT (Short-Time Fourier Transform) analysis-synthesis method, where the original pitch is being preserved during the processing [8]. PRAAT scripts were run for accomplishing all the above processing steps.

For /SV/ set, the acoustic segments for modification were: Burst Duration (BD), Voice Onset Time (VOT), and Formant Transition Duration (FTD). The release burst was identified as the short segment characterized as a 'spike' in the time domain and a sudden, sharp vertical line in the spectrogram [9]. The segmentation of a burst was performed visually by examining both the waveform and the spectrogram. VOT was identified as duration from the end of burst to the beginning of the vowel (the beginning of first waveform period) [10]. It is to be noted that the silence or closure interval of plosives cannot be defined for isolated CV syllables. The current stage of investigation reported that, the release burst was longer for voiceless than voiced plosives; VOT durations were longer for velars than alveolar, which in turn were longer than for labials; formant transitions were longer for voiced than voiceless plosives.

For /FV/ set, the main acoustic cues-Noise Duration (ND) and Formant Transition Duration (FTD) were reported to affect perception of fricatives [11]. ND is the high frequency noise measured as the difference between the fricative onset time and fricative offset time. The onset time is the point at which the high frequency energy appeared on the spectrogram and/or the point at which the number of zero crossings rapidly increased, while the offset time is the intensity minimum immediately preceding the onset of vowel periodicity, for voiceless fricative the earliest pitch period exhibiting a change in waveform from that seen throughout the initial frication, zero crossing of the preceding pitch was designated as fricative offset [12].

The Formant Transition Durations (FTD) were measured by simultaneous consultation of time domain waveform, spectrogram, linear-predictive coding (LPC) spectra, and Short-Time Fast-Fourier transform (ST-FFT) spectra [8] The LPC spectrum was constituted for a prediction order of 10 (at least twice as the number of spectral peaks that we want to detect), analysis window of 12.5 ms and 5 ms step, +6dB/octave filtering above 50 Hz. The three formants were originally located by examining the LPC spectra, FFT spectra, and spectrogram. The steady-state point of the vowel was centered at 100 ms after the onset. Formant analysis was performed for the detection of formant transition duration. After proper settings, formant contour was extracted and the formant values were written to a text file. Utilizing this data, the duration of the transitions and their onset and offset points were determined, and we then applied a time warp to all formants over the determined duration of the transition. The acoustic segmentations and measurements were done using PRAAT software. The temporal waveforms and spectrograms are presented in Figures 3- 5 for /SV/, Figures 6, 7 for /FV/ syllables below. The top panel displays the baseline (original) syllable while the middle panel 50% time expanded and the bottom panel 100% time expanded waveforms. The length of acoustic segments for /pa/ syllable was determined experimentally as Burst Duration: 4.5ms, VOT: 9ms, FTD: 30ms, hence time-expansions with 50%/ 100% (compared to original duration) are evident from the figures.

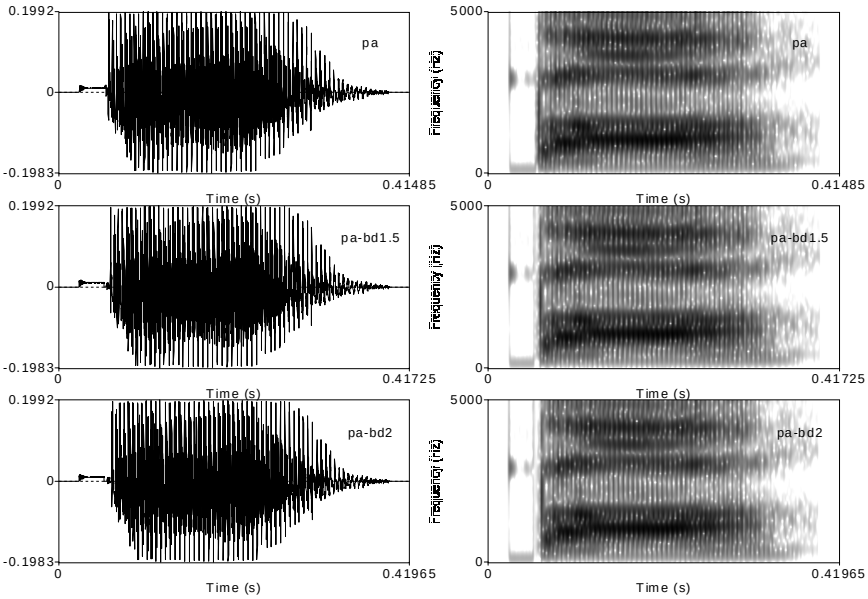

Figure 3. BDM Paradigm: Temporal waveforms and spectrograms for /pa/ syllable

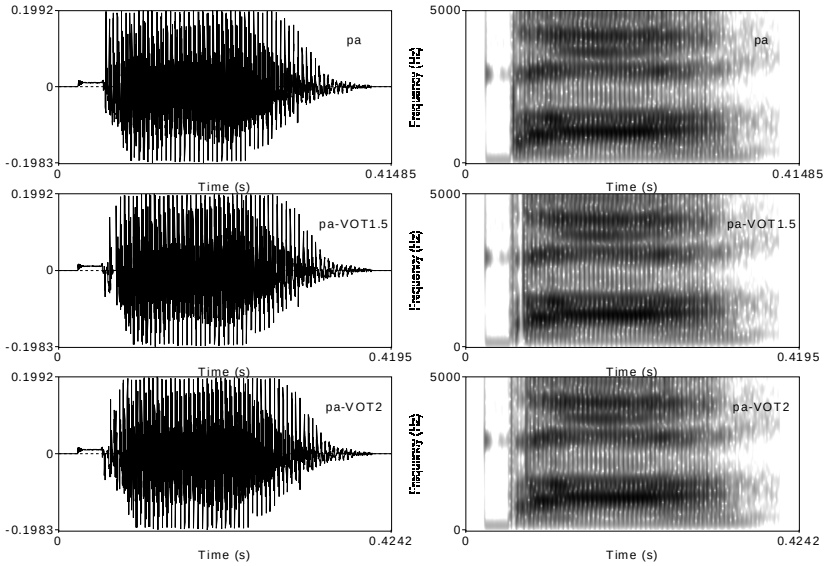

Figure 4. VOTM Paradigm: Temporal waveforms and spectrograms for /pa/ syllable

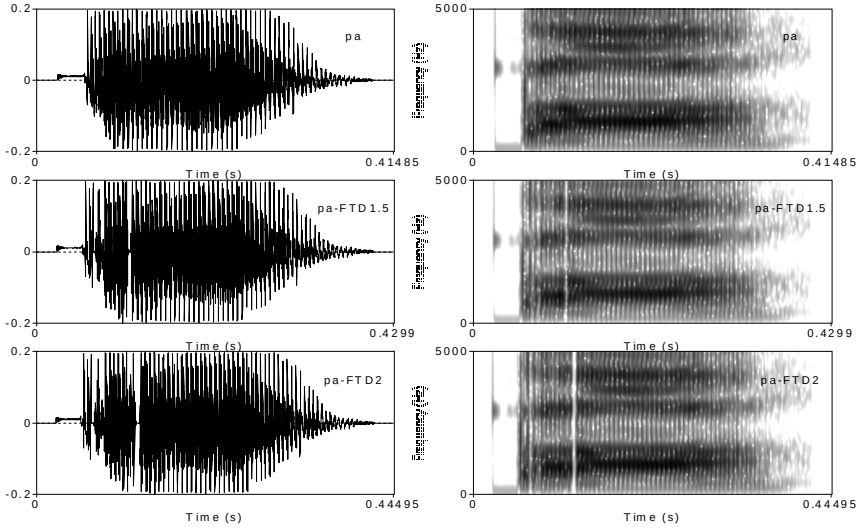

Figure 5. FTDM Paradigm: Temporal waveforms and spectrograms for /pa/ syllable

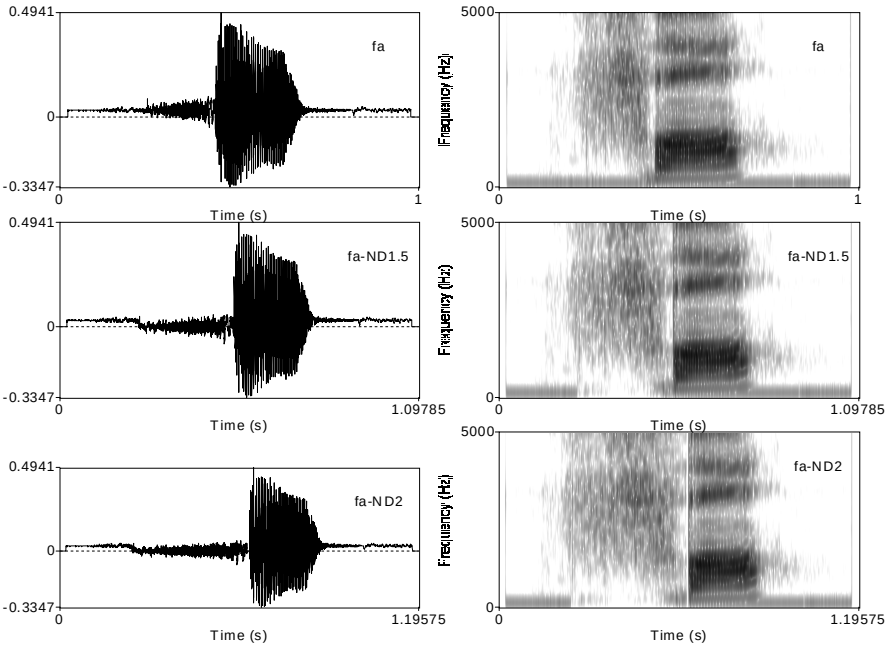

Figure 6. NDM Paradigm: Temporal waveforms and spectrograms for /fa/ syllable

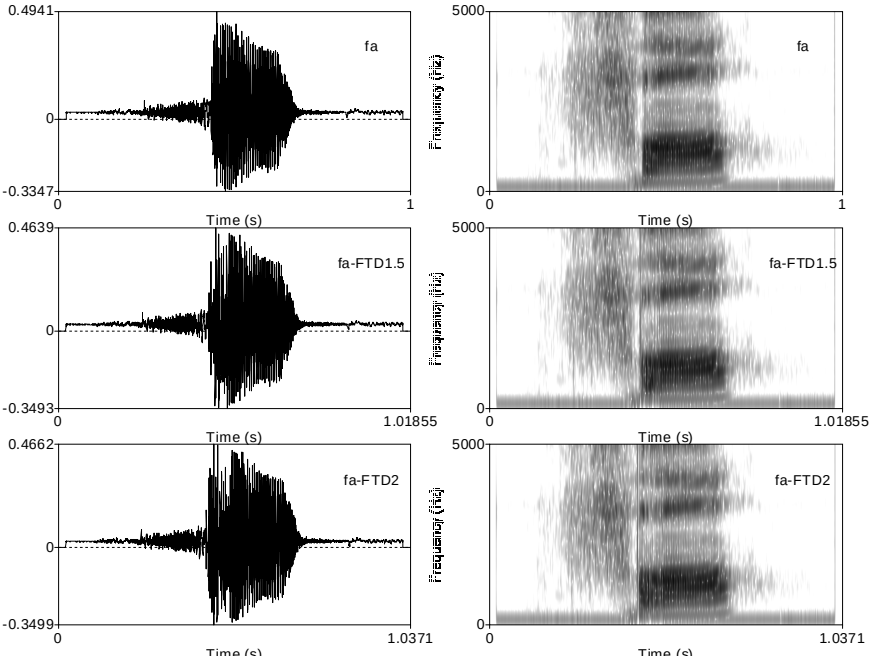

Fig.7 FTDM Paradigm: Temporal waveforms and spectrograms for /fa/ syllable

2.4 Speech in Noise Task

For Type 1 context, time-expanded stimuli from previous stage in the presence of no-noise served as test stimuli. The stimuli corpus for /SV/ context held 162 tokens (18*3*3) categorized under three schemes (BDM/ VOTM/ FTDM) and single listening no-noise condition ; also /FV/- CD modification held 108 tokens (18*3*2), categorized under two schemes (NDM/ FTDM) and single listening no-noise condition.

For Type 2 context, Hearing-Impairment in normal-hearing listeners was simulated. To provide a simple model for some of the perceptual effects of hearing impairment, gaussian white-noise masker was mixed with the stimuli. In other words, in order to simulate some effects of hearing impairment, three noise levels, no-masking noise, +12 dB and +6dB SNR were adopted. The PRAAT scripts were run for the generation of noise and for simulation process of mixing noise and stimuli. The stimuli corpus for /SV/ context held, 486 tokens (18*3*3*3) categorized under Three schemes (BDM/ VOTM/ FTDM) and 9(3*3) Listening conditions ; also /FV/ context held, 324 tokens (18*3*3*2), categorized under Two schemes (NDM/ FTDM) and 9(3*3) listening conditions.

3. EXPERIMENTAL SESSIONS

The second phase of the work utilized the processed speech data with the developed facility to evaluate the effects of time-expansion on speech perception in noise (SPIN). The SPIN experimentation was conducted using computerized testing procedure developed using MATLAB. Stimuli were presented using the computerized testing procedure at the most comfortable listening level of 75 dB to 85 dB SPL for the listeners. The test procedure used a similar protocol for all the experiments. Each experiment referred to single paradigm for eg BDM1/ BDM1.5/ BDM2 in no-noise/ +12dB/,+6dB masking level. Subjects were played token with ten randomized replications, they were prompted to choose from the set of choices displayed on the computer screen. Each run lasted for 20 min-25 min, spanning a period of nearly 4hrs for the entire experiment for one listener. Results were cast into three groups of six by six confusion matrices (CM) per run; sub-matrices (3*3) can be derived for analyzing the effect on the production-based categories.

3.1 Speech Intelligibility Measures

Speech discrimination test results were summarized as the percentage of correct responses for many experimental runs. The diagonal cell entries in the stimulus-response confusion matrix correspond to the correct responses and the off-diagonal entries correspond to the confusion errors. The results of each run were cast into stimulus-response confusion matrix, which were evaluated for percent-correct recognition data based on two intelligibility measures: Recognition scores and Relative information transmitted. While Recognition Scores are easiest to calculate and interpret, Relative Information Transmitted measures the covariance between the stimuli and responses and hence takes into account the relatedness of the two. The Relative information transmitted of the input stimulus X and output response Y are defined in terms of the mean logarithmic probability MLP given by,

$$I(X;Y) = -\sum_i \sum_j p(x_i, y_j) \log_2 \left(\frac{p(x_i)\, p(y_j)}{p(x_i, y_j)} \right) bits \quad .. (1)$$

The Relative Information Transmission (RIT) from X to Y is given by ,

$$I_{tr}(X;Y) = \frac{I(X;Y)}{I_s(X)} \quad ..(2)$$

Where, $Is(x)$ is the information measure of the input-stimulus in terms of MLP.

3.2. Results of CD Modifications on Stop-Vowel Syllables

3.2.1. Speech Perception in Type- 1 Listeners

The consonant recognition scores averaged across Type 1 listeners quantized in terms of Relative Information Transmitted scores are presented in Table 1 below. The scoring pattern reported that BDM paradigm has significant improvement in 50% and 100% lengthening (w r t original length) for voiced and voiceless stops in vowel contexts - /a/, /e/ with maximum intelligibility benefit equal to +26 percent points . The VOTM paradigm reported significant improvement in 50% lengthening in vowel contexts - /a/ , /e/,/o, with maximum intelligibility benefit of +33 percent points. The FTDM paradigm reported low improvement under 50% for voiceless stops in /a/ context only, with intelligibility benefit equal to +16 percent points.

Table 1 CD Modifications - HI Subjects- / SV/ Syllables/- RIT scores pattern with BDM/VOTM/FTDM Modification schemes for voiceless/voiced syllables

Information transmission analysis:/SV/:Test CV9										
		Relative information transmitted (%)								
		No-masking noise			No-masking noise			No-masking noise		
		BDM (%)			VOTM (%)			FTDM (%)		
Test Stimuli	Vowel Context	0	50	100	0	50	100	0	50	100
Unvoiced stop-vowels	/a/	14	20	40	14	33	13	14	30	17
	/e/	44	53	43	44	47	50	44	40	33
	/o/	53	50	57	53	83	60	53	53	27
Voiced stop-vowels	/a/	59	60	80	59	60	33	59	33	43
	/e/	27	33	50	27	60	0	27	0	17
	/o/	100	20	23	100	20	0	100	10	3

3.2.2. Speech Perception in Type- 2 Listeners

The Consonant Duration Modifications on /SV/ set have established mixed results**.** The conclusion summary of paper [13] based on the perceptual and statistical results suggested that BDM by 50% (compared to original duration) reported significant intelligibility benefit, while VOTM by 50% and 100% could not report significant benefit in the presence of noise, hence may be detrimental. The third scheme-FTD lengthening by 100% reported significant benefit in the presence of no-noise, and +12dB noise**.** The above results suggested that of the three acoustic segments considered here, lengthening BD and FTD yielded positive results. At lower SNRs, Burst Duration and Formant Transition Duration are found to be dominant cues for lengthening consonant duration. A detailed analysis is presented in previous papers [13].

3.3 RESULTS OF CD MODIFICATIONS ON FRICATIVE-VOWEL SYLLABLES

3.3.1 Speech Perception in Type-1 Listeners

The consonant recognition scores averaged across listeners and in terms of Relative Information transmitted scores are presented in Table 2. The scoring pattern reported no significant benefit with FTDM paradigm while NDM paradigm reported low benefit in 50% & 100 % with vowel context/i/ only.

3.3.2 Speech Perception in Type- 2 Listeners

The conclusion summary of paper [14] based on the perceptual and statistical results suggested that Consonant Duration Modifications on /FV/ set have reported that fricative NDM reported no significant benefit in the absence or in the presence of noise; hence such alterations may be detrimental. On the other hand, FTDM by 50% (compared to original duration) reported consistent significant benefit in the presence of +6dB noise. The above results suggested that of the two acoustic segments considered here, Based on the consistency of scores, 50% FTD can be treated as a candidate for consonant duration modification in lower SNR (higher level of SNHL), but not lengthening ND. A detailed analysis is presented in the previous paper **[**14].

Table 2 CD Modifications- HI_Subjects- / FV/ Syllables: RIT scores pattern with NDM/FTDM modification schemes for voiceless/voiced syllables

Information transmission analysis :/FV/:CV9							
		Relative information transmitted (%)					
	Vowel Context	No-masking noise			No-masking noise		
		NDM (%)			FTDM (%)		
Test Stimuli		0	50	100	0	50	100
Unvoiced Fricative-vowels	/a/	93	77	57	93	87	100
	/i/	50	60	70	50	23	23
	/u/	73	77	67	73	60	73
Voiced Fricative-vowels	/a/	100	83	93	100	77	83
	/i/	57	50	40	57	3	13
	/u/	100	97	90	100	87	77

4. DISCUSSION

In spite of not a very encouraging background, an attempt to perform duration modifications was being investigated in current paper. As it was felt that it would be more effective to apply temporal modifications to enhance speech intelligibility only to consonant distinctions that are cued by duration differences. Thus, it is worthwhile to explore a few of recent studies in correlation with the present investigational results. However, it is crucial to understand that the variability in benefits across different studies depends on speaker- listener effects, signal-dependant effects, implementation of clear speech strategies etc.

Krause and Braida [15] assessed the role of speaking rate on intelligibility by eliciting clear speech at normal (conversational) speaking rates naturally, thereby avoiding some of the pitfalls of signal-processing techniques. Clear

speech at normal/conversational speaking rates increased intelligibility for normal hearing listeners with simulated hearing losses(in noise), albeit to a slightly smaller degree compared to clear speech at slow rates. The intelligibility tests indicated 18-percentage-points advantage for clear/slow relative to conv/normal speech; while a 14-point advantage for clear/normal relative to conv/normal speech, and 12-point advantage for clear/slow relative to conv/slow speech. The study concluded that at normal rates, none of the alternative speaking modes tested provided as large or as consistent of an intelligibility advantage over conversational speech as clear speech.

Liu and Zeng [16] employed time-scaling algorithms to digitally compress (clear sentences) and stretch (conversational sentences) the experimental stimuli by inserting silent intervals into the conversational sentences to cause the overall duration to be equal to that of the clear speech. They concluded that, time compression was found to be more detrimental than time stretching in terms of processing reversibility and degree of performance degradation. Consistent with previous findings, they found that clear speech was more advantageous over conversational speech for normal-hearing listeners. In contrast to previous studies, they found that an increase in the number of pauses has a beneficial effect on intelligibility.

Smiljanic and Bradlow [17], [18] conducted an in-depth comparison of clear speech production and perception in English and Croatian. Sentences-in-noise test results showed that spontaneously produced clear speech enhanced intelligibility equally for both English and Croatian listeners in their respective native languages. Acoustic analyses revealed that talkers of both languages enhanced the overall salience of speech signal through a decrease in speaking rate, expansion of pitch range, expanded F1 x F2 vowel space.

Maniwa and Jongman [19] conducted experiments to characterize the adaptations in the clear speech production of American English fricatives in a carefully controlled range of communication situations. The study demonstrated that there were systematic acoustic-phonetic modifications in the production of clear fricatives. There were consistent overall style effects, several of which (consonant duration, spectral peak frequency, and spectral moments) were consistent with previous findings and a few (notably consonant-vowel intensity ratio) of which were not.

In the present investigation, time expansion on consonants demonstrated that, for the hearing-impaired listeners longer stops (with Burst Duration alteration) has been beneficial for intelligibility improvement, with a benefit of +26 percent points(for stop consonants), while the rest of the modifications such as VOT alteration (for stop consonants) and Formant transition alteration(for stops and fricatives), Noise Duration alteration (for fricative consonants) degraded consonant intelligibility or lead to perceptual errors. On the other hand, for normal listeners in simulated impairment ,Burst Duration by 50% (for stop consonants), FTD alteration by 100% (for stop consonants) , FTD by 50% (for fricative consonants) reported significant benefits. Reliable intelligibility advantages were not reported for VOT alteration (for stop consonants) and Noise Duration alteration (for fricative consonants). The tests reported maximum intelligibility benefit in relative information transmitted for overall consonant recognition as equal to +13 percent points (for stop consonants with BD lengthening), +8 percent points (for stop consonants with FTD lengthening), and +25 percent points (for fricative consonants with FTD lengthening).

5 CONCLUSIONS

Finally, Based on the correlation of experiment results for HI and NH listeners, it was asserted that only longer stops (with Burst Duration alteration) as beneficial cue for intelligibility. However, VOT alteration (for stop consonants) and Noise Duration alteration (for fricative consonants), Formant Transition Duration (for stops and fricatives) degraded consonant intelligibility. Hence the findings suggested that efforts to emphasize potentially weak consonant duration through 'Burst duration' should be beneficial in surmounting some of the speech recognition difficulties of hearing impaired listeners with sensorineural hearing loss. The finding also suggested the fact that hearing-impaired listeners may have difficulty integrating amplitude and spectral cues, and may generally place less weight on formant transitions than normal hearing listeners. In agreement with the previous work[20}, it can be concluded that the listeners with sensorineural hearing loss have elevated thresholds, and reduced dynamic range in regions relevant to fricative perception.

REFERENCES

[1] Liu, S., and Zeng, F., "Temporal properties in clear speech perception", Journal of Acoustic Society of America, 120(1), 424-432, 2006
[2] J C Krause & L D Braida, " Investigating alternative forms of clear speech:the effects of speaking rate and speaking mode on intelligibility", Journal of Acoustic Society of America., vol 112, 2165-2172, 2002.
[3] J C Krause, L D Braida., "Accoustic properties of naturally produced clear speech at normal speaking rates", Journal of Acoustic Society of America., vol 115 (1), 362-378, 2004.
[4] Stevens, K.N.: "Acoustic phonetics", MIT Press, Cambridge, MA, 1998.
[5] Jintao Jiang, Chen, M., and Alwan, A., "On the perception of voicing in syllable-initial plosives in noise", Journal of Acoustic Society of America , 119(2),1092-1105, 2006.

[6] Chaba, "Speech perception aids for the hearing-impaired people: current status & needed research", Journal of Acoustic Society of America , 90, 637-685, 1991.
[7] P Boersma, & D Weenik, PRAAT: Doing Phonetics by computer, http://www.praat.org
[8] Liu, S. and Fan-Gang Zeng, "Temporal properties in clear speech", Journal of Acoustic Society of America , 120(1), pp 424-432, 2006.
[9] Jiang, J. Chen, M. and Alwan, A, "On the perception of voicing in syllable-initial plosives in noise", Journal of Acoustic Society of America , 119(2), pp 1092-1105, 2005.
[10] Thomas, T.G., " Experimental Evaluation of improvement in speech perception with consonantal intensity and Duration modification", Ph.D. Thesis. Department of Electrical Engineering. Indian Institute of Technology, Bombay, 1996.
[11] Van Heuven, V.J.. "Reversal of the rise-time cue in the affricative-fricative contrast: An experiment on the silence of sound", The Psychophysics of speech perception, Martinus Nijhoff, Dordrecht, pp 181-187. 1987.
[12] Jongman,A.,Spence,M.,Wang,Y.,Kim,B., and Schenck,D., "Perceptual properties of English fricatives', Journal of Acoustic Society of America.,105, 1401(A),1999.
[13] Shobha, N.H., Thomas, T.G., and Subbarao, K., "Effect of Consonant Duration Modifications on Speech Perception in Noise-I", International Journal of. Electronics Engineering (ISSN NO. 0973-7383), Vol-I, Issue-II, pp 179-184, 2009.
[14] Shobha, N.H., Thomas, T.G., and Subbarao, K. "Effect of Consonant Duration Modifications on Speech Perception in Noise- II", International Journal of. Electronics Engineering (ISSN NO. 0973-7383). 2010.
[15] Krause, J.C., & Braida, L.D. (2002). "Investigating alternative forms of clear speech: the effects of speaking rate & speaking mode on intelligibility", Journal of Acoustic Society of America, 112, 2165-2172.
[16] Liu, S., & Zeng, F.(2006), "Temporal properties in clear speech perception", Journal of Acoustic Society of America 120(1), 424-432.
[17] Smiljanic, R., & Bradlow, A.R. (2005), "Production & perception of clear speech in Croatian & English", Journal of Acoustic Society of America., 118(3), 1677-1688.
[18] Smiljanic, R., & Bradlow, A.R.(2008), "Stability of temporal contrasts across speaking styles in Croatian & English", Journal of Phonetics., 36(1), 91-113.
[19] Maniwa, K., & Jongman, A. (2009). "Acoustic characteristics of clearly spoken English fricatives", Journal of Acoustic Society of America, 125(6), 3962-3973.
[20] Dubno, Dirks, & Langhoffer, "Evaluation of hearing-impaired listeners using nonsense syllable test II. Syllable recognition & consonant confusion patterns", Journal of Speech & Hearing Research, 25, 141-148,1982.

BIOGRAPHY OF AUTHOR

Dr N H SHOBHA obtained her Bachelor's in Electronics and Communication Engineering from Mysore University, Master's in Power Electronics from Bangalore University. She obtained her PhD from Osmania University, Hyderabad in Speech Perception/ Psychoacoustics' domain. Her thesis titled 'Effects of Consonant-Vowel Intensity Ratio and Consonant-Duration Modifications on Speech Intelligibility for the Hearing-Impaired' addressed the social problem of hearing-impairment and focused on developing appropriate speech signal processing mechanisms to improve speech perception for the advantage of those individuals. She has rich experience in teaching, research and administration in Karnataka and Hyderabad. Presently, working as Professor and Head in ECE dept. at Methodist College of Engineering, Hyderabad. Her expertise includes Speech signal processing, Digital signal processing, Signals and systems, Microprocessors, Automatic control systems. She has published 13 research papers indexed in IEEE,IEI, AES . She is the life member of ISTE, JASA, JASI

International Journal of Application or Innovation in Engineering & Management (IJAIEM)
Web Site: www.ijaiem.org Email: editor@ijaiem.org
Volume 4, Issue 8, August 2015 **ISSN 2319 - 4847**

Speech Intelligibility Enhancement in the context of Hearing -Impairment

Dr N H SHOBHA

Department of Electronics & Communication Engineering, Methodist college of Engineering & Technology, Hyderabad, India

ABSTRACT

The current paper focuses on the enhancement of an important attribute of clear speech, consonant-vowel Intensity Ratio on listeners suffering from Sensorineural hearing loss. This work is an extension of author's previous papers. A case for synthetic clear speech in the context of hearing impairment was tested on (i) Hearing Impaired subjects, and (ii) Normal hearing subjects in the presence of masking noise (+6dB, +12 dB). Consonant recognition in noise free and noisy situations using non-sense syllable test was investigated. The Stops and Fricative consonants of English language with cardinal vowels were processed for consonant-vowel intensity modifications ranging from 0dB to + 12dB at 3dB step. The speech perception in noise tests were quantified in terms of Consonant Recognition scores and Information transmission analysis measures. The results reported that the consonant-vowel intensity ratio modification of +9 to +12dB has positive effect on speech intelligibility improvement for both Hearing-impaired and Normal-hearing listeners. The maximum intelligibility benefit in Information transmitted scores were reported as 44, 45 percent points for HI listeners and 18, 31 percent points for masked normal-hearing listeners for /SV/ and /FV/ syllables respectively.

Keywords:- Consonant-vowel intensity ratio; Non-sense syllable test; Speech perception in noise; Speech intelligibility; Consonant Recognition

1.INTRODUCTION

Listeners almost always listen to speech, which is degraded by the addition of competing speech and non-speech signals. Unfortunately, hearing-impaired listeners often have the greatest difficulty in understanding speech in noisy environments as they have difficulty in isolating a specific speech signal from the background noise and understanding what is said. Sensorineural hearing losses (SNHL) are due to reduced sensitivity of the neural receptor that distorts the perception of sounds. The SNHL is characterized by compression in dynamic range, elevated hearing threshold, poor frequency and temporal resolutions. SNHL are not amenable to medical intervention and patients need to use the hearing-aids for speech perception. Owning to the complexity of the speech perception in general and consonant perception in particular, there is a need for more efficient algorithms in hearing aids. The present work is one such contribution to a broad research line whose aim is to develop improved hearing aids for people suffering from SNHL.

When listeners are confronted with difficult environments or when speaking to hearing-impaired person, humans instinctively change the way they speak and adopt a speaking style called *clear speech*. The acoustic analysis show that naturally produced clear speech typically involves a wide range of acoustic & articulatory adjustments or special attributes [1,2,3] such as more salient consonant contrasts (enhanced consonant-vowel intensity ratio-CVR, longer formant transitions, less vowel reduction[1,4,5],decrease in speaking rate (longer segments), wider dynamic range, greater sound-pressure levels, more salient stop releases, greater rms intensity of non-silent portions(release burst, frication, and/or aspiration) of obstruent consonants. Pre-processing speech for some of these parameters is expected to improve speech intelligibility for impaired listeners [1,4,5] and speech development in HI children[6] .

Two important temporal attributes of clear speech that are found to increase at phoneme level are the consonant-vowel Intensity ratio (CVR) and the consonant duration (CD). The process of strengthening CVR and CD are said to increases the salience of the consonant cues to weaken the masking effect or in other words results in reducing the vowel emphasis. Vowel perception is relatively simple for the hearing impaired while consonant perception is an area of continuing controversy. The present work focused on the role of CVR Modifications on speech perception in the context of hearing-impairment.

2. METHOD

2.1 Subjects

Two category of subjects such as Type 1 and Type 2 participated in listening/perception tests. Type 1 listeners were Hearing Impaired (HI) listeners, and Type 2 were Normal Hearing (NH) listeners. None of the subjects were experienced with perceptual experiments; subjects went through a speech token familiarization training session before the experiment started.

Figure 1 below illustrates the hearing losses and their associated thresholds in human beings, (i) Normal hearing :-10

to 25dB, (ii) Mild hearing loss: 26 to40 dB, (iii) Moderate hearing loss: 41 to 55dB, (iv)Severe hearing loss: 56 to 90dB, (v) Profound hearing loss: >91dB.

Type -1 Subjects: Five senior citizens in the age group of 58- 62 years, native listeners with hearing impairment ranging from moderate to severe hearing loss ranging from 45 dB to 85 dB in both ears. These listeners underwent audiological investigation with Pure Tone Audiometry (PTA) tests in speech and hearing clinic.

Type- 2 Subjects: Five subjects in the age group of 16 -45 years, native normal hearing individuals, participated in the listening experiments. They were tested for normal hearing as per PTA tests with less than 25dB hearing thresholds indicative of normal hearing ability.

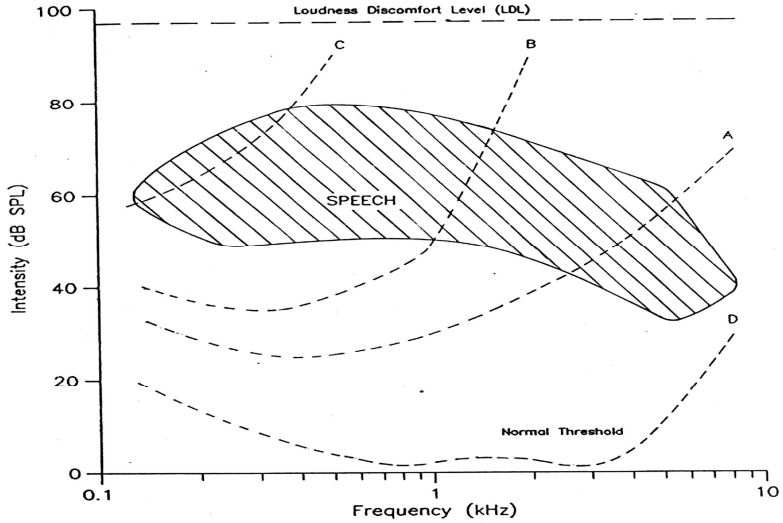

Figure 1. Sensorineural Hearing Thresholds: Hatched portion- Normal speech spectrum , Curve A-Mild to Moderate HL;B-Severe HL, C-Profound HL;D-Normal Hearing [6]

2.2 Target Stimuli System

The Stop consonants - /p, t, k, b, d, g/, and the Fricative consonants - /f, θ , s, v, ð, z/, with the accompanying cardinal vowels /a, ɛ, o/ and /a, i, u/ respectively, to form nonsense syllables were used as target stimuli system. The baseline set of 18 syllables are referred as Stop-Vowels (/SV/) and Fricative-Vowels (/FV/), further grouped into voiceless and voiced sub-sets. In total, the baseline stimuli in /SV/ context are: (i) voiceless sub-set: /pa, p ɛ , po, ta, t ɛ , to, ka, k ɛ , ko/ / (ii) voiced sub-set: /ba, b ɛ , bo, da, d ɛ, do, ga, gɛ , go/; similarly in /FV/ context are: (i) voiceless sub-set: /fa, fi, fu, θa, θi, θu, sa, si, su/ and (ii) voiced sub-set: /va, vi, vu, ða, ði, ðu, za, zi, zu/.

Stops and Fricative consonants are short speech sounds and people suffering from hearing loss are often said to have greatest difficulty in identifying them. 'Stops' are produced by first forming a complete closure in the vocal tract via a constriction at the place of constriction, during which there is a either silence or a low-frequency hum called voice bar. The vocal tract is then opened suddenly releasing the pressure built up behind the constriction; this is characterized acoustically by a transient and /or a short duration noise Burst. 'Fricatives' are produced when the turbulent air-flow occurs at a point of narrow constriction in the vocal tract. Fricative consonants are characterized by a high frequency noise of sufficient duration. In general, stops and fricatives are both characterized by high frequency random noise, which occurs due to opening of oral cavity. The duration of the high frequency noise is longer and its intensity is greater for voiceless than for voiced for stops/fricatives. These consonants are common to all regional accents in Indian English.

2.3 Speech Signal Processing

The experiment constituted two phases, in the first phase or the signal processing phase, the speech stimuli were processed for CVR modifications comprising of selection and modifications of consonant segments. In the second phase the developed database was subjected to perception tests and the results were analyzed quantitatively to assess the benefit on speech intelligibility. A detailed explanation is as below

In the first stage of signal processing, the natural speech tokens were recorded and were subjected to resynthesis. The natural stimuli were recorded in a quiet room, sampled at 44.1 kHz, using a Praat monosound recorder. The best utterance out of 20 utterances of the author (middle aged, female) was selected based on the clarity and stress. The speech tokens were subjected to resynthesis using the procedure of LPC (linear prediction) analysis-synthesis as provided in Praat [7]. The idea behind the resynthesis was to get synthetic copy which renders efficient and independent manipulation of the spectral, temporal and intensity characteristics, and sounds as similar as possible to a human utterance. After the process of resynthesis, the synthesized tokens referred as baseline syllables were normalized

to 70 dB Intensity level to avoid the signal clipping in subsequent processing stages.

In the second stage of signal processing, consonant-vowel intensity modifications (CVRM) were carried out on the baseline syllables set. CVR is defined as the difference in decibels between either the power/energy of the consonant and that of the adjoining vowel. CVRM can be achieved either by reducing the intensity of vowel or by increasing the intensity of the preceding consonant. The latter method has been reported to be more efficient over the former [8, 9]. The baseline syllables were manipulated under five CVRMs such as, 0 dB, +3 dB, +6 dB, +9 dB, and +12 dB, where 0 dB refers to the unmanipulated set (natural). In the process, the consonant and vowel segments were identified on simultaneous consultation with timing and spectrogram waveforms with repeated visual and auditory monitoring. The intensity of the vowel segment was fixed while that of the consonant segment was adjusted to the required CVR level. CVR modification was restricted to +12 dB so as to avoid the possibility of weak-vowel cue [10].

CVR modifications and their effects on syllable intensities are displayed for some syllables /ba/ and /va/ in Figures 2 and 3. These sample graphs obtained for /SV/ and /FV/ set, have established an enhancement in consonant intensity with respect to the proceeding vowel intensity with respect to five modification levels(0 dB, +3 dB, +6 dB, +9 dB, +12 dB) under study.

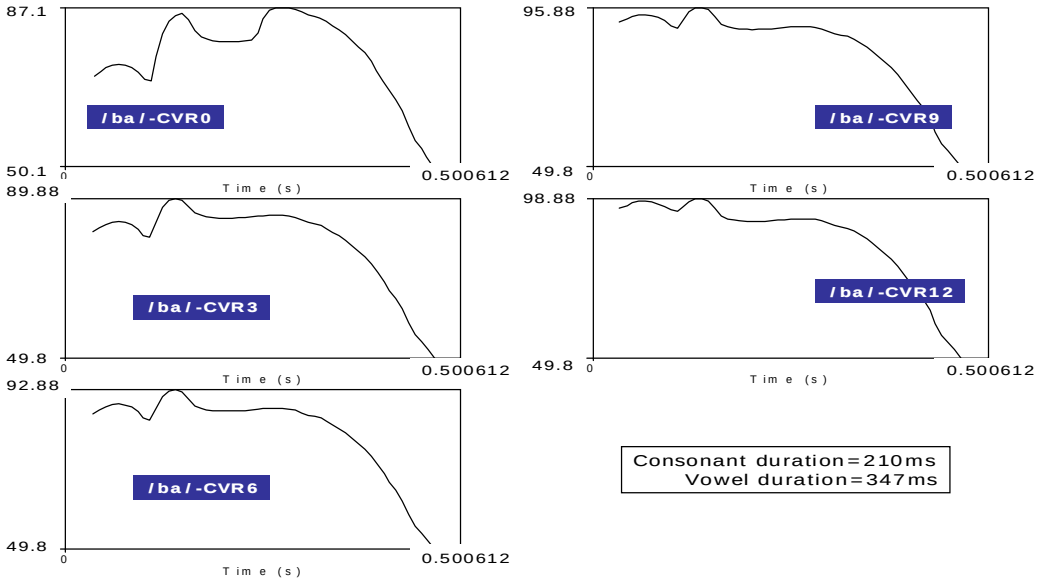

Figure 2. Intensity-time plots for stop-vowel syllable /ba/ for 0 to 12 dB CVR modifications

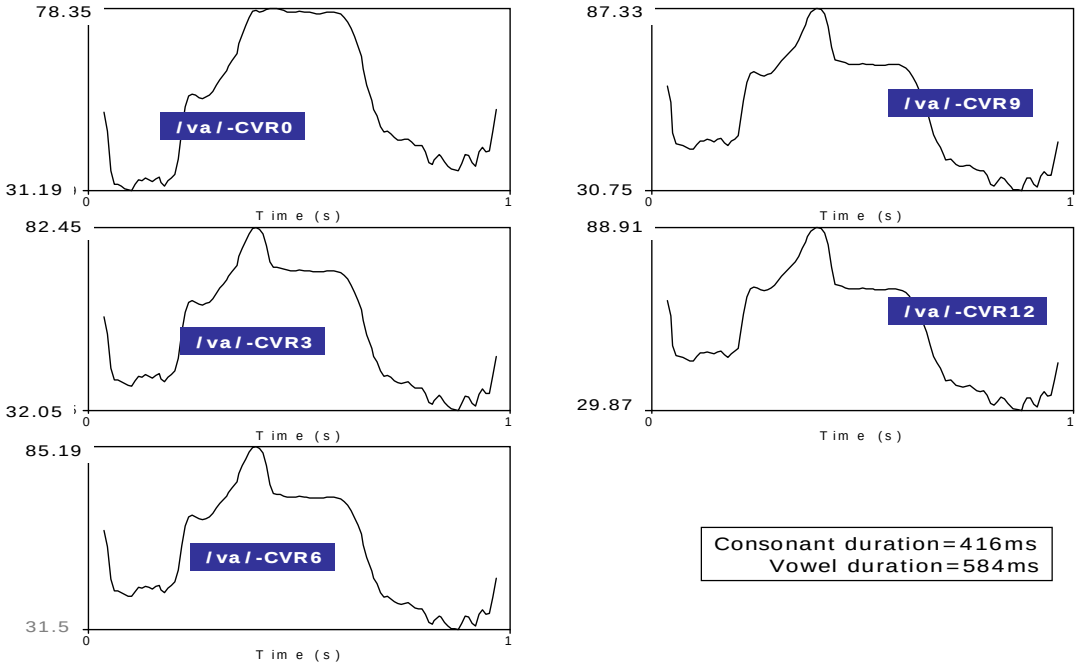

Figure 3. Intensity-time plots for fricative-vowel syllable /va/ for 0 to 12 dB CVR modifications

2.4 Speech in Noise Task

The third stage of processing holds relevance for Type 2 (NH) context stimuli but not for Type 1 (HI) context. In other words, the processed/CVR modified stimuli from the second stage served as test stimuli for Type 1 without the presence of noise masking . Thus Type 1 stimuli corpus held 90 (=18*5) tokens for /SV/ and /FV/ syllables respectively.

For Type 2 context, this stage of processing was designed to simulate hearing impairment by reducing the acoustic dynamic range. As reported in the literature, the reduction of the acoustic dynamic range (elevated hearing threshold) can be simulated by addition of white (Gaussian) noise [11, 12]. This masking noise responsible for the threshold elevation is believed to be predominantly of cochlear origin [11]. Some researchers have employed multi-talker babble instead of white noise [13, 14, 15]. However, due to its non-stationary nature, the effective masking it may provide during stimulus presentation is unpredictable. Simulation of hearing impairment is a complicated phenomenon. However, noise masking does to some extent; provide a partial model for some of the perceptual effects of hearing impairment. Hence, it was decided to use white noise masker, Praat script was run for the generation of white noise [16] . The CVR modified tokens from the second stage were now additively mixed along with the synthesized noise at three noise conditions, *ie*, no-masking noise, +12 dB and +6dB SNRs, where noise free (natural) tokens were considered to be those at no-masking noise.. The SNR refers to the ratio of the average power in CV token to the average power of the noise token in decibels.

$$SNR_{dB} = 10 \log_{10} (P_{Avg\text{-}CV} / P_{Avg\text{-}Noise}) \quad \ldots\ldots (1)$$

The average power level of the speech token was fixed while that of the noise was adjusted for fixing the SNR to the required value. The process of mixing processed syllable with masking noise was accomplished by a PRAAT script [16]. In this algorithm, sounds are summed up by point-to-point values, preserving real time across different time domains and sampling rate. Finally, for Type 2 context, the stimuli corpus holds 270(=18*5*3) tokens spanning across 18 baseline stimuli with 5 CVR modifications and 3 SNR conditions.

3. EXPERIMENTAL SESSIONS

The perception tests were automated using MATLAB code with graphic user interface. Stimuli were presented using computerized testing procedure at the most comfortable listening level of 75 dB to 85 dB SPL for the listeners. The set of tokens at one CVR level (0/3dB/6dB/9dB/12dB) and one SNR level (noise free/+12dB/+6dB) were administered to listeners at one test run. Subjects were played tokens with ten randomized replications of each token; they were prompted to choose from the set of choices displayed on the computer screen. Each run lasted for 20 -25 min, spanning a period of 6 -8 hrs for the entire experimentation per listener. Results were cast into three groups of six by six confusion matrices (CM) per run; sub-matrices (3*3) were derived for analyzing the effect on the production-based categories [17].

3.1 Experimental Measures

Speech discrimination test results were summarized as the percentage of correct responses for many experimental runs. The diagonal cell entries in the stimulus-response confusion matrix correspond to the correct responses and the off-diagonal entries correspond to the confusion errors.

Recognition Score: The sum of these diagonal elements gives the empirical probability of correct responses, known as Recognition Score RS (or articulation score). Though computation of RS is simple, it obscures the detailed and important information on the distribution of errors among the off-diagonal cells [17] ,also it is sensitive to the subject's bias or chance scoring (an artificially high score).

$$Rs = \sum_{i=1}^{n} P(Xi;Yj) \quad \ldots\ldots (2)$$

Relative information Transmission Score:

The Information Transmission analysis approach [10, 17, 18, 19] provides a measure of covariance between stimuli and responses. It takes into account the pattern of errors and the score in a probabilistic manner. The covariance measure of intelligibility can be applied to the sub matrices derived from the original matrix by grouping the stimuli in accordance with certain desired features[10,17,18, 19]. The information measures of the input stimulus X and output response Y are defined in terms of the mean logarithmic probability MLP,

$$I(X;Y) = -\sum_i \sum_j p(x_i, y_j) \log_2 \left(\frac{p(x_i)\, p(y_j)}{p(x_i, y_j)} \right) bits \quad \ldots\ldots (3)$$

The Relative information Transmission (Rtr) score from X to Y is given by,

$$Rtr\left(X\ ;Y\right)=\frac{I\left(X\ ;Y\right)}{I_s\left(X\right)} \qquad \ldots\ldots (4)$$

where, $I_s(x)$ is referred as the information measure of the input-stimulus in terms of MLP.

4. RESULTS

The speech perception in noise tests (SPIN) were quantified using two intelligibility scores (i) RS: Recognition scores, (ii) Rtr: Relative Information Transmitted scores. As per the previous discussion, even though relative information transmitted scores are better estimates of intelligibility measures, in this paper both the scores are analyzed. The perceptual ability of subjects with five versions of CVRM (0, +3, +6, +9, +12 dB) are reported in Tables 1, 2 and 3. The Intelligibility benefit which was defined as the percentage rise in Mean Score for CVR modification from 0 dB to the new CVR level under consideration (+3/+6/+9/+12dB).

4.1 Type- 1 Subjects

For Type -1 (HI) listeners, Recognition Scores and Relative Information transmitted scores are reported in Tables 1 and corresponding graphs in Figures 4. The mean scores for voiced and voiceless /SV/ and /FV/ syllables averaged across all listeners for individual vowel context are reported in the table. The scoring pattern reported the effect of CVRM on 'voiceless/voiced syllable' recognition and their vowel dependency. The stimuli included voiced and voiceless consonants under a single vowel context forming three subsets of 6 syllables for /SV/ and /FV/ syllables. For /SV/ set syllable subsets were, {/pa/, /ta/, /ka/, /ba/, /da/, /ga/}, {/pɛ/, /tɛ/, /kɛ/, /bɛ/, /dɛ/, /gɛ/}, {/po/, /to/, /ko/, /bo/, /do/, /go/}; similarly for /FV/ set subsets were, {/fa/, /θa/, /sa/, /va/, /ða/, /za/}, {/fi/, /θi/, /si/, /vi/, /ði/, /zi/}, {/fu/, /θu/, /su/, /vu/, /ðu/, /zu/}.

The results of the perceptual analysis for hearing impaired subjects were analyzed with two scoring patterns, Recognition scores and Relative information transmission scores .Table 1 and Figure 4 have summarized these scores for /SV/ and /FV/ syllables, where the identification ability of subjects were compared across five versions of CVRM's 0, +3, +6, +9, +12 dB. The perceptual analysis results have reported positive benefit on speech intelligence ranging from marginal to significant levels with CVR modifications. The maximum intelligibility benefit in Recognition Scores (RS) were, 56% (for Stops) and 47% (for fricatives) ; while maximum intelligibility improvement in Relative information transmitted scores (Rtr) were 44% (for stops) and 45% (for fricatives) .

4.2 Type- 2 Subjects

For Type-2 (NH) listeners, Recognition Scores are summarized in Tables 2 and the corresponding graphs in Figure 4; while the Relative Information transmitted scores are summarized in Tables 3 and the corresponding graphs in Figure 5. The mean scores for voiced and voiceless consonants averaged across all listeners for individual vowel context are recorded in these tables. The scoring pattern reported the effect of CVRM on 'voiceless/voiced syllable' recognition and their vowel dependency as a function of SNR (no-noise, +12dB, +6dB). The perceptual analysis results have reported positive benefit in speech intelligence albeit by different amounts.

According to Table 2, maximum intelligibility benefits in RS at 6 dB and 12 dB SNRs are summarized as follows, /SV/ syllables reported :15% (SNR=6dB) and 19% (SNR=12dB) for unvoiced stop syllables /o/context; while /FV/ syllables reported: 15% (SNR=6dB) and 16% (SNR=12dB) for voiced fricative consonant in /i/ context.

According to Table 3, maximum intelligibility improvement in Rtr at 6dB and 12 dB SNRs are summarized as follows, /SV/ syllables reported: 17% (SNR=6dB) and 18% (SNR=12dB) for unvoiced stop consonant in /o/context; while /FV/ syllables reported: 31% (SNR=6dB) and 27% (SNR=12dB) for unvoiced fricative consonant in /i/context.

4.3 Implication of Results

The results of our investigation based on the perceptual analysis tested on HI (Type- 1) and masked NH (Type- 2) listeners, involving two sets of stimuli (Stops and Fricatives), analyzed with two intelligibility scores (RS and Rtr) have altogether indicated a positive impact on speech intelligibility with CVR enhancement. The results suggest that there is an improvement in scores with respect to increasing CVR for voiceless and voiced consonant recognition, as well as the overall consonant recognition.

For stops and fricatives, the CVR modification of +9 and +12dB have contributed significant improvement of intelligibility in the presence of noise. It is also to be noted that the improvements due to processing are more for higher level of masking noise(+6dB), indicating an improvement in listening condition with processing. Though both the stops and fricatives have reported positive intelligibility improvement, the benefits were higher for fricatives compared to stops, in other words fricatives have reported better intelligibility improvement in the presence of noise. Further, in the presence of masking noise - the voiceless and voiced syllables exhibited nearly equal percent-benefits for stop-vowels; while voiceless syllables exhibited higher benefit than their voiced counterparts for fricative-vowels.

Table 1. Type-1 Subjects: Recognition scores and Relative information transmitted scores

Test Stimuli	Vowel context	Test CV9 Consonant Recognition Scores(%) CVR (dB) 0	3	6	9	12	Test CV9 Rel. Infor. Transmitted(%) CVR (dB) 0	3	9	12
Voiceless stop-vowels	/a/	43	60	73	67	60	14	24	54	58
	/ɛ/	50	53	67	53	50	44	19	20	22
	/o/	67	73	87	97	93	53	60	90	80
Voiced stop-vowels	/a/	73	60	70	77	100	59	44	54	100
	/ɛ/	27	83	73	83	73	27	59	61	60
	/o/	100	100	100	93	80	100	100	84	61
Voiceless Fricative-vowels	/a/	73	100	83	100	97	52	100	100	90
	/i/	30	60	70	77	63	15	59	54	58
	/u/	50	73	70	70	87	56	65	60	75
Voiced Fricative-vowels	/a/	100	100	97	97	100	100	100	100	100
	/i/	50	67	100	100	97	45	58	100	90
	/u/	97	100	100	100	100	90	100	100	100

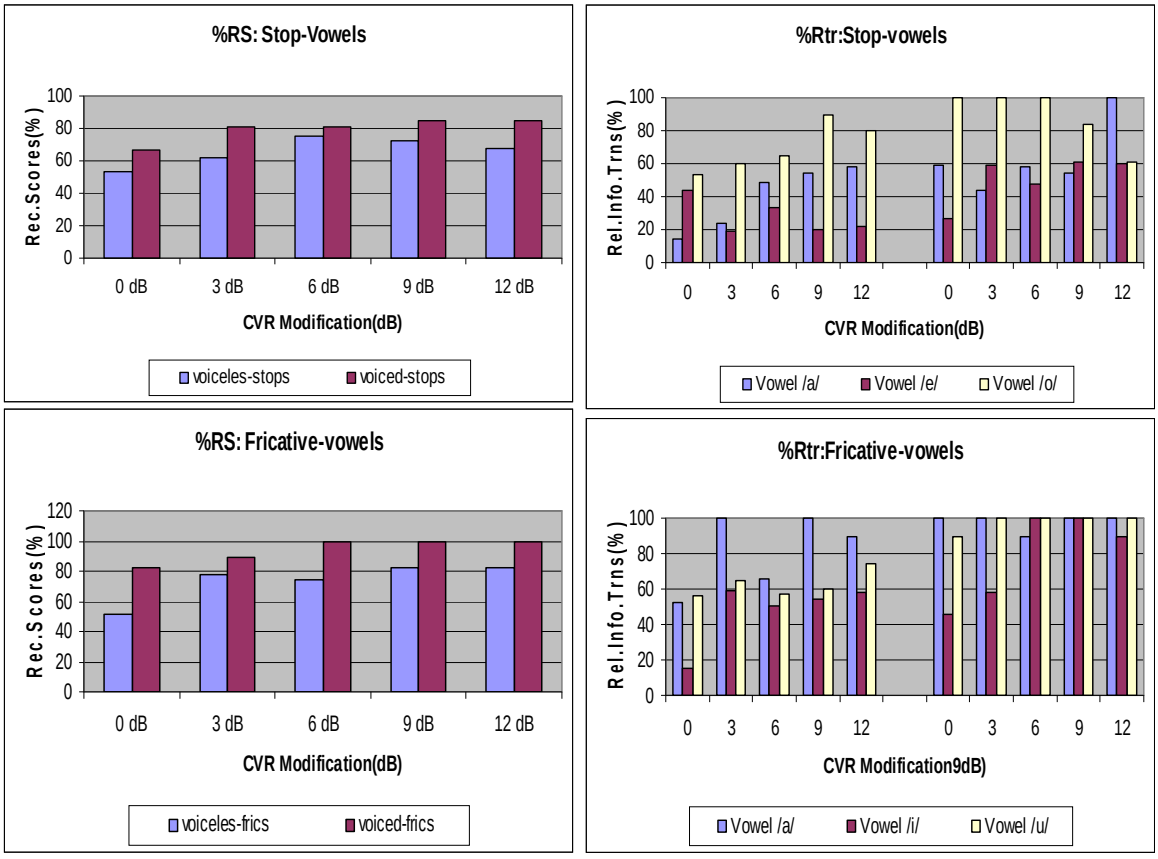

Figure 4. Recognition scores and Relative information transmitted pattern corresponding to Table 1
Top panel: - /SV/ syllables, Bottom panel: - /FV/ syllables

Table 2. Type-2 Subjects: Recognition score pattern for voiceless/voiced syllables

Consonant Recognition Scores :CV9																
Test Stimuli	Vowel context	No masking noise					SNR=12 dB					SNR=6 dB				
		CVR (dB)					CVR (dB)					CVR (dB)				
		0	3	6	9	12	0	3	6	9	12	0	3	6	9	12
Voiceless stop-vowels	/a/	88	98	98	97	99	81	83	86	87	86	78	82	83	85	85
	/ɛ/	95	97	98	99	99	92	94	95	96	97	87	90	93	94	93
	/o/	97	99	97	100	100	70	73	75	82	89	69	73	74	78	84
Voiced stop-vowels	/a/	94	96	98	98	98	71	75	78	77	78	68	70	73	75	77
	/ɛ/	97	99	97	99	99	89	91	91	94	99	87	89	89	92	93
	/o/	97	99	98	98	97	89	89	92	95	96	87	90	91	94	95
Voiceless Fricative-vowels	/a/	99	98	99	100	97	77	79	83	87	93	81	82	84	86	87
	/i/	97	99	96	97	95	77	78	81	87	89	77	86	86	87	87
	/u/	100	100	99	97	98	79	81	90	89	87	77	82	82	84	87
Voiced Fricative-vowels	/a/	94	97	98	98	96	81	83	85	87	91	80	81	81	85	89
	/i/	97	99	94	95	100	78	80	81	83	94	74	85	86	88	89
	/u/	98	97	99	99	100	86	86	89	90	95	89	88	82	87	92

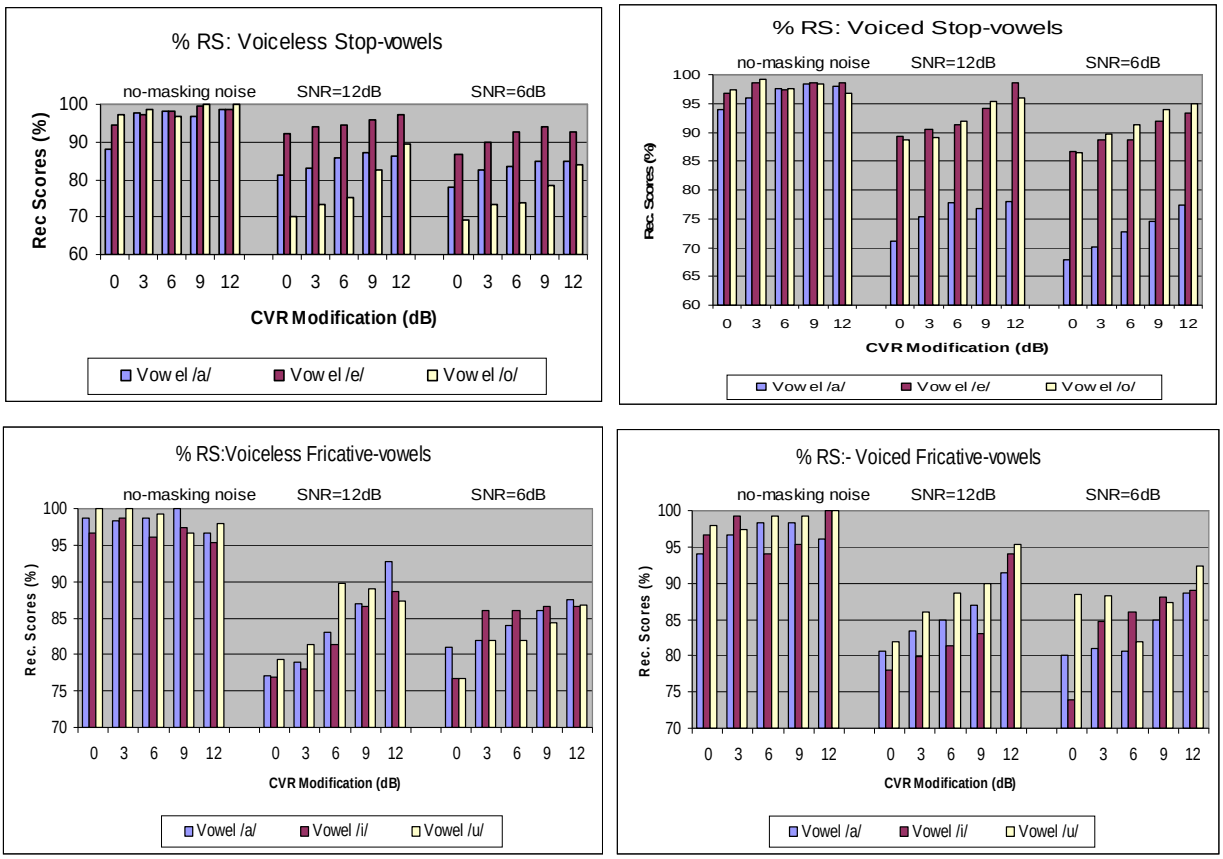

Figure 5. Recognition score Graphs with reference to Table 2 Top panel: - /SV/ syllables, Bottom panel: - /FV/ syllables

Table 3. Type-2 Subjects: Relative information transmitted scores pattern for voiceless/voiced syllables

Information transmission analysis: CV9																
Test Stimuli	**Vowel context**	**Relative information transmitted (%)**														
		No masking noise					**SNR=12 dB**					**SNR=6 dB**				
		CVR (dB)					**CVR (dB)**					**CVR (dB)**				
		0	**3**	**6**	**9**	**12**	**0**	**3**	**6**	**9**	**12**	**0**	**3**	**6**	**9**	**12**
Voiceless Stop-vowels	**/a/**	100	100	100	100	100	90	93	94	93	96	89	91	92	94	95
	/ɛ/	96	95	96	98	98	90	93	90	89	96	79	87	88	89	87
	/o/	100	98	98	100	100	65	69	67	71	83	58	61	62	71	75
Voiced Stop-vowels	**/a/**	100	100	98	100	98	94	94	96	98	98	82	85	87	93	96
	/ɛ/	100	100	100	96	100	91	92	92	94	96	83	87	87	88	88
	/o/	96	100	100	98	98	92	94	95	97	96	90	94	94	95	96
Voiceless Fricative-vowels	**/a/**	100	100	100	100	100	93	95	95	100	100	89	88	97	98	98
	/i/	97	95	96	98	98	73	96	98	98	100	67	85	87	91	98
	/u/	100	98	100	98	100	77	89	94	97	97	74	80	85	90	98
Voiced Fricative-vowels	**/a/**	100	100	100	100	98	92	92	93	92	98	92	88	96	94	100
	/i/	100	100	98	100	100	78	94	96	96	98	79	83	95	98	100
	/u/	99	100	100	100	100	90	91	92	96	99	88	91	92	94	99

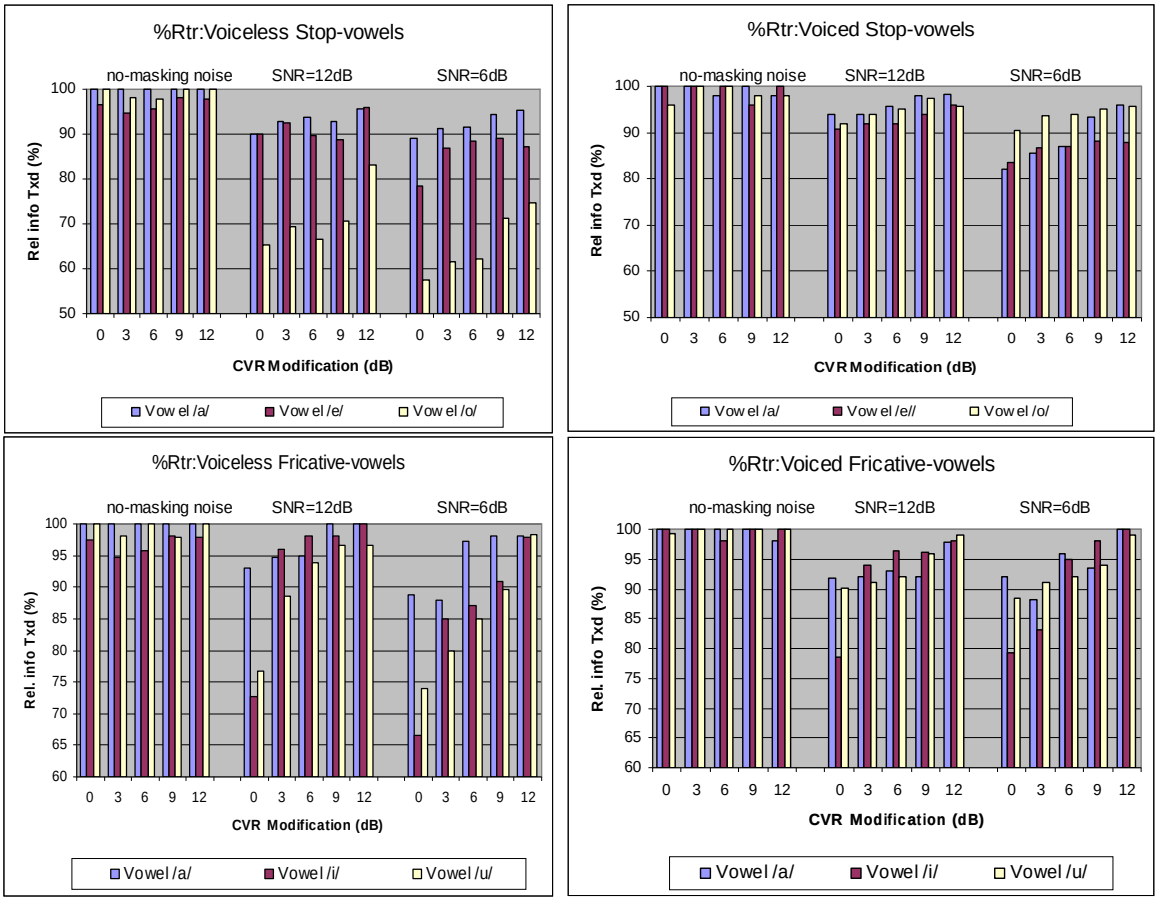

Figure 6. Relative information transmitted pattern with reference to Table 3
Top panel: - /SV/ syllables, Bottom panel: - /FV/ syllables

4.4 Discussion

A substantial body of previous research, has provided with important insights into the characteristics and benefits of clear speech. It is worthwhile to explore a few of recent studies in correlation with the present investigational results. However, it is crucial to understand that the variability in benefits across different studies depends on speaker- listener effects, signal-dependant effects, implementation of clear speech strategies etc. The focus of the reviewed studies shown below has exclusively used recorded speech material; on shifting the focus to synthesized clear speech material as in the present investigation, effectively revealed what acoustic-phonetic features are present/absent and how their manipulation affected intelligibility.

In a notable work by Ferguson and Kewley-port [20], conversational and clear vowels were recorded by one male talker in a CVC context and mixed with 12-talker babble. The stimuli were presented to young normal hearing adults and elderly HI listeners, they found that listeners with normal hearing enjoyed a 15 percent points clear speech advantage for vowels presented in noise, while elderly HI listeners showed no clear speech benefit.

In a detailed exploration of talker variability, Ferguson [21], collected conversational and clear speech from 41 talkers, thus created a large database that allows assessments of the relationship between acoustic-phonetic variations across talkers' variability in intelligibility. The study showed that for 41 talkers, clear speech vowel intelligibility for normal hearing listeners in noise varied widely from 12 to 33 percent points. Female talkers tended to produce more intelligible clear speech compared to male talkers despite having similar conversational intelligibility scores. Similar variability in clear speech intelligibility across talkers was found for words and sentences by Gagne et al. (1994), Schum, (1996), suggesting that intelligibility variability is characteristic of individual talker's production rater than vowel intelligibility only.

Bradlow et al. [22] explored clear speech perception in children with and without learning disabilities, in order to see whether they would be able to utilize clear speech cues to the same extent as the more experienced adults. Although, children with learning disabilities exhibited lower intelligibility scores compared to children with no deficits, the clear speech effect was substantial for both groups: 9% and 16-18%. This study demonstrated that speech perception for children with learning problems may be enhanced in everyday communication by employing a simple strategy of speaking clearly, which can be adopted in clinical settings and in educational settings.

Liu et al. [23] compared clear speech perceptual benefits for normal hearing adults and adults with cochlear implants varied in age of implant use. Using a slightly different approach in this study, conversational and clear speech intelligibility was measured as a function of S/N ratios. Both groups of listeners a significant clear speech advantage, although listeners with cochlear implants needed somewhat better S/N ratios in order to perform at the same level as normal-hearing adults.

Thomas et al. [24] studied the role of the two important attributes of clear speech namely, the consonant-to-vowel intensity ratio (CVR) and the consonant duration (CD) for dasiasynthetic clear speechpsila in the context of the persons with hearing impairment. The results suggested that the CVR and the formant transition duration play an important role in speech perception.

Maniwa et al. [25] conducted two experiments to determine whether clear speech enhances fricative intelligibility for normal hearing and for listeners with simulated impairment. The experiments measured babble signal-to-noise ratio thresholds for fricative minimal pair distinctions for 14 normal-hearing listeners and 14 listeners with simulated sloping, recruiting impairment. Results indicated that clear speech helped both groups overall. However, for impaired listeners, reliable clear speech intelligibility advantages were not found for non-sibilant pairs. Correlations between acoustic and perceptual data were less consistent for listeners with simulated impairment, and suggested that lower-frequency information may play a role.

Based on the present and past investigations of the author[19,26], CVR enhancement by +9 to +12dB levels have enjoyed significant intelligibility benefit in the context of hearing impairment, albeit by different amounts. The tests have reported that the maximum intelligibility benefit in relative information transmitted as 44, 45 percent points (for HI listeners) and 18, 31 percent points (for masked normal-hearing listeners) for /SV/ and /FV/ syllables respectively. The complex interactions between C-V modification, consonant feature, and vowel context indicate that the benefits of clear speech are not uniform for all features and contexts.

5. CONCLUSIONS

The work focused on speech perception on people with varying degree of hearing loss, using synthetic or digitally manipulated features of natural speech to the clear speech advantage. The avenue of research focused on an interesting approach to create more intelligible speech, based on clear speech attribute- consonant vowel intensity ratio. The results of the investigation involving two sets of stimuli analyzed with two intelligibility scores have altogether indicated a positive impact on speech intelligibility. For stops and fricatives, the CVR modification of +9 and +12dB have contributed significant improvement, hence an adjustment of the C-V intensity ratio can yield significant improvement in consonant recognition for hearing-impaired listeners in quiet, and for normal hearing listeners in noise [27-31]. The CVR level for hearing benefit for both hearing-impaired and masked normal-hearing listeners have been almost

equivocal. In summary, the findings suggested that efforts to emphasize potentially weak consonant amplitude should be beneficial in surmounting some of the speech recognition difficulties of hearing impaired listeners with sensorineural hearing loss.

REFERENCES

[1] Liu, S., and Zeng, F., "Temporal properties in clear speech perception," Journal of Acoustic Society of America, 120(1), 424-432, 2006
[2] J C Krause & L D Braida,, "Investigating alternative forms of clear speech:the effects of speaking rate and speaking mode on intelligibility," Journal of Acoustic Society of America., vol 112, 2165-2172, 2002.
[3] J C Krause, L D Braida., "Accoustic properties of naturally produced clear speech at normal speaking rates," Journal of Acoustic Society of America , vol 115 (1), 362-378, 2004.
[4] M I Picheny, N I Dulach and L D Briada. "Speaking Clearly for the Hard of Hearing I : Intelligibility Differences between Clear and Conversational Speech." Journal of Speech Lang and Hear Res, vol 28, 1985.
[5] J C Krause and L D Braida. "Accoustic Properties of Naturally Produced Clear Speech at Normal Speaking Rates," Journal of Acoustic Society of America, vol 115, no 1, 2004.
[6] N Schiavetti, R L Whitehead and D E Metz. "The Effects of Simultaneous Communication on Production and Perception of Speech," Journal of Deaf Studies and Deaf Education, vol 3, 2004.
[7] P Boersma and D Weenik. "Praat : Doing Phonetics by Computer" vol 4.4.22, 2005.
[8] M I Picheny, N I Dulach and L D Briada. "Speaking Clearly for the Hard of Hearing I : Intelligibility Differences between Clear and Conversational Speech," Journal of Speech Lang and Hear Res, vol 28, 1985.
[9] M I Picheny, N I Dulach and L D Briada. "Speaking Clearly for the Hard of Hearing II : Acoustic Characteristics of Clear and Conversational Speech," Journal of Speech Lang and Hear Res, vol 29, 1986.
[10] T G Thomas. "Experimental Evaluation of Improvement in Speech Perception with Consonantal Intensity and Duration Modification," Ph D Thesis, Department of Electrical Engineering, Indian Institute of Technology Bombay, 1996.
[11] S DeGennaro, L D Braida and N I Dulach. "Study of Multi-band Compression with Simulated Sensorineural Hearing Loss," Journal of Acoustic Society of America, vol 69, 1981, S16.
[12] A J Oxenham and B C J Moore. "Modelling the Effects of Peripheral Non-linearity in Listeners with Normal and Impaired Hearing. W Jesteadt (ed)." N J Mahwah. 'Modelling Sensorineural Hearing Loss.' Lawrence Earlbaum Associates, 1987, p 273.
[13] H Flecher. "The Perception of Sounds by Deafened Persons," J Acoust Soc Am, vol 24, 1952, p 490.
[14] S A Simpson and M Cooke. "Consonant Identification in N-talker Babble in a Non-monotonic Function of N," Journal of Acoustic Society of America ,vol 118, no 5, 2005, p 2775.
[15] H D Lewis, V A Benignus, K E Muller and C M Malott. "Babble and Random Noise Masking of Speech in High and Low Content Cue Identifications," Journal of Speech and Hearing Response, vol 31, 1988, p 108.
[16] http://www.lifesci.Sussex.ac.uk/home/Chris_Darwin/praatscripts/
[17] G A Miller and P E Nicely. "An Analysis of Perceptual Confusions among Some English Consonants," Journal of Acoustic Society of America , vol 27, no 2, 1955, p 338.
[18] R C Bilger and M D Wang. "Consonant Confusions in Patients with Sensorineural Hearing Loss," Journal Speech and Hearing Res, vol 19, 1976, p 718.
[19] N H Shobha, T G Thomas and K Subbarao. "Influence of Consonant-vowel Intensity Ratio on Speech Perception for Hearing Impaired Listeners," Proceedings of 2008 Congress in Image and Signal Processing, Hainan, CHINA, 2008, p 342.
[20] Ferguson,S.H., & Kewley-port, D. "Vowel intelligibility in clear &conversational speech for normal-hearing & hearing-impaired listeners," Journal of Acoustic Society of America , 112, 259-271.
[21] Ferguson. (2004). "Talker differences in clear & conversational speech; vowel intelligibility for normal-hearing listeners," Journal of Acoustic Society of America , 116(4), 2365-2373.
[22] Bradlow, A.R., Kraus. N., & Hayes. E. "Speaking clearly for children with learning disabilities: Sentence perception in noise," Journalof Speech Lang. Hear. Res. 46, 80-97.
[23] Liu, S., Del Rio, E., Bradlow, A.R., Zeng, E.G. "Clear speech perception in acoustic & electrical hearing," Journal of Acoustic Society of America, 116, 2374-2383.
[24] Thomas, T.G., Sekhar, S.C. " Perception studies on the attributes of synthetic clear speech for the hard of hearing," Proc. Signal processing & its Application, ISSPA, 1-4.
[25] Maniwa, K., & Jongman, A. " Perception of clear fricatives by normal-hearing & simulated hearing-impaired listeners," Journal of Acoustic Society of America , 123(2), 1114-1125,2008.
[26] N H Shobha, T G Thomas and K Subbarao ."Experimentation to Improve Consonant Recognition for the Hearing Impaired listeners", International Interdisciplinary Journal, Institute of Engineers-INDIA, May 2010.

http://www.ieindia.info/public.asp
[27] R L Freyman and G P Nerbonne. "The Importance of Consonant Vowel Intensity Ratio in the Intelligibility of VoicelessConsonants," Journal of Accost Speech Hear Res, vol 32, 1989.
[28] R L Freyman, G P Nerbonne and H A Cote. "Effect of C-V Ratio Modification on Amplitude Envelope Cues for Consonant Recognition," Journal of Accost Soc Am, vol 34, 1991.
[29] E Kennedy, H Levitt, Neumann and Weiss. "C-V Intensity Ratios for Maximizing Consonant Recognition by Hearing Impaired Listeners," Journal of Accost Soc Am, vol 103, no 2, 1998, p 1098.
[30] Uma Balakrishnan, Freyman, Chiang and Patrick Kelly. "Consonant Recognition for Spectrally Degraded Speech as a Function of C-V Intensity Ratio," Journal of Accostic Society of America, vol 99, no 6, 1996.
[31] AA Montgomery and R A Edge. "Evaluation of Two Speech Enhancement Techniques to Improve Intelligibility for Hearing-impaired Adults," Journal of Speech and Hearing Res, vol 31, 1988.

BIOGRAPHY OF AUTHOR

Dr N H SHOBHA obtained her Bachelor's in Electronics and Communication Engineering from Mysore University, Master's in Power Electronics from Bangalore University. She obtained her PhD from Osmania University, Hyderabad in Speech Perception/ Psychoacoustics domain. Her thesis titled 'Effects of Consonant-Vowel Intensity Ratio and Consonant-Duration Modifications on Speech Intelligibility for the Hearing-Impaired' addressed the social problem of hearing-impairment and focused on developing appropriate speech signal processing mechanisms to improve speech perception for the advantage of those individuals. She has rich experience in teaching, research and administration in Karnataka and Hyderabad. Presently, working as Professor and Head in ECE dept. at Methodist College of Engineering, Hyderabad. Her expertise includes Speech signal processing, Digital signal processing, Signals and systems, Microprocessors, Automatic control systems. She has published 14 research papers indexed in IEEE,IEI, AES .

IOSR Journal of Mechanical and Civil Engineering (IOSR-JMCE)
e-ISSN: 2278-1684,p-ISSN: 2320-334X, Volume 12, Issue 2 Ver. VI (Mar - Apr. 2015), PP 05-10
www.iosrjournals.org

Influence of Microstructure on Mechanical Properties of Martensitic Stainless Steel Welds

A. Rajasekhar
Prof. Mechanical Engg. St.Marten Engg College, Kompally, Ranga Reddy, Telangana, India.

Abstract: *The mechanical properties of welds in martensitic stainless steels are critically dependent upon the microstructure developed in the weld metal and heat affected zone. Hence it is essential to understand the transformations that take place during the welding cycle.*
The purpose of the present paper is to present an overview of the phase transformations which take place in the weld metal or heat affected zones of martensitic stainless steels and their influence on mechanical properties of the welds.
Keywords: *Martensitic stainless steel; mechanical properties, delta ferrite; retained austenite*

I. Introduction:

Fusion welding involves localized heating, melting and cooling with the thermal cycle experienced varying over a wide range depending on the thickness of the material being weld and the welding process employed. In practice, all the metals and alloys which experience welding display some metallurgical change between the base metal and weld and HAZ region and hence the joint properties of these regions will differ significantly from those of the base metal.

Metallurgical transformation will take place during both heating and cooling, however for weld metal it is only the cooling cycle that is of concern. The metallurgical changes during welding may be mainly of two types, the first one is the major phase changes that occur and secondly the involvement of second phase particles either dissolution on heating or precipitation on cooling.

Because the properties of welds in steels are critically dependent upon the microstructure developed in the weld metal and heat affected zone, it is essential to understand the transformations that take place during the welding cycle.

The purpose of the present paper is to present an overview of the phase transformations which may take place in the weld metal or heat affected zones of martensitic stainless steels and their influence on mechanical properties of the welds.

II. Phase Transformations

Phase transformations take place during the original solidification process of the weld metal, and solid state transformations may occur in both the weld metal and heat affected zone. The predominant phase transformation in the martensitic stainless steel welds is the austenite-to-martensite transformation that occurs in the fusion zone and regions of the HAZ that have been heated into the austenite phase field.

2.1 Fusion Zone

The fusion zone of martensitic stainless steel with a nominal 11 to 14 wt% Cr and 0.1 to 0.25 wt% C solidify as delta ferrite. Segregation of C and other alloying elements during solidification can in some cases result in the formation of austenite, or a mixture of ferrite and austenite, at the end of solidification. As the weld metal cools in the solid state, the δ-ferrite transforms into fully austenite structure below about 1100^0C. The austenite will transform to martensite upon further cooling. This transformation is represented by the following sequence.

Transformation path 1: fully martensitic microstructure
L→ L + Fp→ Fp +A → A → martensite
Where, Fp is primary ferrite, and A is austenite.
However complete transformation to austenite will be influenced by

i. Segregation during solidification resulting in the formation of ferrite, which remains stable during cooling and remain at dendritic axes [1]. On the other hand, some of the ferrite stabilizers are also rejected into the liquid during solidification, so that the inter dendritic regions also can become ferrite, with some of the ferrite remaining at room temperature [2]. The amount of ferrite will depend on the ratio of ferrite to austenite promoting elements and the solidification conditions. This transformation is represented by the following sequence.

Transformation path 2: Two phase martensite + eutectic ferrite microstructure

$L \rightarrow L + Fp + (A + Fe) \rightarrow F_p + A + Fe \rightarrow A + Fe \rightarrow M + Fe$

Where, Fe is eutectic ferrite.

ii. The transformation of δ-ferrite to austenite during cooling is completed if the cooling rate is lower. However, cooling rate being higher at elevated temperatures; some non-equilibrium δ- ferrite can remain [1]. This transformation is represented by the following sequence.

Transformation path 3: Two phase martensite + primary ferrite microstructure

$L \rightarrow L + Fp \rightarrow F_p \rightarrow A + Fp \rightarrow M + Fp$

Depending upon cooling rate some carbide precipitation may also occur on cooling to room temperature [3]. These carbides are normally of the type $M_{23}C_6$ or M_7C_3 where M is predominantly chromium and Fe. The M_7C_3 carbides are usually restricted to the high carbon alloys (greater than 0.3 wt %C).

The probability of the presence of untransformed austenite increases, when the content of alloying elements increase and in some cases it may require to cool the weld below room temperature, to obtain fully transformed structure.

2.2 Heat Affected Zone:

In the as-welded condition, depending upon the maximum temperature attained and the duration of the welding cycle, the heat affected zone of martensitic stainless steel welds can exhibit a number of distinct micro structural regions. A macrograph of an autogenously weld in a 12Cr-1Mo stainless steel is shown in Fig. 1 [4]. The various micro structural regions of this alloy are:

Region 1: It is a region which is adjacent to the fusion boundary. The microstructure at elevated temperature consists of austenite, but some ferrite may be present at the austenite grain boundaries. Upon cooling to room temperature, the austenite transforms to martensite and some of the ferrite remains in the microstructure. The fraction of ferrite in the HAZ increases with increased welding heat input, since a longer time at high temperatures allows diffusion to make the transformation to ferrite more complete, while the reverse reaction on cooling is very sluggish [5]. In fact the high temperature ferrite remains stable to room temperature, possibly because the formation of alloy carbides at the ferrite-austenite interface immobilizes the interface [6]. The amount of ferrite that is present at room temperature will be a function of the amount that was present initially and the rate of dissolution of this ferrite as it cools through the austenite phase field. The presence of ferrite can promote local softening relative to the adjacent fusion zone and HAZ.

In region 2 of the HAZ, the microstructure will be fully austenitic at elevated temperature. The temperatures in this region of the HAZ are sufficiently high resulting in base metal carbide dissolution and consequent grain growth. Upon cooling, this region will be fully martensitic. Because all or most of the carbon will have gone back into solution in the austenite, the peak HAZ hardness will generally occur in this region.

Region 3 of the HAZ is also heated into the austenite phase field during welding, but because the temperature is lower than in region 2, carbide dissolution will be incomplete and austenite grain growth will not be so pronounced. This reduction in grain growth is due to both the lower temperature experienced and the pinning effect of the undissolved base metal carbides. Failure to dissolve the carbides results in a lower austenite carbon concentration and a subsequent reduction in the hardness of the martensite that forms upon cooling.

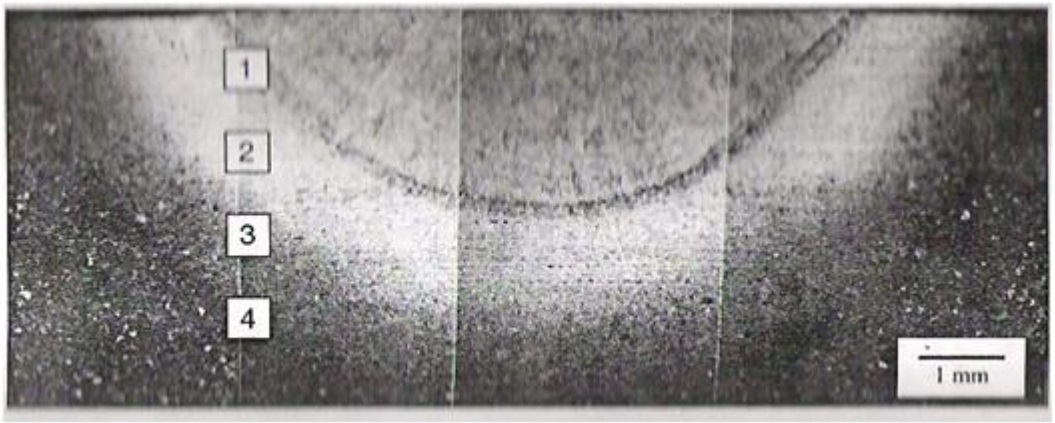

Fig. 1. Macrograph of an autogenous GTA weld in a 12Cr-1Mo stainless steel showing distinct regions in the HAZ [Lippold, 1984]

In region 4, little or no transformation to austenite occurs. Within this temperature regime [800 to 950^0C] carbide coarsening can occur, resulting in some local softening relative to the base metal.

If alloys with higher carbon content are considered, the two-phase austenite + ferrite region will shrink and eventually disappear. This will result in elimination of the softened region at the fusion boundary, since untempered martensite will extend all the way to the fusion boundary. An alloy of 0.4 wt% C, for example, will have no ferrite in the HAZ near the fusion boundary. At lower carbon contents, considerable ferrite may form in the HAZ near the fusion boundary, resulting in more pronounced softening.

III. Influence of Phases on Mechanical Properties

3.1 Martensite

Martensite is the desired predominant phase in martensitic stainless steels. Its presence is a consequence of the diffusion less transformation of austenite during cooling to room temperature.

Martensitic transformation in these steels is athermal i.e., the amount of martensite formed depends only on the under cooling below the Ms temperature and not on the time at temperature. This behavior is expressed in the Koistinen and Marburger equation [7]

$$Vm = \exp(-0.011^* (Ms - Tq))$$

Where Vm is the fraction of martensite and Tq is the quenching temperature below Ms.

Depending upon carbon content, the martensite in these steels present in various forms i.e., lath martensite, plate martensite or a combination of lath and plate martensite. In alloys containing less than about 0.6 wt% C, the martensite forms as laths which are aligned parallel to one another. The schematic illustration of the microstructural features of lath martensite is shown in Fig. 2[8] and the optical structure is shown in Fig. 3.

Plate martensite structure is normally present in high carbon steels and in alloys with low Ms temperature [9-13]. The structure is shown in Fig. 4 [14]. Medium carbon steels may contain a mixture of lath and plate martensite so that their structure is unusually complicated, as shown in Fig.5[14]. The relative amounts of plate martensite increase when elements such as nickel are added that lower the Ms temperature [14].

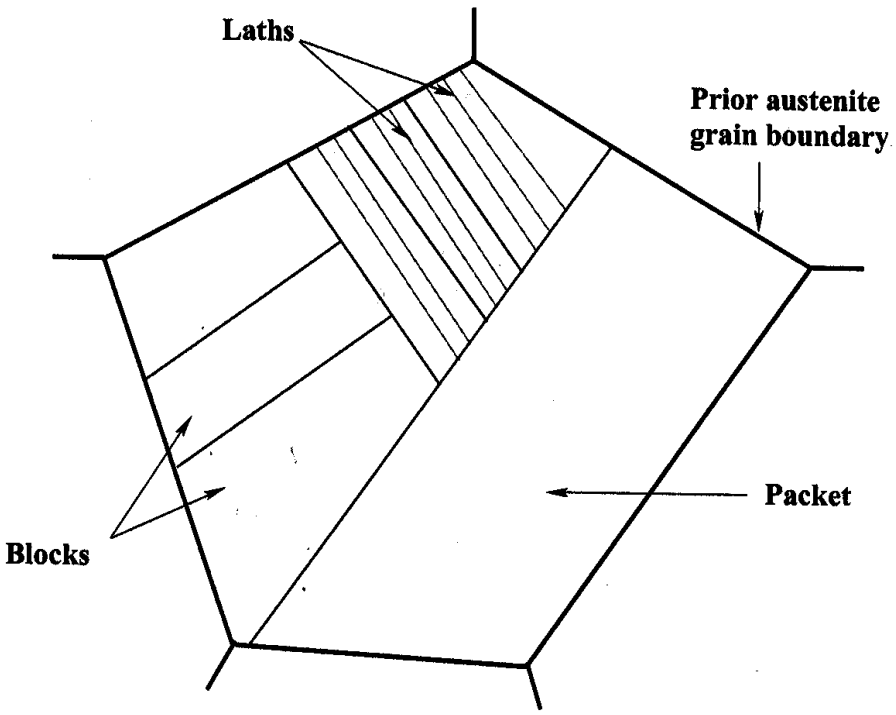

Fig. 2 Schematic illustration of the microstructural features of lath martensite [Maki. et al., 1980]

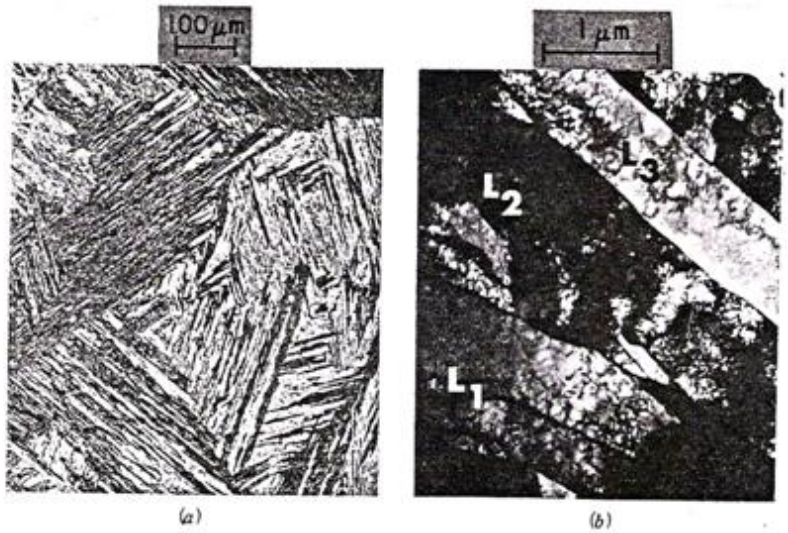

Fig. 3. Structure of lath martensite in 0.02% Mn steel. [Speich, G. R, et al., 1972] (a) Light micrograph. (b) electron transmission micrograph {L1,L2, L3 represents separate laths; the laths are separated by high-angle boundaries but each lath may contain many low –angle dislocation cells.

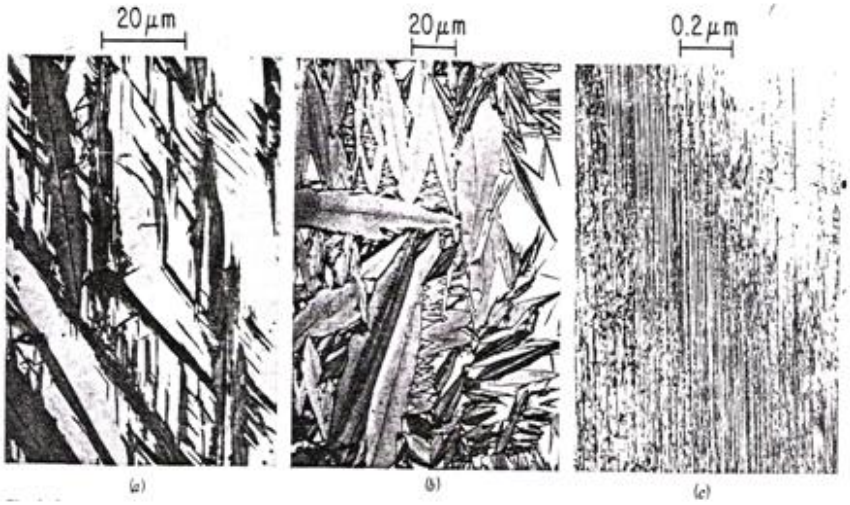

Fig. 4: Structure of plate martensite: (a) 1.2 %C steel, light micrograph; (b) Fe-30%Ni alloy, light micrograph; (c) Fe-30%Ni alloy, electron transmission micrograph. [Speich, et al., 1972]

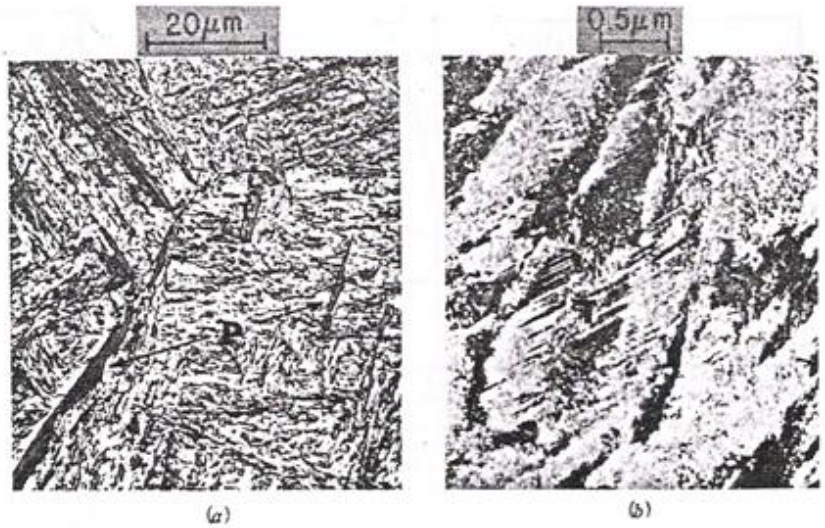

Fig. 5: Mixed lath and plate martensite structure in 0.57%C steel; (a) light micrograph (b) electron transmission micrograph (plate martensite labeled P; twinned substructure labeled T) [Speich, et al., 1972]

3.2 Retained Austenite

Depending upon the temperature at which the welding operation finishes and the precautions taken to avoid cracking, the weld can consist of martensite or a mixture of martensite and untransformed austenite. The probability of the presence of untransformed austenite increases, when the content of alloying elements increases and in some cases it may require to cool the weld below room temperature, to obtain fully transformed structure. Particularly, higher carbon grades are likely to retain large amounts of untransformed austenite in the as quenched structure, frequently as much as 30 % by volume. The Ms temperature is the primary factor affecting the level of retained austenite in martensitic stainless steel welds, and numerous empirical equations have been proposed to model the effect of a given element on the Ms temperature [14]. If an alloy element lowers the Ms temperature, retained austenite levels are increased within the steel, and vice versa [9].

Large increase in fracture and impact toughness in structural steels has been attributed to the presence of stable, retained austenite [15-18]. It has been shown that retained austenite decreases the yield strength in tension for heat treated low alloy steel [19].

The increased amount of retained austenite have been reported [20] to impart higher impact toughness when the steel is tempered at low temperatures, but the yield strength is lowered when the retained austenite is present in stainless steels of type AISI 431 [21-23]

3.3 δ-Ferrite

The amount of δ- ferrite retained is a function of both temperature and time, and is dependent upon the initial homogeneity of the steel and the extent to which equilibrium conditions are approached [24]. The presence of ferrite may be detrimental [25]. Studies have shown that small amounts of ferrite significantly improve the toughness of these steels at room temperature but ferrite presence in excess of 10 % can result in an approximate 50 % reduction in impact toughness [1, 26]. Its presence also decreases the tensile and fatigue strength [27]. Presence of significant amounts of delta ferrite results in low transverse strength and ductility, and also lower corrosion resistance [21, 28]. Hence it is not desirable for the welds to contain too much delta ferrite, both in the form of intra and inter dendritic form, since it doesn't harden during heat treatment.

3.4 Carbides

Depending upon cooling rate some carbide precipitation may also occur on cooling to room temperature [3]. These carbides are normally of the type $M_{23}C_6$ or M_7C_3 where M is predominantly chromium and Fe. The M_7C_3 carbides are usually restricted to the high carbon alloys (greater than 0.3 wt %C). The microstructure consisting of undissolved carbides is deleterious to toughness, particularly if the carbide phase is present as a network at the original austenite grain boundaries, or at inter lath boundaries [21, 29].

IV. Conclusions:

This paper presented an overview of the phase transformations which may take place in the weld metal or heat affected zones of martensitic stainless steels and their influence on mechanical properties of the welds. Depending upon the maximum temperature attained and the duration of the welding cycle, the various phases present in weld and HAZ of martensitic stainless steels include martensilte, retained austenite, delta–ferrite and carbides. The influence of these phases on mechanical properties has been discussed.

References:

[1]. Castro, R and J.J.de.Cadenet: 'Welding Metallurgy of Stainless and Heat-Resisting Steels', Cambridge University Press, 1974

[2]. Lippold, J. C.: 'Transformation and Tempering Behavior Of 12Cr-1Mo- 0.3V Martensitic Stainless Steel Weldments', J. Nucl. Mater., 1981, vol 103 and 104, P 1127-1132

[3]. Lippold, John C. and Damian J.Kotecki: 'Welding Metallurgy and Weldability of Stainless Steels, A John Wiley & Sons. Inc. Publication, 2005

[4]. Lippold, J.C.: 'The effect of post weld heat treatment on the Microstructure and properties of the heat-affected zone in 12Cr-1Mo-0.3V (ht9) weldments', proc. Topical conference on ferritic alloys for use in nuclear energy technologies, TMS, 1984, p 497-506

[5]. Fenn, R and Jordan, M. F.: 'Microstructure of weld heat-affected zone in 12Cr- 1Mo steel', Met. Technol., 1982, Vol 9 (No. 8), P 327-337

[6]. Villafuerte, J. C. and Kerr, H. W.: 'Phase transformations in stainless steel weld metal and HAZ', Engg. Materials, 1992, vols. 69 & 70, p 29-148

[7]. Koistinen, P. P and Marburger, R. E: 'A General Equation Prescribing The Extent of The Austenite-Martensite Transformation in Pure Iron-Carbon Alloys and Plain Carbon Steels', Acta Metallurgica, 1959, 7:59–60.

[8]. Maki. T, Tsuzaki. K and Tamura. I.: 'The Morphology of Microstructure Composed of Lath Martensites in Steels', ISIJ, 20:207–214, 1980.

[9]. Speich, G. R., and Leslie, W. C.: Mater. Trans. A, 1972, 3A, 1043-1052

[10]. Speich, G. R., and Swann, P. R.: J. Iron Steel Inst., 1965, vol. 203, pp. 480-485.

[11]. Speich, G. R., and Warlimont, H: J. Iron Steel Inst., 1968, vol. 206, pp. 385-392.

[12]. Marder, A. R., and Krauss, G: Trans. ASM, 1967, vol. 60, pp. 651-659.

[13]. Marder, A. R., and G. Krauss, G: Trans. ASM, 1969, vol. 62, pp. 957-963.

[14]. Andrews, K. W : J. Iron Steel Inst., 1965, 203, pp721-732

[15]. McMahon, J and Thomas, G: Proc. Third International conference on strength of metals and alloys, Inst. of metals, London, 1973, vol.1, pp. 180-184
[16]. Rao, B. V. N and Thomas, G: Metall.Trans. A, 1980, vol. 11A, pp. 441-457.
[17]. Lai, G. Y., Wood, W. E., Clark, R. A., Zackay, V. F., and Parker, E. R: Metall.Trans., 1974, vol. 5, pp. 1663-1670
[18]. Sarikaya, M., Steinberg, B. G., and Thomas, G: Metall.Trans. A, 1982, vol. 13A, pp. 2227-2237.
[19]. Castleman, L. S., Averbach, B. L., and Morris Cohen: 'Effect of retained austenite upon mechanical properties', Transactions, American Society for Metals, 1952, vol.44, p 240-263.
[20]. Bloom, F. K.: 'Effect of heat treatment and related factors on straight chromium stainless steels', Corrosion, 1953, vol.9, no.2, p. 56-65.
[21]. Dieter, G. E.: 'Effect of microstructure and heat treatment on the mechanical properties of AISI type 431 stainless steels', Transactions of ASM, vol.50, 1958, p. 722-737.
[22]. Kulmburg, A. Korntheuer, F. Gr¨undler, O and Hutterer, K.: Umwandlungsund Ausscheidungsverhalten von Weichmartensitischen und Hochfesten Korrosionsbestandigen St¨ahlen. Berg. u. huttenm. Mh., 126:104–108, 1981.
[23]. Leymonie, C. Lecocq, M. C. and Ottmann, M. C.: 'Relations entre la Structure et les Proprietes Mecaniques de Deux Aciers a 16%Cr - 4%Ni. Traitement thermiques', 165:57–62, 1982.
[24]. Chernyavskaya, S.G.: Met. Sci. Heat Treat., 1972, 14, (9-10), 812
[25]. Streicher, M.A.: Stainless Steels' 77, Climax Molybedenum Co., New York, 1978,1
[26]. Hashizume, S: 'A New 15 %Cr Martensitic Stainless Steel Developed for OCTG', CORROSION 1991, paper 28, NACE International, 1991.
[27]. Rickett, R. L., White, W. F., Walton, C. S., and Butler, J. C.: 'Isothermal Transformation, Hardening and Tempering of 12% chromium steel', Trans. ASM, 1952, 44, 138
[28]. Angstadt, C. C: Met. Prog. , 1959,75,(6),86
[29]. Narasimha Rao, B. V., and Thomas, G: Material Science and Engineering, 20, 1975, 195-202

International Journal of VLSI System Design and Communication Systems

ISSN 2322-0929
Vol.03, Issue.06,
August-2015,
Pages:0892-0896

www.ijvdcs.org

Error Detection and Correction using STI in Cache Memory

D. VISHWAKALA[1], CH. SURESH[2], K. HYMAVATHI[3]

[1]PG Scholar, Dept of VLSI System Design, Swami Ramananda Tirtha Institute of Science and Technology, Telangana, India, Email: vishwakala431@gmail.com.

[2]Assistant Professor, Dept of ECE, Swami Ramananda Tirtha Institute of Science and Technology, Telangana, India.

[3]Assoc Prof & HOD, Dept of ECE, Swami Ramananda Tirtha Institute of Science and Technology, Telangana, India.

Abstract: With continued technology scaling to the nanometer regime, computer systems are becoming vulnerable to transient errors. Especially, cache memories are vulnerable because they operate at low voltage levels and their sizes increase due to popular use of multilevel cache hierarchy and multi-core architecture even in embedded/mobile systems. To combat against transient errors, cache memories typically employ error protection mechanisms, such as parity codes and single-bit error correction and double-bit error detection (SEC–DED) codes. However, these schemes are not efficient in terms of area overhead and error protection coverage. Thus, many techniques are proposed to reduce such inefficiency and enhance protection coverage. With the trend of increasing transient error rate, it is becoming important to prevent transient errors and provide a correction mechanism for hardware circuits, especially for SRAM cache memories. Caches are the largest structures in current microprocessors and, hence, are most vulnerable to the transient errors. Tag bits in cache memories are also exposed to transient errors but a few efforts have been made to reduce their vulnerability. In this paper, we propose to exploit prevalent same tag bits to improve error protection capability of the tag bits in the caches. When data are fetched from the main memory, it is checked if adjacent cache lines have the same tag bits as those of the data fetched. This same tag bit information is stored in the caches as extra bits to be used later. When an error is detected in the tag bits, the same tag bit information is used to recover from the error in the tag bits. The proposed scheme has small area, energy, and performance overheads with error protection coverage of 97.9% on average. Even with large working sets and various cache sizes, our scheme shows protection coverage of higher than 95% on average.

Keywords: Cache memory, reliability, tag bits, transient Errors.

I. INTRODUCTION

With continued technology scaling, caches are becoming more vulnerable to transient errors. There have been many efforts made to address transient errors in the data arrays of the caches. However, errors in the tag bits of the caches are critical for data integrity, too. For example, transient errors in the tag bits can lead to false misses in the dirty cache lines and, consequently, stale data can be consumed. Therefore, addressing transient errors in the tag bits are critical for correction execution. By our experiments with embedded benchmarks on an Intel X-scale-based simulator, most tag bits in the data caches have their replica in other cache sets. In other words, when a cache line is accessed or replaced, we can find an adjacent cache line with the same tag bits as those of the cache line accessed in a upper or lower cache set than the current set. This is called tag bits similarity in this paper. Tag bits similarity can be exploited for improving tag bits vulnerability against transient errors. For instance, when an error is detected using the conventional parity check bits, the error could be corrected if the same tag bits were present in one of adjacent cache lines. Faulty tag bits are simply replaced with correct tag bits from the adjacent cache line for error correction. To exploit similar tag bits for transient error protection, we augment the conventional cache architecture with four simple hardware components. To access cache lines in a upper and/or lower cache set than currently accessed cache set, a shifter right after the decoder of a cache or a up/down counter is required. Second, an encoder for generating similarity information between tag bits is needed. Third, a small circuit is necessary for handling similarity bits on cache replacements. Finally, an error correction unit corrects transient errors in the tag bits using the same tag bits from adjacent cache lines. These extra components are simple structures and incur little energy, area, and latency overheads. We evaluated our proposed scheme with in-cache replication (ICR), which was originally proposed to reduce data array vulnerability but can also be applied to reduce tag bits vulnerability. From our experimental results, our scheme shows high error protection coverage of 97% with no virtual performance hit while ICR degrades overall system performance by around 10% and increases DRAM energy consumption by around 20%, on average.

II. RELATED WORK

Different techniques are proposed to protect against transient errors in microprocessors. Protection is generally achieved by employing redundancy; this redundancy may be

in time, in area, or in information. Error Detection Code (EDC) and Error Correction Code (ECC) are used widely for protecting caches against transient errors. However, the conventional ECC protection imposes significant area and latency penalties, making it practical only for large memories and second-level (L2) caches where the increased latency has little impact on performance. To prevent latency increasing, first level (L1) caches tend to employ parity check codes that allow bit error detection, but no correction. Bhattacharya et al. investigate in detail multi-bit soft error rates in large L2 caches and propose a framework based on the amount of redundancy present in the memory hierarchy.

Table I. Error Protection Techniques for Tag Bits

Technique	No Detection		Parity		SECDED		Parity+SimTag		SECDED+SimTag		Parity+ICR		SECDED+ICR	
Cache Line	*Clean*	*Dirty*	*Clean*	*Dirty*	*Clean*	*Dirty*	*Clean*	*Dirty*	*Clean*	*Dirty*	*Clean*	*Dirty*	*Clean*	*Dirty*
False Hit	Error		Hit → Miss		Hit → Miss		Hit → Miss		Hit → Miss		Hit → Miss		Hit → Miss	
False Miss	Ignore	Error	Ignore	Error	Ignore	Correct only 1-Bit Error	Ignore	Correct Odd bits error if same tag exists	Ignore	Correct 2-bit error if same tag exists	Ignore	Correct Odd bits error if Replica exists	Ignore	Correct 2-bit error if replica exists
Replacement Error	Ignore	Error	Ignore	Error	Ignore	Correct only 1-Bit Error	Ignore	Correct Odd bits error if same tag exists	Ignore	Correct 2-bit error if same tag exists	Ignore	Correct Odd bits error if Replica exists	Ignore	Correct 2-bit error if replica exists

Despite the fact that most of the previous work has studied effectiveness in terms of performance, energy, and area overheads, it targets data bits reliability with the assumption that tag bits are intact. However, tag bits also are vulnerable in caches and they have different inherent properties compared to data bits. Kim et al. classify tag bits faults into pseudo-hit, pseudo miss (also called false-hit or false-miss), and multi-hit. Asadi et al. present L1 and L2 cache vulnerability computation algorithms and also deal with algorithms forag vulnerability computation. They analyze in detail the sources of tag bits vulnerability. In-Cache Replication (ICR) has been proposed to replicate frequently accessed cache blocks to dead blocks. Replicated blocks can be used to correct tag bits errors in the active blocks. However, the dead block prediction technique is not always accurate. Thus, ICR increases cache miss and write-back rates resulting in large performance loss and increased energy consumption.

III. OUR PROPOSED APPROACH

A. Effects of tag bits corruptions

Transient errors in tag bits manifest themselves as false hits, false-misses, and replacement errors. A false-miss makes cache hit as a cache miss because of transient error in tag bits. Consequently, the data path gets wrong data on a read and updates a wrong location on a write. A false-hit refers to a cache hit that is actually a miss in the absence of a transient error. If tag bits are corrupted after the line is modified, it may write back to a wrong location in the next level of memory, which is classified as a replacement error. Table I shows tag bits error protection techniques including our proposed scheme and ICR. Except for no detection, clean cache lines do not need error recovery. If erroneous data are in a clean cache line, they can be recovered by invalidating the cache line and by fetching correct data from the next level of memory. If an error occurs in a dirty cache line, hardware exception will be generated and an error handling mechanism will take over for error recovery. Parity check code can cover transient errors on clean caches but it cannot protect dirty cache lines. Single Error Correction Double Error Detection (SECDED) can detect 2-bit errors and correct 1-bit errors.

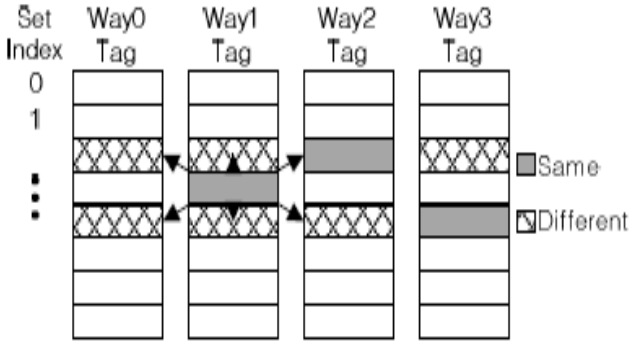

Fig.1. Same tag bits in the adjacent sets

These error codes can be augmented with our proposed technique. If single or multi-bit errors are detected by parity or SEC-DED, our technique will correct the errors using the same tag bits from adjacent cache lines. Our scheme and ICR use location information for error protection. However our scheme exploits prevalent same tag bits while ICR replicates tag bits into other locations by force.

B. Exploiting spatial locality

It is highly probable that same tag bits exist in adjacent cache sets (see Fig.1). This is a consequence of spatial locality of programs. The basic idea of our scheme is to exploit the same tag bits in an adjacent set for correcting erroneous tag bits. Additional bits are required to encode location information which points to exact location of the same tag bits in a upper or lower set. These extra bits are called "Same Tag Information" (STI). STI bits consist of three logical parts; a valid bit, a set location bit, and way location bits. The valid bit indicates that tag bits have the same bits in an adjacent set. The set location bit denotes a lower or upper set and way location bits represent a specific cache way which has the same tag bits. To find same tag bits and set STI bits properly, extra components are required. The tag bits of the missed data are compared with the tag bits of adjacent sets during fetching data from the next level of memory on a cache miss. If there is a match, the STI bits for

the missed data are generated and stored in the data cache. It is possible that replaced tag bits are indicated by the STI bits of adjacent sets (A). If this situation is not handled properly, the STI bits will point non-existing tag bits. To solve this problem, another extra component reads STI bits from lower and upper sets A. If there are matching STI bits, new STI bits are generated. All of these procedures are performed while pipelines are stalled due to cache misses. Therefore, there is no performance degradation virtually.

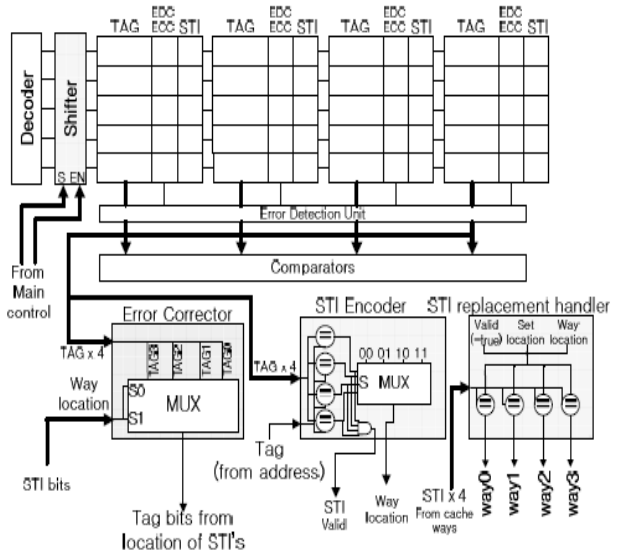

Fig.2. Detailed architecture of Sim Tag.

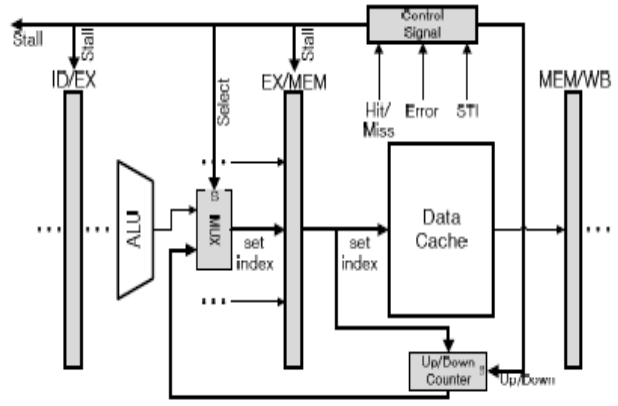

Fig.3. Counter-based technique to access adjacent sets

C. Proposed architecture

In this subsection, we present our proposed architecture and explain additional components which are required to implement it. Fig.2 shows the micro-architecture-level schematic of our architecture called **Sim Tag**. Detailed operation of each component is described below. **Shifter** Our approach uses a shifter for accessing lower or upper cache lines. This is simple and intuitive but it may increase the critical path of data cache access. An alternative approach is to use a counter for hiding the decoding latency. Fig.3 shows the counter-based technique for set index control. Basic operation is same as in the shifter approach but it operates in parallel with cache access.

STI Encoder: To generate STI bits, STI encoder compares the tag bits of cache missed data with the tag bits from lower and upper sets during pipelines are stalled due to cache misses.

STI Replacement Handler: STI replacement handler checks the STI bits in the upper and lower sets on cache replacement. If the STI bits point to replaced tag bits in question, then simply invalidate the STI valid bits and generate new STI bits by finding other same tag bits.

Error Corrector: When errors are detected, this component fetches uncorrupted tag bits from an adjacent cache set by using STI bits (if same tag bits exist) for error correction.

Main Controller: On cache misses or tag bits errors, the pipelines are stalled and, at the same time, the main controller signals the additional shifter (or counter) to access adjacent sets.

There is little area overhead due to the additional components. A set index bits-wide shifter or counter is put into the cache. A 4-to-1 tag bits-wide multiplexer is used for tag matching in the Error Corrector. STI Encoder uses a 2-bits multiplexer, a 1-bit AND gate and tag bits-wide comparators.

Table II. Baseline System Configuration

Configuration Parameter	Value
Processor	
Functional unit	1 Integer/Floating-point ALU 1 Multiply-Accumulate (MAC) Unit
Frequency	600MHz
Cache and Memory Hierarchy	
L1 Instruction Cache	32KB, 32-way, 32byte blocks
L1 Data Cache	8KB, 4-way, 32byte blocks Write-back
Memory	32M SDRAM

Also, STI bits-wide comparators are required for STI Replacement Handler. A few bits are required for the way location. These bits depend on the number of sets inside the data cache. If there are M sets, the size of way location bits is log2 (M)

IV. RESULTS

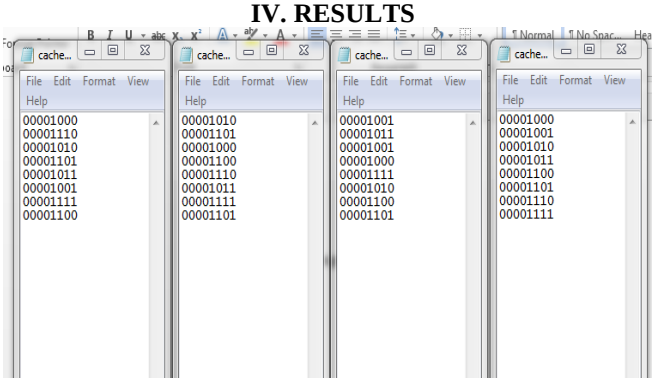

Fig.4. Cache memory.

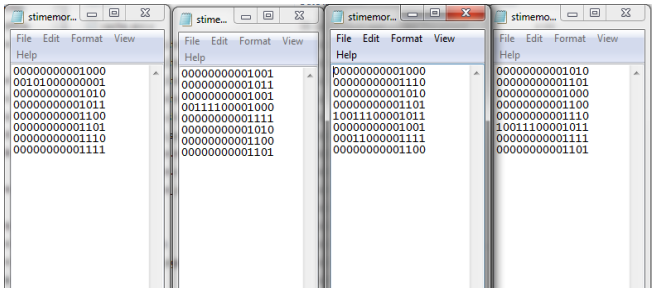

Fig.5. STI memory

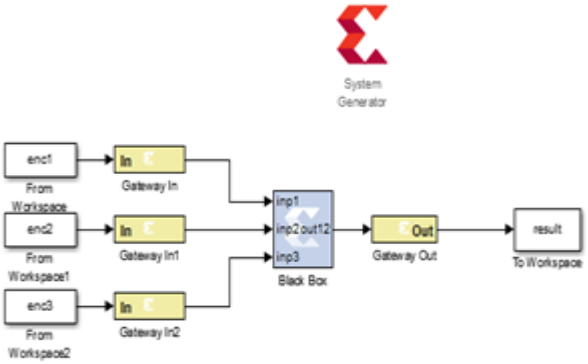

Fig.6. Encoder Design.

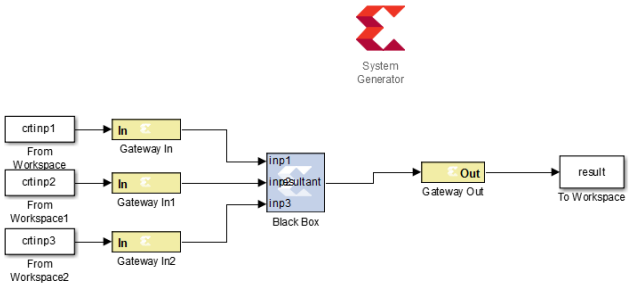

Fig.7 Corrector.

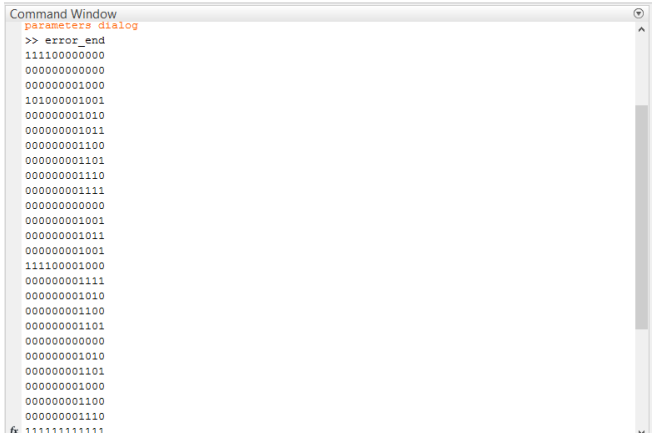

Fig.8. Error correction result

V. CONCLUSION AND FUTURE SCOPE

A. Conclusion

It is becoming important to provide error detection and correction capability for hardware circuits, especially for cache memories. Traditionally, parity or SEC–DED code has been widely used for caches against transient errors. Many techniques are proposed to reduce performance, energy, and area overheads of the conventional error protection mechanisms. However, most of the techniques consider only data bits without considering tag bits corruption. To improve tag bits reliability, this paper exploits tag bits similarity. Most of the tag bits in the data caches have their replica in adjacent cache sets due to spatial locality of programs. Hence, when an error is detected using the conventional parity check bits, the error can be corrected if the same tag bits were present in adjacent cache sets. Faulty tag bits are simply replaced with correct tag bits from the adjacent cache sets for error correction. We evaluate and compare our proposed architecture with the ICR scheme. With the trend of increasing soft error rate, it is becoming important to provide error detection and correction capability for hardware circuits, especially for cache memories. However, most of the previous techniques focus only on data bits without considering tag bits corruption. Most tag bits in the data caches have their replica in adjacent cache sets from our experiments. We exploit this tag bits similarity against transient errors. Faulty tag bits are simply replaced with correct tag bits from the adjacent cache lines for error correction.

B. Future scope

Processor caches already play a critical role in the performance of today's computer systems. At the same time, the data integrity of words coming out of the caches can have serious consequences on the ability of a program to execute correctly, or even to proceed. The integrity checks need to be performed in a time-sensitive manner to not slow down the execution when there are no errors as in the common case, and should not excessively increase the power budget of the caches which is already high. A novel solution to this problem by allowing in-cache replication, wherein reliability can be enhanced without excessively slowing down cache accesses or requiring significant area cost increases. The mechanism is fairly power efficient in comparison to other alternatives as well. In particular, the solution replicates data that is in active use within the cache itself while evicting those that may not be needed in the near future. Our experiments show that a large fraction of the data read from the cache has replicas available with this optimization.

VI. REFERENCES

[1] Jeongkyu Hong, Jesung Kim, and Soontae Kim, Member, IEEE, "Exploiting Same Tag Bits to Improve the Reliability of the Cache Memories", IEEE Transactions on Very Large Scale Integration (VLSI) Systems.

[2] Z. Herczeg, A. Kiss, D. Schmidt, N. Wehn, and T. Gyimóthy, "XEEMU: An improved X-Scale power simulator," in PATMOS (Lecture Notes in Computer Science), N. Azémard and L. J. Svensson, Eds. Springer-Verlag, 2007, pp. 300–309.

[3] S. Kim and A. Somani, "Area efficient architectures for information integrity in cache memories," in Proc. Int. Symp. Comput, Archit., 1999, pp. 246–255.

[4] W. Zhang, S. Gurumurthi, M. Kandemir, and A. Sivasubramaniam, "ICR: In-cache replication for enhancing data cache reliability," in Proc. Int. Conf. Dependable. Syst. Netw., 2003, pp. 291–300.
[5] B. Gold, M. Ferdman, B. Falsafi, and K. Mai, "Mitigating multi-bit soft errors in L1 caches using last-store prediction," in Proc. Workshop Archit. Support Giga scale Integr, 2007, pp. 1–8.
[6] S. Mukherjee, J. Emer, T. Fossum, and S. Reinhardt, "Cache scrubbing in microprocessors: Myth or necessity," in Proc. Int. Symp. Dependable Comput, 2004, pp. 37–42.
[7] C. Slayman, "Cache and memory error detection, correction, and reduction techniques for terrestrial servers and workstations," IEEE Trans. Device Math. Rel., vol. 5, no. 3, pp. 397–404, Sep. 2005.
[8] N. Wang and S. Patel, "ReStore: Symptom-based soft error detection in microprocessors," IEEE Trans. Dependable Sec. Comput., vol. 3, no. 3, pp. 188–201, Jul. 2006.
[9] H. Asadi, V. Sridharan, M. B. Tahoori, and D. Kaeli, "Vulnerability analysis of L2 cache elements to single event upsets," in Proc. Des., Autom., Test Eur., 2006, pp. 1–6.
[10] T. Austin, "DIVA: A reliable substrate for deep submicron micro-architecture design," in Proc. 32nd Annu. Int. Symp. Micro-architecture, 1999, pp. 196–2007.
[11] O. Ergin, O. Unsal, X. Vera, and A. Gonzaez, "Exploiting narrow values for soft error tolerance," IEEE Comput. Archit. Lett., vol. 5, no. 2, pp. 1–12, Dec. 2006.
[12] C. Weaver, J. Emer, S. S. Mukherjee, and S. K. Reinhardt, "Techniques to reduce the soft errors rate in a high-performance microprocessor," in Proc. 31st Annu. Int. Symp. Comput, Archit., Jun. 2004, pp. 264–275.

Author's Profile:

D.Vishwakala, PG Scholar, Dept of VLSI System Design, Swami Ramananda Tirtha Institute of Science and Technology, Telangana, India,
Email: vishwakala431@gmail.com.

Ch. Suresh, Received B.Tech degree in Electronics & Communication Engineering from sri venkateshwara engineering college, surypet, Nalgonda and M.Tech degree in VLSISD Systems from netaji institute of engineering college, nalgonda ,and currently working as an Assistant Professor, Department of Electronics and Communication Engineering in Swami Ramananda Tirtha Institute of Science and Technology, Nalgonda. Area of interest includes communication Systems.

K. Hymavathi, Received B.E degree in Electronics & Communication Engineering from Osmania University, Hyderabad and M.Tech degree in Digital Systems and Computer Electronics from Jawaharlal Nehru Technological University, Hyderabad and currently working as an Associate Professor and Head of the Department of Electronics and Communication Engineering in Swami Ramananda Tirtha Institute of Science and Technology, Nalgonda. Area of interest includes Analog and Digital Communications.

International Journal of Science and Research (IJSR)
ISSN (Online): 2319-7064
Index Copernicus Value (2013): 6.14 | Impact Factor (2013): 4.438

Corrosion Behavior of Martensitic Stainless Steels – Role of Composition and Heat Treatment Procedures

A. Rajasekhar

Professor, St. Marten Engineering College Kompally, R.R., A.P.-509 217, India

Abstract: ***Martensitic stainless steels are used in many applications which demand high strength-toughness combination along with good corrosion resistance. Selection of these steels for corrosive environment is generally based on the carbon and chromium content of the steel, and their resistance to corrosion in the heat treated conditions, as the corrosion resistance of these steels depends on carbide volume fraction dissolved in matrix after austenitizing and on the carbide precipitation during tempering. This paper reviews the influence of the composition and the heat treatment procedures which are being followed to get optimum corrosion resistance of these steels.***

Keywords: Corrosion; Martensitic stainless steel; Austenitizing; Tempering;

1. Introduction

Martensitic stainless steel has become increasingly attractive for a number of industry sectors due to their excellent mechanical properties like high strength, adequate ductility and toughness apart from good corrosion resistance. These are used in various industries such as in chemical plants, power generation equipments in gas turbines and compressor blades and discs, aircraft engine components and fittings in marine components [1]. However, the need for superior properties combined with good corrosion resistance in specific applications (e.g. steam generators, mixer blades, etc.) led to wide research on the performance improvement of these steels.

Table 1: The corrosion rate of Cr and Cr-Ni steels during 120 h in 100% H_2S at atmospheric pressure [Naumann, 1938]

Material, Wt.%	Corrosion Rate (mm/yr)	
	344^0C	500^0C
5 Cr	6.10	25.40
9 Cr	5.08	17.78
12 Cr	3.30	10.16
17 Cr	2.29	5.08
25 Cr	-	2.54
18 Cr- 9 Ni	2.03	6.10
26 Cr- 20 Ni	1.50	2.54

Chromium confers the stainless steel it's most important property of being resistant to corrosion. From the point of view of general corrosion, the higher the chromium content of the steel the greater will be its resistance to corrosion. The existence of chromium as chromium carbide particles may be beneficial to stainless steel from the point of view of certain mechanical properties but as far as corrosion resistance is concerned it is beneficial if chromium exists in solid solution [2]. The corrosion resistance of martensitic stainless steels depends on carbide volume fraction dissolved in matrix after austenitizing and on the carbide precipitation during tempering [3-4]. Therefore, for maximum corrosion resistance, the carbon content and heat treatment condition of stainless steel are two important factors to be taken into account while considering martensitic stainless steel for any structural application.

This paper reviews the influence of composition and the heat treatment methods which influence the corrosion resistance of martensitic stainless steels.

2. Effect of Chemical Composition

Increasing chromium in stainless steels increases resistance to atmospheric corrosion in an industrial atmosphere [5]. Data presented in Table 1 [6] indicate that the resistance of stainless steels to corrosion by hydrogen sulphide (H_2S) at elevated temperatures increases with increasing amount of chromium. Chromium increases the resistance of stainless steels to sulphur vapor in flue gases. The protective chromium oxide film imparting resistance to stainless steel from general aqueous corrosion increases with increase in chromium in oxidizing environments. However, the effect is negative in reducing environment.

Increased chromium resists pitting corrosion [2] and stress corrosion cracking in these steels (SCC) [7]. Chromium also increases resistance to oxidation at 1000ºC in the manner as shown in Fig. 1 "A" [8]. For a number of steels maximum temperature without producing excessive scaling is presented in Fig. 1.18 "B" [9] which indicates the beneficial effect of 16% Cr over 12% Cr steel.

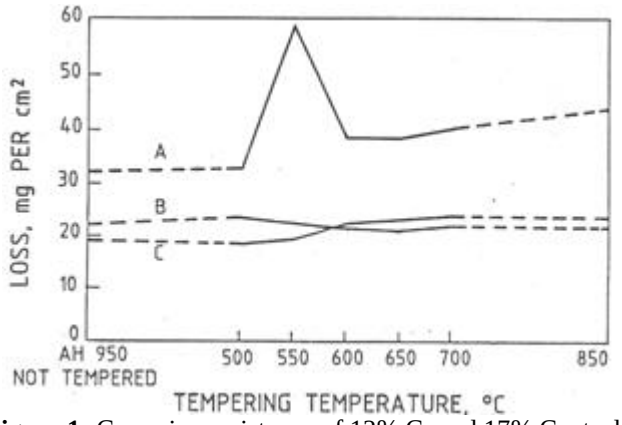

Figure 1: Corrosion resistance of 12% Cr and 17% Cr steels in hardened and tempered conditions [Monypenny, 1951]

Increasing nickel content of 12% Cr steels from 2.5% to 4.5% is found to improve resistance to marine atmosphere corrosion [10]. Brasunas et al. [11] showed that nickel improved scaling resistance in stainless steels with wide range of Cr (11-31%) in air at 532^{0}C. Nickel in stainless steels is found to improve both general corrosion resistance as well as SCC [10]. It is reported that the small amounts of silicon and manganese (1.0%) in martensitic stainless steels have no noticeable effect on corrosion resistance [2].

C.X. Li' and T. Bell [12] have investigated the corrosion properties of plasma nitided AISI 410 martensitic stainless steel and found that the nitrided samples showed higher corrosion potentials and, higher pitting potentials. The improved corrosion resistance was believed to be related to the iron nitride compound layer formed on the martensitic stainless steel surface during plasma nitriding, which protected the underlying metal from corrosive attack under the testing conditions.

3. Influence of Austenitizing and Tempering Temperature on Corrosion Behavior

In 12% chromium steels carbon in the usual limit of 0.2% goes into solution when austenitized at 1000-1050^{0}C. Steel in quenched condition, therefore has all the chromium in solid solution for effective corrosion resistance. On tempering up to 500^{0}C, the hardness remains more or less the same as that of hardened steel and therefore the steel does not show any change in its corrosion resistance. However, on tempering at 550^{0}C, the corrosion resistance is found to drop considerably [2]. On tempering at higher temperatures viz., 600-700^{0}C, the corrosion resistance is found to improve again. The explanation given for this behavior of steel by Monypenny is that maximum precipitation of chromium carbide occurs at the tempering temperature of 550^{0}C. Therefore, with higher tempering temperatures the precipitated carbide particles only grow. As the carbide particles are more electropositive compared to steel matrix, electro-chemical action leading to corrosion can take place on the steel portion [2]. Therefore, the possibility of corrosion is maximum when finer and larger number of carbides are precipitated on tempering at 550^{0}C, causing a larger surface area of the carbide particles. With higher tempering temperatures growth of carbide particles reduce the surface area of carbides. Moreover, on transformation of carbides from Cr_7C_3 to $M_{23}C_6$ with higher tempering temperature, Cr substitution by Fe in $M_{23}C_6$ is also affected. Thus the effective chromium content of matrix is improved with raise in tempering temperature.

Lim et al.[13] have reported a tempering map for AISI 403 martensitic stainless steel containing 12% Cr and 0.1%C (Fig.2). According to this map for 2 hours tempering between 600-660^{0}C, the steel becomes sensitized and its resistance to inter granular corrosion gets impaired.

The speed of sensitization in martensitic stainless steel is much more rapid as compared to austenitic stainless steel because the carbides form rapidly within the martensitic laths and along the lath boundaries. The resulting corrosion can be intergranular, transgranular or mixed [14-16]. Healing of chromium depleted zone in 12% Cr steel is seen to be occurring only at temperatures above 680^{0}C, which may recover the microstructure from the effect of sensitization but would also result in considerable loss in strength owing to tempering at very high temperature.

Effects of austenitizing treatment temperatures on aqueous corrosion properties of martensitic stainless steels were investigated by Yoon-Seok Choi, et.al [17] and found that the breakdown potential increased with the increased austenitizing temperature. This indicates the increased relative resistance to initiation of localized corrosion. The samples austenitized at higher temperatures exhibits larger polarization resistance value than samples austenitized at lower temperatures at passive and breakdown states. This was caused by decreasing the amount of Cr-rich $M_{23}C_6$ carbide which acts as preferential sites for pitting corrosion.

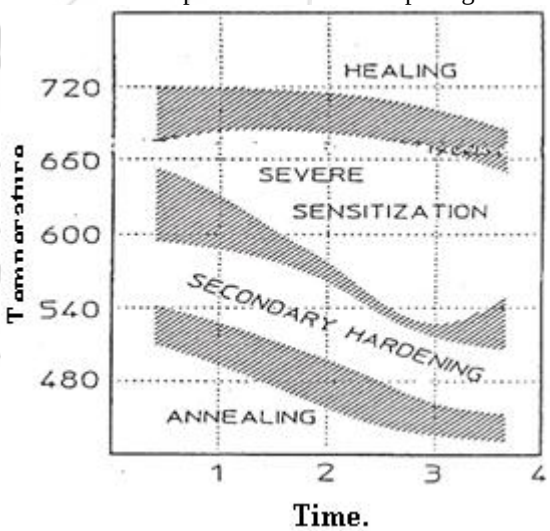

Figure 2: Tempering map of 12Cr-0.1C martensitic stainless steels [Lim et al., 1993]

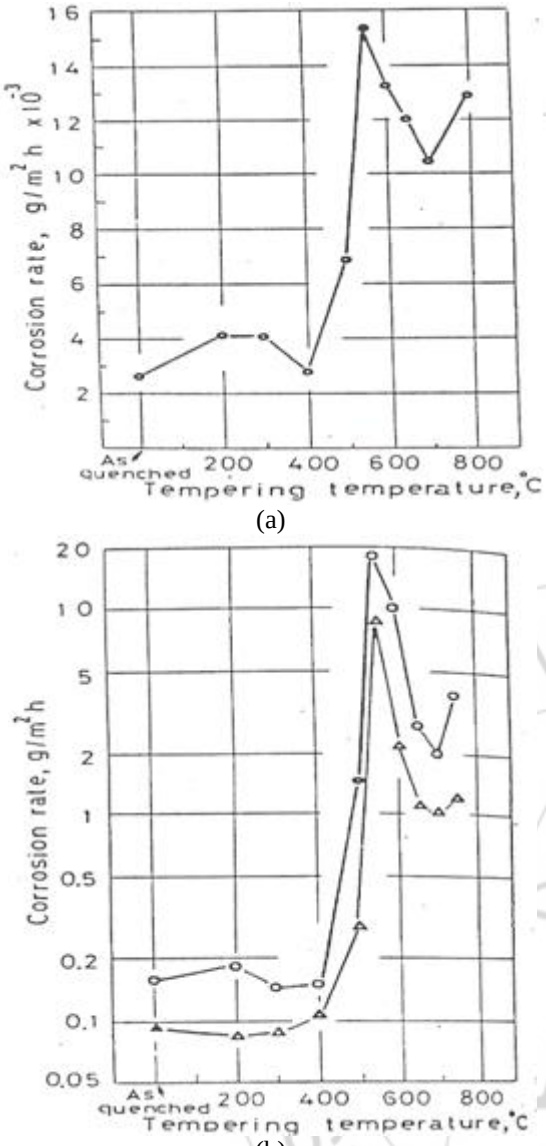

Figure 3: Variation in corrosion rate as a function of tempering temperature for 16Cr-2Ni steel in (a) 3% NaCl solution at 22^0C for 405 hours, and (b) 0.1 N H_2So_4 (o) and 0.1 N HCl ( ) solutions at 22^0C for 24 hours[Ogino, et. al., 1987]

Jee-Yong Park, and Yong-Soo Park [18] have investigated the effects of heat-treatment parameters on corrosion resistance and phase transformation in relation to the dissolution and re-precipitation of carbides in 14Cr–3Mo martensitic stainless steel. It is observed that the corrosion resistance of the experimental alloy was found to be improved at higher austenitizing temperatures. However, it was deteriorated at the specific austenitizing temperatures of 1000 and 1050 °C when the cooling rate was 10 K/s. The deterioration of corrosion resistance was caused by the impaired balance between the matrix and the retained austenite.

Of all the hardenable martensitic stainless steels, 16Cr-2Ni steel is the most resistant to general types of corrosion [19]. 16 Cr-2 Ni steel is slightly superior to the straight chromium alloy of equal chromium content but marginally inferior to the austenitic stainless steels of 18-8 type in most media. However, under certain conditions of tap water, steam, food products and particularly salt spray, the alloy compares very favorably with the 18-8 type stainless steels [19].

Solution and precipitation of carbide is expected to occur in a similar manner in 16Cr-2Ni steel as that of 12% Cr steel. However, since chromium is more in this steel compared to 12%Cr steels, even with all the carbon (up to 0.25%) precipitated as chromium carbide; the steel would be having sufficient chromium to resist corrosion.

The results shown in Fig. 1 illustrate the better corrosion resistance of 16Cr-2Ni steel compared to 12%Cr steel at all heat treated conditions [2]. Thus for applications which are to resist sea water or to be reasonably immune from electrochemical action due to contact with copper alloys, and also nitric acid, 16%Cr steels are preferred to 12%Cr steels [Monypenny, 1951][2].

Tests in acid medium was carried out by Ogino et al [20] on cylindrical specimens of diameter 10 mm and height 15 mm of 16Cr-2Ni steel and the results obtained are shown in Fig.3. It is evident from the data that tempering up to 400^0C (for two hours at each temperature) has negligible effect on the corrosion resistance of the steel. The data also reveal that the highest tempering temperature which provided maximum corrosion resistance in this steel is 400^0C. The reason attributed to this behaviour is that chromium depletion from the matrix is minimal at 400^0C tempering. Between 550-600^0C, where fine carbide precipitation (M_7C_3) in the steel causes substantial chromium depletion, shows minimum corrosion resistance (Fig.3). Tempering beyond 600^0C induces some improvement in corrosion resistance relative to 500-600^0C tempering due to precipitation of equilibrium carbide ($M_{23}C_6$) in which some amount of chromium is replaced by iron i.e., $(Cr, Fe)_{23}C_6$, causing less amount of chromium depletion from the steel. However, tempering beyond 600^0C, shows much lower corrosion resistance as compared to tempering up to 400^0C.

The pitting corrosion resistance of 16Cr-2 Ni steels after austenitizing at various temperatures followed by double tempering was studied by Rajasekhar et.al [21]. The results show that double austenitization followed by double tempering resulted high pitting corrosion resistance as compared to single austenitization temperatures (followed by double tempering). The reason attributed to this behavior is that chromium depletion from the matrix is low in double austenitization treatment that results precipitation of equilibrium carbides $M_{23}C_6$ in which some amount of chromium is replaced by Fe, causing less chromium depletion from the matrix.

4. Conclusions

A review on the present published information on corrosion behavior of martensitic stainless steels indicates that the corrosion resistance depends on carbide volume fraction dissolved in matrix after austenitizing and the carbide precipitation during tempering. Corrosion resistance can be improved by adopting proper heat treatment procedures

depending upon the application for which the material is selected.

References

[1] Brickner, K. G.: 'Stainless steel for room and cryogenic temperatures', Metals Engineering Quarterly, May 1968, pp 25-45
[2] Monypenny, J. H. G.: 'Stainless Iron and Steel', Chapman and Hall ltd., London, 1951, vol. 1, p 24
[3] Dieter, G. E.: 'Effect of microstructure and heat treatment on the mechanical properties of AISI type 431 stainless steels', Transactions of ASM, vol.50, 1958, p. 722-737.
[4] Sarikaya, M., Steinberg, B. G., and Thomas, G: Metall.Trans. A, 1982, vol. 13A, pp. 2227-2237.
[5] Binder, W. O. and Brown, c. M., "Atmospheric Corrosion Tests on high Chromium Steels", ASTM Proc., vol.46, 1946, p 593.
[6] Naumann, F. K : Chem. Fabr., 1938, vol. 11, p 365
[7] Lillys, P. and Nehrenberg, A.E.: Trans. ASM, 1956,vol.48, p 327
[8] Crafts, W: Chromium in steels, Metals handbook, ASM, Cleveland, Ohio, 1948, p460
[9] Mc Gannon, H. E., Ed.: 'The making, shaping and treating of steel', 9th ed., United States Steel Corp., Pittsburg, Pa, 1971, p 1163
[10] Edwin Snape: 'Effect of Nickel on the structure and properties of wrought and cast stainless steels', Handbook of stainless steels, Ed: Donal Peckner and Bernstein, F. M., McGraw Hill, New York, 1977, p12-1 to 12-40
[11] Brasunas, A, de S, Gow, J.T., and Harder, D. E.: Symp. Materials Gas Turbines, ASTM, 1946.
[12] C.X. Li' and T. Bell., "Corrosion properties of plasma nitrided AISI 410 martensitic stainless steel in 3.5% NaCl and 1% HCl aqueous solutions", Corrosion Science, Volume 48, Issue 8, August 2006, Pages 2036–2049
[13] Lim, L. C. Lai, M. O. Ma, J Northwood, D. O and Miao, B.: Material Science and Engineering, A 171**,** 1993, p 13.
[14] Truman, J.E., Br. Corros, J.: 1976, vol. 11, No. 2, p 92
[15] Briant, C. L., and Ritter, A. M.: Scripta Materialia, 1979, vol. 13, p177
[16] Briant, C. L., and Ritter, A. M.: Metall. Trans. A., 1980,vol. 11, p 2009
[17] Yoon-Seok Choi, Jung-Gu Kim' ' , Yong-Soo Park, Jee-Yong Park, "Austenitizing treatment influence on the electrochemical corrosion behavior of 0.3C–14Cr–3Mo martensitic stainless steel, Materials Letters, Volume 61, Issue 1, January 2007, Pages 244–247
[18] Jee-Yong Park' , and Yong-Soo Park, "The effects of heat-treatment parameters on corrosion resistance and phase transformations of 14Cr–3Mo martensitic stainless steel", Materials Science and Engineering: A Volumes 449–451, 25 March 2007, Pages 1131–1134
[19] Alloy Digest, Inc., Upper Montclair, New Jercy, May 1959
[20] Ogino, Hida, A., and Kishima, S.: "Susceptibility of type 431 stainless steel to erosion-corrosion by vibratory cavitation in corrosive media", Wear, vol. 116, 1987, p 299
[21] Rajasekhar, A., and G. M.Reddy: 'The effect of single and double austenitization temperatures on the microstructure, mechanical properties and pitting corrosion of AISI electron beam welds', Proc.IMechE vol.224 Part L; Journal of Materials: Design and Applications, Page no.9-18

Author Profile

A.Rajasekhar completed his graduation and post graduation from Osmania University in the year 1992 and 1999 respectively. Ha has completed his Ph.D from the same university in the year 2009. He has received best paper award in 2008 from IIT,Madras in the Int. Symposium. His research areas are welding & welding metallurgy of stainless steels and aluminum alloys, unconventional machining processes especially Abrasive jet machining and Abrasive water jet machining. Presently, he is working as Professor, Mechanical Engineering Department, St.Martin's Engineerirng College, Kompally Telangana ,India

Available online www.ejaet.com

European Journal of Advances in Engineering and Technology, 2015, 2(3): 46-50

Research Article ISSN: 2394 - 658X

Orthogonal Frequency Division Multiplexing Modulation Scheme for 4G/5G Cellular Network

Santosh M Nejakar[1], Prabhu G Benakop[2] and Sharanabasappa R R[1]

[1]Department of E&TC, Sanjay Ghodawat Institutions, Atigre, Kolhapur, India
[2]Department E&C, Indore Institute of Engineering and Technology, Hyderabad, India
nejakarganu@gmail.com

ABSTRACT

The next generation wireless communications systems need to be of a higher standard in order to provide the customers with the multitude of high quality services they demand. Orthogonal frequency division multiplexing (OFDM) is a key technique for achieving high data rates and spectral efficiency requirements for wireless communication systems OFDM is becoming the chosen modulation technique for wireless communications. OFDM can provide large data rates with sufficient robustness to radio channel impairments. The purpose of this paper is to implement the basic processing involved in the transmission and reception of an OFDM technique. The implementation of OFDM is done in MATLAB.

Key words: Orthogonal frequency division multiplexing (OFDM), fast Fourier transformer (FFT), frequency division multiplexing (FDM)

INTRODUCTION

With the rapid growth of digital wireless communication in recent years, the need for high-speed mobile data transmission has increased. In the wireless environment signals are usually impaired by fading and multipath delay phenomenon, traditional single carrier mobile communication systems do not perform well. In such channels, extreme fading of the signal amplitude and Inter Symbol Interference (ISI) occurs at the receiver side. This leads to a high probability of errors and the system's overall performance becomes very poor. Techniques like channel coding and adaptive equalization have been widely used as a solution to these problems. However, due to the inherent delay in the coding and equalization process and high cost of the hardware, it is quite difficult to use these techniques in systems operating at high bit rates [5] New modulation techniques are being implemented to keep up with the desire more communication capacity Orthogonal Frequency Division Multiplexing (OFDM) is a key technique for achieving high data rates and spectral efficiency requirements for wireless communication systems. Orthogonal Frequency Division Multiplexing (OFDM) transmissions are emerging as important modulation technique because of its capacity of ensuring high level of robustness against any interference [4]

In an OFDM scheme a large number of sub channels or sub-carriers are used to transmit digital data. Each sub-channel or sub-carriers divide the available bandwidth and each sub-carrier is orthogonal to every other. They are closely spaced and narrow band. The separation of the sub-channels is as minimal as possible to obtain high spectral efficiency. The purpose of this project is to implement the basic processing involved OFDM technique. The implementation of OFDM is done in MATLAB.

The aim of this paper is to implement a baseband OFDM processing. Including FFT (Fast Fourier Transform) and IFFT (Inverse Fast Fourier Transform), which satisfy to overcome from ISI (Inter Symbol Interference) and avoiding overlapping of signals.

THEORY OF OFDM

In classical parallel data system, the total signal frequency band is divided into N non-overlapping frequency sub-channels. Each sub-channel is modulated with a separate symbol, and then the N sub-channels are frequency multiplexed. It seems good to avoid spectral over-lap of channels to eliminate inter-channel

interference. However it leads to inefficient use of available spectrum. As like in Frequency Division Multiplexing (FDM), shown in Fig. 1, requires separation of the channels. In radio-based FDM, there must be a space, or guard band between channels to avoid interference from adjacent channels. These empty spaces are not efficient use of the spectrum [1]. So to cope up with this inefficiency, the idea is to use parallel data and FDM with overlapping sub-channels. One modulation scheme of recent interest is Orthogonal Frequency Division Multiplexing (OFDM). OFDM is a multicarrier modulation technique, which divides the bandwidth into many carriers; each one is modulated by a low rate data stream and each sub-carrier is orthogonal to every other so can achieve overlapping of sub-channels. As shown in Fig. 2. This modulation is one of several that can support high data rates [2].

Fig. 1 Frequency division multiplexing

Fig. 2 Orthogonal frequency division multiplexing

Orthogonality

The key to OFDM is maintaining orthogonality of the carriers. If the integral of the product of two signals is zero over a time period, then these two signals are said to be orthogonal to each other. Two sinusoids with frequencies that are integer multiples of a common frequency can satisfy this criterion. Therefore, orthogonality is defined by [3]

$$\int \cos(2\pi n f_0 t)\cos(2\pi m f_0 t)dt = 0 \qquad (n \neq m) \qquad (1)$$

Multiple Path Effect

This affects the transmission in case of the wireless transmission system. The received radio signals from the transmitter consist of a direct signal and reflections from the objects such as mountings; building, and other structures. The reflected signal arrives at a later time than the direct signal because of the extra path length. This gives rise to slightly different arrival times which spreads the received energy in time. Delay spread is thus the time spread between the arrival of the first and last significant multipath signal seen by the receiver. In digital systems, the delay spread leads to the inter-symbol interference. This causes significant errors in bit rate [2].

Inter Symbol Interference (ISI)

Inter-Symbol Interference takes place when a given transmitted symbol is distorted by other transmitted symbols.

BLOCK DIAGRAM OF OFDM

The implementation of OFDM is carried out as follows the Fig. 3.

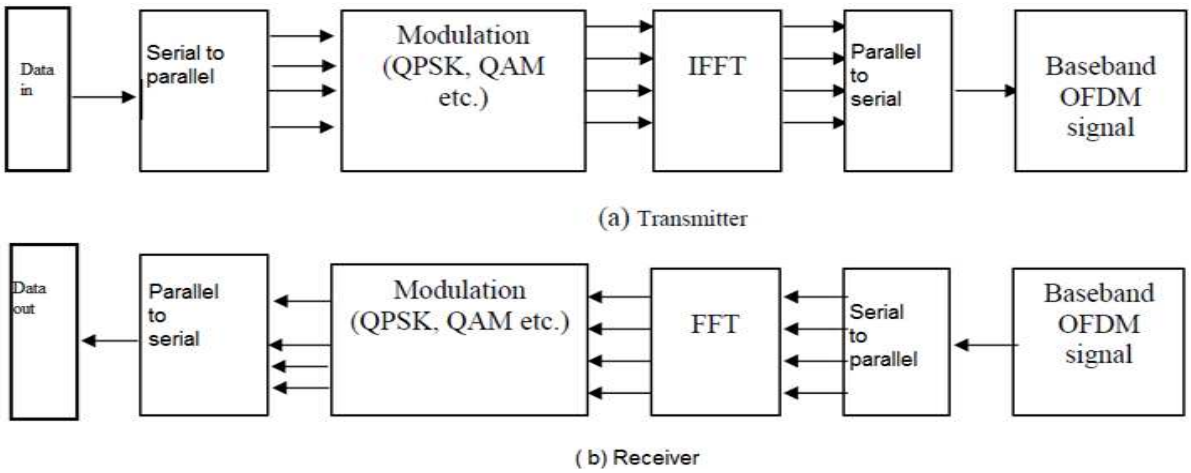

Fig. 3Orthogonal Frequency Division Multiplexing system (a) Transmitter, (b) Receiver

Data In

Stream of binary sequence are generated. Here 64 bits of binary sequence (0's and 1's) are generated and feed to serial to parallel converter.

Serial to Parallel

Here we convert the input serial bit stream into several parallel bit streams to divided whole bandwidth among the individual carriers. The data allocated to each symbol on individual carriers depends on the modulation scheme used and the number of subcarriers.

Modulation

Modulation is the process of modifying some properties of the high frequency carrier signal in accordance with the baseband signal [2]. Here QPSK modulation is used. This modulation scheme is characterized by the fact that the information carried by the transmitted wave is contained in the phase. The phase of the carrier takes one of the equally spaced values, such as π /4, 3 π /4, 5 π /4 and 7 π /4 as shown by

$$S_n(t) = \sqrt{\frac{2E_s}{T_s}} \cos(2\pi f_c t + (2n-1)\frac{\pi}{4}) \qquad \text{(n =1, 2, 3, 4...)} \qquad (2)$$

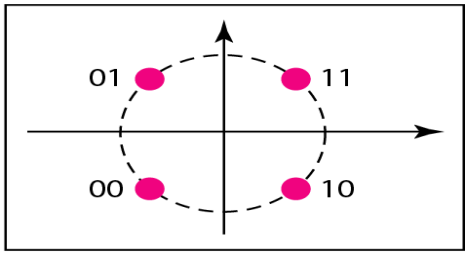

Fig. 4 QPSK Signal-Constellation

Inverse Fast Fourier Transform (IFFT)

The IFFT takes an N symbols at a time where N is the number of subcarriers in the system. The IFFT output is the summation of all N sinusoids. Thus, the IFFT block provides a simple way to modulate data onto N orthogonal subcarriers. The block of N output samples from the IFFT make up a single OFDM symbol. IFFT is given by [3]

$$X_n = \frac{1}{N} \sum_{p=0}^{N-1} X_p e^{j\frac{2\pi}{N} np}, \; n \in \{0, 1, 2 \ldots\ldots N-1\} \qquad (3)$$

After the IFFT guard bits are added and feed to parallel to serial. Here the guard bits added by using period time of zero amplitude transmission. This was to allow for symbol timing to be easily recovered by receiver.

Parallel to Serial

Once the guard bit has been added to the sub-carrier channels, they must be transmitted as one signal. Thus, the parallel to serial conversion stage is the process of summing all sub-carriers and combining them into one signal. This is the base band signal for the OFDM transmission.

Fast Fourier Transform (FFT)

At the receiver, an FFT block is used to process the received signal and bring it into the frequency domain. Ideally, the FFT output will be the original symbols that were sent to the IFFT at the transmitter. FFT is given by

$$X_p = \sum_{n=0}^{N-1} X_n e^{-j\frac{2\pi}{N} np}, \; p \in \{0, 1, 2 \ldots\ldots N-1\} \qquad (4)$$

Demodulation

This process is the juts reverse of the modulation process. It is carried out on the receiver side of the system and is done in the frequency domain.

IMPLEMENTATION AND RESULT

The below flow chart shows the steps performed to implement. According to the binary sequence, the QPSK modulated output is shown in Fig.5.After the performing the IFFT the output received is shown in Fig.6. After the removing of guard bits at the receiver side the output is shown in Fig.7 and Fig. 8 depicts the output after the performing FFT at receiver ends.

CONCLUSION

In this paper OFDM with QPSK modulation is demonstrated .The key building blocks of an OFDM transmitter and OFDM receiver has been implemented in MATLAB and the functionality of the each blocks are studied. The modulation of data can be modelled with the help of a modulation matrix that is computed based on a given pulse shaping filter and data block size. Based on the transmitter model, known ways of receiving the signal can be applied. However, all three standard methods may, depending on the system parameters, yield strong performance degradation when compared to FFT, IFFT. Output of the QPSK modulation IFFT with adding guard bits can be calculated.

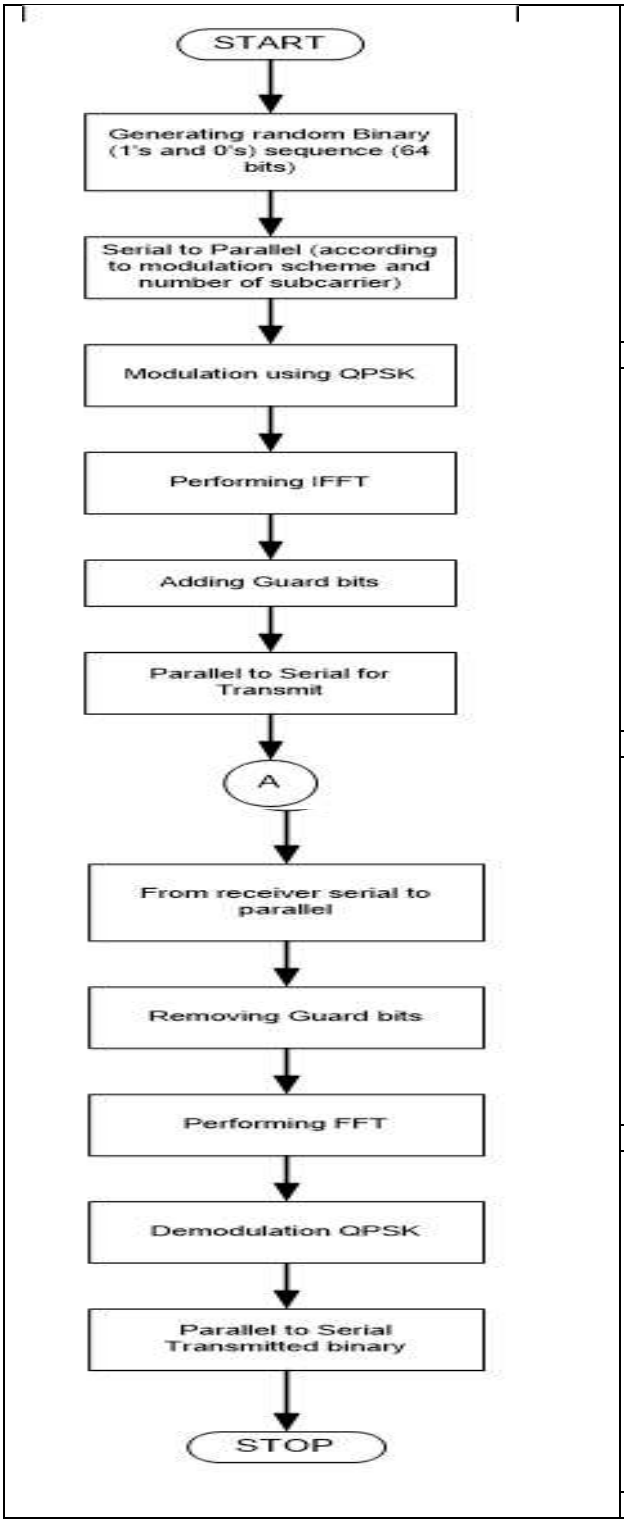

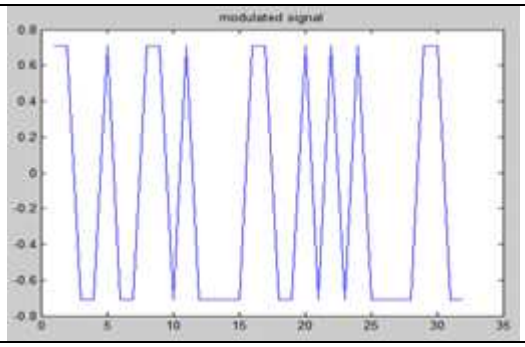

Fig. 5

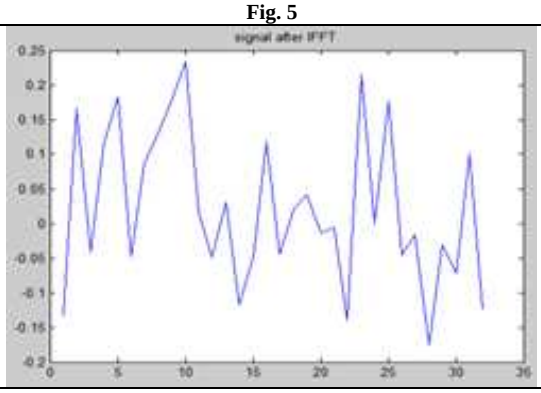

Fig. 6

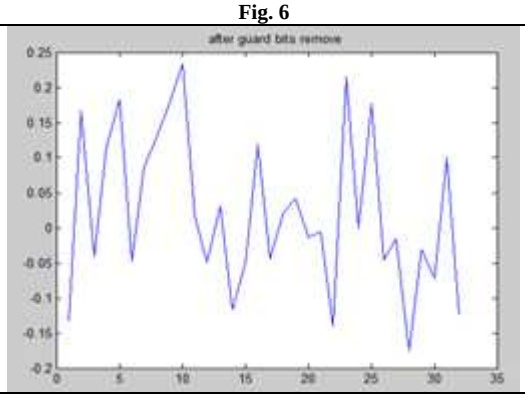

Fig. 7

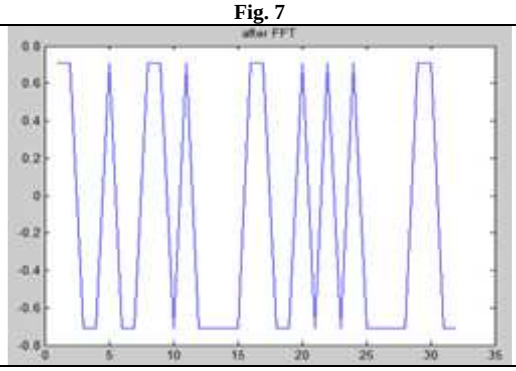

Fig. 8

REFERENCES

[1] Ender Bolat, Study of OFDM Performance over AWGN Channels, Eastern Mediterranean University, Cyprus, 2003.
[2] Simon Haykin *Digital communications*, 4th edition, Mc Graw Hill, India, **2002**.
[3] John G. Proakis *Digital communications*, 5th edition, Pearson, India, **2001.**
[4] OFDM Simulation using MATLAB http://users.ece.gatech.edu/~mai/tutorial/OFDM/Tutorial_web.pdf, **2003**.
[5] SS.Riaz Ahamed, Performance Analysis of OFDM, *Journal of Theoretical and Applied Information Technology***, 1982,** 4, 52-59.

[6] T Schmid and D Cox, Robust Frequency and Timing Synchronization for OFDM, *IEEE Trans.* Comm., **1997**, 45(12), 1613–1621.
[7] H Minn, M Zeng and V Bhargava, On Timing Offset Estimation for OFDM Systems, *IEEE Communication* Letter, **2000**, 4(7), 242–244.
[8] A Awoseyila, C Kasparis and B Evans, Improved Preamble-Aided Timing Estimation for OFDM Systems, IEEE Communication Letters, **2008**, 12(11), 825–827.
[9] C Kasparis and BG Evans, A cross-correlation approach for improved timing estimation in, OFDM broadcasting systems, 24th AIAA International Communications Satellite Systems Conferences (ICSSC), **San Diego, USA, 2006**, 1039–1048.

Heat Treatment Methods Applied To AISI 431 Martensitic Stainless Steels

A.Rajasekhar

Abstract: Martensitic stainless steels are widely used in industrial applications due to their ability to be heat treated to different strength levels, coupled with good corrosion and oxidation resistance. AISI 431 is one of the most potentially attractive steels in this class used extensively for parts requiring a combination of high tensile strength, good toughness and corrosion resistance. However, high alloy content of these steels causes the transformation to be so sluggish, and the hardenability to be so high, that maximum hardness is produced by air cooling. By applying suitable heat treatment procedures, the properties of martensitic stainless steels are greatly modified. This paper reviews the various heat treatment methods applied to AISI 431 martensitic stainless steels and their influence on the microstructure and mechanical properties.

Keywords: Martensitic stainless steel, heat treatment, austenitizing, tempering.

1.0 INTRODUCTION

Martensitic stainless steels occupy a unique status as engineering materials by virtue of their excellent combination of properties such as high strength, adequate ductility, toughness and good corrosion resistance. These steels find extensive application in chemical plants, power generation equipments, in gas turbines as turbine and compressor blades and discs, aircraft engine components and fittings and in marine components [1]. These steels can be heat treated to obtain a wide range of mechanical properties to meet the requirements of specific application [1, 2].

AISI 431 is one of the most potentially attractive steels in this class used extensively for parts requiring a combination of high tensile strength, good toughness and corrosion resistance [3].

Unlike other types of stainless steels, the properties of martensitic stainless steels are greatly modified by normal heat treatment procedures. The heat treating of martensitic stainless steel is essentially the same as for plain-carbon or low-alloy steels, in that maximum strength and hardness depend chiefly on carbon content. However, high alloy content of these steels causes the transformation to be so sluggish, and the hardenability to be so high, that maximum hardness is produced by air cooling.

The various heat treatment methods applied to martensitic stainless steels, in particular to the AISI 431 type steel and their influence on microstructure and mechanical properties, are reviewed in this paper.

Professor, Mech. Engg. St.Marten Engg. College, Kompally, Ranga Reddy, Telangana, India; E-mail: arsekhar06@gmail.com

2.0 AUSTENITIZING

Martensitic stainless steels are normally hardened by heating in the austenitizing range of 925 to 1065^{0}C and then cooled in air or oil. When maximum corrosion resistance and strength are desired, the steel should be austenitized at the high end of the temperature range. For alloys that are to be tempered above 565^{0}C, the low side of the austenitizing range is recommended because it enhances ductility and impact properties.

In structural steels it is observed that higher austenitizing temperatures greater than 900^{0}C can be beneficial to the mechanical properties [4-6]. By high temperature (>1100^{0}C) treatment, coarse alloy carbides can be dissolved completely, and a compositionally homogeneous structure can be achieved [5-6]. However, a very high austenitizing temperature leads to an increase in grain size. Yield strength and fracture toughness (CVN) values increase and DBTT decreases with a decrease in prior austenite grain size [7]. Once a compositionally homogeneous structure is achieved by heat treatments, grain refinement increases the amount of retained austenite. [5] Therefore, double austenitizing, i. e., high temperature austenitizing and quenching followed by low temperature austenitizing, can be applied to obtain the benefits of both treatments. [8]

2.1 Soaking times:

Soaking times employed in the hardening of martensitic stainless steels represent a compromise between achieving maximum solution of chromium-iron carbides for maximum strength and corrosion resistance, and avoiding decarburization, excessive grain growth, retained austenite, brittleness, and quench cracking. For sections of 13 mm thick and under, a soaking time of 30 to 60 min is

sometimes recommended. For most parts, adding 30 min for each additional inch of thickness or fraction thereof has proved adequate. However, soaking times should be doubled if parts to be hardened have been fully annealed or isothermally annealed.

2.2 Quenching.

Because of their high hardenability, martensitic stainless steels can be quenched in either oil or air. These steels may precipitate carbides at grain-boundary areas if heavy sections are cooled slowly through the temperature range of about 870^{0}C to 540^{0}C. Although oil quenching is preferred, air cooling may be required for large or complex sections to prevent distortion or quench cracking.

3. TEMPERING

In the hardened condition, the strength and hardness of martensitic stainless steels are high but the ductility and toughness are low. In order to obtain useful engineering properties, these steels are normally tempered. The tempering temperature range for martensitic stainless steels is normally from 480-750^{0}C. [9] With in this range, the hardness of the martensite decreases as a function of time, with more rapid tempering occurring at higher temperatures. Care must be taken not to temper higher-Cr alloys for excessive times since sigma phase precipitation in the ferrite is possible. This will result in embrittlement of the structure. [9]

4. PROBLEMS IN AISI 431 (16CR-2NI) STEELS

By virtue of its high chromium content, 16Cr-2Ni steel would invariably contain considerable amount of δ-ferrite when cooled to room temperature from liquid metal during solidification or while processing at high temperature [10]. δ-ferrite is known to reduce the transverse ductility [11] and the attainable strength of the steel [12-13]. Angstadt [10] summarized that lower strength is due to interfaces of δ – ferrite with martensitic matrix providing weak paths for crack propagation.

Due to high alloy contents and a significant amount of carbon the 16Cr-2Ni steel requires a high austenitizing temperature to allow carbides to go into solution. This would result in lower Ms and Mf temperatures resulting in retention of high levels of austenite on quenching [12]. It is reported that the steel could retain as high as 20% austenite when quenched from 1060^{0}C [14] which is known to decrease the yield strength [15].

Due to the presence of nickel, the Ac_1 temperature of the steel is low (about 600^{0}C) [16, 14]. Lower Ac_1 imposes a restriction on tempering temperatures since high temperatures could result in re-austenitization [16, 9]. The austenite formed during tempering can transform to martensite on cooling thereby reducing the ductility of the steel. Thus the two problems posed by 16Cr-2Ni steel are (a) formation of δ-ferrite and (b) retention of austenite. Compositional balance and optimum processing parameters are essential requisites to achieve the desired properties.

Table 1 Chemical composition (Wt %) [Brownrigg, 1976]

5. HEAT TREATMENT OF AISI 431 (16CR-2NI) STEELS

Heat No.	C	Si	Mn	P	S	Ni	Cr	N
N9657	0.14	0.35	0.80	0.030	0.024	2.6	16.2	0.032
N9765	0.15	0.41	0.79	0.023	0.026	2.6	15.4	0.035
N9927	0.14	0.27	0.77	0.030	0.029	2.6	15.8	0.032

5.1 Hardening:

Brownrigg [14] and Liu Ning et al. [17] have studied on the heat treatment methods applied to these steels. The composition of the steels chosen for study by Brownrigg and Liu Ning et al are given in Table 1 and 2 respectively.

Table 2 Chemical composition (Wt %) [Liu Ning et al., 1991]

C	Si	Mn	P	S	Cr	Ni
0.16	0.37	0.45	0.025	0.010	16.52	2.25

The austenitization temperature of 16Cr-2Ni steel has been reported typically as 1050^{0}C [Brownrigg, 1976]. Despite the fact that the Ac_1 and Ac_3 temperatures in Brownrigg's study were 607^{0}C and 835^{0}C, the selection of a much higher austenitizing temperature was to allow dissolution of all the carbides in the solid solution. The variation in hardness with increasing austenitizing temperature is shown in Fig. 1. There is a pronounced hardness peak found between 1000^{0}C-1100^{0}C for all the three steels. The increased hardness in this temperature range is explained to be due to carbon enrichment of the austenite resulting in a harder martensite. The lower hardness below 1000^{0}C is due to undissolved carbides resulting in softer martensite. The decrease in hardness above 1100^{0}C was attributed to increased amount of δ-ferrite and / or retained austenite formation.

In the studies carried out by Brownrigg [1976] Heat nos. N 9657 and N 9927 contained varying amounts of δ-ferrite at different austenitization temperatures (Fig.2), which can be attributed to variation in their Cr concentration. δ-ferrite content was found to increase in the steel with increase in austenitizing temperature.

Retained austenite content of only one composition N 9765 (Table 1) has been reported which was less than 2.0% after austenitizing at 1050^{0}C and quenching. Ms temperature reported for the steels N 9765 and N 9657 were 188^{0}C and 162^{0}C respectively.

The volume fraction of all the major phases, as function of austenitization temperature is shown in Fig. 3. [Liu Ning et al., 1991]. The volume fraction of δ-ferrite was not found to change when the austenitizing temperature was less than 1100^{0}C, thereafter it increased with austenitizing temperature. The volume fraction of retained austenite increased with austenitizing temperature between 950^{0}C and 1200^{0}C, while the martensite content decreased.

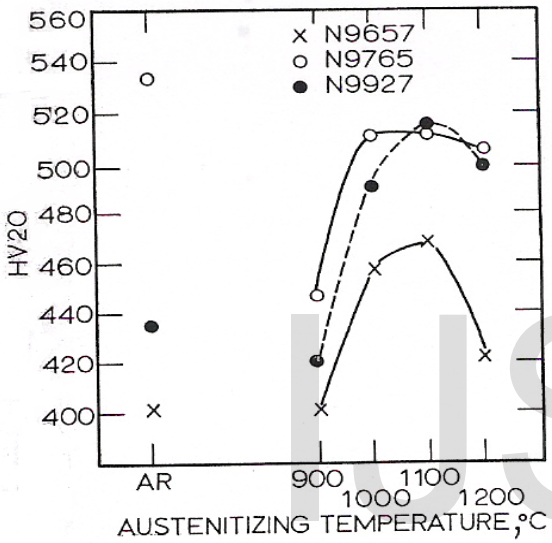

Fig. 1. Variation in hardness as a function of austenitization temperature in as-quenched 16Cr-2Ni steel [Brownrigg, 1976]

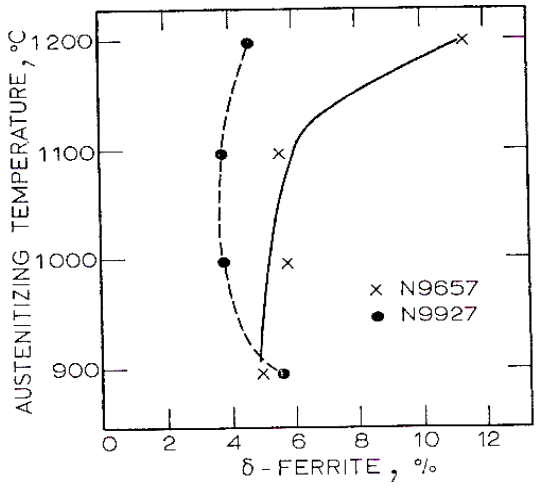

Fig. 2 Volume fraction of major phases as a function of austenitization temperature in 16 Cr-2 Ni steel [Brownrigg, 1976]

Comparing Brownrigg's data [1976] with Liu Ning et al.'s data [1991] it is seen that for a given austenitizing temperature of 1050^{0}C, the δ-ferrite content in Liu Ning et al.'s steel was about 15% whereas it was only 4.7% in Brownrigg's steel.

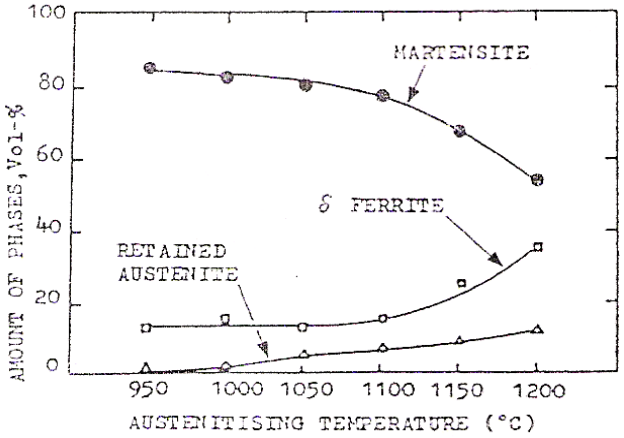

Fig.3 Variation in δ-ferrite content with austenitization temperature for 16Cr-2Ni steel [Liu Ning et al., 1991]

The significant difference could only be attributed to chemical composition of the steels [Table 1 and 2]. In the case of Liu Ning et al., [1991], the steel had about 16.52% Cr whereas the Cr content was only 15.4 to 16% in the steels studied by Brownrigg [1976]. This indicates that increase in chromium content has a marked effect on increase in δ-ferrite content in these steels.

The retained austenite content of Brownrigg's steel N 9765 is relatively less (2%) compared to 7% reported by Liu Ning et al., [1991]. It is also observed from Liu Ning et al.'s [1991] data that retained austenite content increases with increase in austenitizing temperature. At constant austenitizing temperature of 1050^{0}C, the only variable affecting retained austenite content is the composition of the steel. Alloying additions constituted about 19.5% in Brownrigg's steel compared to 19.75% in Liu Ning et al.'s steel. In addition, the individual content of major alloying elements viz., C, Cr and Ni being at similar levels, their individual effects on Ms temperature in case of the steels studied by them is expected to remain the same. Ms temperature reported by Brownrigg is 188^{0}C while Liu Ning et al., have reported it to be 355^{0}C. Thus, there is contradiction on the effect of alloying elements on the Ms temperature, and calls for critical reassessment.

Liu Ning et al. [1991] have reported increase in strength of the steel with increase in austenitizing temperature reaching a peak value at 1100^{0}C; thereafter the strength is found to be decreasing with further increase in austenitizing temperature. The hardness is reported to be 510 HV when austenitized at 1050^{0}C for steel N 9765

[Brownrigg, 1976]. The hardness obtained for the same austenitizing temperature is reported to be about 425 HV (converted from tensile strength value) by Liu Ning et al. [1991]. The difference in hardness reported by the two authors could be attributed to the difference, again, in chemical composition of the steels.

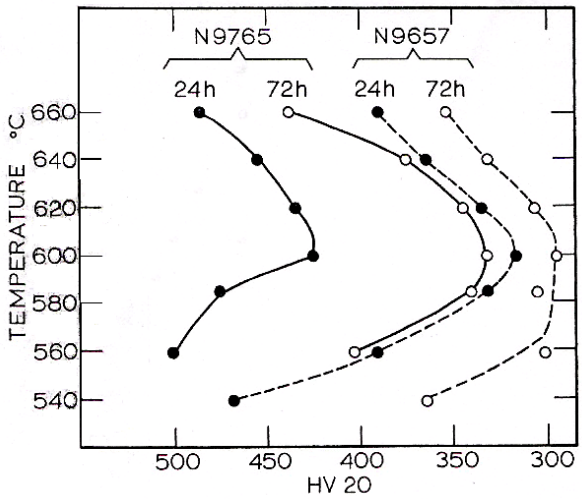

Fig. 4 Kinetics of isothermal softening in 16 Cr- 2Ni steel austenitized at 1050^0C for 30 minutes [Brownrigg, 1976]

Brownrigg's steel contained lower chromium and higher nickel content resulting in lower δ-ferrite content in the microstructure. Liu Ning et al.'s steel contained higher chromium and lower nickel content resulting in about 15% δ-ferrite in the steel. The decrease in hardness could be attributed to lower dissolution of carbides during austenitization coupled with higher amount of δ-ferrite content in Liu Ning et al.'s steel. Whereas higher amount of carbides in solution coupled with negligible amount of δ-ferrite resulted in higher hardness of Brownrigg's steel.

Thus, it can be seen from the studies of Brownrigg [1976] and Liu Ning et al., [1991] that chemical composition plays a major role on the microstructure of 16Cr-2Ni steel for a given heat treatment which influences the mechanical properties. Therefore, a critical control over the chemical composition remains a prime criteria in the alloy design of 16Cr-2Ni steels.

5.2 Isothermal transformation behavior

Isothermal transformation experiments were carried out by Brownrigg [1976] by dilatometry, metallography and hardness measurements. 4 mm disc specimens were austenitized at 1050^0C for 30 minutes and then immediately transferred to lead bath in the temperature range of 540^0C-660^0C. Specimens were removed at different intervals and then characterized.

The experiments showed that there was no $\gamma \rightarrow \alpha$ isothermal transformation and the bulk of the austenite transformed to martensite on cooling to room temperature. The transformation on long holding periods caused carbon depletion of austenite by the reaction-

$$\gamma \rightarrow M_{23}C_6 + \alpha$$

This caused rise in the Ms temperature allowing transformation of γ to martensite. The precipitation showed C-curve kinetics (Fig. 4), with a maximum rate at 600^0C. It was also observed that the alloy which contained some amount of δ-ferrite along with austenite softened more rapidly on isothermal holding compared to the one having only austenite in its microstructure. This was probably due to larger nucleation site available at δ-ferrite/austenite boundaries apart from the prior austenite grain boundaries. Moreover, the δ-ferrite containing steels showed finer prior austenite grain boundaries thereby providing greater nucleation area for the precipitates.

Isothermal transformation of 16% Cr steels has been studied by Castro and Tricot [1974][18] in detail and a comprehensive report has been published which is summarized below.

5.2.1 Decomposition between 950-800^0C:

During isothermal holding of the steel at any temperature between the ranges of 950-800^0C, a fine intergranular precipitation occurs very rapidly at the $\gamma \rightarrow \delta$ and $\delta \rightarrow \delta$ interfaces due to the transformation of δ - ferrite which follows the reaction-

δ-ferrite → $M_{23}C_6$ carbides + γ′ austenite

(the notation ′ is used here only to differentiate this transformation product from the initial austenite). The product $M_{23}C_6$ carbides + γ′ austenite is lamellar and has been called as delta eutectoid or generally as D-aggregate.

Simultaneously outside these areas the regression of the austenite to δ-ferrite takes place by the reaction γ-austenite → δ - ferrite.

The identification of lamellar carbides has shown that these are (Cr, Fe) $_{23}C_6$ with a Cr: Fe ratio of about 2.3. The inter lamellar spacing of the carbides decreases with the isothermal holding temperature. The D-aggregate nucleus forms at grain and phase boundaries and the number of nuclei increases with decreasing temperature. This results in more numerous and finer precipitation of D-aggregate.

5.2.2 Decomposition between 700-550^0C

During short holding periods (1-3 minutes) a very fine and granular precipitation takes place on the boundaries of austenitic areas and edges of γ - δ boundaries which is termed as the G-aggregate

$\gamma \rightarrow$ fine carbides $M_{23}C_6 + \alpha$

The carbides are of the type $(Cr, Fe)_{23}C_6$ with a Cr: Fe ratio of about 1.6 at 650^{0}C. The morphology and position of the G-aggregate indicate the limited diffusion rate of carbon at these temperatures. The growth of this aggregate, of limited extent, ceases after about 10 minutes. The remaining austenite transforms either to ferrite by regression, or an aggregate of a pearlitic nature consisting of Cr_2N and ferrite, which is also called as the nitrogen-pearlite.

$\gamma \rightarrow \alpha$-ferrite and $\gamma \rightarrow Cr_2N$ + ferrite

The pearlitic transformation exhibits all the characteristics of reaction by nucleation and growth.

5.2.3 Decomposition below 550^{0}C

Below 550^{0}C, decomposition is very slow. At 550^{0}C, 24 hours holding produced a fringe of G-aggregate and incipient regression.

5.3 Tempering behavior

The reported data on the variation of mechanical properties with tempering temperature [19-20] are shown in Fig. 5.

The results reported [Harvey, 1982][19] show that there is a drop in tensile strength and hardness up to 300^{0}C tempering beyond which a secondary hardening peak is attained at 450-500^{0}C tempering (Fig.5.a). Whereas, the yield strength more or less remains constant up to 400^{0}C, tempering beyond which causes the yield strength to follow a similar trend as those of hardness and tensile strength. In all the three properties viz., hardness, yield strength and tensile strength, there is a steep fall beyond 500^{0}C and up to 600^{0}C tempering. Between 600-700^{0}C tempering, the properties stabilize. Percentage elongation (%El) shows gradual increase with increasing tempering temperature, while the percentage reduction area (%RA) gradually increases up to 400^{0}C tempering.

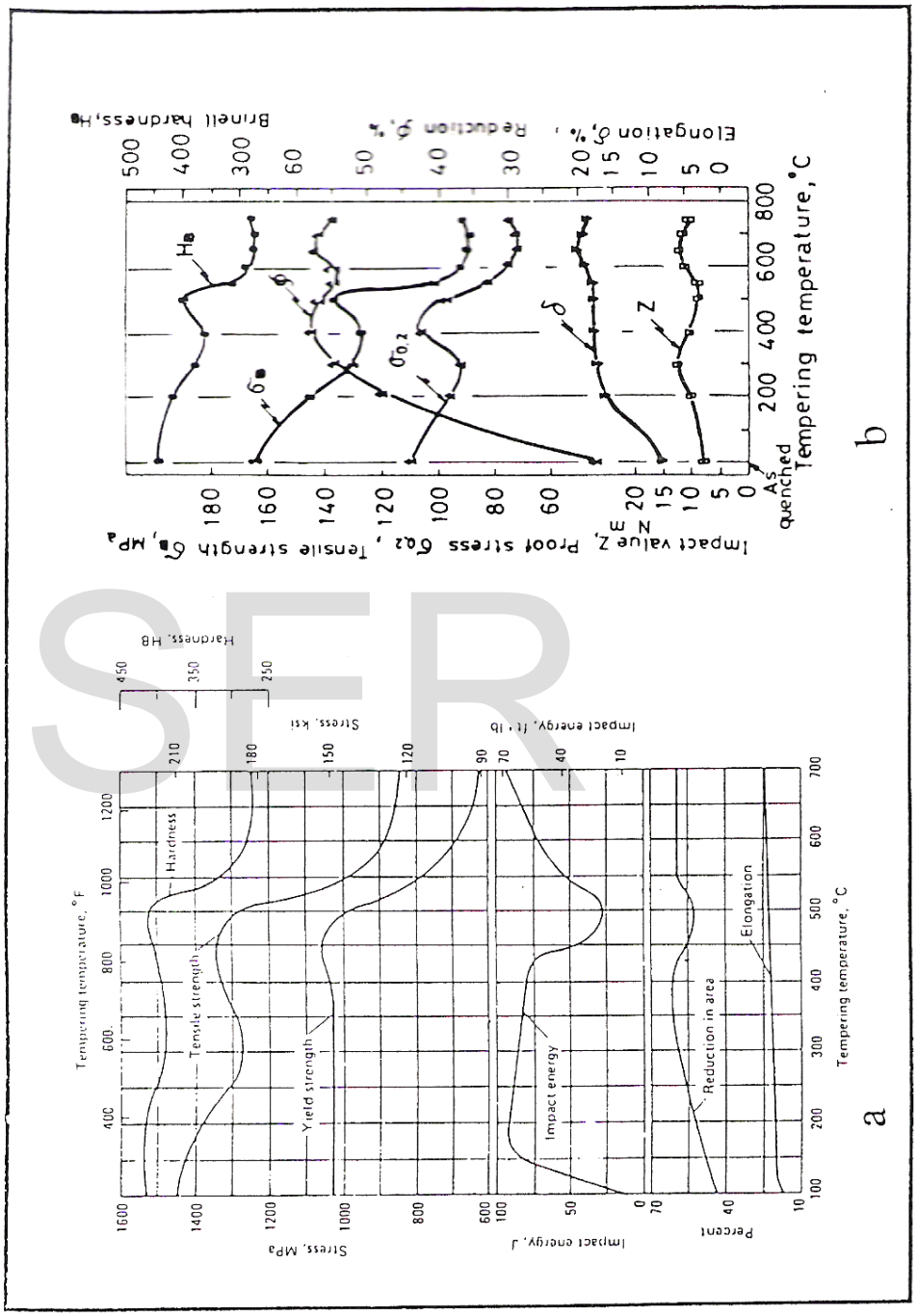

Fig. 5. Effect of tempering temperature on the mechanical properties of 16Cr – 2Ni steel. (a) Harvey[1982], (b) Ogino et al.[1987]

Tempering between 400 to 550^{0}C causes a slight decrease in %RA, beyond which the ductility is restored and remains unchanged when tempered up to 700^{0}C.

The results of Ogino et al. [1987][20] show that hardness, tensile strength and yield strength initially decrease on tempering at all temperatures up to 300^{0}C, after which they increase. The strength parameters reach a peak between 400-500^{0}C. On tempering beyond 500^{0}C, there is a steep fall in strength and hardness up to 600^{0}C tempered

condition. The values more or less stabilize between 600-700^{0}C tempering.

With increase in tempering temperature, %El shows a progressive increase. %RA increases steeply up to tempering temperature 400^{0}C. Tempering between 400 and 600^{0}C causes a dip in %RA, beyond which the ductility gets restored condition. The values more or less stabilize between 600-700^{0}C tempering. With increase in tempering temperature,.

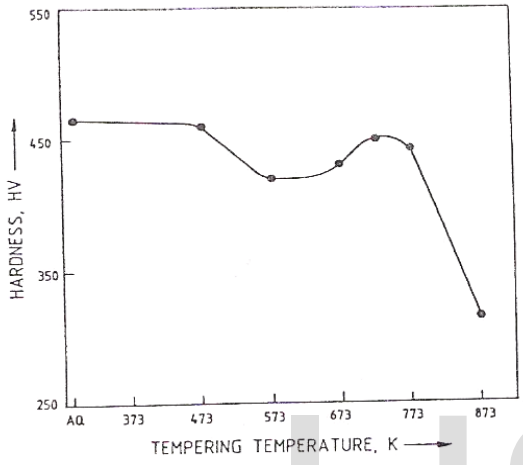

Fig. 6. Variation in hardness with increasing tempering temperature.

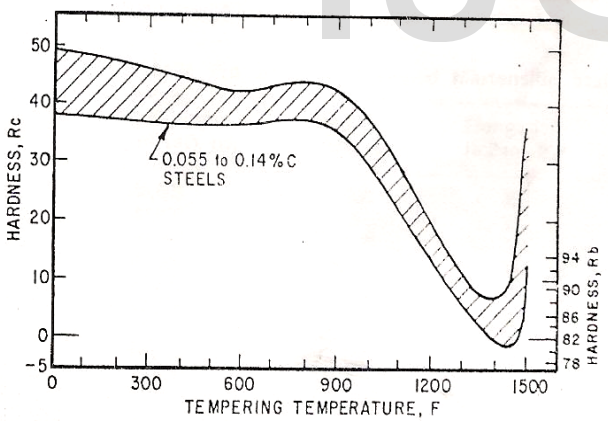

Fig. 7. Effect of tempering temperature (2-hour temper) on the hardness of 12 % Cr steels [Rickett, et. al., 1952]

It is understood from these plots that it is difficult to control the strength between 500-600^{0}C during tempering. Since it is a critical range, tempering within this temperature interval is not practiced [BS 5 S 80, 1976].

The plots in Fig. 5.(a and b) show that the impact energy progressively decreases between 300-500^{0}C temper conditions reaching a minimum at 500^{0}C, beyond which the energy increases. The steel shows poor notch toughness at room temperature when tempered between 300-500^{0}C.

The variation of hardness with increasing tempering temperature for 16%Cr – 2%Ni martensitic stainless steels is shown in Fig. 6 [21]. The graph suggests that as quenched hardness dropped on tempering at 573 K (300^{0}C), secondary hardening occurs when tempered between 673 K-773 K (400 - 500^{0}C) and finally, the hardness decreases sharply on tempering above 773 K (500^{0}C). Similar trends are observed on tempering 12% Cr steels as shown in Fig. 7 [22]. Tempering below 600^{0}C is essentially ineffective in reducing the hardness.

The tempering temperature also has a large influence on the retained austenite content. The variation of retained austenite content with tempering temperature for 16%Cr – 2%Ni martensitic stainless steels is shown in Fig. 8 [21]. The retained austenite content decreases on tempering at 573 K, increases dramatically on tempering between 673-773 K and finally decreases to below 2% on tempering at 873 K.

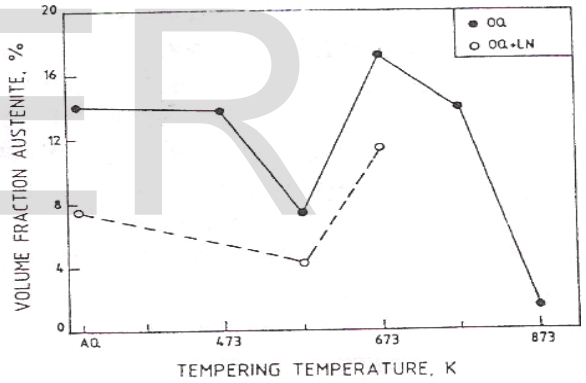

Fig. 8. Variation in austenite content with increasing tempering temperature. [Balan, 1998]

5.4 Temper embrittlement

16Cr-2Ni steel is stated to be susceptible to temper embrittlement between 370-595^{0}C [23]. Although the specification BS 6S80 [1990] has indicated the susceptibility of the steel to temper embrittlement above 350^{0}C, the exact temperature range has not been indicated. In the study carried out by Liu Ning et al. [1991], the author has reported temper embrittlement of the steel on tempering at 550^{0}C. The embrittlement has been manifested in the steel by a minimum in room temperature charpy impact energy and fracture toughness when tempered at 550^{0}C. Typical intergranular fracture of the CVN impact specimen and Auger spectroscopy confirmed the temper embrittlement of the steel following tempering at 550^{0}C. The temper embrittlement was not attributed by the author to either precipitation of fine carbides ($M_{23}C_6$ or M_7C_3) in the

microstructure or to the transformation of retained austenite (as retained austenite transformation was complete on tempering at 500^{0}C).

The embrittlement is believed to be caused by segregation of phosphorus to prior austenite grain boundaries during austenitizing of the steel. The susceptibility of the steel to temper embrittlement is also enhanced by segregation of alloying elements, particularly manganese and chromium, to prior austenite grain boundaries. Apparently the embrittling elements are arranged near the grain boundaries and move to the embrittling configuration only in the temperature range 370^{0}C-565^{0}C. Below about 370^{0}C the mobility of the embrittling elements is restricted and above about 565^{0}C they return to the un-embrittling configuration [24]. Auger spectroscopy confirmed the segregation of Cr, Ni and P on prior austenite grain boundaries during 550^{0}C tempering, which is therefore concluded to be the cause of temper embrittlement of the steel.

6.0 CONCLUSIONS

A comprehensive review of present published information on heat treatment of AISI 431 martensitic stainless steels indicates that the mechanical properties of this material can be greatly modified by careful control of heat treatment methods. The major factors which influence the mechanical properties are formation of delta ferrite and retention of austenite. They can be well addressed by careful selection of austenitising temperatures and tempering temperatures. Further it is noted that the chemical composition has a vital influence on the volume fraction of the phases existing and hence a critical control over the chemical composition remains a prime criteria in the alloy design of 16 Cr-2Ni steels.

References:

1. Brickner, K. G.: Metals Engineering Quarterly, May 1968, 8 (2), 1-29
2. Pickerring, F. B.: International Metals Review No.211, 1976, 227-268
3. Bloom, F.K., "Effect of heat treatment and related factors on straight chromium stainless steels," Corrosion, vol.9, no.2, 1953, p. 56-65
4. Narasimha Rao, B. V., Miller, R. W., and Thomas, G: Proc. 16 th International Heat Treatment Conference, The Materials Society, London, 1976,pp. 75-85.
5. Rao, B. V. N and Thomas, G: Metall.Trans. A, 1980, vol. 11A, pp. 441-457.
6. Lai, G. Y., Wood, W. E., Clark, R. A., Zackay, V. F., and Parker, E. R: Metall.Trans., 1974, vol. 5, pp. 1663-1670
7. Carlson, M., Rao, B. V. N., Ritchie, R. O., and Thomas, G: Proc. International Conf. on Strength of Metals and Alloys, Nancy, France, 1976, vol.5, pp. 509-515.
8. Sarikaya, M., Steinberg, B. G., & Thomas, G: Metall.Trans. A, 1980, vol. 13A, pp. 2227-2237.
9. Lippold, John C. and Damian J.Kotecki, Welding Metallurgy and Weldability of Stainless Steels, A John Wiley & Sons. Inc. Publication, 2005
10. Angstadt, C. C.: Met. Prog. , 1959,75,(6),86
11. Dieter, G. E., "Effect of microstructure and heat treatment on the mechanical properties of AISI type 431 stainless steels," Transactions of ASM, vol.50, 1958, p. 722-737.
12. Sorokin, M. I., Kuikova, M. N., Rubenchik, A. E., Liporoty, V. H and Polonkaya, S. M.: Metallurgy, 1977, vol.12, p 22 (Russian)
13. Pickering, F. B.: 'The Metallurgical Evolution of Stainless Steels', Ed., Pickering, F. B., ASM and The Metals Society of London, 1979, p1
14. Brownrigg, A., Proc. 16th Int. Conf. on 'Heat treatment 76', 86, The Metals Society, Stratford- upon- Avon, (1976).
15. Dieter, G. E., "Effect of microstructure and heat treatment on the mechanical properties of AISI type 431 stainless steels," Transactions of ASM, vol.50, 1958, p. 722-737.
16. Irvine, K. J., Crowe, D. J., and Pickering, F. B.,. J. Iron and steel Inst. 195 (1960) 386
17. Liu Ning, Deng Zhonggang, and Huang Menggen, Material Sc. & Tech., **7**, 1057 (1991).
18. Castro, R., and Tricot, R. 1962. Metallurgie, Part 1, 59: 571-586; Part 2, 59:587-596
19. Harvey, Philip, D., Ed.: Engg. properties of steels, ASM., Metals Park, Ohio, 1982, p 331-357
20. Ogino, Hida, A., and Kishima, S.: "Susceptibility of type 431 stainless steel to erosion-corrosion by vibratory cavitation in corrosive media", Wear, vol. 116, 1987, p 299
21. Balan, K. P., Venugopal Reddy, A and Sarma, D. S., "Austenite precipitation during tempering in 16Cr – 2Ni martensitic stainless steels", Scripta Mater, 1998 vol. 39, No. 7, pp. 901-905.
22. Rickett, R. L., White, W. F., Walton, C. S., and Butler, J. C.: 'Isothermal Transformation, Hardening and Tempering of 12% chromium steel', Trans. ASM, 1952, 44, 138
23. Wei, R. P.: Aerospace Structural Metals Handbook, Code 1404, Beifour Stulen Inc, 1973, p 1
24. Speich, G. R., and Leslie, W. C.: Mater. Trans. A, 1972, 3A, 1043-1052

NOVATEUR PUBLICATIONS
INTERNATIONAL JOURNAL OF INNOVATIONS IN ENGINEERING RESEARCH AND TECHNOLOGY [IJIERT]
ISSN: 2394-3696
VOLUME 2, ISSUE 7, JULY-2015

LPC Models and Different Speech Enhancement Techniques- A Review

Mr. Arjun Ghule
Research Scholar, Department of ECE, J.N.T.U., Hyderabad, India
Dr.Prabhu Benakop
Director, Aurora`s Engineering College, Bongir, Hyderabad, India

Abstract

Author has already published one review paper on the quality enhancement of a speech signal by minimizing the noise. This is a second paper of same series. In last two decades the researchers have taken continuous efforts to reduce the noise signal from the speech signal. This paper comments on, various study carried out and analysis proposals of the researchers for enhancement of the quality of speech signal. Various models, coding, speech quality improvement methods, speaker dependent codebooks, autocorrelation subtraction, speech restoration, producing speech at low bit rates, compression and enhancement are the various aspects of speech enhancement. We have presented the review of all above mentioned technologies in this paper and also willing to examine few of the techniques in order to analyze the factors affecting them in upcoming paper of the series.

Key words: LPC models, coding, speaker dependent codebooks, autocorrelation subtraction, speech restoration, compression and enhancement of speech

Introduction

In last two decades, various models have been developed by the researchers for speech enhancement. Many people have worked for analysis of the models and few others have commented on the advantages and disadvantages of the models. We are writing the review of some models developed and principles used while developing them. The source filter model of speech is widely used for digital coding of speech; the popularity of the LPC method stems from its computational efficiency in determining the synthesis filter parameters [2]. Speech enhancement algorithms that reduce the level of noise present in a speech signal captured in the presence of background noise have several applications [5].

Literature Review

Evangelos E. Milios and Alan V. Oppenheim [1] The work carried out by various researchers has demonstrated the importance of the long-time phase of speech. The possibility of using the long-time phase of the LPC residual signal in speech synthesis is investigated by author.

The importance of the various parts of the long-time spectrum of the residual is also suggested. The potential for synthesizing high-quality speech using the phase-only residual has been demonstrated. It is recommended that coding the long-time phase together with either the

smoothed long-time magnitude alone or the smoothed long-time magnitude augmented by some more accurate low frequency magnitude information.

V. K. Jain, R. Hangartner [2] The introduction of multipulse excitation for LPC coders has increased the quality achievable for digitally coded speech at bit rates in the 9.6 kbs range. A simplified multipulse analysis is proposed with particular prominence on the speech model developed as a result of a two pass method. In the first pass, estimated LPC parameters generated by conventional covariance analysis are used to generate the forward prediction error; the multi—pulse sequence is them detected by thresholding the residual. The second pass generates the final LPC parameters by a covariance analysis incorporating knowledge of the estimated pulse locations and amplitudes along with perceptual synthesis error weighting. Experimental results are presented to demonstrate the method.

Rizwan Ishaq and Begofia Garcia Zapirain [3] The vocal fold modulates the air source from lungs to produce voicing source for speech production. The vocal fold essential part of speech production resides in larynx. The larynx cancer treatment necessitates removal of larynx, in consequences normal speech production destroyed due to no voicing source available. The new voicing source provided artificially or by use of Paryngo-esophageal (PE) segments. The voicing source or residual signal for Esophageal (E) speech uses PE segment, has irregular behavior, and produces degraded quality speech. This paper discussed and evaluated the residual signal or voicing source enhancement of E speech by incorporating speech enhancement method Adaptive Gain Equalizer (AGE), in time frequency and modulation frequency along with formants modification by Line Spectral Frequencies (LSF) and Linear Predicative Coding (LPC). The system validated by measuring Harmonic to Noise Ratio (HNR) temporally and maximum of 4dB enhancement has been observed in comparison to Kalman filtering based enhancement where enhancement observed maximum of 2dB.
The improved HNR has validated the system capability to improve quality of E speech. The system successfully removed noise, as well tried to enhanced residual signal for better and intelligible E speech signal. The MAGE modulation frequency system provides better enhancement in comparison to AGE and overall both systems outperformed Kalman filtering based system [4]. Along with voicing source enhancement, formant enhancement significantly improves quality of E speech in comparison to poles modification by shifting upward [4] when conducted listening test. Although LPC analysis/synthesis provides good estimation of voicing source signal, but as comparison to normal speech this estimation in not perfect and modeling of PE segment can provides better voicing source signal which can be improved and modified through this system. The future can be to provide optimized value of L opt by having noise information from modeling of PE segment.

D. Hanumantha Rao Naidu, G. V. Prabhakara Rao, Sriram Srinivasan [5] Speech enhancement techniques that employ trained codebooks of speech and noise linear predictive coefficients have been previously shown to provide good performance in non stationary noise environments. The speech codebooks are typically trained using data from a large number of speakers. For noise reduction systems in personal devices such as mobile phones, the use of speaker dependent codebooks is appealing as such devices are typically owned by a single user.

It is however not straightforward whether the use of speaker dependent codebooks translates into an observable benefit in terms of noise reduction. Moreover, it is of interest to quantify the improvement obtained over speaker independent codebooks. In this paper, the benefit of using speaker dependent codebooks is analyzed in terms of the resulting improvement in noise reduction when compared to using speaker independent codebooks.

The hypothesis that the use of speaker dependent (SD) codebooks can provide improved performance compared to speaker independent (SI) codebooks when used for speech enhancement has been validated through experimental results. It has been seen that the ability of SD codebooks to better model the spectral shapes corresponding to a particular speaker's data also translates into improvements in noise reduction using a codebook-based speech enhancement method. SD codebooks provide a significant improvement over SI codebooks in terms of all three performance measures considered in this paper: segmental signal-to-noise ratio, log spectral distortion and PESQ scores, and indicate that the benefits justify the added complexity in training the SD codebooks on-line. In fact, depending on the input SNR, it was seen that an SD codebook of half the size of an SI codebook is sufficient to provide a similar level of performance. Reducing the codebook size can significantly reduce the computational complexity of the speech enhancement algorithm. This is desirable as the resulting savings more than compensate for the added complexity in adapting the speech codebooks to the user's voice, which only needs to be done when the user changes. Our results indicate that speaker dependent approaches are promising for applications such as speech enhancement for personal devices, e.g., mobile phones. Future work will extend the investigation to gender and language dependent codebooks. Another interesting extension is when the number of users is larger than one, but limited to a small number. Examples of such applications include VoIP calls on a PC or home telephony systems, where the users could be the members of a family. Future work will investigate the use of one speech codebook per person, where the system automatically determines the appropriate codebook to be used based on the input signal.

C. K. Mn and K. Y. Choi [6] A robust linear predictive coding (LPC) method that can be used in noisy as well as quiet environment has been studied. In this method, noise autocorrelation coefficients are first obtained and updated during non speech periods. Then, the effect of additive noise in the input speech is removed by subtracting values of the noise auto correlation coefficients from those of autocorrelation coefficients of corrupted speech in the course of computation of linear prediction coefficients. When signal-to-noise ratio of the input speech ranges from 0 to 10 dB, a performance improvement of about 5 dB can be gained by using this method. The proposed method is computationally very efficient and requires a small storage area. Authors have studied linear predictive coding in noisy environment and proposed a method to reduced gradation caused by additive white noise. The approach is based on subtraction of autocorrelation coefficients of noise from those of corrupted speech after estimation of noise periodogram during intervals of non-speech activity. By using the proposed method, one can improve the performance of an LPC vo coder by about 5 dB in SNR.

A.B. Premkumar, Ang Eeluang and A. S. Madhukumar[7] Restoration of speech parameters that have been degraded by noisy channel is of paramount importance, since mutilated speech parameters such as Linear Predictive Coefficients may render speech totally irrecoverable. The

objective of this paper is to provide a technique using discrete dyadic wavelet transforms as a preprocessing stage prior to LPC extraction. We show that this step makes the speech parameters more robust to noise perturbation in the channel and hence makes recovery of speech possible. We discuss the effects of applying a single level and a three level transformation to speech prior to compression and compare the quality of recovered speech in both cases. We also apply Wiener filter to the wavelet coefficients and show that the recovered speech is of appreciable quality.

Speech recovery from channel noise has been studied. Recovery has been made possible using DWT techniques. Applying DWT analysis prior to the extraction of LPC parameters and synthesizing speech from the inverse DWT coefficients has proved effective in combating channel noise. This method works well so long as the formant information in speech is not completely destroyed by noise affecting the LPC coefficients

Siva Sushma G, D R Sandeep [8] Over the past several years there has been considerable attention focused on compression and enhancement of speech signals. This interest is progressed towards the development of new techniques capable of producing good quality speech at the output. Speech compression is a process of converting human speech into efficient encoded representations that can be decoded to produce a close approximation of the original signal. In this paper the simulated vo coder (LPC) using mat lab was implemented for compression. The result obtained from LPC was compared with other implemented speech compression using Wavelet transform in terms of quality. Speech enhancement means improving the quality or value of the signal in a noisy environment. In this paper we proposed spectral subtraction (S.S) and wavelet transform methods for de-noising and the result of one method was compared with other. From the results we see that in both compression and enhancement, the performance of wavelet transform was better than other.

In this paper, speech compression using LPC, Wavelets and enhancement using S.S, wavelet transforms was presented. In both compression and enhancement of speech signals using wavelet transforms, we have chosen DB20 wavelet and then the performance was tested and the following points were observed. From the output signals of Lpc, we can observe that the noise in the synthesized files is stronger than in the actual signals, but in wavelets the noisy feeling is low. By this we can say that the signal to noise ratio (as one of the most important measurements of the performance) of the Wavelet transform has high values comparable to LPC and high compression is achieved using wavelet transforms. From the enhancement results, we can observe that the signal to noise ratio of spectral subtraction is low when compared to wavelets. By this we can say, that the spectral subtraction works poorly in de-noising when compared to the wavelets. The analysis that we undertook for wavelets in both compression and enhancement includes only the compactly supported wavelets. An improvement in the performance can be done by studying the effects of other wavelets on compression and enhancement.

Bishnu S. Atal and Joel R. Remde [9] The excitation for LPC speech synthesis usually consists of two separate signals - a delta-function pulse once every pitch period for voiced speech and white noise for unvoiced speech. This manner of representing excitation requires that speech segments be classified accurately into voiced and unvoiced categories and the pitch period of voiced segments be known. it is now well recognized that such a rigid idealization of the vocal

excitation Li often responsible for the unnatural quality associated with synthesized speech. This paper describes a new approach to the excitation problem that does not require a priori knowledge of either the voiced-unvoiced decision or the pitch period. All classes of sounds are generated by exciting the LPC filter with a sequence of pulses; the amplitudes and locations of the pulses are determined using a non-iterative analysis-by-synthesis procedure. This procedure minimizes a perceptual-distance metric representing subjectively-important differences between the waveforms of the original and the synthetic speech signals. The distance metric takes account of the finite-frequency resolution as well as the ditTerential sensitivity of the human ear to errors in the formant and inter-formant regions of the speech spectrum.

Our work on developing a new model of LPC excitation for producing high quality speech is as yet very preliminary. We find that speech quality can be significantly improved by using multi pulse excitation signal. Moreover, the locations and amplitudes of the pulses in the multi-pulse excitation can be determined by using a computationally efficient non-iterative analysis-by synthesis procedure that can minimize the perceptual difference between the natural and the synthetic speech waveforms. The difficult problems of voiced-unvoiced decision and pitch analysis are eliminated.

Conclusion

Author has already published one review paper on the quality enhancement of a speech signal by minimizing the noise. This is a second paper of same series. This paper comments on various models and methodologies of the speech enhancement techniques. The various models proposed by the scholars were working on various factors and the researchers also commented on the methods for improving the performance of the models. All the models are good for various surrounding conditions and there are several factors affecting the performance of each model. We have presented the review of various mentioned technologies in this paper and also willing to examine few of the techniques in order to analyze the factors affecting them in upcoming paper of the series.

References

1] *"The Phase-only Version of the LPC Residual in Speech Coding*"- Evangelos E. Milios and Alan V. Oppenheim, ICASSP 83, BOSTON

2] *"Efficient Algorithm for multi—pulse LPC analysis of speech*", V. K. Jain, R. Hangartner, ICASSP— 84

3] *"Adaptive Gain Equalizer for Improvement of Esophageal Speech",* Rizwan Ishaq and Begofia Garcia Zapirain, 978-1-4673-5604-6/12 ©20 12 IEEE.

4] B. Garcia and A. Mendez, "*Oesophageal speech enhancement using poles stablization and kalman filtering,"* ICASSP, pp. 1597-1600, 2008.

5] *"Speech Enhancement Using Speaker Dependent Codebooks"*, D. Hanumantha Rao Naidu, G. V. Prabhakara Rao, Sriram Srinivasan, 978-1-4577-0274-7/11/©2011 IEEE, DSP 2011.

6] "Improving Lpc Nalysis Of Noisy Speech By Autocorrelation Subtraction Method", C. K. Mn and K. Y. Choi , CH161O-5/81/0000-1082 © 1981 IEEE

7] "Speech Restoration From Lpc Parameters Corrupted By Channel Noise", A. B. Premkumar, Ang Eeluang and A. S. Madhukumar, 1999 IEEE TENCON

8] *"Compression and Enhancement of Speech Signals"*, Siva Sushma G, D R Sandeep, Chennai and Dr.MGR University Second International Conference on Sustainable Energy and Intelligent System (SEISCON 2011) , Dr. M.G.R. University, Maduravoyal, Chennai, Tamil Nadu, India. July. 20-22, 2011.

9] "A New Model Of Lpc Excitation For Producing Natural-Sounding Speech At Low Bit Rates", Bishnu S. Atal and Joel R. Remde, CH 1746-718210000 . 0614 © 1982 IEEE

International Journal of Technical Research and Applications e-ISSN: 2320-8163,
www.ijtra.com Volume 3, Issue 3 (May-June 2015), PP. 280-285

EFFECT OF WELDING PROCESS AND POST WELD HEAT TREATMENTS ON MICROSTRUCTURE AND MECHANICAL PROPERTIES OF AISI 431 MARTENSITIC STAINLESS STEEL

A. Rajasekhar
Professor, Department of Mechanical Engg.,
St. Marten Engineering College
Kompally, R.R., A.P.-509 217, India; E-mail: arsekhar06@gmail.com; Tel: +91 99894 21206

Abstract **- Evaluation of mechanical properties and metallurgical changes, which occur in AISI 431 martensitic stainless steel as a result of the welding processes consisting of electron beam welding (fusion welding) and friction welding (solid state welding) is carried out. In addition, the influence of post weld heat treatments on microstructure and mechanical properties has also been investigated. Weld center in EB welding exhibited a cast dendritic structure with ferrite network in a matrix of un-tempered martensite. In friction welding, the weld center exhibited thermo-mechanical effected structure consists of fine intragranular acicular martensite in equiaxed prior austenite grains. In both the welding processes, post weld tempering treatment resulted in coarsening of the martensite which increases with increase in tempering temperature. In the as-weld condition, both EB and Friction welds exhibited high strength and hardness and poor impact toughness. Increase in impact toughness and decrease in strength and hardness is observed with an increase in tempering temperature. However, high strength and hardness observed in friction welds as compared to EB welds, which may be due to fine grain size of the welds due to thermo-mechanical work the weld undergoes during welding. Low impact toughness is observed in friction welds as compared to EB welds, due to presence of fine grained martensite.**

Key words: **Martensitic stainless steel; Electron beam welding; Friction welding; Tempering temperature; Microstructure; Mechanical properties.**

I. INTRODUCTION

Martensitic stainless steels are widely used when the application requires good tensile strength, creep and fatigue strength in combination with good corrosion resistance. They have been primarily used as structural material in various industry sectors, various parts in steam turbines, gas turbines and petro chemical equipment.

Conventional arc welding characteristics of martensitic stainless steels have been examined by several researchers [1-4]. Though these processes can be employed for welding of martensitic stainless steels, special precautions are necessary to avoid hydrogen cracking and the propensity of forming fine and brittle martensite even in normal air cooling conditions [5].

These steels can be used as structural material and hence focus was thrown to use the material in the as welded condition by reducing the carbon content [1,6]. However, at low carbon levels, the steel becomes fully ferritic which exhibits extensive grain growth in the weld and heat affected zones of fusion welds. Further, the toughness and ductility of these steels welded by conventional welding processes are low and they do not effectively respond to post weld heat treatments due to high ferrite content.

Research is focused to improve toughness in these steels by controlling heat input, employing multi-pass deposition to encourage additional austenite formation and tempering of martensite in the reheated areas [5,7]. Both preheat and post weld heat treatments (PWHT) can be employed to reduce the hardness of these martensitic regions thereby ensuring the structural integrity of the weld region during service. Optimum combination of high strength and high toughness in the steel can only be achieved under carefully controlled heat treatment conditions.

Electron beam welding process has a lower heat input, and hence a greater control is expected over grain coarsening and distortion. Solid state welding process like friction welding due to its slow cooling rate can offer a solution to the problem of low toughness encountered in conventional fusion welding. Hence this study is focused on the metallurgical changes, which occur in AISI 431 martensitic stainless steel as a result of the welding processes consisting of electron beam welding (fusion welding) and friction welding (solid state welding). In addition, the influence of post weld heat treatments on microstructure and mechanical properties has also been investigated.

II. EXPERIMENTAL PROCEDURE

A. Material

The parent material employed in this study is martensitic stainless steel type AISI 431 whose chemical composition is 0.17C-0.6Si-1.0Mn-17.0Cr-2.0Ni-0.03S-0.04P(wt.%). The material was received in the form of 20 mm diameter rods in fully annealed condition.

For preparing welds by electron beam welding, as received rods were forged at 1200^0C into 5 mm thick plates. The forged plates were annealed at 670^0C for 1 hour and air cooled prior to welding.

B. Welding Processes

In the present study, electron beam welding (high power density fusion welding) and continuous drive friction welding (solid state welding) processes are employed.

C. Electron Beam Welding

Autogenous bead on plate full penetration electron beam welds were made in 5mm thick plates of AISI 431 martensitic stainless steel. The welding parameters employed for EB welding are given in Table 1. Initial low power welding has been adopted to preheat the material.

Machine settings/ parameters	
Gun to work distance (mm)	283
Accelerating Voltage (kV)	55
Beam Current (mA)	35 mA (first pass for pre heating) ; 65mA (for penetration)
Focus	Slightly above the surface
Speed (m min^{-1})	1.0
Vacuum level (mbar)	10^{-4} mbar and less
Heat Input (J min^{-1})	214.5

Table 1. Welding parameters for EB welding

D. Friction Welding

Welding was carried out on a continuous drive rotary friction welding machine with continuous variable speed capability up to 2400 rpm. The maximum axial force of the machine was150 KN.

Prior to welding, the mating faces of all the specimens were machined perpendicular to the rotational axis and the samples were degreased with acetone and dried. The weld parameters employed to weld 20 mm diameter rods are: Friction force – 30 kN, Upset force – 50 kN, Rotational speed – 1350 rpm and burn - off –5 mm.

E. Post weld heat treatment (PWHT)

Welded samples were austenitized at 950 ^{0}C for one hour followed by air cooling. The air cooled samples were subsequently subjected to various tempering treatments at 400^{0}C (HT/400), 600^{0}C (HT/600) and double tempering at 670^{0}C + 600^{0}C (HT/DT) for two hours followed by air cooling. For comparison purpose parent metal was also subjected to similar heat treatment.

F. Metallography

The welds were subjected to standard metallographic sample preparation to examine the microstructure under LEITZ optical microscope and stereomicroscope. To observe the microstructure in the etched condition gleseresia (glycerol–15ml, HCl-10ml, HNO_3-5ml, and acetic acid-5 ml) was employed for friction welds and Kallings reagent (cupric chloride-1.5g, HCl-33ml, ethanol-33ml and distilled water-33ml) was employed for EB welds. After different mechanical tests the fractured surfaces were examined under scanning electron microscope (SEM).

G. X-Ray Diffraction

The phases present in the parent metal and welds in various conditions were identified by X-ray diffraction using Philips PW 3020 machine with Cu Kα radiation. Retained austenite (γ_r) content in the welds and parent metal in various heat treated conditions was estimated using Stress Tech 3000 X-ray system using Cr Kα radiation. The volume fraction of austenite was estimated from measurements of the integrated intensities of martensite, austenite and delta ferrite peaks assuming they are the only phases present.

H. Mechanical testing

Tensile strength, hardness and Charpy 'V'-notch impact properties of welds were evaluated. ASTM Standard specimen configurations were employed for tensile and impact testing. Hardness measurements included survey of hardness across the joint interface at the centre.

III. RESULTS AND DISCUSSION

A. Visual examination

Visual examinations of welded joints revealed that, the welds are of high quality and were free from cracks, incomplete bonding and other micro-structural defects.

B. Microstructure and XRD analysis

The transverse sectional view of the welds in the as-welded condition along with micro structural details in the centre and fusion boundary region of EB welds are presented in Fig. 1 and in the centre, mid-radius and periphery regions of friction welds are presented in Fig. 2. EB welds exhibited cast dendritic structure with ferrite network in a matrix of un-tempered martensite (Fig. 3). The as-welded microstructure contains about 10% dark regions within a martensitic matrix. Friction welds in the as-welded condition exhibited thermo mechanical effected structure which consists acicular martensite in equiaxed prior austenite grains at the periphery region, while the central region contains fine intragranular martensite.

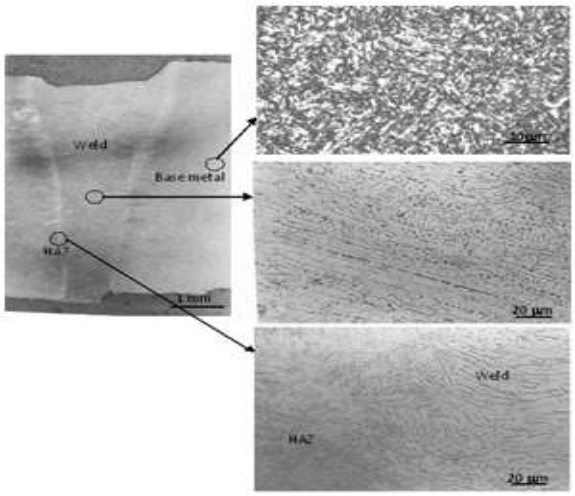

Fig. 1 Electron beam weld and its cross sectional view (as-welded condition)

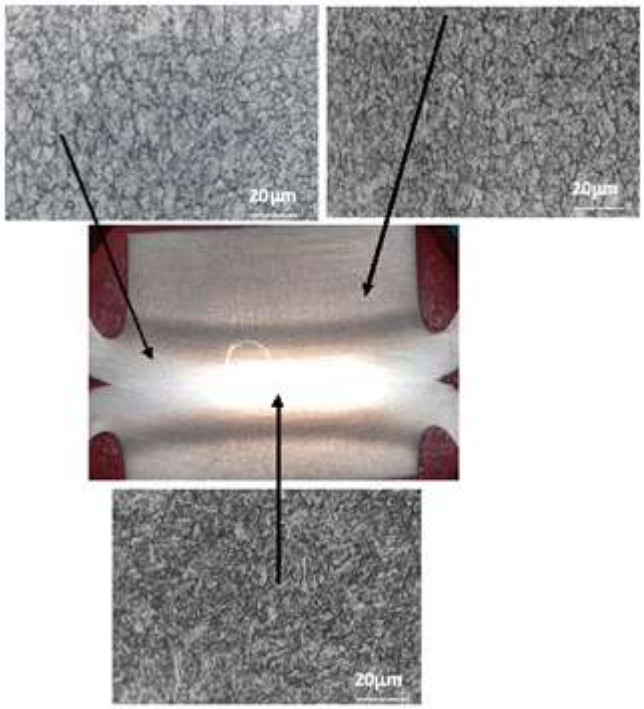

Fig. 2. Friction weld and its cross sectional view (as-welded condition)

The microstructures of the central region of welds in different post weld heat treatment conditions are presented in Fig. 4 (EB welds) and 5 (friction welds). From the figures it is revealed that with heat treatment, dendritic microstructure features in EB welding disappeared. The martensitic microstructure in both EB and friction welds experienced coarsening after heat treatment. The degree of coarsening increased with an increase in the tempering temperature.

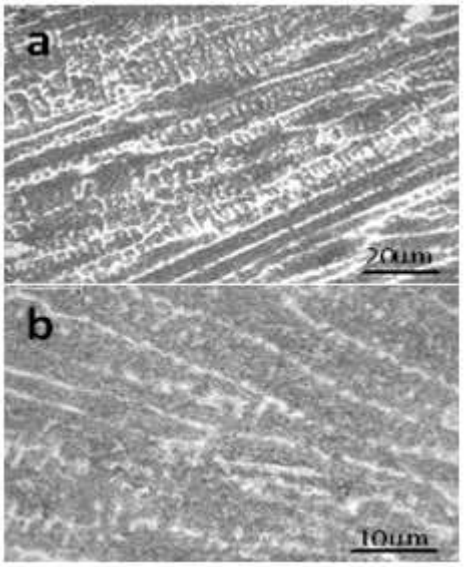

Fig. 3 Optical microstructure of EB welds in as-weld condition. a) 500x b) 1000x

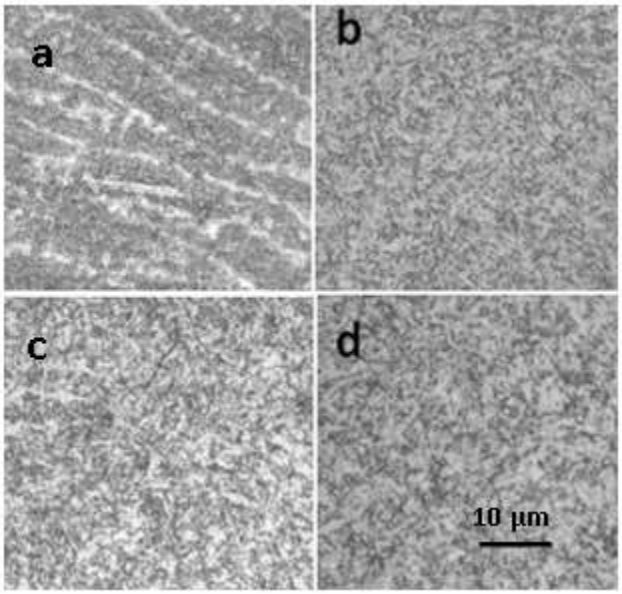

Fig. 4 Optical microstructures of EB welds (central region) (a) As-weld (b) HT/T400 (c) HT/T600 (d) HT/ T (670+600) conditions

Material condition	Phases Present (hkl)		
	Parent Metal	EB welds	Friction welds
As- received	Martensite (110) Austenite (200),(220), (311)		
As-weld		Martensite (110) Austenite (200),(220), (311) Ferrite (200),(221)	Martensite (110) Austenite (200),(220), (311)
HT/400	Martensite (110) Austenite (200),(220), (311)	Martensite (110) Austenite (200),(220) , (311) Ferrite (200),(221)	Martensite (110) Austenite (200),(220), (311)
HT/600	Martensite (110)	Martensite (110) Ferrite (200), (221)	Martensite (110)
HT/DT	Martensite (110)	Martensite (110) Ferrite (200), (221)	Martensite (110)

Table 2. Various phases present in parent metal and weld in different heat treated conditions.

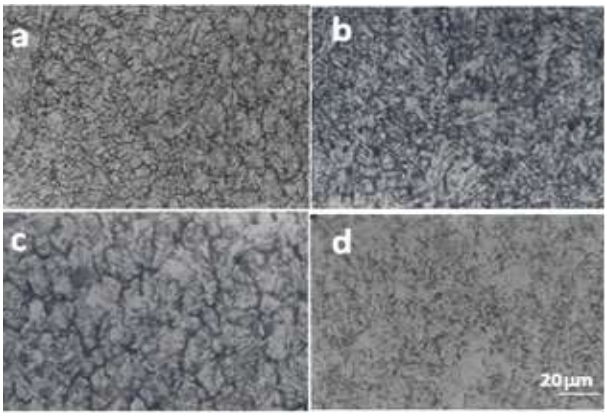

Fig. 5 Optical microstructure of friction welds (central region) (a) as-weld (b) HT/T400 (c) HT/T600 (d) HT/T(670+600) conditions

X-ray diffraction data summarized in Table 2 reveals the presence of delta ferrite and retained austenite along with martensite in EB welds and presence of retained austenite with martensite in friction welds. The effect of post weld heat treatment (PWHT) on the distribution of phases is also evident from the table.

Material condition	0.2 % Yield strength (MP		Ultimate tensi strength (MP		Elongation %	
	EB welds	FW welds	EB welds	FW welds	EB welds	FW welds
As-weld	730	859	1050	996	6.9	12
HT/400	1162	1158	1432	1448	15.3	14
HT/600	794	831	1010	1038	5.0	14
HT/DT	664	749	929	971	6.8	17

Table. 3 Variation in Retained austenite in parent metal and welds in different post weld heat treatments.

The influence of PWHTs on retained austenite is presented in Table 3. It is observed that retained austenite content is high in as weld condition and it is reduced with increase in PWHT. The high austenite percentage in the as weld condition is due to the fact that the welding experiences high temperatures, and at these temperatures carbon exists in the form of solid solution. Carbon is an austenite stabiliser and reduces Ms temperature, as alloying elements which are austenite stabilisers lower Ms temperature. Tempering at 400^0C did not result in significant reduction in retained austenite content. The reduction of retained austenite content in double tempered condition to the level of 2% can be attributed to the transformation of retained austenite to martensite during first tempering and decomposition of this martensite to ferrite and carbides during subsequent low temperature tempering.

C. Hardness

Hardness survey across EB and Friction welds in the as welded and different post weld heat treated conditions are shown in Fig. 6. In the as-welded condition the weld and HAZ regions exhibit higher hardness than the parent metal. The high temperatures experienced in welding allow the carbides to get dissolved and a carbon rich martensite formed that results in higher hardness. Hardness is observed to decrease with PWHT. Hardness reduction is predominant at high tempering temperatures. In HT/DT the hardness of the weld, HAZ and parent metal is equal. Tempering at 400^0C is ineffective in reducing the hardness. Hardness plots reveal that hardness of friction welds is slightly more as compared to EB welds in all the conditions. This may be due to fine grained microstructure of friction welds as compared to EB welds.

D. Tensile properties

The tensile properties of both EB and friction welds in different post weld heat treatments are presented in Table 4. From the results it is observed that in all the conditions, friction welds exhibited higher tensile strengths as compared to EB welds except in as-weld condition. From the elongation data it is observed that EB welds in general have low ductility as compared to friction welds in the corresponding PWHT conditions with the exception of weld in HT/400 condition in that, the EB weld exhibits higher ductility than the friction weld in the same heat treated condition.

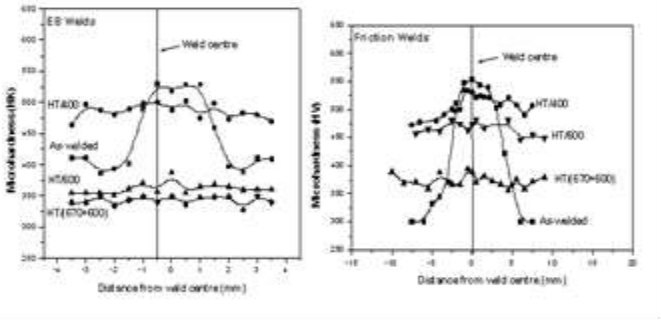

Fig. 6. Micro hardness survey across the weld joint (a) EB weld (b) Friction weld

Material condition	Impact toughness (Joules)	
	EB welds	Friction welds
As-weld	32	4
HT/400	24	15
HT/600	52	45
HT/DT	72	68

Table 4. Tensile properties of EB and friction welds (FW) in different heat treated conditions

Material condition	Retained Austenite (%)		
	Parent metal	EB welds	Friction welds
As-received	16		
As-weld		18	24
HT/400	12	14	18
HT/600	5	8	10
HT/DT	<2	<2	<2

Table 5. Impact properties of EB and Friction welds in different heat treated conditions

High transverse strengths and elongations of friction welds may be due to fine grain microstructure and absence of □-ferrite. Presence of significant amounts of □-ferrite in EB welds resulted in low transverse strength and ductility, and also lower corrosion resistance [8-9]. The high tensile strength in EB welds in as-weld condition as compared to as-welded friction welds is thought to be due to presence of carbon in solid solution which increases the strength and hardness.

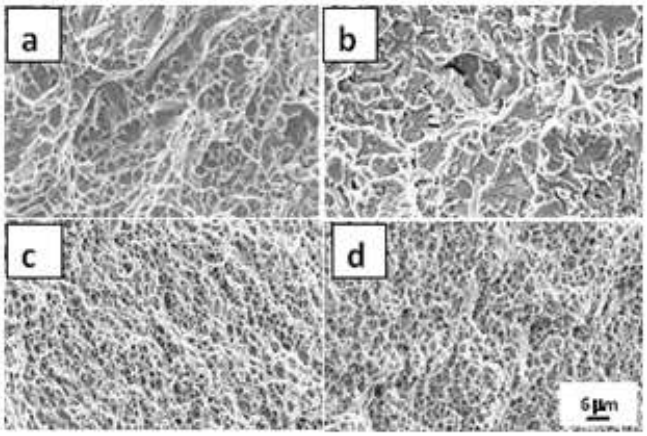

Fig. 7 Fracture features of impact samples of EB welds in various heat treated conditions (a) as-weld (b) HT/T400 (c) HT/T600 (d) H/T(670+600)

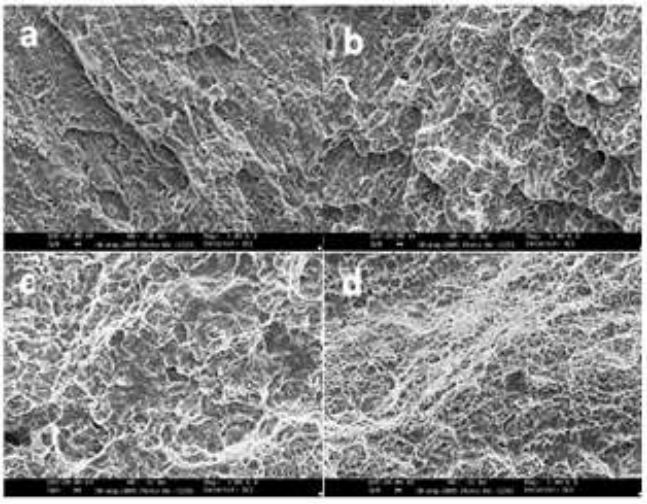

Fig. 8. Fracture features of impact samples of friction welds in various heat treated conditions (a) as-weld (b) HT/ T400 (c) HT/T600 (d) HT/ T(670+600)

E. Impact toughness

The impact properties of EB and friction welds are presented in Table 5. Welds in as-weld condition exhibited lower impact toughness. Post weld heat treatments resulted in improved toughness. The toughness is in the order: HT/DT > HT/600 > HT/400. Double tempering resulted in maximum improvement in toughness. Fractographs presented in Fig. 7 and Fig. 8 suggests that ductile features increased with an improvement in impact toughness. Improvement in toughness was accompanied by a corresponding decrease in hardness and strength which is similar to other engineering metals and alloys [10-19]. Intergranular cracks observed in 400^0C tempered condition suggest that the material experienced temper embrittlement.

The observed reduction in strength and improvement in toughness at high tempering temperatures is thought to be due to tempering of martensite to ferrite and alloy carbides.

Friction welds did not respond to heat treatments as much as EB welds, as revealed from toughness trends. This behaviour could be due to combined effects of fine grain size and aligned microstructural features that developed due to the application of axial pressure in these welds (Fig. 9).

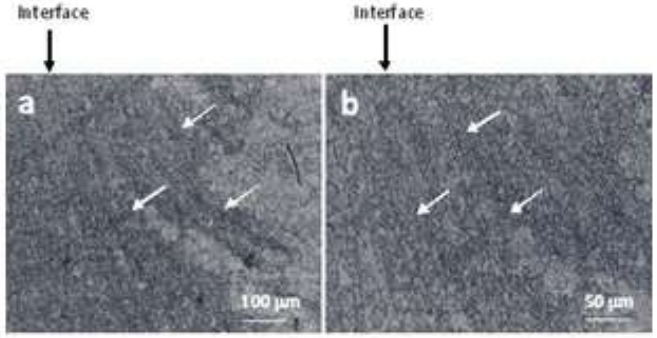

Fig.9. Typical optical micrograph at the interface of the friction weld (as-welded condition) arrow indicates aligned grain structure (a) low magnification (b) higher magnification

IV. CONCLUSIONS

AISI 431 martensitic stainless steel can be successfully welded by both friction welding and electron beam (EB) welding processes.

EB welding resulted a cast dendritic structure which consists of ferrite network in a matrix of un-tempered martensite. In friction welding, the weld centre exhibited thermo-mechanical effected structure consists of fine intragranular acicular martensite in equiaxed prior austenite grains.

Presence of δ-ferrite along with martensite and retained austenite phases is observed in EB welds, where as friction welds resulted only martensite and retained austenite phases.

In all the specimens, martensitic microstructure experienced coarsening when subjected to post weld heat treatments. The degree of coarsening increased with an increase in the tempering temperature.

Hardness of friction welds is slightly more as compared to EB welds in all the conditions due to fine grained microstructure.

EB welds exhibited lower tensile strengths and elongation rates as compared to friction welds due to course grained structure and presence of δ-ferrite.

Poor impact toughness resulted in both the welding processes in as welded condition. Double tempering exhibited better toughness due to coarsening of martensite during PWHT. However, friction welds did not respond to heat treatments as much as EB welds as revealed from toughness trends due to combined effects of fine grain size and aligned microstructural features.

REFERENCES

[1] P.D.Bilmes, M.Solari, C.C. Liorenke: Material Characterization, 2001, **46**, 285 – 296
[2] L.Beres, A.Balogh and W.Irmer: Welding Journal, 80, Aug. (2001), pp 191s-195s.
[3] R.Fenn , M.F.Jordan: Metals Technology , 9, Aug. (1982), pp 327-337
[4] J.E.Ramirez: Welding Journal,.86, May (2007), pp. 125s-134s.
[5] R. Castro and de Cadenet.J.J: Welding Metallurgy of Stainless and Heat Resisting Steels, 56- 57, (1974), Cambridge University Press**,** Cambridge, U.K.
[6] C.G. Kreischer: Welding Journal, 1961, **40** (11) Pages: 489s – 496s
[7] O.M. Akselsen, G. Rorvik, P.E. Kvaale and C. Vander E.J.K: Welding Journal, May 2004, 161s-167s
[8] Angstadt, C. C: Met. Prog. , 1959,75,(6),86
[9] Dieter, G. E.: 'Effect of microstructure and heat treatment on the mechanical properties of AISI type 431 stainless steels', Transactions of ASM, vol.50, 1958, p. 722-737.
[10] G. Madhusudhan Reddy and T. Mohandas: Proc. on Symp. on 'Joining of materials', Welding Research Institute, Bharat Heavy Electricals Ltd. Tiruchirappalli, India, July.2004, WMA2
[11] K. Yoshikawa, T. Mizoguchi, S. Ohta and E. Sato: Journal of Society of Material Science, Japan, 1982, **231**, 265-272
[12] Y. Kawabe, S. Muneki and J. Takahashi: Journal of Iron and Steel Institute, Japan, 1983, **69**, 145-151
[13] E. Breslaner and A. Rosen: Material Science and Technology, May 1991, 7 (1-6), 441-446
[14] M. Ninomi, I. Inagahi and T. Kobayashi: Materials Science and Technology, Sep 1988, **4** (7-12), 803 – 810
[15] V.V. Satyanarayana, G. Madhusudhan Reddy, T. Mohandas and G. Venkata Rao: Science and Technology of Welding and Joining, 2003, **8** (3),184-193
[16] M. Niinomi, T. Kobayashi and N. Sasaki: Material Science and Engineering, 1988, **100**, 45 - 55 [16]
[17] G. Madhusudhan Reddy and T. Mohandas: Proc.on Int. Welding Symposium (IWS 2K5), Hyderabad, India, February, 2005, WP 16
[18] G. Madhusudhan Reddy and T. Mohandas: Proc. Int. Welding Symposium (IWS 2K5), Hyderabad, India, February, 2005, WM 01
[19] T. Mohandas, M.S. Kulkarni, G. Madhusudhan Reddy: 'Welding studies on a super-duplex stainless steel', DMRL TR 2003 338, Defence Metallurgical Research Laboratory Hyderabad, India, August 2003, 1-34

Available online at www.sciencedirect.com

ScienceDirect

J Materiomics 1 (2015) 348–356

www.ceramsoc.com/en/

www.journals.elsevier.com/journal-of-materiomics/

Electrical transport properties of nano crystalline Li–Ni ferrites

G. Aravind [a], M. Raghasudha [b,*], D. Ravinder [a]

[a] Department of Physics, Osmania University, Hyderabad, 500 007, Telangana, India
[b] Department of Chemistry, Jayaprakash Narayan College of Engineering, Mahabubnagar, 509001, Telangana, India

Received 18 April 2015; revised 18 September 2015; accepted 19 September 2015
Available online 14 October 2015

Abstract

Nickel substituted lithium nano ferrites with the chemical composition $Li_{0.5-0.5x}Ni_xFe_{2.5-0.5x}O_4$ ($0.0 \leq x \leq 1.0$) were prepared by Citrate-gel method. The single phase cubic spinel structure of the ferrites was confirmed by X-ray diffraction analysis. Surface morphology and particle size of the samples was studied using Transmission Electron Microscopy (TEM). The TEM micrographs reveal that the particle size of the samples was in the nanometric range confirming the nano crystalline nature. The FTIR spectra shows the two significant absorption bands in the wave number range of 400–600 cm^{-1} arising due to the inter-atomic vibrations in the tetrahedral and octahedral coordination compounds. The dielectric parameters like dielectric constant (ε'), dielectric loss tangent (tan δ) and AC conductivity (σ_{ac}) of the samples were measured using LCR meter at room temperature in the frequency range 20 Hz–2 MHz ε', tan δ and σ_{ac} of the samples show a normal dielectric behavior of ferrites with frequency which indicates the fact that the dielectric dispersion is due to the hopping of electrons between the Fe^{2+} and Fe^{3+} ions. Thermo Electric Power (TEP) studies of Li–Ni ferrites were measured using differential method in the temperature range of 473–873 K. Seebeck coefficient (S) of the prepared ferrites was increased with increasing temperature.

Keywords: Ferrites; Citrate gel method; X-ray diffraction; Dielectric behavior; Thermo electric power

1. Introduction

Ferro-spinels have interesting structural, electrical and magnetic properties. They are widely used in many important applications such as microwave devices like circulators, phase shifters, memory cores, magnetic recording media, transformers, choke coils, high frequency instruments, data storage, noise filters and recording heads, owing to their high magnetic permeability and low magnetic loss [1]. The usefulness of a ferrite material for microwave devices is influenced by physical and chemical properties which in turn depend on the method of preparation [2]. For obtaining the required properties, selection of the ferrite composition and nature of substituent ion is most important besides sintering temperature and time. The valence state of doping ions in the selected ferrite composition influences the structural, electrical and magnetic properties of ferrite material.

Ferrite materials are low mobility semiconducting iron oxides. Unlike most materials, they possess high permeability and moderate permittivity at different frequencies. Due to their small eddy current losses, they possess wide range of electronic applications in terms of energy production, transmission and telecommunication applications. At present, 'nano ferrites' has been the subject of many scientists all over the world because of novel properties exhibited by nano-particles. The properties of bulk material vary drastically when their size approaches the nano-scale [3]. In ferrites, grain size reduction and grain boundary modifications results in high frequency properties such as resistivity and quality factors. Smaller grain size will provide large number of grain boundaries as barriers for the electron hopping between the different ions so as to increase the resistivity and decrease the eddy current losses in ferrites [4].

* Corresponding author. +919550083100 (mobile).
E-mail address: raghasudha_m@yahoo.co.in (M. Raghasudha).
Peer review under responsibility of The Chinese Ceramic Society.

http://dx.doi.org/10.1016/j.jmat.2015.09.003

Lithium ferrites and substituted Lithium ferrites have become most attractive materials for microwave applications especially as a replacement for garnets. Mixed lithium ferrites have low cost, square hysteresis loop, high Curie temperature that make them promising materials for microwave applications [5–7].

Nano-crystalline ferrite materials can be synthesized by various preparation techniques including glass-ceramic method [8], hydrothermal method [9], sol–gel method [10], co-precipitation method [11], and citrate-gel method [12]. Many scientists have studied the frequency dependence on the dielectric properties of Li–Co [13], Li–Mg [14], Li–Ge [15]. Among the various preparation methods citrate-gel auto-combustion method has attracted the attention of solid state chemist, physicist and material scientist etc. due to the fact that the product with high purity, good homogeneity and low particle size can be obtained. This is because the mixing of constituent cations takes place on atomic scale in the precursor itself, thereby lowering the sintering temperature during the formation of required ferrites. Moreover, novel properties for the product were observed in this method of preparation [16]. Some authors have synthesized nickel substituted lithium ferrites by ceramic method with high sintering temperature [17]. However, there is no detail report on Ni substituted Lithium nano ferrites prepared by citrate-gel auto combustion method with low sintering temperature.

In the present work, the authors report the structural properties of Li–Ni nano crystalline ferrites with XRD, TEM and FTIR analysis with the detailed investigation of the composition. Frequency dependence of the dielectric properties and thermo electric power studies of the samples with the results were discussed.

2. Experimental

Ni substituted Lithium ferrites with compositional formula $Li_{0.5-0.5x}Ni_xFe_{2.5-0.5x}O_4$ (where x = 0.0 to 1.0) with a step increment of 0.2 have been prepared by low temperature citrate gel auto combustion method with the following raw materials as starting chemicals:

(i) Ferric nitrate ($Fe(NO_3)_2 9H_2O$)
(ii) Nickel nitrate ($Ni(NO_3)_2 6H_2O$)
(iii) Lithium nitrate ($LiNO_3$)
(iv) Citric acid ($C_6H_8O_7 \cdot H_2O$) and Ammonia solution (NH_3).

The detailed procedure for the preparation of ferrites by citrate-gel auto-combustion method was explained in our earlier publication [18]. The synthesized powders were sintered at 500 °C for 4 h in air at a slow heating rate of 5 °C/min and then furnace cooled. X-ray diffraction analysis of the prepared ferrite powders were performed by using Philips X-ray diffractometer with Cu K_α radiation of wavelength 1.5405 A°. The average crystallite size of the ferrites was determined from the measured width of their diffraction pattern using the Debye Scherer's formula

$$D = \frac{0.91\lambda}{\beta \cos\theta} \quad (1)$$

Where λ-the wavelength of the x-ray used for diffraction,

β – full width half maximum (FWHM) in radians.
θ – diffraction angle.

The lattice constant 'a' was calculated using the following relation

$$a = d\left(h^2 + k^2 + l^2\right)^{1/2} \quad (2)$$

where d-inter planar distance, hkl-miller indices

Hopping length for tetrahedral site (d_A) and octahedral site (d_B) can be calculated using

$$d_A = 0.25a\sqrt{3}A^0 \quad \& \quad d_B = 0.25a\sqrt{2}A^0 \quad (3)$$

The morphology of prepared ferrites was investigated using Transmission Electron Microscopy with a JEOL 2000 electron microscope operating at 200 kV.

The FTIR spectra of the ferrite samples as pellets in KBr were recorded by SHIMADZU FTIR spectrophotometer in the frequency range of 400–600 cm^{-1}

For the thermo electric power measurements, the synthesized powders were made in the form of circular pellets (diameter – 13 mm and thickness – 2 mm) using 2% polyvinyl alcohol (PVA) as binder under a pressure of 5 tons for 1–2 min. These pellets were finally sintered at 500 °C for 4 h and then slowly cooled to room temperature. Pellets were then coated on either side with a thin layer of silver paste to have good electrical contact.

Agilent E4980A Precision LCR meter was used for the dielectric measurements of the prepared pellets by using bellow formulae [19,20].

$$\text{Real part of dielectric constant } (\varepsilon') = C\,d/A\,\varepsilon_0 \quad (4)$$

$$\text{Imaginary part of dielectric constant } \varepsilon'' = (\varepsilon')\tan\delta \quad (5)$$

$$\text{AC conductivity} \quad \sigma_{ac} = 2\pi f\,\varepsilon_o(\varepsilon')\tan\delta \quad (6)$$

Where C – capacitance of the pellet in faraday

$\tan\delta$ – dielectric loss tangent.
ε_0 – permittivity of free space = 8.85×10^{-12} F/m
f – frequency

Thermo electric power measurement studies on the prepared pellets were carried out by differential method from 320 K to well beyond Curie temperature. The pellet was kept between the hot and cold junctions of the method. The temperature difference between two ends of the sample was kept at 10 K throughout the measured temperature range. The thermo emf was produced across the sample as the charge carriers (electrons or holes) diffused from the hot junction to the cold junction due to the temperature gradient ΔT in degree Kelvin maintained across the sample.

The thermo electric power or Seebeck coefficient (S or α) was calculated using the following relation [21].

$$S = \frac{\Delta E}{\Delta T}(\mu V/K) \quad (7)$$

where ΔE is the thermo electro motive force produced across the two ends of the sample which is measured by using a digital micro voltmeter and the ΔT is the temperature difference between the two surfaces of the pellet which is measured by two chromel-alumel thermocouples that were kept very close to the sample. For achieving good thermal stability, thermo emf values were measured while cooling.

The carrier concentration values of the prepared samples were calculated using the following relation

$$n = Ne^{(-Se/K)} \quad (8)$$

where N – concentration of electronic levels involved in the conduction process

S – Seebeck coefficient
e – electron charge, K – Boltzmann constant.

Ferrites are low mobility semiconductors having exceedingly narrow bands or localized levels, so value of N can be taken as 10^{22}/mL [22].

3. Results and discussions

3.1. X-ray diffraction analysis

The X-ray diffraction pattern of the prepared Ni substituted Lithium nano ferrites were shown in Fig. 1.

The diffraction patterns confirmed the well defined homogeneous single phase cubic spinel structure of the samples without any impurity peak belonging to the space group $P4_332$ (confirmed by JCPDS No.88-0671).

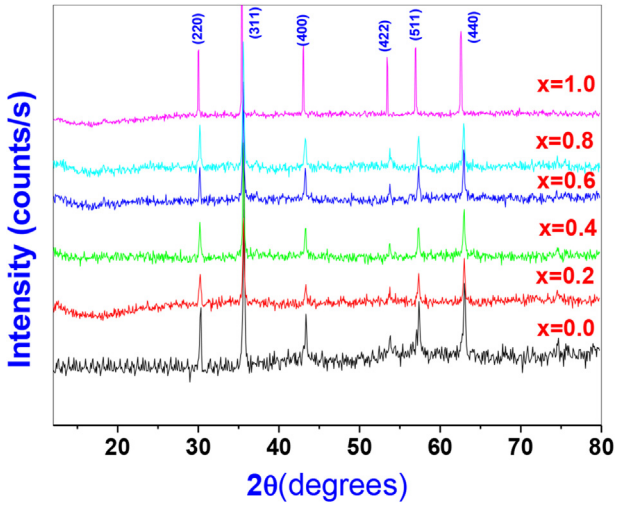

Fig. 1. XRD pattern of the nano crystalline $Li_{0.5-0.5x}Ni_xFe_{2.5-0.5x}O_4$ ferrites.

Table 1
Lattice parameter, Crystallite size and hoping length for $Li_{0.5-0.5x}Ni_xFe_{2.5-0.5x}O_4$ ferrites.

Ferrite composition	Lattice parameter (Å)	Crystallite size (nm)	Hopping length	
			A-site (d_A)	B-site (d_A)
$Li_{0.5}Fe_{2.5}O_4$	8.356	41.90	3.618	2.953
$Li_{0.4}Ni_{0.2}Fe_{2.4}O_4$	8.356	39.54	3.618	2.954
$Li_{0.3}Ni_{0.4}Fe_{2.3}O_4$	8.358	45.35	3.619	2.954
$Li_{0.2}Ni_{0.6}Fe_{2.2}O_4$	8.361	49.90	3.620	2.955
$Li_{0.1}Ni_{0.8}Fe_{2.1}O_4$	8.368	41.30	3.623	2.958
$NiFe_2O_4$	8.374	43.01	3.626	2.960

All the diffraction peaks were indexed as (220), (311), (400), (422), (511) and (440) that confirm the pure spinel phase of the prepared ferrites. Crystallite size of the prepared samples measured from the X-ray analysis by Debye Scherer's formula was in the range of 39–49 nm as shown in Table 1. From the table it is clear that with increase in Ni composition in the Li–Ni ferrites, Lattice parameter of the prepared samples was increased. This was expected because six fold co-ordinated ionic radius of the Ni^{2+} (0.78 Å) was greater than the six fold co-ordinated ionic radii of the Li^+ (0.76 Å) and Fe^{3+}(0.67 Å) ions.

Hopping length of A-site and B-site was observed to be increased with increase in the Ni composition. This is because, hopping length of the sites were directly proportional to the lattice parameters of the samples. The variation of lattice parameter (Å) and hopping length of A-site with Ni compositions were shown in Fig. 2a and b respectively.

3.2. FTIR spectral analysis

The FTIR spectra of nickel substituted lithium ferrites measured in the frequency range of 400 cm^{-1}–600 cm^{-1} were shown in Fig. 3. From the figures, it is noticeable that the two main absorption bands appeared common in almost all spinel ferrites of the ferrite system under investigation. These absorption bands are observed around 600 cm^{-1} and 400 cm^{-1} respectively and are summarized in Table 2. These bands correspond to the stretching vibrations of tetrahedral (A) (ν_1) and octahedral (B) (ν_2) sites respectively which represent the characteristic feature of single phased spinel ferrites [23].

The observed larger ν_1 values of the prepared ferrites compared to the ν_2 values indicates the normal mode of vibration in these ferrites. This is because of shorter bond length of A-site compared to that of B site. In Li–Ni ferrites, an absorption band ν_3 was observed for $x < 0.6$, the values of which are summarized in Table 2. According to Tarte [24], the recorded band ν_3 indicates the presence of Li–O complexes on the octahedral sites. The intensity of this band goes on decreasing with increase in the nickel substitution in the system. This is because, Li^+ content decrease with increase in x, so it persists only up to $x = 0.6$ and then it completely disappears [25]. The shift occurred in the absorption band ν_1, ν_2 for each A and B sites are due to the perturbation occurring in the Fe–O band by introducing Ni composition in the Li–Ni mixed ferrites.

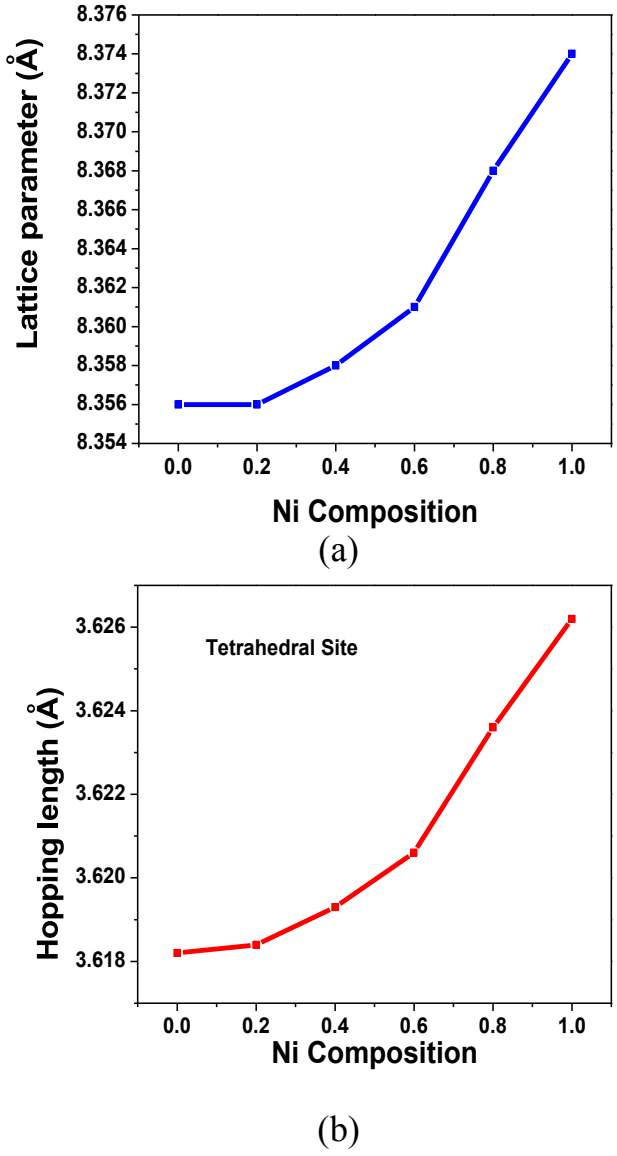

Fig. 2. a. Variation of lattice constant of $Li_{0.5-0.5x}Ni_xFe_{2.5-0.5x}O_4$ ferrites with Ni composition. b. Variation of hopping length of A site (d_A) of $Li_{0.5-0.5x}Ni_xFe_{2.5-0.5x}O_4$ ferrites with Ni composition.

From Table 2, one can observe that the tetrahedral vibrational band (ν_1) appeared in the range of 549–552 cm^{-1}, octahedral vibrational band (ν_2) in the range of 414–430 cm^{-1} and Li–O band (ν_3) in the range of 444–458 cm^{-1}.

3.3. TEM analysis of Li–Ni ferrites

The particle size, shape and size distribution are important morphological characteristics for a nano scaled material [26]. Transmission electron microscopy (TEM) provides a direct information about these characteristics. TEM micrographs of the prepared Li–Ni ferrite samples annealed at 500 °C for 4 h are shown in Fig. 4 which are nearly spherical in shape. The average particle size observed from the TEM micrographs suggests the formation of single crystals [27].

3.4. Dielectric properties

The dielectric properties of the ferrites depends on the several factors including method of preparation, sintering time, sintering temperature, particle size, type and amount of substitution, etc. Dielectric parameters at room temperature in the frequency range of 20 Hz–2 MHz were calculated using the relations 4, 5, 6. The frequency dependence of real part of dielectric constant (ε') and imaginary part of dielectric constant (ε'') at room temperature were shown in Fig. 5 (a) and (b). From the figures, it is clear that the value of ε' and ε'' decreases continuously with increasing frequency. After certain frequency, the dielectric parameters do not change with frequency i.e. become independent of frequency. This fact shows a normal behavior of ferromagnetic materials.

The variation of dielectric constant with frequency may be explained on the basis of space-charge polarization phenomenon [28]. According to this, dielectric material has well conducting grains separated by highly resistive grain boundaries. On the application of electric field, space charge accumulates at the grain boundaries and voltage drops mainly at grain boundaries [29]. Koops proposed that grain boundary affect is more at low frequencies [29]. As the frequency increased beyond a certain limit the electron exchange between Fe^{2+} and Fe^{3+} ions does not follow the variations in applied field, so the value of dielectric constant becomes constant.

The variation in the dielectric parameters with frequency in ferrites was through a mechanism similar to the conduction process [30]. The electron exchange between Fe^{2+} and Fe^{3+} ions results in local displacement of electrons in the direction of applied field that determines polarization. The Polarization decreases with increasing frequency, and then reaches a constant value. It is due the fact that beyond a certain frequency of external field, the electron exchange $Fe^{2+} \leftrightarrow Fe^{3+}$ cannot follow the alternating field. The high value of dielectric constant at lower frequency is due to the predominance of the species like Fe^{2+} ions, oxygen vacancies, grain boundary defects, etc [31] while the decrease in dielectric constant with frequency is natural, i.e. any species contributing to the polarizability is found to show the applied field lagging behind at higher frequencies [32]. Hence, the electron conduction mechanism can be explained by electron hopping between the same element having the different ionic states (Fe^{3+}/Fe^{2+} and Ni^{2+}/Ni^{+}) [33].

Variation of loss tangent of the material with frequency was shown in Fig. 6. From the figure, it is observed that tan δ decrease with increase in frequency and the values were very small at high frequencies. Hence, these materials are desirable for high frequency microwave device applications. The variation of dielectric constant of Li–Ni nano ferrites with Ni composition was shown in Fig. 7. From the figure, it is observed that room temperature dielectric constant decreased with increase in Ni concentration after an initial rise of Ni concentration from 0.0 to 0.2. It is seen that as Ni content is increased there is a decrease in the Fe^{3+} ions at the B-sites thereby decreasing the hopping of electrons, that results in

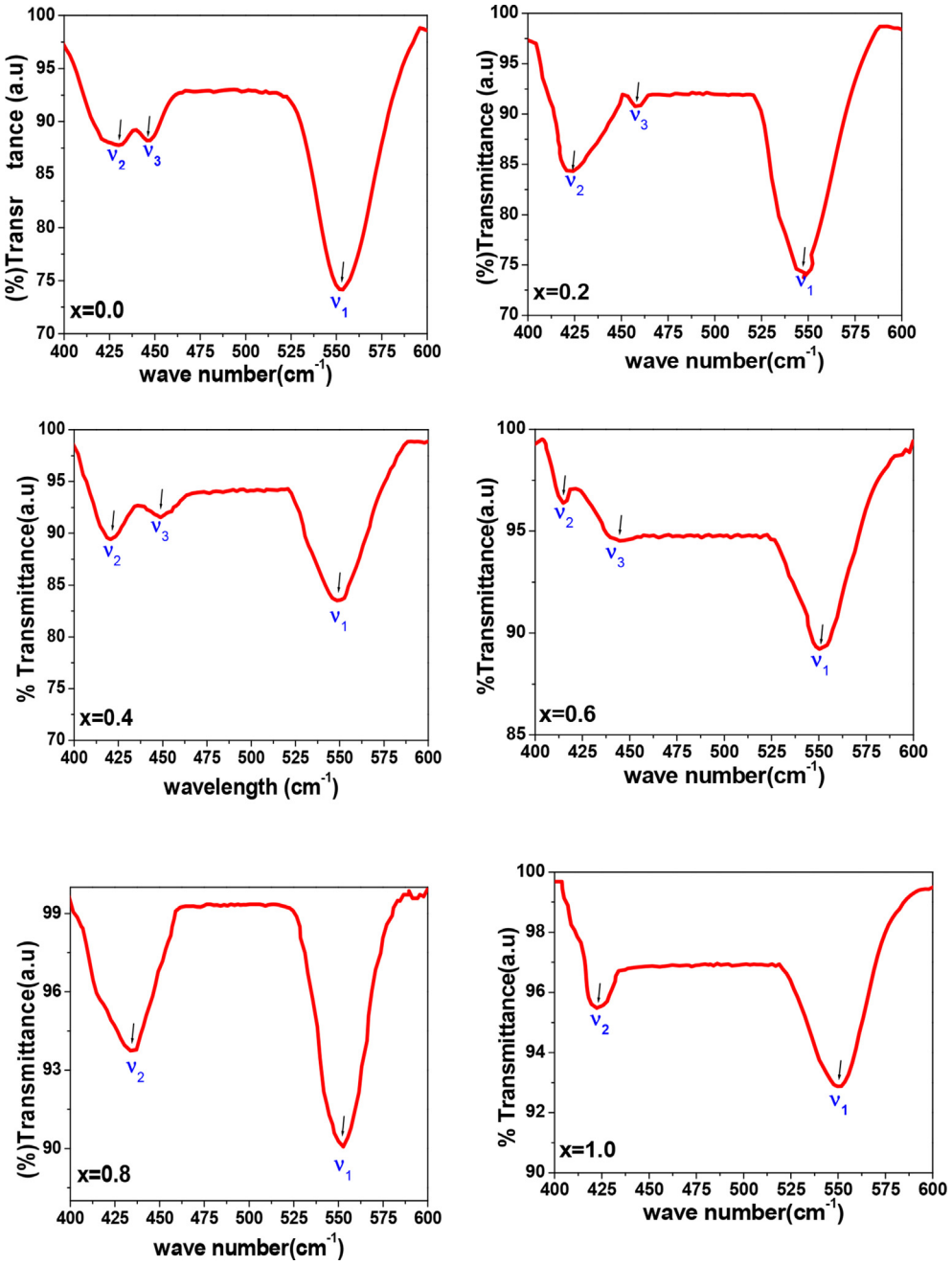

Fig. 3. FTIR absorption spectra of the $Li_{0.5-0.5x}Ni_xFe_{2.5-0.5x}O_4$ ferrite samples ($0.0 \leq x \leq 1.0$).

decrease in piling up of electrons at the grain boundary. Therefore, the dielectric constant decreases. The same anomalous behavior was also observed by some researchers [34].

Table 2
Band positions of the Li–Ni ferrites estimated from the FTIR spectroscopy.

Composition	ν_1 (cm^{-1})	ν_2 (cm^{-1})	ν_3 (cm^{-1})
$Li_{0.5}Fe_{2.5}O_4$	552	430	446
$Li_{0.4}Ni_{0.2}Fe_{2.4}O_4$	549	423	458
$Li_{0.3}Ni_{0.4}Fe_{2.3}O_4$	550	420	449
$Li_{0.2}Ni_{0.6}Fe_{2.2}O_4$	552	414	444
$Li_{0.1}Ni_{0.8}Fe_{2.1}O_4$	553	433	–
$NiFe_2O_4$	550	422	–

Frequency dependence of AC conductivity of the prepared ferrites was shown in Fig. 8. From the figure, it is observed that the AC conductivity of the prepared samples shows dispersion with respect to frequency. At lower frequencies, AC conductivity is almost constant. But, after certain frequency it increases rapidly. This behavior can be explained by Koop's theory [35], which supported that the ferrite material act as a bilayer condenser. According to Koop's bilayer model in ferrite, first layer is a conducting layer consisting conducting ferrite grains which is separated by a second layer of poorly conducting intermediate grain boundaries. Koops proposed that grain boundary effect dominates at lower frequencies resulting in low conductivity. With increase in frequency the

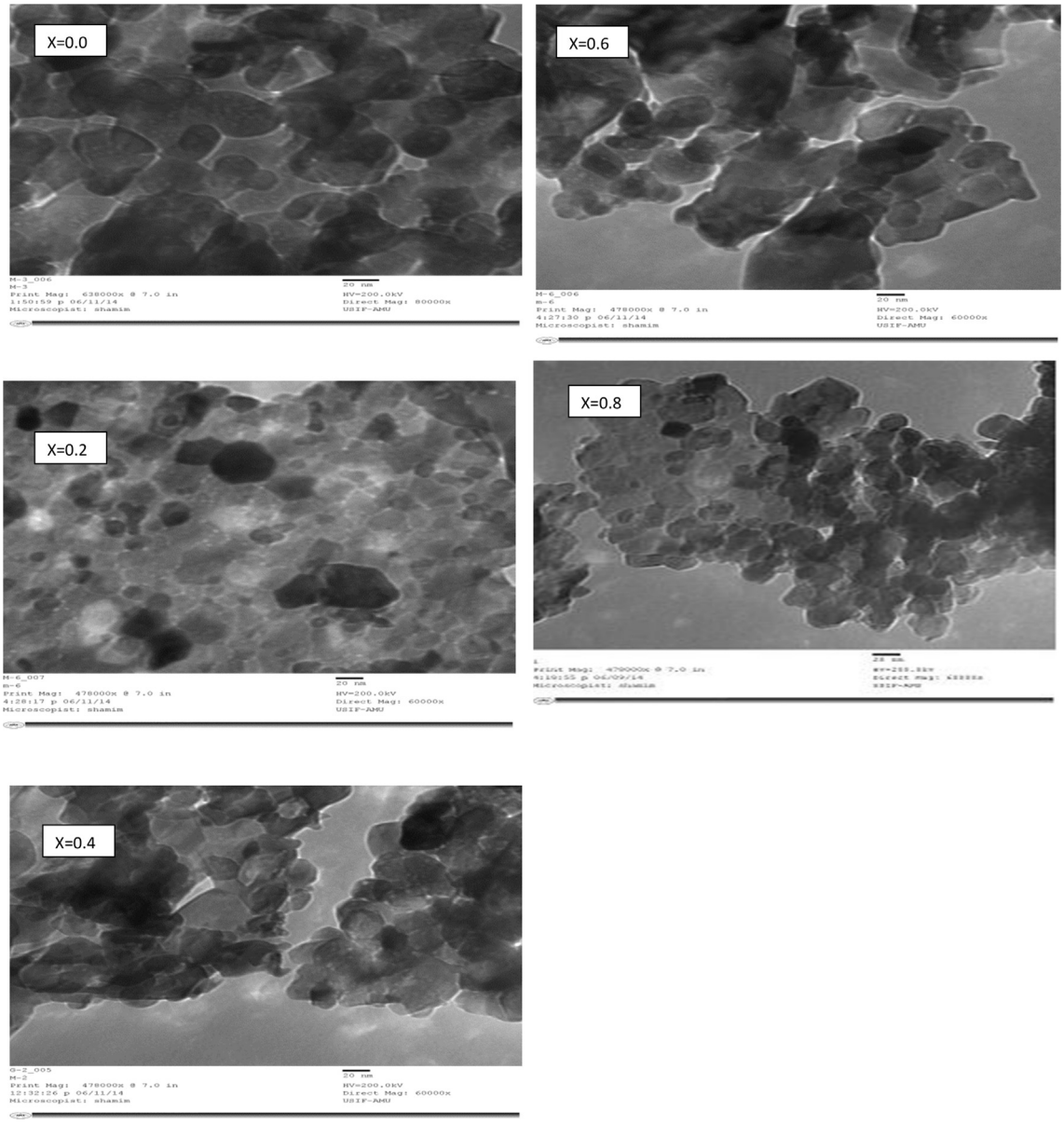

Fig. 4. TEM micrographs of nano crystalline $Li_{0.5-0.5x}Ni_xFe_{2.5-0.5x}O_4$ ferrites (x = 0.0 to 0.8).

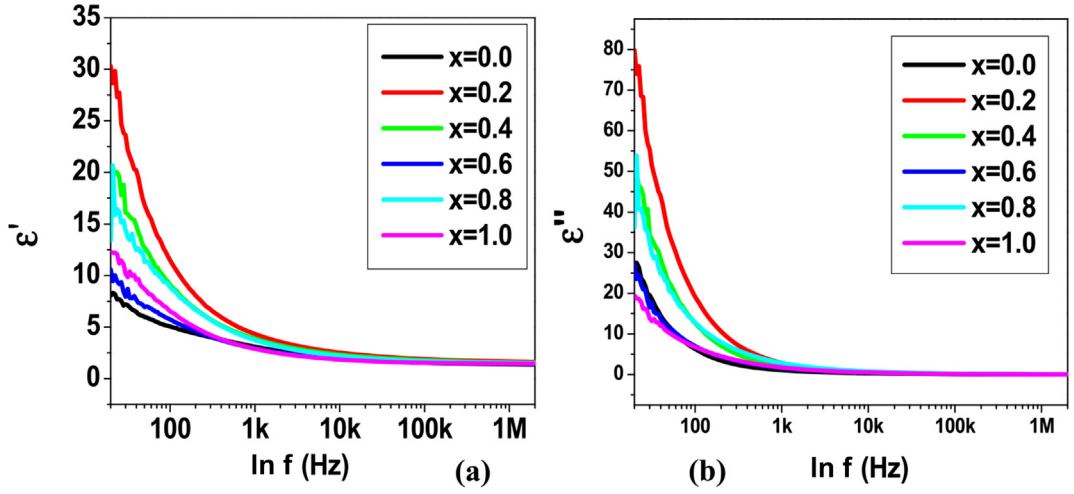

Fig. 5. Variation of (a) real part of dielectric constant (ε') and. (b) imaginary part of dielectric constant (ε'') with frequency.

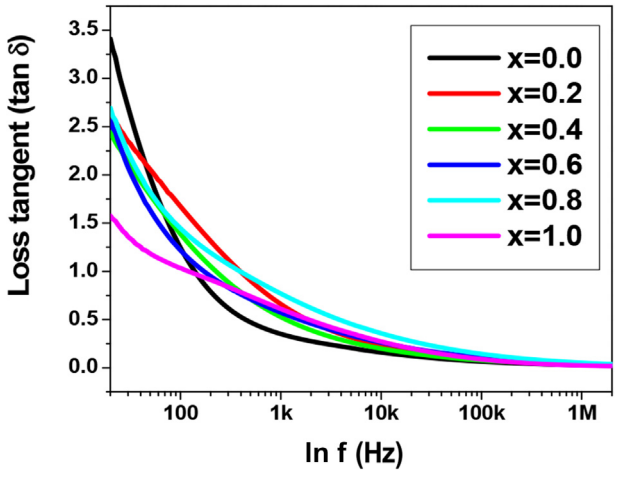

Fig. 6. Variation of Loss Tangent with frequency of $Li_{0.5-0.5x}Ni_xFe_{2.5-0.5x}O_4$ ferrites.

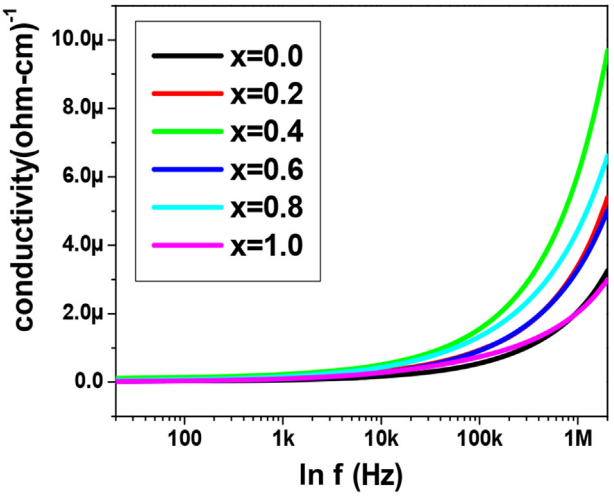

Fig. 8. Variation of AC conductivity with frequency of $Li_{0.5-0.5x}Ni_x$-$Fe_{2.5-0.5x}O_4$ ferrites.

conductive grains becomes more dominating resulting in promoting the hopping between Fe^{2+} and Fe^{3+} ions and hence the conductivity increases.

3.5. Thermo electric power studies

The Variation of Seebeck coefficient (S) with temperature of the prepared Li–Ni ferrites was shown in Fig. 9. From the figure, it was observed that all the samples show similar thermal variation with S and the value of S increases with increase in the temperature.

At low temperature, positive value of S shows p-type semi conducting nature of the prepared ferrites. By increasing the temperature, the sample has changed to n-type semiconductor behavior. The probable conduction mechanisms in the spinel ferrite system under investigation are

$$Fe^{2+} \leftrightarrow Fe^{3+} + e^{-} (n-\text{type or electron exchange mechanism})$$

$$Ni^{2+} \leftrightarrow Ni^{1+} + e^{+} (p-\text{type or hole exchange mechanism})$$

The preponderance of one mechanism over the other depends upon the concentration of substituted cation and temperature. If the hole exchange mechanism dominates over the electron exchange mechanism, the ferrite composition might conduct as p-type semiconductor or vice versa. On increasing the temperature the n-type of conduction mechanism becomes more probable which generates electrons and the material behaves as n-type semiconductor at higher temperature. Hence the material was behaving as p-type semiconductor at low temperature region and changes to n-type at high temperature region.

Li–Ni ferrite samples show an increasing trend in Seebeck coefficient with temperature which indicates that more n-type charge carriers (electrons) are released with an increase in temperature. At a particular temperature an abrupt change was occurred which is called Curie temperature. From the figure, one can say that

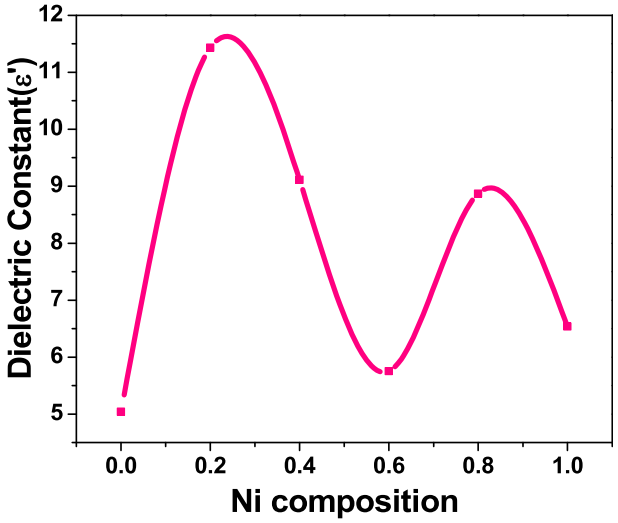

Fig. 7. Variation of dielectric constant (ε') with Ni composition.

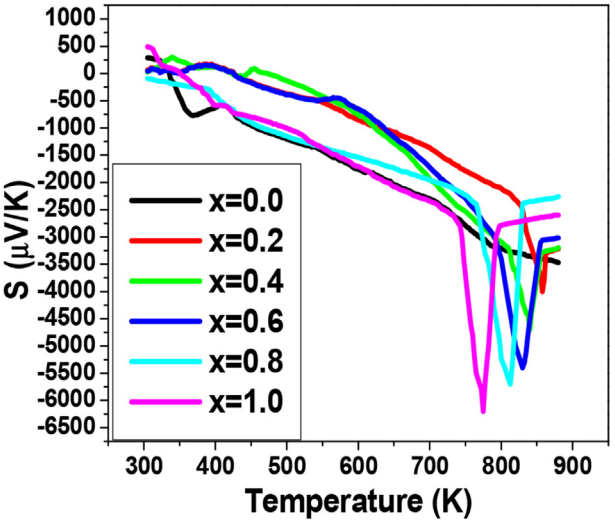

Fig. 9. Variation of Seebeck coefficient with temperature of $Li_{0.5-0.5x}Ni_xFe_{2.5-0.5x}O_4$ ferrites.

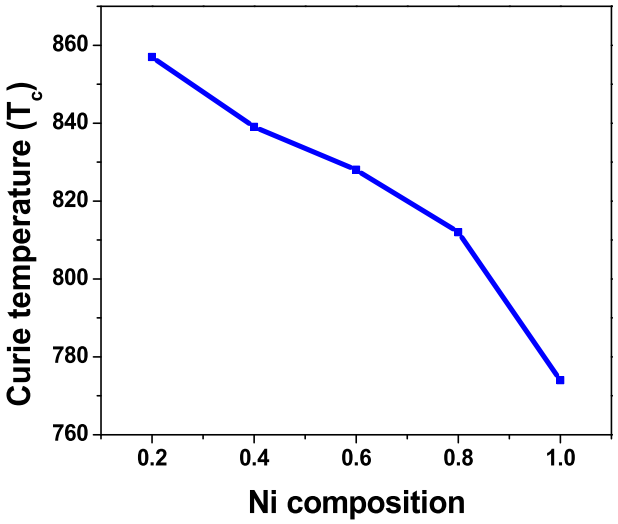

Fig. 10. Variation of Curie temperature with Ni composition.

the Curie temperature of the prepared samples decreased with increase in the Ni concentration in the Li–Ni ferrite system (see Table 3).

Variation of Curie temperature with Ni composition of the prepared ferrites was shown in Fig. 10. The decrease in Curie temperature by increasing the Ni doping can be understood on the basis of the number of magnetic ions present in the two stable sub lattices and mutual interaction. An increase in the Ni^{2+} at the octahedral site has replaced the Fe^{3+} at this site. This leads to the decrease in the AB interaction of the type $Fe_A^{3+} - O^{2-} - Fe_B^{3+}$. Curie temperature depends on overall strength of AB exchange interaction, so the weakening of the $Fe_A^{3+} - O^{2-} - Fe_B^{3+}$ interaction results in a decrease in Curie temperature of prepared Li–Ni ferrites [36].

Carrier concentration of the prepared samples was calculated at 500 K. It can be seen from the Table 3 that among all the mixed Li–Ni spinel ferrites, the composition$Li_{0.1}$ $Ni_{0.8}Fe_{2.1}O_4$was having the highest values of carrier concentration.

4. Conclusions

Ni^{2+} ions when substituted in the basic lithium ferrite affect its structural and dielectric properties. The crystallite size of the prepared samples was in the range of 39–49 nm which reveals the nano crystalline structure. An increase in the Ni concentration increase the lattice parameter and hopping length of A-site and B-site. The dielectric constant and dielectric loss tangent were observed to decrease with the increase in frequency, which was the common nature of any semiconducting ferrites. The AC conductivity of the prepared samples was observed to increase with increasing the frequency. Seebeck coefficient of the prepared Li–Ni ferrite samples were increased with increase in temperature. Curie temperature of the samples was observed to be decreased with increasing Ni concentration in the Li–Ni nano crystalline ferrites.

Table 3
Seebeck coefficient, Carrier concentration, Curie temperature of Li–Ni ferrites.

Composition	Seebeck coefficient (μV/K)	Carrier concentration (n)	Curie temp (K)
$Li_{0.5}Fe_{2.5}O_4$		3.26×10^{22}	>900
$Li_{0.4}Ni_{0.2}Fe_{2.4}O_4$	3974	1.59×10^{22}	857
$Li_{0.3}Ni_{0.4}Fe_{2.3}O_4$	4648	1.15×10^{22}	839
$Li_{0.2}Ni_{0.6}Fe_{2.2}O_4$	5350	1.61×10^{22}	828
$Li_{0.1}Ni_{0.8}Fe_{2.1}O_4$	5670	3.64×10^{22}	812
$NiFe_2O_4$	6100	3.04×10^{22}	774

Acknowledgment

The authors are very grateful to Prof. R.Sayanna, Head, Department of Physics, University College of Science, Osmania University, Hyderabad. The authors are very thankful to UGC, New Delhi, for their financial assistance through Major research Project (M.R.P).

References

[1] Goodenough JB. In: Cotton FA, editor. Magnetism and the chemical bond, interscience monographs on chemistry, inorganic chemistry section, vol. I. New York: Interscience-Wiley; 1963.
[2] Liu C, Lan Z, Jiang X, Yu Z, Sun K, Li L, et al. Effects of sintering temperature and Bi_20_3 content on microstructure and magnetic properties of Li–Zn ferrites. J Magn Magn Mater 2008;320:1335.
[3] Kumar AM, Verma MC, Dube CL, Rao KH, Kashyap SC. Development of Ni–Zn nano ferrite core material with improved saturation magnetization and DC resistivity. J Magn Magn Mater 2008;320:1995.
[4] Yang YJ, Sheu CI, Cheng SY, Chang HY. Si–Ca species modification and microwave sintering for Ni–Zn ferrites. J Magn Magn Mater 2004;284:220.
[5] Jadhav SA. Magnetic properties of Zn-substituted Li–Cu ferrites. J Magn Magn Mater 2001;224:167.
[6] Shaikh AM, Kanamadi CM, Chougule BK. Electrical resistivity and thermo electric power studies of Zn substituted Li–Mg ferrites. Mater Chem Phys 2005;93:548.
[7] Jadhav SA. Structural and magnetic properties of Zn substituted Li–Cu ferrites. Mater Chem Phys 2000;65:120.
[8] El-Sayed Ahmed M, Hamzawy Esmat MA. Structure and magnetic properties of Nickel–Zinc ferrite nanoparticles prepared by glass crystallization method. Monatsh für Chemie/Chemical Mon 2006;137:1119. http://dx.doi.org/10.1007/s00706-006-0521-1.
[9] Hu Chaoquan, Gao Zhenghong, Yang Xiaorui. One-pot low temperature synthesis of MFe_2O_4 (M=Co, Ni, Zn) superparamagnetic nano crystals. J Magn Magn Mater 2008;320:L70.
[10] Batoo Khalid Mujasam, Kumar Shalendra, Lee Chan Gyu, Alimuddin. Finite size effect and influence of temperature on electrical properties of nano crystalline Ni–Cd ferrites. Curr Appl Phys 2009;9:1072.
[11] Soibam I, phanjoubam S, Prakash C. Magnetic and Mössbauer studies of Ni substituted Li–Zn ferrite. J Magn Magn Mater 2009;321:2779.
[12] Raghasudha M, Ravinder D, Veerasomaiah P. Characterization of chromium substituted cobalt nano ferrites synthesized by citrate-gel auto combustion method. Adv Mater Phys Chem 2013;3:89–96.
[13] Venudhar YC, Satya Mohan K. Dielectric behavior of lithium–cobalt mixed ferrites. Mater. Lett 2002;54:135.
[14] Bellad SS, Chougule BK. Composition and frequency dependent dielectric properties of Li–Mg–Ti ferrites. Mater Chem Phys 2000;66:58.
[15] Ravinder D, Chandrashekhar Reddy A. Dielectric properties of Li–Ge ferrites. Mater Lett 2003;57:2855.
[16] Singh Amarendra K, Goel TC, Goel TG, Mendiratta RG, Thakur OP, Prakash Chandra. Dielectric properties of Mn-substituted Ni–Zn ferrite. J Appl Phys 2002;91:6626.

[17] Bhatu SS, Lakhani VK, Tanna AR. Effect of nickel substitution on structural, infrared and elastic properties of lithium ferrite. Indian J Pure Appl Phys 2007;45:596. IPC code GO1J3/28.
[18] Raghasudha M, Ravinder D, Veerasomaiah P. Characterization of nanostructured magnesium-chromium ferrites synthesized by citrate-gel auto combustion method. Adv Mat Lett 2013;4:910. http://dx.doi.org/10.5185/amlett.2013.5479.
[19] Raghasudha M, Ravinder D, Veerasomaiah P. FTIR studies and dielectric properties of Cr substituted cobalt nano ferrites synthesized by citrate-gel method. Nanosci Nanotech 2013;3:105. http://dx.doi.org/10.5923/j.nn.20130305.01.
[20] Pervaiz Erum, Gul IH. Enhancement of electrical properties due to C^{r3+} substitution in Co-ferrite nanoparticles synthesized by two chemical techniques. J Magn Magn Mater 2012;324:3695.
[21] Raghasudha M, Ravinder D, Veerasomaiah P. Thermoelectric power studies of Co–Cr nano ferrites. J Alloys Compd 2014;604:276.
[22] Morin FJ, Geballe TH. Electrical conductivity and seebeck effect in $Ni_{0.8}Fe_{2.2}O_4$. Phys Rev 1955;99:467.
[23] Priyadarshini P, Pradeep A, Sambasivarao P, Chandrasekaran G. Structural, spectroscopic and magnetic study of nanocrystalline Ni–Zn ferrites. Mater Chem Phys 2009;116:207.
[24] Tarte P. Infra-red spectrum and tetrahedral coordination of lithium in the spinel $LiCrGeO_4$. Acta Crystallogr 1963;16:228.
[25] Mazen SA, Abu-Elsaad NI. IR spectra, elastic and dielectric properties of Li–Mn ferrite. ISRN Condens Matter Phys 2012:9. http://dx.doi.org/10.5402/2012/907257. Article ID 907257.
[26] Kumar V, Rana A, Kumar N, Pant RP. Investigations on controlled size precipitated cobalt ferrite nano particles. Int J Appl Ceram Technol 2011;8:120.
[27] Samsonov D, Zhdanov S, Morfill G, Steinberg V. Levitation and agglomeration of magnetic grains in a complex (dusty) plasma with magnetic field. New J Phys 2003;5:24.1. http://dx.doi.org/10.1063/1.1763577.
[28] Rezlescu N, Rezlescu E. Dielectric properties of copper containing ferrites. Phys Status Solidi A 1974;23:575.
[29] Gul IH, Maqsood A, Naeem M, Naeem Ashiq M. Optical, magnetic and electrical investigation of cobalt ferrite nanoparticles synthesized by co-precipitation route. J Alloys Comp 2010;507:201.
[30] Iwauchi K. Dielectric properties of fine particles of Fe_3O_4 and some ferrites. Jap J Appl Phys 1971;10:1520.
[31] Maxwell JC. Electricity and magnetism, 1. Oxford: Oxford University Press; 1929 (section 328).
[32] Baruwati B, Reddy KM, Manorama SV, Singh RK, Prakash O. Tailored conductivity behavior in nanocrystalline nickel ferrite. App Phys Lett 2004;85:2833.
[33] Jonker GH. Analysis of the semiconducting properties of cobalt ferrite. J Phys Chem Solids 1959;9:165.
[34] Soibam I, Phanjoubam S, Sharma HB, Sarma HNK, Laishram R, Prakash C. Effects of cobalt substitution on the dielectric properties of Li–Zn ferrite. Solid State Comm 2008;148:399.
[35] Koops CG. On the dispersion of resistivity and dielectric constant of some semiconductors at audio frequencies. Phys Rev 1951;83:121.
[36] Sharifi Ibrahim, Shokrollahi H. Nanostructural, magnetic and Mössbauer studies of nanosized $Co_{1-x}Zn_xFe_2O_4$ synthesized by co-precipitation. J Magn Magn Mater 2012;324:2397.

Dr. M. Raghasudha is working as Associate Professor in Chemistry, Jayaprakash Narayan college of Engineering, Mahabubnagar, Telangana, India. She obtained her M.Sc. in Chemistry (1997) from Kakatiya University, Telangana, M.Phil. in Chemistry (2007) from Alagappa University, Tamil Nadu and Ph.D. from Osmania University, Hyderabad, Telangana, India in 2014. To her credit she has published 15 research papers in International Journals, attended 20 national and international conferences and has 19 years of teaching experience. Her current area of research is on electrical and magnetic properties of ferrite nano materials and thin films by citrate-gel method.

Prof. D. Ravinder is working as Professor and Head, Department of Physics, Nizam college, Osmania University, Hyderabad, Andhra Pradesh, India. His research work is on magnetic and electrical properties of ferrites, thin films, GMR materials, Cu-Co alloy thin films and nano-materials by pulsed laser deposition, sol gel, citrate precursor method and electro deposition. To his credit, he has published 195 research papers in International Journals. He has been awarded Young Scientist award received by Dr. Abdual Kalam (former president of India), for outstanding contributions in the field of science and Technology, UGC research award, Boyscast by DST (Department of science and technology), Government of India, JSPS fellowship Japan and Royal Society fellowship, UK. He also visited USA, UK, Sweden, Ireland, Singapore and Japan for Collaborative Research and invited talks.

Dr.G. Aravind is working as Asst. Professor in Physics, Methodist College of Engineering and Technology, Affiliated to Osmania University, Hyderabad. Telangana, India. He completed his M.Sc in 2007 and Ph.D. in 2015 from Osmania University, Hyderabad, Telangana, India. He published 5 international papers and attended 13 national and international conferences. He has four years teaching experience.

NOVATEUR PUBLICATIONS
INTERNATIONAL JOURNAL OF INNOVATIONS IN ENGINEERING RESEARCH AND TECHNOLOGY [IJIERT]
ISSN: 2394-3696
VOLUME 2, ISSUE 7, July-2015

A REVIEW OF LPC METHODS FOR ENHANCEMENT OF SPEECH SIGNALS

Mr. Arjun Ghule
Research Scholar, Department of ECE, Jawaharlal Nehru Technological University, Hyderabad, India,

Dr.Prabhu Benakop
Director, Aurora`s Engineering College, Bongir, Hyderabad, India

Abstract

This paper presents a review of LPC methods for enhancement of speech signals. The purpose of all method of speech enhancement is to improve quality of speech signal by minimizing the background noise. This paper especially comments on Power Spectral Subtraction, Multiband Spectral Subtraction, Non-Linear Spectral Subtraction Method, MMSE Spectral Subtraction Method and Spectral Subtraction based on perceptual properties. As the spectral subtraction produces the Residual noise, Musical noise, Linear Predictive Analysis method is used to enhance the Speech.

Keywords: Power Spectral Subtraction, Multiband Spectral Subtraction, Non-Linear Spectral Subtraction Method, MMSE Spectral Subtraction Method and Spectral Subtraction based on perceptual properties

Introduction

Linear prediction coding methods needs highly efficient LPC filter and its excitation to provide high quality of speech at minimum cost. [1] In an abandoned surrounding the speech signals includes the noise, mixing of speech from other speakers and many other unwanted components. [2] This presence of noise reduces clarity and quality of signal. Removing or reducing such noise signal in order to improve the clarity of speech without losing its quality is really a challenge. [3]

Methods of Speech improvement are classified on the criteria such as number of input channels, time domain or frequency domain, adaptive or non adaptive and some additional constraints.

Various ways such as spectral subtraction method, subspace methods, Hidden Markov modeling, wavelet-based methods etc. were proposed for speech enhancement and further more improvements, revisions are done in proposed methods in order to achieve most efficient solution. The spectral subtraction method is widely used enhancement methods for all types of noise, has been chosen for its simplicity of implementation and low computational load [3]. Speech coding has been and still is a major issue in the area of digital speech processing. As a result, a greater emphasis is being placed on the design of new and efficient speech coder for voice communication and transmission. [4]

Literature Review

The several models proposed for minimization of noise present in the speech signal are having their own advantages and disadvantages; one has to analyze the methods and models depending upon the practical application where we are actually willing to utilize the models. Few models are discussed below in detail.

Power Spectral Subtraction Method:

Spectral subtraction is a method for restoration of the power spectrum or the magnitude spectrum of a signal observed in additive noise, through subtraction of an estimate of the average noise spectrum from the noisy signal spectrum. [5] This method is one of the oldest or firstly introduced methods for reducing the noise from the speech signal. The method proposed by Boll is very popular due to simplicity and high effectiveness in improving the speech due to noise addictiveness. The basic principle of this method is that one can approximate and renew the noise band when speech signal is not present and deduct it from the noisy speech signal to obtain clean speech signal spectrum. [6]The assumptions are to be made such that the noise signal is additive and noise is time invariant or slowly varying with time. The block diagram drawn below explains the method in better sense.

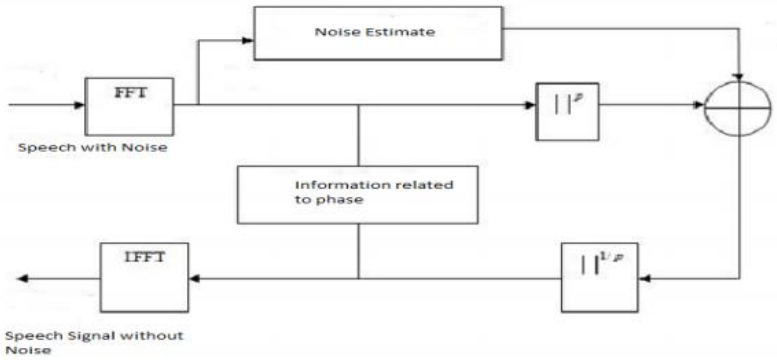

Figure 1: Block Diagram of Spectral Subtraction

In this method the noise signal is suppressed from the speech by subtraction of the approximate noise or estimated noise from the noisy speech signal. The noise band is estimated and modernized, for the duration of the periods when the signal is not present or when only noise is present. [7] These algorithms undertaking to be a universal way out for all types of noise surroundings. The limitation of this method is, the practical noise present in the surrounding is not constant and it is really challenging to suppress the noise present in speech.

Multiband Spectral Subtraction Method

This model also considered as one of the earliest proposed model for the suppression of noise. Here the speech signal is divided in to x samples and subtraction of pre calculated sample noise signal is subtracted from each sample. [8]

There are four stages for execution of this method. In the first stage, the signal is windowed and FFT used to estimate the magnitude spectrum. In the second stage to calculate the over subtraction factor, we divide the noise and speech into different frequency band. The third stage includes processing the individual frequency bands by subtracting the corresponding noise spectrum from the noisy speech spectrum and in the last stage the modified frequency bands are recombined and the time signal is obtained by using the noisy phase information and taking the IFFT.

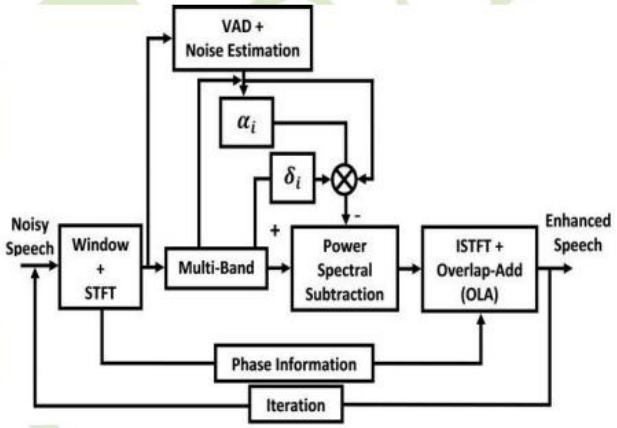

Figure2: Block Diagram of Multi-band Spectral Subtraction Method

Non-Linear Spectral Subtraction Method

The use of spectral subtraction in its basic form may cause deterioration in the quality and the information content of a signal. For example, in audio signal restoration, the musical noise can cause degradation in the perceived quality of the signal, and in speech recognition the basic spectral subtraction can result in deterioration of the recognition accuracy. In the literature, there are a number of variants of spectral subtraction that aim to provide consistent performance improvement across a range of SNRs. These methods differ in their approach to estimation of the noise spectrum, in their method of averaging the noisy signal spectrum, and in their post processing method for the removal of processing distortions. Non-linear spectral subtraction methods are heuristic methods that utilize estimates of the local SNR, and the observation that at a low SNR over subtraction can produce improved results. [5]

MMSE Spectral Subtraction Method

Minimum Mean Square Error (MMSE) Spectral subtraction method is proposed by Sim. [9] A method for selecting the subtractive parameters in the mean error sagacity. [10] In this method the mean square of the predefined error signal is subtracted from speech signal in order to improve the efficiency of the system by achieving a better quality speech signal.

Spectral Subtraction based on perceptual properties

In the previous methods, the subtractive parameters were computed experimentally, based on short term SNR levels [11] or obtained optimally in a mean square error sense [9]. No perceptual properties of the auditory system have been considered. An algorithm proposed by Virag [12] that incorporates psycho acoustical properties of speech signal, in the spectral subtraction process. The main objective of this algorithm is to remove the residual noise perceptually inaudible and improve the intelligibility of enhanced speech by taking into account the properties of the human auditory system [13]. Method proposed by Virag [12] was based on idea that, if the estimated masking threshold at a particular frequency is low, the residual noise level might be above. The threshold and will therefore be audible. The subtraction parameters should therefore attain their maximal values at that frequency. Similarly, if the masking threshold level is high at a certain frequency, the residual noise will be masked and will be inaudible. The subtraction parameters should attain their minimal values at that frequency.

Conclusion

This paper presents a review of LPC methods for enhancement of speech signals by minimizing the noise present in the speech. The purpose of all method of speech enhancement is to improve quality of speech signal by minimizing the background noise. This paper especially comments on Power Spectral Subtraction, Multiband Spectral Subtraction, Non-Linear Spectral Subtraction Method, MMSE Spectral Subtraction Method and Spectral Subtraction based on perceptual properties. All the methods discussed in this paper are having several advantages and disadvantages, moreover defining the method depending upon the application and utilizing it with full of its efficiency is big challenge.

References

1] *"A new model of LPC excitation"* Jun Xu, Yuancheng Zheng, Hangui Liang, Biqing Lin, Baozhong Yuan, China 1991 International Conference on Circuits and Systems, June 1991, Shenzhen, China.

2] Anuradha R. Fukane, Shashikant L. Sahare *"Different Approaches of Spectral Subtraction method for Enhancing the Speech Signal in Noisy Environments"* International Journal of Scientific & Engineering Research, Volume 2, 1 ISSN 2229-5518,Issue 5, May-2011.

3] Vimala.C, V.*Radha "A Family of Spectral Subtraction Algorithms for Tamil Speech Enhancement"* International Journal of Soft Computing and Engineering (IJSCE) ISSN: 2231-2307, Volume-2, Issue-1, March 2012.

4] "Compression and Enhancement of Speech Signals" Siva Sushma G, D. R. Sandeep Chennai and Dr.MGR University Second International Conference on Sustainable Energy and Intelligent System (SEISCON 2011) , Dr. M.G.R. University, Maduravoyal, Chennai, Tamil Nadu, India. July. 20-22, 2011.

5] *"Advanced Digital Signal Processing and Noise Reduction",* Second Edition. Saeed V. Vaseghi Copyright © 2000 John Wiley & Sons Ltd ISBNs: 0-471-62692-9 (Hardback): 0-470-84162-1 (Electronic)

6] S.F. Boll, *"Suppression of acoustic noise in speech using spectral subtraction",* IEEE Transactions on Acoustics, Speech and Signal Processing, Vol. 27, No. 2, pp. 113-120, 1979

7] Ekaterina Verteletskaya, Boris Simak *"Noise Reduction Based on Modified Spectral Subtraction Method"* IAENG International Journal of Computer Science, 38:1, IJCS_38_1_10.

8] GANGA PRASAD, SURENDER *"A Review of Different Approaches of Spectral Subtraction Algorithms for Speech Enhancement"* Department of Electronics, Madhav Institute of Technology & Science Vol 01, 57-64, Issue 02 April 2013

9] Sim B, Tong Y, chang J., Tan C.(1998) *"A parametric formulation of the generalized spectral subtraction method"* IEEE. Trans. Speech Audio Process,6(4), 328-337

10] Martin, R(2002) *"Speech Enhancement Using MMSE Short Time Spectral Estimation with Gamma Distributed Speech Priors*", in Proc. IEEE Intl. Conf. Acoustics, Speech, Signal Processing (ICASSP), vol. I, pp. 253–256, 2002

11] Berouti,M. Schwartz,R. and Makhoul,J.,*"Enhancement of Speech Corrupted by Acoustic Noise"*, Proc ICASSP 1979, pp208-211,.

12] Virag, N., (1999). *"Single channel speech enhancement based on masking properties of the human auditory system"*. IEEE. Trans. Speech Audio Process, 7(3), 126-137.

13] Phillips C Loizou *"Speech enhancement theory and practice"* 1st ed. Boca Raton, FL.: CRC, 2007. Releases Taylor & Francis

Journal of Magnetism and Magnetic Materials 378 (2015) 278–284

Contents lists available at ScienceDirect

Journal of Magnetism and Magnetic Materials

journal homepage: www.elsevier.com/locate/jmmm

Synthesis, characterization and FC–ZFC magnetization studies of cobalt substituted lithium nano ferrites

G. Aravind [a], M. Raghasudha [b], D. Ravinder [a,*]

[a] Department of Physics, Osmania University, Hyderabad 500007, Telangana, India
[b] Department of Chemistry, Jayaprakash Narayan College of Engineering, Mahabubnagar 509001, Telangana, India

ARTICLE INFO

Article history:
Received 11 July 2014
Received in revised form
8 November 2014
Accepted 14 November 2014
Available online 20 November 2014

Keywords:
Citrate-gel auto-combustion technique
Nano ferrites
Magnetic properties
Field cooled (FC)
Zero field cooled (ZFC) Magnetization
Superparamagnetism

ABSTRACT

Cobalt substituted Lithium Nano ferrites with the chemical composition $[Li_{0.5}Fe_{0.5}]_{1-x}Co_xFe_2O_4$ (where $x=0.0, 0.2, 0.4, 0.6, 0.8, 1.0$) were synthesized through Citrate-Gel auto combustion technique. Structural characterization of the prepared ferrites was carried by X-ray diffraction analysis (XRD) and Scanning Electron Microscopy (SEM). XRD analysis has confirmed the formation cubic spinel structure of the ferrite compositions with a particle size ranging from 37 nm to 42 nm. The SEM images represent large agglomeration of the nano particles of the ferrite samples with broader grain size distribution. Temperature dependent magnetic properties of $[Li_{0.5}Fe_{0.5}]_{1-x}Co_xFe_2O_4$ for two compositions with cobalt content $x=0.8$ and $x=1.0$ were carried out using Vibrating sample magnetometer (VSM). The magnetization as a function of an applied field ± 10 T was carried out at temperatures 5 K and 310 K. Field cooled (FC) and Zero field cooled (ZFC) magnetization measurements under an applied field of 100 Oe and 1 KOe in the temperature range of 5–375 K were performed. These measurements have resulted the blocking temperature (T_b) at around 350 K i.e. above room temperature for both the ferrites. Below this temperature the ferrites show ferromagnetic behavior and above which superparamagnetic behavior where the coercivity and remanence magnetization are almost zero. Such behavior makes the ferrites to be desirable for biomedical applications.

1. Introduction

In recent years, magnetic nano particles have gained much attention due to their fundamental, technological and scientific importance. Among the various types of magnetic nanoparticles, spinel ferrite nanoparticles are most fascinating materials. The unusual optical, electrical and magnetic properties of ferrite nano particles such as superparamagnetism, low saturation magnetization make the nano-ferrites, a subject of research interest [1]. Properties of spinel ferrites are susceptible to be modified very easily for their wide range of potential applications. This is because, the spinel crystal structure of the ferrites is complex and adaptive, thus can be modified in many ways resulting in novel properties [2].

Lithium ferrite and substituted lithium ferrites have become the candidates of the most attractive materials for microwave applications especially as a replacement for garnets. Their low cost, square hysteresis loop, superior high-temperature performance due to the high Curie temperature are the other prominent properties that make them such promising candidates for microwave devices, for example; isolators, circulators, gyrators and phase shifters [3–4].

Various divalent metal ions such as Co^{2+}, Cd^{2+}, Cu^{2+}, Mg^{2+}, etc. can be used as substituent in lithium ferrites to tailor its properties for device applications. Several investigations on the substitution of different metal ions in lithium ferrites have been carried out and reported to improve the electrical and magnetic properties of lithium ferrite [5–11]. The Co^{2+} being a fast relaxing ion, enhances the microwave properties [12].

Moreover, to the author's knowledge a very little information is available on the low temperature magnetization study of Cobalt substituted lithium ferrites which show the super paramagnetic behavior. This fact motivated the author to study the effect of Co^{2+} on the magnetic properties of the lithium ferrite.

The properties of the spinel ferrites are also dependent on its microstructure, which in turn is sensitive to the method of preparation. Different techniques have been developed for the synthesis of the nano ferrites viz., sol–gel method, micro emulsion, double sintering, hydrothermal, co-precipitation, ball milling and microwave heating to improve the performance of the nano-ferrites [13–16]. Sol–gel auto-combustion is the simple and

* Corresponding author.
E-mail addresses: raghasudha_m@yahoo.co.in (M. Raghasudha), ravindergupta28@rediffmail.com (D. Ravinder).

http://dx.doi.org/10.1016/j.jmmm.2014.11.052
0304-8853/

economic method to synthesize the nanoferrites with good homogeneity at low processing temperature [17]. The present work reports the synthesis, characterization of cobalt substituted lithium ferrites synthesized by Citrate-gel auto combustion method. It also reports FC and ZFC magnetization studies of $[Li_{0.5}Fe_{0.5}]_{1-x}Co_xFe_2O_4$ for two compositions with cobalt content $x=0.8$ and $x=1.0$.

2. Materials and methods

Cobalt substituted Lithium ferrites with the chemical composition $[Li_{0.5}Fe_{0.5}]_{1-x}Co_xFe_2O_4$ where $x=0.0$, 0.2, 0.4, 0.6, 0.8, 1.0 were synthesized through Citrate-Gel auto combustion technique using $LiNO_3$, Co $(NO_3)_2 6H_2O$, Fe $(NO_3)_2 9H_2O$, $C_6H_8O_7 \cdot H_2O$ and NH_3 as starting materials of high purity. Calculated quantities of individual metal nitrates and citric acid were dissolved in double distilled water separately. The stoichiometric calculation during the preparation of the samples gives nominal chemical composition which can be confirmed by Energy Dispersive Spectroscopy measurements. All these solutions were thoroughly mixed together on a magnetic stirrer to result in a citrate nitrate homogeneous solution. Ammonia solution was then added to this solution to adjust its pH to 7. The solution was heated to about 100 °C with constant stirring on magnetic hot plate where all the water molecules were evaporated resulting in the formation of a viscous gel. The gel was continued to heat on the hot plate up to 200 °C. The viscous gel started foaming when all the water molecules were removed from the mixture. The gel has undergone a flame less auto combustion reaction that has started in the hottest portion of the beaker and propagated like a volcanic eruption from the bottom to the top. The reaction has completed just in minute resulting in a loose puffy powder. Finally the burnt ash is subjected to calcination at 500 °C for 4 h in a muffle furnace to obtain spinel

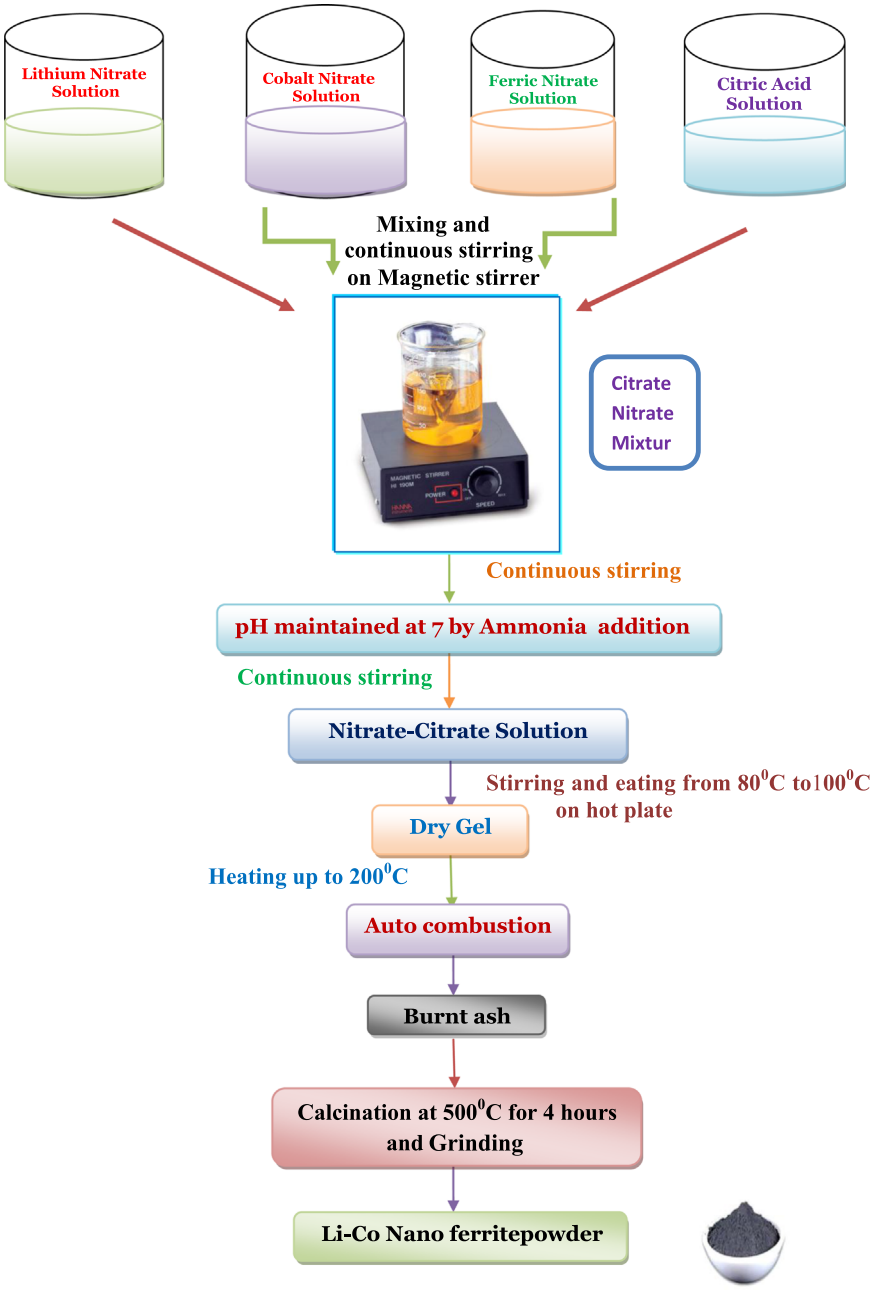

Fig. 1. Flow Chart for the synthesis of Li–Co Nano ferrites.

phase. After calcinations the samples were cooled at a slow rate, as rate of cooling affects the electrical and magnetic properties of the ferrites. Slow cooling results in the formation of ferrites with low particle size, good electrical and magnetic properties. After attaining the room temperature, the samples were taken out off the furnace and ground thoroughly to obtain nano ferrites in spinel phase. The synthesis of Li–Co nano ferrites is shown in Fig. 1 in the form of a flow chart.

3. Characterization

In order to investigate the phase and crystallite size of the synthesized nano ferrites, the structural characterization was performed by X-ray diffractometer (PW3710 Phillips Diffractometer 3710). The experiment was carried out at room temperature by continuous scanning in the range of 2θ°–85θ° using Cu Kα radiation of wave length 1.5405 Å. Structural morphology of the prepared samples was studied by using Scanning Electron Microscope (SEM). Vibrating Sample Magnetometer was used for the ZFC–FC magnetization measurements of two specific ferrite compositions in the temperature range of 5–360 K at different applied fields.

4. Calculation

Using the X-ray diffraction data, the crystallite size of the synthesized samples was calculated using maximum intensity peak from Scherrer's formula [18] as mentioned below

$$\text{Crystallitesize} = D = \frac{0.91\lambda}{\beta Cos\theta} \quad (1)$$

Where λ=the wavelength of X-ray,

β=Full width and half maxima in radians,
θ=Bragg's angle at the peak position.

Lattice parameter 'a' of the individual composition can be calculated using the following expression [18]:

$$a = d\sqrt{h^2 + k^2 + l^2} \quad (2)$$

Where a is lattice parameter, d is inter planar distance, *hkl is* miller indices

The X-ray density (d_x) is calculated using the following relation [18]:

$$x - \text{raydensity} = d_x = \frac{8M}{Na^3}\text{gm/cc} \quad (3)$$

Where M is molecular weight of the sample, N is Avogadro number, a is lattice parameter

Volume of the unit cell 'V' is calculated using the following expression [18]:

$$v = a^3 \quad (4)$$

5. Results and discussion

5.1. XRD analysis

The X-ray diffraction patterns of all the synthesized ferrites were shown in Fig. 2. The diffraction pattern and the crystalline phases were identified in comparison with the standard data from the JCPDS No. 88-0671 of Lithium ferrites. The XRD patterns

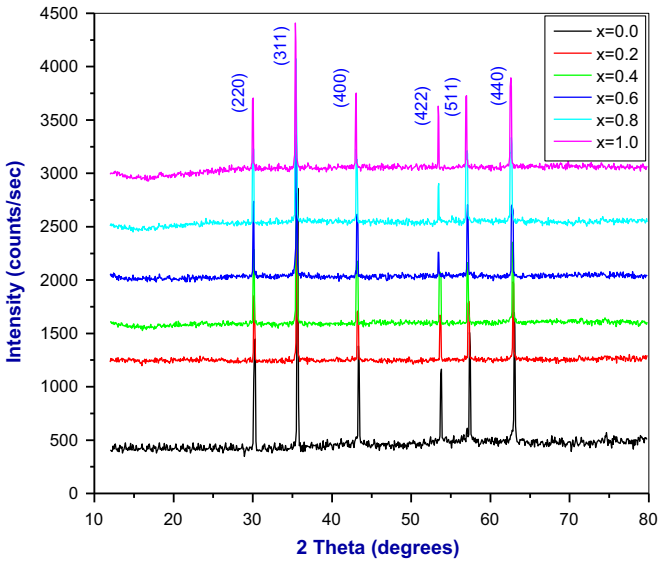

Fig. 2. XRD patterns of $[Li_{0.5}Fe_{0.5}]_{1-x}Co_xFe_2O_4$ where x=0.0, 0.2, 0.4, 0.6, 0.8, 1.0.

indicate formation of well defined peaks of crystalline phase confirming the spinel cubic structure of the samples. All the peaks in the XRD patterns were indexed with reference to the standard data as (220), (311), (400), (422), (511) and (440). These reflections indicate the presence of single phase cubic spinel structure without any impurity peak (311) plane has the maximum intensity which indicates the spinel phase. The crystallite size (D) of all the ferrite compositions was calculated using the Eq. (1) considering the (311) plane. The crystallite size was in the range of 37–42 nm as clear from Table 1.

Lattice parameter of the individual compositions was calculated using the relation 2 and was shown in Table 1. The calculated value of lattice parameter for Lithium ferrite was in good agreement with the standard data 8.33 Å from JCPDS No. 88-0671. It is clear that the calculated lattice parameter was 99.7% precise with a least error of 0.3%. It is observed that with an increase in Co composition from x=0.0–1.0 in $[Li_{0.5}Fe_{0.5}]_{1-x}Co_xFe_2O_4$, the lattice parameter has increased from 8.356 to 8.404 Å. This can be explained based on the ionic radii of the metal ions. The ionic radii of Li^+ ion (0.06 Å) and Fe^{3+} ion (0.64 Å) are smaller than that of the Co^{2+} ion (0.72 Å) which is acting as a dopant. That is, smaller ions are replaced by bigger ion, resulting in an increase in lattice parameter of synthesized individual ferrites with an increase in Co content from x=0.0 to 1.0. The variation of lattice parameter with Co composition is shown in Fig. 3.

X-ray density of the samples is calculated using the relation 3 and the values are recorded in the Table 1. It is observed that with an increase in Co (x) content, the X-ray density has also increased as evident from the Table 1 and Fig. 4. From the relation 3, it is clear that X-ray density depends on the molecular weight of the sample and lattice parameter. With the increase in Co content in $[Li_{0.5}Fe_{0.5}]_{1-x}Co_xFe_2O_4$ferrite system, the molecular weight of the sample is increased and the lattice parameter has also increased. The increase in X-ray density with the increase in Co content in the present ferrite system is because the increase in mass is more than the increase in volume of the unit cell. Similar behavior in the variation of lattice parameter and X-ray density with Co content was observed for cobalt substituted lithium ferrites synthesized by conventional ceramic technique as reported by Song et al. [19].

Volume of the unit cell is calculated from the relation 4 which depends on lattice parameter. It is observed that with an increase in Co content (x), the lattice parameter has increased. Hence there

Table 1
Crystallite size (D), Lattice parameter (a), X-ray density (d_x) and Volume of the unit cell (V) of $[Li_{0.5}Fe_{0.5}]_{1-x}Co_xFe_2O_4$ nano ferrites where $x=0.0, 0.2, 0.4, 0.6, 0.8, 1.0$.

Cr content	Ferrite composition	Molecular weight	Crystallite size-D (nm)	Lattice parameter-a (Å)	X-ray density-d_x (gm/cc)	Volume of the unit cell-V (Cm^3)
$X=0.0$	$Li_{0.5}Fe_{2.5}O_4$	207.079	41.90	8.356	4.713	583.44
$X=0.2$	$Li_{0.4}Co_{0.2}Fe_{2.4}O_4$	212.587	43.01	8.370	4.815	586.38
$X=0.4$	$Li_{0.3}Co_{0.4}Fe_{2.3}O_4$	218.095	38.44	8.375	4.931	587.43
$X=0.6$	$Li_{0.2}Co_{0.6}Fe_{2.2}O_4$	223.603	37.57	8.386	5.035	589.75
$X=0.8$	$Li_{0.1}Co_{0.8}Fe_{2.1}O_4$	229.111	37.06	8.395	5.144	591.65
$X=1.0$	$CoFe_2O_4$	234.619	36.90	8.404	5.250	593.55

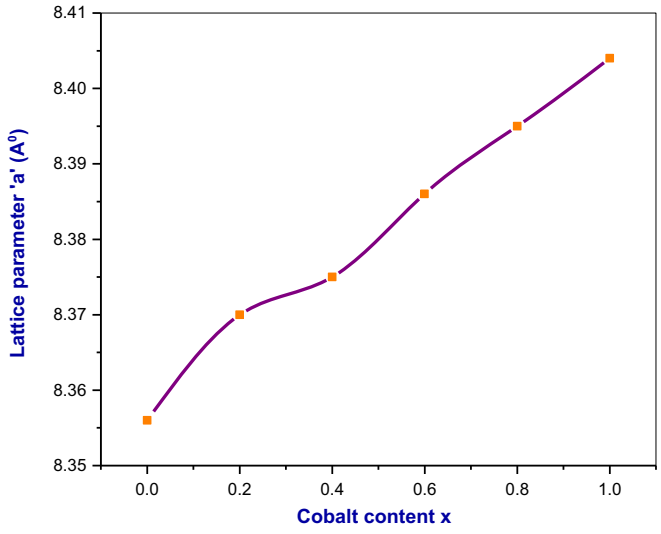

Fig. 3. Variation of lattice parameter with cobalt content for $[Li_{0.5}Fe_{0.5}]_{1-x}Co_xFe_2O_4$ where $x=0.0, 0.2, 0.4, 0.6, 0.8, 1.0$.

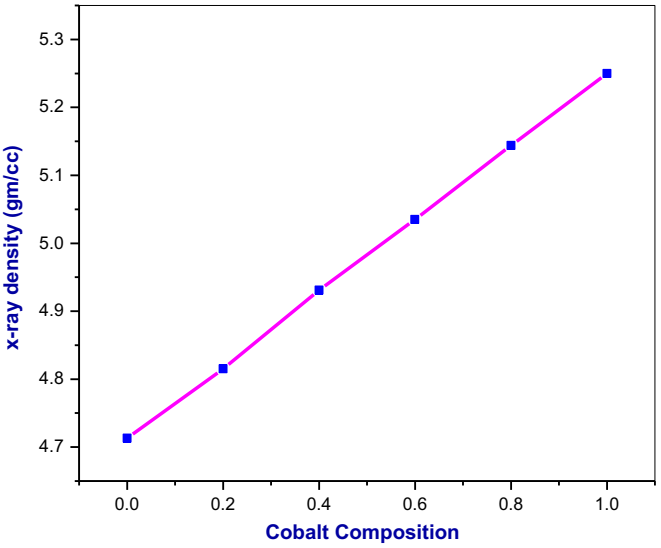

Fig. 4. Variation of X-ray density with cobalt content for $[Li_{0.5}Fe_{0.5}]_{1-x}Co_xFe_2O_4$ where $x=0.0, 0.2, 0.4, 0.6, 0.8, 1.0$.

is an increase in volume of the unit cell as clear from the Table 1 and Fig. 5.

5.2. Morphology by SEM

SEM images of the ferrite compositions under investigation were shown in Fig. 6. From the figure it is clear that the surface morphology of the particles is similar. The images represent large

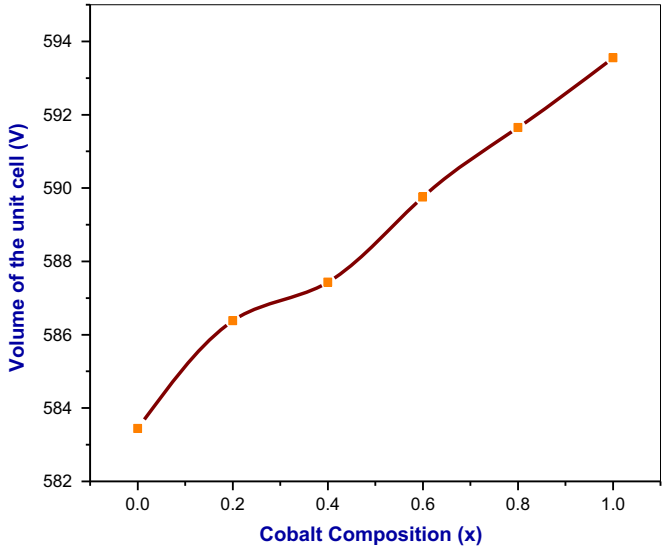

Fig. 5. Variation of volume of the unit cell with cobalt content for $[Li_{0.5}Fe_{0.5}]_{1-x}Co_xFe_2O_4$ where $x=0.0, 0.2, 0.4, 0.6, 0.8, 1.0$.

agglomeration of the nano particles of the ferrite samples where the distribution of the grain size is broad and not uniform. Such broader particle size of the samples confirms the formation of mechanically activated nano sized particles. The particles experience a permanent magnetic moment that is proportional to their volume resulting in the agglomeration of particles. Magnetic properties of the nano particles were affected by the Agglomeration of the ferrite nano particles. Agglomeration of the ferrites makes different ferrites with different alignments to come close to each other. This results in an increase in magneto crystalline anisotropy [20].

5.3. FC–ZFC magnetization study of $[Li_{0.5}Fe_{0.5}]_{1-x}Co_xFe_2O_4$ with $x=0.8$ and 1.0

Among the prepared lithium-cobalt nano ferrites of all compositions, the samples with Cobalt content $x=0.8$ and $x=1.0$ have the crystallite size of 37.06 nm and 36.9 nm. Ferrites with Such low particle size are expected to show superparamagnetic behavior. This has motivated the author to investigate the superparamagnetic behavior of these samples by performing Zero Field Cooled (ZFC) and Field Cooled (FC) magnetization measurements using the Vibrating Sample Magnetometer. Superparamagnetism is a phenomenon in which the magnetic materials behave as paramagnetic materials below the Curie temperature, unlike the general transition of a magnetic material from ferromagnetic to paramagnetic above its Curie temperature.

In the ZFC process, the ferrite sample is cooled in the absence of magnetic field. Then, the temperature is gradually raised by

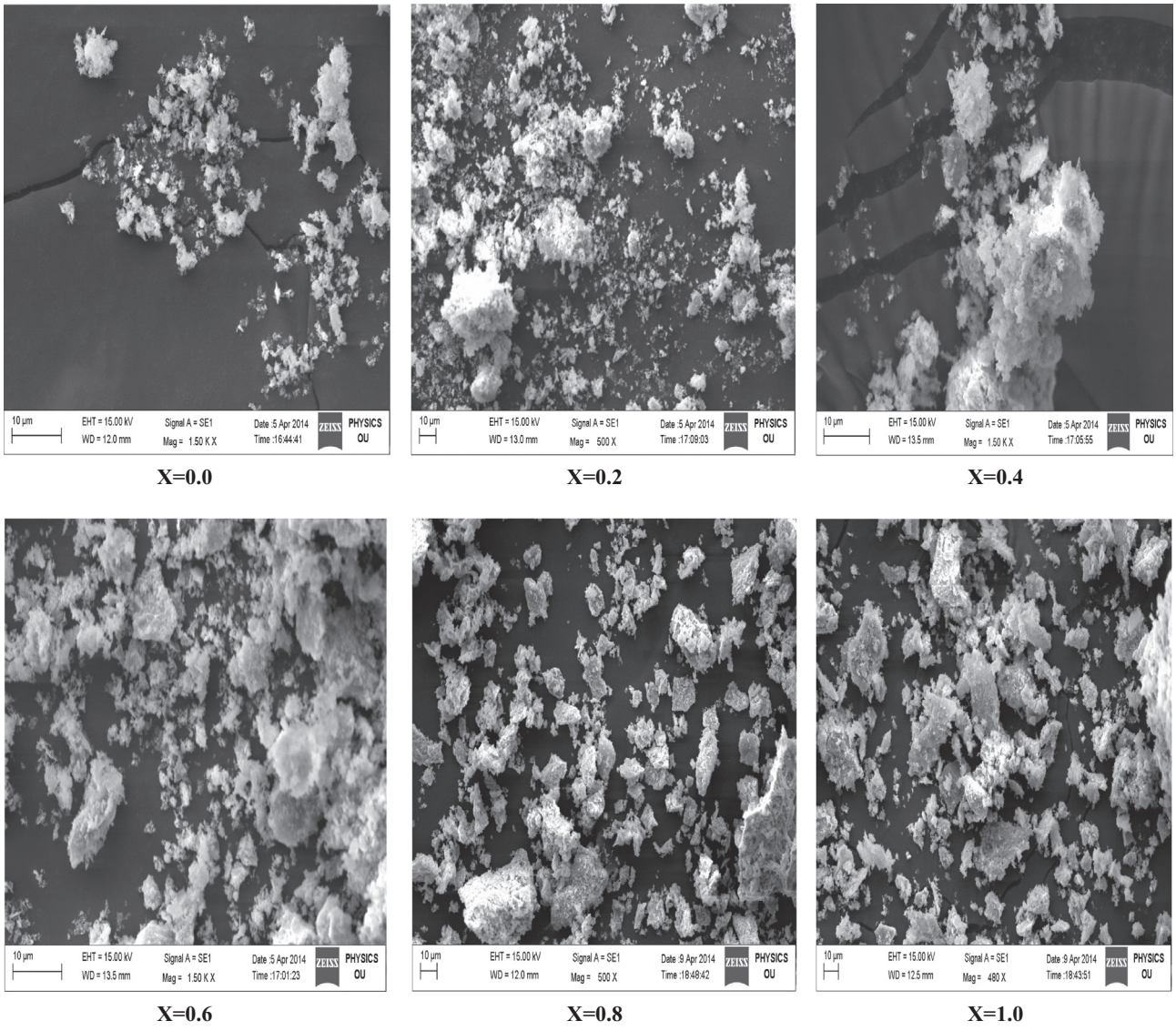

Fig. 6. SEM images for $[Li_{0.5}Fe_{0.5}]_{1-x}Co_xFe_2O_4$ where $x=0.0$, 0.2, 0.4, 0.6, 0.8, 1.0.

applying a moderate measuring field and the magnetization values (M) were recorded. In the FC process, the sample is cooled in the presence of a non-zero magnetic field and the same procedure is followed as in case of ZFC process.

Figs. 7 and 8 show the Magnetization–Temperature curves recorded in FC and ZFC modes for the samples $Li_{0.1}Co_{0.8}$ $Fe_{2.1}O_4$ and $CoFe_2O_4$ in an external magnetic field of 100 Oe and 1 KOe respectively.

In ZFC mode, the two ferrite samples under investigation i.e. $Li_{0.1}Co_{0.8}$ $Fe_{2.1}O_4$ and $CoFe_2O_4$ were cooled from 375 K down to 2 K in the absence of magnetic field. Then, a measuring field of 100 Oe and 1 KOe were applied and the magnetization measurements were made in the warming cycle. Whereas, in FC mode the samples were cooled from 375 K down to 2 K in the presence of the measuring field and then magnetization measurements were recorded as a function of rising temperature.

From the figures, it is clear that both the FC and ZFC magnetization decrease by decreasing the temperature for both the samples under two different applied fields (100 Oe and 1 KOe).

There exists a bifurcation between the FC and ZFC modes as evident from the figures owing to the magnetic relaxation nature of the nano particles and confirms their superparamagnetic nature. The temperature at which this bifurcation in the two modes is observed is defined as bifurcation temperature or blocking temperature (T_b). It is observed that the blocking temperature did not change with the increase in applied field, but shows a strong bifurcation in the FC and ZFC curves under higher applied field i.e. at 1 KOe, showing irreversibility of FC and ZFC magnetization curves. For both the samples the bifurcation or blocking temperature is observed at 350 K.

Figs. 9 and 10 show Magnetization Hysteresis curves for $Li_{0.1}Co_{0.8}$ $Fe_{2.1}O_4$ and $CoFe_2O_4$ samples at 5 K and 310 K. It is observed that the coercivity is more at lower temperature and it decreases with increase in temperature. The values of Coercivity (H_c) and remanence (M_r) were measured from the hysteresis curves and were recorded in Table 2. From the table it is clear that H_c and M_r values at 310 K for both the samples is very less which will approach zero at above room temperature. Zero coercivity and Zero remanence is the characteristic feature of the superparamagnetic behavior of the magnetic nano particles [21]. By comparing the FC–ZFC data and hysteresis curves data it is clear that below blocking temperature i.e. <350 K the material shows some hysteresis and hence behaves as ferromagnetic material. Above blocking temperature i.e. >350 K, hysteresis disappears

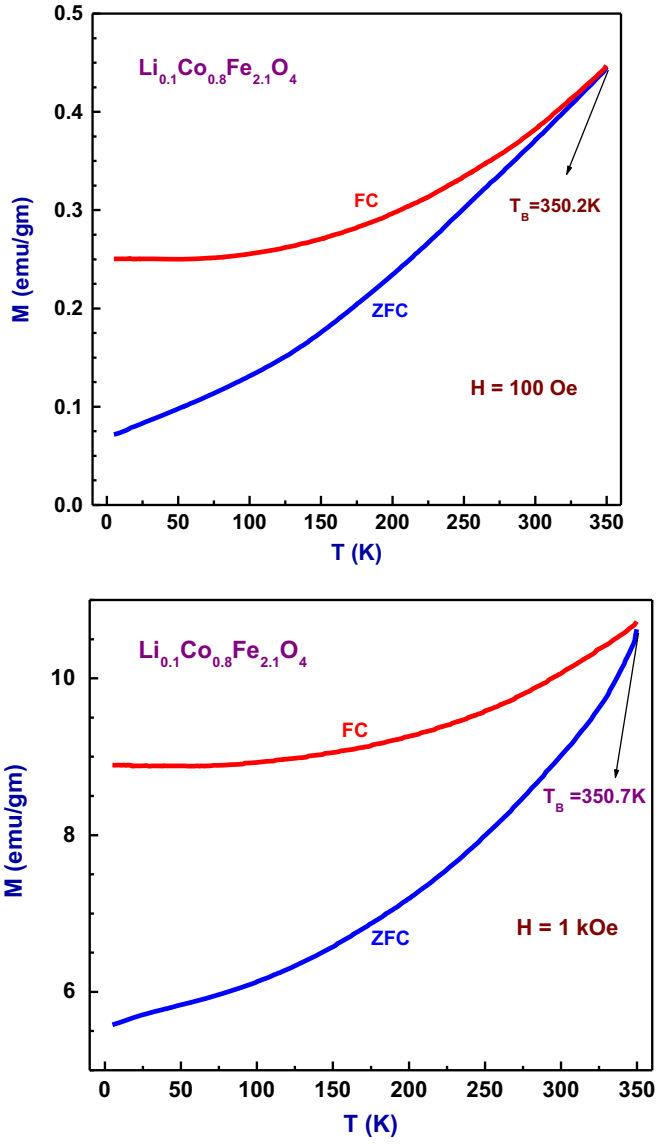

Fig. 7. Magnetization–Temperature curves recorded in FC and ZFC modes for the sample $Li_{0.1}Co_{0.8}$ $Fe_{2.1}O_4$ in an external magnetic field of 100 Oe and 1 KOe.

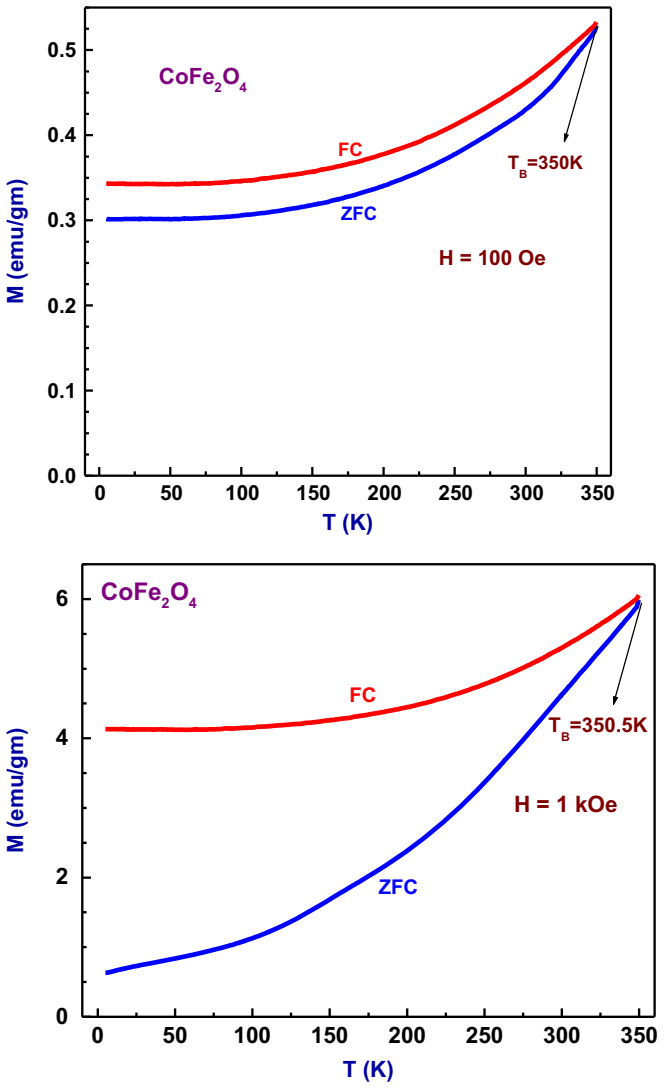

Fig. 8. Magnetization–Temperature curves recorded in FC and ZFC modes for the sample $CoFe_2O_4$ in an external magnetic field of 100 Oe and 1 KOe.

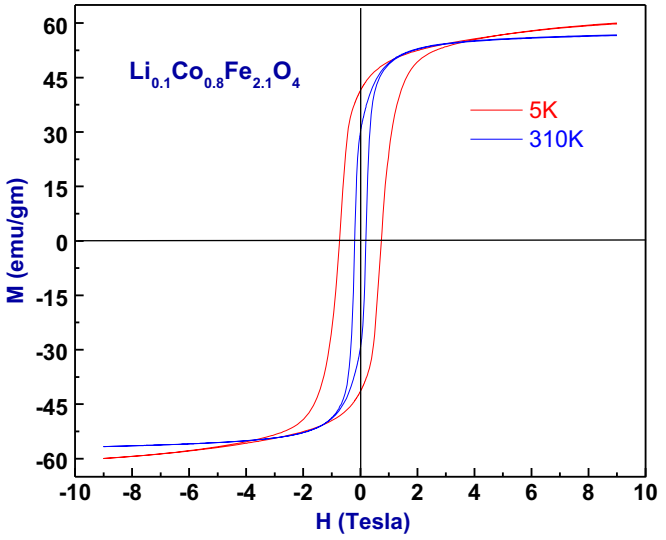

Fig. 9. Magnetization Hysteresis curves for $Li_{0.1}Co_{0.8}$ $Fe_{2.1}O_4$.

and the material behaves as superparamagnetic. Hence, Li–Co nano ferrites with superparamagnetic behavior are desirable for bio-medical applications.

6. Conclusion

Li–Co nano ferrites with the chemical composition $[Li_{0.5}Fe_{0.5}]_{1-x}Co_xFe_2O_4$ $x=0.0$, 0.2, 0.4, 0.6, 0.8, 1.0 were successfully prepared by Citrate gel auto-combustion technique with a crystallite size ranging from 37 to 42 nm. X-ray diffraction studies confirmed the formation of single phased cubic spinel structure of the ferrites without any impurity peak. The SEM analysis reveals the large agglomeration of the nano particles. Field cooled (FC) and Zero field cooled (ZFC) magnetization measurements on $Li_{0.1}Co_{0.8}$ $Fe_{2.1}O_4$ and $CoFe_2O_4$ nano ferrites under an applied field of 100 Oe and 1 KOe in the temperature range of 5–375 K have resulted the blocking temperature (T_b) at around 350 K i.e. above room temperature for both the ferrites. These two ferrites show ferromagnetic behavior below blocking temperature i.e. 350 K and show

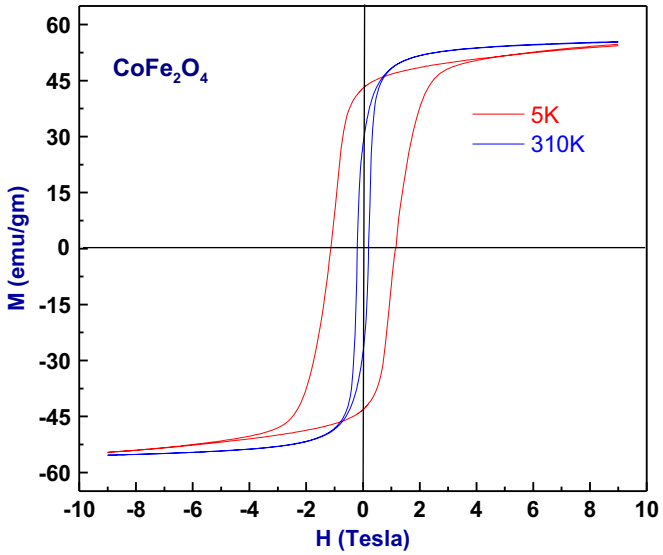

Fig. 10. Magnetization Hysteresis curves for $CoFe_2O_4$.

Table 2
Coercivity (H_c) and Remanence (M_r) of $Li_{0.1}$ $Co_{0.8}Fe_{2.1}O_4$ and $CoFe_2O_4$ from the Hysteresis curves.

Magnetic parameters	$Li_{0.1}$ $Co_{0.8}Fe_{2.1}O_4$		$CoFe_2O_4$	
	5 K	310 K	5 K	310 K
Coercivity (H_c)	0.74T	0.19T	1.11T	0.18T
Remanence (M_r) (emu/gm)	41.63	29.1	43.52	29.9

superparamagnetic behavior above 350 K. Hence, these ferrites are desirable for bio-medical applications.

Acknowledgment

The authors are very grateful to Prof. K. Venugopal Reddy, Head, Department of Physics, University College of Science, Osmania University for his support in carrying out the research work. Authors are thankful to Dr. V. Siruguri, Centre Director, UGC-DAE, Consortium for Scientific Research, Mumbai Centre and to Dr. P. D. Babu, Scientist, Mumbai centre for providing Low temperature Magnetic measurements. The authors are thankful to UGC, New Delhi for their financial assistance through Major Research Project.

References

[1] M. Raghasudha, D. Ravinder, P. Veerasomaiah, J. Magn. Magn. Mater. 355 (2014) 210.
[2] I. Soibam, S. Phanjoubam, C. Prakash, J. Magn. Magn. Mater. 321 (2009) 2779.
[3] A.M. Shaikh, C.M. Kanamadi, B.K. Chougule, Mater. Chem. Phys. 93 (2005) 548.
[4] S.A. Jadhav, Mater. Chem. Phys. 65 (2000) 120.
[5] N. Singh, A. Agarwal, S. Sanghi, P. Singh, J.Magn.Magn.Mater. 323 (2011) 486.
[6] A.M. Shaikh, S.S. Bellad, B.K. Chougule, J. Magn. Magn. Mater. 195 (1999) 384.
[7] K. Mohan, Y.C. Venudhar, J. Mater. Sci. Lett. 18 (1999) 13.
[8] S.S. Bellad, R.B. Pujar, B.K. Chougule, Mater. Chem. Phys. 52 (1998) 166.
[9] S.A. Mazen, F. Metawe, S.F. Mansour, J. Phys. D 30 (1997) 1799.
[10] S.A. Mazen, A. Elfalaky, A.Z. Mohamed, H.A. Hashem, Mater. Chem. Phys. 44 (1996) 293.
[11] C.S. Liu, W.B. Shu, M.J. Tung, M.Y. Ke, J. Appl. Phys. 67 (1990) 5506.
[12] S.C. Watawe, B.D. Sarwade, S.S. Bellad, B.D. Sutar, B.K. Chougule, J.Magn.Magn. Mater. 214 (2000) 55.
[13] M.C. Dimri, A. Verma, S.C. Kashyap, D.C. Dube, O.P. Thakur, C. Prakash, Mater. Sci. Eng. B 133 (2006) 42.
[14] L. Zhao, Y. Cui, H. Yang, L. Yu, W. Jin, S. Feng, Mater. Lett. 60 (2006) 104.
[15] R.S. Devan, Y.D. Kolekar, B.K. Chougule, J. Phys. Condens. Mater. 18 (2006) 9809.
[16] L. Yin, Q. Tai, Chin. Phys. 16 (2007) 3837.
[17] M. Raghasudha, D. Ravinder, P. Veerasomaiah, Adv. Mat. Lett. 4 (12) (2013) 910.
[18] M. Raghasudha, D. Ravinder, P. Veerasomaiah, Adv. Mat. Phy. Chem. 3 (2013) 89.
[19] J.M. Song, J.G. Koh, J. Magn. Magn. Mater. 152 (1996) 383.
[20] Sonal Singhal, Sheenu Jauhar, Jagdish Singh, Kailash Chandra, Sandeep Bansal, J. Mol. Stru. 1012 (2012) 182.
[21] C.P. Bean, I.S. Jacobs, Appl. Phys. 27 (1956) 1448.

Hadoop Architecture and its Functionality

Dr. B V Ramana Murthy,
Department of CSE
Jyothishmathi College of Engg and Technology, Shamirpet, India

Mr. V Padmakar
Department of CSE,
Guru Nanak Institutions Technical Campus, Hyderabad

Mr. M Abhishek Reddy
Department of CSE,
Jyothishmathi College of Engg Technology, Shamirpet, India.

Abstract:
Hadoop is nothing but a "framework of tools" and it is a java based programming framework (In simple terms it is not software). The main target of hadoop is to process the large data sets into smaller distributed computing. It is part of the Apache project sponsored by the Apache Software Foundation. As we observe in database management system, all the data are stored in organized form by following the rules like normalization , generalizations etc., and hadoop do not bother about the DBMS features as it stores large amount of data in servers. We are studying about Hadoop architecture and how big data is stored in servers by using this tools and the functionalities of Map Reduce and HDFS (Hadoop File System).

Keywords: Big Data, HDFS, Map Reduce Task Tracker, Job Tracker, Data Node, and Name Node.

Introduction-

Big Data Introduction: We probably heard about Big Data[1], but we may wondering what is it and why we should care. Ok, for starters big data is like data is getting bigger for a while now. From dawn of a time to less than a decade ago mankind generated about 5 Exabyte's of data. In 2012 global data brought to 2.7 Zetta byte of data which is 500 times more data than all data ever generated in 2003. And it has grown 3 times bigger in 2015. Some of the reasons that data is getting bigger[2] is that continuously being generated more sources and more devices. Much back data is like videos, photos, comments and social media comments on web sites is unstructured. That means data is stored in structures pre defines tables, instead it's often made up of volumes of text dates numbers in fact they are typically free from by nature. Certain data sources are arriving so fast not even a time to store the data before applying analytics to it. That is why traditional data management and analytics tools unable to store, process and analyze big data. So we could just ignore big data after all it's worth the efforts? Turns out, it is. A recent study concluded only 10-15% organization would take full advantage of big data. In order to generate that level of insight and competitive advantage from big data innovative new approach and technologies are required because big data we looking at is like a mountain.

http://sites.google.com/site/ijcsis/
ISSN 1947-5500

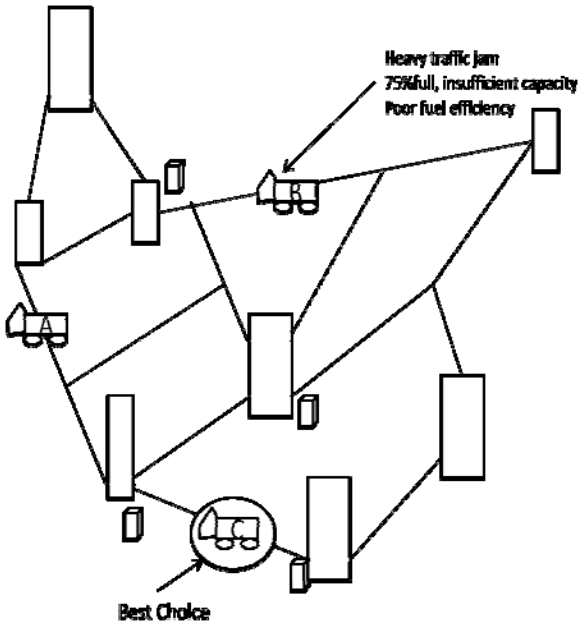

Imagine a logistic company mining data on truck pickup and delivering schedule on real time traffic patterns. The data they are using combines real time GPS speed from trucks. Public traffic pattern data or if I take cargos from data. Imagine they get a call from a new pickup, which truck should they send? The closest one right. So what if the route to the closets truck has heavy traffic jam? What if the cargo loaded on that truck doesn't allow space for new data? May be the route for that truck involve a series of great changes. In that case closest truck is not the best choice. They might b more costly less efficient or unable to service the customer needs. But the only way to arrival of optimal decision is to analyze multiple big data sources in real time.

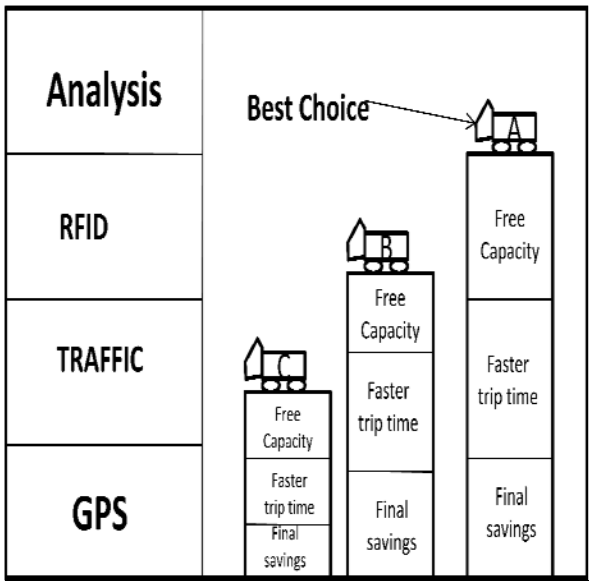

Big Data = Big Impact

INTRODUCTION

As we see in our daily routine entire world has become an E-world (electronic world in common terms). So we can say increase in E-World in directly proportional to increase in data, so we required large no of servers to save the data.

To overcome this problem hadoop came into existence. Hadoop is so profound and powerful java tool which process large data into small data computations. Hadoop was created by Doug Cutting and Mike Cafarella in 2005 and Doug Cutting, who was working at Yahoo at the time named it after his son's toy elephant. And later they donated hadoop to apache so now we can say that hadoop is directed under the control of apache.

Hadoop architecture is playing a very important role in breaking of large data in to small data sets. In this paper we will know about architecture how the data[7] will get spitted and get computed and all its functionality.

http://sites.google.com/site/ijcsis/
ISSN 1947-5500

Here comes a question in mind, how does Facebook, Google, Online marketing (retails), and all does store large amount of data?

The reason behind is all these frameworks uses hadoop system. The main reason hadoop came into existence of 3 factors.

They are velocity volume and verity. Velocity, large amount of data is coming with very high speed. Volume, large amount of data increasing day by day with huge volume. Verity, Data which are lots of verity. Ex: Audio, Video and etc.

Big data is creating large and growing files which are measured in terabytes (10^12) and petabytes (10^15) and the data is unstructured, we do not need relational models. This huge data is coming from tons of sources like users, applications like Facebook, yahoo, twitter etc, system, sensors and on and on.

The main problem hadoop is fixing is that in traditional hard disk transfer rate of data will be approx 60-100 MB/s and in hadoop there will be around 250-500 MB/s.

A. Reasons for hadoop evolution

Traditional Approach: when an enterprise will have a powerful computer it will process with very high speed it performance will be high and we can say computer is scalable. But there will be a certain point even a powerful computer cannot process Big Data. Now we can say computer is not scalable. This was one of the main reason hadoop came into existence.

Hadoop Approach: The main target of hadoop is to break Big Data[4] into smaller pieces and store into Commodity Hardware (Numerous Low Cost Computers known as Commodity Hardware). We do not require any powerful computers. At the same time all the computations are done on distributed system as well. All these computations are done at the same time and results send back to the application[6].

B. Hadoop simple Architecture

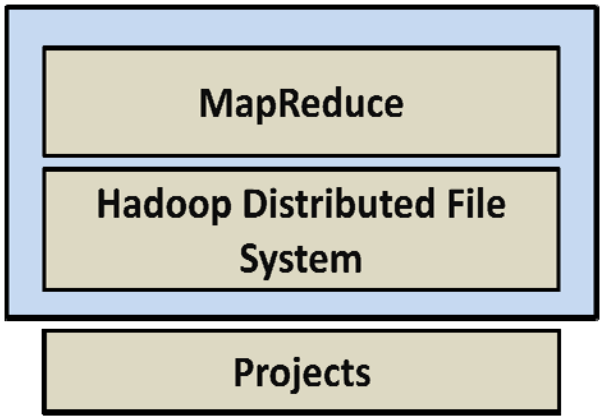

Figure 1: Hadoop Architecture

Hadoop Architecture consisting of three simple things i.e. MapReduce, HDFS, Projects. Hadoop MapReduce is a software framework for easily writing applications which process vast amounts of data (multi-terabyte data-sets) in parallel on large clusters (thousands of nodes) of commodity hardware in a reliable, fault-tolerant manner. Hadoop Distributed File System (HDFS) is a Java-based file system that provides scalable and reliable data storage that is designed to span large clusters of commodity servers. Finally the projects, as we said hadoop is framework of tools so all the tools come under this project. Some examples for projects are Hive, HBase, Mahout, Pig, Oozie, Flume, Sqoop etc.

Hadoop consisting of two nodes:-

1. Slave node
2. Master node.

1. Slave Node: Slave node are having two major components

- Task Tracker.
- Data Node.

http://sites.google.com/site/ijcsis/
ISSN 1947-5500

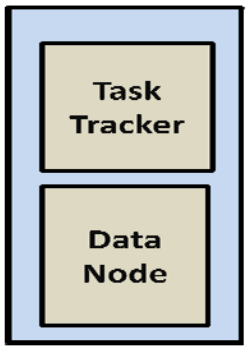

Figure 2: Slave node

1.1 Task Tracker: The job of task tracker is to processes the piece of task that has been given to this particular node.

1.2 Data Node: The job of data node is to manage piece of data that has been given to this particular node.

There can be n number of slave nodes. Here data is clustered in to these numerous slaves.

2. Master Node: The reason this is said to be a master node is that, master node having two another major components along with task tracker and data node.
1.1 Job Tracker.
1.2 Name Node.

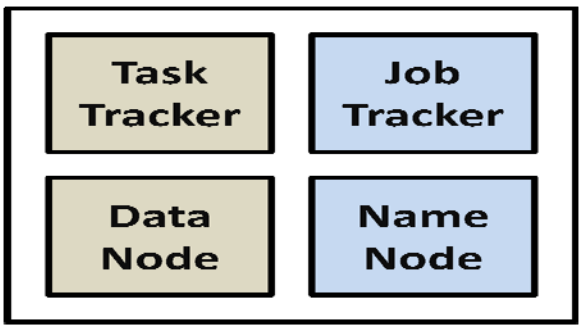

Figure 3: Master

1.1 Job Tracker: The role of job tracker component is to break higher task into smaller pieces and it will send each small computation to task trackers including its own. And after completing it will send back its results to the job tracker and it will combine the results and it will send back to application.

1.2 Name Node: It is responsible of keep an INDEX of which data is resigning on which data node.

Interaction between Master node and Slave node

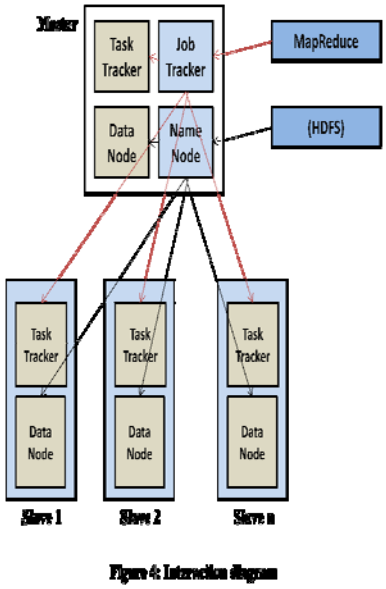

Job Tracker and Name Node functionality and interaction between them is observed in figure

MapReduce: Task Tracker and Job Tracker are the part of high level i.e. map reduce. So they all fall under the umbrella of map reduce.

File System: Data Node and Name Node are the part of high level i.e. map reduce. So they all fall under the umbrella of file system called HDFS.

Batch Processing:
One of the attribute of hadoop is that is a "Batch Processing" set of tools. So application would assign or provide a task for hadoop to in form of a QUEUE.

Once the task is completed it will inform application and results will be given back to application.

http://sites.google.com/site/ijcsis/
ISSN 1947-5500

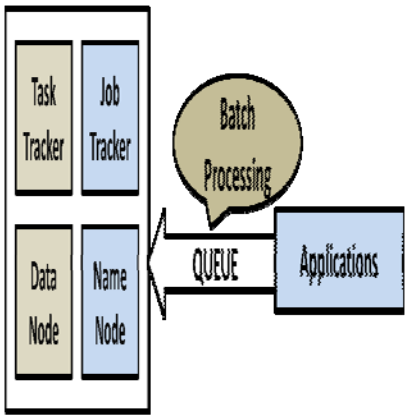

Figure 4: Batch Processing

Direction flow of data:

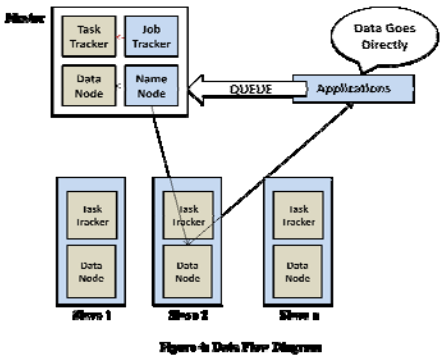

Figure 4: Data Flow Diagram

Here data flow directly when application comes in contact with master node and check the index on name node about the required information on which data node the data is residing. After the required information is gathered it directly goes to the application i.e. application doesn't wait for the name node to give back result. This is one of the important features is that; time optimizing in getting back result.

Fault Tolerance for Data and Master Backup:

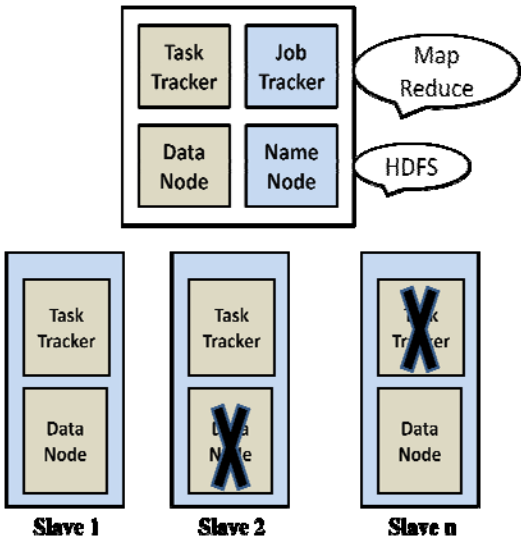

Figure 5: Fault Tolerance and Master Backup

One of the basic and important thing that hadoop keeps in mind is Fault Tolerance. If any of the Data Node gets failed, system doesn't go in to stop state by default Hadoop maintain 3 copies of each file and these copies are scattered along different computers. If any one of the task trackers gets failed to do its task, job tracker will detect the failure and it assigns the same task to other task tracker. When Master node gets failed then the tables that are maintained by name node which contain tables are backed up and copied over different computers. The enterprise version of hadoop also keeps two masters. One the main master and other the backup master.

Advantages of Hadoop:

One of the main advantages of hadoop to the programmers is

- Programmer need not worry about where the file is located name node will take care of it.
- Programmer need not worry about how to manage files; hadoop will take care of it.
- Programmer need not worry about how to break computations into pieces hadoop will take care of it.

http://sites.google.com/site/ijcsis/
ISSN 1947-5500

- Programmer need not worry about writing the scalable programmers.

Consistency: - Component failures during execution of a job will not affect the outcome of the job.

Scalability: - Hadoop is highly scalable. As the no of slave nodes increases scalability also increases. Scalability of hadoop is linear, as we required processing speed to be increased then increase the no of computers.

Usage Areas:
There are tons of wide areas[3] where hadoop is used some of them are

- Social Media: Facebook, Twitter, yahoo, YouTube etc.
- Retail: e-Bay, Amazon etc.
- Searching Tools: Google.
- Companies: IBM etc.

And many more like American Airlines, The New York times and on and on. There are tons of users[5] who are using hadoop.

Conclusion
In this paper we have studied the entire architecture of hadoop and its functionality. It clearly explains that managing of big data in to clusters, how data is stored in numerous low cost computers (Commodity Hardware). Hadoop achieved Scalability and Consistency of data. As we seen in Database Management System we required organized data (following rows and columns) to store in server, we need follow normalizations techniques but where as in hadoop a programmer need not worry about relational data models.

Future Scope: - According to Yahoo point of view by the year 2015 50% of the enterprise[8] will processed by hadoop.

Biblography:-

[1] Advancing Discovery in Science and Engineering. Computing Community Consortium. Spring 2011.

[2] Drowning in numbers -- Digital data will flood the planet—and help us understand it better. The Economist, Nov 18, 2011. http://www.economist.com/blogs/dailychart/2011/11/big-data-0

[3] Computational Social Science. David Lazer, Alex Pentland, Lada Adamic, Sinan Aral, Albert-László Barabási, Devon Brewer,Nicholas Christakis, Noshir Contractor, James Fowler, Myron Gutmann, Tony Jebara, Gary King, Michael Macy, Deb Roy, and Marshall Van Alstyne. Science 6 February 2009: 323 (5915), 721-723.

[4] Big data: The next frontier for innovation, competition, and productivity. James Manyika, Michael Chui, Brad Brown, Jacques Bughin, Richard Dobbs, Charles Roxburgh, and Angela Hung Byers. McKinsey Global Institute. May 2011.

[5] Folowing the Breadcrumbs to Big Data Gold. Yuki Noguchi. National Public Radio, Nov. 29, 2011. http://www.npr.org/2011/11/29/142521910/the-digital-breadcrumbs-that-lead-to-bigdata

[6] The Search for Analysts to Make Sense of Big Data. Yuki Noguchi. National Public Radio, Nov. 30, 2011. http://www.npr.org/2011/11/30/142893065/the-search-for-analysts-to-make-sense-of-big-data

[7] The Age of Big Data. Steve Lohr. New York Times, Feb 11, 2012. http://www.nytimes.com/2012/02/12/sunday-review/big-datas-impact-in-the-world.html

[8] A Sustainable Future. Computing Community Consortium. Summer 2011.

http://sites.google.com/site/ijcsis/
ISSN 1947-5500

[9] Windows Azure Platform: http://www.microsoft.com/windowsazure/

[10] Microsoft Service Bus and Access Control for Windows Azure platform AppFabric : http://www.microsoft.com/windowsazure/whitepapers/

[11] Windows Azure Tools – Constraints: http://msdn.microsoft.com/en-us/library/dd203058.aspx

[12] Microsoft Azure Comparison: http://cloudenterprise.info/2008/10/29/microsoft-azure-vs-amazon-google-and-vmware/

[13] Geneva Framework: http://download.microsoft.com/download/7/d/0/7d0b5166-6a8a-418a-addd-95ee9b046994/GenevaFrameworkWhitepaperForDevelopers.pdf

[14]SQL Azure: http://www.microsoft.com/windowsazure/sqlazure/

[15]WCF Data Services: http://msdn.microsoft.com/en-us/data/aa937697.aspx

[16]Windows Azure Platform AppFabric Services: http://msdn.microsoft.com/en-us/library/dd630576.aspx

Conclusion-

Windows Azure runs on machines in Microsoft data centers. Rather than providing software that Microsoft customers can install and run themselves on their own computers, Windows Azure is a service: Customers use it to run applications and store data on Internet-accessible machines owned by Microsoft. Those applications might provide services to businesses, to consumers, or both.

Dr. B. V.Ramana Murthy has done his PhD from Osmania University, presently he working as Professor in Computer Science and Engineering, has 18 years of experience in Teaching and R&D. His primary area of interest is Software Engineering & Web Engineering.

Mr. V Padmakar is pursuing PhD in CSE and has done his M Tech (CSE) from JNTUH, presently working as Professor in Computer Science and Engineering has 17 years of experience in Teaching and Industry. His primary area of interests is Software Engineering, Network Security and Data mining

Mr. Abhishek Reddy Mirupati is a Computer Science and Engineering student at Jyothishmathi College of Engineering and Technology pursuing his Bachelor of Technology in CSE. His primary area of interest is Object Oriented Programming and Data Base Management System.

http://sites.google.com/site/ijcsis/
ISSN 1947-5500

www.amlett.com, www.vbripress.com/aml, DOI: 10.5185/amlett.2015.5610 Published online by the VBRI press in 2015

Impact of transition metal ion doping on electrical properties of lithium ferrite nanomaterials prepared by auto combustion method

G.Aravind[1], Abdul Gaffoor[1], D. Ravinder[1*], V. Nathanial[2]

[1]*Department of Physics, Osmania University, Hyderabad 500007, Telangana, India*
[2]*Department of Physics, University College of Science, Sifabad, O.U, Hyd, Telangana, India*

[*]Corresponding author. Tel: (+91) 9246162228; E-mail: ravindergupta28@rediffmail.com

Received: 18 August 2014, Revised: 30 September 2014 and Accepted: 10 November 2014

ABSTRACT

Nano crystalline cobalt substituted lithium ferrites having chemical formula $[Li_{0.5}Fe_{0.5}]_{1-x}\ Co_x\ Fe_2O_4$ (where x=0.0, 0.2, 0.4, 0.6, 0.8 and 1.0) have been prepared by the citrate gel auto combustion method at low temperature (180 ^oC). The prepared samples were sintered at 500 ^oC for 4 hours. Single phase of these samples were confirmed by x-ray powder diffraction technique and found that lattice parameter increases with increasing with the Cobalt substituted concentration, and the values of crystallite size, x-ray density, bulk density and porosity of the prepared samples were calculated from the XRD analysis. The dc electrical resistivities of the prepared Li-Co ferrites were studied by using the two probe method in the temperature range of 473-873 K (200-600 ^oC). A plot of log (σT) vs inverse of temperature yields a almost straight line which reveals the semiconducting behavior of prepared ferrite samples. The dielectric properties namely dielectric constant (ε'), dielectric loss tangent ($\tan \delta$) of these Li-Co nano crystalline ferrites have been studied using an LCR meter from the room temperature to 700 K at various selected frequencies up to 5 MHz. The dielectric constant (ε') of all prepared samples was increased with increasing in temperature. These results have been explained on the basis of Koop's theory, concentration of Fe^{+2} and Fe^{+3} ions on the octahedral site and hoping frequency of charge carriers (electrons) between Fe^{+2} and Fe^{+3} ions. Copyright © 2015 VBRI press.

Keywords: Citrate gel method; nano ferrite; XRD studies; dc resistivity; dielectric properties.

G. Aravind is a research scholar under the supervision of Prof. D. Ravinder, in Department of Physics, Osmania University, Hyderabad, Telangana, India. He obtained his M.Sc. from Osmania University in 2007. He has published 4 research papers in International Journals and has 4 years of teaching experience.

D. Ravinder is working as a professor in Department of Physics, Osmania University, Hyderabad, Telangana, India. His research work is on magnetic and electrical properties of ferrites,thin films, GMR materials, Cu-Co alloy thin films and nano-materials by pulsed laser deposition, sol-gel, citrate precursor method and electro deposition. To his credit, he has published 150 research papers in International Journals. He has been awarded Young Scientist award received by Dr. Abdual Kalam, for outstanding contributions in the field of science and Technology, UGC research award, Boyscast by DST (Department of science and technology), Government of India, JSPS fellowship Japan and Royal Society fellowship, UK . He also visited USA, UK, Sweden, Ireland, Singapore and Japan for Collaborative Research and invited talks.

Introduction

Magnetic spinel ferrites have captured the global market and grabbed the attention of many researchers due to their fascinating and exotic electromagnetic properties. The unique properties of nano-scaled magnetic ferrite particles have generated more interest in the science and engineering community because these nano-crystalline particles have a high surface to volume ratio which results novel properties contrary to those bulk particles. The excellent electrical and dielectric properties of the some of the nano ferrites make them suitable for the high frequency applications in the field of telecommunications. The properties of ferrites depend on several factors which include method of preparation, sintering temperature/time, pH value, amount

and type of substitution, and most important being the distribution of metal cations at tetrahedral and octahedral sites in the spinel lattice of the ferrites etc to obtain desired properties for specific applications **[1].** These nano crystalline magnetic ferrites have been used as permanent magnets in various devices as these are regarded as better magnetic materials than pure metals because of their large value of resistivity and larger efficiency and reasonable cost. Lithium ferrites and substituted lithium ferrites have proved to be very good alternatives for garnet ferrites in microwave applications due to their low cost. Lithium ferrite belongs to the group of soft ferrite materials extensively used in many applications such as microwave devices computer memory chips, magnetic recording media, radio frequency coil fabrication, transformer cores rod antennas and many branches of telecommunication and electronic engineering **[2-6].** Several researchers have studied transition metal substituted lithium ferrites to enhance their properties such as Li-Cr **[7, 8],** Li-Cd **[9],** Li-Zn **[10],** Li-Mg **[11],** Li-Co **[12,13].** Several preparation methods are used for synthesizing nano sized spinel ferrites such as co-precipitation, sol-gel, micro emulsion, hydrothermal, citrate-gel, reverse micelle methods **[14-16]**. Among the all the preparation methods, citrate gel method is very adequate for the preparation of nano crystalline ferrites. This method has a special significances (i) in yielding ultrafine single phase nano crystalline ferrites (ii) no ball milling is required, (iii) better purity, (iv) gives homogeneous mixture of metal ions, (v) narrow grain size distribution, (vi) low temperature processing which reduces the lithium volatilization and (vii) relatively low cost process as compared with other wet chemical synthesis processes.

The objective of present work is to obtain cobalt substituted lithium ferrite systems having compositional formula $[Li_{0.5}Fe_{0.5}]_{1-x}\ Co_x\ Fe_2O_4$ (where x=0.0, 0.2, 0.4, 0.6, 0.8 and 1.0) prepared by citrate gel auto combustion method at lower sintering temperature. Literature is accessible on structural properties of investigated system. To the best of our knowledge, investigations on detailed electrical and dielectric properties of Li-Co ferrite system prepared by citrate gel method have not been reported. The present study reports on detailed synthesis, structural, electrical and dielectric properties of Li-Co ferrite nano particles.

Table 1. Raw material information.

S.No	Chemical Name	Purity (%)	Manufacturer name	Placeof Manufacture
1	Lithium-nitrate ($LiNO_3$)	98.8	SIGMA-ALDRICH	Spruce street,St.Louis,USA.
2	Ferric-nitrate ($Fe(NO_3)_29H_2O$)	99.0	CentralDrug House (P) Ltd	New Delhi, India
3	Cobalt-nitrate ($Co(NO_3)_26H_2O$)	99.0	Sdfine-CHEM LIMITED	Mumbai, India.
4	Citric-acid ($C_6H_8O_7.H_2O$)	99.7	S d fine-CHEM LIMITED	Mumbai, India.
5	Ammonia solution (NH_3).	99.7	Sdfine-CHEM LIMITED	Mumbai, India

*These chemicals were used in the material synthesis without further purification.

Experimental

Materials and methods

Nano crystalline cobalt substituted lithium ferrites having chemical formula $[Li_{0.5}Fe_{0.5}]_{1-x}\ Co_x\ Fe_2O_4$ (where x=0.0, 0.2, 0.4, 0.6, 0.8 and 1.0) have been prepared by the citrate gel auto combustion method at low temperature (180^{o}C). In this method of preparation, an exothermic reaction takes place between the oxidant and reductant in which NO^{3-} ions are acts like the oxidant and the carboxyl group is the reductant. The enthalpy of exothermic reaction is used to synthesize materials in nano form.

Raw materials

The starting materials information viz. their purity, manufacturer name and place of manufacturing are given in the **Table 1**.

Method of synthesis

Stoichiometric amounts of the metal nitrates along with citric acid were dissolved in minimum amount of distilled water. Molar ratio of metal nitrates and citric acid was taken as 1:1 **[17]**. The resulting clear solution was mixed and heated at 80^{o}C with continuous stirring by using a magnetic stirrer with hot plate. The pH value of the solution was controlled at 7 by addition of ammonia drop by drop. A change in the viscosity and color of the solution was observed and converted to a gel after stirring for some hours. By increasing the temperature up to 180 ^{o}C, the gel ignited on drying due to self combustion with the evolution of gases giving rise to a dark gray ash as product. This resultant ash powder samples were sintered for 4h at a temperature of 773K at default heating rate of 4K/min using a temperature programmed box furnace. The powdered materials were characterized by various techniques.

Table 2. Structural parameters of the prepared Li-Co ferrite sample.

Composition	Mol.wt (gm/mol)	Crystallite size(nm)	Lattice Parameter(A^o)	X-ray Density(d_x) (gm/cc)	Experimental Density(d_e) (gm/cc)	Porosity (P)
$Li_{0.5}Fe_{2.5}O_4$	207.079	41.90	8.356	4.713	4.286	9.00
$Li_{0.4}Co_{0.2}Fe_{2.4}O_4$	212.587	43.01	8.370	4.815	4.379	9.10
$Li_{0.3}Co_{0.4}Fe_{2.3}O_4$	218.095	38.44	8.374	4.931	4.388	11.00
$Li_{0.2}Co_{0.6}Fe_{2.2}O_4$	223.603	37.57	8.386	5.035	4.393	12.70
$Li_{0.1}Co_{0.8}Fe_{2.1}O_4$	229.111	37.06	8.394	5.144	4.580	10.90
$CoFe_2O_4$	234.619	36.90	8.404	5.250	4.685	10.70

Characteristic techniques

The X-ray diffraction analysis of the prepared samples were performed on a Philips X pert PRO diffractometer using Cu Kα as radiation source to study the phase developed of the synthesized nano particles and to calculate the structural parameters. The crystallite size of the Li-Co nano ferrite samples was investigated based on the X-ray diffraction line broadening and calculated using the Debye-Scherer's formula **[18]**. Structural parameters like lattice parameter, X-ray density, Porosity have been calculated by using XRD data and given in the **Table 2**. For measuring the electrical properties, powders were added with a small amount 2 % PVA as a binder to press the prepared powders into circular

pellets having 13 mm diameter and 2.5 mm thickness by applying a pressure of 4 tons. The prepared pellets were sintered at 500 ^{o}C for 4 hours in air in muffle furnace for the densification of the sample. For having a good ohmic contact silver paste was applied on both sides of the pellet. The dielectric properties of the sample were measured by using Agilent E4986 precession LCR meter from room temperature to 725 K at different frequencies up to 5 MHz. DC resistivity of the prepared samples was measured by using two probe methods in the temperature range 473-873 K.

Results and discussion

XRD analysis

The phase identification and determination of structural parameters of the prepared samples were measured by the X-ray diffraction analysis. The X-ray diffraction pattern of the prepared cobalt substituted lithium ferrite samples were shown in below **Fig. 1**. The strong diffraction from the (220), (311), (400), (422), (511), and (440) planes confirms the pure spinel phase of the prepared samples. The XRD pattern perfectly matches with the standard pattern with JCPDS reference code 00-013-0207.

It can be seen that the location of the peaks in XRD pattern of all samples are coincident, which indicate that there were no distinct differences in phase structure of Li-Co nano crystalline ferrites with different cobalt composition. It was observed that cobalt ions in the lattice were partly replaced by iron and lithium ions and then increased the lattice constant. The XRD analysis of the prepared Li-Co nano crystalline samples provides the estimation of the crystallographic lattice constant (a), crystallite size (D), X-ray density (d_x) and experimental density (d_e) etc as given in **Table 2**.

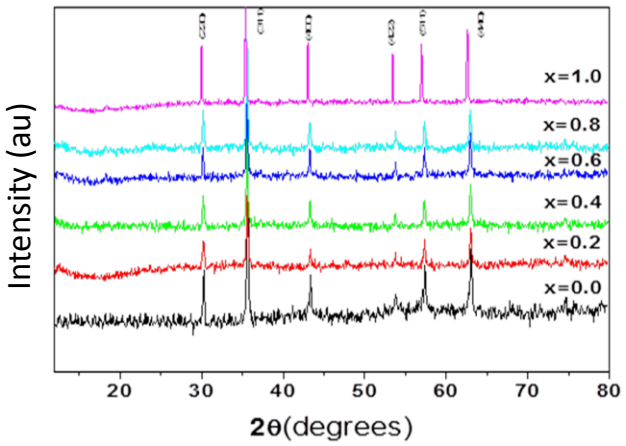

Fig. 1. XRD pattern of the $[Li_{0.5}Fe_{0.5}]_{1-x}$ Co_x Fe_2O_4 nano ferrites.

The values of the crystallite size which are calculated from the Debye-Scherer's formula were in the range of 36-43 nm which confirm the nano crystalline form. The lattice parameter of the samples increases with cobalt composition which obeys the Vegard's law **[19]**. From the **Table 2** we observed that lattice parameter of the prepared samples increases with increase in the cobalt composition because ionic radii of the six-fold coordinated Co^{+2} (0.82A^o) being larger than the six-fold coordinated Fe^{+3} (0.64A^o) and Li^{+1}(0.76A^o) similarly X-ray density of the prepared samples increases with cobalt composition because molar masses of the substituted cobalt ions were larger than that of iron ions. The experimental density of the samples were observed to be less than the X-ray density which reveal that the some porous nature of the prepared samples. The variation of lattice parameter and experimental density of the prepared samples with cobalt composition was shown in below **Fig. 2**.

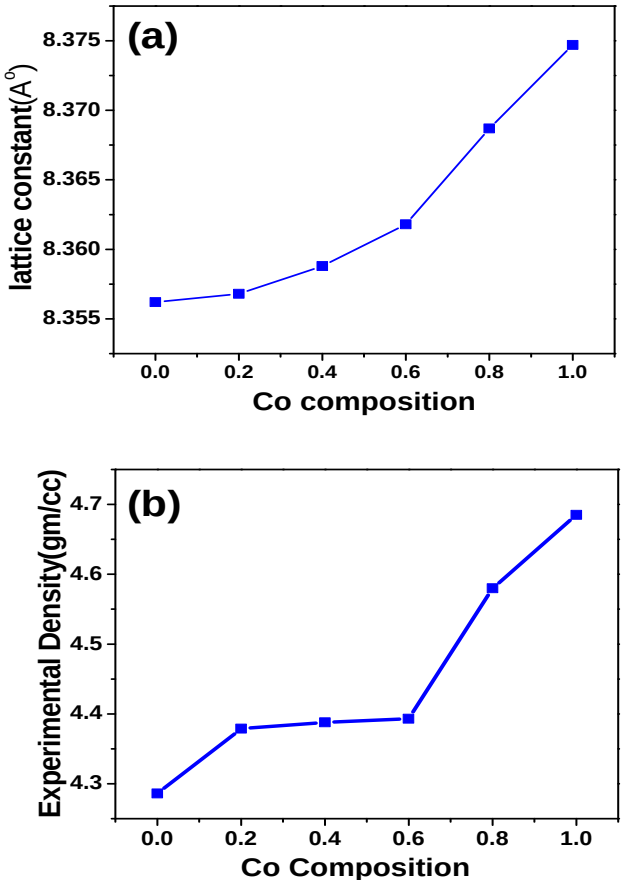

Fig. 2. Variation of (a) Lattice parameter and (b) Experimental density with Co composition of $[Li_{0.5}Fe_{0.5}]_{1-x}$ Co_x Fe_2O_4 ferrites.

DC resistivity studies

The dc electrical resistivity was the important property to study the conduction mechanism in ferrites. The conduction mechanism in ferrites was due to the hopping of charge carriers (electrons), between the ions of same element, present in more than more valence state, distributed randomly over equivalent crystallographic sites in lattice. The probability of hopping depends on the separation between the involving ions and activation energy **[33]**.The electrostatic interaction between the conduction electron and nearby ions may result in the polarization of the surrounding region so the electron present at the center of the polarization well. This electron is transferred to the neighboring site by thermal activation. This mechanism in conduction is called hopping mechanism **[20].**

The cation distribution of lithium ferrite and cobalt substituted lithium ferrite having the inverse spinel structure were given by $(Fe_{1.0}{}^{+3})[Li_{0.5}{}^{+}Fe_{1.5}{}^{+3}]O_4{}^{-2}$ and $(Fe^{+3}{}_{1.0-x+y}Co^{+2}{}_{x-y})[Li_{0.5-0.5x}Fe^{+3}{}_{1.5+0.5x-y}Co_y{}^{+2}]O_4{}^{-2}$ for x=0

and x>0 respectively, where the parenthesis denote the A-sites and square brackets denote the B-sites **[34]**. For lithium ferrite, the conduction mechanism taking place between the Fe^{+2} and Fe^{+3} ions present in the equivalent crystallographic sites in the structure of the ferrite.

$$Fe^{+2} \leftrightarrow Fe^{+3} + e^{-}$$

In ferrites the electrons transfer between the adjacent B-sites in the spinel structure. Local displacement of electrons in the direction of applied electric field can be obtained that occur due to the displacement in determining the polarization effect in ferrite **[21]**.

In this article we discussed the electrical conductivity of the prepared samples in the temperature range 200-600 ^{o}C, which reveal that the electrical conductivity of the prepared samples increases with increasing temperature, which indicated the semiconducting nature of the prepared samples. The dc electrical conductivity of the of materials has a general form $\sigma=\sigma_o \exp(-E_a/kT)$ where E_a is the thermal activation energy, σ_o is the pre exponential factor depending on material nature and k is the Boltzmann constant. The temperature dependence of the electrical conductivity of the prepared samples were studied by plot a graph between the Log (σT) vs 1000/T which shown in **Fig. 3**, which yields a straight line whose slope can be used to calculate thermal activation energies of the ferrite samples.

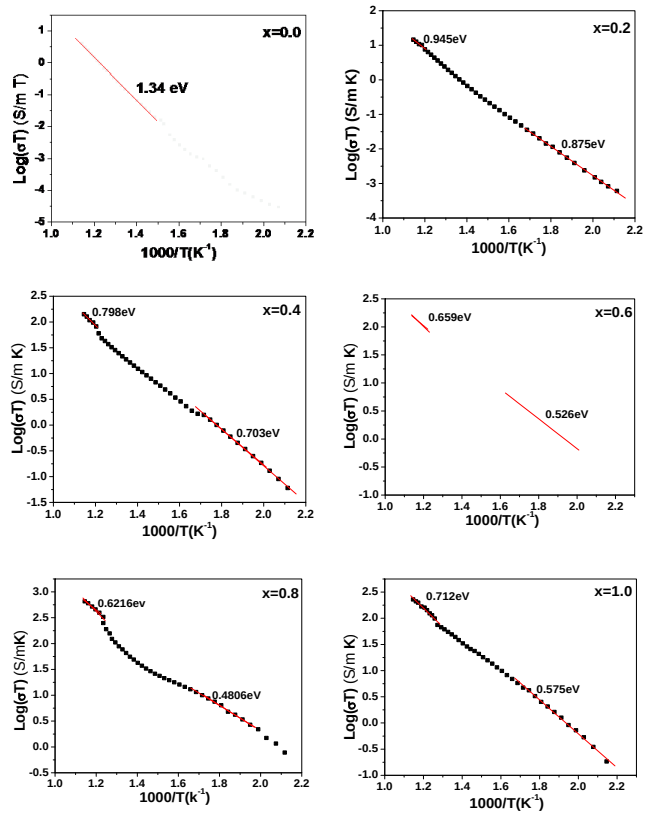

Fig. 3. Arrhenius plots for electrical conductivities of nano crystalline $[Li_{0.5}Fe_{0.5}]_{1-x}$ Co_x Fe_2O_4 ferrites.

According to **Fig. 3** except the pure lithium ferrites, Arrhenius plots for electrical conductivities of cobalt substituted lithium ferrites shows a discontinuity (kink occurs) in the straight line which shows two different regions with a variation in the activation energies. The temperature where the discontinuous kink occur was called transition temperature (T^*). V.R.K. Murthy et al. **[22]** reported that discontinuity in the Arrhenius plot may be due to the change in the conduction mechanism. For $T< T^*$ region the conduction mechanism may be due to the electron hopping between the Fe^{+2} and Fe^{+3} ions in the octahedral sites of the crystal lattice. For $T> T^*$ region the conduction mechanism may be probably due to the ionic conduction caused by the lithium and cobalt ions in the B-sites **[23].** But according to Raghasudha et al. **[24]** proposes that a discontinuity in the Arrhenius plot may be due to the ferri to para magnetic transition from low to high temperature. This transition temperature (T^*) represents the Curie temperature (T_c). Therefore it suggests that change in slope due to the magnetic transition. Similar transitions near the Curie temperature have also been observed by several investigators for different ferrites **[25, 26]**.

The variation of dc resistivity with cobalt concentration was shown in **Fig. 4** which reveals that dc resistivity of the prepared Li-Co samples decreases with Co composition. This may be due to the hoping of electrons between the $Fe^{+2} \leftrightarrow Fe^{+3}$ and $Co^{+2} \leftrightarrow Co^{+3}$ increases in the octahedral sites of the prepared samples with increase in the Co composition **[27]**.

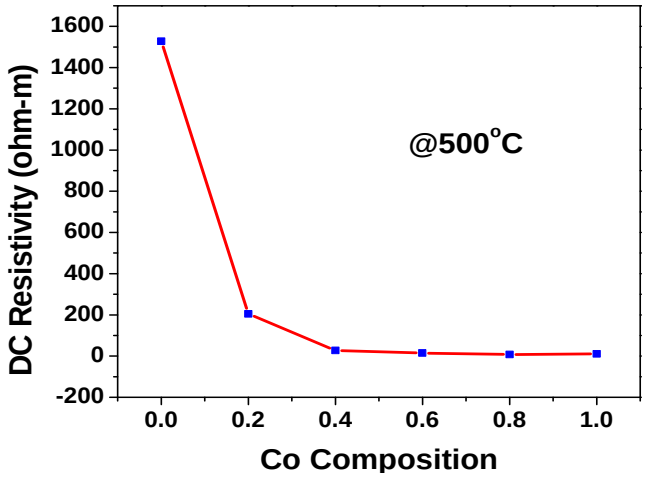

Fig. 4. Variation of dc resistivity with cobalt composition.

Table 3. Curie temperature and activation energies of Li-Co nano ferrites.

S.N0	Composition	Curie Temp (°C)	Activation Energy(eV)	
			Paramagnetic	Ferrimagnetic
1	$Li_{0.5}Fe_{2.5}O_4$	>600		1.340
2	$Li_{0.4}Co_{0.2}Fe_{2.4}O_4$	572	0.945	0.875
3	$Li_{0.3}Co_{0.4}Fe_{2.3}O_4$	560	0.798	0.703
4	$Li_{0.2}Co_{0.6}Fe_{2.2}O_4$	553	0.659	0.526
5	$Li_{0.1}Co_{0.8}Fe_{2.1}O_4$	540	0.621	0.480
6	$CoFe_2O_4$	521	0.712	0.575

The **Table 3** summarizes the activation energies in ferri magnetic and paramagnetic regions and Curie temperatures

of the Li-Co ferrites. From **Table 3** one can observed that activation energy of the paramagnetic region is larger than the ferri magnetic region **[28]**. This is because ferri magnetic state was an ordered state one while the para magnetic state is disordered one hence charge carriers require more energy for conduction in paramagnetic state compared to ferri magnetic state.

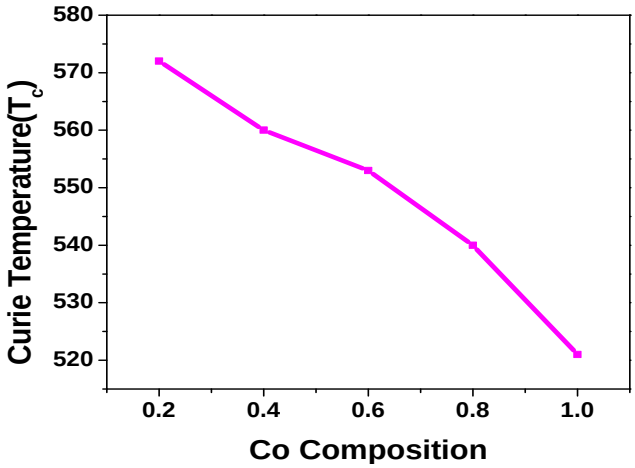

Fig. 5 Variation of Curie temperature with Co composition.

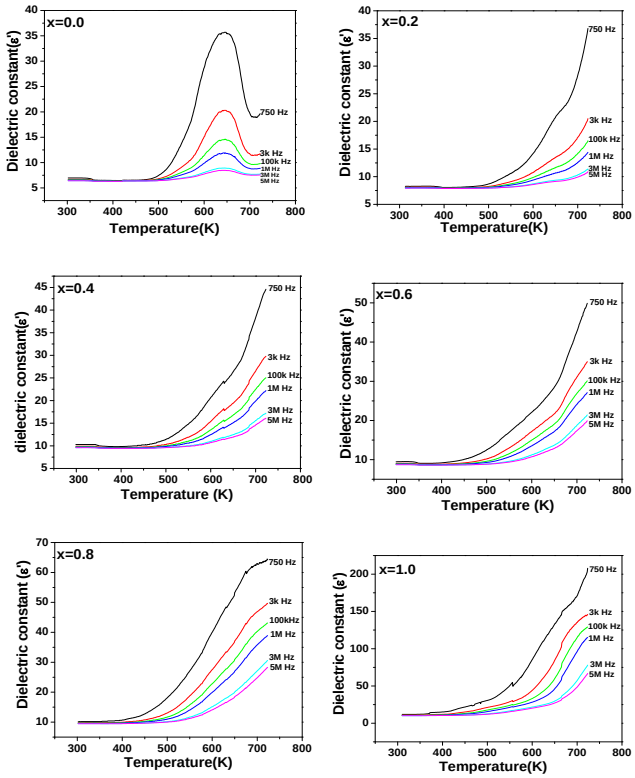

Fig. 6. Variation of Dielectric constant with temperature of $[Li_{0.5}Fe_{0.5}]_{1-x}$ Co_x Fe_2O_4 ferrites.

From the **Fig. 5** we can observe that Curie temperature of the prepared samples was observed to be decrease with the increase in cobalt composition. This can be explained on the basis of the number of magnetic ions present in the two sub-lattices and their mutual interaction. An increase in the cobalt composition at the B-site has replaced the Fe^{+3} ions at this site, which leads to reducing the AB interaction of the type $^{+3}$(A)-O^{-2}- Fe^{+3}(A). Since T_c depends on the strength of AB exchange interaction, so the weakening the interaction results in a decrease in Curie temperature (T_c).

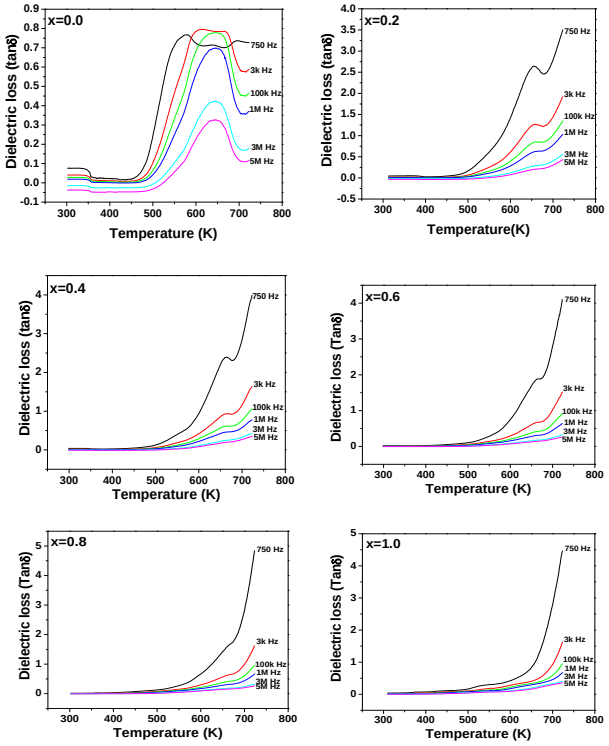

Fig. 7. Variation of Dielectric loss (tan δ) with temperature of $[Li_{0.5}Fe_{0.5}]_{1-x}$ Co_x Fe_2O_4 ferrites.

Dielectric studies

The dielectric parameters of the prepared samples were depends on the temperature and frequency. The temperature dependence of the dielectric constant of the prepared Li-Co ferrites was shown in **Fig. 6**. From this **Fig. 6** one can be concluded that except the pure lithium ferrite, dielectric constant of the cobalt substituted lithium ferrite increases with increasing the temperature. In case of pure lithium ferrites dielectric constant was increases up to certain temperature beyond that temperature, dielectric constant going to decrease **[29]**. Similar behavior can be observed by the various researchers for different compositions **[30]**. The hopping of electrons between the Fe^{+2} and Fe^{+3} ions present in the octahedral sites is thermally activated by increasing temperature which causes local displacements in the direction of external field, which enhances their contribution to the space charge polarization thereby leading to increase in the dielectric constant **[31]**. The variations of dielectric loss with temperature of the prepared samples were shown in **Fig. 7** this behavior is similar to that of variation of dielectric constant with temperature shown in **Fig. 6**.

The frequency dependent dielectric constant (ε') and dielectric loss tangent (tan δ) of the prepared Li-Co ferrite samples for x=0.2 were shown in **Fig. 8** remaining samples show similar behavior (not shown). From the **Fig. 8** one can be concluded that dielectric parameters like dielectric constant and loss tangent were observed to be decrease with increase in frequency which can be understood by

Maxwell-Wagner two layer models in agreement with the Koop's theory **[32]**. According to this theory, ferrite structure was made up of well conducting grains separated by poor conducting grain boundaries. The high dielectric constant comes from the space charge polarization produced at the grain boundary.

During the hopping mechanism, the electrons have to pass through the grains and grain boundaries of the dielectric medium. Due to the high resistance to the grain boundary, the electrons were accumulating at the grain boundary and produce space charge polarization. It was well known that the grain boundaries were more effective at low frequency and grains were more effective at the high frequency. Therefore due to the grain boundary effect the dielectric constant decreases rapidly in the low frequency region and at high frequency the grains come into action and also exchange of electrons cannot follow the applied ac field hence dielectric constant decreases and frequency independent.

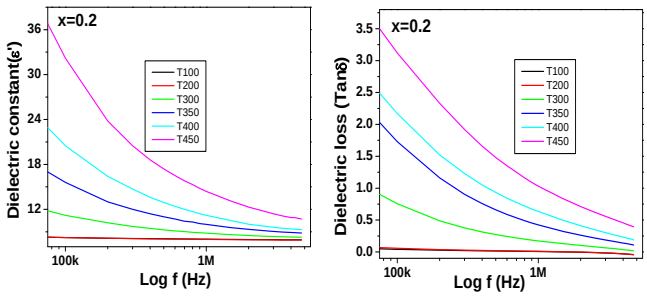

Fig. 8. Variation of dielectric parameters with frequency of $[Li_{0.5}Fe_{0.5}]_{1-x}$ Co_x Fe_2O_4 ferrites at x=0.2.

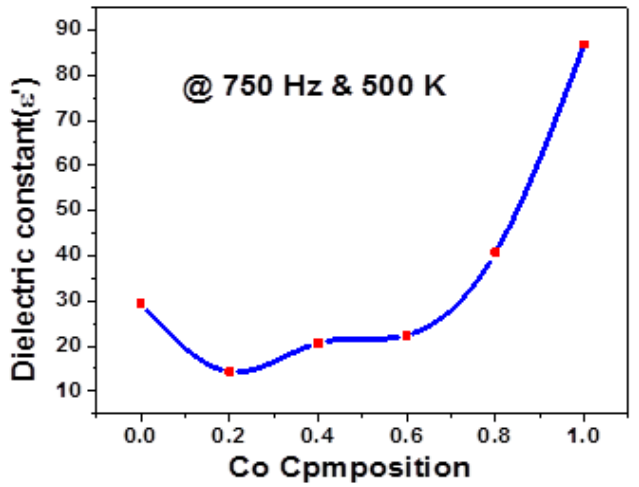

Fig. 9. Variation of dielectric constant with Co composition.

The variation of dielectric constant with cobalt concentration of the prepared samples was shown in **Fig. 9**. From this we concluded that the dielectric constant of the prepared samples increases with cobalt composition in lithium ferrites. This is because in Li-Co ferrites Li^{+1} ions occupy B-site and Co^{+2} ions have prefer to occupy both A and B sites. With increase of Co^{+2} compositions, some of the Co ions occupy A-site and displace the Fe^{+3} ions from the A-site to B-site. Thus more Fe^{+3}- Fe^{+2} ion pair are available at B-site for hopping of electrons resulting in the increase of dielectric polarisation which results a increase of dielectric constant.

Conclusion

Citrate gel auto combustion method was a very suitable technique for the preparation of nano sized (36-43 nm) cobalt substituted lithium ferrite at low sintering temperature. The lattice parameter of the prepared samples observed to increases with increasing the cobalt composition which obeys the Viguard's law. The dc electrical resistivity of the prepared samples was decreases with increasing the temperature which shows the semiconducting nature of the samples. A plot of Log (σT) vs 1000/T shows straight line and the discontinuity in the straight line shows a Curie temperature at which ferri magnetic state of the material shift to paramagnetic state. The dielectric parameters such as dielectric constant and dielectric loss tangent were observed to be increased with increasing temperature and decreased with increasing frequency. Finally by observing the results of these measurements one can say that dc resistivity is inversely proportional to the dielectric constant of the prepared samples.

Acknowledgements

The authors are very grateful to Prof.R.Sayanna, Head, Department of Physics, University College of Science, OsmaniaUniversity,Hyderabad. The authors are very thankful to UGC, New Delhi, for their financial assistance through Major Research Project (M.R.P).

Reference

1. Navneet Singh, Ashish Agarwal, Sujatha Sanghi, Currnet *Applied Physics* **2011,** 11, 783
DOI: 10.1016/j.cap.2010.11.073
2. S.T.Assar,H.F.Abosheiasha, m.K.El Nimr, *J of Mag and Mag Materials* **2014,** *350*, 12.
DOI: 10.1016/j.jmmm.2013.09.022
3. S.C.Watawe, U.A.Bamne, S.P.Gonbare,R.B.Tangsali, *Mater Chem and Phys* **2007,** *103*, 323.
DOI: 10.1016/j.matchemphys.2007.02.037.
4. Yen-Pei Fu, *Mater Chem and Phys* **2009,** *115*, 334.
DOI: 10.1016/j.matchemphys.2008.12.023.
5. P.P.Hankare,R.P.Patil, U.B.Shankpal, S.D.Jadhav, P.D.Lokhande, K.M.Jadhav, R.Sasikala, *J of Solid State Chem* **2009,** *182*, 3217.
DOI: 10.1016/j.jssc.2009.08.034
6. Vivek Verma, M.Abdullah dar, Vibhav pandey, Anterpreet Singh, S.Annapprni, R.K.Kotnala, *Mater Chem and Phys* **2010,** *122*, 133
DOI: 10.1016/j.matchemphys.2010.02.057
7. P.P.Hankare,R.P.Patil,U.B.Shankpal,K.M.Garadkar,R.Sasikala,A.K. Tripathi, I.S.Mulla. *J of Magn.magn.Mater.* **2010,** *322*, 2629.
DOI: 10.1016/j.jmmm.2010.03.005
8. A.M.Rais, A.Addou,M.Ameri, *Inter J of Mater and Chem* **2012**,*2*, 72.
DOI: 10.5923/j.ijmc.20120202.05
9. S.Akhter,M.A.Hakim, *Mater Chem and Phys* **2010,** *120*, 399.
DOI: 10.1016/j.matchemphys.2009.11.023
10. D.Ravinder, *J Mater Scince Letters*, **1992,** *11*, 1498.
DOI: 10.1007/BF0072927
11. P.Vijay Bhaskar Reddy, D.Ravinder, *J of Mag Mag Materials*, **2003,** *263*, 127.
DOI: 10.1016/S0304-8853 (02)01545-7
12. Kwang Pyo Chae, Woo Hyum Kwon, Jae-gwang Lee, *J of Mag Mag Materials* **2012,** *324*, 2701.
DOI: 10.1016/j.jmmm.2012.03.024
13. Nutan Gupta, S.C.Kashyap, D.C.Dude, *Phys.stat.sol(a)* **2007,** *204*, 2441.
DOI: 10.1002/pssa.200622146

14. E.VeenaGopalan,I.A.Al-Omari,K.A.Malini,P.A.Joy,D.Shakti Kumar, Y.Yoshida, M.R.Anantharaman, *J. of Magnetism and Mag Mater* **2008,** *321*, 1092.
DOI: 10.1016/j.jmmm.2008.10.031
15. E.VeenaGopalan,K.A.Malini,S.Saravanan,D.Shaktikumar,Y.Yashida, M.R.Anantharaman, *J of Physics, D:Applied Physics*, **2008,** *41*, 185005.
DOI: 10.1088/0022-3727/41/18/185005
16. Manish Srivasthava,S.chaubey,Animesh K.Ojha, *Material Chemistry and Phy*, **2009,** *118*, 174.
DOI: 10.1016/j.matchemphys.2009.07.023
17. Zhenxing Yue, Ji Zhou,Longtu Li, Hongguo Zhang Zhilum Gui, *J Magn Magn Matr* **2000,** *208*, 55.
DOI: 10.1016/S0304-8853(99)00566-1
18. B.D.Cullity,Elements of X-ray diffraction, Addision-Wasely Publishing Co.Inc.1976 (chapter 14,**1976**)
19. K.Wykpis,A.Budnoik,E.lagiewka, Mater,Science, Forum.636 **2010** 1053-1058.
DOI: 10.4028/www.scientific.net/MSF.636-637.1053
20. Ferrite Material Science and Technology, Narosa publishing house , New Delhi, **1990**
21. R.K.Kontala,V.Verma,V.Pandev, V.P.S.Awana, P.P.Aloysis, P.C.Kothari, *Solid State Commun.***2007,** *143*, 527.
DOI: 10.1016/j.ssc.2007.07.007
22. Manjula,V.R.K.Murthy, Shobanadri, *J of Appl Physics* **1986,** 59, 2929.
DOI: 10.1063/1.336954
23. Yen Pei-Fu, *Material Chemistry and Physics* **2009,** *115*, 334.
DOI: 10.1016/j.matchemphys.2008.12.023
24. M.Ragasudha, Ph.D thesis, dept of chemistry, osmania university Aug-**2013**.
25. S.A.mazen, H.A.Dawoud, *Mater Chem Phys* **2003,** *82*, 557.
DOI: 10.1016/S0254-0584 (03) 00200-1
26. A.M.Shaik,C.M.Kanamadi,B.K.Chougale, *Mater Chem and Phys* **2005,** *93*, 548.
DOI: 10.1016/j.matchemphys.2005.04.005
27. S.T.Assar,H.F.Abosheisha,M.K.El Nimr *J of magMag Mater* **2014,** *354*, 1.
DOI: 10.1016/j.jmmm.2013.10.029
28. K.Rama krishna et al, *Advances in Materials Physics and Chemistry*, **2012**, *2*, 185.
DOI: 10.4236/ampc.2012.23028
29. Vivek Verma, Vibhav Pandey, V.N.Shukla, S.Annapoorni, R.K.Kotnala, *Solid State Commun*, **2009,** *149*, 1726.
DOI: 10.1016/j/ssc.2009.06.010
30. Ibetombi Soibam, Sumitra Phanjoubam, H.B.Sharma, H.N.K.Sarma, *Solid State Communs* **2008,** *148*, 399.
DOI: 10.1016/j.ssc.2008.09.029
31. K.M.Batoo, S.Kumar,C.G.Lee,Alimuddin, *Curr Appl Phy* **2009,** *9*, 1397.
DOI: 10.1016/j.cap.2009.03.012
32. C.G.Koop's *Phys Rev* **1951,** *83*, 121.
33. Sheenu Jauhar, Ankitha Goyal, N.Lakshmi, Kailash Chandra, Sonal Singhal, *Materials Chem and Phy*,**2013,** *139*, 836.
DOI: 10.1016/j.matchemphys.2013.02.041
34. Mazen, S.A.; Abu-Elsaad, N.I.; *ISRN Condensed Matter Physics*, Vol **2012**, ID 907257,
DOI: 10.5402/2012/907257

Smart Phone Based Authentication System Using Gestures

Sandeep Ravikanti[1] Rajashekar Deva[2]
[1,2]Assistant Professor
[1,2]Department of Computer Science and Engineering
[1,2]Methodist College of engineering and technology, Hyderabad, Telangana, India

Abstract— Because of the developments in Mobile advancements, Gestures assume a vital part for the Authentication in the cell phones. With expanding prominence of the Authentications, the security dangers are likewise developing and that is clear in the episodes of UnAuthentication as far as different sorts. Along these lines it is vital to have a versatile based Authentication framework [1] for security. Motions permit clients to cooperate with your application by controlling the screen objects [2] you give. This paper presents components that assistance to synchronize with your own information, search for representatives by name, see their points of interest, add them to your contacts, and see their manager and employees, and also call, content, or email them.

Key words: Gestures, Intents

I. INTRODUCTION

For traditional web apps (delivered through a browser), Twitter Bootstrap can help. But what about Mobile apps? I explored Android here. Depending on what you are looking for, it may or may not be the right solution: jQM[8] provides mobile skins, but they don't look native. It's also more of a full stack framework than lightweight UI toolkit [9] that you can easily layer on top of your app.

The alternative to using an existing UI toolkit is to roll your own styles to make your application look and behave like a native app[1].

Employee Details always accesses the employee data from a SQLite[7] on your Android Mobile. The information is always available. The application comes with a sample dataset to provide an "out-of-the-box" experience, and with a simple offline synchronization mechanism to sync with your own data.

SQLite is a in-process library that implements a self-contained, serverless, zero configuration, transactional SQL database engine. The code for SQLite is in the public domain and is thus free for use for any purpose, commercial or private. SQLite is currently found in more applications than we can count, including several high-profile projects.

SQLite is an embedded SQL database engine. Unlike most other SQL databases[4], SQLite does not have a separate server process. SQLite reads and writes directly to ordinary disk files. A complete SQL database with multiple tables, indices, triggers, and views, is contained in a single disk file. The database file format is cross-platform - you can freely copy a database between 32-bit and 64-bit systems or between big-endian and little-endian architectures[6]. These features make SQLite a popular choice as an Application File Format. Think of SQLite not as a replacement for Oracle but as a replacement for fopen().

SQLite is a compact library. With all features enabled, the library size can be less than 350KiB, depending on the target platform and compiler optimization settings. (64-bit code is larger. And some compiler optimizations such as aggressive function inlining and loop unrolling can cause the object code to be much larger.) If optional features are omitted, the size of the SQLite library can be reduced below 300KiB. SQLite can also be made to run in minimal stack space (4KiB) and very little heap (100KiB), making SQLite a popular database engine choice on memory constrained gadgets such as cellphones, PDAs, and MP3 players. There is a tradeoff between memory usage and speed. SQLite generally runs faster the more memory you give it. Nevertheless, performance is usually quite good even in low-memory environments.

SQLite is very carefully tested prior to every release and has a reputation for being very reliable. Most of the SQLite source code is devoted purely to testing and verification. An automated test suite runs millions and millions of test cases involving hundreds of millions of individual SQL statements and achieves 100% branch test coverage. SQLite[7] responds gracefully to memory allocation failures and disk I/O errors. Transactions are ACID even if interrupted by system crashes or power failures. All of this is verified by the automated tests using special test harnesses which simulate system failures. Of course, even with all this testing, there are still bugs. But unlike some similar projects (especially commercial competitors) SQLite is open and honest about all bugs and provides bugs lists including lists of critical bugs and minute-by-minute chronologies of bug reports and code changes.

The SQLite code base is supported by an international team of developers who work on SQLite full-time. The developers continue to expand the capabilities of SQLite and enhance its reliability and performance while maintaining backwards compatibility with the published interface spec, SQL syntax, and database file format.

II. RELATED WORK

The Employee Directory in JAVA page flow

(1) Search Page -> Employee Page -> Reports Page -> Employee Page -> …
(2) Search Page -> Employee Page -> Employee Page (manager) -> Reports
(3) Search Page -> Employee Page -> Employee Page (manager) -> Employee Page (manager's manager) -> …

The employee directory in java has o be governed by the external devices for the authentication. It needs a server to run the application where the front end is the HTML.

For storing the data it has to use the large databases like MYSQL and SQL[3].

III. PROPOSED WORK

The Employee Directory page flow is more random.

– Gesture Login ->Search Page -> Employee Page -> Reports Page -> Employee Page -> …

- Gesture Login ->Search Page -> Employee Page -> Employee Page (manager) -> Reports
- Gesture Login ->Search Page -> Employee Page -> Employee Page (manager) -> Employee Page (manager's manager) -> …
- Exploring the mechanism for internal and external detection.

Android supports gestures. To use this support your application must use the view "GestureOverlayView"[6]. In this view place you're other views.

Gestures are defined by binary resources which can be created with an example program from the Android SDK[1]. In your activity you can load Gestures via GestureLib.fromRawResource()[6]. If a gesture is detected then the method "onGesturePerformedListener" is called. For this the activity must implement the interface "OnGesturePerformedListener" and must register itself at the GestureOverlayView with the method "addOnGesturePerformedListener()".

Android shows the gestures in yellow for recognized gestures and a ligher yellow for not recognized gestures. You can turn this off, via setGestureColor(Color.TRANSPARENT) or setUncertainGestureColor(Color.TRANSPARENT) on the GestureOverlayView.

If you create the gesture in the Android simulator via the program "GestureBuilder"[6]. You can create several gestures with the same name. That may help you to determine the right one. If you create an Android Emulator for Android 1.6 this application will be preinstalled on your device. Make sure to create a device with sdcard otherwise you cannot save gestures. All gestures will be saved in a file called *gestures* on your emulator.

You can copy the gestures from the emulator via the ADB[9] onto your local machine via the command:

./adb pull /sdcard/gestures ~/test

The gesture file must be copied into your application under "res/raw". Afterwards it can be used in your GestureOverlayView[6].

IV. Problem Definition and Assumptions

Authentication is essential in Mobiles. How can we provide the authentication for the mobile devices? Because the biometric is work properly with the mobile devices which use android. How can we manage the Employees in an organization in a compact way? The problem of Authentication is solved by using gestures instead of the biometric and the compact version of employees can be managed by using the Employee details. In Employee details look for employees by name, view their details, add them to your contacts, and see their manager and direct reports, as well as call, text, or email them.

V. Gestures Detection Algorithm

A. Creating a View: Gesture View

An easy way to get a Canvas object to drawing on is by overriding the onDraw() method of a View object. Conveniently, this method has a single parameter: the Canvas object. Drawing a Bitmap graphic on a Canvas object[9][3] is as easy as calling the drawBitmap() method of the Canvas object.

```
private class GestureView extends View {
   private Matrix translate;
   private Bitmap droid;
   protected void onDraw(Canvas canvas) {
      canvas.drawBitmap(droid, translate, null);
      Matrix m = canvas.getMatrix();
      Log.d(DEBUG_TAG, "Matrix: "+translate.toShortString());
      Log.d(DEBUG_TAG, "Canvas: "+m.toShortString());
   }
}
```

Fig. 1: Shows How to create a Gesture View

B. Configuring the Gesture View

A GestureDetector is an Android class that can take motion events, do some mathematical magic to determine what they are, and then delegate calls to a GestureListener object as specific gesture or other motion callbacks. The GestureListener object[5], a class we implement, receives these calls for specific gestures that the GestureDetector[6] recognizes and allows us to react to them as we see fit (in this case, to move a graphic around within our PlayAreaView). Although the GestureDetector[5] handles the detection of certain motions, it doesn't do anything specific with them nor does it handle all types of gestures.

```
public GestureView(Context context) {
   super(context);
   translate = new Matrix();
   gestures = new GestureDetector(GestureFunActivity.this,
         new GestureListener(this));
   droid = BitmapFactory.decodeResource(getResources(),
         R.drawable.droid_g);
}
```

Fig. 2: Shows GestureView Constructor

C. Connecting to a Gesture Detector

GestureDetector[6] object receives the motion data it needs to do its gesture recognizing magic. GestureDetector object called gestures to receive events[1].

```
@Override
public boolean onTouchEvent(MotionEvent event) {
   return gestures.onTouchEvent(event);
}
```

Fig. 3: Shows Gesture Detection Object

D. Implementing the Gesture Listener

In order to react to the events recognized by the GestureDetector class, we need to implement the GestureListener class. The motion events[2] we are most interested in are double taps and gestures of any kind. To listen for these types of motion events, our GestureListener class must implement both the OnGestureListener and OnDoubleTapListener interfaces[3].


```
private class GestureListener implements
GestureDetector.OnGestureListener,
      GestureDetector.OnDoubleTapListener {
   GestureView view;
   public GestureListener(GestureView view) {
      this.view = view;
   }
}
```

Fig. 4: shows Gesture Listener

E. Handling Motion Events

A scroll event occurs when the user touches the screen and then moves their finger across it. This gesture is also known as a drag event. This event comes in through the onScroll() method of the OnGestureListener interface[5].

```
@Override
public boolean onScroll(MotionEvent e1, MotionEvent e2,
      float distanceX, float distanceY) {
   Log.v(DEBUG_TAG, "onScroll");
   view.onMove(-distanceX, -distanceY);
   return true;
}
```

Fig. 5: Shows onScroll()

VI. IMPLEMENTATION

A. Admin

1) Add Gesture

The admin has the permission to add the Gesture signature of all the Employees and can view all the details of the employee.

Fig. 6: Adding the Signature

Each and every Employee will have a particular signature. Based on the signature the employee login. The Employee signatures are added by the Admin.

2) Add Employee

The Admin has permissions to add all the Employees. For adding the Employee the following details need to be entered First Name, Last Name, Department, Manager id, Phone Number and Email

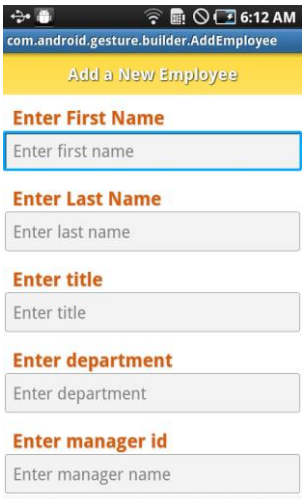

Fig. 7: Adding the Details of the Employee

3) Home Activity

In this page there will four sub modules

(1) Employee Reports
(2) Employee Full Details
(3) Add Employee
(4) Save Signature

Fig. 8: Other Modules page

B. Employee

The Employee has to enter the Gesture signature for login. If the Employee Login Gesture Signature is correct then the Employee will be redirected to the next page where the employee can view the other employee details along with their details and their manager.

1) Employee Login

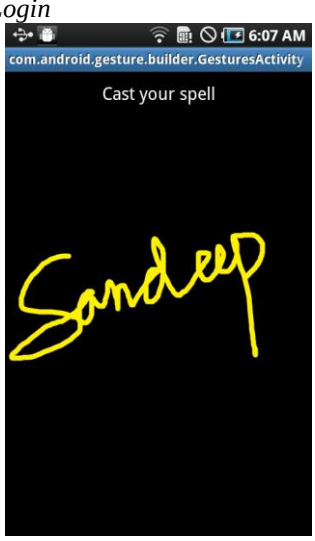

Fig. 9: Signature of the Employee

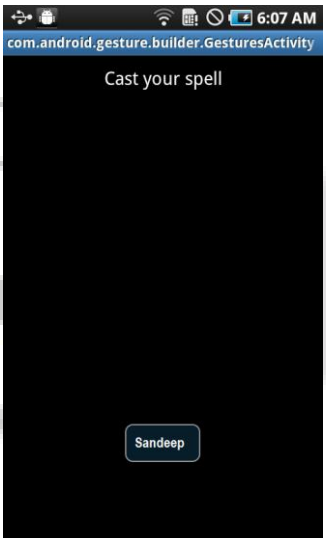

Fig. 10: Employee Login Successful

If the Employee Login Gesture Signature[6] is correct then the Employee will be redirected to the next page where the employee can view the other employee details along with their details and their manager.

C. Employee Reports

The Employee can view all other Employee details and the designation of the Employees. The Employee can even search the other employees. Based on the selection of the Employees the corresponding details will be displayed.

The display of elements in lists is a very common pattern in mobile applications. The user sees a list of items and can scroll through them. If he selects one item, this can update the ActionBar[9] or triggers[3] a detailed screen for the selection.

Android provides the ListView[2] class which is capable of displaying a scrollable list of items. These items can be of any type.

The Alphabetic search bar is used for displaying the list with the selected Alphabet on the right side of the screen.

Fig. 11: Employee Reports.

D. AutoCompleteSearch

A text field allows the user to type text into your app. It can be either single line or multi-line. Touching a text field places the cursor and automatically displays the keyboard. In addition to typing, text fields allow for a variety of other activities, such as text selection (cut, copy, paste) and data look-up via auto-completion.

An editable text view that shows completion suggestions automatically while the user is typing. The list of suggestions is displayed in a drop down menu from which the user can choose an item to replace the content of the edit box with.

The drop down can be dismissed at any time by pressing the back key or, if no item is selected in the drop down, by pressing the enter/dpad center key[1].

The list of suggestions is obtained from a data adapter and appears only after a given number of characters defined by the threshold.

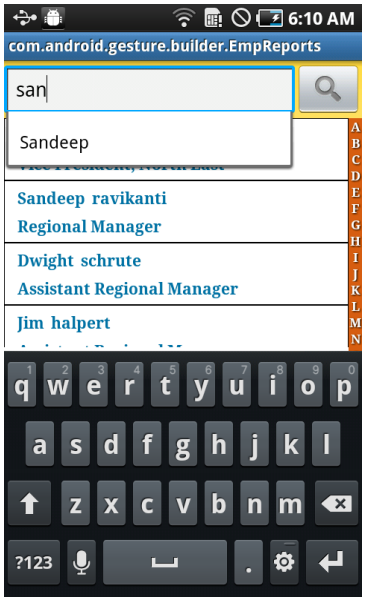

Fig. 12: Auto Complete Search

Based on the search the user can view the list populated down in the ListView

Fig. 13: Result based on Auto Complete Search

E. Employee Results

The Employee Results shows the Employee name, Designation, Phone Number and view reports.

From this activity we can Call, Send SMS and Send Email.

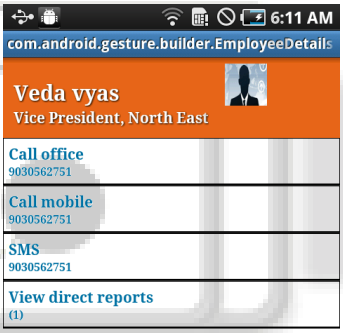

Fig. 14: Employee Results Page.

F. View Reports

We can view the Manager details of a particular Employee and can view the manager details based on the selection of the ListView[2].

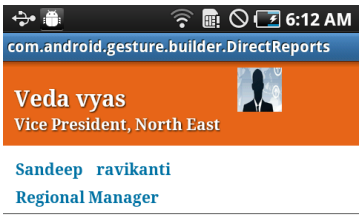

Fig. 15: shows View Reports

G. Employee Full Details

We can search the Employee and can view full details of the Employee.

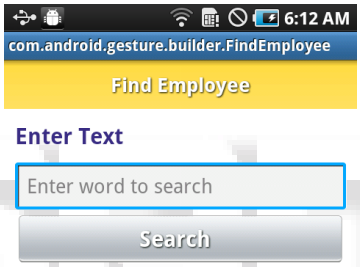

VII. CONCLUSION

Authentication is Important in the Mobile Technology. This paper presents the Gestures [6] Authentication for Login and compact view of the Employee Details. The effectiveness of the simulation model is tested with simulations using a custom-built[1] simulator developed in Android. The results revealed that the proposed analytical model is effective and can be used in real world applications.

REFERENCES

[1] http://developer.android.com/index.html
[2] http://www.vogella.com/articles/AndroidListView/article.html
[3] http://mobile.tutsplus.com
[4] http://stackoverflow.com
[5] http://www.vogella.com/tutorials/AndroidIntent/article.html

[6] http://www.tutorialspoint.com/android/android_gestures.htm
[7] http://www.androidhive.info/2011/11/android-sqlite-database-tutorial/
[8] http://demos.jquerymobile.com/1.2.0/docs/pages/popup/
[9] http://www.xda-developers.com/

ISSN(Online): 2320-9801
ISSN (Print): 2320-9798

International Journal of Innovative Research in Computer and Communication Engineering

(An ISO 3297: 2007 Certified Organization)

Vol. 3, Issue 7, July 2015

Future's Smart Objects in IOT, Based on Big-Data and Cloud Computing Technologies

Sandeep Ravikanti, Gadasu Preeti

Assistant Professor, Dept of CSE, Methodist College of Engineering &Technology, Hyderabad, India

ABSTRACT: The Internet of Things (IoT)[1] is simply known "smart[3]". How does IoT affect and change the relation between humans and objects. The IoT introduces issues that lead us to turn a philosophical eye to those 50 billion objects which are predicted in near future: Big Data[6] flowing from sensors[7] and other smart devices[3], RFID[2], IPV6[2], cloud computing[7]. like technology trends , Security, Privacy and other important technological challenges such as Arrive and operate[2], Interoperability, Software complexity and many more challenges of smart objects used in everyday life. This paper discusses the basics, architecture, the challenges, applications, and building blocks of the "Internet of Things"[1] The full deployment of the IoT is likely to bring about a set of new issues such as the autonomy of humans in a world where smart objects that make a ratio of 1: 10; the 'right to be forgotten' in a scenario of billions of things exchanging one's data; trust in the things that will decide on behalf of the humans or for them. Finally, as IoT evolves through a combination of big data and cloud computing**.**

KEYWORDS: Sensors, RFID, IPV6, cloud computing, big-data, MDM.

I. INTRODUCTION

Imagine a world where billions of objects can sense, communicate and share information, all interconnected over public or private Internet Protocol (IP)[1] networks. These interconnected objects have data regularly collected, analyzed and used to initiate action, providing a wealth of intelligence for planning, management and decision making. This is the world of the Internet of Things (IOT)[2]. The Internet of Things (IoT) is a technological revolution that represents the future of computing and communications. Its development depends on the dynamic technical innovation in a number of important fields, from wireless sensors to nanotechnology. The concept of the IoT comes from Massachusetts Institute of Technology (MIT)'s Auto-ID[9] Center in 1999. The MIT Auto-ID Laboratory is dedicated to create the IoT using Radio Frequency Identification (RFID)[4] and Wireless Sensor Networks[3]. IoT is a foundation for connecting things, sensors, actuators, and other smart technologies, thus enabling Machine to machine, machine to infrastructure, machine to environment communications. A new dimension has been added to the world of Information and Communication Technologies (ICTs)[4]: anyone can access the information from anywhere, any device anytime what you want? It's happening, and its potential is huge. We see the IoT as billions of smart, connected "things" (Includes People, Location (of objects) ,Time Information (of objects) ,Condition (of objects))that will encompass every aspect of our lives, and its foundation is the intelligence that embedded processing provides. The IoT is comprised of smart machines interacting and communicating with other machines, objects, environments and infrastructures. As a result, huge volumes of data are being generated, and that data is being processed into useful actions that can "command and control" things to make our lives much easier and safer—and to reduce our impact on the environment.

"The Internet of Things (IoT) is a scenario in which objects, animals or people are provided with unique identifiers and the ability to transfer data over a network without requiring human-to-human or human-to-computer interaction. IoT has evolved from the convergence of wireless technologies, micro-electromechanical systems (MEMS) and the Internet of Things Will Change the Way We Work [5]"

ISSN(Online): 2320-9801
ISSN (Print): 2320-9798

International Journal of Innovative Research in Computer and Communication Engineering

(An ISO 3297: 2007 Certified Organization)

Vol. 3, Issue 7, July 2015

So now many people are concentrating on the phrase "Internet of Things" which refers to general idea of things specially the objects which we are using in our daily life are readable, recognizable, locatable, addressable, and/or controllable via the Internet, irrespective of the communication means[1]. Everyday objects include not only the electronic devices we encounter or the products of higher technological development such as vehicles and equipment but things that we do not ordinarily think of as electronic at all - such as food and clothing. These "things[3]" of the real world shall seamlessly integrate into the virtual world, enabling anytime, anywhere connectivity. In 2010, the number of everyday physical objects and devices connected to the Internet was around 12.5 billion. Cisco forecasts that this figure is expected to double to 25 billion in 2015 as the number of more smart devices per person increases, and to a further 50 billion by 2020[10].

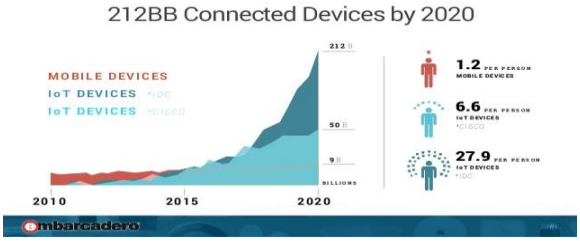

Figure 1 number of connected devices to internet by 2012

1.1 IOT Architecture

IOT architecture consists of different technologies in different layers these technologies will provide support to IOT and all these technologies related to each other and communicate the scalability, modularity and configuration of IOT deployments in different cases[2].The below IOT architecture shows the functionality of each and every layer. This architecture mainly consists of three layers [2].

Reference image is taken form ref [2]

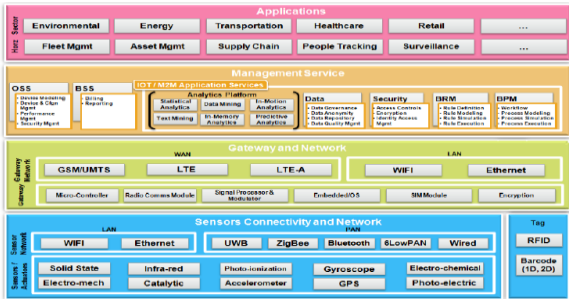

1. **Applications layer**: this is the top layer in iot architecture .it layer mainly deals with the different applications of IOT[1] where smart devices are in widely use like home automation, health care, intelligent communication, industry automation, government sector, fleet management etc.
2. **Networking layer:** This layer acts as interface between sensor and application layer. This layer again sub divided into two layers they are

A) Gateway and network layer B) Management service layer

ISSN(Online): 2320-9801
ISSN (Print): 2320-9798

International Journal of Innovative Research in Computer and Communication Engineering

(An ISO 3297: 2007 Certified Organization)

Vol. 3, Issue 7, July 2015

A) Gateways and Network Layer: Massive volume of data will be produced by these tiny sensors and this requires a robust and high performance wired or wireless network infrastructure as a transport medium. Current networks, often tied with very different protocols, have been used to support machine-to-machine (M2M)[3] networks and their applications. With demand needed to serve a wider range of IOT services and applications such as high speed transactional services, context-aware applications, etc, multiple networks with various technologies and access protocols are needed to work with each other in a heterogeneous configuration. These networks can be in the form of a private, public or hybrid models[4] and are built to support the communication requirements for latency, bandwidth or security. A possible deployment could consist of a converged network infrastructure that resolves the fragmentation by integrating disparate networks into a single network platform. Converged network layer abstraction allows multiple organizations to share and use the same network independently for their information to be routed without compromising their privacy, security and performance requirements. Each organization thus utilizes the network as if it is a private network resource to them.

B) **Management Service Layer:** The management service renders the processing of information possible through analytics, security controls, process modeling and management of devices[2]. One of the important features of the management service layer is the business and process rule engines[1]. IOT brings connection and interaction of objects and systems together providing information in the form of events or contextual data such as temperature of goods, current location and traffic data. Some of these events require filtering or routing to post-processing systems such as capturing of periodic sensory data, while others require response to the immediate situations such as reacting to emergencies on patient's health conditions [8]. The rule engines support the formulation of decision logics and trigger interactive and automated processes to enable a more responsive IOT system. In the area of analytics, various analytics tools are used to extract relevant information from massive amount of raw data and to be processed at a much faster rate. Analytics such as in-memory analytics allows large volumes of data to be cached in random access memory (RAM) rather than stored in physical disks[4]. In-memory analytics reduces data query time and augments the speed of decision making. Streaming analytics is another form of analytics where analysis of data, considered as data-in-motion, is required to be carried out in real time so that decisions can be made in a matter of seconds. For example, this requirement is typical in the transportation sector where real-time traffic information enables drivers to optimize their routes and travelling times. Analytics can be carried out at other layers within the IOT architecture [2]. For example, analytics may be carried out in the smart object layer, i.e., local hub or edge device, so that subsets of the information can be carried through the network for further processing. At this layer, analytics helps to reduce the stress placed on the network layer, reduce power needs of sensors by less frequent communication backend and allow faster responses to data received by the sensors. Data management is the ability to manage data information flow. With data management in the management service layer, information can be accessed, integrated and controlled.

3. **Sensor Layer: The** lowest layer is made up of smart objects[3] integrated with sensors[4]. The sensors enable the interconnection of the physical and digital worlds allowing real-time information to be collected and processed. The miniaturization of hardware has enabled powerful sensors to be produced in much smaller forms which are integrated into objects in the physical world. There are various types of sensors for different purposes. The sensors have the capacity to take measurements such as temperature, air quality, movement and electricity. In some cases, they may also have a degree of memory, enabling them to record a certain number of measurements. A sensor can measure the physical property and convert it into signal that can be understood by an instrument. Sensors are grouped according to their unique purpose such as environmental sensors, body sensors, home appliance sensors[8] and vehicle telemetric sensors, etc.Massive volume of data will be produced by these tiny sensors and this requires a robust and high performance wired or wireless network infrastructure as a transport medium. Current networks, often tied with very different protocols, have been used to support machine-to-machine (M2M) networks[3] and their applications. With demand needed to serve a wider range of IOT services and applications such as high speed transactional services, context-aware applications, etc, multiple networks with various technologies and access protocols are needed to work with each other in a heterogeneous configuration. These networks can be in the form of a private, public or hybrid models and are built to support the communication requirements for latency, bandwidth or security.

ISSN(Online): 2320-9801
ISSN (Print): 2320-9798

International Journal of Innovative Research in Computer and Communication Engineering

(An ISO 3297: 2007 Certified Organization)

Vol. 3, Issue 7, July 2015

Figure 3.IOT architecture with example devices in each layer [10]

II. RELATED WORK

From ref[2] Moving into the future, RFID has the potential to provide streams of data that will provide information systems with real-time, item-specific data and be flexible enough to be placed in extremely small spaces and locations, i.e., coil-on-chip technology. With technology developments in areas such as chip design, energy usage and preservation, RF[4] technologies and manufacturing, new ways of RFID usage will emerge for applications such as automatic meter reading, remote home automation and real-time vehicle tracking. Neither the buzzword nor the concept of the "Internet of things"[1] is new. Since the Internet emerged back in the 1990s (and before), we found it interesting to connect Coke machines and coffee pots, among other items. These days, everything comes with some kind of network connection option. This includes our thermostats, TVs, refrigerators, and even coffee makers. The real progress is being made in the area of industrial equipment, such as those sold by GE and other manufacturers that have pushed this concept in the last few years.

The idea is to go beyond simple monitoring of these, well, things, to advanced analytical services(like Big-Data) that let devices provide critical information about how they are functioning and what they are doing. That, in turn, let's automated corrective action take place based on remote analysis of this data. The more "things" that we connect the greater use of cloud computing and Big-Data analytics. The cloud, Big-data[7] and the things are tightly coupled in the "**Internet of things"**.

With the help of special-purpose clouds and Big-Data tools we can focus on connecting devices and machines. They'll gather data quickly, likely streaming off devices with very little structure, as well as performing quick analysis of the data with the ability to instantly respond to the device by considering all these we wrote one paper related to smart objects future in coming years. This is perhaps the most interesting aspect of cloud computing. Our ability to connect pretty much anything lets us operate devices that have much more intelligence than machines from just a few years ago. These smart devices operate more effectively and can even self-repair. So we are saying the use of the **cloud and Big-Data** will play an important role in every human life in coming generations.

III. TECHNOLOGIES USED TO SHAPE INTERNET OF THINGS

1. Smart Objects: A Smart Object [3] is an object that enhances the interaction with not only people but also with other Smart Objects. It can not only refer to interaction with physical world objects but also to interaction with virtual (computing environment) objects. A smart physical object may be created either as an artifact or manufactured product or by embedding electronic tags such as RFID[2] tags or sensors into non-smart physical objects. Smart virtual objects are created as software objects that are intrinsic when creating and operating a virtual or cyber world simulation or game. The concept of a smart object has several origins and uses. There are also several overlapping terms, like Smart device, Tangible Object or Tangible User Interface and Thing as in the Internet of Things. Characteristics of smart objects[3]:

1. Humans use models of smart objects situated in the physical world to enhance human to physical world interaction; versus how

2. Smart physical objects situated in the physical world can model human interaction in order to lessen the need for human to physical world interaction; versus how

ISSN(Online): 2320-9801
ISSN (Print): 2320-9798

International Journal of Innovative Research in Computer and Communication Engineering

(An ISO 3297: 2007 Certified Organization)

Vol. 3, Issue 7, July 2015

3. Virtual smart objects by modeling both physical world objects and modeling humans as objects and their subsequent interactions can form a predominantly smart virtual object environment.

2. Radio Frequency Identification (RFID)

Radio Frequency Identification (RFID)[1][2] technology is of particular importance to IOT as one of the first industrial realizations of IOT is in the use of RFID technology to track and monitor goods in the logistics and supply chain sector. RFID frequency bands range from 125 kHz (low frequency/LF) up to 5.8 Ghz/super high frequency (SHF)[4] and the tags have at least three basic components:

- The chip holds information about the object to which it is attached and transfers the data to reader wirelessly via an air interface.
- The antenna allows transmission of the information to/from a reader.
- The packaging encases chip and antenna, and allows the attaching of the tag to an object for identification. Today, the one dimension bar (ID) code has made a significant contribution to the supply chain and other businesses such as asset management. Two dimension (2D) bar codes have provided a richer source of data but, once printed, are not up-datable. RFID, with its ability to permanently collect and process data in its environment, is proving to be the next technology for the identification of goods. Many industry verticals, especially in the logistics and supply chain, have been using RFID[2] as tagging solutions to improve their tracking and monitoring processes. Moving into the future, RFID has the potential to provide streams of data that will provide information systems with real-time, item-specific data and be flexible enough to be placed in extremely small spaces and locations, i.e., coil-on-chip technology. With technology developments in areas such as chip design, energy usage and preservation, RF technologies and manufacturing, new ways of RFID usage will emerge for applications such as automatic meter reading, remote home automation and real-time vehicle tracking.

3. Internet Protocol version 6 (IPv6) The IPv4[2] address pool is effectively exhausted, according to industry accepted indicators. The final allocations under the existing framework have now been made, triggering the processes for the Internet Assigned Numbers Authority (IANA) to assign the final five IPv4/8 blocks, one to each of the five regional registries. With the exhaustion of the IANA pool of IPv4 addresses, no further IPv4 addresses can be issued to the regional registries that provide addresses to organizations. IPv6 is the next Internet addressing protocol that is used to replace IPv4. With IPv6[1][2], there are approximately 3.4×1038 (340 trillion trillion trillion) unique IPv6 addresses, allowing the Internet to continue to grow and innovate. Given the huge number of connected devices (50 billion), IPv6 can potentially be used to address all these devices (and systems), eliminating the need of network address translation (NAT) [4]and promoting end-to-end connectivity and control. These features provide seamless integration of physical objects into the Internet world.

4. **Security and Privacy:** Today, various encryption and authentication technologies such as Rivest Shamir Adleman (RSA)[2] and message authentication code (MAC) protect the confidentiality and authenticity of transaction data as it "transits" between networks. Encryptions such as full disk encryption (FDE)[1] is also performed for user data "at rest" to prevent unauthorized access and data tampering.

For data privacy, policy approaches and technical implementations exist to ensure that sensitive data is removed or replaced with realistic data (not real data). Using policy approaches, Data Protection Acts are passed by various countries such as the USA and the European Union to safeguard an individual's personal data against misuse. For technical implementations, there are Privacy Enhancing Techniques (PETs) [2]such as anonymisation and obfuscation to de-sensitize personal data. PETs use a variety of techniques such as data substitution, data hashing and truncation to break the sensitive association of data, so that the data is no longer personally identifiable and safe to use. For example, European Network and Information Security Agency (ENISA)[4] has proposed to approach data privacy by design22, using a "data masking" platform which uses PETs to ensure data privacy.

IV. TECHNOLOGICAL CHALLENGES RELATED TO IOT

Scalability: An Internet of Things potentially has a larger overall scope than the conventional Internet of computers. But then again, things cooperate mainly within a local environment. Basic functionality such as communication and service discovery therefore need to function equally efficiently in both small-scale and large-scale environments[1].

ISSN(Online): 2320-9801
ISSN (Print): 2320-9798

International Journal of Innovative Research in Computer and Communication Engineering

(An ISO 3297: 2007 Certified Organization)

Vol. 3, Issue 7, July 2015

Arrive and operate: Smart everyday objects should not be perceived as computers that require their users to configure and adapt them to particular situations. Mobile things[2], which are often only sporadically used, need to establish Connections spontaneously, and organize and configure themselves to suit their particular environment.

Interoperability: Since the world of physical things is extremely diverse, in an Internet of Things each type of smart object is likely to have different information, processing and communication capabilities. Different smart objects would also be subjected to very different conditions such as the energy available and the communications bandwidth required. However, to facilitate communication and cooperation, common practices and standards are required. This is particularly important with regard to object addresses. These should comply with a standardized schema if at all possible, along the lines of the IP standard [2] used in the conventional Internet domain.

Discovery: In dynamic environments, suitable services for things must be automatically identified, which requires appropriate semantic means of describing Their functionality. Users will want to receive product-related information, and will want to use search engines that can find things or provide information about an object's state.

Software complexity: Although the software systems in smart objects will have to function with minimal resources, as in conventional embedded systems, a more extensive software infrastructure will be needed on the network and on background servers in order to manage the smart objects and provide services to support them.Data volumes: While some application scenarios will involve brief, infrequent communication, others, such as sensor networks, logistics and large-scale "real-world awareness" scenarios, will entail huge volumes of data on central network nodes or servers.

Security and personal privacy: In addition to the security and protection aspects of the Internet with which we are all familiar (such as communications confidentiality, the authenticity and trustworthiness of communication partners, and message integrity), other requirements would also be important in an Internet of Things. We might want to give things only selective access to certain services, or prevent them from communicating with other things at certain times or in an uncontrolled manner; and business transactions involving smart objects would need to be protected from competitors' prying eyes[1].

V. WAYS THE INTERNET OF THINGS WILL CHANGE THE WAY WE WORK

The "Internet of Things" (IoT) may sound like the futuristic wave of talking refrigerators and self-starting cars, but Internet-connected devices that communicate with one another will affect our lives outside the "smart home[8]" as well. For workers, IoT[1] will change the way we work by saving time and resources and opening new opportunities for growth and innovation[5].

1. Know where everything is, all the time
"IoT has the potential to make the workplace life and business processes much more productive and efficient [5]" One significant way IoT will increase productivity and efficiency is by making location tracking much simpler and seamless. As currently done in hospitals, Internet-connected equipment and devices will all be geographically tagged, which will save workers time hunting things down and save money by reducing the loss rate. "Companies can track every aspect of their business, from managing and fulfilling orders as quickly as possible to locating and deploying field service staff. Tools and factories and vehicles will all be connected and reporting their locations [8]".

2. Get anywhere faster IoT is the next big thing in your daily commute. The interconnectivity of mobile devices, cars and the road you drive on will help reduce travel time, thus enabling you get to work faster or run errands in record time.Today, the "connected car" is just the start of IoT capability. "AT&T, together with automotive manufacturers such as GM and BMW, are adding LTE connectivity

to the car and creating new connected services, such as real-time traffic information and real-time diagnostics for the front seat and infotainment for those in the back seat," said Macario Namie, vice president of marketing at Jasper Wireless, a machine-to-machine (M2M)[4] platform provider. In the future, IoT will integrate everything from streets to stoplights."Imagine a world in which a city's infrastructure installed roadside sensors, whose data could be used to analyze traffic patterns around the city and adjust traffic light operations to minimize or perhaps eliminate traffic jams," Namie said. "This could save a few minutes, if not hours of our day."

ISSN(Online): 2320-9801
ISSN (Print): 2320-9798

International Journal of Innovative Research in Computer and Communication Engineering

(An ISO 3297: 2007 Certified Organization)

Vol. 3, Issue 7, July 2015

3. Cheaper, greener manufacturing
Thanks to IoT, device interconnectivity will facilitate the adoption of "smart grid" technologies, which use meters, sensors and other digital tools to control the flow of energy and can integrate alternative sources of power, such as solar and wind."The Internet of Things[2] will drastically lower costs in the manufacturing business by reducing wastage, consumption of fuel and the discarding of economically unviable assets," Namie said. "IoT can also improve the efficiency of energy production and transmission and can further reduce emissions by facilitating the switch to renewable[5]."

4. Completely remote mobile device management (MDM)
IT departments may have remote access to computers and mobile devices, but IoT will also enable remote control of other Internet-connected devices, said Roy Bachar, founder and chief executive officer of MNH Innovations and member of the Internet of Things Council.Bachar, who also works with CommuniTake, a startup that provides remote-access technology, said that the cutting-edge technology that has given them full control over smart phones and tablets now allows remote management over other devices, including Android cameras and set-top boxes, among others. Soon[4], MDM technologies will extend to the remote management of IoT devices, which will introduce changes for IT departments and IoT connected employees."It's clear that the telecommunication giants will play a major role in the IoT domain and they are all introducing solutions. I believe that as early 2014, we will see the introduction of platforms for managing the IoT applications as well as solutions offered by companies, such as CommuniTake, for remote management of IOT devices [1]".

5. Increased device management complexity
As the number of connected devices grows, so does the complexity of managing them. For instance, today workers use smart phones for communication, productivity and entertainment. With IoT, they will have an additional function: controlling IoT-connected devices. "Many of the future IoT-connected devices will not have a screen. The way to take control over the device will be via smart phones"."The complexity will also increase due to the variety of operating systems," he added. Thus, employees and IT departments will have a broader range of platforms to deal with, not just Android or iOS.Both of these instances may require training for employees to learn how to control and manage connected, cross-platform devices [2].

6. Save time and get more out of your day Other than controlling other IoT devices, your smartphone will also be much like a remote control for your life, said Brendan Richardson, co-founder and chief executive officer of PsiKick, a Charlottesville, Va.-based startup that develops IoT wireless sensors.One of the most convenient aspects of IoT is that you have devices that "know" you and will help save time by allowing you to get in and out of places and conduct transactions faster using a mobile device[5]."The iPhone or Android will increasingly interact with a whole range of sensors that you never see and don't own, but which provide your smartphone with valuable information and act on your behalf through an app,".With these sensors, even just getting your morning coffee will eliminate the need to wait in line for a less stressful start to your day. For instance, wireless sensors can detect when you walk into a Starbucks, which alert the barista of your likely order based on your order history. You can then confirm or choose a different order, and then pay for it using your phone.

V. INTERNET OF THINGS AND BIG DATA

The significant increase in connected devices that's due to happen at the hands of the Internet of Things will, in turn, lead to an exponential increase in the data that an enterprise is required to manage. Here's where IoT[2] intersects wonderfully with big data – and where it becomes evident that the two trends fit one another like a glove."Once the Internet of things gets rolling, stand back. "We're going to have data spewing at us from all directions - from appliances, from machinery, from train tracks, from shipping. In short, for most businesses, the timing has never been better to look into the adoption of a big data strategy [10].

ISSN(Online): 2320-9801
ISSN (Print): 2320-9798

International Journal of Innovative Research in Computer and Communication Engineering

(An ISO 3297: 2007 Certified Organization)

Vol. 3, Issue 7, July 2015

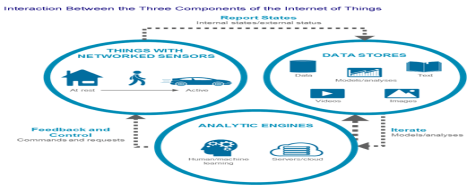

IoT Needs Big Data

While larger enterprises like Coca-Cola, General Electric [8], and Domino's Pizza have managed to tap into its value, most businesses will have to wait some time before they can really enjoy the advantages of embedded sensor technology. In the meantime, it's imperative that those businesses prepare by adopting a big data strategy – and looking into analytics technology. Big Data [6] capacity is, in essence, a prerequisite to tapping into the Internet of Things. Without the proper data-gathering in place, it'll be impossible for businesses to sort through all the information flowing in from embedded sensors. What that means is that, without Big Data, the Internet of Things can offer an enterprise little more than noise [6].

VI. INTERNET OF THINGS AND CLOUD COMPUTING

Ten years from now, things will be different. These days we wake up in the morning, jump in the shower, reach for the shower gel and only then do we realize the bottle's empty. "Dimmit", you'll curse to yourself before making a mental note to buy some more and hoping that you don't forget. In the future, we won't have to rely on ourselves to remember such trivial (but annoying) things, because everything will be automated. Your shower will already know about your washing habits[8], and most likely it'll be able to tell you when the shower gel's about to run out. There'll be a sensor that can recognize the sounds you make when desperately squeezing the remaining dregs out of the bottle, and most likely that same sensor will pick up on your frustration too. But your shower will do more than just make a mental note for you. It'll let you know exactly where to buy that shower gel by checking local store inventories for your favorite brand's availability. It'll also cross-reference your list of appointments that day to identify which is the most convenient store to drop by during the day. This "task" will automatically be filed, and synced with your laptop, Smartphone, iPad or smart car to ensure you don't forget [7].This is the future of the Internet of Things, but it won't be made possible by a jumble of wires. What makes it possible is cloud computing, combined with the glut of sensors and applications all around you that collect, monitor and transfer data to where it's needed. All of this information can be sent out or streamed to any number of devices and services, all update before you've even finished drying yourself off with the towel. Of course, this means that there's going to be an awful lot of data flying around out there, data that needs to be processed quickly so that manufacturers, suppliers and everyone else in your shower gel's supply chain can ensure that you never run out. The problem is exacerbated somewhat by the fact that you're not the only out there taking a shower – think about, between 6am and 8am, how many millions of people are going through exactly the same routine as you are? Millions of them are busy scrubbing themselves clean, which means gigabytes of data streaming in from showers up and down the country. This is why the cloud is so important. The cloud can easily get a handle on the speed and volume of the data that's being received. It possesses the ability to ebb and flow according to demand, all the while remaining accessible anywhere from any device[7]

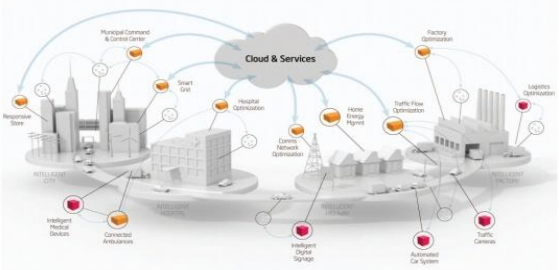

ISSN(Online): 2320-9801
ISSN (Print): 2320-9798

International Journal of Innovative Research in Computer and Communication Engineering

(An ISO 3297: 2007 Certified Organization)

Vol. 3, Issue 7, July 2015

But it's not just you who needs this cloud. Manufacturers do too. In the shower gel example, there are lots of insights that can be gleaned from this, for example how long does it take the average person to get through a bottle of the stuff, will that person buy the same brand again, the same bottle size again, or does he or she prefer something different? Using these insights, retailers and manufacturers will come up with customized special offers for certain types of people, and deliver these to their Smartphone in time for when they go shopping later that afternoon.Such insights can only be extracted using Big Data technologies, and cloud solutions will be an essential partner to this. Cloud software[7] is the only technology capable of handling this data and delivering it where it needs to be in real time.The Internet of Things[2] still has some way to go before we reach this point, but it's getting there and cloud computing will be driving it every step of the way.

VIII. REAL LIFE APPLICATIONS OF IOT WITH BIG-DATA AND CLOUD

1. Smart home: Smart Home clearly stands out, ranking as highest Internet of Things application on all measured channels. More than 60,000 people currently search for the term "Smart Home[3]" each month. This is not a surprise. The IoT Analytics company database for Smart Home includes 256 companies and startups. More companies are active in smart home than any other application in the field of IoT. The total amount of funding for Smart Home startups currently exceeds $2.5bn. This list includes prominent startup names such as Nest or AlertMe as well as a number of multinational corporations like Philips, Haier, or Belkin.

2. Wearable's: Wearables [8] remain a hot topic too. As consumers await the release of Apple's new smart watch in April 2015, there are plenty of other wearable innovations to be excited about: like the Sony Smart B Trainer, the Myo gesture control, or Look See bracelet. Of all the IoT startups, wearable maker Jawbone is probably the one with the biggest funding to date. It stands at more than half a billion dollars!

3. Smart City: Smart city spans a wide variety of use cases, from traffic management to water distribution, to waste management, urban security and environmental monitoring. Its popularity is fueled by the fact that many Smart City [8] solutions promise to alleviate real pains of people living in cities these days. IoT solutions in the area of Smart City solve traffic congestion problems, reduce noise and pollution and help make cities safer.

4. Smart grids: Smart grids are a special one[2]. A future smart grid promises to use information about the behaviors of electricity suppliers and consumers in an automated fashion to improve the efficiency, reliability, and economics of electricity. 41,000 monthly Google searches highlight the concept's popularity. However, the lack of tweets (Just 100 per month) shows that people don't have much to say about it.

5. Industrial internet: The industrial internet is also one of the special Internet of Things applications. While many market researches such as Gartner or Cisco[8] see the industrial internet as the IoT concept with the highest overall potential, its popularity currently doesn't reach the masses like smart home or wearable do. The industrial internet however has a lot going for it. The industrial internet gets the biggest push of people on Twitter (~1,700 tweets per month) compared to other non-consumer-oriented IoT concepts [4].

6. Connected car: The connected car is coming up slowly. Owing to the fact that the development cycles in the automotive industry typically take 2-4 years, we haven't seen much buzz around the connected car yet. But it seems we are getting there. Most large auto makers as well as some brave startups are working on connected car solutions. And if the BMWs and Fords of this world don't present the next generation internet connected car soon, other well-known giants will: Google, Microsoft, and Apple have all announced connected car platforms [8].

7. Connected Health (Digital health/Telehealth/Telemedicine: Connected health remains the sleeping giant of the Internet of Things applications. The concept of a connected health care system and smart medical devices bears enormous potential (see our analysis of market segments), not just for companies also for the well-being of people in general. Yet, Connected Health [5] has not reached the masses yet. Prominent use cases and large-scale startup successes are still to be seen. Might 2015 bring the breakthrough?.

ISSN(Online): 2320-9801
ISSN (Print): 2320-9798

International Journal of Innovative Research in Computer and Communication Engineering

(An ISO 3297: 2007 Certified Organization)

Vol. 3, Issue 7, July 2015

8. Smart retail: Proximity-based advertising as a subset of smart retail is starting to take off. But the popularity ranking shows that it is still a niche segment. One LinkedIn post per month is nothing compared to 430 for smart home.

9. Smart supply chain: Supply chains have been getting smarter for some years already. Solutions for tracking goods while they are on the road, or getting suppliers to exchange inventory information have been on the market for years. So while it is perfectly logic that the topic will get a new push with the Internet of Things, it seems that so far its popularity remains limited.

10. Smart farming: Smart farming is an often overlooked business-case for the internet of Things because it does not really fit into the well-known categories such as health, mobility, or industrial. However, due to the remoteness of farming operations and the large number of livestock that could be monitored the Internet of Things could revolutionize the way farmers work. But this idea has not yet reached large-scale attention. Nevertheless, one of the Internet of Things applications that should not be underestimated. Smart farming [8] will become the important application field in the predominantly agricultural-product exporting countries.

IX. CONCLUSION

In conclusion, Internet of Things is the concept in which the virtual world of information technology connected to the real world of things. The technologies of Internet of things such as RFID [2] and Sensor make our life become better and more comfortable. This paper discusses the Internet of Things which is one of the upcoming concepts in the field of Internet. We analyzed the general architecture, challenges of IOT, ways the IOT change our way of work, and real life applications that can be used to implement internet of things and the actual technologies that can be used to implement IOT like RFID, IPV6[1]. We also found relationship between big data [6] and Internet of things and Cloud Computing [7] and Internet of things how these two fields related to each other.

REFERENCES

[1].https://www.ida.gov.sg/~/media/Files/Infocomm%20Landscape/Technology/TechnologyRoadmap/InternetOfThings.pdf
[2].http://www.freescale.com/files/32bit/doc/white_paper/INTOTHNGSWP.pdf
[3].https://en.wikipedia.org/wiki/Smart_objects
[4].https://en.wikibooks.org/wiki/A_Bit_History_of_Internet/Chapter_8_:_Internet-of-Things
[5].http://www.businessnewsdaily.com/4858-internet-of-things-will-change-work.html
[6].http://www.datamation.com/applications/why-big-data-and-the-internet-of-things-are-a-perfect-match.html
[7].http://siliconangle.com/blog/2013/07/17/cloud-computing-the-internet-of-things-go-hand-in-hand/
[8].http://iot-analytics.com/10-internet-of-things-applications/
[9].http://internetofthingsphilosophy.com/keynote-speakers/
[10]https://www.googleimags.com
[11] http://www.infoworld.com/article/2608029/cloud-computing/the-cloud-is-the-secret-weapon-in-the-internet-of-things.html

BIOGRAPHY

Sandeep Ravikanti received his Masters degree in Computer Science & Engineering in 2012 from HITAM College, Hyderabad, India. Presently, he is working as Assistant Professor in the Department Of CSE, Methodist College of engineering and technology Hyderabad, Telangana, India.

Gadasu Preeti received her Masters degree in Computer Science & Engineering in 2012 from JNTUH – School Of IT, Hyderabad, India. Presently, she is working as Assistant Professor in the Department Of CSE, Methodist College of engineering and technology Hyderabad, Telangana, India.

ISSN: 2321-7782 (Online)
Volume 3, Issue 7, July 2015
International Journal of Advance Research in Computer Science and Management Studies
Research Article / Survey Paper / Case Study
Available online at: www.ijarcsms.com

An Incremental Framework for Internet of Things (IOT) and Big Data - A business Intelligence (BI) Prospective

Gadasu Preeti[1]
Assistant Professor,
Dept of Computer Science Engineering,
Methodist College of Engineering &Technology,
Hyderabad, Telangana. India

Sandeep Ravikanti[2]
Assistant Professor,
Dept of Computer Science Engineering,
Methodist College of Engineering &Technology,
Hyderabad, Telangana. India

Abstract: ***Internet of Things (IoT) covers every aspect of our lives and to generate a paradigm shift towards a hyper-connected society. IoT has become a mainstream topic. This growing credit is due to the impact the IoT had on business analytics and the prospective that still remains untouched. Each day, new machines, sensors, and devices come online and feed information into data systems. As organizations get on new IoT initiatives and work to abstract more insight from huge data volumes, an architectural approach is shown. Traditional databases and analytics architectures will always be fundamental, but the IoT calls for specific capabilities to handle varied data constantly streaming from various numbers of sources. In this paper we address technological rootmap from IoT – Bigdata to Business Intelligence that leads to bigdata analytics.***

I. INTRODUCTION

"The Internet Of Things Takes Over Big Data As The Most Hyped Technology". Big data has moved down the "trough of disillusionment," replaced by the Internet of Things at the top of the hype cycle.The term Internet of Things was coined by the British technologist Kevin Ashton in 1999, to describe a system where the Internet is connected to the *physical* world through ubiquitous *sensors*.Today, the huge amounts of data we are producing and the advances in mobile technologies are bringing the idea of Internet connected devices into our homes and daily lives.RFID and sensor technology enabling computers to observe, identify and understand the world without the limitations of human-entered data.However, people took it beyond the capture of "physical" events/data. An envision of network of things that was wholly dependent on human beings for information and expanded to involve anything that touched a person.Capturing the behavior of people will need broader collection of data beyond sensor technology ,beyond the "physical" that is web server clickstream data, e-commerce transaction data, customer service call logs, search logs, video surveillance, documents, etc.To understand the behavior of people, you need to capture data from any touch point, gaining a holistic view of that person. Gaining a 360 degree of your customers or a 360 degree view of your business by leveraging an environment of structured data that can be analyzed. IoT of physical devices becomes a subset of the data sources available to such a project.

Big Data: [1] Is a term used to describe the massive growth and availability of structured and unstructured data. While the term refer to the volume of data, it also refers to the technology (tools and processes) that an organization requires to handle these data volumes and storage facilities. Big Data spans three dimensions: Volume, Velocity and Variety. **Importance of Big Data: [1]** Everyone is talking about Big Data trends, from challenges to the tools required for Big Data projects. Businesses understand that Big Data infrastructure will help them make better decisions. When Big Data platforms is effectively and efficiently captured, processed and analyzed, organizations gain a clear and complete understanding of their business which would lead to efficiency improvements, lower costs, increased sales and better customer service. **Business Intelligence:** Business intelligence (BI) [2] is an umbrella term used to encompass the processes, methods, measurements and systems businesses use to more easily view, analyze and understand information relevant to the history, current performance or future

projections for a business.The goal of BI is to help decision-makers make more informed and better decisions to guide the business. Business intelligence software and software-as-a-service (SaaS) solutions achieve this by making it simpler to aggregate, see, and slice-and-dice the data. Thus makes it easier to identify trends and issues, discover new insights, and fine-tune operations to meet business goals.

II. Related Work

1) IoT a Subset of Big Data

A simple incremental view of how IoT feeds Big Data which then feeds a broader analytic platform. Imagine IOT as a bunch of customized data sources (sensors and machines) leveraging customized collectors that feed a comprehensive platform (e.g. Hadoop vendors like Cloudera and Hortonworks) which, in turn, allow us to feed downstream analytic, BI, and visualization platforms.

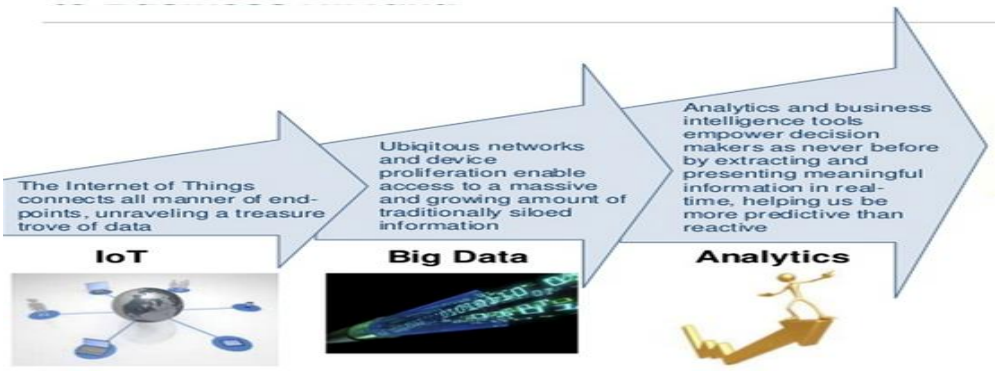

Figure1: Reference image is taken form ref [12] : Incremental View

2) *Sensors the core of Iot*

A sensor[13] is technically any device which converts one form of energy to another form, the end being usually being an electrical form mainly for measurement, control or monitoring purposes. Consider a typical temperature sensor like a gas pressure based tube sensor which expands or contracts to convert the temperature into a mechanical motion which can be displayed, recorded or used for control as required. Translation a thermostat as used in a refrigerator. The raw electrical signal from a physical sensor is usually in analog form, and can be conveniently processed further and displayed on a meter or other suitable indication device or recorded on paper or other media such as magnetic tape or more advanced digital systems as required. The sensor[13] is classified as per its application and there could be many different types of sensors, with their own inherent advantages or disadvantages for a particular application. Putting it simply, the sensor generates an output which can be conveniently displayed, recorded or used to control or monitor the application at the point where the sensor is installed. What's so special about sensors? You can translate the analog physical world into a digital computer world ,where we convert the sensor's analog signals in to digital signals so, the computer can be able to read it and then we feed that with other digital signals into a Big Data platform."Technologies that operate upon the physical world are a key component of the digital business opportunity." I think IoT requires a lot of talent on the many types of physical sensors and how they are ultimately converted into a form that the emerging Big Data platforms can consume and analyze them.

3) IoT Needs a Big Data Platform

Getting your fridge to talk to you through sensors is one thing, getting your plants to talk to your heating system and to you is quite another. As we map the spread of the IoT, it starts to get more difficult and barriers appear with the centralized big data platform or halt progress JeffHagins Founder and [5] CTO of SmartThings, described the data platform he has been working on that should help expand the IoT and help product designers work out new ways of connecting machines and people. He believes that the Internet of Things has got to be built on a platform that is easy, intelligent and open. The evolving Big Data platforms will become a standard for IoT-based applications and IoT is just that, a set of specialized sensor connectors and Big Data

applications. The blurring the physical and virtual worlds are strong concepts in this point. Physical assets become digitalized and become equal factors in understanding and managing the business value chain alongside already-digital entities, such as big data systems and next-generation applications.

III. Business Intelligence And Internet Of Things

For business intelligence (BI) [8] we inten

d the set of methods and models that explore the data in order to obtain information and then knowledge .Internet of Things: a global network of interconnected objects. In the year 2008, for the first time more object than people were connected to Internet. Merging the concepts from those two fields will provide new ideas and methods to solve problems.

Technology roadmap of IoT

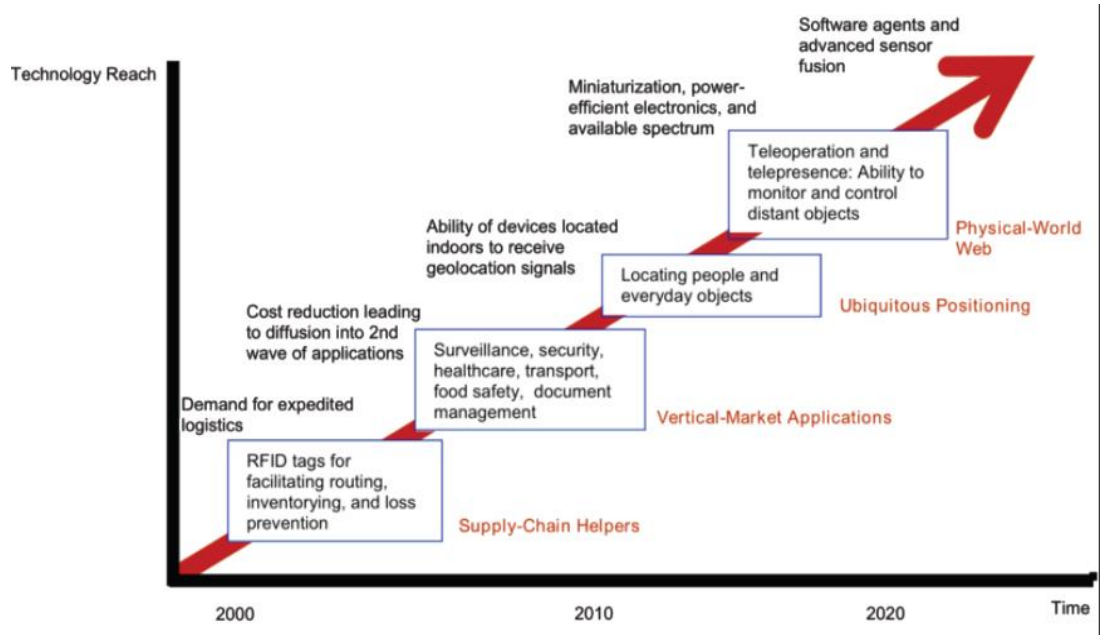

Figure2: Technology moves of Iot

Enabling Factors of BI and IoT

Tagging, sensing, shrinking, connecting have made easier to access and share large amounts of data.

» Data available from many sources, but heterogeneous in origin, content and representation.

» Commercial transactions, financial, administrative.

» Transport & energy.

» Clinical data.

» Their presence opens scenarios and opportunities that were unthinkable before.

IV. Big Data To Business Intelligence

In older tools and in most current solutions BI tells you what happened in a specific segment of your business. With how quickly business is moving today, that kind of BI is as problematic as driving down the freeway by looking only in your rear-view mirror. With new technology and new expectations, BI is moving toward a more predictive model that shows you what will happen. New BI systems are now beginning to show how all the various parts of your organization work together to produce an outcome, and business leaders can finally see the big picture and make faster, better-informed decisions.

V. Architecture And Related Discussions

The data components of a BI architecture [3] include the data sources that corporate executives and other end users need to access and analyze to meet their business requirements. Important segment in the source selection process include data currency, data quality and the level of depth in the data. Both structured and unstructured data may be required as part of a BI architecture, as well as information from both internal and external sources. Information management architectural components are used to transform raw transaction data into a consistent and coherent set of information that is suitable for BI uses. For example, this part of a BI architecture [3] typically includes data integration, data cleansing and the creation of data dimensions and business rules that conform to the architectural guidelines. It may also define structures for data warehousing that aggregates information in virtual databases instead of physical data warehouses or data marts.

The technology components are used to show information to business users and enable them to analyze the data. This includes the BI software suite or BI tools [4] to be used within an organization as well as the supporting IT infrastructure – i.e., hardware, database software and networking devices. There are various types of BI applications that can be built into an architecture: reporting, ad hoc query, data mining and data visualization tools, and online analytical processing (OLAP) software, business intelligence dashboards and performance scorecards.

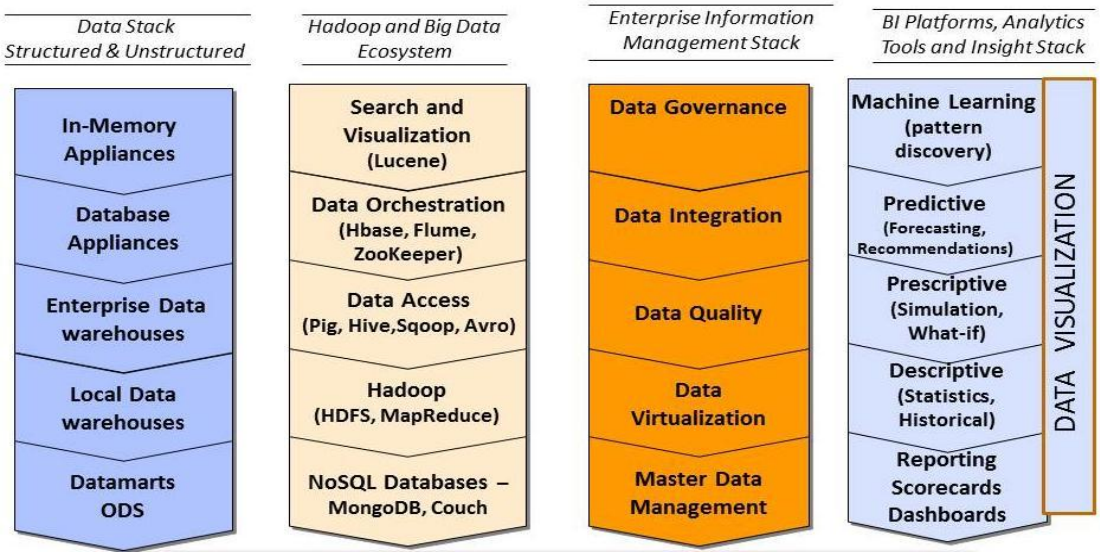

Figure3: Structured and Unstructured Data [3], BI architecture

Whether the IoT and sensors are Big Data: The discussion [4] is on architecture challenges–from device to data to data consumer–created by the start of millions (or billions) of connected sensors and smart things. Connected devices bring back some standard engineering challenges back. How do you transmit data securely and with low power consumption.How do you handle lossy networks and cut-off transmissions. Everything is not smartphone application transmitting JSON over HTTP. How do you handle communication myriad protocols, each of which could be using a near-infinite variety of data encoding formats. IoT data is messy. Devices get cut off in mid-transition or repeat. How do you detect this–and clean it up–as data arrives. IoT data is of high volume. By 2020, we will have 4x more sensor and IoT data than enterprise data. We already get more data today from sensors than we do from PCs. How do we scale to consume and use this. In addition, connected devices are not always smart or fault-tolerant. How do you ensure you are always ready to catch all that data (i.e., you need a zero-downtime IoT utility).IoT and sensor and of itself is not terribly useful. It is rarely in a format that a business analyst would even be able to read. It would be incredibly wasteful to store all this as-is in a business warehouse, DropBox repo, etc.. IoT and sensor data needs context. Knowing device Knowing that FE80:0000:0000:0000:0202:B3FF:FE1E:8329 is at GPS location X,Y is of no

use. You need to marry it to data about the "things" to get useful insights. IoT data is in two view points: what does this mean right now and what does this imply for the big picture. The Lambda Architecture [6] is an ideal tool to handle this.

VI. TECHNOLOGIES

The Lambda Architecture, first proposed by Nathan Marz, attempts to provide a combination of technologies that together can provide the characteristics of a web-scale system that can satisfy requirements for availability, maintainability, and fault-tolerance. Big data analytical ecosystem architecture [7] is in early stages of development. Unlike traditional data warehouse / business intelligence (DW/BI) architecture which is designed for structured, internal data, big data systems work with raw unstructured and semi-structured data as well as internal and external data sources. Moreover, organizations may need both batch and (near) real-time data processing capabilities from big data systems. Lambda architecture provides a clear set of architecture principles that allows both batch and real-time or stream data processing to work together while building immutability and recomputation into the system.

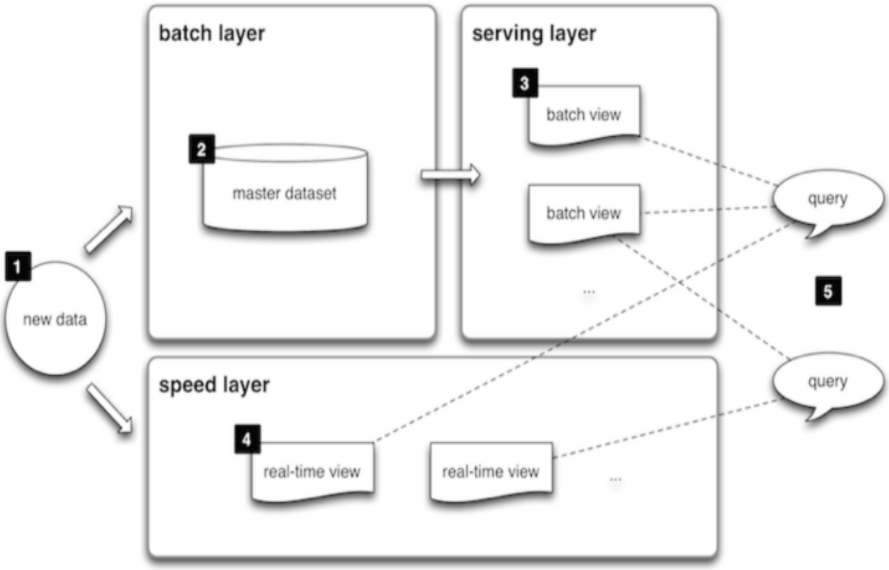

Figure4: Lambda Architecture[7] ; various layers

Batch processes high volumes of data where a group of transactions is collected over a period of time. Data is collected, entered, processed and then batch results produced. Batch processing requires separate programs for input, process and output. An example is payroll and billing systems. In contrast, real-time data processing involves a continual input, process and output of data. Data must be processed in a small time period (or near real-time). Customer services and bank ATMs are examples. Lambda architecture has three (3) layers:

» Batch Layer

» Serving Layer

» Speed Layer

Batch Layer (Apache Hadoop): [7] Hadoop is an open source platform for storing massive amounts of data. Lambda architecture provides "human fault-tolerance" which allows simple data deletion (to remedy human error) where the views are recomputed (immutability and recomputation).The batch layer stores the master data set (HDFS) and computes arbitrary views (MapReduce). Computing views is continuous: new data is aggregated into views when recomputed during MapReduce iterations. Views are computed from the entire data set and the batch layer does not update views frequently , resulting in latency.

Serving Layer (Real-time Queries): The serving layer indexes[7] and exposes precomputed views to be queried in ad hoc with low latency. Open source real-time Hadoop query implementations like Cloudera Impala, Hortonworks Stinger, Dremel

(Apache Drill) and Spark Shark can query the views immediately. Hadoop can store and process large data sets and these tools can query data fast. At this time Spark Shark outperforms considering in-memory capabilities and has greater flexibility for Machine Learning functions. Note that MapReduce is high latency and a speed layer is needed for realtime.

Speed Layer(Distributed Stream Processing):[7] The speed layer compensates for batch layer high latency by computing real-time views in distributed stream processing open source solutions like Storm and S4. They provide:

» Stream processing

» Distributed continuous computation

» Fault tolerance

» Modular design

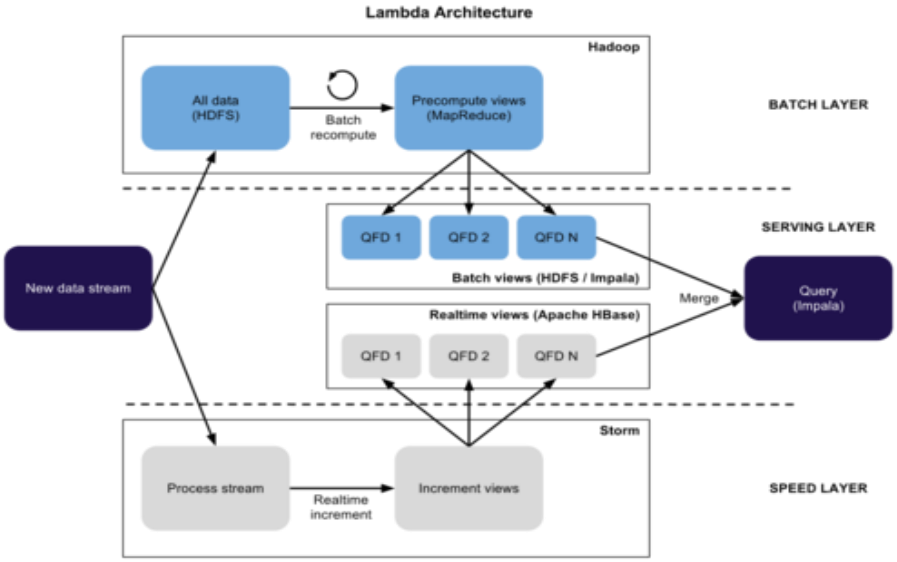

Figure5: Layers in Detail

In the speed layer real-time views are incremented when new data received. Lambda architecture provides "complexity isolation" where real-time views are transient and can be discarded allowing the most complex part to be moved into the layer with temporary results. The decision to implement Lambda architecture depends on need for real-time data processing and human fault-tolerance. There are significant benefits from immutability and human fault-tolerance as well as precomputation and recomputation. Lambda implementation issues include finding the talent to build a scalable batch processing layer. We can work with Hadoop, MapReduce, HDFS, HBase, Pig, Hive, Cascading, Scalding, Storm, Spark Shark and other new technologies.

VII. BIG DATA ANALYTICS INFRASTRUCTURE

Big data analytics [8] refers to the science and analysis of both internal and external data to obtain valuable, actionable insights that allows the organization to make better decisions. Recent surveys suggest the number one investment area for both private and public organizations is the design and building of a modern data warehouse (DW) / business intelligence (BI) / data analytics architecture that provides a flexible, multi-faceted analytical ecosystem.

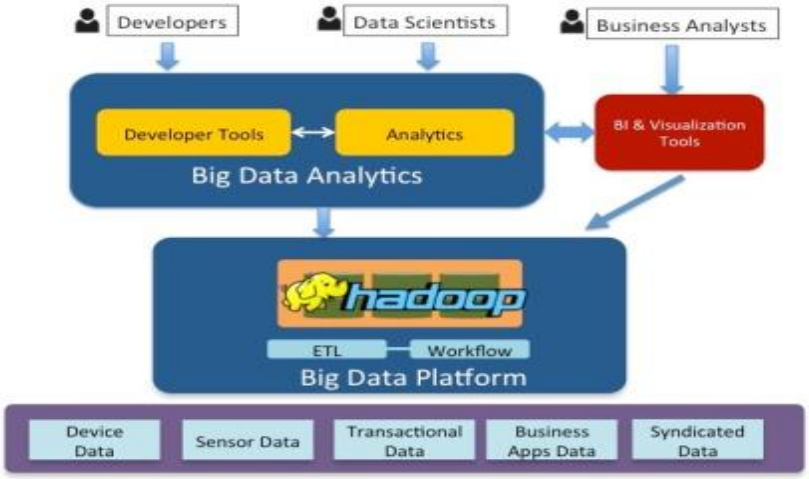

Figure6: Bigdata Analytics[8]

The goal is to leverage both internal and external data , as well as structured and unstructured data - to gain competitive advantage and make better decisions. While traditional business intelligence (BI) technologies provide historical, current and descriptive views of business operations, big data analytics focuses on data science, predictive analytics, data mining, decision optimizing processes and business performance management.

Five key benefits to data science and business analytics:

1. Improving the decision-making process.
2. Speeding up the decision-making process.
3. Better alignment of resources with strategies.
4. Realizing cost efficiencies.
5. Responding to user needs for availability of data on a timely basis.

By embracing data science, decision optimizing processes and an analytical approach, companies identify their most profitable customers, accelerate product innovation, optimize supply chains and pricing, and identify the true drivers of financial performance.

VIII. APPLICATIONS

The COMPOSE project: [10] It has built a cloud platform that helps developers find their way smoothly through the booming, Internet of Things (IoT). Their mission is simple: to allow developers to create apps that provide people with Internet services and launch them into the market quickly , whether that be shopping or traffic information systems, or home-based apps .'We give developers a one-stop shop where it is easy to design and deploy IoT applications, providing building blocks so they can create their own dream apps.[8] . We hope that opening the door to this realm for smaller developers will lead to higher innovation. For this, COMPOSE (Collaborative Open Market to Place Objects at your SErvice) has developed and uploaded libraries of software, all of which can be downloaded free from its open source code repository, GitHub, the largest code host in the world. The project is continually adding new items to GitHub so users can acquire COMPOSE smart 'objects' or modules from the repository. They can combine these to create their own apps easily and quickly. It saves building any app from scratch, avoiding wasting time and development money in the process, by using basic blocks that have been developed by programmers in the past and shared through the COMPOSE project.

Shopper behaviour, car sharing and happy skiers: COMPOSE [8] is conducting three pilot projects. One of these involves the start-up U-Hopper, which has won awards for its COMPOSE-based retail analytics platform, RetailerIN, currently on trial at the SAIT-COOP supermarket in Trento, Italy. Shoppers' carts and baskets are tracked to create a heat map of where customers spend their time in the store. From the office, the store manager can monitor the effectiveness of displays and campaigns, and the queues forming at various counters, changing the supermarket's strategies to suit. The second pilot involves car sharing among around 750 staff and students at the University of Tarragona in Spain. Through social media, the app encourages car sharing by linking it to reserving spaces in the university car park, thus reducing the number of vehicles travelling to the university every day. In the third pilot in a resort of Trentino, Italy, skiers get real-time snow and weather conditions fed to their smartphones from a network of meteorological stations. The app, Go2Ski, also helps friends meet up and share photos, and even informs on the length of queues at ski lifts. And it is truly an app for all seasons. When the snow melts it uses the same meteorology network, but for warmer weather sports such as cycling.

IX. CONCLUSION

In conclusion, Internet of Things is the concept in which the virtual world of information is connected to the real world of things. The technologies of Internet of things such as sensors, bigdata make our life more comfortable. This paper discusses the Internet of Things which is one of the upcoming concepts in the field of Internet. We analyzed the architecture, its technologies and real life applications. An incremental view of Iot and Bigdata to Business intelligence leads to Big data analytics [8] that refers to the science and analysis of both internal and external data to obtain valuable, actionable insights that allows the organization to make better decisions.

References

1. http://www.happiestminds.com/Insights/Big-Data/
2. http://www.smallbusinesscomputing.com/News/Software/article.php/3896051/What-is-Business-Intelligence-and-Why-Should-You-Care.htm
3. http://www.savi.com/2015/how-to-architect-for-the-internet-of-things-iot/
4. http://www.b-eye-network.com/
5. www.ctosmartthings.org
6. http://www.dbta.com/Columns/Big-Data-Notes/Real-Time-Big-Data-With-the-Lambda-Architecture-99798.aspx
7. http://www.datasciencecentral.com/profiles/blogs/lambda-architecture-for-big-data-systems
8. http://www.rosebt.com/big-data-analytics-infrastructure.html
9. www.ibmresearch.com
10. http://www.libelium.com/smart-city-urban-resilience-smart-environment/(app final)
11. http://www.meetup.com/Internet-of-Things-DC/messages/boards/thread/49041291/(app)
12. https://www.googleimags.com
13. www.datamation.com

ISSN(Online) : 2319-8753
ISSN (Print) : 2347-6710

International Journal of Innovative Research in Science, Engineering and Technology

(An ISO 3297: 2007 Certified Organization)

Vol. 4, Issue 7, July 2015

Evaluating the Performance of Reactive Unicast Routing Protocols with OPNET Simulator in MANETS under VOIP

Sandeep Ravikanti, Gadasu Preeti

Assistant Professor, Department of CSE, Methodist College of Engineering and Technology, Hyderabad, Telangana, India

Assistant Professor, Department of CSE, Methodist College of Engineering and Technology, Hyderabad, Telangana, India

ABSTRACT: Mobile Ad Hoc Networks (MANETs)[2] are an emerging type of wireless networking, in which mobile nodes associate on an extemporaneous or ad hoc basis. MANETs are self-forming and self-healing, enabling peer-level communications between mobile nodes without reliance on centralized resources or fixed infrastructure. Many ground breaking applications have been suggested for MANETs including the Voice over Internet Protocol (VoIP)[7]. In order to support VoIP application over MANETs a suitable routing protocol is essential. Several routing protocols have been proposed for MANETs. In this paper, the performances of different routing protocols have been investigated and compared for VoIP application. Some popular routing protocols namely Dynamic Source Routing (DSR)[9], Ad hoc On-demand Distance Vector (AODV)[6], Temporally-Ordered Routing Algorithm (TORA)[7] have been considered in this investigation. The OPNET simulation results show that the TORA protocol is a good candidate for VoIP application.

KEYWORDS: AODV, DSR, MANETs, VOIP, Qos metrics, OPNET, TORA.

1. LITERATURE SURVEY

MODERN wireless communication [2] systems are rapidly evolving day by day. The main objective of this evolution is to provide a user with communication services at anytime and from anywhere of the World. Technological advancements and the popularity of the portable computing devices have made this objective an attainable one. In MANETs [6] performance is sensitive to mobility, scalability and traffic load. Examining different protocols performance in dynamic environment plays a vital role in efficient routing. The main objective is to access the performance of protocols whether varying with network size, node speed, traffic, and mobility and simulation time [8].MANET routing protocols are classified into three categories. They are;

1) Proactive routing protocols 2) Reactive routing protocols 3) Hybrid routing protocols
Main related work in our paper is focused only on RIP and OLSR [5] routing protocols. In this paper, we conduct a performance evaluation of RIP[9] and OLSR routing protocols. Goal of the paper is to analyze the DSR, AODV [6] AND TORA routing protocols in MANET [2] on TCP, UDP and FTP traffic under Voice over Internet Protocol. In our paper,
The first work will be to analyze the performance of existing routing protocols RIP and OLSR confined to performance metrics like package delivery ratio, end to end delay, throughput etc. by using OPNET[8] simulator.
Secondly in designing and implementing the network scenarios by varying number of nodes, traffic loads, simulation time etc.

ISSN(Online) : 2319-8753
ISSN (Print) : 2347-6710

International Journal of Innovative Research in Science, Engineering and Technology

(An ISO 3297: 2007 Certified Organization)

Vol. 4, Issue 7, July 2015

Finally CBR, FTP uses TCP[3] for denial of service in existing routing protocols. We are also concentrating on the impact of traffic at two different layers (application and transport layers) to analyze the performance of MANET [4] routing protocols.

Related Work

- To analyze throughput, medium access delay, end to end delay on varying network size, throughput, and simulation time.
- To investigate the impact of mobility on throughput and delay.

II. INTRODUCTION

Cellular Wireless Networks are Infrastructure dependent network. These networks are Single-Hop Wireless links. This network provides guaranteed bandwidth (designed for voice traffic). These runs with Circuit-Switching (evolving toward packet switching) process. Developing these networks are High cost and time of deployment. Seamless connectivity (low call drops using handoffs). Reuse of frequency spectrum through geographical channel reuse. Cellular networks[8] are easy to achieve the time synchronization. These networks are easy to employ bandwidth reservation. Application domains include mainly civilian and commercial sectors. Maintenance of these networks is of high cost while compared to other networks maintenance (backup power source, staffing etc.). Major goals of routing and call admission are to maximize the call acceptance ratio and minimize the call drop ratio. Cellular Networks are widely deployed and currently in the third generation of evolution.

Ad-Hoc Networks[4] are Multi-hop radio relaying and without support of infrastructure. These are of two types:
–Wireless Mesh Networks
–Wireless Sensor Network

Ad-Hoc networks are Infrastructure Less and Multiple-hop wireless links. Ad-Hoc networks are shared radio channel which are more suitable for best-effort data traffic. These are running with Packet-Switching (evolving towards the emulation of circuit switching)[3]. Developing this network is quick and cost-effective deployment. There are frequent path breaks due to mobility in Ad-Hoc networks. These networks reuse Dynamic frequency based on carrier sense mechanism.

In this, time synchronization is difficult and consumes bandwidth which causes some problems. To reserve the bandwidth in Ad-Hoc network[2], it requires complex medium access control protocols. Major application domains include battlefields, emergency search and rescue operations and collaborative computing etc. Mobile Hosts require more intelligence (should have a transceiver as well as routing/switching capability). Self-organization and maintenance properties are built into the network. Main aim of routing is to find paths with minimum overhead and also quick re-configuration of broken paths.

Mobile ad-hoc networks (MANET)

Opposed to the infrastructure wireless networks where each user directly communicates with an access point or base station, a mobile ad-hoc network, or MANET is a kind of wireless ad-hoc network. It is a self configuring network of mobile routers connected by wireless links with no access point. Every mobile device in a network is autonomous. The mobile devices are free to move haphazardly and organize themselves arbitrarily. In other words, ad-hoc network do not rely on any fixed infrastructure (i.e. the mobile ad-hoc network is infrastructure less wireless network. The Communication in MANET is take place by using multi-hop paths.

Nodes in the MANET share the wireless medium and the topology of the network changes erratically and dynamically. In MANET, breaking of communication link is very frequent, as nodes are free to move to anywhere. The density of nodes and the number of nodes are depends on the applications in which we are using MANET.

ISSN(Online) : 2319-8753
ISSN (Print) : 2347-6710

International Journal of Innovative Research in Science, Engineering and Technology

(An ISO 3297: 2007 Certified Organization)

Vol. 4, Issue 7, July 2015

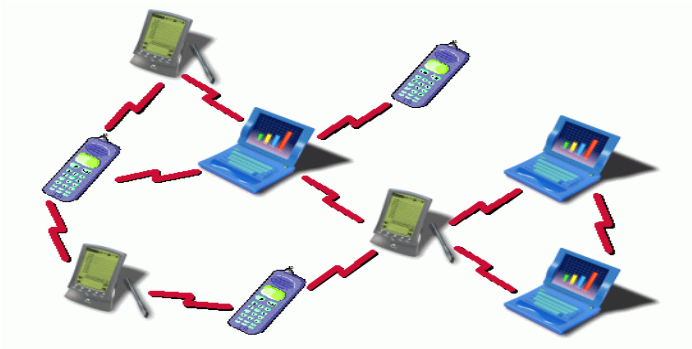

Fig 1.Mobile Ad-Hoc Network

CHALLENGES OF MOBILE AD-HOC NETWORK:

Regardless of the variety of applications and the long history of mobile ad hoc network, there are still some issues and design challenges that we have to overcome. This is the reason MANET is one of the elementary research field. MANET is a wireless network of mobile nodes; it's a self organized network. Every device can communicate with every other device i.e. it is also multi hop network.

As it is a wireless network it inherits the traditional problem of wireless networking:[4]

- The channel is unprotected from outside signal.
- The wireless media is unreliable as compared to the wired media.
- Hidden terminal and expose terminal phenomenon may occur.
- The channel has time varying and asymmetric propagation properties.

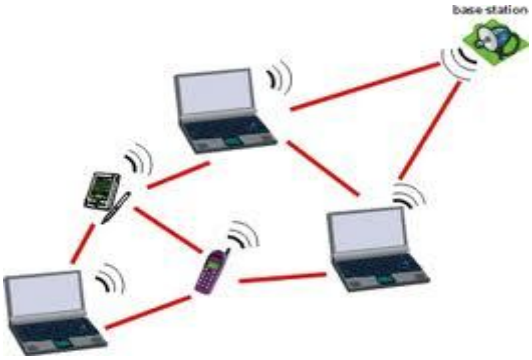

Fig 2.Wireless Network

III. ROUTING PROTOCOLS IN MANET's

Routing is the process of selecting paths in a network along which to send network traffic [5]. The process of finding a route or path along which the data or control packets can be delivered between nodes in the network is also known as routing. Again routing is the process of creating or updating the table, called routing table, which contains the information that a router needs to route packets, that helps in forwarding (the way a packet delivered to the next station). The information may include the network address, the cost, and the address of next hop and so on.

CLASSIFICATION OF ROUTING PROTOCOLS IN MANET'S:Routing protocols typically fall under two classifications first one is unicast Routing Protocol[5], second one is multicast Routing Protocol. Different routing protocols try to solve the problem of routing in mobile ad hoc network in one way or the other. Unicast routing protocols are divided into proactive, reactive and hybrid routing protocols[7], and the multicast routing protocol are divided into proactive, reactive, and hybrid routing protocol gives a classification on routing protocol is based on unicast and multicast routing

ISSN(Online) : 2319-8753
ISSN (Print) : 2347-6710

International Journal of Innovative Research in Science, Engineering and Technology

(An ISO 3297: 2007 Certified Organization)

Vol. 4, Issue 7, July 2015

protocol. Proactive routing[5] that means route available immediately. Reactive routing that means discovers the route when needed. And hybrid routing that means combination of both, such as proactive for neighborhood, reactive for far away.

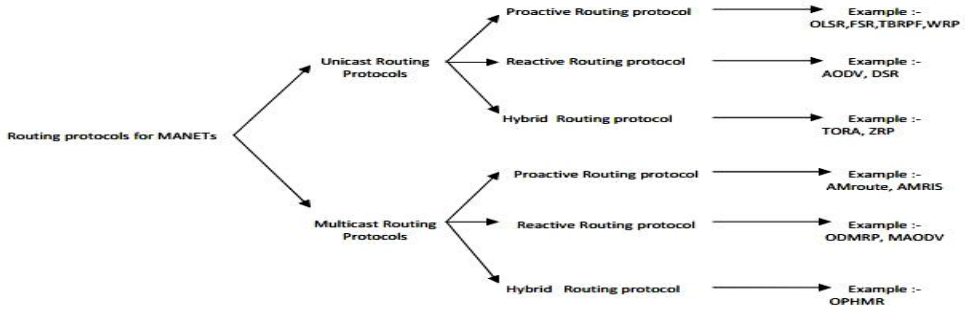

Fig 3.Classification of Routing protocols for MANET's

3.1 UNICAST ROUTING PROTOCOLS

Most applications in the MANET are based upon unicast communication. Thus, the most basic operation in the IP layer of the MANET [2] is to successfully transmit data packets from one source to one destination. The forwarding procedure is very simple in itself: with the routing table [3], the relay node just uses the destination address in the data packet to look it up in the routing table.

3.1.1PROACTIVE UNICAST ROUTING PROTOCOLS:

The following table shows the unicast routing protocols scope, organization, nighbour detection method, broadcasting based on optimized route, route freshness etc for all OLSR, FSR, and TBRPF protocols.

	OLSR	FSR	TBRPF
Scope	Large and dense MANETs	Large scale MANETs with high mobility	MANETs with hundreds of nodes and high mobility
Organization Of the network	Flat	Hierarchical	Flat
Neighbor Detection method	Periodical HELLO messages	Periodical link state updates	Differential HELLO messages
Optimized Broadcast	Multipoint relaying	Combined with neighbor Detection	Combined with HELLO messages
Broadcast Information	MPR selector list	Link state update	(Partial) Spanning tree
Route freshness	Up-to-date	Maybe not up-to-date	Up-to-date

Characteristic Comparison of Proactive Unicast Routing Protocol

3.1.2 REACTIVE UNICAST ROUTING PROTOCOLS:

Due to the frequently changing topology of the Mobile Ad hoc Network, the global topology information stored at each node needs to be updated frequently, which consumes lots of bandwidth, because the link state updates received expire before the route between itself and another node is needed. To minimize the wastage of bandwidth, the concept of on demand or reactive routing protocol is proposed. In On demand protocols the routing is divided into the following two steps: first one is route discovery and second one is route maintenance. The most distinctive On Demand unicast routing protocols are Dynamic Source Routing (DSR)[9] protocol, Ad hoc On Demand Distance Vector Routing (AODV)[6] protocol and Temporally Ordered Routing Algorithm etc., in Table 2, gives the Characteristic comparison of Reactive Unicast Routing Protocols.

The following are the three protocols we selected for this paper.

ISSN(Online) : 2319-8753
ISSN (Print) : 2347-6710

International Journal of Innovative Research in Science, Engineering and Technology

(An ISO 3297: 2007 Certified Organization)

Vol. 4, Issue 7, July 2015

A) DYNAMIC SOURCE ROUTING PROTOCOL (DSR) :

Dynamic Source Routing (DSR) is an On Demand unicast routing protocol that utilizes source routing algorithm. In source routing algorithm, each data packet contains complete routing information to reach its dissemination. Additionally, in DSR[9] each node uses caching technology to maintain route information that it has discovered. For example, the intermediate nodes cache the route towards the destination and backward to the source. Furthermore, because the data packet contains the source route in the header, the overhearing nodes are able to cache the route in its routing cache.

B) AD-HOC ON-DEMAND DISTANCE VECTOR ROUTING PROTOCOL (AODV):

The Ad Hoc On-demand Distance Vector Routing (AODV) protocol is a reactive unicast routing protocol for mobile ad hoc networks. As a reactive routing protocol, AODV[6] only needs to maintain the routing information about the active paths. In AODV, routing information is maintained in routing tables at nodes. Every mobile node keeps a next-hop routing table, which contains the destinations to which it currently has a route. A routing table entry expires if it has not been used or reactivated for a pre-specified expiration time. Moreover, AODV [6] adopts the destination sequence number technique used by DSDV in an on-demand way.
We used this below algorithm in TORA to calculate results and analysis.

C.TEMPORALLY ORDERED ROUTING ALGORITHM (TORA):

Temporally Ordered Routing Algorithm (TORA) is a On Demand routing algorithm based on the concept of link reversal. This Routing protocol improves the partial link reversal method by detecting partitions and stopping non-productive link reversals. TORA can be used for highly dynamic mobile ad hoc networks. TORA[4] has three basic steps: route creation, route maintenance and route erasure. In TORA[6] the DAG provides the capability that many nodes can send packets to a given destination and guarantees that all routes are loop-free. Because of node mobility the DAG in TORA may be disconnected. So, route maintenance step is a very important part of TORA.This routing protocol has the unique feature that control messages are localized into a small set of nodes near the topology changes occurred.

	DSR	AODV	TORA
Updating of Destination at	Source	Source	Neighbors
Multicast Capability	No	Yes	No
Control Hello Message Requirement	No	No	Yes
Design Structure	Flat	Flat	Flat
Unidirectional link	Yes	No	Yes
Multiple Route	Yes	Yes	Yes

Characteristic Comparison of Reactive Unicasting Routing Protocols

3.2 MULTICAST ROUTING PROTOCOLs:

Although multicast transmission has not been widely deployed in the current MANETs, it will become very important in multimedia communications in the near future. To send a same data packet to multiple receivers in the MANET simultaneously, the simplest method is to broadcast the data packets.

However, broadcast consumes considerable bandwidth and power, which should be avoided as much as possible. Multicast can be use for save the bandwidth while transmitting same data packets to multiple receivers. Fig. 10 shows the multicast process, data packet is replicated by the network. There have been many multicast routing protocols

ISSN(Online) : 2319-8753
ISSN (Print) : 2347-6710

International Journal of Innovative Research in Science, Engineering and Technology

(An ISO 3297: 2007 Certified Organization)

Vol. 4, Issue 7, July 2015

proposed for MANET. They could be divided into three groups: first one is proactive multicast, second one is reactive multicast and last one is hybrid multicast routing protocol.

3.2.1 PROACTIVE MULTICAST ROUTING PROTOCOLS:

Conventional routing protocols such as Ad-hoc Multicast Routing (AM Route)[8][3], Core-Assisted Mesh Protocol (CAMP) and Ad-hoc Multicast Routing Protocol Utilizing Increasing id-numbers (AMRIS) are proactive multicast routing protocols. Periodic broadcast of network topology updates are needed to compute the shortest path from the source to every destination, which consumes a lot of bandwidth.

A) Ad-hoc Multicast Routing (AM Route)

B) Ad-hoc multicast routing protocol utilizing increase id numbers (AMRIS)

IV. QOS METRICS

A) PACKET DELIVERY RATIO:

It is defined as the ratio of number of data packets [1] delivered to all the receivers to the number of data packets supposed to be delivered to the receivers.

This ratio represents the routing effectiveness [1][3] of the protocol:

$$PDR = \frac{\text{Packets delivered}}{\text{Packets sent}}$$

B) AVERAGE END-TO-END DELAY:

It is the average time taken for a data packet to move from the source to the receivers [1]:

$$\text{Avg. EED} = \frac{\text{Total EED}}{\text{No. of packets}}$$

C) THROUGHPUT:

Throughput refers to how much data can be transferred from the source to the receiver(s) in a given amount of time[1]:

$$\text{Throughput} = \frac{\text{Number of packets sent}}{\text{Time Taken}}$$

V. SIMULATION RESULTS AND ANALYSIS

The performances of different routing protocols for VoIP applications have been investigated via OPNET simulator. The default parameters used in the simulations are listed in the table

Simulation parameters and values

Parameters	values
Number of nodes	50
Network size	1000m*1000m
Mobility	. Placed in row an column based model
Communication model	Random way point model with continus movement
Placed in row an column based model	Selection by strict channel match 300m 600 simulation sec

ISSN(Online) : 2319-8753
ISSN (Print) : 2347-6710

International Journal of Innovative Research in Science, Engineering and Technology

(An ISO 3297: 2007 Certified Organization)

Vol. 4, Issue 7, July 2015

SIMULATED APPLICATION AND PROTOCOLS

Parameters	values
Physical layer	Segmented calculation of the signal power and SNR
MAC layer	IEEE802.11 DCF with transmission rate of 12 Mbps for voice application
Routing	AODV,DSR,TORA
Applications	Applications
Codec	G.711 and GSM-EFR
Compression and Decompression delay	0.02sec
Type of service(TOS)	Interactive voice,unicast
Frame size	20ms

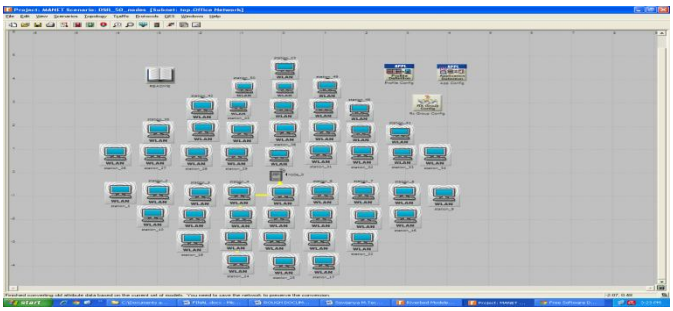

DSR simulations: sample DSR scenario with 50 nodes

The below snapshot of the opnet simulator shows the 50 nodes that are connected in the network for finding the performance of the network based in the unicast dynamic source routing protocol .

End to end delay in DSR

The below snapshot of the opnet simulator shows the data transmission delay from one end to another end when we are using the unicast routing protocol dynamic source routing(DSR).at the time of starting of the process the delay is high for finding the node and after some time the delay becomes constant from end to end showed in below graph.

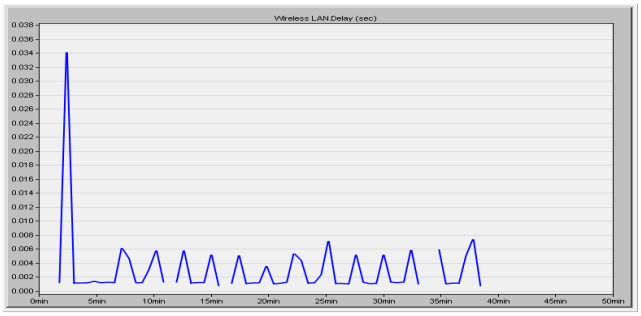

Load vs Medium Access Delay in DSR

This snapshot of the opnet simulator shows the load on the network along with medium access delay when we are trying to deliver the data from one end to another in this DSR method the node it self has to wait when the medium is busy so,in the below graph the node has to wait when the medium is busy at that yime delay graph is raised to high.

ISSN(Online) : 2319-8753
ISSN (Print) : 2347-6710

International Journal of Innovative Research in Science, Engineering and Technology

(An ISO 3297: 2007 Certified Organization)

Vol. 4, Issue 7, July 2015

Throughput with load in DSR [9]

This snapshot in opnet simulator shows the throughput of the route when we use DSR routing protocol. here the red line in the graph shows the load on the network and blue line shows the throughput of the network.

TORA Results

This following graph shows the performance of routing TORA protocol [4] under load, thoughput, and delay like qos metrics.

Load with throughput in TORA

The below snapshot in opnet simulator shows the throughput of the network under the load condition when we are using the TORA routing protocol for sending the data from one end to another end here if we observe carefully the load and throughput are going equally.

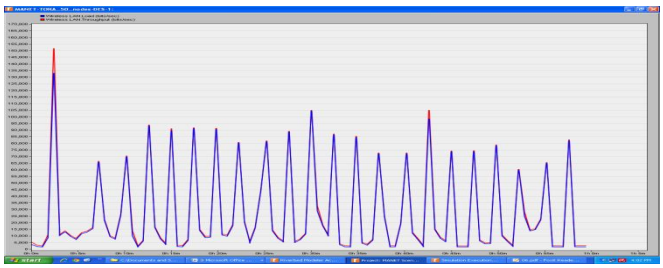

End to end delay with Medium Access delay inTORA.

This below snapshot in opnet simulator shows the end to end delay when the medium is busy with data. In this case for accessing that medium for node will take lot of time so here the delay goes to high state. After getting access to medium it will ready to transfer.

ISSN(Online) : 2319-8753
ISSN (Print) : 2347-6710

International Journal of Innovative Research in Science, Engineering and Technology

(An ISO 3297: 2007 Certified Organization)

Vol. 4, Issue 7, July 2015

AODV Results

These below graphs show results in case of AODV [6] routing algorithm when we run in TORA [9] routing algorithm.

End-to-End delay with Medium Access delay in AODV [6]
This below snapshot in opnet simulator shows the end to end delay when the medium is busy with data. In this case for accessing that medium for node will take lot of time so here the delay goes to high state. After getting access to medium it will ready to transfer if we observe carefully the delay in AODV and DSR is almost same.

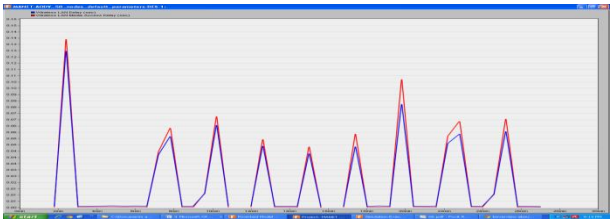

Load with throughput in AODV
The below snapshot in opnet simulator shows the throughput of the network under the load condition when we are using the AODV routing protocol for sending the data from one end to another end here if we observe carefully the throughput is good even though the load is high.

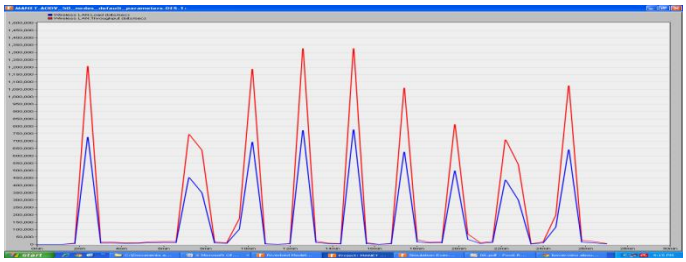

VI. CONCLUSION AND FUTURE WORKS

In this paper, the performances of different popular routing protocols have been investigated for VoIP application in MANET scenario. After studying all the performance matrices we can conclude that TORA protocol is a good candidate compared to other protocols that we have investigated in this work. The TORA[2] protocol uses the optimized routing algorithm to adjust the heights of routers to improve routing algorithm. This kind of adaptive routing algorithm makes TORA more suitable for VoIP application over MANETs[2][4] compared to other routing protocols. The TORA protocol also minimizes the overhead control messages that results in low delay. On the other hand the performance of DSR protocol is the poorest compared to other routing protocols. Hence, the DSR protocol (in its

ISSN(Online) : 2319-8753
ISSN (Print) : 2347-6710

International Journal of Innovative Research in Science, Engineering and Technology

(An ISO 3297: 2007 Certified Organization)

Vol. 4, Issue 7, July 2015

current form) is not suitable for VoIP application over MANET in both small scale and large scale scenarios. The reactive nature and failure to control overhead messages make the DSR protocol poorly performs in terms of QoS parameters. In addition, the traffic loads and node mobility degraded the performances of the DSR protocol. In large scale condition GRP and OLSR[7] performs better than small scale condition for their proactive nature and position based routing respectively. But, the performances of these two protocols are not comparable with those of TORA protocol. Although this investigation goes in favor of TORA protocol, for using voice codes G.711 and GSM-EFR[1] in small and large network respectively we need do to a more comprehensive study to confirm this claim. We need to investigate the other routing protocols proposed in the literatures.

REFERENCES

[1] D. Chalmers and M. Sloman, "A survey of quality of service in mobile computing environments," IEEE Communications Surveys and Tutorials, Vol. 2, No. 2, Second Quarter 1999, pp. 2-10
[2] S. Corson. And J. Macker. "Mobile Ad Hoc Networking (MANET): Routing Protocol Performance Issues and Evaluation Consideration", available at http://www.ietf.org/rfc/rfc2501.txt
[3] E.M. Royer, C-K. Toh, "A Review of Current Routing Protocols for Ad Hoc Mobile Wireless Networks", IEEE Personal Communications Magazine, April 1999, pp. 46-55.
[4] Aftab Ahmad. "Wireless and Mobile Data Networks." John Wiley & Sons, Inc., Hoboken, NJ, USA, 2005.
[5] T. Clausen, and P. Jacquet, "Optimized Link State Routing Protocol (OLSR)", IETF, RFC 3626, 2003.
[6] C. E. Perkins, E. M. Belding-Royer, and S. R. Das, "Ad hoc On-Demand Distance Vector (AODV) routing," Internet Engineering Task Force (IETF) draft, November 2002.
[7] T. Camp, J. Boleng, and V. Davies, "A survey of mobility models for ad hoc network research," Wireless Communications and Mobile Computing (WCMC): Special issue on Mobile Ad Hoc Networking: Research, Trends and Applications, Vol. 2, No. 5, 2002, pp.483-502
[8] I. D. Aron and S. K. S. Gupta, "On the scalability of on-demand routing protocols for mobile ad hoc networks: an analytical study," Journal of Interconnection Networks, Vol. 2, No. 1, pp. 5-29, 2001.
[9] J. Broch, D. B. Johnson, and D. A. Maltz, "The Dynamic Source Routing (DSR) protocol for Mobile Ad hoc Networks", IETF Mobile Ad hoc Network (MANET) working groups, Dec. 1998.

International Journal of Emerging Research in Management &Technology
ISSN: 2278-9359 (Volume-4, Issue-12)

Research Article | **December 2015**

Various Research Trends of Electrical Discharge Machining (EDM)– A Review

BSV Ramarao*
Associate Professor, Dept of Mech,
ASTI, Hyderabad, India

Dr. P Shailesh
Professor, Dept of Mech,
MCE, Hyderabad, India

Dr. M Sreenivasarao
Professor & Head, Dept of Mech
JNTUH, Hyderabad, India

Abstract—

Electrical discharge machining (EDM) is one of the oldest non-traditional machining processes. EDM process is basically done through the thermoelectric energy between the work piece and an electrode. In electrical discharge machining (EDM), a process utilizing the removal phenomenon of electrical discharge in dielectric, the working fluid plays an important role affecting the material removal rate and the properties of the machined surface. Selection of the right dielectric fluid is important for successful operations. This paper presents a literature survey on the various concepts with current research trends and also their effects in electrical discharge machining characteristics.

Keywords— DOE, RSM, GFRG, GRA, ANFIS, CACO, DEA, WLT, SCD, WG, EW & OC

I. INTRODUCTION

Electrical discharge machining

The electrical discharge machining (EDM) is one of the popular manufacturing processes widely used in die and mold making industry to generate deep complex cavities in various classes of materials under roughing and finishing operations

The EDM process is most widely used by many of the industries like mold-making tool and die industries, but is becoming a general method of making prototype and production parts, especially in the aerospace, auto-mobile and electronics industries in which production quantities are relatively low. It is also used for coinage die making, metal disintegration machining, etc. There are few types of EDM available which is discussed below.

Sinking EDM: In the sinking EDM process, a mirror image of tool shape occurs on the surface of work piece. In this process, copper or graphite is generally used as electrode material. The numerical control monitors the gap conditions (voltage and current) and synchronously controls the different axes and the pulse generator. The dielectric liquid is filtrated to remove debris particles and decomposition products. In this process electrical energy turns into thermal energy through a series of discrete electrical discharges occurring between the electrode and work piece immersed in a dielectric fluid. The thermal energy generates a channel of plasma between the cathode and anode. When the pulsating direct current supply is turned off, the plasma channel breaks down. This causes a sudden reduction in the temperature allowing the circulating dielectric fluid to implore the plasma channel and flush the molten material from the workpiece surface.

Wire EDM: Wire-cut EDM (WEDM) is one of the most favorable variants owing to its ability to machine conductive, exotic and high strength and temperature resistive (HSTR) materials with the scope of generating intricate shapes and profiles. It uses a thin continuously traveling wire feeding through the work piece by a micro-processor eliminating the need for elaborate reshaped electrodes, which are required in the EDM. The wire-cut EDM process uses a thin copper wire of diameter about 0.1–0.3 mm as the electrode and the workpiece is mounted on a controlled worktable, enabling complex two dimensional shapes can be cut on the work piece by controlled the movement of the X–Y worktable. Wire EDM process is widely applied not only in tool and die-making industry, but also in the fields of medicine, electronics and the automotive industry.

Micro EDM: The recent trend in reducing the size of products has given micro-EDM a significant amount of research attention. Micro-EDM is capable of machining not only micro-holes and micro-shafts as small as 5 _m in diameter but also complex three-dimensional (3D)micro cavities. Micro EDM process is basically of four types: micro-wire EDM, die-sinking micro-EDM, micro EDM drilling and micro-EDM milling. In micro-wire EDM, a wire which has a diameter down to 0.02 mm is used to cut through a work piece. Indie-sinking micro-EDM, an electrode is used containing micro-features to cut its mirror image in the work piece. In micro EDM drilling, micro-electrodes (of diameters down to 5–10 _m) are used to 'drill' micro-holes in the work piece. In Micro-EDM milling, micro-electrodes (of diameters down to 5–10 _m) are employed to produce 3D cavities by adopting a movement strategy similar to that in conventional milling.

Powder mixed EDM (PMEDM) : The mechanism of PMEDM is totally different from the conventional EDM. A suitable material in the powder form is mixed into the dielectric fluid of EDM. When a suitable voltage is applied, the spark gap filled up with additive particles and the gap distance setup between tool and the work piece increased from 25–50 to50–150 mm. The powder particles get energized and behave in a zigzag fashion. These charged particles are accelerated by the electric field and act as conductors. The powder particles arrange themselves under the sparking area and gather in clusters. The chain formation helps in bridging the gap between both the electrodes, which causes the early explosion. Faster sparking within discharge takes place causes faster erosion from the workpiece surface.

Dry EDM: In this process a thin walled pipe is used as tool electrode through which high-pressure gas or air is supplied. The role of the gas is to remove the debris from the gap and cooling of the inter electrode gap. The technique was developed to decrease the pollution caused by the use of liquid dielectric which leads to production of vapors during machining and the cost to manage the waste

II. LITERATURE

Gostimirovic et al. (1) investigated the effects of electrical process parameters on the performances of die-sinking electrical discharge machining process with RC pulse generator while machining manganese-vanadium tool steel workpiece using graphite tool electrode. They found that the discharge current and pulse duration have highly influenced the material removal rate of the EDM process.

Puertas et al. (2) carried out a study on the influence of the factors of current intensity, pulse time and duty cycle over the material removal rate, surface quality and electrode wear rate. They modeled the relationship between the input parameters and response parameters in the die-sinking EDM process using response surface methodology. It has been concluded that the lower values of the current intensity and the machining time have to be used in order to obtain a good surface finish.

Patel et al. (3) presented a detailed experimental investigation of machining characteristics such as surface integrity and material removal mechanisms of advanced ceramic composite Al2O3–SiCw–TiC with EDM process. It has been concluded that the surface roughness and material removal rate have been increased with pulse duration in EDM process.

A Yahya et al. (4) explained the use of the dimensional analysis for investigating the effects of the electrical and the physical parameters on the material removal rate of a die-sinking EDM process has been described by Yahya and Manning. From the experimental results, it has been found that the material removal rate has been increased with discharge current, gap voltage and pulse on time.

Patel et al. (5) investigated the feasibility of fabricating micro holes in SiCp–Al composites using electrical discharge machining with a rotary tube electrode [31]. They have investigated the material removal rate, electrode wear rate and hole tapper as the responses for the study. The experimental results have revealed that pulse on duration has significantly affected the response characteristics involved in EDM process.

Pelicer et al. (6) focused on investigating the influence of EDM process parameters and electrode geometry on feature micro accuracy on tool steel for mold fabrication purposes. A set of designed experiments with varying process parameters such as pulse current, open voltage and pulse duration have been carried out in H13 steel using different shaped copper electrodes. It has been concluded that the triangular shaped electrode would produce highly inefficient output, since the fast wearing nature of the electrode edges.

Kuppan et al. (7) reported about the experimental investigation of small deep hole drilling of Inconel 718 with electrolytic copper tool electrode using the electrical discharge machining process [30]. The experimental results have shown that the material removal rate has been increased with the increase in the peak current and duty factor.

Wang et al. (8) carried out a series of experiments to investigate the impacts of machining polarity, electrode rotation speed and nominal capacitance on the material removal rate and tool wear rate with poly crystalline diamond. It has been demonstrated that favorable machining performance of EDM process on the workpiece could be achieved in tool with negative polarity as compared to the positive polarity.

Batish et al. (9) investigated the effect of process parameters and mechanism of material deposition in electric discharge machining on surface properties of EN31, H11 and high carbon high chromium die steel materials [38]. It has been discussed about material transfer mechanism involved in EDM process. It has been found that die steels have been machined effectively with copper tool electrode using EDM process.

Jahan et al. (10) conducted an experimental investigation with the view of obtaining fine surface finish in die-sinking EDM process of tungsten carbide using different tool electrodes such as tungsten, copper tungsten and silver tungsten. It has been found that the surface finish has been influenced by the discharge energy during machining process. It has been realized that the lower discharge energy has produced good surface finish.

Yeo et al. (11) discussed about the machining of zirconium based bulk metallic glass by EDM process with different tool electrodes such as copper, brass and tungsten rod electrode. The experimental results have shown that the usage of lower input energy has produced the lower surface roughness and electrode tool wear.

Khanra et al. (12) investigated the influence of energy input on the workpiece surface during the machining in the EDM process. In this experimental investigation, a well-polished mild steel (C – 0.18%) plate has been used for machining by EDM. It has been observed that the energy input has influenced the debris particle size in the EDM process.

Popa et al. (13) showed the importance of optimizing the process parameters that could influence the quality of the EDM process. They formulated the equation of crater depth in terms of discharge energy in EDM process. From the relation, it has been observed that the crater depth has been increased with the discharge current flowing through the work piece and tool electrode.

Kojima et al. (14) described about the spectroscopic measurement of arc plasma diameter in EDM. They found that the arc plasma has been increased with increasing discharge current. It has been verified that crater diameter and depth decrease with increasing gap width due to the increased plasma diameter. The arc plasma diameter has been increased with increasing spark gap and thus clarified the reason for lower material removal rate and smoother surface finish with longer spark gap.

Wong et al. (15) developed a single spark pulse generator using resistance–capacitance arrangement to study the erosion characteristics in the EDM process from the crater size. The volume and size of the craters have been found to be

more consistent at lower energy discharge sparks than the higher energy discharge sparks. The higher energy pulse leads to the micro surface crack on the work surface.

Guu et al. (16) aimed to investigate the machining characteristics of manganese–zinc ferrite magnetic materials using electrical discharge machining process. The experimental results have indicated that the morphology of debris revealed the mechanism of material removal. It has been observed that the better machined surface has been obtained by setting process parameters at low pulse energy.

H Singh et al. (17) The theoretical modeling of the EDM process based upon the heat transfer equations has been established by Singh. In the study, the input energy equation has been developed as a function of pulse duration, current, polarity of electrode and properties of the work piece and tool electrodes. This model has been helpful to calculate the optimal process parameters for obtaining optimum discharge energy.

Fenggou et al. (18) presented a method to automatically determine and optimize the process parameters on the EDM sinking process with the application of artificial neural network [58]. The experimental results have proved that automatic determination of current value would be the efficient method on improving EDM performance.

Caydas et al. (19) developed an adaptive neuro-fuzzy inference system model for the prediction of the surface roughness of machined surface using wire EDM process as a function of process parameters such as open circuit voltage, pulse duration and wire feed rate. From the experimental results, it has been found that the proposed control system has improved the surface quality in EDM process.

Zhou et al. (20) developed an adaptive control system which directly and automatically has regulated the tool down time for improving the process performance in EDM process. It has been observed that this adaptive system would improve the machining rate, due to the automatic adjustment of spark gap.

Yilmaz et al. (21) introduced a used friendly intelligent system based on the knowledge of the skilled operators for the selection of the EDM process parameters for machining AISI 4340 stainless steel. The system has been provided with a compact selection tool based on expert rules and enabled an unskilled user to select necessary parameters which lead to lower electrode wear rate and better surface quality.

Behrens et al. (22) proposed a neuro-fuzzy based gap width controller for a highly efficient removal mechanism in EDM process. The experimental results have indicated that the proposed controller has enhanced EDM process to achieve the better surface finish of workpiece.

Kao et al. (23) monitored the discharge current in electrical discharge machining using high speed data acquisition with high frequency response. From the experimental results, it has been found that decrease in air gap between tool and workpiece has improved the material removal rate in EDM process.

Chang et al. (24) designed a proportional derivative controller of the spark gap between an electrode and a workpiece to analyze the non-linearity involved in EDM process. They concluded that this non-linearity has reduced the effective discharge in electrical discharge machining process.

Tong et al. (25) designed an experimental system with a macro/ micro dual feed spindle to improve the machining performance of servo scanning micro EDM process, which utilized an ultrasonic linear motor as the macro drive and a piezoelectric actuator as micro feeding mechanism. Based on LabVIEW software package, a real time control system has been developed to control coordinately the dual-feed spindle to drive the tool electrode.

Spadlo et al. (26) developed a thermo model for brush electrical discharge alloying process. It has been realized that material removal depends on the discharge current pulse flowing through the dielectric medium.

Salonitis et al. (27) developed the thermal based model for the determination of the material removal rate and average surface roughness achieved as a function of the process parameters in the EDM process.

Liu et al. (28) constructed a plate capacitor model for electrical discharge machining process. The correlation actions of process parameters and energy distribution have been discussed based on the field electron emission theory. It has been observed that machining time plays a major role to improve the process efficiency.

Matoorian et al. (29) presented the application of the Taguchi robust design methods to optimize the precision and accuracy of the EDM process for machining of precise cylindrical forms on hard and difficult-to-machine materials. They found that the current intensity of the EDM process affects the material removal rate greatly.

Muthuramalingam et al. (30) and Mohan developed Taguchi-DEAR methodology based optimization of electrical process parameters.

Tzeng et al. (31) described about the application of the fuzzy logic analysis coupled with Taguchi methods to optimize the precision and accuracy of the high speed electrical discharge machining process. The most important factors affecting the precision and accuracy of the high speed EDM process have been identified as duty cycle and peak current.

Most number of research works have been carried out to optimize the electrical process parameters in EDM process. Marafona et al. (32) described an investigation into the optimization of material removal rate in the electric discharge machining process with copper tungsten tool electrode. From the experimental results, it has been proved that large current intensity would result in higher material removal rate.

R. Landfried et al. (33) conducted an experiment to find the influence of TiC particle size on the material properties and also on electrical discharge machining. They have focused the same of ZTA-TiC ceramics with 24% TiC, 17% ZrO2 and 59% Al2O3. It was shown that reducing the size of electrical conductive grains strongly increases the electrical conductivity and slightly decreases mechanical properties and also it have considerable impact on the machinability by EDM and at the end concluded that the size of the particle should not be reduced below a threshold.

K. Palanikumar et al. (34) studied machining characteristics of WC/Co composites on Electrical Discharge Machining. They have performed experiments on a newly designed experimental set up developed in their own lab using response

surface methodology to identify the most influenctial parameters for maximizing metal removal rate and to minimize the surface roughness. Their experiments were carried out using a Box–Behnken experimental strategy. At the end they have concluded that the effect of machining parameters such as flushing pressure, pulse on-time, peak current and electrode rotation on MRR and surface quality of the WC/Co composites was analyzed using 3-D response graphs

M. Merkleina et al. (35) presented a research on influence of machining process on residual stresses in surface of cemented carbides for the purpose of investigation and description of correlation between manufacturing process and surface properties in a quantitative way. During their study they have found that grinding is accompanied by compressive stresses as it achieves higher removal rates and lower surface roughness and also tool geometries of low complexity should be machined by grinding. They have concluded that, both machining methods reveal that hard machined surfaces are not sufficient for application in cold forging. Consequently a final polishing step is required. After fine machining both surface types reveal compressive stresses in the top layer.

Jambeswar Sahu et al (36) applied a approach called DEA for optimization of multiple responses in EDM of AISI D2 steel to select a best process parameters in multi response situation. They have conducted experiments on DSEDM under different conditions of process parameters. During their study, A response surface methodology (RSM) is adopted to establish effect of various process parameters such as discharge current (Ip), Pulse on time (Ton), Duty factor and flushing pressure on four important responses like material removal rate (MRR), tool wear rate (TWR), surface roughness (Ra) and circularity (r1/r2) of machined componentThus, DEA method has the ability to hold the multiplicity of inputs and outputs and an easy optimization technique to find the best alternatives.

Abdus Sabur et al. (37) investigated of MR characteristics in EDM of non conductive ceramics. Electro discharge machining (EDM) technique, a noncontact machining process, is applied for processing nonconductive ceramic ZrO2 using assisting electrode. in this technique, pyrolytic carbon layer on the ceramic surface formed by the cracked carbon from the carbonic dielectric, plays the key role for continuous EDM. In this study, experiments were done to investigate the effect of input power on the material removal rate (MRR) and to explore the material removal mechanism. At the end, the experimental results show that the material is removed in EDM of nonconductive ZrO2 ceramic mostly by spalling and it increases with the increase of input power. They have concluded that, using adhesive copper foil as assisting electrode and copper tool electrode with –ve polarity in kerosene dielectric, EDM of nonconductive ZrO2 ceramic is done effectively and also The material removal can be increased by increasing the input power keeping other parameters constant

Sengottuvel.Pa et al. (38) presented a research paper on optimization of multiple characteristics of EDM parameters for the super alloy Inconel 718 based on desirability approach and fuzzy modeling. They have investigated the effects of various EDM input parameters as well as the influence of different tool geometry on Material Removal Rate(MRR), Tool Wear Rate(TWR) and Surface Roughness(SR) on machining of Inconel 718 material by using copper electrode. Five EDM parameters, namely pulse on time (TON), pulse off time (TOFF), peak current (A), flushing pressure (P) and electrode tool geometry (Geo), were considered here. Tool geometry of the electrodes was circle (C), square (S), rectangle (R) and triangle (T). They have concluded that, higher current (15A) and flushing pressure was preferred. Medium pulse on time was suitable for copper electrode. Rectangular tool geometry was best for copper electrode. The contribution of peak current was high followed by pulse on time. At the end they have concluded that the tool geometry was not the most significant factor to affect the performance measures.

Chinmaya P Mohanty et al. (39) conducted experiments to determine the machinability of Inconel 718 in EDM using a multi objective particle swarm optimization (MOPSO) algorithm. A Box-Behnkin design of response surface methodology has been used to collect data for the study. The machining performances of the process are evaluated in terms of material removal rate (MRR) and surface quality.Their proposed model shows the interactive and complex effects of various important process variables viz. open circuit voltage (V), discharge current (Ip), pulse-on-time (Ton) and tool material on responses justified through experimentation and analysis.

Milan Kumar Dasa et al. (40) applied ABV algorithm for optimization MRR and surface roughness in EDM of EN31 tool steel. For experimentation, they have considered machining parameters viz., pulse on time, pulse off time, discharge current and voltage are varied based on central composite design (CCD). Second order response equations for MRR and surface roughness are found out using response surface methodology (RSM). Empirical equations for MRR and Ra in terms of four important EDM parameters viz. pulse on time, pulse off time, current and voltage are obtained. The optimum values obtained from the analysis show good agreement with that of experimental values. It is seen that MRR and Ra are proportional to pulse on time and discharge current in the experimental regime. Finally, surface morphology is studied using SEM images.

V. Muthukumara et al. (41) presented a Mathematical Modeling for Radial Overcut on Electrical Discharge Machining of Incoloy 800 by Response Surface Methodology. The experiments were planned as per central composite design (CCD) method. After conducting 30 experiments, a mathematical model was developed to correlate the influences of these machining parameters and ROC. The significant coefficients were obtained by performing ANOVA at 5% level of significance. From the obtained results, It was found that current and voltage have significant effect on the radial overcut. The predicted results based on developed models are found to be in good agreement with the predicted values match the experimental results reasonably well with the coefficient of determination 0.9699 for ROC.

M. Munza et al. (42) conducted experiments to find Machinability of ZTA-TiC ceramics by electrical discharge drilling. During their study electrically conductive ceramic ZTATiC composites were machined by EDM drilling with variation of pulse shape, discharge current, discharge time and flushing conditions. Their results show the strong influence of machining parameters on the machining quality, the economical performance and the accuracy of the EDM

process. They have concluded that the triangular pulses with a discharge current of 20 A or lower are more suitable for EDM drilling of ZTA-TiC than rectangular pulses, since rectangular pulses do not allow a broad variation of parameters to adjust the parameters fine enough. And also, the drill oversize and the feed rate during machining mainly depend on the correct flushing conditions controlled by the volumetric flow rate.

F. Klockea et al. (43) done Experimental research on the electrochemical machining of modern titanium- and nickel-based alloys for aero engine components. In their paper modern hard to machine alloys for aero engine components were analyzed in terms of their electrochemical machinability. Therefore at first the basic research platform at WZL with the associated ECM-tool has been presented. With the help of this platform the feed rate - current density curves for several titanium and nickel-based alloys have been examined. Experimental results were compared to theory according to Faraday's law and among each other by effective material removal rates. For all analyzed titanium materials the effective material removal rates were almost equal to $V_{eff,Ti} \approx 1.78$ mm³/(Amin). They have concluded that, in case of nickel-based alloys it turned out that the more fine grained the microstructure of the material the better its electrochemical machinability.

M. Iwai et al. (44) examined EDM properties of newly developed PCD made up of electrically conductive diamond particles. They have studied material properties and electrical discharge machinability of EC-PCD. Their result shows that the EC-PCD is superior in heat resistance to conventional PCD by a factor of about 200°C. And the EC-PCD shows low frictional wear at high temperature in a sliding test against a stainless steel disk. They have concluded that the processing speed of EC-PCD is more than 7 times higher than that of conventional PCD in EDM.

M. Iwai et al. (45) presented a research paper on Improvement of EDM properties of PCD with electrode vibrated by ultrasonic transducer. During their series of EDM experiments, three types of ultrasonic vibration modes were selected (axial vibration, flexural vibration and complex vibration). From the experimental results, it was found that EDM efficiency became 3 times higher than the ordinary EDM (no vibration given to the electrode) under the two specific vibration modes, namely, 1) the axial vibration (large) mode and 2) the complex vibration (axial vibration: large + flexural vibration: small) mode. At the end it was shown that the effects resulted from not only the cavitation effect of the working fluid but also the vibrational action of the electrode itself.

Shailesh Dewangan et al. (46) obtained Multi-response optimization of surface integrity characteristics of EDM process using grey-fuzzy logic-based hybrid approach. During their study, grey-fuzzy logic-based hybrid optimization technique is utilized to determine the optimal settings of EDM process parameters with an aim to improve surface integrity aspects after EDM of AISI P20 tool steel. The experiment is designed using response surface methodology (RSM) considering discharge current (Ip), pulse-on time (Ton), tool-work time (Tw) and tool-lift time (Tup) as process parameters. Various surface integrity characteristics such as white layer thickness (WLT), surface crack density (SCD) and surface roughness (SR) are considered during the current research work. Grey relational analysis (GRA) combined with fuzzy-logic is used to determine grey fuzzy reasoning grade (GFRG). They have concluded that the optimal solution based on this analysis is found to be Ip ¼ 1 A, Ton ¼ 10 ms, Tw ¼ 0.2 s, and Tup ¼ 0.0 s. Analysis of variance (ANOVA) results clearly indicate that Ton is the most contributing parameter followed by Ip, for multiple performance characteristics of surface integrity.

R. Teimouri et al. (47) performed Optimization of magnetic field assisted EDM using the continuous ACO algorithm. During their study, a rotary tool with rotary magnetic field has been used to better flushing of the debris from the machining zone in electrical discharge machining (EDM) process. Two adaptive neuro-fuzzy inference system (ANFIS) models have been designed to correlate the EDM parameters to material removal rate (MRR) and surface roughness (SR) using the data generated based on experimental observations. And then continuous ant colony optimization (CACO) technique has been used to select the best process parameters for maximum MRR and specified SR. Experimental trials divided into three main regimes of low energy, the middle energy and the high energy. At the end, results show that the proposed ANSIS models have an acceptable performance to prediction of the MRR and SR in terms of three input parameters.

L. Li et al. (48) presented a paper on Surface Integrity Evolution and Machining Efficiency Analysis of WEDM of Nickel-based Alloy. Their study focused on the evolution process of surface integrity and machining efficiency of W-EDM in machining IN718 by one rough cut (RC) mode followed by three trim cut (TC) modes. Material removal efficiency, surface roughness, surface topography, surface alloying, and micro hard ness have been characterized. Their results show that high material removal efficiency can be achieved in W-EDM. Six-sigma distribution of Ra in RC mode is different from that of TC modes. The high toughness of IN 718 would be the major contributing factor to the absence of micro cracks in the TC modes. Thick white layers (6-8μm) with micro cracks in RC mode and very thin white layers (0-2μm) free of those defects in TC2 mode can be observed, while white layer is nearly invisible in TC3 mode. They have concluded that the micro hardness of white layer in TC mode is higher than that in MC mode.

M. Kunieda et al. (49) preseted a paper on Advancing EDM through Fundamental Insight into the Process. According to them, these EDM phenomena are not in thermal equilibrium, but include transitions between solid, liquid, gas, and plasma, chemical reactions, mass transfer, and displacement of boundaries. they have concluded that, compared to other discharge phenomena such as glow discharge in dry etching processes and arc discharge in welding processes, physics involved in EDM processes are obviously most complicated, rendering observation and theoretical analysis extremely difficult.

Harminder Singh (50) have conducted an Experimental study of distribution of energy during EDM process for utilization in thermal models. During their study they have experimentally calculated the distribution of input discharge energy during electric discharge machining, using heat transfer equations. The results obtained especially of fraction of

energy transferred to the workpiece (Fcw) for different machining parameters are in good concurrence with the results obtained by other authors for the effect of Fcw, i.e., MRR, for same combination of electrodes.

Vineet Srivastava et al. (51) conducted Study of ultrasonic assisted cryogenically cooled EDM process using sintered (Cu–TiC) tooltip. During their research, the process performance of sintered copper (Cu)–titanium carbide (TiC) electrode tip in ultrasonic assisted cryogenically cooled electrical discharge machining (UACEDM) has been studied. The performance parameters studied are electrode wear ratio (EWR), material removal rate (MRR), surface roughness (SR), out of roundness and surface integrity. During their work, cermet electrode tip of sintered copper (Cu)- titanium carbide (TiC) was successfully fabricated and brazed with copper rods to perform as electrodes. At the end the electrodes with modified tooltip were tested for UACEDM process and compared with electrodes having Cu tooltip.

M.P. Jahan et al (52) presented a paper on a study on the fine-finish die-sinking micro-EDM of tungsten carbide using different electrode materials. During their study, investigations have been conducted with view of obtaining fine surface finish in the micro-EDM of WC using tungsten (W), copper tungsten (CuW) and silver tungsten (AgW) electrodes and it was found that the surface characteristics are dependent mostly on the discharge energy during machining. The fine-finish micro-EDM requires minimization of the pulse energy supplied into the gap. In addition, the surface finish was found to be influenced greatly by the electrical and thermal properties of the electrode material. And also the performance of the electrodes for the finishing micro-EDM was evaluated based on the achieved surface roughness and surface characteristics with respect to material removal rate (MRR) and electrode wear ratio (EWR) and it was found that AgW electrode produces smoother and defect-free nano surface with the lowest Ra and Rmax among the three electrodes. They have concluded that a minimum amount of material migrates from the AgW electrode to the WC work piece during the finishing micro-EDM.

J. Murray et al. (53) presented a paper on Work piece debris deposition on tool electrodes and secondary discharge phenomena in micro-EDM. Their work furthers the understanding of the little understood discharge gap phenomena by investigating the attachment of machined material back onto the tool electrode surface and explains the mechanism of this attachment. After the machining of high-aspect ratio slots, SEM and EDS techniques along with single discharge and cross-sectional analysis were used to explain that debris reattachment onto the tool electrode does not occur randomly but is dependent on its re-melting in the dielectric by the secondary discharge process. They have concluded that the bonded material is present mainly in the centre of the discharge crater, with no attachment occurring outside of discharge affected regions.

Yin Qingfeng et al.(54) conducted a Research of lower tool electrode wear in simultaneous EDM and ECM. In their manuscript, a new method to reduce the electrode wear and suppress excessive electrolytic-erosion is investigated. Electrolyte with a much higher conductivity than deionized water is utilized as machining fluid in the method, while electro-deposition is used to compensate for tool electrode wear in the processing. Besides, nanosecond voltage pulse and tool electrode with side-insulation are adopted to suppress excessive electrolytic-erosion. Experiment results show that this new method can reduce electrode wear and suppress excessive electrolytic-erosion effectively. And concluded that Excessive electrolytic-erosion can be suppressed in SEDCM by using tool electrode with side-insulation.

S. Dewangan et al. (55) presented a paper on Study of Surface Integrity and Dimensional accuracy in EDM using Fuzzy TOPSIS and Sensitivity Analysis. Their work aims at investigating the influence of various EDM process parameters like pulse current (Ip), pulse-on time (Ton), tool work time (Tw) and tool lift time (Tup) on various aspects of surface integrity like white layer thickness (WLT), surface crack density (SCD) and surface roughness (SR). The dimensional accuracy, characterized by over cut (OC), has also been studied in the similar way. A response surface methodology (RSM) - based design of experiment has been considered for this purpose. Their study also recommends an optimal setting of EDM process parameters with an aim to improve surface integrity aspects after EDM of AISI P20 tool steel. That was achieved by simultaneous optimization of multiple attributes (i.e. WLT, SCD, SR and OC) using Fuzzy-TOPSIS-based multi-criteria decision making (MCDM) approach. The optimal solution was obtained based on five decision makers' preferences on the four responses (i.e. WLT, SCD, SR, and OC. Furthermore, sensitivity analysis is also carried out to study the sensitivity or robustness of five decision makers' preference of optimal machining parameters. Form their study, decision makers' preference for surface crack density has been found to be the most sensitive response and therefore should be chosen first and analyzed very carefully.

M Manohara et al. (56) conducted an Experimental study to assess the effect of Electrode bottom profiles while machining Inconel 718 through EDM Process. During their study, it was observed that the bottom surface profile of the electrode was contributing towards many aspects like Material Removal Rate (MRR), Electrode Wear Rate (EWR), surface roughness and surface integrity. Certainly such process improvements would contribute a lot in the shop-floor in terms of productivity and product-quality, while machining Inconel 718 alloy. It was concluded that the adverse effects caused due to the erosion of flat profile electrodes on the machined surfaces could be overcome by employing convex profile electrodes; concave profile electrodes almost simulate the condition of eroded flat-profile electrode; convex profile electrodes produce machined surfaces of better quality in terms of higher surface finish, thinner recast-layer and closer geometry, in addition to higher MRR compared to flat profile or concave profile electrodes.

Mao-yong LIN et al. (57) presented a research paper on Optimization of electrical discharge machining of Inconel 718 by Grey-Taguchi method. The optimization of electrical discharge machining (EDM) process parameters of Inconel 718 alloy was done to achieve multiple performance characteristics such as low electrode wear, high material removal rate and low working gap was investigated by the Grey-Taguchi method. The influences of peak current, pulse on-time, pulse off-time and spark gap on electrode wear (EW), material removal rate (MRR) and working gap (WG) in the electrical discharge machining of Inconel 718 were analyzed.

Peng-fei BAI et al (58) presented a paper on Solid-phase sintering process and forced convective heat transfer performance of porous-structured micro-channels. According to them, a solid-phase sintering process for the low-cost fabrication of composite micro-channels was developed. Three kinds of composite micro-channels with metallic porous structures were designed. The sintering process was studied and optimized to obtain porous-structured micro-channels with high porosity. The flow resistance and heat transfer performance in the composite micro-channels were investigated. At the end, the composite micro-channels show acceptable flow resistance, significant enhancement of heat transfer and dramatic improvement of flow boiling stability, which indicates a promising prospect for the application in forced convective heat transfer.

III. CONCLUSION

Good number of researchers have worked on the study of various concepts of EDM process. The review of the research trends in EDM in different concepts and research trends of EDM along with the various methods of optimization is presented. The remarkable machining rates have been achieved mostly with the tap water. Machining with water acting as dielectric has the possibility to achieve zero electrode wear while using copper tool is connected to the negative polarity. Surface roughness of the Work piece is also dependent on the type of dielectric fluid. It produced with deionised water is generally lower than that with hydrocarbon oils. Various methods have been used for optimization like DOE, RSM, ANOVA, GFRG, GRA, ANFIS, CACO and DEA with input parameters like pulse current (Ip), pulse-on time (Ton), tool work time (Tw) and tool lift time (Tup) on various aspects for the output parameters like Material Removal Rate (MRR), white layer thickness (WLT), surface crack density (SCD), working gap (WG), Electrode wear (EW) , overcut (OC) and surface roughness (SR).

REFERENCES

[1] M. Gostimirovic, P. Kovac, B. Skoric, M. Sekulic, Effect of electrical process parameters on the machining performance in EDM, Indian Journal of Engineering and Materials Sciences 18 (2012) 411–415.

[2] I. Puertas, C.J. Luis, L. Alvarez, Analysis of the influence of EDM parameters on surface quality, MRR and EW of WC-Co, Journal of Materials Processing Technology 153/154 (2004) 1026–1032.

[3] K.M. Patel, P.M. Pandey, P.V. Rao, Surface integrity and material removal mechanisms associated with the EDM of Al2O3 ceramic composite, International Journal of Refractory Metals and Hard Materials 27 (2009) 892–899.

[4] A. Yahya, C.D. Manning, Determination of material removal rate of an electro discharge machine using dimensional analysis, Journal of Physics D: Applied Physics 37 (2004) 1467–1471.

[5] K.M. Patel, P.M. Pandey, P.V. Rao, Understanding the role of weight percentage and size of silicon carbide particulate reinforcement on electro-discharge machining of aluminium based composites, Materials and Manufacturing Processes 23 (2008) 665–673.

[6] N. Pelicer, J. Ciurana, T. Ozel, Influence of process parameters and electrode geometry on feature micro-accuracy in electro discharge machining of tool steel, Materials and Manufacturing Processes 24 (2009) 1282–1289.

[7] P. Kuppan, A. Rajadurai, S. Narayanan, Influence of EDM process parameters in deep hole drilling of Inconel 718, International Journal of Advanced Manufacturing Technology 38 (2008) 74–84.

[8] D. Wang, W.S. Zhao, L. Gu, X.M. Kang, A study on micro hole machining of poly crystalline diamond by micro- electrical discharge machining, Journal of Materials Processing Technology 211 (2011) 3–11.

[9] A. Batish, A. Bhattacharya, V.K. Singla, G. Singh, Study of material transfer mechanism in die steels using powder mixed electric discharge machining, Materials and Manufacturing Processes 27 (2012) 449–456.

[10] M.P. Jahan, Y.S. Wong, M. Rahman, A study on the quality micro-hole machining of tungsten carbide by micro-EDM process using transistor and RC-type pulse generator, Journal of Materials Processing Technology 209 (2009) 1706–1716.

[11] S.H. Yeo, P.C. Tan, E. Aligiri, S.B. Tor, N.H. Loh, Processing of zirconium based bulk metallic glass using micro electrical discharge machining, Materials and Manufacturing Processes 24 (2009) 1242–1248.

[12] A.K. Khanra, L.C. Pathak, M.M. Godkhindi, Micro analysis of debris formed during electrical discharge machining, Journal of Materials Science 42 (2007) 872–877.

[13] M.S. Popa, G. Contiu, G. Pop, P. Dan, New technologies and applications of EDM process, The International Journal of Material Forming 2 (2009) 633–636.

[14] A. Kojima, W. Natsu, M. Kunieda, Spectroscopic measurement of arc plasma diameter in EDM, CIRP Annals – Manufacturing Technology 57 (2008) 203–207.

[15] Y.S. Wong, M. Rahman, H.S. Lim, H. Han, N. Ravi, Investigation of micro-EDM material removal characteristics using single RC-pulse discharges, Journal of Materials Processing Technology 140 (2003) 303–307.

[16] Y.H. Guu, K.L. Tsai, L.K. Chen, An experimental study on electrical discharge machining of manganese–zinc ferrite magnetic material, Materials and Manufacturing Processes 22 (2007) 66–70.

[17] H. Singh, Experimental study of distribution of energy during EDM process for utilization in thermal models, International Journal of Heat and Mass Transfer 55 (2012) 5053–5064.

[18] C. Fenggou, Y. Dayong, The study of high efficiency and intelligent optimization system in EDM sinking process, Journal of Materials Processing Technology 149 (2004) 83–87.

[19] U. Caydas, A. Hascalik, Modeling and analysis of electrode wear and white layer thickness in die-sinking EDM process through response surface methodology, International Journal of Advanced Manufacturing Technology 38 (2008) 1148–1156.
[20] M. Zhou, F. Han, Adaptive control for EDM process with a self tuning regulator, International Journal of Machine Tools and Manufacture 49 (2009) 462–469.
[21] O. Yilmaz, O. Eyercioglu, N.N.Z. Gindy, A user friendly fuzzy based system for the selection of electro discharge machining process parameters, Journal of Materials Processing Technology 172 (2006) 363–371.
[22] A. Behrens, J. Ginzel, Neuro-fuzzy processes control system for sinking EDM, Journal of Manufacturing Processes 5 (2003) 33–39.
[23] C.C. Kao, A.J. Shih, Sub-nano second monitoring of micro-hole electrical discharge machining pulses and modeling of discharge ringing, International Journal of Machine Tools and Manufacture 46 (2006) 1996–2008.
[24] X.F. Chang, Mixed H2/H1 optimization approach to gap control on EDM, Control Engineering Practice 13 (2005) 95–104.
[25] H. Tong, Y. Li, Y. Wang, D. Yu, Servo scanning 3D micro-EDM based on macro/micro dual feed machine, International Journal of Machine Tools and Manufacture 48 (2008) 858–869.
[26] S. Spadlo, J. Kozak, P. Mlynarczyk, Mathematical modelling of the electrical discharge mechanical alloying process, Procedia CIRP 6 (2013) 423–427.
[27] K. Salonitis, A. Stournaras, P. Stavropoulos, G. Chryssolouris, Thermal modeling of the material removal rate and surface roughness for die-sinking EDM, International Journal of Advanced Manufacturing Technology 40 (2009) 316–323.
[28] S. Liu, Y. Huang, Y. Li, A plate capacitor model of the EDM process based on the field emission theory, International Journal of Machine Tools and Manufacture 51 (2011) 653–659.
[29] P. Matoorian, S. Sulaiman, M.M.H.M. Ahmed, An experimental study for optimization of electrical discharge turning process, Journal of Materials Processing Technology 204 (2008) 350–356
[30] T. Muthuramalingam, B. Mohan, Multi response optimization of electrical process parameters on machining characteristics in EDM using Taguchi-DEAR methodology, Journal of Engineering Technology 3 (2013) 57–60.
[31] Y.F. Tzeng, F.C. Chen, Multi objective optimisation of high speed electrical discharge machining process using Taguchi fuzzy based approach, Materials and Design 28 (2007) 1159–1168.
[32] J. Marafona, C. Wykes, A new method of optimizing material removal rate using EDM with copper–tungsten electrodes, International Journal of Machine Tools and Manufacture 40 (2000) 153–164.
[33] R. Landfried □, F. Kern, R. Gadow, Electrically conductive ZTA–TiC ceramics: Influence of TiC particle size on material properties and electrical discharge machining, Institut für Fertigungstechnologie keramischer Bauteile, Universität Stuttgart, Allmandring 7b, D-70569 Stuttgart, Germany
[34] K. Palanikumar and J. Paulo Davim, Electrical discharge machining: study on machining characteristics of WC/Co composites , Published by Woodhead Publishing Limited, 2013
[35] M. Merkleina & K. Andreasa, Influence of machining process on residual stresses in the surface of cemented carbides, 1st CIRP Conference on Surface Integrity (CSI), 2012 Published by Elsevier Ltd.
[36] Jambeswar Sahu, Chinmaya P. Mohanty & S.S. Mahapatra, A DEA approach for optimization of multiple responses in Electrical Discharge Machining of AISI D2 steel, Chemical, Civil and Mechanical Engineering Tracks of 3rd Nirma University International Conference on Engineering (NUiCONE 2012), Procedia Engineering 51 (2013) 585 – 591
[37] Abdus Sabur,* Mohammad Yeakub Ali, Md. Abdul Maleque, Ahsan Ali Khan, Investigation of material removal characteristics in EDM of nonconductive ZrO2 ceramic, 5th BSME International Conference on Thermal Engineering, © 2012 The authors, Published by Elsevier Ltd.
[38] Sengottuvel.Pa*, Satishkumar.Sb, Dinakaran.Dc, Optimization Of Multiple Characteristics Of EDM Parameters Based On Desirability Approach And Fuzzy Modeling, International Conference On DESIGN AND MANUFACTURING, IConDM 2013, Procedia Engineering 64 (2013) 1069 – 1078, © 2013 The Authors. Published by Elsevier Ltd.
[39] Chinmaya P Mohanty*, Siba Shankar Mahapatra, Manas Ranjan Singh, An Experimental Investigation of Machinability of Inconel 718 in Electrical Discharge Machining, 3rd International Conference on Materials Processing and Characterisation (ICMPC 2014), Procedia Materials Science 6 (2014) 605 – 611
[40] Milan Kumar Dasa, Kaushik Kumarb, Tapan Kr. Barmana*and Prasanta Sahooa, Application of Artificial bee Colony Algorithm for Optimization of MRR and Surface Roughness in EDM of EN31 tool steel, 3rd International Conference on Materials Processing and Characterization (ICMPC 2014), Procedia Materials Science 6 (2014) 741 – 751
[41] V. Muthukumara*, N. Rajesha, R. Venkatasamya, A. Sureshbabub , N. Senthilkumarc, "Mathematical Modeling for Radial Overcut on Electrical Discharge Machining of Incoloy 800 by Response Surface Methodology, 3rd International Conference on Materials Processing and Characterization (ICMPC 2014), Procedia Materials Science 6 (2014) 1674 – 1682
[42] M. Munza, M. Ristoa, R. Haasa, R. Landfriedb*, F. Kernb, R. Gadowb, "Machinability of ZTA-TiC ceramics by electrical discharge drilling", The Seventeenth CIRP Conference on Electro Physical and Chemical Machining (ISEM), Procedia CIRP 6 (2013) 77 – 82

[43] F. Klockea, M. Zeisa,*, A. Klinka, D. Veselovaca, " Experimental research on the electrochemical machining of modern titanium- and nickel-based alloys for aero engine components", The Seventeenth CIRP Conference on Electro Physical and Chemical Machining (ISEM), Procedia CIRP 6 (2013) 368 – 372

[44] M. Iwaia*, S. Ninomiyab, K. Suzukib, "EDM properties of newly developed PCD made up of electrically conductive diamond particles", The Seventeenth CIRP Conference on Electro Physical and Chemical Machining (ISEM), Procedia CIRP 6 (2013) 140 – 145

[45] M. Iwai, S. Ninomiya, K. Suzuki, " Improvement of EDM properties of PCD with electrode vibrated by ultrasonic transducer", The Seventeenth CIRP Conference on Electro Physical and Chemical Machining (ISEM), Procedia CIRP 6 (2013) 146 – 150

[46] Shailesh Dewangan, Soumya Gangopadhyay*, Chandan Kumar Biswas 1, Multi-response optimization of surface integrity characteristics of EDM process using grey-fuzzy logic-based hybrid approach ,Engineering Science and Technology, an International Journal xxx (2015) 1e8

[47] R. Teimouri & H. Baseri, Optimization of magnetic field assisted EDM using the continuous ACO algorithm, Applied Soft Computing 14 (2014) 381–389

[48] L. Li*, X.T. Wei, Z.Y. Li, Surface Integrity Evolution and Machining Efficiency Analysis of WEDM of Nickel-based Alloy

[49] M. Kunieda, B. Lauwers, K. P. Rajurkar, B. M. Schumacher, Advancing EDM through Fundamental Insight into the Process.

[50] Harminder Singh, Experimental study of distribution of energy during EDM process for utilization in thermal models, International Journal of Heat and Mass Transfer 55 (2012) 5053–5064

[51] Vineet Srivastava, Pulak M. Pandey, Study of ultrasonic assisted cryogenically cooled EDM process using sintered (Cu–TiC) tooltip

[52] M.P. Jahan, Y.S. Wong, M. Rahman∗, A study on the fine-finish die-sinking micro-EDM of tungsten carbide using different electrode materials, journal of materials processing technology 2 0 9 (2 0 0 9) 3956–3967.

[53] J. Murray, D. Zdebski, A.T. Clare, Workpiece debris deposition on tool electrodes and secondary discharge phenomena in micro-EDM, Journal of Materials Processing Technology 212 (2012) 1537– 1547

[54] Yin Qingfeng∗, Wang Baorui, Zhang Yongbin, Ji Fang, Liu Guangmin," Research of lower tool electrode wear in simultaneous EDM and ECM, Journal of Materials Processing Technology 214 (2014) 1759–1768

[55] S. Dewangan,S. Gangopadhyay and C. K. Biswas, Study of Surface Integrity and Dimensional accuracy in EDM using Fuzzy TOPSIS and Sensitivity Analysis

[56] M Manohara, T Selvarajb , D Sivakumara, Shibu Gopinatha and Koshy M Georgea, Experimental study to assess the effect of Electrode bottom profiles while machining Inconel 718 through EDM Process, 3rd International Conference on Materials Processing and Characterisation (ICMPC 2014), Procedia Materials Science 6 (2014) 92 – 104

[57] Mao-yong LIN , Chung-chen TSAO, Chun-yao HSU, Ai-huei CHIOU, Peng-cheng HUANG, Yu-cheng LIN, Optimization of micro milling electrical discharge machining of Inconel 718 by Grey-Taguchi method, Trans. Nonferrous Met. Soc. China 23(2013) 661−666

[58] Peng-fei BAI, Zi-chuan YI, Biao TANG, Guo-fu ZHOU, Solid-phase sintering process and forced convective heat transfer performance of porous-structured micro-channels, Trans. Nonferrous Met. Soc. China 24(2014) 900−906

ISST Journal of Mechanical Engineering, Vol. 6 No. 2, (July - December 2015), p.p. 11-22
ISSN 0976-7371 © Intellectuals Society for Socio-Techno Welfare

EFFECT OF EXHAUST GAS RECIRCULATION ON COMBUSTION CHARACTERISTICS AND EMISSIONS OF DI DIESEL ENGINE ADOPTING DIFFERENT AIR FILTERS

[1] P. Ravi Chander, [2] B. Sudheer Prem Kumar and [2] K. Vijaya Kumar Reddy
[1] Research Scholar, JNTUH, India
[2] Professor, Mechanical Engineering Department, JNT University, Hyderabad, Telangana, India
[2] Professor, Mechanical Engineering Department, JNT University, Hyderabad, India.
E-mail: vira755@gmail.com

ABSTRACT

The exhaust gas recirculation technique has proven a better solution to reduce NOx emission in diesel engines. EGR method is taken for the study to investigate the engine behavior on its combustion and emissions. In this paper the combustion characteristics such as heat release rate (HRR), cylinder pressures, the exhaust gas emissions such as CO, CO_2, NOx, UBHC, O_2, and smoke are presented and discussed. The discussion is presented and supported by experimental results. In the experimentation variation in EGR percentage for different air filters is selected for the study. The engine is run by adopting one type of filter at once at different loads for different percentages of EGR such as 5%, 10% and 15%.

Key words*: Diesel engine, Air filters, Emissions, EGR.*

INTRODUCTION

Unlike SI engine the CI engine emits smokes and particulate matter along with CO, HC & NOx. Though CO_2 is not an emission for local environment, but as a greenhouse gas, it contributes to global warming. These emissions severely affect human health and the lives of animal and plant. The severity of emission effects depend on their concentration and the time of exposure simultaneously. The actual magnitudes of the emissions from SI and CI engines vary due to the difference in their mixture preparation and combustion mechanisms. Air filters play an important role in minimizing exhaust specially particulate matter.

The air filter separation efficiency was studied for particle size of 50 and 100µm, it was found to be 94.4%. The study was made with both experimental and simulation methods. Pressure drop in the analysis was well matched with experimental results [1]. The air filters (SAE J726 & J1669) used in automotive cabin and engine are investigated for their standards and filtration behaviors. The actual air filter performance and their definitions are related to the real time conditions. In the investigation relation between primary function of the air filter and defined one are analyze and the changes for the recommended [2]. The air filter design is critical because of the factors like limited space availability in the induction system for higher velocity of aerosol passing in the primary air filter but this increased velocity causes re-trapping of dust particles and increased dust penetration through the filter [3]. The frequency of replacing the air filter depends on its optimum usage which can reduce its cost and extended its life. The experiments conducted in optimizing geometrical configuration of intake system to keep reduced pressure drop and improved utilization of filter area. CFD analysis was made to improve air flow characteristics through the filters. An eccentricity was suggested in the filter element The eccentricity place a role of maintaining air velocity at constant in annular portion. This constant value of velocity resulted in lowering pressure drop was found to be higher for an eccentricity placed at 15mm distanced from the inlet [4]. When Exhaust Gas in which the Recirculation (EGR) on the performance and emissions of a single cylinder naturally aspirated constant speed diesel engine is studied. The results showed that EGR would be one option to reduce the nitrous oxide emissions, but with a rise in EGR rate the CO, UHC concentrations in the engine exhaust are increased [5 & 6]. When the effects of hot and cold EGR methods on emissions and efficiency of the engine is provided for obtaining different EGR methods in which the performance parameters were studied with and without exhaust gas recirculation of different methods with 10%, 15% and 20% of EGR[7& 8]. The technology adopted for the reticulated foam multilayer filters calls for no servicing and maintenance throughout the life of

the vehicle i.e, 150000 miles. The technology adopted for these type of filters facilitates sum unique advantages compare to traditional air filters [9]. The restriction for air flow will be naturally higher in old filter than that of new [10]. When investigation made on air filters and their traps in different locations with different vegetation zones to study the efficiency of air filters used in motor cars. It was revealed that on efficiency filter traps will capture only the airborne particles. The contamination due to vegetation is also consider along with animal derived debris [11]. In this paper the performance characteristics and the exhaust gas emissions of stationary diesel engine are presented and discussed which is supported by experimental results. In the experimentation variation in EGR percentage for different air filters is selected for the study. The engine is run by adopting one type of filter at once at different loads for different percentages of EGR such as 5%, 10% and 15%.

EXPERIMENTAL SETUP

The experimentation is carried out on a single cylinder, four stroke, water cooled, DI engine. The test set up is developed to carry out set experimentation procedures. The layout of the experimental set up is shown in the Fig. 2.1. and Fig. 2.2 shows Photographic View of Computerized Experimental Diesel Engine Setup.

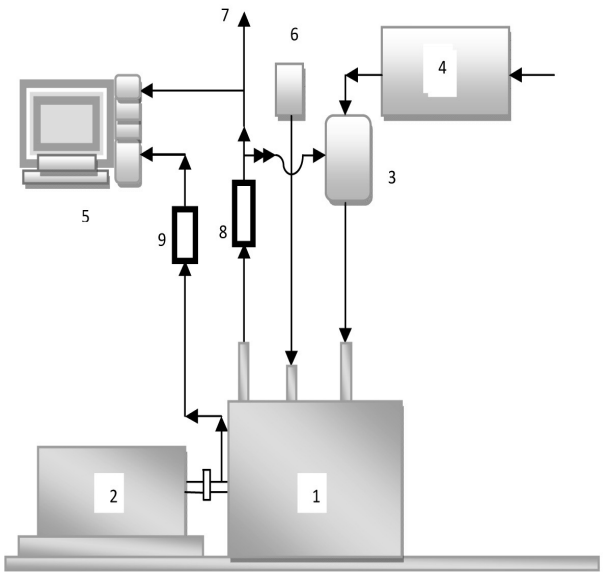

Fig: 2.1 Layout of Experimental Set up

1) Engine, 2) Dynamometer, 3) Air Filter Housing, 4) Air surge tank, 5) Computerized data acquisition,
6) Diesel fuel tank, 7) Exhaust Manifold, 8) Exhaust gas recirculation unit, 9) Crank angle encoder.

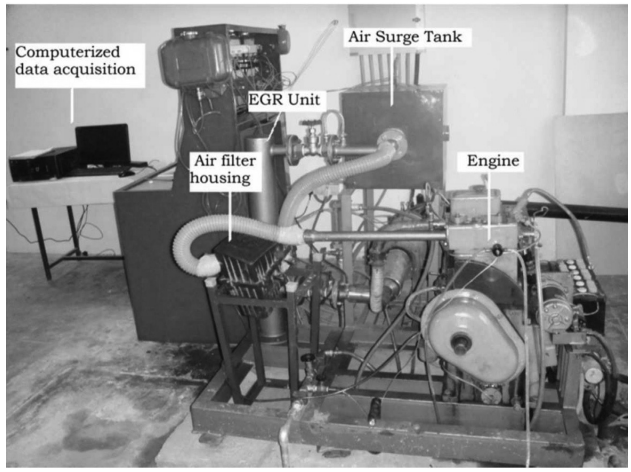

Fig: 2.2 Photographic View of Computerized Diesel Engine Setup with Air Filter Housing Arrangements and EGR Facility

Table.1 Engine specification:

Make	Kirloskar AV-1
Engine type	4- stroke single cylinder diesel engine(water cooled)
Rated Power	3.7KW, 1500rpm
Bore & stroke	80mmx110mm
Compression rate	16.5:1 (Variable From 14.3to20)
Cylinder Capacity	553cc
Dynamometer	Electrical-AC alternator

2.2 EXPERIMENTATION PROCEDURE

The experiments are conducted on test engine in different stages. The engine is experimented without air filter considering as baseline operation to make the comparison study. In second stage the engine is run by adopting the air filter of type 1 (AFM1) - Model No. NF 1004 both with new and clogged filters one after the other. In third stage the engine is run by adopting the air filter of type 2 (AFM2) - Model No. NF615 both with new and clogged filters one after the other. In fourth stage the engine is run by adopting the air filter of type 3 (AFM3) - Model No. NF560 both with new and clogged filters one after the other. . In fifth stage the engine is run by adopting the air filter of type 4 (AFM4) - Model No. 0313AC2261N both with new and clogged filters one after the other.

Fig: 2.4(a) AFM1 (OLD& NEW)

Fig: 2.4 (b) AFM2 (OLD& NEW)

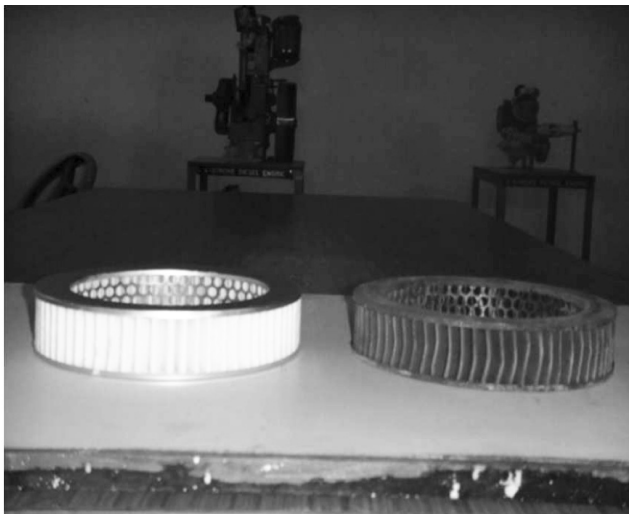

Fig: 2.4 (c) AFM3 (OLD& NEW)

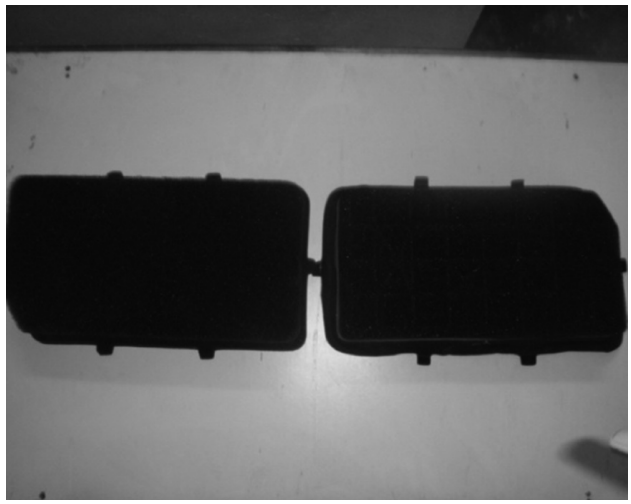

Fig: 2.4 (d) AFM4 (OLD& NEW)

3. RESULTS AND DISCUSSION

3.1 Combustion Characteristics

3.1.1 Cylinder pressure

The variation of cylinder pressure against crank angle of the engine for different filters, AFM1, AFM2, AFM3 and AFM4 with varying percentages of exhaust gas recirculation is presented and discussed below. The exhaust gas percentage is varied by 5, 10 and 15 percentages in the inlet.

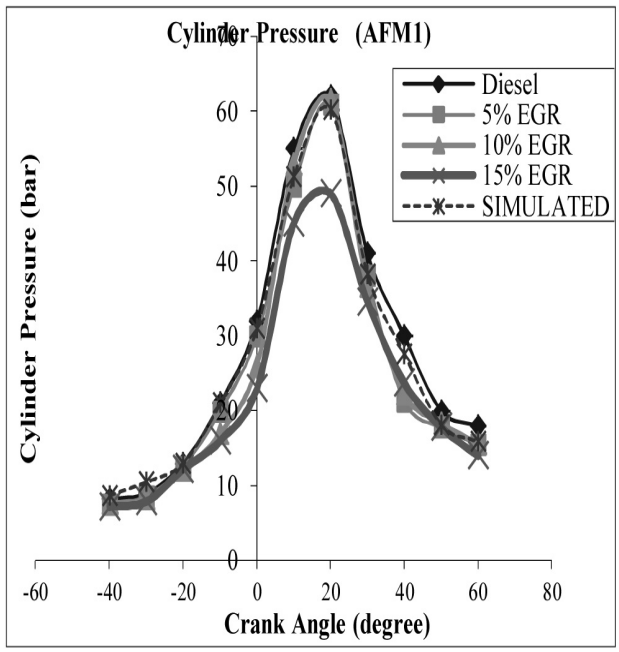

Fig: 3.1.1(a)

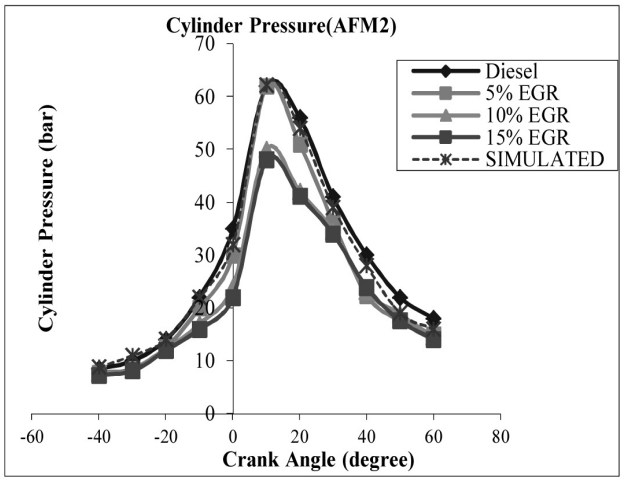

Fig: 3.1.1(b)

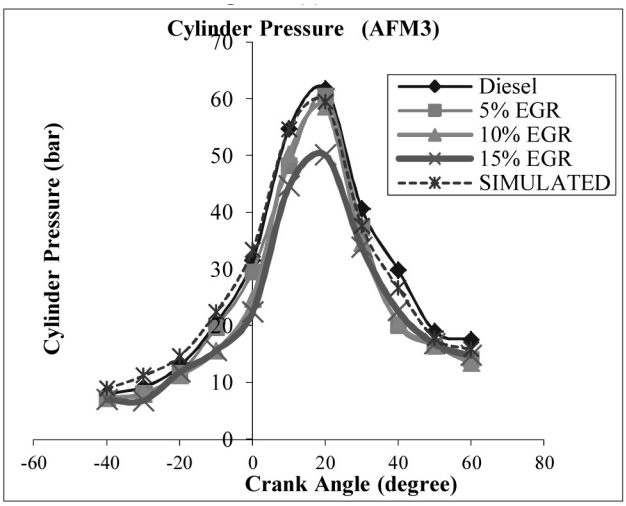

Fig: 3.1.1(c)

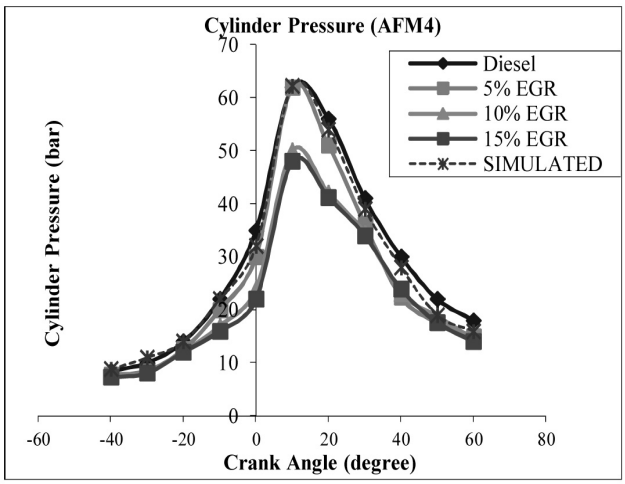

Fig: 3.1.1(d)

Fig: 3.1.1(a) to Fig: 3.1.1(d) Effect of EGR percentage on cylinder pressure adopting AFM1, AFM2, AFM3 & AFM4

The cylinder pressure as a function of crank angle is presented in figure 3.1.1(a) to 3.1.1(d). In the figure 3.1.1(a) the effect of percentage of exhaust gas recirculation on cylinder pressure for the filter AFM1is presented. For each percentage of EGR the graphs are plotted against crank angle the simulated values are also compared. As the percentage of EGR increases the cylinder pressure found to be decreasing marginally for 5, 10 & 15% percent of EGR when compared to diesel fuel operation without EGR. The decrease in cylinder pressure was recorded in the range of 2 to 5%. The values at crank angle 18 ATDC for 5, 10 & 15% percent of EGR were 62, 65 and 53 bar when compared to 65 of diesel operation without EGR. The values are well matched with simulated results.

In the figure 3.1.1(b) the effect of percentage of exhaust gas recirculation on cylinder pressure for the filter AFM2 is presented. For each percentage of EGR the graphs are plotted against crank angle the simulated values are also compared. As the percentage of EGR increases the cylinder pressure found to be decreasing for 5, 10 & 15% percent of EGR when compared to diesel fuel operation without EGR. The decrease in cylinder pressure was recorded in the range of 4 to 9%. The values at crank angle 18 ATDC for 5, 10 & 15% percent of EGR were 60, 50 and 49 bar when compared to 62 of diesel operation without EGR. The values are well matched with simulated results.

In the figure 3.1.1(c) the effect of percentage of exhaust gas recirculation on cylinder pressure for the filter AFM3 is presented. For each percentage of EGR the graphs are plotted against crank angle the simulated values are also compared. As the percentage of EGR increases the cylinder pressure found to be decreasing marginally for 5, 10 & 15% percent of EGR when compared to diesel fuel operation without EGR. The decrease in cylinder pressure was recorded in the range of 2 to 6%. The values at crank angle 18 ATDC for 5, 10 & 15% percent of EGR were 60, 58 and 50 bar when compared to 62 of diesel operation without EGR. The values are well matched with simulated results.

In the figure 3.1.1(d) the effect of percentage of exhaust gas recirculation on cylinder pressure for the filter AFM4 is presented. For each percentage of EGR the graphs are plotted against crank angle the simulated values are also compared. As the percentage of EGR increases the cylinder pressure found to be decreasing for 5, 10 & 15% percent of EGR when compared to diesel fuel operation without EGR. The decrease in cylinder pressure was recorded in the range of 4 to 10%. The values at crank angle 18 ATDC for 5, 10 & 15% percent of EGR were 50, 45 and 51 bar when compared to 56 of diesel operation without EGR.

The values are well matched with simulated results.

3.1.2 Heat release rate

The variation of heat release rate against crank angle of the engine for different filters, AFM1, AFM2, AFM3 and AFM4 with varying percentages of exhaust gas recirculation is presented and discussed below. The exhaust gas percentage is varied like 5, 10 and 15 percentages in the inlet.

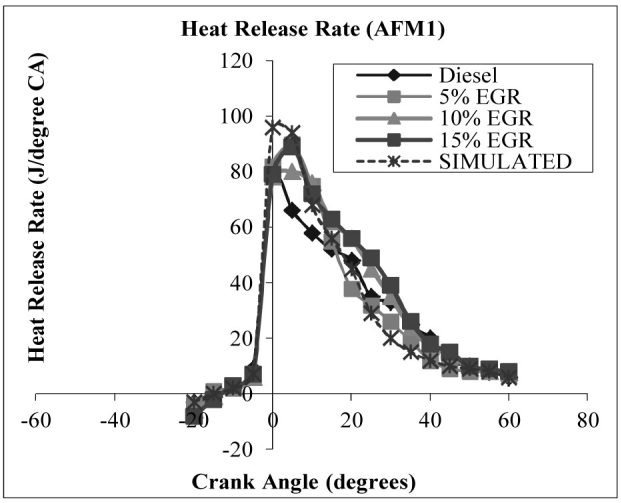

Fig: 3.1.2(a)

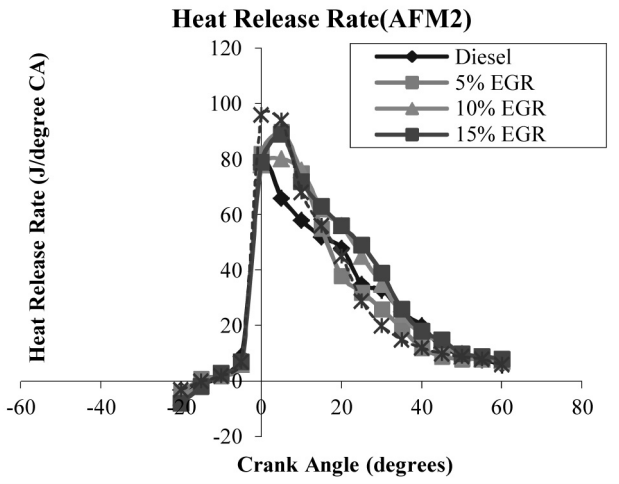

Fig: 3.1.2(b)

In the figure 3.1.2(a) the effect of percentage of exhaust gas recirculation on heat release rate for the filter AFM1is presented. For each percentage of EGR the graphs are plotted against crank angle the simulated values are also compared. As the percentage of EGR increases the heat release rate found to be increasing when compared to diesel fuel operation without EGR for 5, 10 & 15% percent of EGR. The increase in heat release rate was recorded in the range of 10 to 30%. The values at crank angle 8 ATDC for 5, 10 & 15% percent of EGR were 75, 76 and 78 J/degree CA when compared to 58 of diesel operation without EGR. The values are well matched with simulated results.

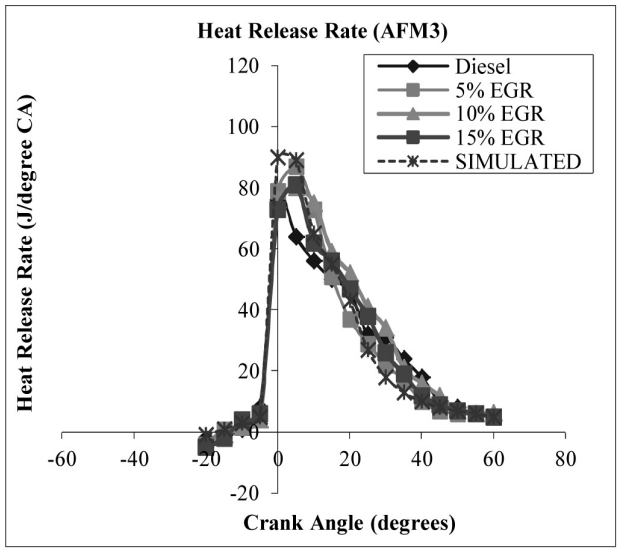

Fig: 3.1.2(c)

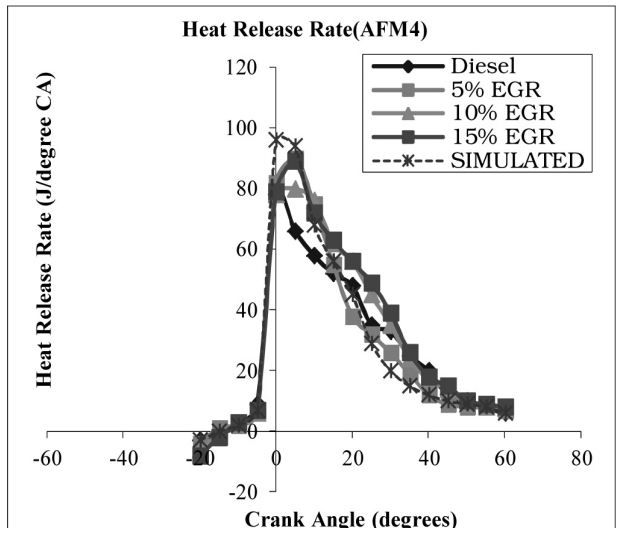

Fig: 3.1.2(d)

Fig: 3.1.2(a) to Fig: 3.1.2(d) Effect of EGR percentage on Heat release rate adopting AFM1, AFM2, AFM3 & AFM4

In the figure 3.1.2(b) the effect of percentage of exhaust gas recirculation on heat release rate for the filter AFM2 is presented. For each percentage of EGR the graphs are plotted against crank angle the simulated values are also compared. As the percentage of EGR increases the heat release rate found to be increasing when compared to diesel

fuel operation without EGR for 5, 10 & 15% percent of EGR. The increase in heat release rate was recorded in the range of 10 to 25%. The values at crank angle 8 ATDC for 5, 10 & 15% percent of EGR were 75, 76 and 78 J/degree CA when compared to 58 of diesel operation without EGR. The values are well matched with simulated results.

In the figure 3.1.2(c) the effect of percentage of exhaust gas recirculation on heat release rate for the filter AFM1is presented. For each percentage of EGR the graphs are plotted against crank angle the simulated values are also compared. As the percentage of EGR increases the heat release rate found to be increasing when compared to diesel fuel operation without EGR for 5, 10 & 15% percent of EGR. The increase in heat release rate was recorded in the range of 15 to 30%. The values at crank angle 8 ATDC for 5, 10 & 15% percent of EGR were 73, 75 and 70 J/degree CA when compared to 56 of diesel operation without EGR. The values are well matched with simulated results.

In the figure 3.1.2(d) the effect of percentage of exhaust gas recirculation on heat release rate for the filter AFM1is presented. For each percentage of EGR the graphs are plotted against crank angle the simulated values are also compared. As the percentage of EGR increases the heat release rate found to be increasing when compared to diesel fuel operation without EGR for 5, 10 & 15% percent of EGR. The increase in heat release rate was recorded in the range of 5 to 25%. The values at crank angle 8 ATDC for 5, 10 & 15% percent of EGR were 75, 76 and 72 J/degree CA when compared to 58 of diesel operation without EGR. The values are well matched with simulated results.

3.2 Exhaust Gas Emissions

3.2.1 Carbon monoxide (CO)

Carbon monoxide is the product of the combustion of a hydrocarbon fuel at intermediate stage. Its presence in the exhaust shows the incomplete or improper combustion. It depends mainly on ratio of air fuel mixture.

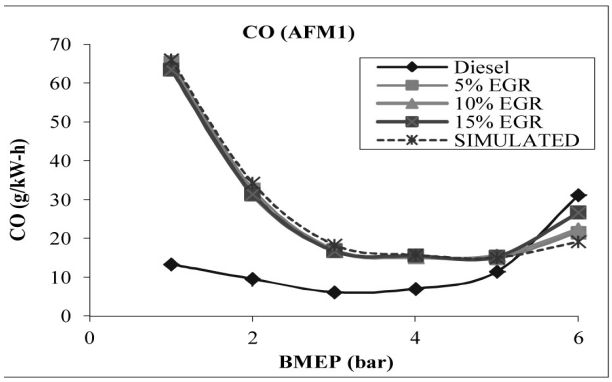

Fig: 3.2.1 (a)

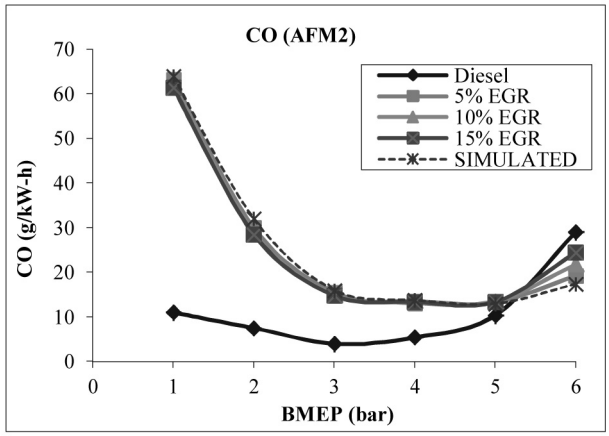

Fig: 3.2.1 (b)

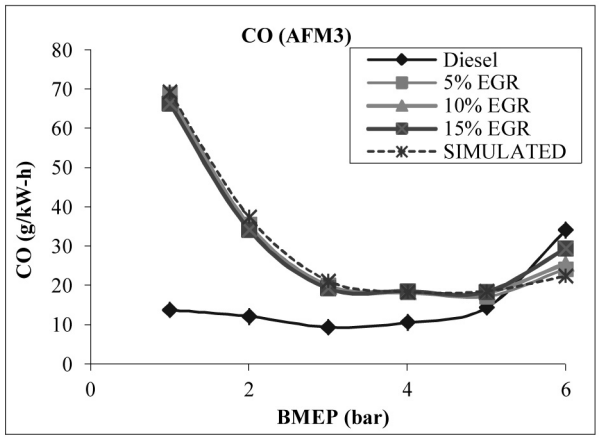

Fig: 3.2.1 (c)

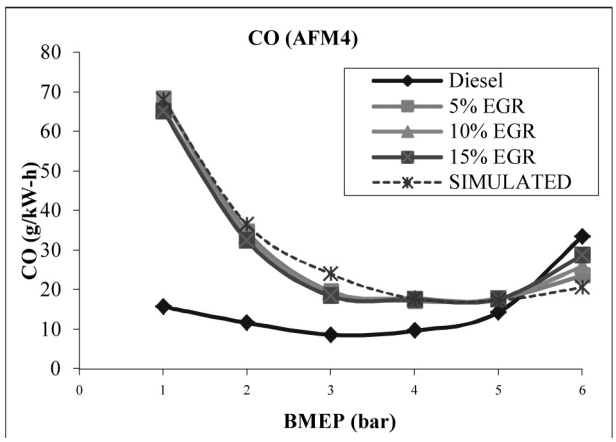

Fig: 3.2.1 (d)

Fig: 3.2.1(a) to Fig: 3.2.1(d) Effect of EGR percentage on CO adopting AFM1, AFM2, AFM3 & AFM4

The figure 3.2.1(a) depicts the effect of percentage of exhaust gas recirculation on Carbon monoxide for the filter

AFM1. For each percentage of EGR the graphs are plotted against bmep the simulated values are also compared. As the percentage of EGR increases the Carbon monoxide found at higher values when compared to diesel fuel operation without EGR. For all the percentages of EGR the carbon monoxide levels were found to be higher at all values of bmep. And the values were recorded very high at smaller values of bmep and were recorded decreasing when bmep values are increased. The values of CO levels are almost similar as the EGR percentage varied. The variation among them is less significant as they recorded in the range of 5 to 10%. But the variation is very large when operated on diesel and are noted 4 to 6 times more than the diesel operation.

The figure 3.2.1(b) depicts the effect of percentage of exhaust gas recirculation on Carbon monoxide for the filter AFM2. For each percentage of EGR the graphs are plotted against bmep the simulated values are also compared. As the percentage of EGR increases the Carbon monoxide found at higher values when compared to diesel fuel operation without EGR. For all the percentages of EGR the carbon monoxide levels were found to be higher at all values of bmep. And the values were recorded very high at smaller values of bmep and were recorded decreasing when bmep values are increased. The values of CO levels are almost similar as the EGR percentage varied. The variation among them is less significant as they recorded in the range of 5 to 10%. But the variation is very large when operated on diesel and are noted4 to 5 times more than the diesel operation.

The figure 3.2.1(c) depicts the effect of percentage of exhaust gas recirculation on Carbon monoxide for the filter AFM3. For each percentage of EGR the graphs are plotted against bmep the simulated values are also compared. As the percentage of EGR increases the Carbon monoxide found at higher values when compared to diesel fuel operation without EGR. For all the percentages of EGR the carbon monoxide levels were found to be higher at all values of bmep. And the values were recorded very high at smaller values of bmep and were recorded decreasing when bmep values are increased. The values of CO levels are almost similar as the EGR percentage varied. The variation among them is less significant as they recorded in the range of 5 to 10%. But the variation is very large when operated on diesel and are noted 5 to 7 times more than the diesel operation.

The figure 3.2.1(d) depicts the effect of percentage of exhaust gas recirculation on Carbon monoxide for the filter AFM4. For each percentage of EGR the graphs are plotted against bmep the simulated values are also compared. As the percentage of EGR increases the Carbon monoxide found at higher values when compared to diesel fuel operation without EGR. For all the percentages of EGR the carbon monoxide levels were found to be higher at all values of bmep. And the values were recorded very high at smaller values of bmep and were recorded decreasing when bmep values are increased. The values of CO levels are almost similar as the EGR percentage varied. The variation among them is less significant as they recorded in the range of 5 to 10%. But the variation is very large when operated on diesel and are noted 4 to 6 times more than the diesel operation.

3.2.2 NO_X

The NO_x percentage in the exhaust is dependent on mean values of cylinder temperature, amount of oxygen availability and residence time of the combustible mixture in the cylinder.

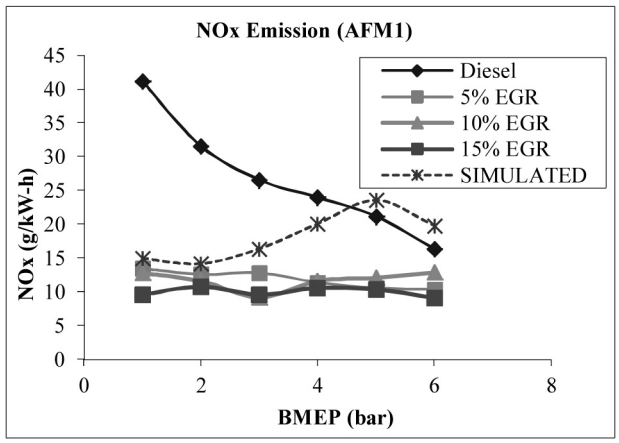

Fig: 3.2.2 (a)

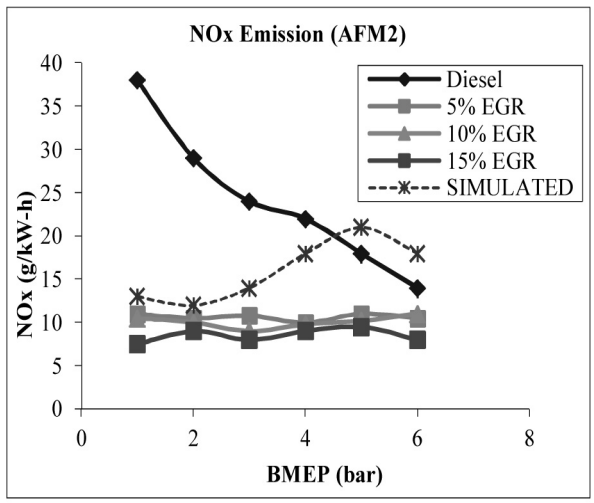

Fig: 3.2.2 (b)

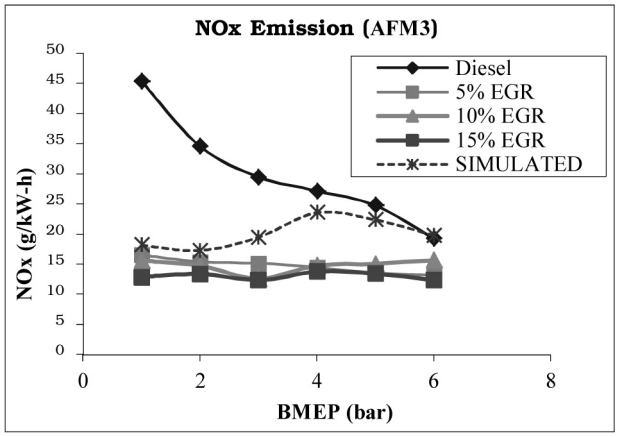

Fig: 3.2.2 (c)

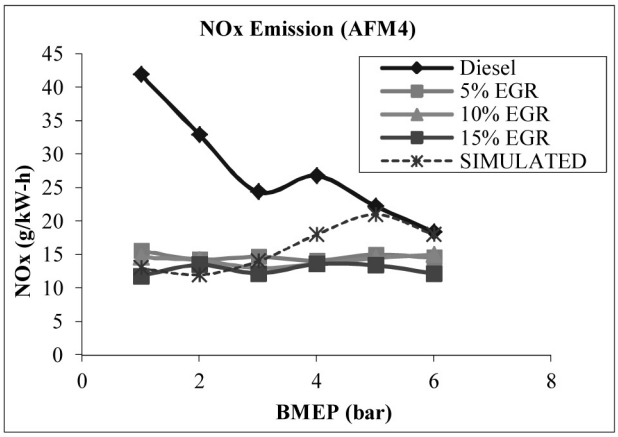

Fig: 3.2.2 (d)

Fig: 3.2.2(a) to Fig: 3.2.2(d) Effect of EGR percentage on NO_X adopting AFM1, AFM2, AFM3 & AFM4

The figure 3.2.2(a) depicts the effect of percentage of exhaust gas recirculation on NO_x for the filter AFM1. For each percentage of EGR the graphs are plotted against bmep the simulated values are also compared. As the percentage of EGR increases the NO_x found to be decreasing when compared to diesel fuel operation without EGR. For all the percentages of EGR the NO_x levels were found to be lower at all values of bmep. And the values were recorded lower at smaller values of bmep and were recorded decreasing as bmep values are increased. The values of NO_x levels are almost similar as the EGR percentage varied. The variation among them is less significant as they recorded in the range of 2 to 5%. But the variation is small when operated on diesel and are recorded 2 to 4 times lower than the diesel operation.

The figure 3.2.2(b) depicts the effect of percentage of exhaust gas recirculation on NO_x for the filter AFM2. For each percentage of EGR the graphs are plotted against BMEP the simulated values are also compared. As the percentage of EGR increases the NO_x found to be decreasing when compared to diesel fuel operation without EGR. For all the percentages of EGR the NO_x levels were found to be lower at all values of bmep. And the values were recorded lower at smaller values of bmep and were recorded decreasing as bmep values are increased. The values of NO_x levels are almost similar as the EGR percentage varied. The variation among them is less significant as they recorded in the range of 2 to 4%. But the variation is small when operated on diesel and are recorded 2 to 4 times lower than the diesel operation.

The figure 3.2.2(c) depicts the effect of percentage of exhaust gas recirculation on NO_x for the filter AFM3. For each percentage of EGR the graphs are plotted against BMEP the simulated values are also compared. As the percentage of EGR increases the NO_x found to be decreasing when compared to diesel fuel operation without EGR. For all the percentages of EGR the NO_x levels were found to be lower at all values of bmep. And the values were recorded lower at smaller values of bmep and were recorded decreasing as bmep values are increased. The values of NO_x levels are almost similar as the EGR percentage varied. The variation among them is less significant as they recorded in the range of 2 to 6%. But the variation is small when operated on diesel and are recorded 2 to 4 times lower than the diesel operation

The figure 3.2.2(d) depicts the effect of percentage of exhaust gas recirculation on NO_x for the filter AFM4. For each percentage of EGR the graphs are plotted against BMEP the simulated values are also compared. As the percentage of EGR increases the NO_x found to be decreasing when compared to diesel fuel operation without EGR. For all the percentages of EGR the NO_x levels were found to be lower at all values of bmep. And the values were recorded lower at smaller values of bmep and were recorded decreasing as bmep values are increased. The values of NO_x levels are almost similar as the EGR percentage varied. The variation among them is less significant as they recorded in the range of 2 to 5%. But the variation is small when operated on diesel and are recorded 2 to 4 times lower than the diesel operation.

3.2.3 UNBURN HYDROCARBON (UBHC)

The diesel engine produces higher unburned hydrocarbons when it runs at lower loads and it is a serious problem which is to be addressed. The UBHC level indicates incomplete burning of the fuel may be due to poor fuel distribution, smaller exhaust temperatures leaner air fuel mixture pockets and crevices in the cylinder. The influence

of EGR on UBHC emission for different filters AFM1, AFM2, AFM3 and AFM4 is presented in the figures from 5.3.3(a) to 3.3.3(d) and the discussion is followed.

The figure 3.2.3(a) depicts the effect of percentage of exhaust gas recirculation on UBHC for the filter AFM1. For each percentage of EGR the graphs are plotted against bmep the simulated values are also compared. As the percentage of EGR increases the UBHC found to be higher when compared to diesel fuel operation without EGR. For all the percentages of EGR the UBHC levels were found to be higher at all values of bmep. And the values were recorded very high at smaller values of bmep and were recorded decreasing when bmep values are increased. The values of UBHC levels are almost similar as the EGR percentage varied. The variation among them is less significant as they recorded below 2%. But the variation is very large when operated on diesel and are noted 4 to 6 times more than the diesel operation.

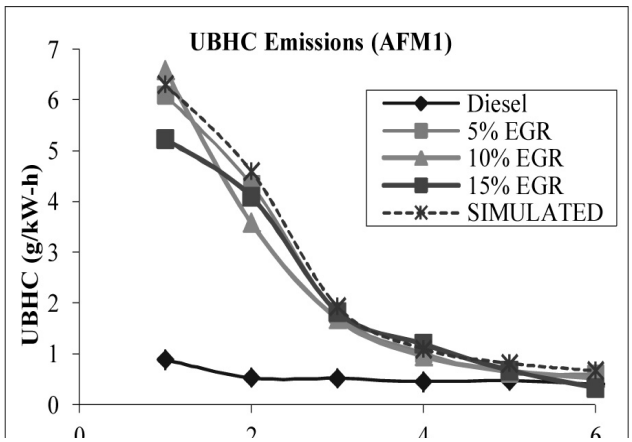

Fig: 3.2.3 (a)

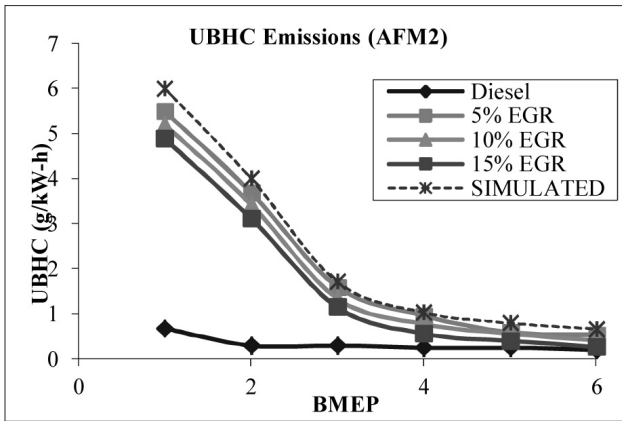

Fig: 3.2.3 (b)

The figure 3.2.3(b) depicts the effect of percentage of exhaust gas recirculation on UBHC for the filter AFM2.

For each percentage of EGR the graphs are plotted against bmep the simulated values are also compared. As the percentage of EGR increases the UBHC found to be higher when compared to diesel fuel operation without EGR. For all the percentages of EGR the UBHC levels were found to be higher at all values of bmep. And the values were recorded very high at smaller values of bmep and were recorded decreasing when bmep values are increased. The values of UBHC levels are almost similar as the EGR percentage varied. The variation among them is less significant as they recorded below 3%. But the variation is very large when operated on diesel and are noted 3 to 6 times more than the diesel operation.

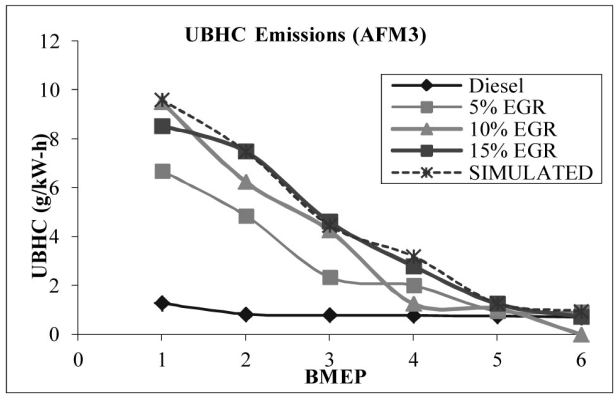

Fig: 3.2.3 (c)

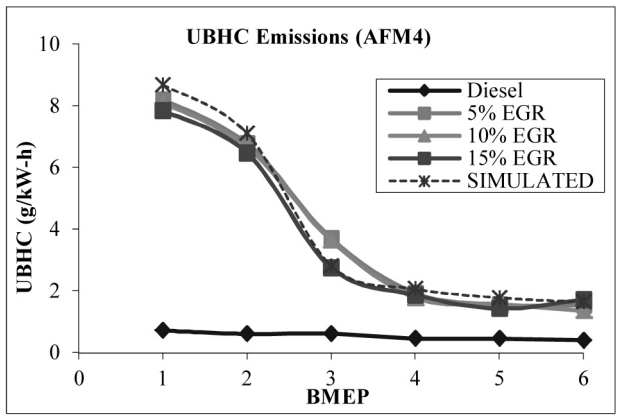

Fig: 3.2.3 (d)

Fig: 3.2.3(a) to Fig: 3.2.3 (d) Effect of EGR percentage on UBHC adopting AFM1, AFM2,AFM3 & AFM4

The figure 3.2.3(c) depicts the effect of percentage of exhaust gas recirculation on UBHC for the filter AFM4. For each percentage of EGR the graphs are plotted against bmep the simulated values are also compared. As the percentage of EGR increases the UBHC found to be higher

when compared to diesel fuel operation without EGR. For all the percentages of EGR the UBHC levels were found to be higher at all values of bmep. And the values were recorded very high at smaller values of bmep and were recorded decreasing when bmep values are increased. The values of UBHC levels are almost similar as the EGR percentage varied. The variation among them is less significant as they recorded below 3%. But the variation is very large when operated on diesel and are noted 4 to 5 times more than the diesel operation.

The figure 3.2.3(d) depicts the effect of percentage of exhaust gas recirculation on UBHC for the filter AFM4. For each percentage of EGR the graphs are plotted against bmep the simulated values are also compared. As the percentage of EGR increases the UBHC found to be higher when compared to diesel fuel operation without EGR. For all the percentages of EGR the UBHC levels were found to be higher at all values of bmep. And the values were recorded very high at smaller values of bmep and were recorded decreasing when bmep values are increased. The values of UBHC levels are almost similar as the EGR percentage varied. The variation among them is less significant as they recorded below 2%. But the variation is very large when operated on diesel and are noted 3 to 5 times more than the diesel operation.

3.2.4 Smoke

The smoke percentage in the exhaust is the indication of deficiency of oxygen locally in the cylinder of a diesel engine. The variation of smoke as the variation in brake mean effective pressure of the engine for different filters, AFM1,AFM2, AFM3 and AFM4 with varying percentages of exhaust gas recirculation is presented and discussed below. The exhaust gas percentage is varied in 5, 10 and 15 percentages at the inlet.

The figure 3.2.4(a) depicts the effect of percentage of exhaust gas recirculation on smoke for the filter AFM1. For each percentage of EGR the graphs are plotted against BMEP the simulated values are also compared. As the percentage of EGR increases the smoke found to be decreasing when compared to diesel fuel operation without EGR. For all the percentages of EGR the smoke levels were found to be lower at all values of bmep. And the values were recorded lower at smaller values of bmep and were recorded increasing as bmep values are increased. The values of smoke levels are almost similar among themselves as the EGR percentage is varied. The variation among them is less significant as they recorded in the range of 5 to 10%. But the variation is smaller when operated on diesel and are recorded 2 to 6 times lower than the diesel operation.

The figure 3.2.4(b) depicts the effect of percentage of exhaust gas recirculation on smoke for the filter AFM2. For each percentage of EGR the graphs are plotted against BMEP the simulated values are also compared. As the percentage of EGR increases the smoke found to be decreasing when compared to diesel fuel operation without EGR. For all the percentages of EGR the smoke levels were found to be lower at all values of bmep. And the values were recorded lower at smaller values of bmep and were recorded increasing as bmep values are increased. The values of smoke levels are almost similar among themselves as the EGR percentage is varied. The variation among them is less significant as they recorded in the range of 5 to 18%. But the variation is smaller when operated on diesel and are recorded 2 to 5 times lower than the diesel operation.

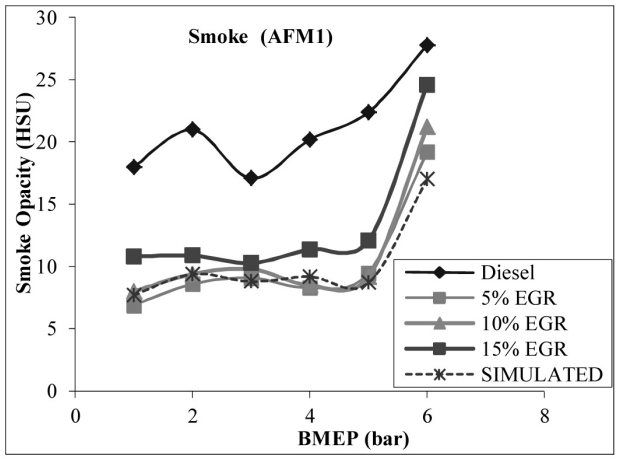

Fig: 3.2.4 (a)

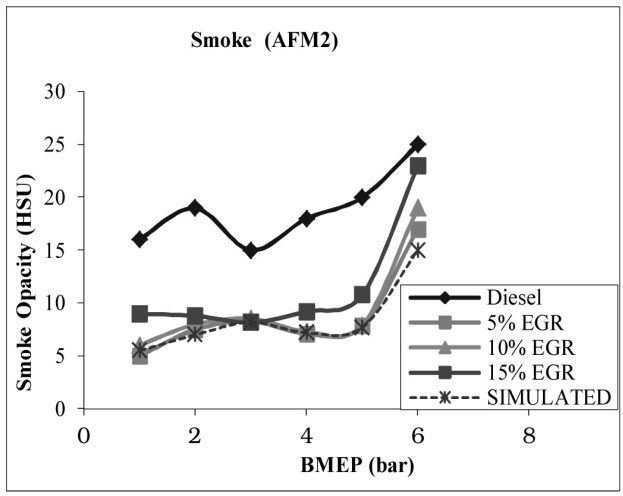

Fig: 3.2.4 (b)

The figure 3.2.4(c) depicts the effect of percentage of exhaust gas recirculation on smoke for the filter AFM3.

For each percentage of EGR the graphs are plotted against BMEP the simulated values are also compared. As the percentage of EGR increases the smoke found to be decreasing when compared to diesel fuel operation without EGR. For all the percentages of EGR the smoke levels were found to be lower at all values of bmep. And the values were recorded lower at smaller values of bmep and were recorded increasing as bmep values are increased. The values of smoke levels are almost similar among themselves as the EGR percentage is varied. The variation among them is less significant as they recorded in the range of 4 to 9%. But the variation is smaller when operated on diesel and are recorded 2 to 6 times lower than the diesel operation.

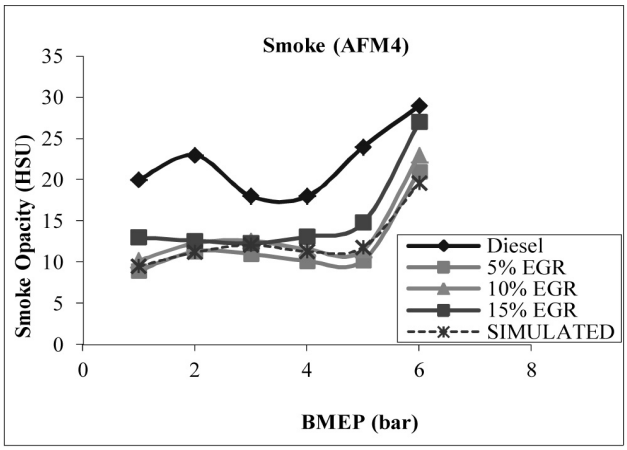

Fig: 3.2.4 (c)

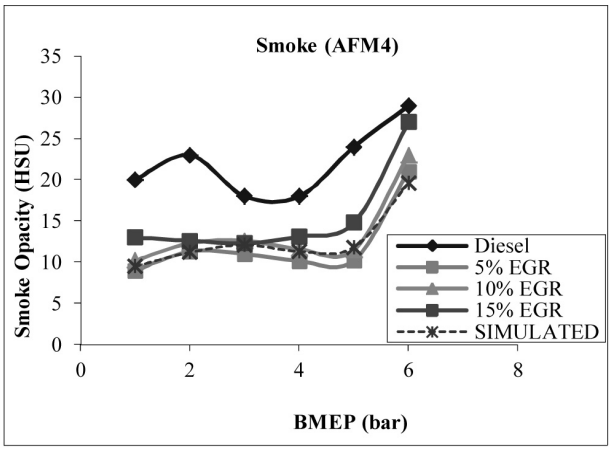

Fig: 3.2.4 (d)

Fig: 3.2.4(a) to Fig: 3.2.4 (d) Effect of EGR percentage on smoke adopting AFM1, AFM2, AFM3 & AFM4

The figure 3.2.4(d) depicts the effect of percentage of exhaust gas recirculation on smoke for the filter AFM4.

For each percentage of EGR the graphs are plotted against BMEP the simulated values are also compared. As the percentage of EGR increases the smoke found to be decreasing when compared to diesel fuel operation without EGR. For all the percentages of EGR the smoke levels were found to be lower at all values of bmep. And the values were recorded lower at smaller values of bmep and were recorded increasing as bmep values are increased. The values of smoke levels are almost similar among themselves as the EGR percentage is varied. The variation among them is less significant as they recorded in the range of 5 to 9%. But the variation is smaller when operated on diesel and are recorded 2 to 5 times lower than the diesel operation.

CONCLUSIONS:

- As the percentage of EGR increases the cylinder pressure for all filters found to be decreasing marginally for 5, 10 & 15% percent of EGR when compared to diesel fuel operation without EGR.
- At 5% of EGR all the filters AFM1, AFM2, AFM3 & AFM4 have given more cylinder pressure by 10 to 15%.
- As percentage of EGR increases the heat release rate for all filters found to be increasing when compared to diesel fuel operation without EGR for 5, 10 & 15% percent of EGR.
- The filter AFM2 has produced uniform cylinder pressure and it is near TDC when compared to other filters.
- Though exhaust gas recirculation has been widely applied in SI engines for reduction of NOx formation, but nowadays in diesel engines it has become common practice. In the investigations it was observed that the use of EGR, NOx reductions are accompanied with an increase in smoke, particulate, unburned hydrocarbon emissions and fuel consumption.

REFERENCES

1. Nagarajan, G., Kumar, S., and Chowdhury, D., "CFD Analysis of Air Filters for an Off-Highway Vehicle," SAE Technical Paper 2007-26-048, 2007.
2. Ptak, T. and Walker, M., "Testing Automotive Engine and Interior Air Filters," SAE Technical Paper 970677,1997.
3. T. Jaroszczyk, J. Wake and M. J. Connor, “Factors Affecting the Performance of Engine Air Filters, Journal of Engineering for Gas Turbines and Power ,Volume 115, Issue 4,Research Paper, J. Eng. Gas Turbines Power 115(4), 693-699 (Oct 01, 1993).
4. M.R.Chopade1, A.P Valavade 2, S. H. Barhatte3, “Performance Enhancement Of Air Filter By Design Optimization”, International Journal of Advanced

Engineering Technology, IJAET, E-ISSN 0976-3945, Vol.III, Issue I, January-March 2012, pp: 68-70.

5. Donepudi Jagadish, Dr.Puli Ravi Kumar, Dr.K.Madhu Murthy., "Performance Characteristics of a Diesel engine operated on Biodiesel with Exhaust gas Recirculation," International Journal of Advanced Engineering Technology, E-ISSN 0976-3945, IJAET/Vol.II/ Issue II/April-June, 2011/202-208.
6. K. Rajan & K. R. Senthilkumar, "Effect of Exhaust Gas Recirculation (EGR) on the Performance and Emission Characteristics of Diesel Engine with Sunflower Oil Methyl Ester," Jordan Journal of Mechanical and Industrial Engineering, ISSN 1995-6665, Volume 3, Number 4, December 2009.
7. R.Senthilkumar, K.Ramadoss & R.Manimaran, "Experimental Investigation of Performance and Emission Characteristics by Different Exhaust Gas Recirculation Methods used in Diesel Engine," Global Journal of Researches in Engineering Mechanical and Mechanics Engineering, ISSN:0975-5861, Volume 13 Issue 1 Version 1.0 Year 2013.
8. A. Paykani, A. Akbarzadeh and M. T. Shervani Tabar, "Experimental Investigation of the Effect of Exhaust Gas Recirculation on Performance and Emissions Characteristics of a Diesel Engine Fueled with Biodiesel" IACSIT International Journal of Engineering and Technology, Vol.3, No.3, June 2011
9. Neville J. Bugli and Gregory S. Green, "Performance and Benefits of Zero Maintenance Air Induction Systems", SAE Technical Paper Series, April 11-14, 2005-01-1139.
10. Marius Toma, Gabriel Anghelache, Raluca Moisescu, "Replacement Period Evaluation of Petrol Engines Air Filters Based on Restriction Measurement", Advances in Automatic Control ISBN: 978-960-474-383-4, pp:71-76.
11. Sandip More1, Kishore Kumar Thapa and Subir Bera1, "Potential of Dust and Soot from Air-Filters of Motor Vehicle Engines as a Forensic Tool", Forensic Research J Forensic Res, Volume 4, Issue 1 1000177.pp:2-7.

INTERNATIONAL JOURNAL FOR TRENDS IN ENGINEERING & TECHNOLOGY
VOLUME 7 ISSUE 1 – JULY 2015 - ISSN: 2349 - 9303

Modified CI Engine Performance by Varying Injection Timing

Md. Fakhruddin H.N / Srinivas Ragahavan
Associate Professor/Assistant Professor
Methodist College of Engineering & Technology
Affiliated to Osmania University Hyderabad, India
mfhnn@yahoo.com

Dr. Mohammed Yousuf Ali / Dr.Manzoor Hussain
Professor& Principal
Nawab Shah Alam Khan College of Engineering & Technology
JNTUH College of Engineering Sultanpur
Hyderabad, India

Abstract— The ever increasing consumption of fossil fuel and petroleum products has been a matter of great concern for India. The huge outflow of foreign exchange on one hand and the increase in the price of crude oil on the other hand have affected the development of the country in contest of energy security. The consumption of diesel fuel is six times higher than that of gasoline in India and even a minute percentage of efficiency improvement for diesel fuel will save a considerable amount of foreign exchange. The energy consumption can be minimized by improving the efficiency of equipment i.e. CI engine. The present work where the modification of C I engine has been done, so as to induce turbulence for enhancing the vaporization characteristics of fuel in a combustible mixture by providing a rotating blade in the crown (bowl) of the reciprocating piston located in the main combustion chamber. The oscillation of the connecting rod causes the blade to rotate by an angle of 60°. This arrangement induces the turbulence in a combustible mixture during engine operation, there by facilitating a better combustion performance. The effects of operating parameters by in turbulence, varying injection pressure and injection timing on performance characteristics of diesel fuelled a compression ignition engine are to be investigated.

Keywords— C I Engine, Piston Crown, Swirl, Injection Pressure, Injection Timing and Performance.

I.INTRODUCTION

First standard engine is fully instrumented and connected to the dynamometer. The experiments are conducted at constant speed and at four different loads levels viz., 20%, 40%, 60% and 80% of full load. The required engine load percentage is adjusted by using the eddy current dynamometer.

Fig.1 shows the schematic diagram of a complete experimental setup for determining the effects of squish and tumble effect on the performance parameters of a compression ignition engine. It consists of a single cylinder, four stroke, water cooled a compression ignition engine connected to an eddy current dynamometer. It is provided with temperature sensors for the measurement of jacket water, calorimeter water, and calorimeter exhaust gas inlet and outlet temperature. It is also provided with pressure sensors for the measurement of combustion gas pressure and fuel injection pressure. An encoder is fixed for crank angle record. The signals from these sensors interfaced with a computer to an engine indicator to display P-Ɵ, P-V and fuel injection pressure versus crank angle plots. The provision is also made for the measurement of volumetric fuel flow. The built-in program in the system calculates indicated power, brake power, thermal efficiency, volumetric efficiency and heat balance. The software package is fully configurable and averaged P-Ɵ diagram, P-V plot and liquid fuel injection pressure diagram can be obtained for various operating condition.

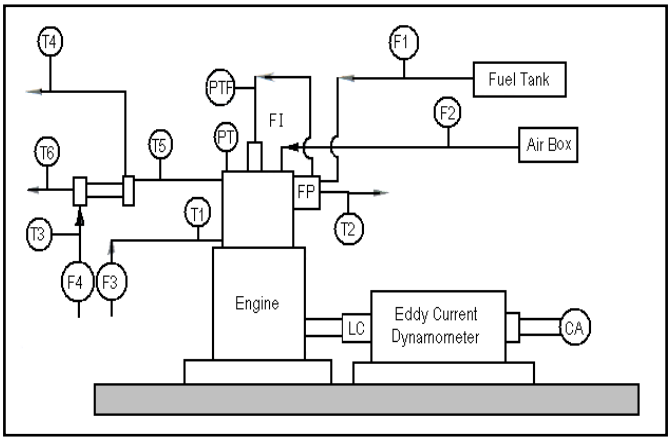

Fig.1

I. ENGINE MODIFICATION

Figure 2 and 3 shows the base line piston and modified piston respectively**.** Base piston is having a simple bowl shaped structure on the crown of it. But the modified piston is made with three chambers at 120 degree to each other. Same aluminum alloy material is used in fabrication of chamber. 2mm thick small strips are used to make the chambers.

Fig2

Fig3

II. EXPERIEMENTAL DETAILS

Experiments are conducted on an IV-stroke1cylinder 3.68Kw Kirlosker water cooled Diesel engine at the rated speed of 1500 RPM. From the experiments observed that combustibility of the fuel is very important in order get a good power output and good thermal efficiencies. The turbulence played an important role here. In the present work it can be obtained by arranging the rotating blades inside the piston bowl of the engine.

III.METHODOLOGY

The engine has a compression ratio of 20.1 and a normal speed of 1500 RPM controlled by the governor. An injection pressure of 250 BAR used. The engine is first run with neat diesel at loading condition such as 20%, 40%, 60% and 80%. Between two load trials the engine is allowed to become stable by running it for 3 minutes before taking the readings. At each loading condition, performance parameters, namely speed, exhaust gas temperature, brake power, peak pressure are measured under steady state condition. The experiments are repeated for various pressures and injection timing. With the above experimental results, the parameters such as total fuel consumption, brake specific fuel consumption, brake specific energy consumption, the brake thermal efficiency is calculated. And finally break specific fuel consumption, the brake thermal efficiency is plotted with respect to loading condition for diesel and each diesel oxygenate blend. From these plots, performance characteristics of the engine are determined.

IV.BRAKE THERMAL EFFICIENCY

The variation of break thermal efficiency with respect to load applied, 20.1 compression ratio, advanced, standard and retard injection timings for normal and modified pistons are shown in graph 1. Turbulence is caused by modified piston. Turbulence enhances mixing and probably produces a leaning effect. The turbulence in the combustion chamber makes the charge into homogeneous and increases the combustibility of fuel. So the brake thermal efficiency of modified piston is 2% more than the normal piston. The brake thermal efficiency is increasing with load applied. Compared to normal piston the efficiency increased by 2.2% for modified piston with 20.1 compression ratio. Thus we can get better improvement in the brake thermal efficiency. The brake thermal efficiency is maximum for the advanced injection timing compared to standard and retard timings. So that the brake thermal efficiency can be increased by more than 2% for modified piston of 20.1 compression ratio and advanced injection timing.

V.VOLUMETRIC EFFICIENCY

The variation of volumetric efficiency with respect to load applied, 20.1 compression ratios, advanced, standard and retard injection timings for normal and modified pistons are shown in graph 2. Volumetric efficiency depends up on the intake air into the combustion chamber. As the intake air into cylinder is more then we get better volumetric efficiency. By Turbulence we get better results. The volumetric efficiency of modified piston is 2-3 % more than the normal piston compared to normal piston the efficiency increased by 2.6% for modified piston with 20.1 compression ratio. For 20.1 compression ratio it is 250 Bar pressure and advance timing, so that the brake thermal efficiency can be increased by more than 2%.

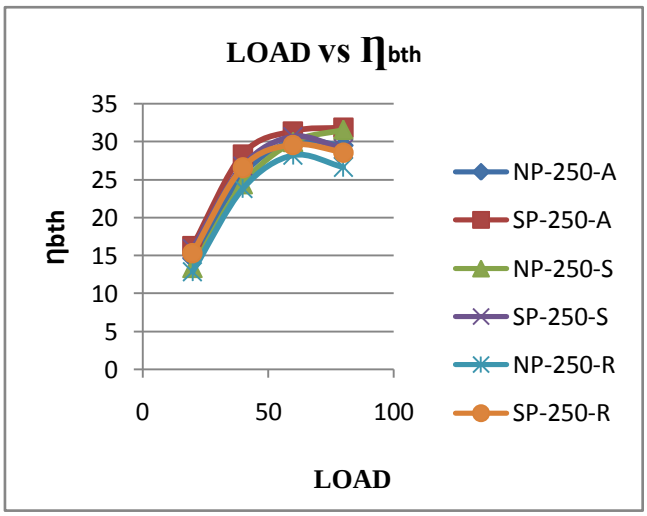

Graph1.comparison of brake thermal efficiencies with load applied for 20.1 Compression ratio and different injection timings of normal & modified pistons

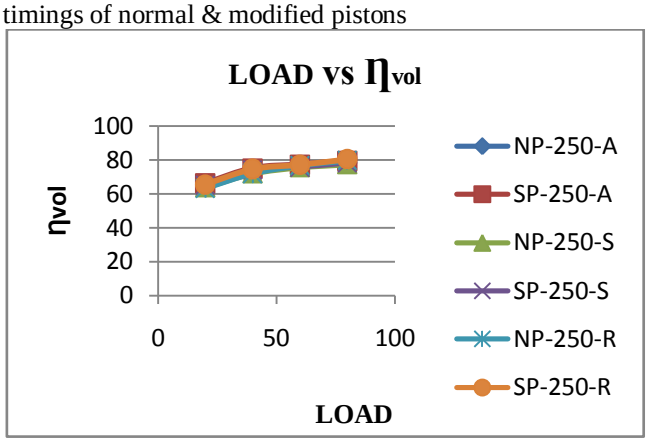

Graph 2.comparison of volumetric efficiencies with load applied for 20.1 compression ratio and different injection timings of normal & modified pistons.

VI.CARBON MONOXIDE (CO) EMISSION

Amount of Carbon monoxide (CO) emission present in the exhaust with respect to load applied, 20.1 compression ratio, advanced, standard and retard injection timings for normal and modified pistons are shown in graph 3. As the more amount of oxygen is available in cylinder results the reduction in CO emission. Due to the turbulence there will be a good amount of oxygen supply to cylinder. Turbulence is caused by modified piston. So that carbon monoxide emission are reduced by 15% Vol with modified piston. Carbon monoxide emission are reduced with load applied. For 20.1 compression ratio the reduction in CO emission is 17% Vol for modified piston. At 250 Bar pressure and the standard injection timing for 20.1 compression ratio, CO emission are reduced by 15 % with modified piston

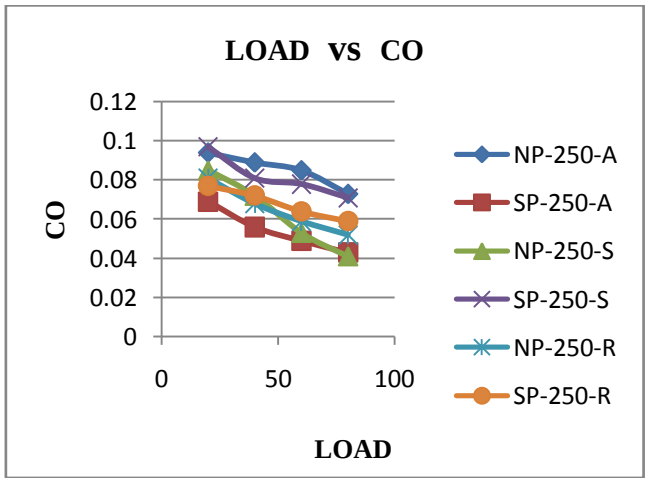

Graph 3.comparison of carbon monoxide emission with load applied for 20.1 compression ratio and different injection timings of normal & modified pistons.

VII. HYDRO CARBON (HC) EMISSION

Amount of Hydro Carbon (HC) emission present in the exhaust with respect to load applied, 20.1 compression ratio, advanced, standard and retard injection timings for normal and modified pistons are shown in graph 4. The HC emission for normal piston is 6 RPM and 4 RPM for swirl piston. This is shown in graph 4. Hence, with the use of swirl piston there has been a considerable decrease of 2 RPM in HC emission.

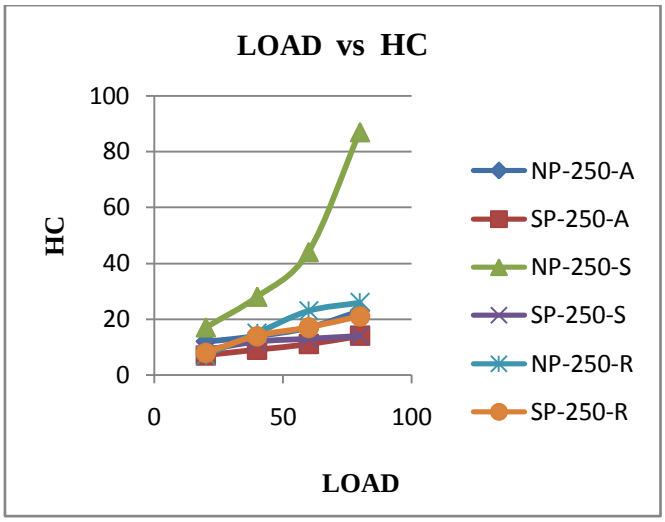

Graph 4.comparison of Hydro carbon emissions with load applied for 20.1 compression ratio and different injection timings of normal & modified pistons.

VIII.CARBON DIOXIDE EMMISION

Amount of Carbon dioxide (CO_2) emission present in the exhaust with respect to load applied, 20.1 compression ratio, advanced, standard and retard injection timings for normal and modified pistons are shown in graph 5. The CO_2 emission are 2.43 % Vol for swirl piston and 3.54 % Vol for normal piston. This is shown in graph 5. There by there is an increase of 1-2 % in CO_2 emission.

IX.OXIDES OF NITROGEN

The amount of Oxides of Nitrogen (NOX) emission present in the exhaust with respect to load applied for 20.1 compression ratios and advanced, standard and retard injection timings for normal and modified pistons is shown in graph 6. NOX is created mostly from nitrogen in the air. NOX is a very undesirable emission, and regulations that restrict the allowable amount continue to become more stringent. Released NOX reacts in the atmosphere to form ozone and is one of the major causes of photochemical smog. Most of this

will be nitrogen oxide (NO), with a small amount of nitrogen dioxide (NO_2), and traces of other nitrogen-oxygen combinations. NOX emission are reduced by 7% with modified piston. For 20.1 compression ratio the reduction in NOX emission is 8% for modified piston. Thus we can get a good reduction in NOX emission at 20.1 compression ratio and standard injection timing.

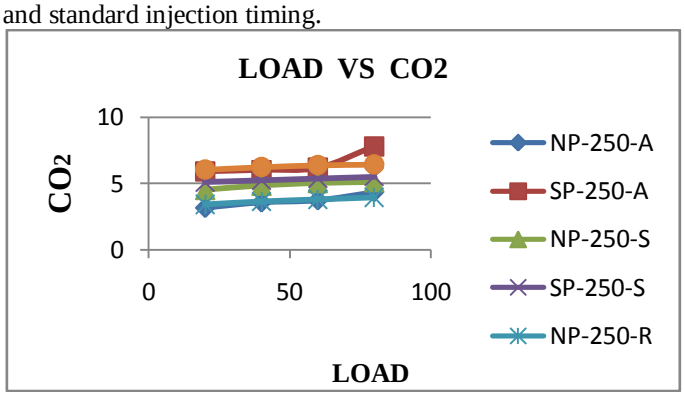

Graph 5.comparison of Carbon dioxide with load applied for 20.1compression ratio and different injection timings of normal & modified pistons.

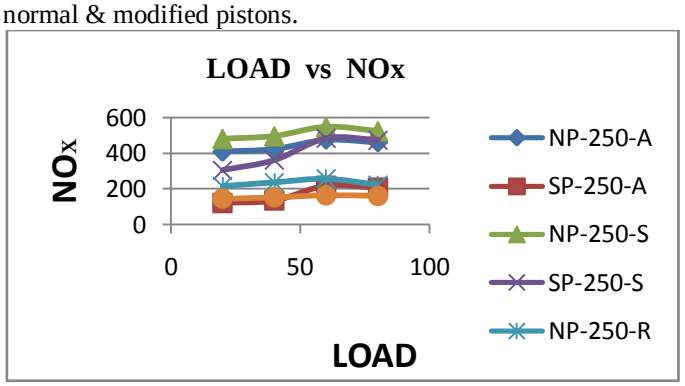

Graph 6.comparison of Oxides of Nitrogen with load applied for 20.1compression ratio and different injection timings of normal & modified pistons.

X.CONCLUSIONS

Fuel economy is most important factor for any I.C. engine. But environmental protection is much more important than fuel economy. It is necessary that modification in the engine may be incorporated so as to minimize the exhaust emission which are of topmost priority. In this connection, the geometry of the piston is modified by accommodating rotating blades in the piston crown to induce turbulence by means of swirl motion of charge.

- With the rotating blades inside the piston, turbulence is generated inside the combustion chamber. This further increases the combustibility of the mixture.
- The homogeneous mixture inside the combustion chamber increases the break thermal efficiency of modified piston by 2% compared to normal piston.
- The turbulence in the combustion chamber provides the homogeneous mixture; this increases the volumetric efficiency by 2% with modified piston.
- The turbulence in the combustion chamber increases the oxygen present in it. With this emissions are drastically reduced.
- The NOx emissions are increased due to the high temperatures in the combustion chamber caused by the turbulence.

REFERENCES

1. Katasuhika Moyamito Yoshiyuki Hosiba, Kiyotaka Hosono, Syunichi Hirao “Enhancement of Combustion by Means of Squish Pistons” MITSUBISHI MOTORS technical review 2006, NO 18.
2. B. Murali Krishna and J. M. Mallikarjuna “Tumble Flow Analysis in an Unfired Engine Using Particle Image elocimetry” World Academy of Science, Engineering and Technology 5-4- 2009.
3. John B. Heywood “Internal combustion Engine fundamentals”. McGraw-Hill International Edition, Automotive technology series. year 1998.
4. S. Baghdar Hosseini, K. Bashirnezhad, A.R. Moghiman, Y. Khazraii, N. and Nikoofal, “Experimental Comparison of Combustion Characteristic and Pollutant Emission of Gas oiland Biodiesel,” International Journal of Mechanical and Materials Engineering 1:1 2010.
5. Lu¨ Xingcai *, Hou Yuchun, Zu Linlin, Huang Zhen “Experimental Study on The Auto-Ignition and Combustion Characteristics in the Homogeneous Charge Compression Ignition (HCCI) Combustion Operation with Ethanol/n-heptanes Blend Fuels,” by Port Injection School of Mechanic and Power Engineering, Shanghai Jiaotong University, Shanghai, People’s Republic of China. Received 2 August 2005; received in revised form 23 April 2006.
6. Z.H.Huang, .W.Wang, H.Y.Chen,L.B.Zhou & D.M.Jiang“Study of combustion characteristics of a compression ignition engine fuelled with dimethyl ether,” Xi'an Jiao tong University Institute of Internal Combustion Engines, School of Energy and Power Engineering Xi'an, People's Republic of China.
7. M. Pugazhvadivu1 and S. Rajagopan Dept. of Mechanical Engineering, “Investigations on a Diesel Engine Fuelled with Biodiesel Blends and Diethyl Ether as an additive,” Dept. of Chemistry, Pondicherry Engineering College, Pondicherry, India- 605 014 ,Vol.2 No 5 (May 2009) ISSN: 0974- 6846.
8. Yi Ren, Zuohua Huang , Deming Jiang, Liangxin Liu, Ke Zeng, Bing Liu, Xibin Wang, “Combustion Characteristics of a Compression-Ignition Engine Fuelled with Diesel–di-Methoxy Methane Blends Under Various Fuel Injection Advance Angles,” State Key Laboratory of Multiphase Flow in Power Engineering, Xi’an Jiaotong University, Xi’an 710049, People’s Republic of China.

9. Kidoguchi Yoshiyuki (univ. Of Tokushima) Miwa Kei (univ. Of Tokushima) Yang.C (zexel corp., jpn) kato ryoji (Isuzu Motor Ltd.)"Effect of High Squish Combustion Chamber on Smoke and NOx Emissions of a Direct-Injection Diesel Engine" ISSN: VOL.2000; NO.Vol.4; PAGE.335-336(2000).

10. Performance and emission characteristics of a 4 stroke C.I. Engine operated on honge methyl Ester using artificial neural network Shivakumar, Srinivas Pai P., Shrinivasa Rao B. R.and Samaga B. S., From ARPN Journal of Engineering and Applied Sciences VOL. 5, NO. 6, JUNE 2010, ISSN 1819-6608.

11. Influence Of Injection Pressure On Performance Of Simarouba Biodiesel Engine, Sharun Mendonca, John Paul Vas, Raghu, Gangadhar Rao, Dr. Thomas Pinto, Dr.C.R.Rajashekar, Ramachandra, International Journal of Scientific & Engineering Research, Volume 4, Issue 7, July-2013 668, ISSN 2229-5518.

12. "Effect of Squish and Tumble on Performance, Combustion & Emission Characteristics of Bio- Diesel (Honge) Fuelled C.I Engine", B.C. Pradeep Kumar, C.R. Rajashekar and T.K. Chandrashekar from International Conference on Challenges and Opportunities in Mechanical Engineering, Industrial Engineering and Management Studies (ICCOMIM-2012),ISBN 978-93-82338-04-8

13. "Experimental Investigation on the Performance & Emission Characteristics of non edible oil (Jatropha Curcus & Honge) as an alternate fuel in variable compression ignition engine" from International Journal of Modern Engineering Research (IJMER),Vol.2, Issue.3 MayJune2012 pp-1375-1380 ISSN: 2249-6645

14. "Studies Of Squish And Tumble Effect On Performance Of Multi Chambered Piston Ci Engine Vinayaka Rajashekhar Kiragi" C.V. Mahesh, C.R. Rajashekhar, Naveen. P, Mohan Kumar S.P from International Journal of Engineering Research and Applications (IJERA) ,ISSN: 2248-9622.

Journal of Basic and Applied Engineering Research
p-ISSN: 2350-0077; e-ISSN: 2350-0255; Volume 2, Number 18; July-September, 2015, pp. 1586-1589

http://www.krishisanskriti.org/Publication.html

4 Stroke Engine with 2 Power Strokes

Md.Fakhruddin H.N. [1], Mohammed Yousuf Ali[2] and A.P.V. Prasad Rao[3]

[1]Methodist College of Engineering & Tech.
[2]Nawab Shah Alam Khan College of Engg. & Tech.
[3]Methodist College of Engineering & Tech.
E-mail: [1]mfhnn@yahoo.com, [2]yousufonline@yahoo.com, [3]prasadraoapv@gmail.com

Abstract—*In today's automobile world it is a great desirable challenge to build an engine having more power generation & less fuel consumption, which are desired parameters for the increased efficiency of the engine. For getting more power engine needs more fuel and if less fuel consumption is needed the power transmitted will be less. In conventional engines the heat energy using is 30% of produced energy and the remaining energy nearly 70% is going as waste. That means, to get more power from engine the fuel resources are wasting by wasting the 70% of produced energy, if less fuel consumption rate is desirable the more power generation should be sacrificed.*

Present innovation namely 4 stroke engine with 2power strokes is introduced in order to overcome these problem, the piston will execute 2nd power stroke without using gasoline fuel. By the introduction of this engine it is more beneficial to the automobile industry because of its more power generation & reduced fuel consumption rates.

1. INTRODUCTION

In the 2 stroke engine the piston makes 2 strokes in cylinder per cycle & the crank shaft makes one complete revolution. Advantage of 2 stoke engine is that the piston executes one power stroke per every 2 strokes of piston & one revolution of crankshaft and Disadvantage is, it consumes more fuel to develop one power stroke in a cycle where as in 4 stroke engine piston makes 4 strokes in cylinder per cycle and crank shaft makes 2 complete revolutions. Advantage of 4 stroke engine is that it consumes less fuel to develop one power stroke in a cycle and the disadvantage of 4 stroke engine is that the power generated by the engine is comparatively low. In the six stroke engine also fuel consumption is less but power generation is less compared to 2 stroke engine.

The present innovation "4 stroke engines with 2 power strokes" overcomes the disadvantages of both 2 stroke and 4 stroke engines. In this engine after 2stokes of the 2stroke engine, hot water is injected into cylinder and by utilizing the high temperatures present in the engine cylinder water changes its phase to steam and it will expand in the cylinder results in another power stroke. According to the experimental results 1ml of water will be converted to 1800 ml of steam when it changes its phase. So that the quantity of water required is also less.

This engine captures the heat energy wasting in case of conventional engine. In this engine a water tube will be placed in such a way that it will be in contact with engine cylinder walls and the other side of water tube will be in contact with an another pipe through which hot exhaust gasses are passing. The water in the water pipe or jacket will capture the heat emitting from engine without releasing it to the environment as waste and on other hand the water also captures the heat from the hot gasses escaping from engine cylinder as exhaust.

2. ADVANTAGES OF THIS ENGINE

1. This engine thermal losses are decreased and thermal efficiency may increased by 40-55%
2. And as the water is using as working fluid for second power stroke, the quantity of fuel require is reduced by 50-60%, resulting the 50-55% increase in the mechanical efficiency
3. Also the need of cooling system is eliminated which further results in reduction in weight of engine by 10%.
4. The environment pollution (by the emission of hot gasses into atmosphere) may be reduced by 45-55%.
5. Two power strokes

Two parallel functions take place, inside and outside the engine cylinder

3. EVENTS OUTSIDE ENGINE CYLINDER

1. Intake of water
2. Heating of water by means of heat exerted by the engine cylinder walls.
3. Heating of water again exhaust emission of fuels
4. Transfering the heated water into engine cylinder

4. EVENTS INSIDE THE ENGINE CYLINDER

Inside the engine cylinder again two functions takes place on both sides of the engine

1. Intake of hot water & power stroke by fuel
2. Compression and transfer of hot water &Exhaust of combustion products
3. Power stroke by steam & intake of fresh charge (Fuel+air)
4. Compression and transfer of charge & Exhaust of steam

5. PRINCIPLE OF 4STR. ENGINE WITH 2 POWER STR.

The 4 stroke engine with 2power strokes captures the heat waste from the 2 stroke engine and utilizes it to produce an additional power stroke of piston. Either steam or Air can be used as working fluid for second power stroke .It is not only giving an additional power stroke but also eliminates the need of a cooling system and makes engine lighter by 5-10 % & also increases the efficiency of the engine by 45-50 % . In this engine piston moves up and down 4 times out of which 2 are power strokes, one by fuel and other by steam. After the exhaust stroke in 2 stroke engine, instead of air fuel mixture hot water (which is converted to steam)will enter from water inlet & is exhausted in 4^{th} stroke. So that, overlapping of ports is reduced & better scavenging is obtained. Because of this action fuel consumption is reduced by 50% - 60 % & huge reduction in the pollution. The variety of fuels can be used to run the engine.

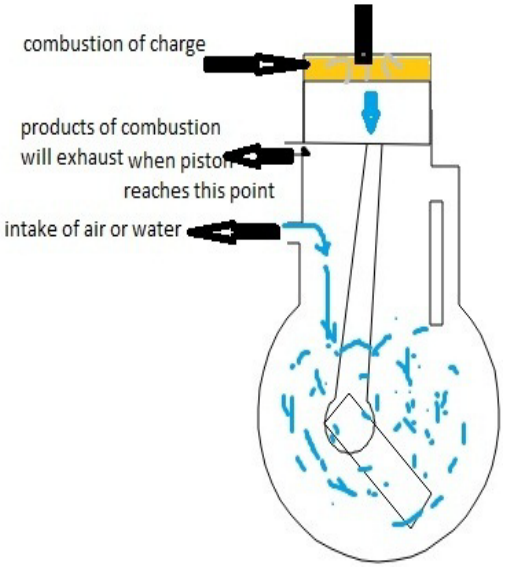

Fig. 1: Working of 4stroke with 2 power stroke

6. MODIFICATIONS IN 4 STROKE ENGINE WITH 2 POWER STROKES

Some modifications are to be done to the specific parts of the 2 stroke engine so as to run the engine successfully. The modifications are:-

1. A water jacket is to be placed around the engine cylinder walls to capture the heat from combustion chamber.
2. A pipe arrangement should be done around the water jacket to heat the water.

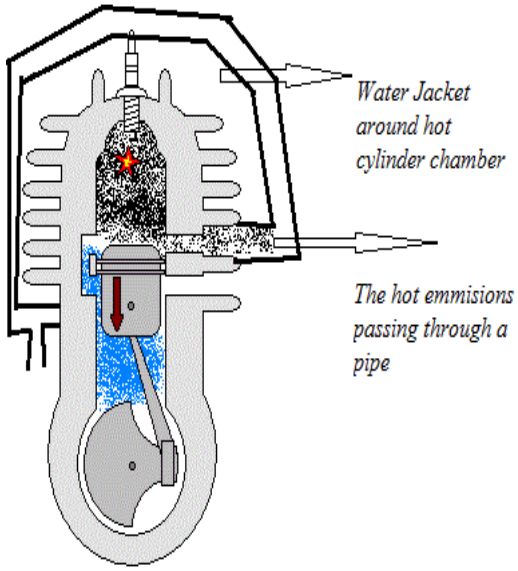

Fig. 2: Water jacket & pipe arrangement around the engine

3. Two solenoid valves are to be placed, one is to pump the (fuel+air) mixture and other is to pump the hot water to the inlet port.
4. The outlets of the two solenoid valves are made to be single pipe & it is to be connected to the inlet port of the engine.

7. WORKING OF THE 4 STROKE ENGINE WITH 2 POWER STROKES

The different strokes of the engine are

First stroke

In this engine two functions will happen on both sides of the piston. On the top side of the piston, combustion of fuel+air will occur resulting in a power stroke by the action of spark plug and on bottom side of the piston hot water will be sucked while the piston moves from TDC to BDC.

Second stroke

In the second stroke the products of combustion will be exhausted on top side of the piston & on the bottom side of the piston the hot water will be transferred to the combustion chamber through transfer port. In this stroke piston moves from BDC to TDC.

Third stroke

In the third stroke, the hot water entered into the combustion chamber will be converted to steam and will expand resulting an another power stroke on top side of the piston. On bottom side of the engine fuel+air mixture will be sucked & compressed. The piston moves from TDC to BDC.

Fourth stroke

In the fourth stroke fuel+air mixture will be sucked into the cylinder on bottom side of piston. And steam products will be exhausted on the top side of the piston. Piston moves from BDC to TDC.

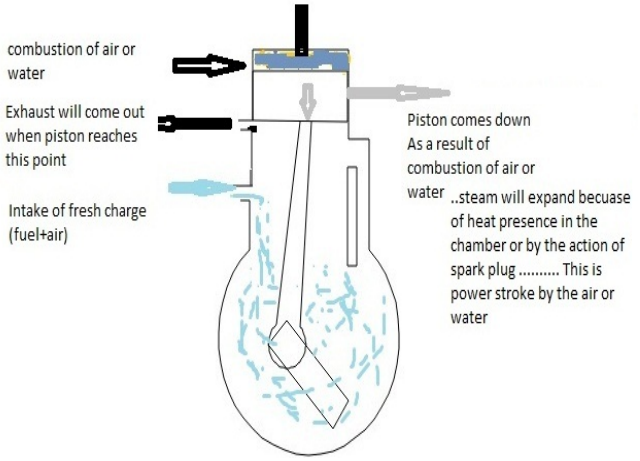

Fig. 3: Working strokes diagram for First stroke

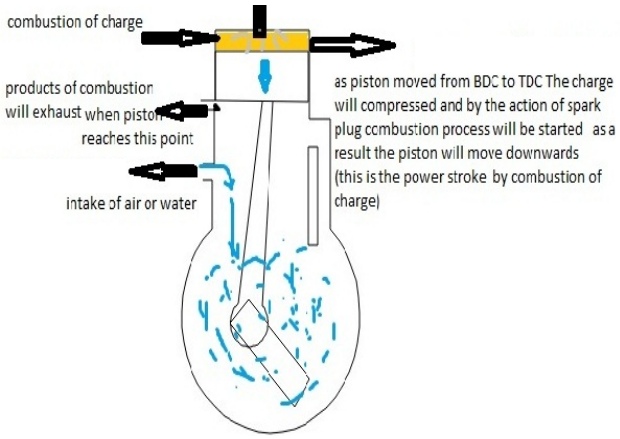

Fig. 4: Working strokes diagram for second stroke

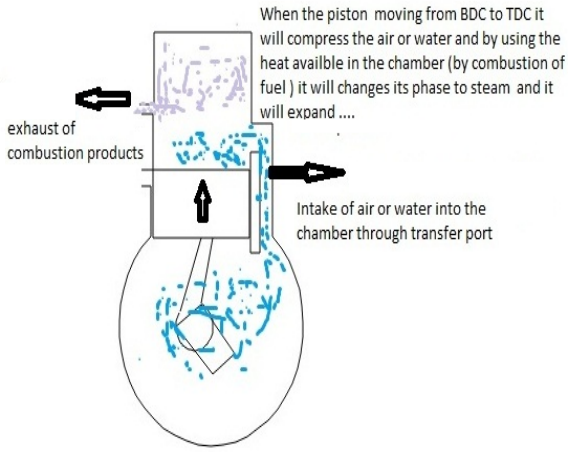

Fig. 5. Working strokes diagram for third stroke

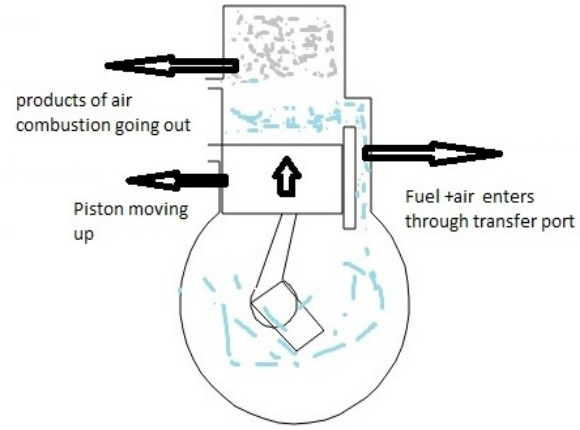

Fig. 6: Working strokes diagram for fourth stroke

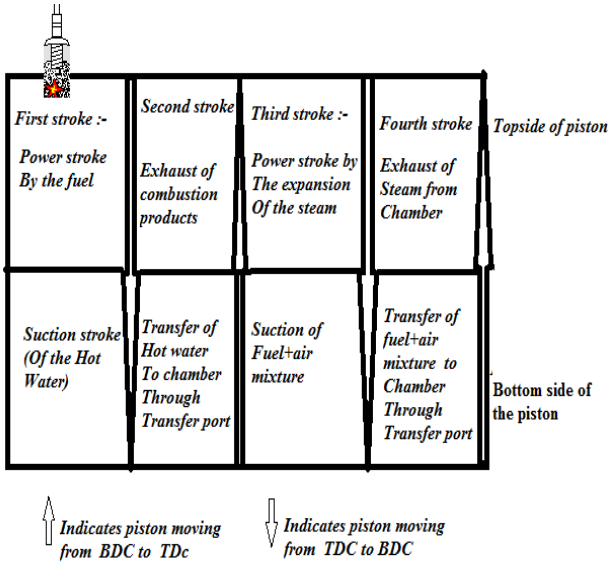

Fig. 7: Sequence of operations diagram

8. ADVANTAGES OF 4 STROKE ENGINE WITH 2 POWER STROKES OVER 2-STROKE,4-STROKE& 6-STROKE ENGINES

1. **Reduction in fuel consumption rate*:***
   As the water is using as working fluid, fuel consumption rate is reduced by 50-60%. It is more compared to 2-stroke, 4-stroke engines & approx. equal to six stroke engine.
2. **Increased torque or power generation:**
   In this engine because of 2 power strokes, the power generation is more compared to 2-stroke engine & as usually as the power generated/cycle in 2-stroke engine is more than 4-stroke and 6-stroke, the power generated/cycle is more in this engine.
3. **Reduction in pollution :**

Noise is reduced in this engine and the thermal pollution is reduced by 40-50 % ,on other hand black smoke, HC, CO,NOX are reduced in the exhaust.

4. **Multi fuel**
   A large variety of fuels can be used in this engine, like vegetable oil, fossil oils & animal grease. Methanol–Petrol mixture and Hydrogen–Petrol mixture are also recommended for this engine.
5. As the fuel consumption is reducing and power generation is more the mechanical efficiency is increased by 50-55%.
6. And as the water jacket is used around the chamber of the cylinder thermal efficiency is increased by 40-55%.also engine is light in weight as the cooling system is removed.

9. CONCLUSION

By the application of this technology the automobile industry has massive change in the both environment and world economy with increased power generation rates.

Wonderingly there is no perfect replacement for the internal combustion engines, to get any specific increase in parameters only the modifications are to be done resulting in improved economy & Eco friendly.

Introduction of this engine into automobile industry would have a enormous change in the efficiencies and the fuel consumption rate, assuming that the mechanical efficiency is increased by 45-55%, thermal efficiency is increased by 50-55 %, the fuel consumption rate is decreased by 50-60% and pollution emissions by 70-90% with increased power generation rates.

REFERENCES

[1] Lu¨ Xingcai *, Hou Yuchun, Zu Linlin, Huang Zhen―Experimental Study on The Auto-Ignition and Combustion Characteristics in the Homogeneous Charge Compression Ignition (HCCI) Combustion Operation with Ethanol/n-heptanes Blend Fuels,‖ by Port Injection School of Mechanic and Power Engineering, Shanghai Jiaotong University, Shanghai, People's Republic of China. Received 2 August 2005; received in revised form 23 April 2006.

[2] Yi Ren, Zuohua Huang , Deming Jiang, Liangxin Liu, Ke Zeng, Bing Liu, Xibin Wang,―Combustion Characteristics of a Compression-Ignition Engine Fuelled with Diesel–di-Methoxy Methane Blends Under Various Fuel Injection Advance Angles,‖ State Key Laboratory of Multiphase Flow in Power Engineering, Xi'an Jiaotong University, Xi'an 710049, People's Republic of China. [3] Marcus, A., *Semantic Driven Program Analysis*, Kent State University, Kent, OH, USA, Doctoral Thesis, 2003.

[3] Katasuhika Moyamito Yoshiyuki Hosiba, Kiyotaka Hosono, Syunichi Hirao―Enhancement of Combustion by Means of Squish Pistons‖ MITSUBISHI MOTORS technical review 2006, NO 18.

[4] NED, University Journal of Research, Volume No. 1, 2008.

[5] George Marchetti and Gilles Saint-Hilaire "A Six-Stroke, High-Efficiency Quasiturbine Concept Engine with Distinct, Thermally-Insulated Compression and Expansion Componets." (September-2005)

[6] Mr.Krishna Kanth, Mr.Shinivas. D. "Six Stroke Engine" (0109), www.Jntuworld.com

[7] James C. Conklin, James P. Szybist " A highly efficient six stroke internal combustion engine cycle with water injection for in-cylinder exhaust heat recovry" Energy 35 (2010) 1658-1664

[8] M.M.Gasim, L.G.Chui, K.A.Bin Anwar " Six Stroke Engine Arrangement" Proceedings of the 15 th Int. AMME Conference, 29-31 May, 2012

[9] M.M.Gasim, L.G.Chui, K.A.Bin Anwar " Six Stroke Engine Arrangement" Proceedings of the 15 th Int. AMME Conference, 29-31 May, 2012

[10] Chinmayee Karmalkar, Vivek Raut "Analysing the implementation of six stroke engine in a hybridcar". (January 10,2014)

[11] Kiran P "A feasibility study on waste heat recovery in six stroke engine" (2013)

[12] Mojtaba TAHAN, Saeed JAVAN, Mojtaba BIGLARI, " A comprehensive study on waste heat recovery from internal combustion engine using organic Rankine cycle ".

[13] http://www.crankshft design, materials, loads and Manufacturing, by EPI INC.Htm

[14] Mojtaba TAHAN, Saeed JAVAN, Mojtaba BIGLARI, " A comprehensive study on waste heat recovery from internal combustion engine using organic Rankine cycle "

[15] http://www.damninteresting.com/the-six-stroke-engine/

[16] P.K. Nagg, Engineering Thermodyanamics

[17] Pandiyaranjan V,Pandian M.C.,Malan E from Experimental Investigation on Heat Thermoelectric Systems for Greener Vehicles, www.greencarcongress.com (accessed 27/11/2011).

Modelling and Control of Higher Rating DC Motor with GA Based Optimized PID Controller

Article · June 2016

CITATIONS
0

READS
76

2 authors, including:

Raghu Chandra Garimella
Methodist College of Engineering and Technology
18 PUBLICATIONS **19** CITATIONS

SEE PROFILE

International Journal of Microelectronics and Digital Integrated Circuits
Vol. 2: Issue 1
www.journalspub.com

Modelling and Control of Higher Rating DC Motor with GA-Based Optimized PID Controller

Garimella Raghu Chandra[1*], *Garimella Atchyut*[2]
[1]Department of Mining Engineering, National Institute of Technology Karnataka, Surathkal, India
[2]SNVT Government College, Tanuku, Andhra Pradesh, India

Abstract

The usage of the common kind dc motors has its extended past. It has been used in the productions for numerous ages currently. They deliver humble means and exact method of controller. In addition, they have high efficiency and have a high starting torque versus falling speed characteristics which helps high starting torque and helps to prevent sudden load rise. But with such characteristics, the dc motors have some deficiencies that needed to be attended to which gave rise to design of some other alternative types of dc motors. For this purpose, a brief perspective will be considered on how the DC motors could be compensated in terms of control and stability. Therefore, this report would present a theoretical background of DC motors, design of simple model of basic DC motors. The PID controller is applied in various fields of engineering, and it is also a very important tool in telecommunication system. If there is a system and stability is desired, then PID could be very useful. The results analysis and discussion is presented.

Keywords: BLDC motor, genetic algorithm, machine modelling, PID controller, ZN method

Corresponding Author
E-mail: raghuchandhra@gmail.com

INTRODUCTION

DC Motors

A brief illustration and mathematical representation of DC motors will be discussed in this section based on the general concepts of electromagnetic induction. The most important part of these components that needs detail attention is the main field and the rotating windings (the stator and the rotor, respectively).

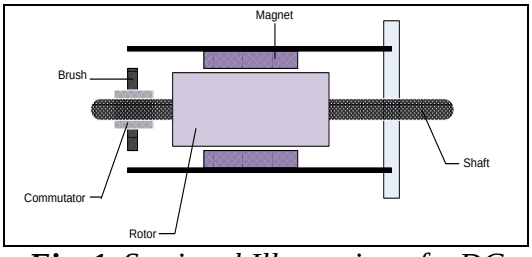

Fig. 1. *Sectional Illustration of a DC Motor.*[1]

As shown in Fig. 1., the stator is formed by the metal carcass with a permanent magnet enclosure which a magnetic field inside the stator windings. At one of the ends is the brush mountings and the brush gear which are used for electrical contacts with the armature (the rotor).[2]

DC MOTOR MODEL

Mathematical Model of a Typical DC Motor

A typical dc motor equivalent circuit is illustrated as shown in the circuit shown below in Fig. .

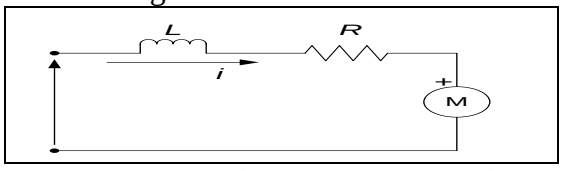

Fig. 2. *A Typical DC Motor Equivalent Electrical Circuit.*

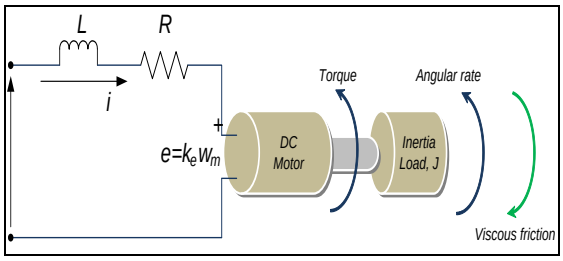

Fig. 3. *A Typical DC Motor Electromechanical System Arrangement.*[3]

The basic component represented are the armature resistance, R and the armature inductance L[4] in addition, there is the back emf, e. From the Fig. , the following equations are used to describe the relationship of operation.

Using the Kirchhoff's Voltage Law, *KVL*, the following Equation (1) is obtained:

$$V_s = Ri + L\frac{di}{dt} + e \quad (1)$$

At steady state (DC state of zero-frequency, $V_s = Ri + e$.
Therefore, for the non-steady state, Equation (1) is rearranged to make provision for the back EMF, as shown in Equation (2) below:

$$e = -Ri - L\frac{di}{dt} + V_s \quad (2)$$

where $V_s is$ the DC Source voltage and is the armature current.

Similarly, considering the mechanical properties of the dc motor, from the Newton's second law of motion, the mechanical properties relative to the torque of the system arrangement in Fig. and Fig. would be the product of the inertia load, J and the rate of angular velocity, ω_m is equal to the sum of all the torques, these follow with Equations (3 and 4) accordingly.

$$J\frac{d\omega_m}{dt} = \sum T_i \quad (3)$$

$$T_e = k_f\omega_m + J\frac{d\omega_m}{dt} + T_L \quad (4)$$

where T_e *is* the electrical torque,
k_f the friction constant,
J the rotor inertia,
ω_m the angular velocity, and T_L is the supposed mechanical load.

Since, the electrical torque and the back emf could be written as:

$$e = k_e\omega_m \text{ and } T_e = k_t\omega_m \quad (5)$$

where k_e is the back emf constant and k_t is the torque constant.

Therefore, re-writing Equations (2 and 3), the Equations (6 and 7) are obtained,

$$\frac{di}{dt} = -i\frac{R}{L} - \frac{k_e}{L}\omega_m + \frac{1}{L}V_s \quad (6)$$

$$\frac{d\omega_m}{dt} = i\frac{k_t}{J} - \frac{k_f}{J}\omega_m + \frac{1}{J}T_L \quad (7)$$

Using Laplace transform to evaluate the two Equations (6 and 7), the following are obtained appropriately (all initial conditions are assumed to be zero):
For Equation (6),[5–8]

$$\mathcal{L}\left\{\frac{di}{dt} = -i\frac{R}{L} - \frac{k_e}{L}\omega_m + \frac{1}{L}V_s\right\} \quad (8)$$

This implies,

$$si = -i\frac{R}{L} - \frac{k_e}{L}\omega_m + \frac{1}{L}V_s \quad (9)$$

For Equation (7),

$$\mathcal{L}\left\{\frac{d\omega_m}{dt} = i\frac{k_t}{J} - \frac{k_f}{J}\omega_m + \frac{1}{J}T_L\right\} \quad (10)$$

This implies,

$$s\omega_m = i\frac{k_t}{J} - \frac{k_f}{J}\omega_m + \frac{1}{J}T_L \quad (11)$$

At no load (for $T_L = 0$); Equation (11) becomes:

$$s\omega_m = i\frac{k_t}{J} - \frac{k_f}{J}\omega_m \quad (12)$$

From Equation (12), i is made the subject for a substitute into Equation (9).

$$i = \frac{s\omega_m + \frac{k_f}{J}\omega_m}{\frac{k_t}{J}} \quad (13)$$

$$\left(\frac{s\omega_m + \frac{k_f}{J}\omega_m}{\frac{k_t}{J}}\right)\left(s + \frac{R}{L}\right) = -\frac{k_e}{L}\omega_m + \frac{1}{L}V_s \quad (14)$$

Equation (14) becomes:

$$\left\{\left(\frac{s^2J}{k_t}+\frac{sk_f}{k_t}+\frac{sRJ}{k_tL}+\frac{k_fR}{k_tL}\right)+\frac{k_e}{L}\right\}\omega_m=\frac{1}{L}V_s \quad (15)$$

And Equation (15) finally resolved to Equation (16):

$$V_s=\left\{\frac{s^2JL+sk_fL+sRJ+k_fR+k_ek_t}{k_t}\right\}\omega_m \quad (16)$$

The transfer function is therefore obtained as follows using the ratio of and the angular velocity, ω_m to source voltage, V_s.

That is,

$$G(s)=\frac{\omega_m}{V_s}=\frac{k_t}{s^2JL+sk_fL+sRJ+k_fR+k_ek_t} \quad (17)$$

From these, the transfer function could be derived accordingly as follows:

That is,

$$G(s)=\frac{\omega_m}{V_s}=\frac{k_t}{s^2JL+(RJ+k_fL)s+k_fR+k_ek_t} \quad (18)$$

Considering the following assumptions:

(1) The friction constant is small, that is, k_f tends to 0, this implies that

(2) $RJ \gg k_fL$, and

(3) $k_ek_t \gg Rk_f$

And the negligible values zeroed, the transfer function is finally written as;

$$G(s)=\frac{\omega_m}{V_s}=\frac{k_t}{s^2JL+RJs+k_ek_t} \quad (19)$$

So by re-arrangement and mathematical manipulation on "*JL*", by multiplying top and bottom of Equation (19) by:

$$\frac{R}{k_ek_t}\times\frac{1}{R}$$

Equation (20) is obtained after the manipulation,

$$G(s)=\frac{\frac{1}{k_e}}{\frac{RJ}{k_ek_t}\frac{L}{R}s^2+\frac{RJ}{k_ek_t}s+1} \quad (20)$$

From Equation (13), the following constants are gotten,

The mechanical (time constant),

$$\tau_m=\frac{RJ}{k_ek_t} \quad (21)$$

The electrical (time constant),

Substituting the Equations (21 and 22) into Equation (20), it yields;

$$G(s)=\frac{\frac{1}{k_e}}{\tau_m\cdot\tau_e\cdot s^2+\tau_m\cdot s+1}$$

constants.m[9]

```
% Start of code
% Sprint Electric flat motor parameters
used in the modeling
%
% Characteristics parameters
R = 120;         % Ohms, Terminal
Resistance phase to phase
L = 0.560;    % Henrys, Terminal
Inductance phase to phase
Kt = 25.5;    % Nm/A, Torque constant
Ks = 374        % rpm/V, Speed constant
tm = 171e-3;    % seconds, s, Mechanical
Time constant
J = 92.5e-7;     % kg.m^2, Rotor
inertia, given in gcm^2
```

evaluatedconstants.m[9]

```
% Evaluated parameters not given
constants
te = L/(R);                % seconds, s,
Electrical Time constant
Ke = (R*J)/(tm*Kt);        % Back emf
constant
```

topenloop.m[9]

```
% Start of code
% includes constant parameters
constants
% includes evaluated constants
evaluatedconstants
% Transfer function
G = tf([1/Ke],[tm*te tm 1]);
% Plots the Step Response diagram
figure;
step(G, 0.5);
title('Open Loop Step Response
diagram');
xlabel('Time, secs')
ylabel('Voltage, volts')
grid on;
```

HIGH RATING DC MOTOR

The DC motor provided for this thesis is the EC 45 flat Ø45 mm, 145 KW, 190 h.p from sprint electric motors. The order number of the motor is 200142. The parameters used in the modelling are

extracted from the datasheet of this motor with corresponding relevant parameters used. Find below in Table 1 the major extracted parameters used for the modelling task.

RATINGS OF DC MOTOR

***Table 1**. Motor Parameters Used.*[8]

	Sprint electric motor data	Unit	Value
	Values at nominal voltage		
1	Nominal Voltage	V	550
2	No load Speed	rpm	4370
3	No load Current	A	15
4	Nominal Speed	rpm	2550
6	Nominal Current (max. continuous current)	A	335
8	Starting Current	A	65
9	Maximum Efficiency	%	89
10	*Terminal Resistance phase to phase*	Ω	120
11	*Terminal Inductance phase to phase*	H	0.560
12	*Torque Constant*	Nm/A	25.5
13	*Speed Constant*	rpm/V	374
14	Speed/Torque Gradient	rpm/Nm	176
15	*Mechanical time constant*	ms	171
16	*Rotor Inertia*	gcm^2	92.5

DC SPRINT ELECTRIC MOTOR MATHEMATICAL MODEL

The mathematical model of the DC motor is modelled based on the parameters from Table 1 using the Equation (23). This is illustrated below:

$$G(s) = \frac{\frac{1}{K_e}}{\tau_m \cdot \tau_e \cdot s^2 + \tau_m \cdot s + 1} \qquad (22)$$

So the values for K_e, τ_m and τ_e need to calculated to obtain the motor model.

From equation,

$$\tau_e = \frac{L}{R}$$

$$\tau_e = \frac{0.560}{120}$$

$$\boldsymbol{\tau_e} = 4.6667 \times 10^{-3} \qquad (23)$$

But τ_m is a function of R, J, K_e and K_t,

Where

R = 120 Ω; J_{Rotor} = 92.5 gcm^2 = 9.25 × 10^{-6} Kgm^2; $K_t = 25.5$ Nm/A; τ_m = 171 $m$secs;

From Equation (21), K_e could be obtained: That is,

$$\boldsymbol{\tau_m} = \frac{R.J}{K_e.K_t} = 0.171\ sec$$

$$\boldsymbol{K_e} = \frac{R.J}{\tau_m.K_t} = \frac{120 \times 9.25 \times 10^{-6}}{0.171 \times 25.5}$$

$$= 2.5455 \times 10^{-3}\ \frac{\text{v} - \text{secs}}{\text{rad}}$$

Therefore, the G(s) becomes:

$$G(s) = \frac{392.85}{4.667 \times 10^{-3} \times 0.171 \cdot s^2 + 0.171 \cdot s + 1}$$

$$G(s) = \frac{392.85}{0.798 \times 10^{-3} \cdot s^2 + 0.171 \cdot s + 1} \qquad (24)$$

The G(s) derived above in the Equation (24) is the open loop transfer function of the DC Sprint Electric motor using all necessarily sufficient parameters available.

OPEN LOOP ANALYSIS OF MOTOR MODEL

The open loop analysis would be done using the MATLAB®/SIMULINK®. And the corresponding stability analysis is given likewise to see the effect thereafter when there is closed loop system incorporation.

Open Loop Analysis Using MATLAB m-File

With the aid of the DC motor parameters provided, the open loop analysis is done by considering the stability factors and making the necessary plots for this analysis. The below plot include the step response. For this, separate m-files were created for the constants, evaluated constants and the main files (Figure 4).

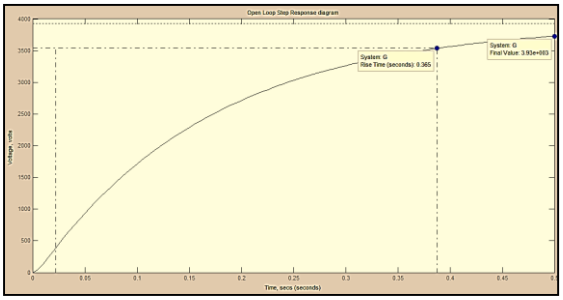

***Fig. 4.** Open Loop Step Response.*

PID DESIGN CONCEPT

The proportional-integral-derivative (PID) controller is about the most common and useful algorithm in control systems engineering. In most cases, feedback loops are controlled using the PID algorithm. The main reason why feedback is very important in systems is to be able to attain a set-point irrespective of disturbances or any variation in characteristics of any form ref.[5]

The PID controller is always designed to correct error(s) between measured process value(s) and a particular desired set-point in a system.

A simple illustration on how the PID works is given below:

Consider the characteristics parameters – proportional (P), integral (I), and derivative (D) controls, as applied to the diagram below in Fig. ***5.***, the system, S is to be controlled using the controller, C; where controller, C efficiency depends on the P, I and D parameters.

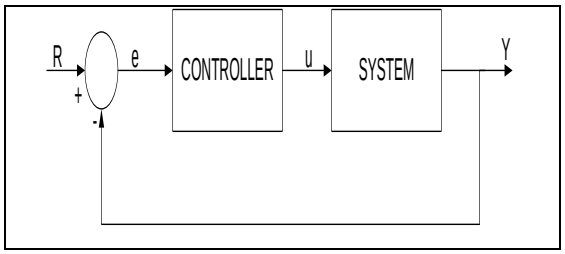

Fig. 5. *A Typical System With a Controller.*

The controller provides the excitation needed by the system and it is designed to control the overall behaviour of the system.

The PID controller has several categories of structural arrangements. The most common of these are the series and parallel structures and in some cases, there are the hybrid form of the series and the parallel structures.

The following shows the typical illustrative diagrams of common PID controller structures. Typically, the function of the form shown in Equation (25) is applicable in this kind of PID controller design.

$$K_P + \frac{K_I}{s} + K_D \cdot s = \frac{K_D s^2 + K_P s + K_I}{s} \qquad (25)$$

where K_P is the Proportional gain,
K_I the Integral gain,
and K_D is the Derivative gain.

$$u = K_P e + K_I \int e dt + K_D \frac{de}{dt} \qquad (26)$$

More also, it should be noted that the major goal of the PID parameters is to obtain a fast rise time with minimum overshoot and no (*almost no*) steady-state error.

PID CONTROLLER TUNING PARAMETERS

Under this section a critical analysis would be done on the PID tuning criteria and the parameters involved.[6] Before a detail analysis is done, a quick look at the tuning methods is considered first and thereafter, specific tuning parameters are computed for the BLDC maxon motor. Some of the generally used tuning methods are the Trial and Error method, the Ziegler-Nichols method (1st), Improved Ziegler-Nichols method (2nd), Cohen-Coon method, Genetic Algorithms and so on. For this work, the Ziegler-Nichols tuning method would be given a priority (Figure 6).[7]

Trial and Error Tuning Methods

This method is crude but could help in getting an overview of what the PID parameters could be like and their effects on the whole system model. It is particularly time consuming because of its trial and format. But a computational stability rule was needed to set a mark for the trial and effect. This is done by using

the Routh-Hurwitz stability rule as shown below. Under this, emphasis would be mainly on the PID combination.

The Routh–Hurwitz stability rule

From the various designs needed for this trial, a brief stability check is needed to make the trial and error at the first instance. It would be observed that the only design near the perfect (open-loop – which is without compensation or controller) is the PID. To have a more appropriate trial and error value, the following steps would be followed for only the PID structure.

From the PID controller Equation (27),

$$K_P + \frac{K_I}{s} + K_D \cdot s = K_P \times \left(1 + \frac{1}{T_I \cdot s} + T_D \cdot s\right) \quad (27)$$

Similarly,

$$K_P + \frac{K_I}{s} + K_D \cdot s = \frac{K_P \cdot s + K_I + K_D \cdot s^2}{s} \quad (28)$$

This is used in the m-file tclosedloopPID_TrialError4.m and it is convuled with the motor model.

Keeping the K_P part, with T_I and T_D set to infinity and zero respectively. A controller gain, K_C could be obtained that would sustain the oscillation output. This value serves as the ultimate gain, K_{CU}. For a proper oscillation, K_C is set to be less than K_{CU}.

Therefore, we have:

$$1 + \mathrm{K_{CU}} \cdot \mathrm{G(s)} = 0 \quad (29)$$

$$1 + K_{CU} \cdot \frac{392.85}{0.798 \times 10^{-3} \cdot s^2 + 0.171 \cdot s + 1} = 0 \quad (30)$$

Equation (30) becomes,

$$0.798 \times 10^{-3} \cdot s^2 + 0.171 \cdot s + 1 + 392.85 \cdot K_{CU} = 0 \quad (31)$$

So, for stability purposes, KCU's range of values could be obtained by using the Routh-Hurwitz condition of stability. This is computed below:

s^2	0.768×10^{-3}	$1 + 392.85 \cdot K_{CU}$
s^1	0.171	0
s^0	$\mathbf{1 + 392.85 \cdot K_{CU}}$	–

According to Routh–Hurwitz condition, the obtained characteristics Equation (31) should be spread into column as shown above and the s0 is evaluated as follows (because it has the assumed unknown KCU which would be evaluated):

$$\mathrm{s^0(1st\ row)} = -\frac{\begin{vmatrix} 0.768 \times 10^{-3} & 1 + 392.85 \cdot K_{CU} \\ 0.171 & 0 \end{vmatrix}}{0.171}$$

$$\mathrm{s^0(1st\ row)} = -\frac{(0.768 \times 10^{-3} \times 0) - (1 + 392.85 \cdot K_{CU})(0.171)}{0.171}$$

$$= 1 + 392.85 \cdot K_{CU}$$

For stability sake, the 1st column after the s-column must not have any sign change (that is, no change from + to – or – to +). Therefore, $\mathrm{s^0(1st\ row)}$, must be greater than zero.

This implied that,

$$1 + 392.85 \cdot \mathrm{K_{CU}} > 0$$

Then,

$$392.85 \cdot \mathrm{K_{CU}} > -1$$

$$\mathrm{K_{CU}} > \frac{-1}{392.85} = -0.002545$$

$$\mathrm{K_U} = \mathrm{abs(K_{CU})} = 0.002545$$

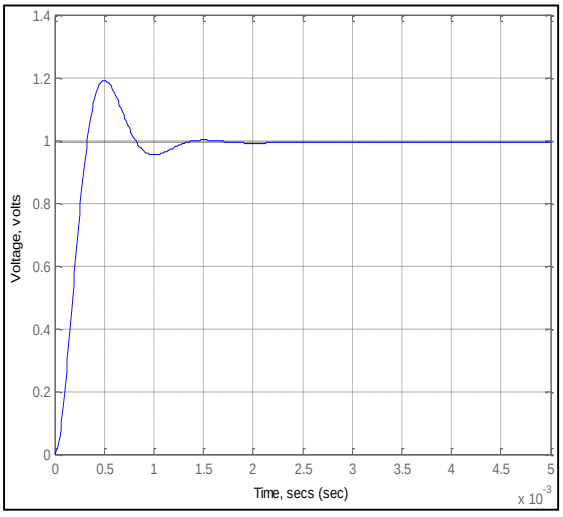

Fig. 6. *Closed Loop Response of the System with PID Controller*

OVERVIEW OF GENETIC ALGORITHM

Genetic algorithms try to imitate the properties of natural selection and natural genetics. It begins with initial population that consists of coded strings of binary numbers, called chromosomes that hold possible solutions of the problem. Their performance is evaluated by a fitness function. Strings with higher fitness value are likely to survive to the next generation as parents. It uses three operators namely selection, crossover and mutation to produce next generations. This procedure is repeated until it finds the optimal solution to the problem.[10]

TUNING OF PID CONTROLLER USING GA APPROACH

The values of the PID controller parameters Kp, Ti and Td are optimized using GA to ensure optimal control performance. The steps involved in evaluating best possible controller gains are listed below.

Initialization of Parameters

To initialize GA, we have to define certain initial parameters. The performance of the designed controller depends heavily on how well we assigned the values to these parameters. Parameters with their assigned values are listed below:

INITIALIZATION PARAMETERS

Generations	*100*
Population size	*30*
Bit length of the considered chromosome	*6*
Maximum number of generations	*0.8*
Selection method	*Arithmetic Crossover*
Crossover probability	*0.8*
Mutation type	*Uniform mutation*
Mutation probability	*0.05*

Objective Function for the GA

To calculate the fitness of each chromosome, selection of objective function is very critical. The objective functions are mean of the Squared Error (MSE), Integral of Time multiplied by Absolute Error (ITAE), Integral of Absolute Magnitude of the Error (IAE), and Integral of the Squared Error (ISE).[4] An integral Absolute Error (IAE) criterion is used in this paper for calculating performance index of controller as mentioned below.

$$IAE = \int_0^T e(t)dt$$

where T = 1 sec.

The Fitness Values

Purpose is to diminish the worth of performance index. The rightest chromosome will be the unique which has minimum value of that performance index,[5] so we can describe fitness value as

$$Fitness\ value = \frac{1}{PerformanceIndex}$$

Termination Criteria

Termination of algorithm takes place when the value of the fitness function for the best point in the current population is less than or equal to fitness limit and the change in the value of fitness function is less than function tolerance. The best member of the population was selected and plotted in the graph. The variation of the PID parameters Kp, Ti and Td are shown, respectively.

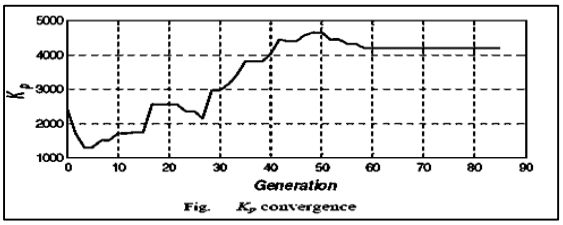

Fig. K_p convergence

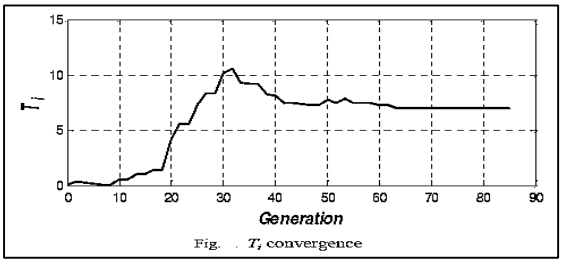

Fig. T_i convergence

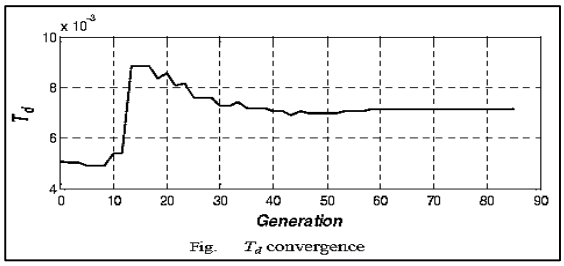

Fig. T_d convergence

PID parameters acquired after GA optimization are listed below:

TABLE OPTIMIZED GAIN USING GENETIC ALGORITHMS

K_p	T_i	T_d
4200	*7*	*0.0071429*

SIMULATION RESULTS AND COMPARISON

With optimized PID gains using GA, the step response of the controlled system is shown in below figure along with the response obtained from ZN method,

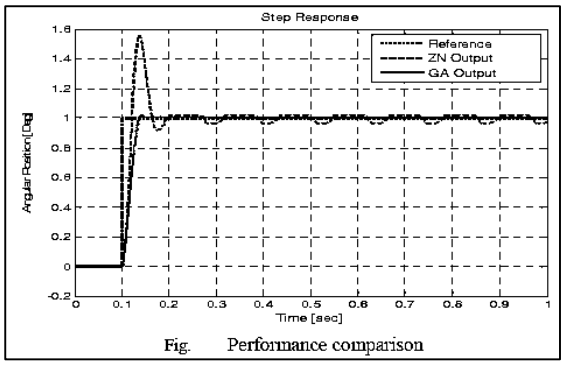

Fig. Performance comparison

It is apparent from the above step response that the controller performance with GA optimized gains is quite efficient as compared to the response obtained from ZN method. It is clear from that the controller designed with ZN method has high overshoots as was observed in the step response, while the controller with GA optimized gains precisely follows the input signal.

CONCLUSION

In this paper, modelling of DC motor and its optimized PID position control design using GA is presented. Comparative study is carried out in which the response of GA-based controller is compared with the controller designed using ZN method. It is obvious from simulation results that the controller performance with GA optimized gains is much more efficient than the ZN method in terms of rise time, settling time, overshoot and set point tracking. However ZN method is good for providing the starting values of PID gains for GA optimization. Hence it can be concluded that GA provides an efficient controller tuning methodology for obtaining improved and accurate performance of a system.

REFERENCES

1. Anon. Basics of DC drives and related products, *Siemens Training Education Program*. STEP 2000 Series, 1994.
2. Anon. *Some Principles of DC Motors.* Crouzet Motor Manuals, 2000.
3. Yedamale P. *DC Motor Fundamentals.* Microchip Technology Incorporated, 2003.
4. Sen P.C. *Principles of Electric Machines and Power Electronics*. John Wiley & Sons; 1997.
5. Anon. *Control Tutorials for MATLAB: PID Tutorial*. Carnegie-Mellon University and University of Michigan Online resources, 2009.
6. Anon. *DSP Solutions for DC Motors*. Texas Instruments Incorporated, 1997.
7. Åstrom K., Hägglund T. *PID Controllers: Theory, Design and Tuning*. 2nd Edn., 1994.
8. Anon. Sprint EC Motor, EC 45 flat Ø45 mm, brushless, 145 KWatt, 190 h.p. flat motor, 2008.
9. Anon. MATLAB/SIMULINK Documentations (Help file), 2008.
10. Srikanth S., Raghu Chandra G. Modelling and PID Control of BLDC Motor with the help of Genetic Algorithm, *IEEE – International Conference on Advances in Engineering, Science and Management.* ISBN: 978-81-909042-2-3, 639-644, India.

Application of High-Speed Videography in Assessing the Performance of Blasts

Article · December 2015

CITATION
1

READS
482

4 authors, including:

Rama Sastry Vedala
National Institute of Technology Karnataka
61 PUBLICATIONS **56** CITATIONS
SEE PROFILE

Raghu Chandra Garimella
Methodist College of Engineering and Technology
18 PUBLICATIONS **19** CITATIONS
SEE PROFILE

Saiprasad Sreekumar Ajitha
National Institute of Technology Karnataka
2 PUBLICATIONS **1** CITATION
SEE PROFILE

International Journal of Geological and Geotechnical Engineering
Vol. 1: Issue 2
www.journalspub.com

Application of High-Speed Videography in Assessing the Performance of Blasts

Vedala Rama Sastry[*], *G. Raghu Chandra, N. Adithya, S.A. Saiprasad*
Department of Mining Engineering, NITK, Surathkal, Mangalore, India

Abstract

Blasting can be considered as the most crucial process in an opencast mine. It is therefore important for mining engineers to understand the effect of geological discontinuities and blast design parameters on the results of blasting. Bench height and burden are very important parameters affecting stiffness of bench. Joints alter the results of blasting, by making explosive energy utilization ineffective. Modern tools like high-speed videography reveal many aspects of fragmentation process, which otherwise are difficult to visualize and understand. An attempt is made through this paper to present some of the research results of model-scale studies, coupled with field study results related to bench height, and joints in order to improve blast results.

Keywords: bench height, burden, gas energy, geological discontinuities, high-speed videography

Corresponding Author
E-mail: vedala_sastry@yahoo.co.in

INTRODUCTION

In this paper, a special emphasis is given to the role of jointing, bench height and delay in blast rounds, the three major parameters in blast design. Detonation of an explosive charge confined in a blasthole releases a vast amount of chemical energy, which is then transformed into gaseous energy.

This gaseous energy exerts an enormous amount of pressure on the blasthole wall. This pressure results in the generation of shockwaves carrying shock energy. According to Sadwin and Junk (1965),[1] the explosive can be categorized in this phase by two pressures:

(1) Detonation pressure: dynamic pressure associated with the detonation wave.
(2) Explosive pressure: pressure developed when the explosive reacts to produce gaseous products.

Thus, the detonation of an explosive under confinement creates two types of energies: strain energy (5–20% of total explosive energy) and gaseous energy (80–95% of total explosive energy).

For an efficient blast, it is necessary to utilize the explosive energy for productive work as much as possible. Design of an efficient blast requires sound knowledge about the role of blast design parameters, explosive characteristics and the structural discontinuities in fragmentation process. Joints, the most commonly occurring discontinuities in the rock mass play a significant role in influencing the blast results.

This study makes an effort at relating various parameters of a blast, which can be used to design an efficient blast, with special emphasis on the usage of high speed videography.

LITERATURE REVIEW

Role of Strain and Gas Energies

Before 1959, it was generally perceived that rock breakage is caused mainly by strain waves. However, Fogelson *et al*. (1959)[2] conducted a series of tests to measure the explosive energy transmitted to rock mass by strain waves, and determined that the strain waves only play a minor role in fragmentation.

Burden rock movement studies by Noren (1956)[3] showed that strain waves cannot be the dominant factor in rock fragmentation, as he showed that it had time to travel the burden distance at least six times before any surface rock movement started. Also, he observed that the burden accelerated continuously during its motion. Had strain waves acted upon it, then the motion would have been discontinuous. Saluja (1963)[4] found out that in case of high explosives, the rock is fractured by a combination of gaseous and strain energy. However, he also showed that in low explosives (gunpowder), the breakage occurs solely due to gaseous energy.[5]

In 1971, Kutter and Fairhurst[6] proposed a more generalized theory based on their experiments. They argued that:

(1) Both strain waves and gaseous energy play an important role in fragmentation.
(2) Strain wave functions to precondition the rock mass by initiating radial cracks.
(3) Gaseous energy then expands and extends the cracks.
(4) Presence of free surfaces favors extension of gas pressurized radial cracks.
(5) In-situ stresses significantly influence the direction of radial crack propagation.

According to the gas pressurization configuration given by Kutter and Fairhurst (1971),[6] gases under high pressure penetrate into radial cracks forming a hydrostatically stressed cylinder of material where the hydrostatic stress is equal to the gas pressure (Figure 1). This large hydrostatically stressed cylinder applies pressure at the back of the burden, inducing bulk rock movement (Figure 2).

Fragmentation of rocks can be explained by another mechanism, known as "Flexural Rupture Mechanism," which involves the transverse fracturing of segments formed by radial cracks (Figure 3).

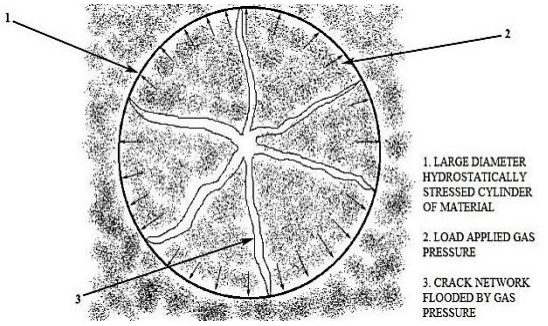

Fig. 1. *Hydrostatic Stress Field Created Around a Blast hole.*[6]

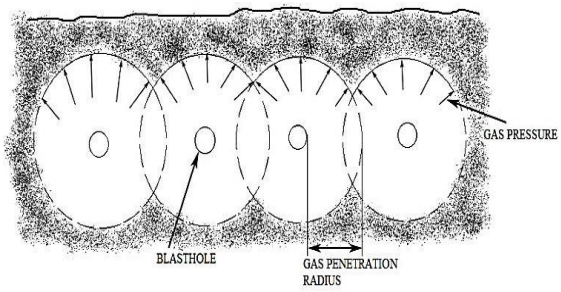

Fig. 2. *Gas Pressure Applied Load at the Periphery of Hydrostatically Stressed Cylinders Causing Rock Movement.* [7]

In this theory, 90% of the total energy required to break the rock was assumed to come from gaseous pressure alone. The sustained gaseous pressure drives radial cracks through the burden upto the free face and displaces the rock through bending, in the direction of the least resistance, generally following the naturally occurring weakness planes.

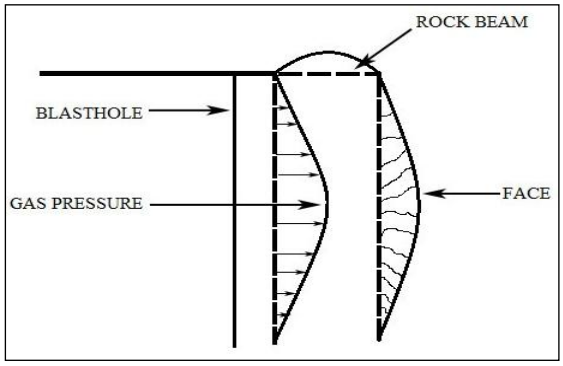

Fig. 3. *Rock Breaking by Flexural Bending.*[8]

Ash and Smith introduced the stiffness theory in 1976,[9] according to which, the degree of fragmentation depended upon the stiffness property of the burden rock. In terms of blasting, *Burden*, *Spacing*, and *Bench Height* are the three main factors affecting the burden rock stiffness. For achieving good fragmentation, the burden to bench height ratio needs to be properly analyzed as the stiffness varies to the third power of this ratio. Reducing burden for a given bench height has been shown to have a positive effect. Thus, increase in bench height reduces the stiffness of burden rock mass.

Effect of Joints

Joints are the most common discontinuities present in rock mass. They create impedance mismatch zones in the strain wave transmitting medium and thereby cause unusual reflection and/or refraction of strain energy. Joints interrupt the development of radial crack network, and thus control the shape and size of the crater to a large extent. The crater formed in the jointed rock mass closely conforms to the network of the weakness planes.[10]

When a blasthole is intersected by joints, explosive energy escapes through joints, opening them up by wedging action causing a sudden drop in blasthole pressure (Figure 4). In some cases, when weak or open joints extend up to the face, premature venting of gases takes place, giving rise to fly rock and air blast problems (Figure 5).

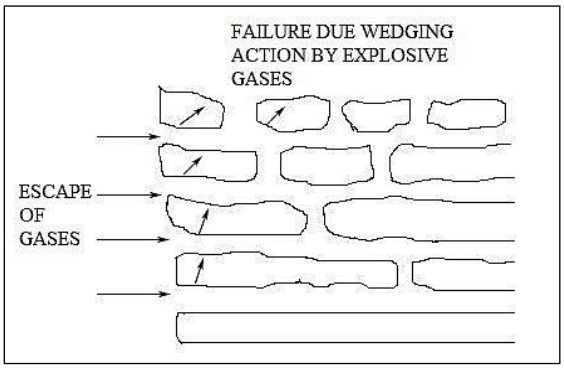

Fig. 4. *Escape of Gases into Joints.*

When there is any open joint opposite to the blast hole, the surfaces of joint cause reflection of the strain wave which in turn interacts with the incoming strain waves. If this intensity is sufficiently strong, fragmentation occurs due to the internal spalling in that zone. As a result, there may be more boulder formation on the other side of the joint.[11,12] Rinehart (1970)[13] analyzed the effects of joints on the wave propagation and observed that localization of fragmentation occurs near joint planes.

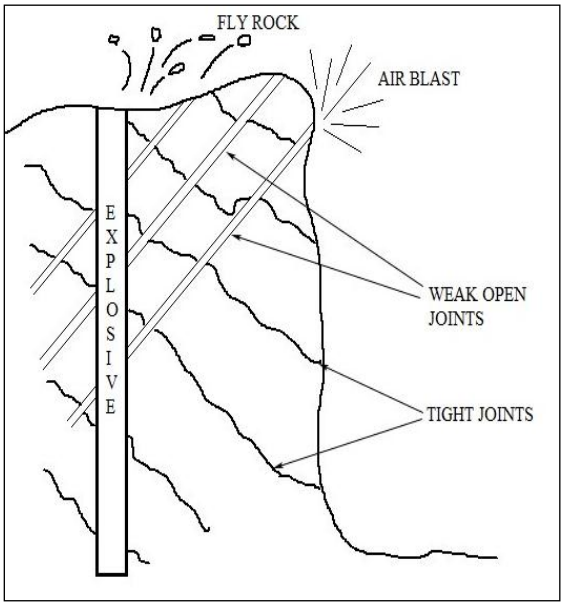

Fig. 5. *Air Blast and Fly Rock Associated With Jointed Rock Mass.*

Similar results were obtained by Sastry (1989)[12] in his laboratory studies on Chunar sandstone models. Pugliese and Atchison (1964)[14] in their comparative studies of explosives in limestone with tight joints found that repeated blasting in the area opened the joints present in the rock mass and thereby affecting the subsequent blasts results.

Emergence of cheaper blasting agents has set a trend toward larger diameter blast holes with increased burdens and spacing. As a result, in blocky strata with large joint spacing, the effects of weakness planes become more pronounced as greater number of joints may be encountered between consecutive blast holes. This result in very poor fragmentation, creating problems to loading, hauling and crushing operations in addition to the unwanted toe formations, as a number of blocks are not penetrated by blast holes (Figure 6). In such cases, small diameter blast holes array with smaller burden and spacing makes the explosive energy distribution more even, giving better results.

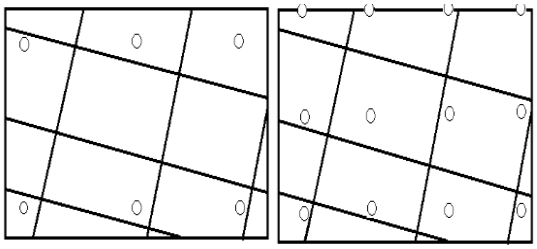

Fig. 6. *Effect of Joints on Blasthole Array.*

Joint planes cause stress concentration zones and create new fractures along the pre-existing flaws. Tests conducted by Barker and Fourney (1978)[15] on Homolite-100 models revealed this phenomenon.

This was also supported by the studies of Lande (1983),[16] who suggested that in jointed and highly fractured rock mass, short delays with smaller burdens give better fragmentation.

Type of Joints

Joints are of three types – tight, open, and filled. The degree of impedance offered to strain waves depends upon the type of joints. Tight joints do not affect the transmission of strain waves as much as open or filled joints. Sometimes the joint plane itself acts as a pseudo-face, especially in the case of open joints, reflecting the strain wave.[12]

Joint filling material, which may be the product of weathering or decomposition of the joint walls, is also a factor exerting considerable influence on the blast results. According to Yang and Rustan (1983),[17] continuity of weakness plane is the major factor affecting fragmentation. Strength of joint, which depends on the filling material, is the next. They observed that open and air filled joints exert a strong control on the fragmentation.

Sastry (1989)[12] observed from the tests on sandstone with four different filling materials (siliceous and calcareous materials, water and air), that the size and shape of bench crater were controlled more by the joint filling material (Figure 7). Larger fragments and larger sockets were observed in models with filled joints.

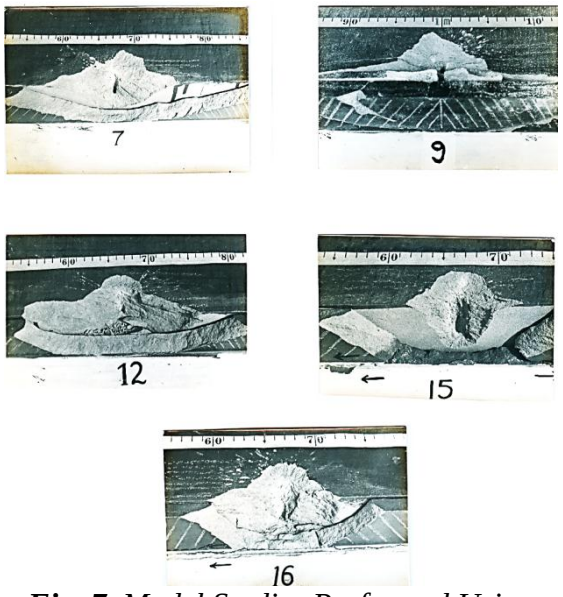

Fig. 7. *Model Studies Performed Using Filling Materials in Joints.*

Joint Spacing

The spacing or frequency of joints plays a vital role in fragmentation of the rock mass. Resistance to the blasting increases as block size increases or joint frequency diminishes.[18] For a successful blast design, data on spacing of joints should be obtained from a joint survey. Also, a detailed study of burden (B), joint spacing (S), and maximum allowable size of block (M) helps in overcoming the problems encountered in blocky formations. In general blasting practice, there are six possible cases of above mentioned variables (Table 1).

Table 1. *Relationships Between Burden (B), Joint Spacing (S), and Maximum Acceptable Fragment Size (M) (Coates, 1981).*[19]

Cases	Relative values of B, S, and M			Dominant Influence	Boulder Formation (size > M)
	Greatest	Intermediate	Smallest		
1	B	M	S	Jointing	Low
2	B	S	M	Jointing	High
3	M	B	S	Jointing	Low
4	M	S	B	Explosive	Low
5	S	B	M	Explosive	Medium
6	S	M	B	Explosive	Low

It is clear from Table 1 that Case 1 is the ideal, due to small amount of boulders and reduced explosive consumption, because joints dominate the fragmentation. Case 2 is not desirable due to the formation of large number of boulders as a result of joint spacing being greater than "M." Cases 3, 4, and 6 have low probability of occurrence in properly designed blasts, because burden "B" is smaller than the accepted block size "M." Case 5 is also rare, for the burden being less than average joint spacing "S" causing undesired boulder formation. Hence, blast design must be done in order to find situations, where $B < M$ and $M < S$, for reducing secondary fragmentation as well as specific explosive consumption.

Joint Orientation

Orientation of weakness planes (joints) has significant influence over size and shape of broken material and excavation.[8,20] Formation and extension of cracks during blasting are controlled by the pattern of joints.[8,21] Bauer *et al*. (1965)[10] and Ash (1973)[8] from their studies concluded that craters formed closely conform to the geometry of weakness planes. When the face is parallel to and on the dip side of the joints, excessive sliding occurs creating significant overbreak problems. When the joints dip away from the face, there may be problems of overhangs toe, etc., but the walls will be more stable (Larson and Pugleise, 1974). Results from small-scale bench blasts showed that when a row of vertical blast holesblast holes was oblique to the joint direction, it resulted in poor fragmentation.[12] By orienting the free face parallel to the marked vertical joint planes, better results may be achieved.[22]

It is reported that in horizontally bedded deposits, vertical lifter holes produce better fragmentation results (Wild, 1976). Thin and horizontally deposited brittle rocks require only horizontal holes, so that the overlying strata slide down by gravity. Rocks like Basalt, which are deposited in the form of thick vertical columns and the rocks with intersecting slips, may require both vertical as well as horizontal holes.

According to Burkle (1980), blasting with dip causes more backbreak, less toe, smooth floor and lower muckpile profile, while blasting against dip creates less

backbreak, more toe, rough floor, and overhangs. Blasting against strike may result in unequal backbreak conditions, saw toothed floor, and unfavorable orientation of face increasing the secondary blasting.

Singh and Sastry (1986a)[11] from their tests on jointed models concluded that the formation of crater, and hence the fragmentation, was highly influenced by joint orientation (Figure 8).

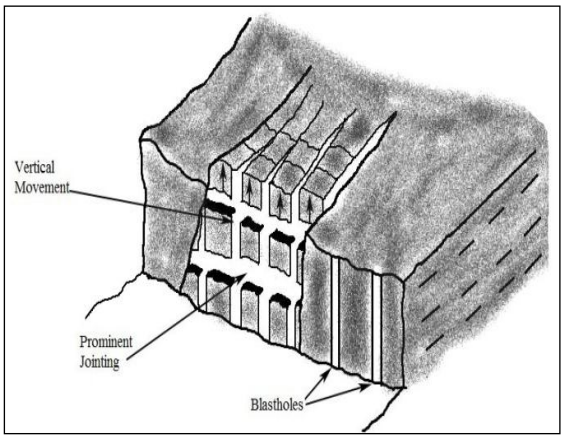

Fig. 8. *Vertical Movement of Rock Mass.*

Singh *et al*. (1986)[23] concluded from their study that both the mass and average fragment size of broken fragments were affected by joint orientation. Singh and Sastry (1986a)[11] have done extensive studies on the effect of joints on Chunar sandstone models incorporating joints running parallel, perpendicular, and angular to the face (Figure 9). They found that:

(1) Minimum yield results, when joints are running perpendicular to the face.
(2) Severe overbreak with uneven face formation results, when orientation of joints is perpendicular to face.
(3) More overbreaks occur in the condition with joints dipping into the face.
(4) Mass of fragments, average fragment size, mass surface area, fine and coarse fragmentation indices were significantly affected by orientation and direction of joints (at 5% level).

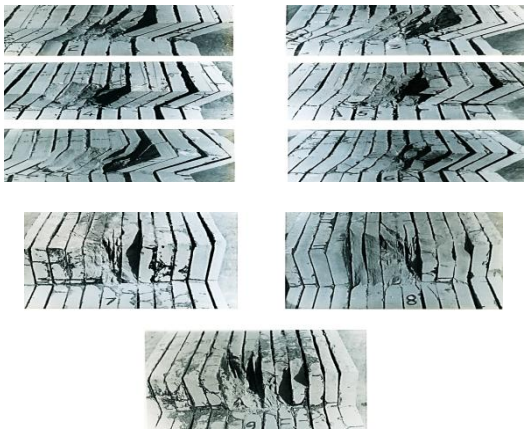

Fig. 9. *Models With Joints Running Perpendicular to Free Face.*

Role of Burden

Burden is one of the most critical geometric parameters of blasting. Burden is considered to have the greatest influence on blast results.[23–25] For any given set of conditions, there exists a burden, which may be termed as "Critical Burden," where the strata get fractured without displacement. According to Rustan *et al*. (1983)[26] critical burden is an important factor when describing blastability nature of any rock. They recommended 40–90% of critical burden as the maximum acceptable burden for satisfactory results.

When the burden falls below its optimum value, then the effectiveness of strain energy increases and gaseous energy decreases. For very small burdens, strain wave fracturing occurs so rapidly in front of the blasthole that, much of the gaseous energy is lost to the atmosphere resulting in excessive throw of rock (fly rock).

In multirow blasts, it is essential to keep the front row burden low in order to achieve proper burden relief and displacement, so that subsequent rows are blasted over smoothly, without any problems.[27] Otherwise, there is a possibility of encountering more fly rock and ground vibrations, in addition to undesired toe formation (Figure 10).

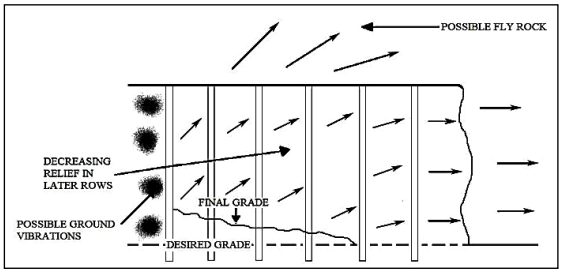

Fig. 10. *Effect of Insufficient Burden Relief.*

Role of Bench Height

Bench height plays a vital role in influencing the blasting results. For each burden, there exists a maximum bench height to produce a full crater.[28] The explosion generated strain in the rock alongside a charge increases as length to diameter ratio of charge increases in the approximate range of 0–20, and remains constant for >20. If it decreases to below 20, the optimum burden distances decreases.

Therefore, when a charge becomes very short (the case with shallow benches), the burden needs to be reduced considerably. The breakage angle for a given burden increases with increase in bench height up to a certain point, beyond which no further significant change occurs (Atchison, 1968).[29] As bench height increases, burden rock stiffness decreases.

Rock Stiffness

Bending mechanism in rock blasting is not new and was recognized long back, even dating to 1898.[30] This mechanism was made popular subsequently by Ash (1973),[8] Ash and Konya (1979),[31] and Smith (1976).[32] Stiffness principle and its use in blasting provide a guideline for the selection of an appropriate combination of burden, spacing, and bench height.

Ash (1973)[8] constructed an analogy between burden rock and structural beam to analyze the effect of bending on rock fragmentation.

Burden on a blasthole was considered as thickness of beam, bench height as its length and average width of crater produced as its width. Cross-section of the burden rock beam was defined by burden and spacing (Figure 11).

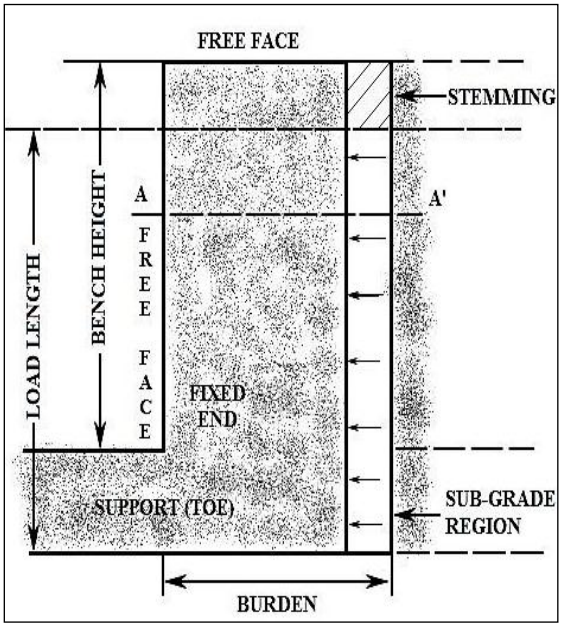

Fig. 11. *Analogy Between Burden Rock and a Structural Beam.*[8]

Smith (1976)[32] correlated the B, S, and BH with stiffness of burden rock as:

$K = CE\ Bx^{a}Sx^{b}/BH$

where K is the stiffness of the burden rock in kg/cm, B the burden dimension in cm, S the spacing dimension in cm, BH the bench height in cm, C the constant depending on the shape and location of the area, a, b the exponential constants depending on the shape of the area, and E is the Young's modulus in kg/cm^2. Breakage in shorter benches will be less than that in taller benches for same burdens, as stiffness decreases in the latter case (Figure 12).

The cause of fly rock and collar overbreak is that the burden rock has become too stiff due to hole depth being too small or relief of burden being inadequate.[33]

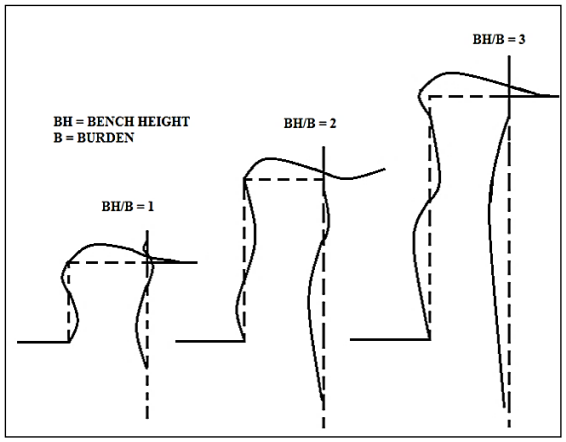

Fig. 12. *Bending Conditions in Blasting.*[32]

INVESTIGATIONS

Role of High-Speed Videography in Assessing Blast Performance

An average blast is completed within seconds and is not possible to analyze the blasting process with naked eye. Ever since the advent of high-speed video cameras (HSCs), it has been possible to view an entire blast in a sequence of frames, making analysis of the blasting process much effective. HSC with a capacity of 1000 FPS is capable of recording blasts, with the ability to capture one frame every millisecond in order to track down the delay performance as well. This enables the user to analyze every tiny movement happening in the blast. The HSC can be used to assess blast performance in terms of:

(1) Tracking of blasted rock mass.
(2) Tracking of burden rock movement.
(3) Checking the credibility of delays.
(4) Assessing the effectiveness of stemming by analyzing stemming/gas ejection during blast.
(5) Determining the displacement of blasted rock mass.

Methodology

Studies were carried out with a series of bench blasts, in one coal and three limestone mines. All blasts were recorded with an S-motion type HSVC, AOS Technologies AG, Switzerland. High-speed videos were analyzed using Pro Analyst software to determine the displacement of burden rock and happenings in bench. An attempt was made to assess the influence of bench height to burden ratio (BH/B) to identify important traits of the blasts and the role of jointing in blasting process. Details of blasts studied are given below (Tables 2–5).

Table 2. *Details of the Blasts in Mine-1 (Coal Mine).*

Sl. no.	Parameter	Blast 1	Blast 2	Blast 3	Blast 4
1	Diameter of blasthole (mm)	250	250	250	250
2	Burden (m)	6	6	7	7
3	Spacing (m)	8	8	9	9
4	Drilling pattern	Staggered	Staggered	Staggered	Staggered
5	Depth of blasthole (m)	11.1	11.1	15	14
6	Stemming (m)	5	3.5	7.5	05
7	No. of rows	6	5	3	4
8	No. of blast holes	25	30	19	70
9	Expl. charge/hole (kg)	276	290	350	410
10	Max. charge/delay (kg)	350	290	390	410
11	Total charge/blast (kg)	6918	8717	7415	22845
12	Initiation system	Shock tube	Shock tube	Shock tube	Shock tube
13	Rock mass movement (m/s)	53.0	111.1	108.3	67.1
14	BH/B ratio	1.85	1.85	2.143	2

Table 3. *Details of the Blasts in Mine-2 (Limestone Mine).*

Sl. no.	Parameter	Blast 1	Blast 2	Blast 3	Blast 4
1	Diameter of blasthole (mm)	115	115	115	115
2	Burden (m)	2.7	2.7	2.5	2.7
3	Spacing (m)	3.7	3.7	3.5	3.7
4	Drilling pattern	Square	Square	Square	Square
5	Depth of blasthole (m)	10.0	10.5	8.0	10.0
6	Stemming (m)	2.5	2.75	3.0	3.25
7	No. of rows	2	2	2	5
8	No. of blast holes	17	14	16	14
9	Expl. charge/hole (kg)	66.17	76.78	48.43	66
10	Max. charge/delay (kg)	463.19	307.12	242.15	264
11	Total charge/blast (kg)	1125	1075	775	925
12	Initiation system	Shock tube	Shock tube	Shock tube	Shock tube
13	Rock mass movement (m/s)	135.7	132.7, 136.9	70.5	108.4
14	BH/B Ratio	3.704	3.889	3.2	3.704

Table 4. *Details of the Blasts in Mine-3 (Limestone Mine).*

Sl. no.	Parameter	Blast 1	Blast 2	Blast 3
1	Diameter of blasthole (mm)	115	115	115
2	Burden (m)	2.7	2.7	2.7
3	Spacing (m)	3.0	3.0	3.2
4	Drilling pattern	Rectangular	Rectangular	Staggered
5	Depth of blasthole (m)	7.5	7.0	9.0
6	Stemming (m)	2	2	2
7	No. of rows	3	2	4
8	No. of blast holes	13	17	43
9	Expl. charge/hole (kg)	54	37.76	55.23
10	Max. charge/delay (kg)	215	294.45	994.14
11	Total charge/blast (kg)	700	642	2315
12	Initiation system	Shock tube	Shock tube	Shock tube
13	Roc mass movement (m/s)	66.2	110.9	77.2, 113.5
14	BH/B ratio	2.778	2.223	3.148
Sl. no.	**Parameter**	**Blast 4**	**Blast 5**	**Blast 6**
1	Diameter of blasthole (mm)	115	115	115
2	Burden (m)	2.7	2.7	2.7
3	Spacing (m)	3.0	3.2	3.2
4	Drilling pattern	Rectangular	Rectangular	Staggered
5	Depth of blasthole (m)	9.5	9.5	8.0
6	Stemming (m)	2	2	2
7	No. of rows	3	2	3
8	No. of blast holes	10	20	18
9	Expl. charge/hole (kg)	62.24	72	44
10	Max. charge/delay (kg)	311.2	506	267
11	Total charge/blast (kg)	622.4	1145	3133
12	Initiation system	Shock tube	Shock tube	Shock tube
13	Rock mass movement (m/s)	122.8, 119.4	125.8	97.0
14	BH/B ratio	3.334	3.519	2.778

Table 5. *Details of the Blasts in Mine-4 (Limestone Mine).*

Sl. no.	Parameter	Blast 1	Blast 2	Blast 3
1	Diameter of blasthole (mm)	115	115	115
2	Burden (m)	2.5	2.5	2.5
3	Spacing (m)	3.0	3.0	3.0
4	Drilling pattern	Square	Square	Square
5	Depth of blasthole (m)	5.0	5.0	5.0
6	Stemming (m)	2.25	2.5	2.0
7	No. of rows	3	2	4
8	No. of blast holes	14	16	29
9	Expl. charge/hole (kg)	28.57	37.5	31.2
10	Max. charge/delay (kg)	114.28	150	156.03
11	Total charge/blast (kg)	400	600	905
12	Initiation system	Shock tube	Shock tube	Shock tube
13	Rock mass movement (m/s)	49.8, 114.0, 71.9	67.0	104.4
14	BH/B ratio	2	2	2

RESULTS AND ANALYSIS

Escape of gas energy was observed through major joints in the bench. Also the escape of gas energy through stemming zone was observed by high speed videos. Figure 13 shows the escape of gaseous energy through weak planes and stemming zone in the bench, causing depletion of blasthole pressure. Both these reasons caused poor fragmentation.

(a)

(b)

(c)

(d)

(e)

Fig. 13. *Escape of Gas Energy Through Weak Planes and Stemming Zone.*

Gas energy is found to escape through horizontal jointing and pushing the beds upwards (Figure 14).

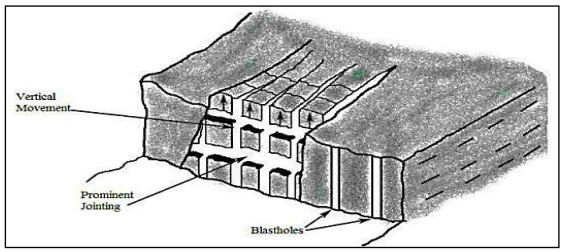

(a)

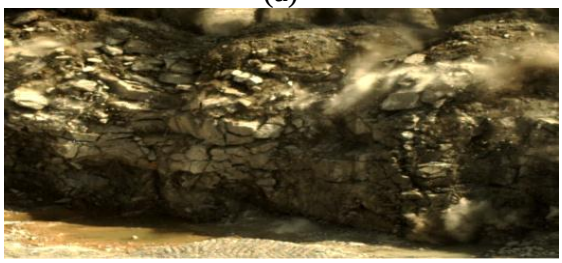

(b)

Fig. 14. *Rock Fragmentation Affected by Jointing (Recorded by HSC).*

The HSC could clearly establish the beam bending mechanism as shown in Figure 15. Also the effect of joints on rock fragmentation could be observed as recorded in one of the blasts in a limestone mine.

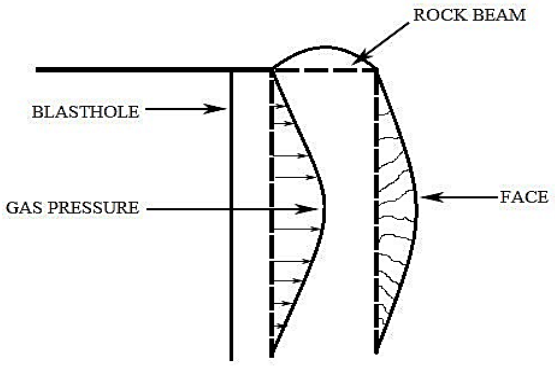

(a)

(b)

(c)

Fig. 15. *Flexural Bending Mechanism.*

It could also be seen from Figure 15 that to a large extent, size of one side of the fragments resulting from the blast is controlled by joint spacing.

Burden Rock Velocity

Analysis of high-speed videography study results revealed that the velocities of blasted rock are higher in case of limestone (7–13 m/s) than in argillaceous sandstone overburden formation (6–10 m/s) (Table 6). This is due to limestone being more compact and stronger than overburden sandstone, and transmission of strain waves is better in limestone formation.

Table 6. *Relationship Between BH/B and Average Velocity of Burden Rock Mass.*

BH/B	BH/B Average	Burden Velocity (m/s)	Avg. Burden Velocity (m/s)
2	2	53.0	79.8
2		111.1	
2		67.1	
2		49.8	
2		114.0	
2		71.9	
2		67.0	
2		104.4	
2.14	2.5	108.3	95.6
2.22		110.9	
2.77		66.2	
2.77		97.0	
3.14	3.2	77.2	100.7
3.14		113.5	
3.20		70.5	
3.33		122.8	
3.33		119.4	
3.51	3.7	125.8	127.9
3.70		135.7	
3.70		108.4	
3.88		132.7	
3.88		136.9	

Effect of BH/B on Delay Timing

Initiation sequence in a blast is very important and is a vital factor to be considered in blast design, since several initiation sequences radically alter effective burden and spacing during the blasting process. It also affects rock movement with respect to face and thereby influences the amount of rock shearing and design boundaries of blast pattern. A systematic release of explosive energy from one hole/row to the other is crucial in maintaining a continuous momentum required for inter-hole/row delay displacements.

It has been suggested by earlier researchers that the burden from first row of blast holes should be displaced by at least one third of the burden distance (1/3 B) before next row of blast holes is fired, for an efficient blast (Figure 16).

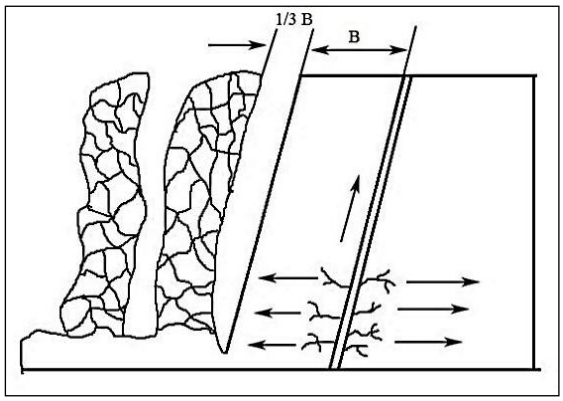

Fig. 16. *Required Burden Movement Before Blasting of Next Row.*

Burden rock velocity was calculated for different conditions by tracking down the movement of burden rock mass. Figure 17 shows some sample screen shots of high speed videographs of some of the blasts recorded in different mines.

ProAnalyst software was used for tracking down the burden rock movement, for determining the velocity of rock mass. Some sample snap shots of the same are shown in Figure 18.

0 ms

100 ms

200 ms

(a)

0 ms

100 ms

200 ms

300 ms

(b)

Fig. 17. *Videographs of Some Blasts Recorded by HSC in Different Mines. (a) Screenshots of Blast-4 Recorded in Mine-1. (b) Screenshots of Blast-5 Recorded in Mine-3.*

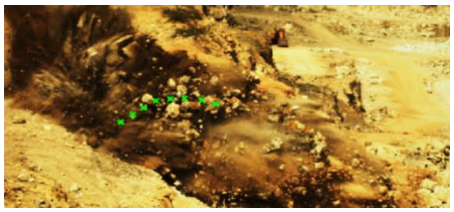

(a)

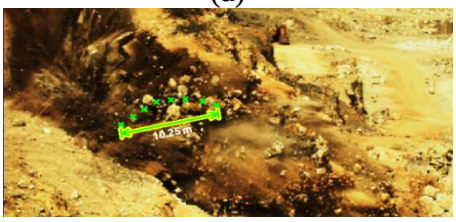

(b)

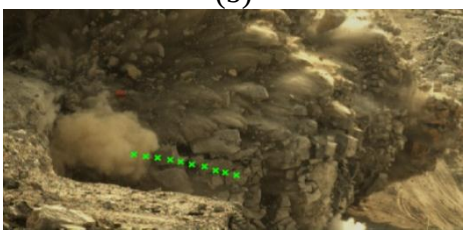

(a)

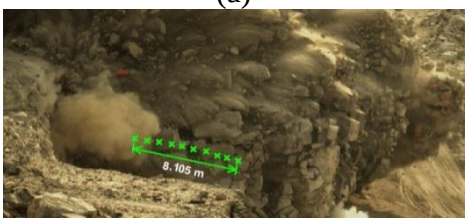

(b)

Fig. 18. *ProAnalyst Analysis of Some Blasts Recorded by HSC in Different Mines. (a) Tracking of Rock Mass Movement (Blast-2 in Mine-3). (b) Tracking of Rock Mass Movement (Blast-3 in Mine-4).*

Based on the burden movement velocity, the minimum delay timing required between rows was analyzed (Table 7). Study has shown that as BH/B ratio increasing, the required delay time per meter distance throw of burden rock mass is decreasing. For a BH/B ratio condition of two, the delay time required was determined as 12.5 ms/m, whereas with BH/B value of 3.75 the required delay reduced to 8 ms per meter distance. This is due to the fact that as BH/B is increasing, the bench is becoming less stiff and more flexible resulting in faster movement of burden rock mass.

Table 7. *Delay Time Required Between Rows Based on High-Speed Videography Data.*

BH/B Ratio	Avg. Burden Velocity (m/s)	Delay Time Required (ms/m)
2.0	79.8	12.5
2.5	95.6	10.5
3.2	100.7	10.0
3.75	127.9	8.0

CONCLUSIONS

Following are the major conclusions drawn from the studies carried out using HSVC in four different mines:

(1) High speed video camera is an excellent tool for analyzing the blast results and designing efficient blasts.

(2) High speed video of the blasts provides clear information about weak zones in the bench being blasted from where escape of gas energy is taking place. Based on this the necessary zones of stemming decks could be finalized.

(3) For small benches, the velocity of blasted rock mass is slower. This is due to the increased stiffness of short benches.

(4) Conversely, for the taller benches, the velocities of blasted rock pieces have been recorded to be higher, as benches are becoming more flexible.

(5) In taller benches, the delay between holes/rows could be 8ms per meter distance. In case of shorter benches the delay time required is about 12ms per meter distance. According to the burden/spacing provided, the necessary delay timing may be adopted.

REFERENCES

1. Sadwin L.D., Junk N.M. Measurement of lateral pressure generated from cylindrical explosive charges, *USBM RI*: 6701; 1965.
2. Fogelson D.E., Atchison T.C., Duvall W.I. Strain energy for explosion generated strain pulses in rock, *USBM RI*: 5514, 1959.
3. Noren C.H. Blasting experiments in granite rock, *Quart Colo Sch Min*. 1956; 51(3): 211–25p.
4. Saluja S.S. Study of mechanism of rock failure under the action of explosives, *Ph.D Thesis*, Univ. Wisconsin; 1963.
5. Clark G.B., Saluja S.S. Blasting mechanisms, *Trans SME/AMIE*. 1964; 229: 78–90p.
6. Kutter H.K., Fairhurst C. On the fracture process in blasting, *Int J Rock Mech Min Sci Geomech Abstr*. 1971; 8: 181–202p.
7. John N.E., Jr. The role of stress waves in explosively induced bulk rock motion, *Proc. 1st Int. Symp. Rock Frag. by Blast*. Lulea, Sweden; 1983, 1: 53–70p.
8. Ash R.L. The Influence of Geological Discontinuition on Rock Blasting, *Ph.D Thesis*, Univ. of Missouri, Rolla, 1973.
9. Ash R.L., Smith N.S. Changing borehole length to improve breakage – a case history, *Proc. 2nd Conf. Expl. and Blast. Tech*. Louisville, Kentucky; 1976, 1–12p.
10. Bauer A., Harries G.R., Lang L., *et al*. How IOC puts crater resarch to work, *E&MJ*. 1965; 166(9): 117–21p.
11. Singh D.P., Sastry V.R. Influence of Sturctural Discontinuities on Rock fragmentation by Blasting, *Proc. Int. Symp. Intense Dynamic Loading and Its Effects.* Beijing, China; 1986a, 980–4p.
12. Sastry V.R. A Study of the Effect of Some Parameters on Rock Fragmentation due to Blasting, *Ph.D. Thesis*. BHU, India; 1989.
13. Rinehart J.S. Fractures and strain generated in joints and layered rock masses bu explosions, *Proc. Symp. Mechanism of Rock Failure by Explosions: Fontineblue*. 1970.
14. Pugliese J.M., Atchison T.C. Comparative studies of explosives in limestone, *USBM RI*: 6395, 1964.
15. Barker D.B., Fourney W.L. *Photoelectric Investigation of Fragmentation Mechanisms, Part-II – Flaw Initiated Network*. Report to NSF: August, 1978
16. Lande G. Influence of structural geology on controlled blasting in sedimentary rocks – case history, *Proc. 1st Int. Symp. Rock Frag. by Blast*. Lulea, Sweden; 1983, 2: 555–63p.
17. Yang Z.G, Rustan A. The Influence from Primary Structure on Fragmentation, *Proc. 1st Int. Symp*. Rock fragmentation by Blasting: Lulea, Sweden; 1983; 2: 581–603p.
18. DaGama C.D. Similitude conditions in models for studies of bench blasting, *Proc. 2nd Cong. Rock Mech*. Belgrade: ISRM; 1970, III: 105–12p.
19. Coates D.F. *Rock Mechanics Principles.* Ottawa: CANNET Energy Mines and Resources; 1981.
20. Gnirk P.F., Pfleider E.D. On the correlation between explosive crater formation and rock properties, *Proc. 9th Symp. Rock Mech.: Col. Sch. Min*. 1968; 321–45p.
21. Dally J.W., Fourney W.L. The Influence of Flaws on Fragmentation, *Proc. 6th Int. Colloq. Gas Dynamics of Explosives and Reactive Systems.* Stockholm, Sweden; 1977.
22. Belland L., Structure as a control in rock fragmentation – coral lake iron

ore deposit, *CIM Bull*. 1966; 59(645): 323–8p.
23. Singh D.P., Saluja S.S., Rao Y.V.A. A Laboratory Study of Effects of Joint on Rock Fragmentation, *Proc. 21st US Symp. Rock Mechanics*. Univ. Missouri, 1986.
24. Allsman P.L. Analysis of explosive action in breaking rock, *Trans AIME*. 1960; 217: 471–3p.
25. Singh D.P., Sastry V.R. An investigation into the effect of blast geometry on rock fragmentation, *J Mines Met Fuels*. 1987; 39(6): 226–33p.
26. Rustan A., Vutukuri V.S., Naarttijarvi T. The influence from specific charge, geometric scale and physical properties of homogeneous rock on fragmentation, *Proc 1st Int. Symp. Rock Frag. by Blast*. Lulea, Sweden, 1983; 1: 115–42p.
27. Hagan T.N. The influence of controllable blast parameters on fragmentation and mining costs, *Proc. 1st Int. Symp*. Rock Frag. by Blast: Lulea, Sweden; 1983, 1: 31–51p.
28. Mason J.M. The effect of explosive charge length on cratering, *M.S Thesis*, Univ. Missouri; 1973.
29. Atchison T.C. In: *Fragmentation Principles, Surface Mining*. Pflieder (Ed.), New York: AMIE; 1968, 355–72p.
30. Daw A.W., Daw Z.W. *The Blasting of Rock: In Mines, Quarries, Tunnels*, Etc., P. 297, London: E. and F.N. Spon. Ltd.; 1898.
31. Ash R.L., Konya C.J. Improper spacing – a major problem with surface blasting, *Proc. 5th Conf. Expl. Blast. Tech*. 1979, 180–3p.
32. Smith, N.S. Burden rock stiffness and its effect on fragmentation in bench blasting, *Ph.D Thesis*, Univ. Missouri, 1976.
33. Lundborg N., Persson P.A., Peterson A.L., *et al*. Keeping the lid on fly rock in open pit blasting, *E&MJ*. 1975.

Available online at www.sciencedirect.com

ScienceDirect

Procedia Earth and Planetary Science 11 (2015) 445 – 456

Procedia Earth and Planetary Science

Global Challenges, Policy Framework & Sustainable Development for Mining of Mineral and Fossil Energy Resources (GCPF2015)

Piezo-Gen - An Approach to Generate Electricity from Vibrations

Raghu Chandra Garimella*, Dr. V.R. Sastry, Mohammed Shoeb Mohiuddin

Department of Mining Engineering, NITK-Surathkal, Mangalore, 575025,Karnataka, India

Abstract

Now-a-days, Generation of Electrical Energy has become a more vital factor in the Power System because of the incremental demands for day-by-day with the population growth in the Electrical Distribution System. Hence, we all knew that Power Generation can be done in much number of ways using different techniques. Many Electrical Professionals developed different technologies for Electrical Energy Generation, which are all frequently fuel consuming apparatus. Here there is a new technique for Generation of Electrical Energy using *Piezo Sensors* from unwanted ground vibrations which may affect the nearby structures or may cause sound pollution. Here with the help of a number of vibratory plates which are well said to be Piezo Sensors, the frequency of different unnecessary vibrations will be converted into Alternating Supply; and then it will be furtherconverted into Direct Supply with the help of Ultra-Fast Switching Diode. The obtained output can be well stored in a Battery for further usage or it can be consumed directly for Loads. Thus, without any Economic Fuel consumption the Electrical Power simply can be generated by utilizing the unwanted vibrations.

Peer-review under responsibility of organizing committee of the Global Challenges, Policy Framework & Sustainable Development for Mining of Mineral and Fossil Energy Resources.

Keywords: Piezoelectric Materials; Piezo Sensors; Polyvinyledene Difluoride; Piezo Electric Generator; Vibrations.

* Tel.: +91 9290796716;
E-mail address: raghuchandhra@india.com

1. Introduction

Piezo-Generation is a new approach to generate Electrical Energy from the sensing cum converting equipment called piezo sensor/piezo buzzer. It mainly works on a principle of Piezo Electric Effect which is creating pressure energy on a crystalline material viz., Quartz Crystal to generate Electricity. Piezo Electric Effect is discovered in 1880 by Jacques and Pierre Curie during studies into the effect of pressure on the generation of electrical charge by crystals (such as quartz).

The word Piezo is derived from the Greek “Piezein”, which means to squeeze or press. The piezo material exhibits both “Direct piezo electric effect” as well as ‘Converse piezo electric effect”. Direct piezo electric effect is the production of electricity when the crystals are mechanically stressed and the converse piezo electric effect is the stress or strain in the crystals when an electric potential is applied. The most common crystals used are lead zirconate titanate crystals.

Peer-review under responsibility of organizing committee of the Global Challenges, Policy Framework & Sustainable Development for Mining of Mineral and Fossil Energy Resources.
doi:10.1016/j.proeps.2015.06.044

The Piezo effect finds many applications such as the production and detection of sound, generation of high voltages, electronic frequency generation, microbalances and ultra-fine focusing of optical assemblies. It is also the basis of a number of scientific instrumental techniques with atomic resolution, the scanning probe microscopes and everyday uses such as acting as the ignition source for cigarette lighters and push-start propane barbecues.

Piezoelectric materials (PZT) can be used as mechanisms to transfer ambient vibrations into electrical energy that can be stored and used to power other devices. With the recent surge of micro scale devices, PZT power generation can provide a conventional alternative to traditional power sources used to operate certain types of sensors/actuators, telemetry and MEMS devices. In this paper, the dynamics of piezoelectric materials for the use of power generation devices has been experimentally investigated. The objectives of this work are to estimate the amount of power that PZT can generate and to identify the feasibility of the devices for real-world applications. The energy produced by the PZT was stored in two different ways. The first was in a capacitor that allows for immediate access to the stored energy and the second method charged a nickel metal hydride battery. The power generated by the vibration of the piezoelectric is shown to be a maximum of 2mW, and provide enough energy to charge a 40mAh button cell battery in one hour.

Piezoelectric materials form transducers that are able to interchange electrical energy and mechanical motion or force. These materials, therefore, can be used as mechanisms to transfer ambient motion (usually vibration) into electrical energy that may be stored and used to power other devices. By implementing power harvesting devices we can develop portable systems that do not depend on traditional methods for providing power, such as the battery, which has a limited operating life. Recent studies, experiments and patents, indicate the feasibility of using PZT devices as power sources. Umeda, yet all uses a free-falling ball to impact a plate with a piezo-ceramic wafer attached to its underside and developed an electrical equivalent model of the PZT transforming mechanical impact energy to electrical power. They also investigated the energy storage characteristics of the PZT with a bridge rectifier and a capacitor. Starner examines the energy available from leg motion of a human being and surveys other human motion sources of mechanical energy including blood pressure.

The author claims 8.4 watts of useable power can be achieved from a PZT mounted in a shoe. Kymissis yet all examine using a piezo-film in addition to the ceramic used in, to provide power to light a bulb in a shoe, entirely from walking motion. Kimura's US Patent centers on the vibration of a small plate, harnessed to provide a rectified voltage signal. The effort seems to be motivated by providing enough energy to run a small transmitter fixed to migratory birds for the purpose of transmitting their identification code and location. This result is also compared to using existing battery technology.

Goldfarb yet all presented a linearized model of a PZT stack and analyzed the efficiency of it as a power generation device. It was shown that the maximum efficiency occurs in a low frequency region much lower than the structural resonance of the stack. The efficiency is also related to the amplitude of the input force due to hysteresis of the PZT. In addition to the force applied in the poling direction (d33 mode), Clark and Ramsay have investigated and compared it with the transverse force (d31 mode) for a PZT generator. There work showed that the d31 mode has a mechanical advantage in converting applied pressure to working stress for power generation. They concluded that a 1-cm2 piezo-ceramic wafer can power MEMS device in the microwatt range. Elvin yet all theoretically and experimentally investigates the use of the self-powered strain energy sensors using PVDF. Their half-rectified circuit was then combined with wireless communication device for human bone strain monitoring. Kasyap yet all formulated a lumped element model to represent the dynamic behavior of PZT in multiple energy domains using an equivalent circuit. Their model has been experimentally verified using a 1-d beam structure with the peak power efficiencies of approximately 20%. Gonzalez yet all analyzed the prospect of piezoelectric based energy conversion and suggested several issues to raise the electrical output power of the existing prototypes to the level that can be theoretically obtained.

Nomenclature

PZT	Lead zirconate titanate (Pb[Zr(x)Ti(1-x)]O3), one of the world's most widely used piezoelectric ceramic materials
MEMS	Micro-Electro-Mechanical Systems
PVDF	Polyvinylidene fluoride

2. Piezo electric effect

Piezoelectricity is defined as a change in electric polarization with a change in applied stress (direct piezoelectric effect) shown in Fig. 1(a). The converse piezoelectric effect is the change of strain or stress in a material due to an applied electric field shown in Fig. 1(b). Another interesting property of piezoelectric material is that they change their dimensions (contract or expand) when an electric field is applied to them. The converse piezoelectric effect describes the strain that is developed in a piezoelectric material due to the applied electric field.

Piezoelectricity is the ability of some materials such as crystals and certain ceramics, to generate an electric potential in response to applied mechanical stress or heat. If the piezo crystals are not short-circuited, the applied charge induces a voltage across the material.

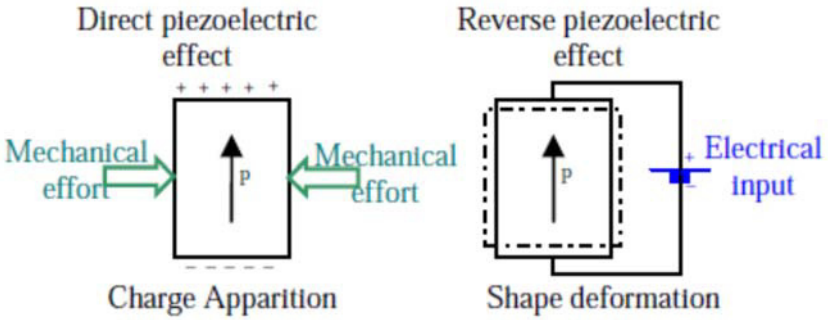

Fig. 1. (a) Piezo Electric Mechanism; (b) Converse Piezo Mechanism.

2.1. Principle of operation

The microscopic origin of the piezoelectric effect is the displacement of ionic charges within a crystal structure. In the absence of external strain, the charge distribution is symmetric and the net electric dipole moment is zero. However, when an external stress is applied the charges will be displaced and the charge distribution will be no longer symmetric and net polarization will be created. In some cases a crystal possesses a unique polar axis even in the unstrained condition. This can result in a change of the electric charge due to a uniform change of temperature. This is called the pyroelectric effect. The direct piezoelectric effect is the basis for force, pressure, vibration and acceleration sensors and the converse effect for actuator and displacement devices.

2.2. Piezo materials

Some examples of practical piezo materials are barium titanate, lithium niobate, polyvinyledenedifluoride (PVDF), and lead zirconate titanate (PZT). There are several different formulations of the PZT compound, each with different electromechanical properties.

3. Mechanism of the proposed system

Mechanical compression or tension on a poled piezoelectric ceramic element changes the dipole moment, creating a voltage. Compression along the direction of polarization or tension perpendicular to the direction of polarization generates voltage of the same polarity as the poling voltage (Fig. 2).

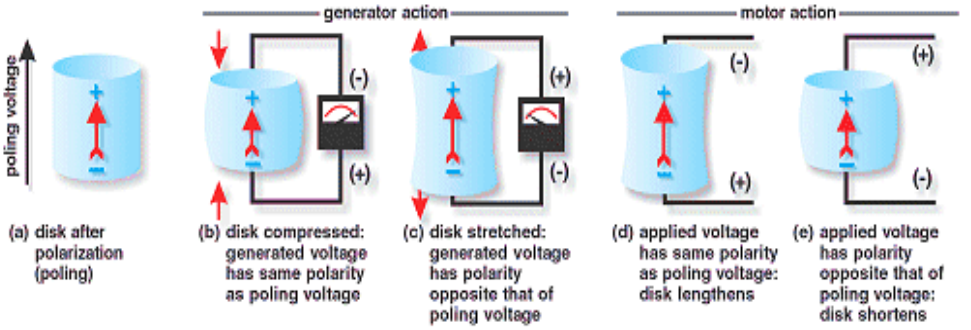

Fig. 2. Working mechanism of simple Piezo Transducer

The principle is adapted to piezoelectric motors, sound or ultrasound generating devices, and many other products. *Generator* action is used in fuel-igniting devices, solid state batteries and other products; *Motor action* is adapted to piezoelectric motors, sound or ultrasound generating devices and many other products.

In addition the superscripts "S, T, E, D" are introduced. They describe an electrical or mechanical boundary condition.

Definition:

S = Strain = constant (mechanically clamped)

T = Stress = constant (not clamped)

E = Field = constant (short circuit)

D = Electrical Displacement = constant (open circuit)

3.1 How it works?

In a piezoelectric crystal, the positive and negative electrical charges are separated, but symmetrically distributed. This makes the crystal electrically neutral. Each of these sides form an electric dipole and dipoles near each other tend to be aligned in regions called “Weiss domains”. The domains are usually randomly oriented, but can be aligned during poling, a process by which a strong electric field is applied across the material, usually at elevated temperatures. When a mechanical stress is applied, this symmetry is disturbed and the charge asymmetry generates a voltage across the material. In Converse piezoelectric effect, application of an electrical field creates mechanical deformation in the crystal.

The most common application of piezo crystals to generate a potential is the electric cigarette lighter. Pressing the button of the lighter causes a spring-loaded hammer to hit a piezoelectric crystal, producing a sufficiently high voltage that electric current flows across a small spark gap, thus heating and igniting the gas. Some substances like quartz can generate potential differences of thousands of volts through direct piezo electric effect.

Flexible Piezoelectric Materials are attractive for power harvesting applications because of their ability to withstand large amounts of strain. Larger strains provide more mechanical energy available for conversion into electrical energy. A second method of increasing the amount of energy harvested from a piezoelectric is to utilize a more efficient coupling mode.

3.2 Types of piezo- sensors

The below figures depicts the various models and types of Piezo transducer system (Fig. 3):

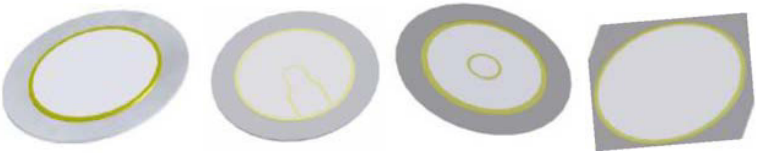

(a) (b) (c) (d)

Fig. 3.(a) Two-terminal circle type, the metal is Stainless Steel, Brass and Nickel Alloy;
(b) Three-terminal circle with brim feedback, the metal is Brass and Stainless Steel;

(c) Three-terminal circle with centre feedback, the metal is Brass and Stainless Steel;
(d) Two-terminal square type, the metal is Nickel Alloy.

All the types of above products can be attached a connector with two or three wires accordingly, also can produce come other dimensions piezo plate (Fig. 4).

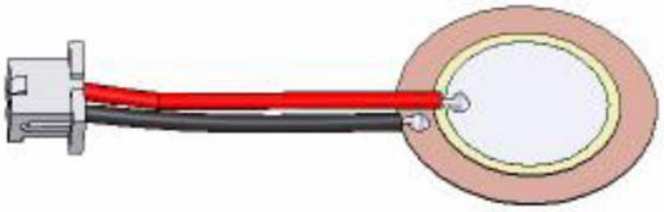

Fig. 4. Connection setup of Piezo-Transducer

4. Construction of the piezo generator

Battery powered mobile devices have recently been rapidly gaining widespread popularity. However, they must always be charged before use. If they are equipped with a generator which transforms mechanical impact energy during travel to electric energy, the batteries can be charged without electrical power sources. For this purpose we have proposed a piezo-generator which transforms mechanical impact energy to electric energy and have discussed its fundamental characteristics. The generator consists of a steel ball and a piezoelectric vibrator. The impact of the ball against the generator produces electrical energy via the piezoelectric effect. By introducing a bridge-rectifier and a capacitor, we have been able to study the energy storage characteristics both theoretically and experimentally. The efficiency and the stored charge are discussed with respect to the initial voltage and the capacity of the capacitor.

Piezoelectric generators (PEGs) are simple, inexpensive and very compact devices. Unlike other explosive power sources, such as magneto-cumulative or ferromagnetic generators, PEGs do not require the use of explosives to produce the required mechanical forces to generate electrical power. However, they are inherently low-energy devices with a maximum energy density of only about 1 J/cm3, which limits their utility to certain specific applications.

To the best of the author's knowledge, work on explosive driven PEGs can be traced back to the early 1960s in the United States, Former Soviet Union and France. All of these early studies had two central themes: using ferroelectric or piezoelectric materials as the working body and using shock waves to depolarize these materials.

Most of the early studies focused on either single crystals or ferro-ceramic materials such as barium titanate, Tibalit, lithium niobate, and lead zirconate titanate (PZT). These materials are still investigated today, but there is also interest in ferroelectric polymers such as PVDF.

One of the early papers that investigated the feasibility of using PEGs as pulsed power supplies was by J.E. Beasancon, J. David, and J. Vedel. Since then, others have investigated their utility as pulsed power devices including A.B. Prishchepenko , B.M. Novac , S. Shkuratov , and Ya. Tkach.

A.B. Prishchepenko and his team probably have the most experience with PEGs with work beginning in 1983 and continuing through the late 1990s. They have used their PEGs to drive capacitive loads and in conjunction with ferromagnetic generators.

It was first observed by B.M. Novac et al that these generators work best when the shock pressures are dampened. They investigated the influence of pressure loading on PZT and found that when the pressure exceeded 50 kbar, the output current dramatically decreased. They theorized that this is caused by internal short circuiting of the generator due to massive generation of electrical charges. Two types of attenuators were used in their experiments: copper-Plexiglas and steel. In this study, it was decided to determine the optimal pressures for PEG operation and it was found that shock pressures are detrimental since they cause the ceramics to fracture and can induce electrical breakdown. Therefore, one of the results of this study was to determine if propellants, rather than explosives, could be efficiently used to generate high voltages from these generators.

The construction of the generation and storage system is shown in Fig. 5. Initially, a steel ball rests at a height 1/1 above a piezoelectric vibrator. The electric output of the vibrator is connected to a capacitor C through a bridge-rectifier.

4.1 Operation

The operation of the system is summarized as follows:

a. The steel ball falls freely toward the center of the vibrator under the effect of gravity.
b. After the collision, a bending vibration is produced in the vibrator and the steel ball bounces up.
c. An alternating current I_g generated by the piezo¬electric effect is supplied to the bridge-rectifier.
d. The rectified current I_c flows into the capacitor C.
e. The voltage across the capacitor increases to V.
f. The steel ball falls again and steps (2)—(5) repeat until the steel ball stops.

4.2 Analysis by an equivalent circuit model

To simulate the generation and storage mechanism, we employ an electrical equivalent circuit model shown in Fig. 6 which was introduced by the authors in the previous study. The load resistance in ref. 1 is substituted by a bridge-rectifier and a capacitor. The input mechanical energy of a falling ball is translated into an initial electrical energy by the equivalent mass in the circuit. The separation of the vibrator and the ball is simulated by changing the parameters in the circuit as described in ref. 1. Only the first bending mode is considered for simplicity of analysis. Hence C denotes the capacity of the capacitor connected to the rectifier. The value of the Cd is the clamped capacitance and Rd is the dielectric loss of the piezo-ceramics. Lm, Cm and Rm express equivalent mass, the equivalent stiffness and the equivalent mechanical loss of the first mode of the vibrator, respectively. v0 is the input voltage to the bridge-rectifier, and Vc is the voltage across the capacitor. The values of im and Ic indicate the currents in each branch.

4.3 Piezo-electric effects

- *Direct Effect* called by the Curies the "primary" effect.-Electric polarization produced by mechanical strain, changing its sign with reversal of the strain.
- *Converse Effect* (sometimes called the "reciprocal" effect)-Mechanical stress produced by the application of an electric field, changing its sign with reversal of field. *All piezo-electric crystals necessarily exhibit both the direct and the converse effect.*
- *Longitudinal Effect*-This term is commonly applied only to those cases where a dilatation in a given direction is -accompanied by an electric polarization in the same direction.
- *Transverse Effect*-As commonly employed this term refers to a dilatation at right angles to the associated electric field

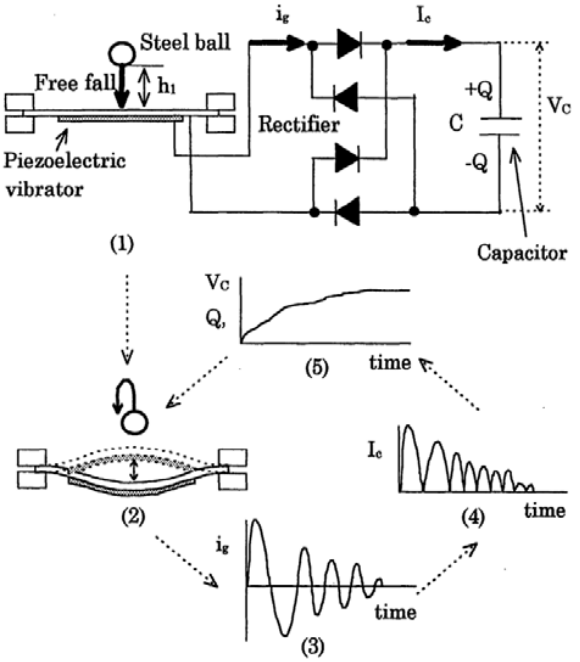

Fig. 5. Principle of generation and storage

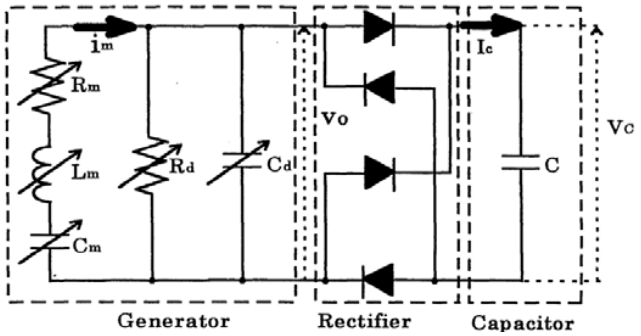

Fig. 6. Equivalent circuit of an generator

5. Types of mechanical vibrations

- *Longitudinal Vibrations* - This term may be applied either to rods or to more extended masses in which the motion of the vibrating particles is parallel to the direction of propagation of the wave, that is, normal to the wave-front. This use of the word "longitudinal" has nothing to do with the longitudinal effect. Vibrations of this type are also called "compressional" and "extensional." Longitudinal vibrations may be produced in either fluids or solids.
- *Transverse Vibrations* - This term is properly related to transverse (distortional) waves in the same manner in which the term "longitudinal vibrations" is related to longitudinal waves. The vibrating particles move in a direction parallel to the wave-front and normal to the direction of propagation. Familiar examples are electromagnetic radiations, vibrating strings, membranes and thin plates. With piezo-electric crystals transverse vibrations may occur when the direction of the electric field is such that the field produces a shearing stress about some axis. If this axis is parallel to one of the principal dimensions of the parallelepiped, the wave propagation may be expected to take place in a direction parallel to another of the dimensions. Such vibrations may also be called "shear vibrations."
- *Flexural Vibrations*- These usually occur in elongated plates or bars and are frequently called "transverse" or "lateral" vibrations. In order to distinguish them from the transverse vibrations described above, it would seem better to use the word "flexural." They are associated with a bending of

the specimen in a certain plane, hence it is best to refer, for example, to "flexural vibrations in the YZ plane."

- *Torsional Vibrations* are those in which a relative angular displacement (shearing strain) about the axis of figure, usually a cylinder or prism, takes place between adjacent cross-sections. For example, we speak of torsional vibrations "about the X-axis."

From what has been said it is evident that it is ambiguous to refer to the "direction of vibration in a crystal," unless the type of vibration is also made clear.

6. Applications

The best-known application of piezo crystals are:

a. Direct piezoelectricity of some substances like quartz, as mentioned above, can generate potential differences of thousands of volts.
b. As sensing elements, Detection of pressure variations in the form of sound is the most common sensor application, e.g. piezoelectric microphones. Sound waves bend the piezoelectric material, creating a changing voltage
c. Ultrasound imaging, Piezoelectric sensors are used with high frequency sound in ultrasonic transducers for medical imaging .For many sensing techniques, the sensor can act as both a sensor and an actuator. Ultrasonic transducers, for example, can inject ultrasound waves into the body, receive the returned wave and convert it to an electrical signal (a voltage).
d. Sonar sensors, Piezoelectric elements are also used in the detection and generation of sonar waves. Applications include power monitoring in high power applications such as medical treatment, sono chemistry and industrial processing etc.
e. As chemical and biological sensors, Piezoelectric microbalances are used as very sensitive chemical and biological sensors. Piezo are also used as strain gauges.
f. Automotive application, automotive engine management systems use a piezoelectric transducer to detect detonation by sampling the vibrations of the engine block. Ultrasonic piezo sensors are used in the detection of acoustic emissions in acoustic emission testing.
g. Piezo-resistive silicon devices, the piezo-resistive effect of semiconductors have been used for sensor devices employing all kinds of semiconductor materials such as germanium, polycrystalline silicon, amorphous silicon and single crystal silicon. Since silicon is today the material of choice for integrated digital and analog circuits the use of piezo-resistive silicon devices has been of great interest. It enables the easy integration of stress sensors with Bipolar and CMOS circuits.
h. Piezo-resistors, Piezo-resistors are resistors made from a piezo-resistive material and are usually used for measurement of mechanical stress. They are the simplest form of piezo-resistive device.
i. In Music instruments, Piezoelectric transducers are used in electronic drum pads to detect the impact of the drummer's sticks.

6.1. The piezo-resistive effect

It is the changing electrical resistance of a material due to applied mechanical stress. The piezo-resistive effect differs from the piezoelectric effect. In contrast to the piezoelectric effect, the piezo-resistive effect only causes a change in resistance; it does not produce an electric potential

6.2. Some other applications in practice

6.2.1. Tokyo Railway Will Have Piezoelectric Power Generators

The tests are concluded in February 2009

The East Japan Railway Company (JR East) has announced that it will outfit the floor of its Tokyo railway station with piezoelectric devices that have the capacity to draw electricity from the steps of those passing in front of ticket booths. For now, the experiment will be fairly limited, covering a small area but, if successful, the system will be implemented at a large scale, probably in all railway or subway stations in Japan, or even worldwide.

According to company officials, the piezoelectric system will be able to supply 1,400 kW/sec under normal traffic condition, which means that it could power up all displays in the station by itself. Of course, the amount of electricity it puts out is directly dependent on the number of people walking over it, to trigger the electric potential of thousands of tiny devices.

Piezoelectric materials, usually crystals or ceramics, have the capability to generate a small amount of current, when they are subjected to mechanical pressure, such as pushing, bending, twisting and turning. Such multiple materials, placed near each other in densely-trafficked areas, could power up even larger structures, provided that the stream of passengers are large enough.

The limitations that these materials have, are the same as for nearly all renewable energy sources – once the "trigger" (the Sun, the wind, human steps etc.) is gone – the power-generating capacity decreases drastically.

The test portion of the railway in Tokyo will only have about 25 sq meters (82 square feet), and it will still be capable of producing sufficient amounts of current.

The piezoelectric materials started testing on December 10th and functioned non-stop until February 2009.

6.2.2. Piezoelectric Crystals Turn Roads into Power Plants

The system is tested in Israel starting January 2009

A new design, devised by HaimAbramovich, a developer at the Technion-Israel Institute of Technology in Haifa, Israel, may hold the key to harnessing the power of moving vehicles to create electricity, he says. Piezoelectric crystals could be used to absorb heavy traffic and convert a 1 kilometer stretch of highway into a 400 kilowatt power plant, much like Japan's railway project.

Innowattech, Abramovich's Haifa-based spin-off company, already announced its intentions of testing the new system as early as January 2009, on a short stretch of highway, about 100 meters long, in Northern Israel. The researcher says that, if successful, the new concept could be implemented in many highways and freeways, through basic maintenance work, without the need for further digs in the pavement.

Piezoelectric materials, crystals and ceramics have the ability to generate a small electric potential when they are subjected to mechanical stress, which makes them suitable for a variety of applications, from harnessing sounds to producing electricity. Piezoelectric concepts include the use of these small devices to capture sound waves from cell phones and convert them into current to feed the battery. This would basically create a self-powering device that would never need re-fuelling.

Critics to the Israeli system say that inserting this type of materials in the surface of the road would basically increase the traction force cars would have to exert on the road, as the surface of the street would resemble that of a mud-covered area. This would mean that fuel consumption would increase, though even opponents admit that powering roadside structures would be very beneficial to everyone.

Regardless of this project, the future of piezoelectric materials looks bright, with studies focusing on their properties and applications even in nanotechnology. If a compromise between the hardness of the road and the make-up of the small devices is reached, then undoubtedly the system will benefit both drivers and the Israeli national power grid.

7. Summarization

With reference to quartz crystals, the terms "X-cut" and "Y-cut" are recommended in place of "Curie cut" and "thirty-degree cut" for plates perpendicular to the X and Y axes respectively. It is suggested that the terms "X-waves", " Y-waves", or "Z-waves " be applied to waves of mechanical vibration the direction of propagation of which is parallel to the X, Y or Z axis respectively, whatever the mode of vibration. For the quantity "meters per millimeter," the name wave-constant, to be designated by the symbol h, is recommended.

It is in general importance for the proper understanding of any paper on piezo-electricity or its applications that the various dimensions of the preparation be clearly specified with respect to the crystal axes, and that the values of the dimensions to be stated. Exceptions may, of course, be made when one of the universally recognized cuts is used and the dimensions of the plates are not essential.

In the first case, we have the cut variously referred to in the literature as "Curie cut," "zero-angle cut," "perpendicular," or "normal" cut. Owing to the evident ambiguity in the use of any of the last three, the term "Curie cut" is preferable. However, a still more concise term would be the "X-cut,"

denoting a plate the normal to whose face, and hence for which the applied electric field, is parallel to an X-axis.

Similarly, the term "Y-cut" would apply to the second type of quartz plate, which has hitherto been referred to as the "30-deg. cut" or "parallel cut." The author ventures to urge that the general adoption of the terms "X-cut" and Y-cut" would at once meet the need for definiteness, brevity and consistency.

Fig. 7 illustrates the X-cut (at the right) and the Y-cut (above) with reference to the crystal axes. The thickness dimensions are parallel to the X- and Y-axes, respectively, while in each case the breadth of the plate is perpendicular to the diagram (parallel to the optic axis).

As is well known, it is exceedingly difficult to cut quartz plates with such precision as to avoid very complex types of vibrations, so that in any given case, owing partly to the effects of elastic reaction and lack of uniformity of the electric field, a wild medley of both longitudinal and transverse waves may be present. Fortunately, the frequencies commonly employed in practice are usually found to have values in fair agreement with those calculated for one or other of the simple vibration modes. In what follows only these simple modes, need be considered.

X-Cut-The chief mode of vibration is longitudinal, in the direction of the X-axis, employing the longitudinal piezo-electric effect; the Y-axis, employing the transverse piezo-electric effect; or the Z-axis, in which case, the vibrations are produced by elastic reaction. The use of the term "transverse vibrations" of quartz plates as applied to longitudinal vibrations which are "transverse" with respect to an electric axis is inconsistent and likely to lead to serious confusion. The characteristic elongation of the plate through the transverse effect is illustrated below in Fig. 7.

One of the most important characteristics of a piezo-electric resonator is that quantity known as the "meters per millimeter," that is, the number of meters of electromagnetic wavelength for the fundamental mode of vibration along any dimension, divided by that dimension expressed in millimeters. For this quantity the term wave-constant is recommended. The term is of course applicable to resonators formed from any kind of crystal. It is suggested that for the wave-constant the symbol has be adopted.

In order to avoid the confusion that arises from attempts at specifying modes of vibration, it is recommended that the term "X-waves", "Y-waves," or "Z-waves" be applied to waves of whatever type whose direction of propagation is parallel to the X, Y or Z axis respectively. For example, instead of the phrase "longitudinal vibrations of a Curie cut plate in the direction of the Y-axis" we would now write "Y-waves in an X-cut plate."

Y-Cut-The only mode of vibration that has received much attention hitherto appears to be a shear vibration, the shearing strain taking place about the Z-axis and the direction of wave propagation being parallel to the Y-axis. The wave velocity, and hence the wave constant for-the fundamental frequency, calculated on the assumption of shear vibrations from the accepted values of the elastic constants of quartz, are in fair agreement with observation. In Fig. 7 the nature of the shearing strain produced in a Y-cut plate is indicated.

8. Rochelle salt

This crystal, when in an electric field is subjected primarily only to a shearing stress, hence in the case of plates cut with all edges parallel to the axes, shear vibrations are the type to be expected in an alternating field, although, through elastic reactions, the possibility of longitudinal vibrations is not excluded. As is well known, plates may also be cut from a Rochelle salt crystal in such a manner as to exhibit resultant extensions and contractions in directions perpendicular to the electric field, so that in this sense one may speak of longitudinal vibrations produced by the transverse effect in Rochelle salt. No longitudinal effect exists with this crystal.

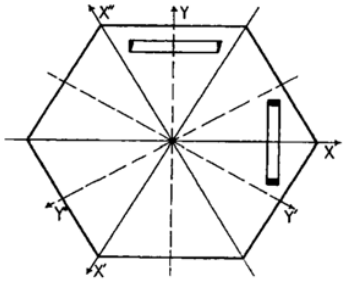

Fig. 7.Rochelle Salt crystalline structure

Strictly, all piezo-electric preparations commonly used in radio are resonators. Nevertheless, in order to avoid the confusion which has already begun to appear in various publications, it is suggested that the term "resonator" be used, as a rule, in a more restricted sense, and that the following definitions be adopted.

Piezo-Electric Resonator- Any device that may be excited piezo-electrical into resonant vibrations at one or more frequencies. In a more restricted sense the term is also applied to such a device when so connected as to exert no appreciable controlling effect upon the applied frequency through its reaction.

Piezo-Electric Oscillator- A circuit containing a resonator and possessing too little regeneration to oscillate of it, but which oscillates through the reaction of the resonator when the latter is vibrating near one of its normal frequencies with energy derived from the circuit. Such a circuit is often called a "crystal-controlled" or "quartz-controlled" circuit, also a "piezo-oscillator." *Piezo-Electric Stabilizer*-A stabilized circuit is one which oscillates without the resonator, but the frequency of which is, usually over a rather narrow range, stabilized when the resonator is connected to the circuit. The resonator itself may, in this case be referred to as a "piezoelectric stabilizer."

Since the distinction between a stabilizer and an oscillator lies largely in the amount of regeneration, it follows that the transition from one to the other may be gradual.

A Crystal Monitor or Piezo-Electric Monitor consists of a resonator in an independent circuit of low power (resonator, stabilizer, or oscillator) serving as a frequency standard to which a generator may be tuned.

A Piezo-Electric Calibrator is a resonator, or set of resonators, so connected as to serve as a frequency standard for the calibration of frequency meters, etc.

9. Conclusions

Experiments on the frequency of piezo-electric elements are described with special reference to the effect due to supersonic sound waves generated in the air gap of the holder and due to its capacity. It is shown that a mechanical load on the crystal increases its thickness frequency and that an air gap has a similar effect. The velocity of the supersonic sound waves is about the same as for ordinary sound waves. The value found is 338.68 meters per second at 24.5C deg.

An appropriate air gap gives even more high frequency output than a mechanically-loaded crystal and procures a steady frequency operation. Two sputtered piezo-electric elements can produce a beat frequency which is correct within a few parts in 100,000. A method is shown by means of which a low-frequency standard can be obtained by harmonic division of a high frequency due to piezo-electric element.

It is possible to generate Electrical Energy by the use of unwanted ground vibrations or simply sound pollution causing vibrations by the use of PIEZO GENERATION. Further, it is also possible to generate Electrical Energy by usual vibration causing works like Message typing in Mobiles, Bike rides, listening music from Audio decks, travelling in conventional trains, etc.,

Hence all the usual and useless works can be effectively turned into most powerful ELECTRICITY (ELECTRICAL ENERGY) GENERATION by the use of Piezo Sensors.

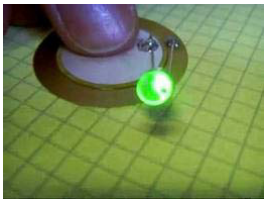

Fig. 8. Piezo-Gen

References

1. Walter G. Cady. Piezo-Electric Terminology, Proceedings of the Institute of Radio Engineers, Volume 18, Number 12 December, 2006.
2. Z.F. Hochfrequenztechnik,Notes on quartz plates, air gap effect, and audio-frequency generation by August Hund (Bureau of Standards, Washington, D. C., Dec. 1996, 178-187; April, 1997, 114-118.
3. Marian Keck, A new approach of a piezoelectric vibration-based power generator to supply next generation tire sensor systems, Department of Micromechanical Systems, Ilmenau Technical University, Germany.
4. APOLLO Project IST-2001-34372, intelligent tyre for accident-free traffic, Final Report, 2005
5. Continental AG, Continental's intelligent tire pressure monitoring system by ootimiles, ABS control and ESC. Press Release available at www.conti-online.com, March 2007
6. S. Koundy and P. K. Wright, A Piezoelectric Vibration based generator for wireless electronics, Smart Mater. Struct. 13, p. 1131-1142, 2004
7. H. A. c. Tilmans, Equivalent circuit representation of electromechanical transducers-part i/ii by J.Micromech. Microeng. 6/7, p. 157-176/285-309, 1996/1997
8. http://news.softpedia.com/cat/Technology/

International Journal of Innovative Technologies
WWW.IJITECH.ORG
ISSN 2321-8665
Vol.03,Issue.11,
December-2015,
Pages:2217-2222

Three Phase H6 Transformer less PVA Grid Connected Inverter

SHASHI KUMAR. K[1], S. RAJESH[2], N. NIREEKSHAN[3]

[1]PG Scholar, Dept of EEE(PE), Siddhartha Institute of Engineering and Technology, Hyderabad, TS, India, E-mail: shashi.psr5@gmail.com.

[2]Associate Professor, Dept of EEE, Siddhartha Institute of Engineering and Technology, Hyderabad, TS, India, E-mail: rajesh118@gmail.com.

[3]Assistant Professor, Dept of EEE, Siddhartha Institute of Engineering and Technology, Hyderabad, TS, India, E-mail: nireekshan222@gmail.com.

Abstract: In this paper a new H6 topology is introduced with sinusoidal PWM (Pulse Width Modulation) technique taking a reference of three phase sin waves, each wave with a phase shift of 120 degrees. The input is considered to be PVA with low voltage magnitude, where the H6 converter converts the DC output voltage of the PVA to three phase AC output. During the conversion the output voltage is boosted with a certain gain value increasing the amplitude of the output AC waveform. The PWM output of the converter is fed to LC filter and converted to sinusoidal wave with reducing the THD (Total Harmonic Distortion). The complete analysis is carried out in MATLAB Simulink 2012a software with all graphical representations and reports.

Keywords: THD (Total Harmonic Distortion), PWM (Pulse Width Modulation), PVA.

I. INTRODUCTION

Nowadays, the invention and development of new energy sources are increasing due to the poisonous results caused by oil, gas and nuclear fuels. This has led the renewable energy sources especially the solar PV systems to the prime position in the generation of electricity [4]. Photovoltaic have applications ranging from small power supplies to power grids. Photovoltaic systems connected to the grid have several advantages such as simplicity in installation, high efficiency, reliability and flexibility [5]. With a reduction in system cost PV technology seems to be an efficient means of power generation. A solar grid connected power generating system usually consists of a solar panel in which the solar cells are arranged to track sunlight, an inverter to convert the DC to AC and the grid. This paper evaluates a single phase transformerless inverter topology called H6, which can minimize the dangerous leakage currents between the solar power generation system and the electrical grid. Transformers are employed in the grid tied systems to provide a galvanic isolation between the PV panel and the grid for safety considerations [2].Line frequency transformers were employed in most of the PV grid tied inverters. But in line frequency transformers due to their low frequency, the size, cost, weight etc. will be higher. The next option is the high frequency transformers. The usage of high frequency transformers increases the number of power stages which affects the efficiency in an adverse manner [1]. When these transformers are eliminated there will be a galvanic connection between the solar module and the grid which results in a potential fluctuation between the PV array and the ground.

The potential variation leads to the flow of common mode leakage currents that has to be eliminated which otherwise leads to electromagnetic distortions, interferences, harmonics and other power quality issues. The H6 transformerless inverter topology with unipolar sinusoidal PWM strategy seems to be a better solution to reduce these leakage currents by maintaining the common mode voltage constant. A simple boost converter is employed to boost the voltage available from the PV panel so as to connect to the grid. The block diagram for the system is shown in fig.1.

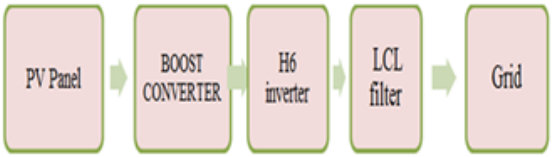

Fig. 1. Operational modules of the inverter.

From the aforementioned analysis, an extra switch S6 is introduced into the H5 inverter topology between the positive terminal of the PV array and the terminal (B) to form a new current path. As a result, a novel H6 transformerless full-bridge inverter topology is derived, as shown in Fig. 2. Similarly, the extra switch S6 can be introduced into the H5 inverter topology between the positive terminal of the PV array and the terminal (A) to form a new current path as well, as shown in Fig. 2. Therefore, a new circuit structure of novel H6 inverter is presented. As a result, the conduction loss of the proposed H6 topologies is higher than HERIC topology and less than H5 topology.

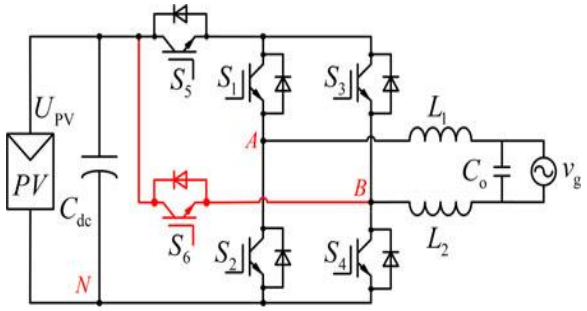

Fig. 2. Proposed H6 topology for one phase.

II. OPERATIONAL MODES

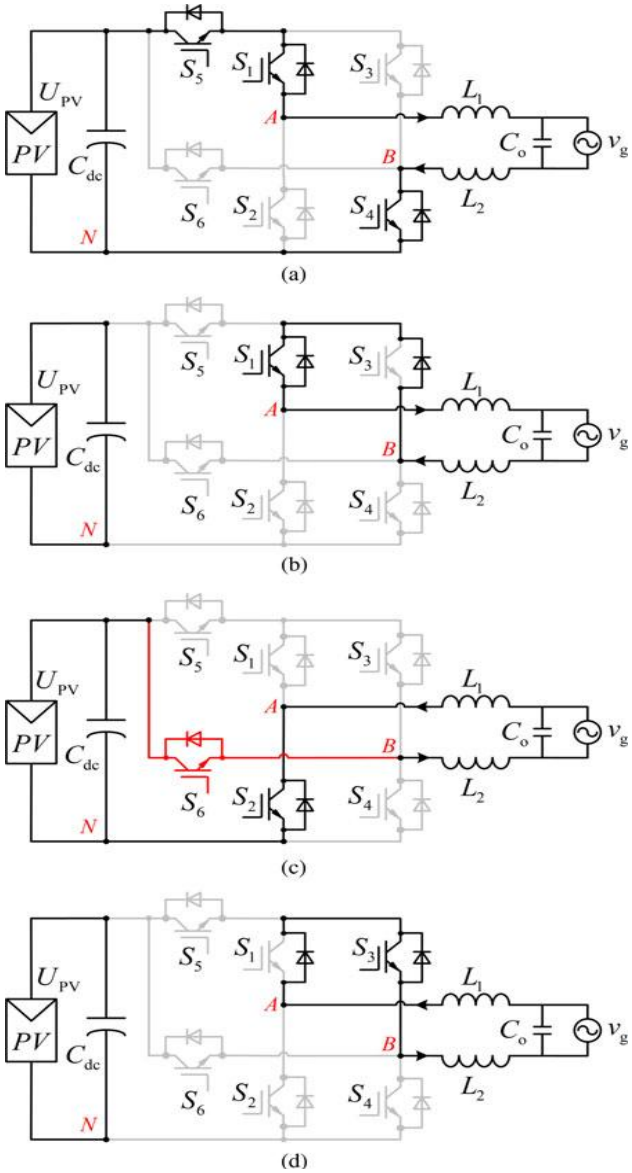

Fig. 3. Equivalent circuits of operation modes. (a) Active mode in the positive half period. (b) Freewheeling mode in the positive half period. (c) Active mode in the negative half period. (d) Freewheeling mode in the negative half period.

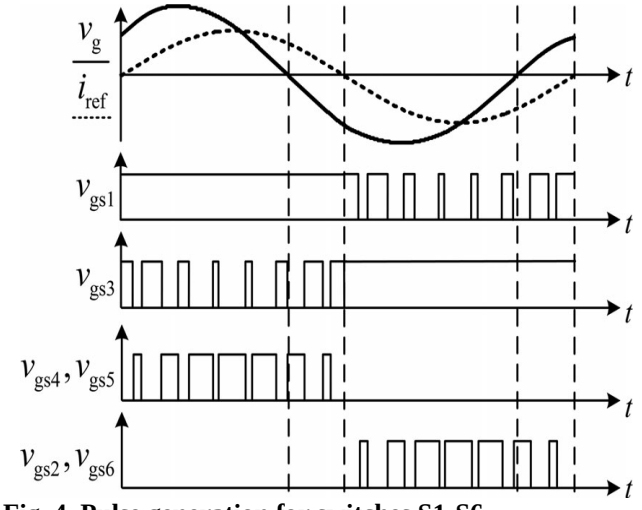

Fig. 4. Pulse generation for switches S1-S6.

The circuit structure of proposed novel H6 inverter topologies shown in Fig. 3(a) is taken as an example to analysis. PV grid-tied systems usually operate with unity power factor. The waveforms of the gate drive signals for the proposed novel H6 topology are shown in Fig. 3, where vg is the voltage of utility grid. iref is the inductor current reference. vgs1 to vgs6 represent the gate drive signals of switches S_1 to S_6, respectively.

- Mode I is the active mode in the positive half period of the utility grid voltage, as shown in Fig. 3(a). S1,S4, and S5 are turned ON, and the other switches are turnedOFF. The inductor current is flowing through S1,S4, and S5. vAN = UPV,vBN = 0; thus, vAB = UPV, and the CM voltage vCM =(vAN + vBN)/2 = 0.5UPV.
- Mode II is the freewheeling mode in the positive half period of the utility grid voltage, as shown in Fig. 3(b). S1 is turned ON; the other switches are turned OFF. The inductor current is flowing through S1 and the antiparalleled diode of S3. vAN = vBN ≈ 0.5UPV; thus, vAB = 0, and the CM voltage vCM =(vAN + vBN)/2 ≈ 0.5UPV.
- Mode III is the active mode in the negative half period of the utility grid voltage, as shown in Fig. 3(c). S2,S3, andS6 are turned ON; the other switches are turned OFF. The inductor current is flowing through S2 and S6. Although S3 is turned ON, there is no current flowing through it, and the switch S3 has no conduction loss in this mode. Nevertheless, in the H5 topology, the inductor current flows through S2,S3, and S5. Therefore, the conduction loss of proposed topology is less than that of H5 topology. In this mode, vAN = 0, vBN = UPV; thus, vAB = −UPV, and theCM voltage vCM=(vAN + vBN)/2 = 0.5UPV.
- Mode IV is the freewheeling mode in the negative half period of the utility grid voltage, as shown in Fig. 3(d). S3 is turned ON, and the other switches are turned OFF. The inductor current is flowing through S3 and the antiparalleled diode of S1. vAN = vBN ≈ 0.5UPV; thus,

vAB = 0, and the CM voltage vCM =(vAN + vBN)/2 ≈ 0.5UPV.Based on the aforementioned analysis, the PV array can be disconnected from the utility grid when the output voltage of the proposed H6 inverter is at zero voltage level and the leakage current path is cut off.

The CM voltage of the proposed topology in each operation mode is equals to 0.5UPV, and it results in low leakage current characteristic of the proposed H6 topologies. The proposed H6 topology with unipolar SPWM method not only can achieve unity power factor, but also has the ability to control the phase shifts between voltage and current waveforms. The modulation strategy is shown in Fig. 4. The drive signal is in phase with the grid-tied current. Therefore, it has the capability of injecting or absorbing reactive power, which meets the demand for VDE-4105 standard.

III. MODELING OF PVA

For efficient renewable power generation PVA is used to generate power from solar irradiation. As the load demand is increasing day by day the power generation also has to be increased, but due to the traditional way of power generation is causing global warming. Due to this the efficiency of the PVA has to be increased by adding silicon surface on the panel. And also employ MPPT techniques to track maximum power during any irradiation and atmospheric conditions. The design of PVA is done in MATLAB with Simulink block, with mathematical representation. Voltage of PVA completely depends on solar irradiation (Sx) and ambient temperature (Tx). PVA (Photo voltaic array) is a combination of series and parallel solar cells arranged in an array to generated the required voltage and current. Each series combination of cells can be considered as photo voltaic module. Increase in series cells increases the voltage and increase in parallel cells increases the current capacity. Formulation for voltage of each cell is given below

$$V_C = \frac{AkT_C}{e}\ln\left(\frac{I_{ph}+I_0-I_C}{I_0}\right)-R_S I_C \quad (1)$$

Where, k = Boltzmann constant (1.38 × 10-23 J/oK).
I_c = cell output current, Amp.
I_{ph} = photocurrent
I_0= reverse saturation current of diode
R_s= series resistance of cell
T_c= reference cell operating temperature
V_c= cell voltage, V.

The Boltzmann constant and the reference temperature have to be in same units ie., either ^{0}C or ^{0}K. The mathematical modeling of the above equation can be constructed using simulink blocks is as below Fig.5. The above design is for a single cell voltage, in order to increase the voltage of the PVA the cell voltage has to be multiplied to a desired values considering each cell voltage as 0.4V. So, the number of series connected cells (Ns) can be calculated as

$$N_s = V_o/0.4 \quad (2)$$

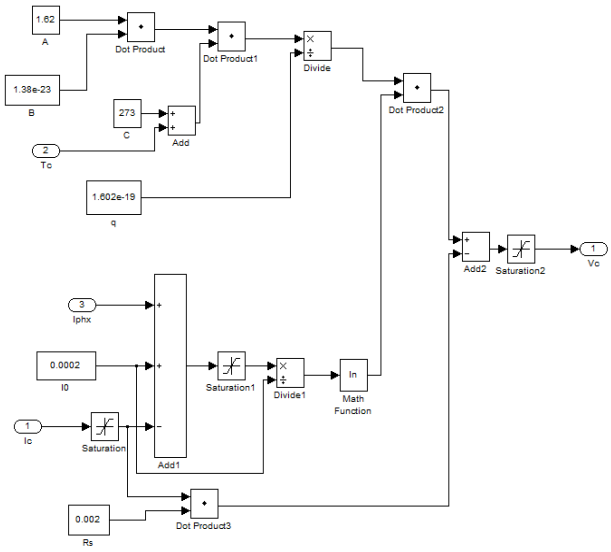

Fig. 5. Simulink model of Vc.

To get each cell current, the total current output from the dependable source has to be divided by number of parallel connected cells (N_p). Therefore, parallel connected cells are considered as

$$N_p = Io/I_{cell} \quad (3)$$

The representation in simulink is taken as shown in Fig.6.

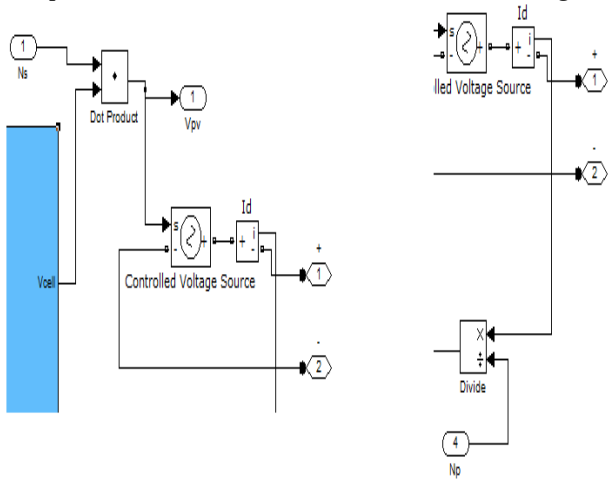

Fig. 6. Simulink modeling of Ns &Np.

For the calculation of Vcx (cell voltage) and I_{phx} (Photocurrent) we need correction factors C_{TV} C_{TI} C_{SV} C_{SI}. The formulation is given as

$$V_{CX} = C_{TV}C_{SV}V_C \quad (4)$$

$$I_{phx} = C_{TI}C_{SI}I_{ph} \quad (5)$$

The correction factors are given as

$$C_{TV} = 1+\beta_T(T_a - T_x) \quad (5)$$

$$C_{TI} = 1+\frac{\gamma_T}{S_C}(T_x - T_a) \quad (6)$$

$$C_{SV} = 1+\beta_T\alpha_S(S_x - S_C) \quad (7)$$

$$C_{SI} = 1 + \frac{1}{S_C}(S_x - S_C) \quad (8)$$

Where, $\beta_T = 0.004$ and $\gamma_T = 0.06$
T_a = reference temperature
T_x = ambient temperature
S_c = reference solar irradiation
S_x = ambient solar irradiation

The values of T_x and S_x changes depending upon the Sun rays which change continuously and unpredictably. The effect of change in solar irradiation varies the cell photocurrent and also the cell voltage (V_c). Let us consider the initial solar irradiation is I_{sx1}& the increase of the irradiation is I_{sx2} which in turn increases the temperature from T_{x1} to T_{x2}, photocurrent from I_{phx1} to I_{phx2}. The mathematical modeling of the correction factors in simulink is given below Fig.7.

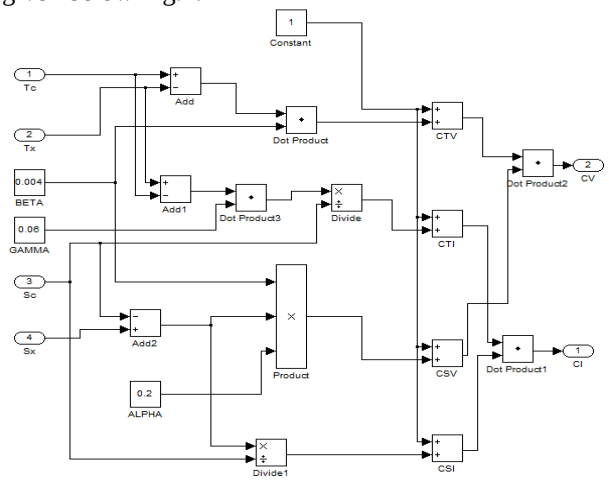

Fig. 7. CI & CV modeling.

Depending upon the solar irradiation and temperature the values of CV & CI are calculated which is fed to V_c block to get the cell voltage value as shown below Fig.8.

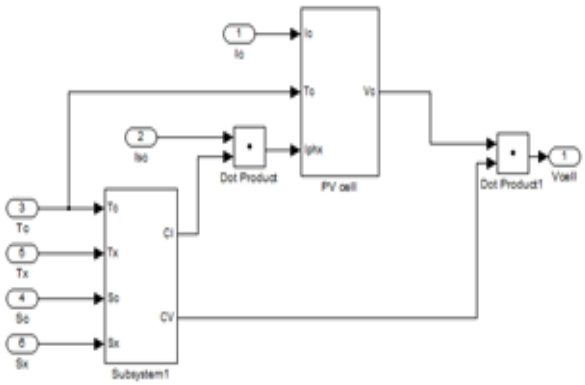

Fig. 8. Combined diagram of CV CI &Vc mathematical models.

The total system diagram of the PVA with all the mathematical formulation are put into a subsystem to make it clear and understandable. The output of the Vc multiplied with the Ns constant block defining the total voltage of the combined cells of the PVA is fed to the voltage controlled voltage source block so as to generate the required voltage. A diode is connected in series at the positive terminal of the PVA to avoid reverse currents passing into the PVA. To reduce the ripples a capacitor can be added later after the diode in parallel as the capacitor doesn't allow sudden change of voltages dV/dt. The complete PVA module with internal block construction is shown in the fig.9 below.

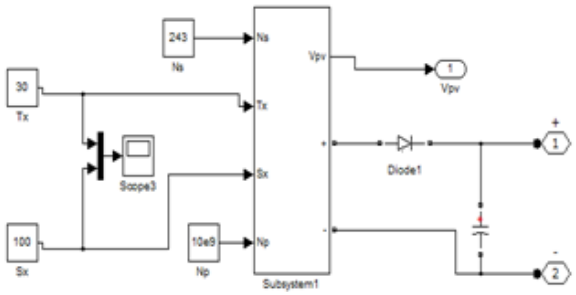

Fig. 9. Complete diagram of PVA.

IV. SIMULINK MODEL AND RESULTS

Simulation results of this paper is as shown in bellow Figs.10 to 13.

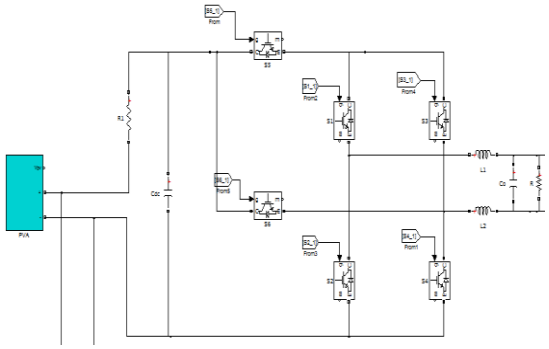

Fig. 10. H6 Simulink model.

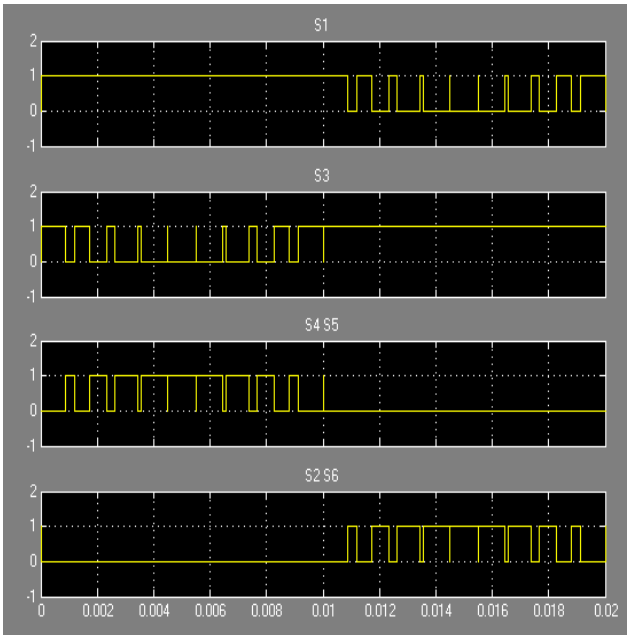

Fig. 11. Pulse waveforms of S1-S6 switches.

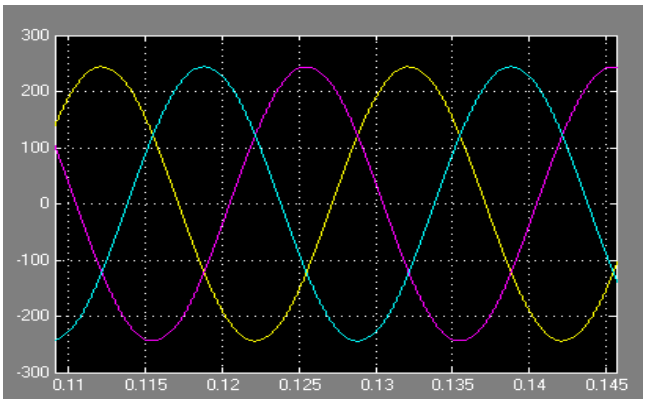

Fig. 12. Three phase output voltages of the three H6 topologies.

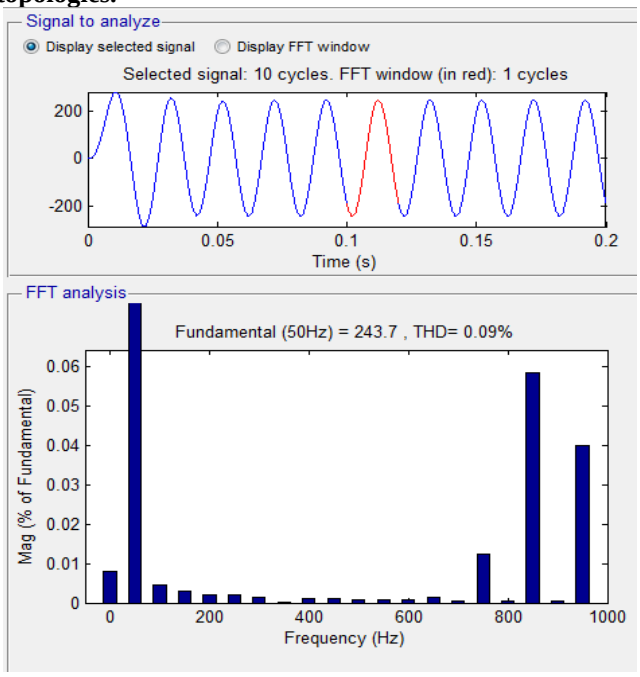

Fig. 13. FFT analysis of phase A voltage (Va).

V. CONCLUSION

With the above results and discussion it can be observed that the output voltages of the three H6 topologies are sinusoidal waveforms with 120 degrees phase shift with a low THD of 0.09%. The LC filter at the output side of the converter minimizes the THD of the H6 topology. As a result the output voltage is boosted to amplitude of 243V from a low voltage of 100V.

VI. REFERENCES

[1]O.Lopez,F.D.Freijedo,A.G.Yepes,P.FernandezComesana , J.Malvar, R.Teodorescu,andJ.Doval-Gandoy, "Eliminating ground current in a transformerless photo voltaic application, "IEEE Trans. Energy Convers., vol.25,no.1,pp. 140–147, Mar.2010.

[2]R.Gonzalez,J.Lopez,P.Sanchis,andL.Marroyo,"Transfor merless inverterforsingle-phase photovoltaic systems," IEEE Trans. Power Electron.,vol.22,no.2, pp.693–697,Mar.2007.

[3]H.XiaoandS.Xie,"Leakage current analytical model and application insingle-phase transformerless photovoltaic grid-connected inverter," IEEETrans.Electromagn. Compat., vol.52, no.4,pp.902–913,Nov. 2010.

[4]VDE-AR-N4105:Power Generation Systems Connected to the Low-Voltage Distribution Network—Technical Minimum Requirements For the Connection to and Parallel Operation with Low-Voltage Distribution Networks, DIN_ VDENormo,2011–08.

[5]B.Yang,W.Li,Y.Gu,W.Cui, and X.He, "Improved transformerless inverter with common-mode leakage current limination for a photovoltaic grid-connectedpowersystem, "IEEETrans.PowerElectron.,vol.27,no.2,pp.752–762,Feb. 2012.

[6]R.Gonzalez,E.Gubia,J.Lopez,andL.Marroyo,"Transforme rlesssingle-phasemultilevel based photovoltaic inverter, "IEEETrans.Ind.Electron.,vol.55,no.7,pp.2694–2702,Jul. 2008.

[7]H.Xiao and S.Xie, "Transformerless split-inductor neutralpointc lamped three-levelPVgrid-connected inverter, "IEEETrans. Power Electron., vol.27,no.4,pp.1799–1808, Apr. 2012.

[8]L.Zhang, K.Sun,L.Feng, H.Wu,and Y.Xing, "A family of neutral point clamped full-bridgetopologies for transformer less photovoltaic grid-tied inverters, "IEEETrans. Power Electron.,vol.28,no.2,pp.730–739,Feb. 2012.

[9]German Patent We chselrichter: DE19642522C1Apr. 1998.

[10]Y.Gu,W.Li, Y.Zhao, B.Yang, C.Li,andX.He, "Transformerless inverter with virtual DC bus concept for cost-effective grid-connected PV power systems, "IEEETrans. PowerElectron.,vol.28,no.2,pp.793–805,Feb. 2012.

[11]M.Victor, F.Greizer, S.Bremicker, and U.H¨ubler, "Method of converting a direct current voltage from a source of direct current voltage, more specifically from a photovoltaic source of direct current voltage, intoaalternatingcurrentvoltage,"U.S.Patent7411802,Aug.12, 2008.

Author's Profile:

K. Shashi Kumar, B.Tech in Electrical and Electronics Engineering in CVR College of Engineering, Hyderabad from JNTUH. Now pursuing M.Tech specialization in power electronics in Siddhartha institute of engineering and Technology. His area of interest is Power electronic and drives systems.

N. Nireekshandone the btech in electrical and electronics in Arjun College of Technology and Science from JNTUH in 2006 and M.Tech specialization in power electronics in lords institute of engineering and technology from JNTUH in 2013 respectively. He done the M.Tech project

unidirectional torque production by using seven level multi level inverter in RV TOPOLOGY technique. He currently serving as Assistant Professor in siddhartha institute of engineering and Technoloy Hyderabad, Telangana, India.He has 3 years teaching experience .

S.Rajesh received the B.Tech degree in Electrical & Electronics Engineering from Jawaharlal Nehru Technological University Hyderabad ,Telangana ,India in 2006 and M.Tech degree in Power Electronics from Jawaharlal Nehru Technological University Hyderabad ,Telangana ,India in 2010 respectively. He has presented nearly 5 papers in National level conferences. His research interests are power electronics applications in distributed power generation and analysis of power converters, control and estimation in induction motor drive and wind turbine driven induction generator. Currently he working on stability studies of Double Fed Induction Generator in Wind power Generation. He is a Student member of IEEE and life Member of ISTE (India). He currently serving as Associate Professor & Head of the Department of Electrical and Electronics engineering in siddhartha institute of engineering and Technology Hyderabad, Telangana, India. He has 8 years experience in teaching.

International Journal of Engineering Research and General Science Volume 3, Issue 4, Part-2, July-August, 2015
ISSN 2091-2730

A HIGH STEP UP RESONANT BOOST CONVERTER USING ZCS WITH PUSH-PULL TOPOLOGY

Maheswarreddy.K , PG Scholar. Suresh.K , Assistant Professor

Department of EEE, R.G.M College of engineering, Kurnool (D), Andhra Pradesh, India

Maheswarreddy.power@gmail.com, karasani.suresh@gmail.com.

Abstract— This dissertation proposes a push-pull boost power factor corrector (PFC). It is composed of two boost converters with a coupled inductor. The two identical modules can share the output power and increase the power capability up to the medium power level applications. The main advantage is coupling the two independent boost inductors into a single magnetic core to substantially reduce the circuit volume and the cost without degrading the conversion efficiency too much, which are the important targets of the modern switching power supply design. The interleaved operations of the switches with a cut-in-half duty cycle can reduce the conduction losses of the switches as well as both the turns and diameters of the inductor windings, which help more to the reduction of the circuit volume. Moreover, the operating frequency of the core, and thus the frequency of the two-phase inductor current ripple, is double that of the switching frequency. Also the ripple current at the input side and the output capacitor size are reduced. The power factor and the power density are improved.

Keywords— push pull topology, coupled inductor, quasi resonant converter

INTRODUCTION

Generally boost converter topology is the most commonly used technique to improve the power factor. It is always necessary to reach power factor as unity a cost effective solution can be obtained for greater than 0.95.In this proposed system we are using the push-pull technique to boost up the voltage level up to 380V dc for an input of 110 V ac supply.

A push–pull converter is a type of DC-to-DC converter that uses a transformer to change the voltage of a DC power supply. The proposed system having the capable of operating three modes of operation they are Continuous Conduction Mode, Discontinuous Conduction Mode and Transition Mode.

Even though Continuous Conduction Mode best suitable for high power applications the inductor value in this mode is high and in case of Discontinuous Conduction Mode the input harmonics level is high. But in case of transition mode the inductor value is moderate and useful for medium power applications so this mode is used for the proposed topology.

Derived from 2 TM boost converters with the interleaved operations, the power rating is increased and the input current and output current are shared equally with lower current ripples. Therefore, the total harmonic distortion (THD) of input current and the output capacitance can be reduced. However, the need of two inductors with two independent cores increases the circuit volume.

In this paper, a push–pull boost PFC composed of two interleaved TM boost PFCs and a coupled inductor is proposed and a single magnetic core is used. The two identical modules can share the output power and promote the power capability up to the medium-power-level applications.

In addition to this coupling of the two distributed boost inductors into a one magnetic core automatically reduces the circuit volume, which is the important goal of the development of switching power supply today. The interleaved operations of the switches act like a push–pull converter. The difference is that the operating frequency of the core is getting double of the switching frequency,

which means that not only the circuit size is reduced and also the operating frequency of the core is getting double of the switching frequency.

The same distributions of the input current and output current, the proposed topology with a cut-in 0.5 duty cycle can reduce the conduction losses of the switches on both the turns and diameters of the inductor windings

It is also maintains the advantages of a TM boost PFC, such as QR valley switching on the switch and zero-current switching (ZCS) of the output diode, to reduce the switching losses and improve the conversion efficiency.

MATLAB/SIMULINK used for the proposed system to simulate for an universal line voltage of 110v ac, a 380-V output dc voltage and a 100-W output power in order to verify its feasibility.

CIRCUIT TOPOLOGY

Fig 1 shows block diagram for push-pull Quasi Resonant converter. Here the power conversion occurs in three segments. In the first segment single phase AC supply is fed to the rectifier, to convert AC to DC. The output from the rectifier is modulated sin wave. This modulated sin wave is given to the quasi resonant converter. Using quasi resonant converter the voltage has been boosted. Then it is given to the load

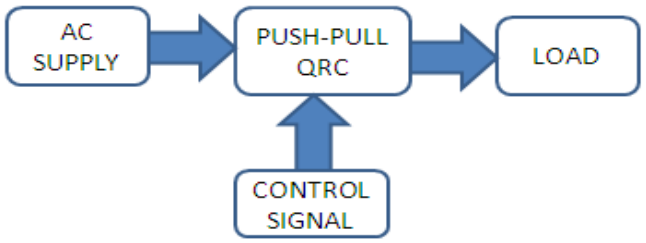

Fig.1. Block diagram of push-pull Quasi Resonant converter

A. Circuit Diagram Of Push-Pull Quasi resonant Converter

The circuit diagram for push- pull quasi resonant converter is shown in fig below. First we are converting ac voltage into dc voltage by using rectifier. The output from the rectifier is modulated sin wave then this supply is given to the push pull quasi resonant converter. This quasi resonant converter boost up the voltage to 380V. The proposed topology is operated by transition mode with constant on time and variable frequency.

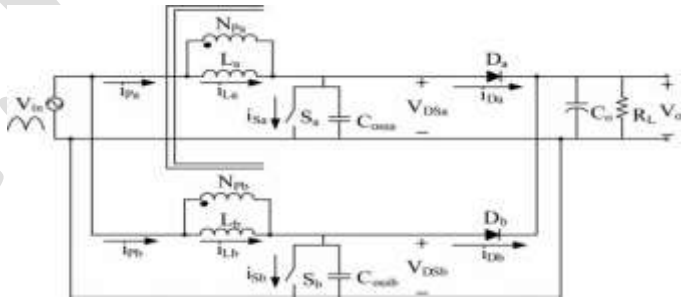

Fig.2.push pull quasi resonant converter

The proposed topology consists of two modules. Module A consists of the switch S_a , the winding $N_{P\,a}$, the inductor L_a , and the output diode D_a . Module B consists of the switch S_b , the winding $N_{P\,b}$, the inductor L_b , and the output diode D_b . These two modules

have a common output capacitor C_o . L_a and L_b are 2 coupled windings wound on the same magnetic core.Theoretically; the same turns of these two windings will lead to the same inductances To analyze the operating principles, there are some assumptions listed as follows.

1)The conducting resistances of S_a and S_b are ideally zero. The conduction time interval is DT_s , where D is the duty Cycle and T_s will be the switching period.

2)The forward voltages of D_a and D_b are ideally zero.

3) The magnetic core for manufacturing L_a and L_b is perfectly Coupled without leakage inductance. In addition, The turns of the windings NPa and NPb will be same. Therefore, L_a and L_b are also matched

OPERATION MODES IN QUASI-RESONANT CONVERTER

The operating modes of the proposed topology are analyzed as follows

A. *Mode 1 operation:* $t_0 < t < t_1$

Referring to Fig4, in module A S_a conducts Thus, the voltage across $N_{P\,a}$ equals to the rectified line- voltage. The inductor current $i_{L\,a}$ increases linearly and D_a is reverse-biased. In module B, S_b is turned OFF. The voltage across NPa is coupled to $N_{P\,b}$. Hence, the voltage across $N_{P\,b}$ is also V_{in}, and the dotted terminal is positive. L_b stores energy as L_a does. The inductor current $i_{L\,b}$ increases linearly and flows into the non dotted terminal of $N_{P\,b}$. By the coupling effect, this current flows into the dotted node of $N_{P\,a}$. Since the voltage across S_b is zero, Db is also reverse-biased. Co supplies the energy to the load . The constant turn-on time of Sa is decided by the management of the controller depending on the rectified line-in voltage Vin. This is the initial mode of operation.

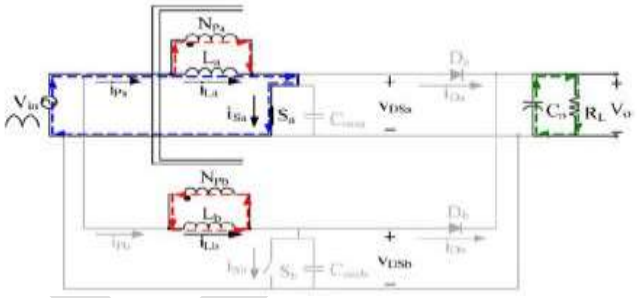

Fig.3. Module A S_a ON, module B S_b OFF

B. *Mode 2 operation:* $t_1 < t < t_2$

As shown in Fig. 5, in module A, S_a is turned OFF. D_a conducts for i_{La} to flow continuously. L_a releases its energy to C_o and the load. The voltage across N_P is ($V_o - V_{in}$) and the dotted terminal is negative. In module B, S_b is still turned OFF the voltage across N_{Pa} is coupled to N_{Pb}. Hence, the voltage across N_{Pb} is also ($V_o - V_{in}$), and the dotted node is negative. D_b is thus forward-biased to carry the continuous i_{Lb}. L_b is also releases its energy to C_o and the load. Both i_{La} and i_{Lb} are decreasing linearly. This state ends until L_a and L_b release their energies completely, and i_{La} and i_{Lb} decrease to zero. in this mode we are boosting the voltage.

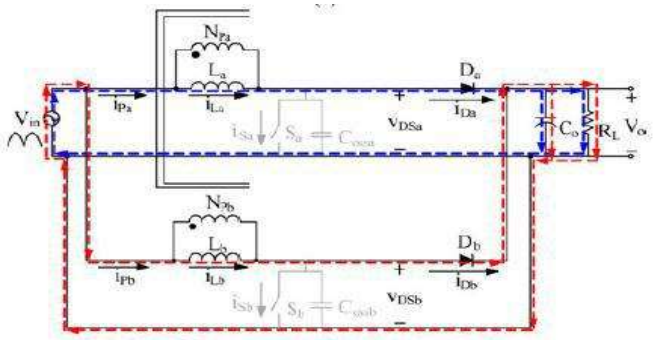

Fig .4.Module A S_a OFF Module B S_b OFF

C. Mode 3 operation: $t_2 < t < t_3$

As shown in Fig. 6, in module A, S_a keeps turned OFF. At t_2, D_a is turned OFF with ZCS since i_{La} decreases to zero naturally. Similarly, in module B, S_b is still turned OFF. D_b is turned OFF with ZCS at t_2 since i_{Lb} decreases to zero naturally, too. In this interval, C_o supplies the energy to the load. At the same time, in module A, the series resonant loop formed by V_{in}, the parallel connection. of L_a and L_b, and the output capacitor switch S_a, C_{ossa}, starts to resonate. Similarly, in module B,the series resonant loop formed by V_{in}, the parallel connection of L_a and L_b, and the output capacitance of the switch S_b, C_{ossb},begins to resonate. Therefore, v_{DSa} and v_{DSb} decrease simultaneously. This mode is helpful to increasing the power factor.

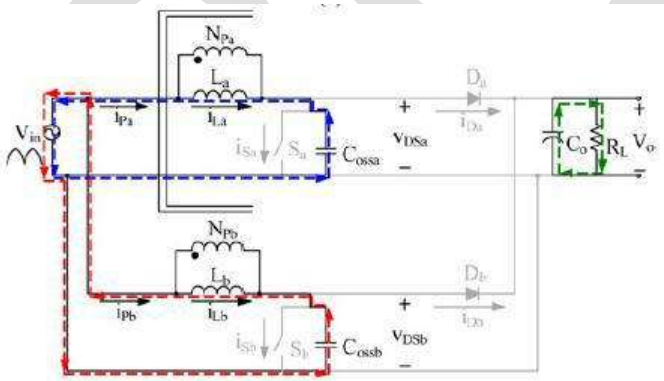

Fig.5.*Module A Sa OFF & Module B Sb OFF*

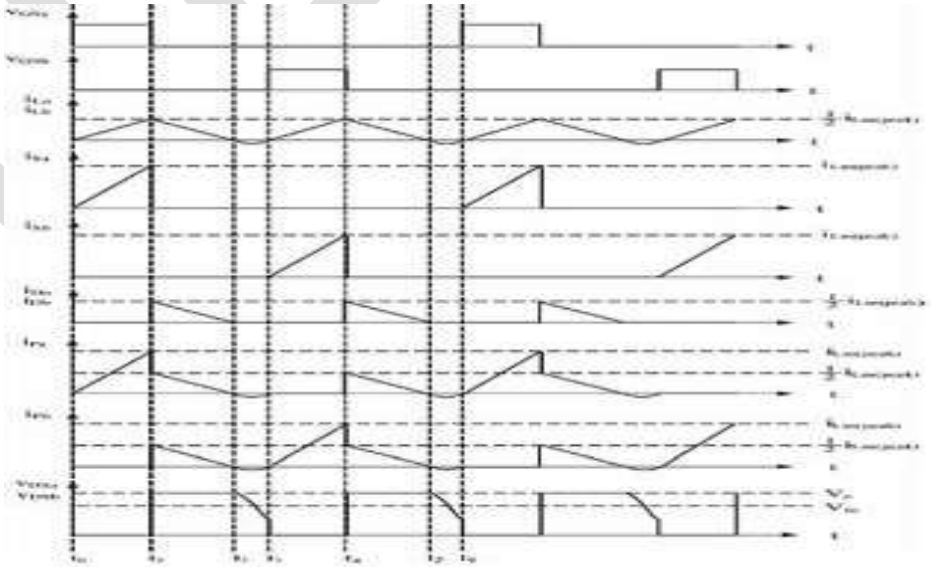

Fig.6.Key wave forms for proposed topology

SIMULATOIN RESULTS

MATLAB/SIMULINK is used for the simulation studies. Fig 7 shows the simulation circuit of push pull quasi-resonant converter with input voltage of 110V AC the corresponding output voltage is 380 dc, Po=100W. The Efficiency of the converter and input current distortion is shown in fig 12 and fig 13.

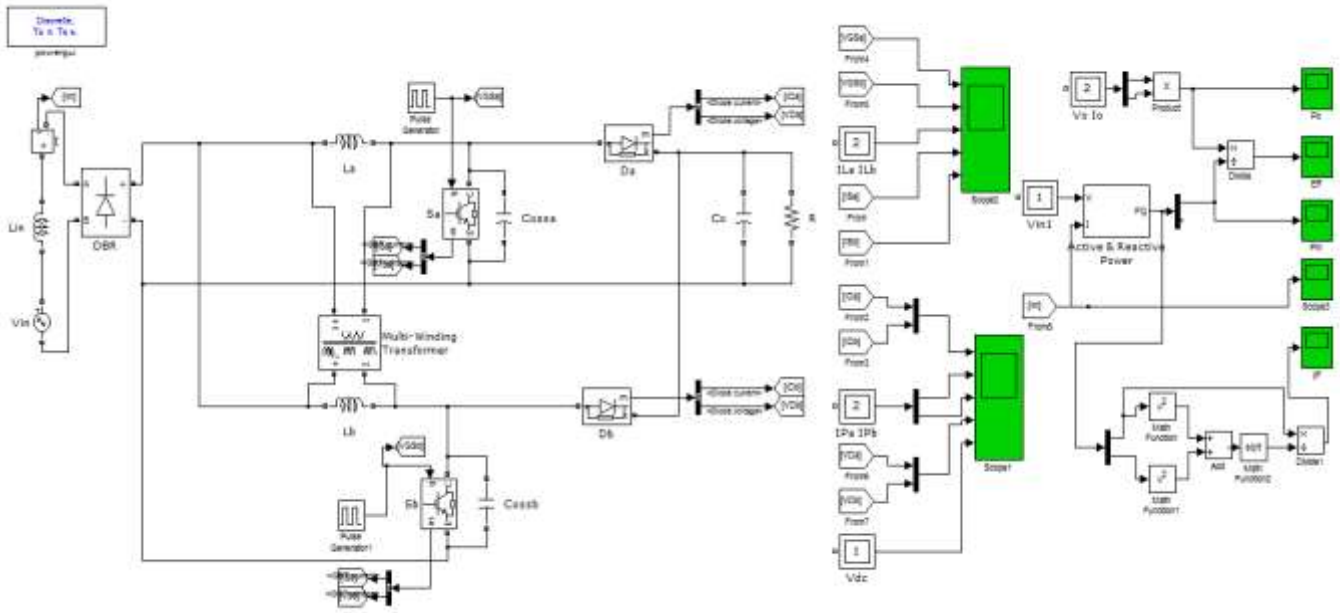

Fig.7.Simulation circuit of push pull quasi resonant converter

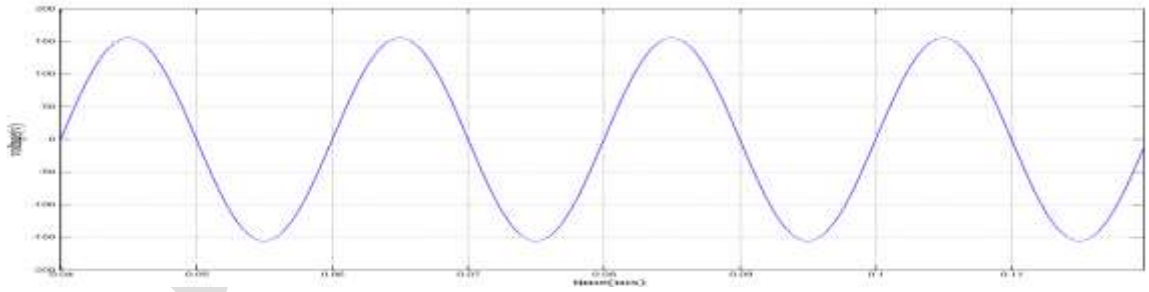

Fig.8.Input voltage of the converter 110 Vac

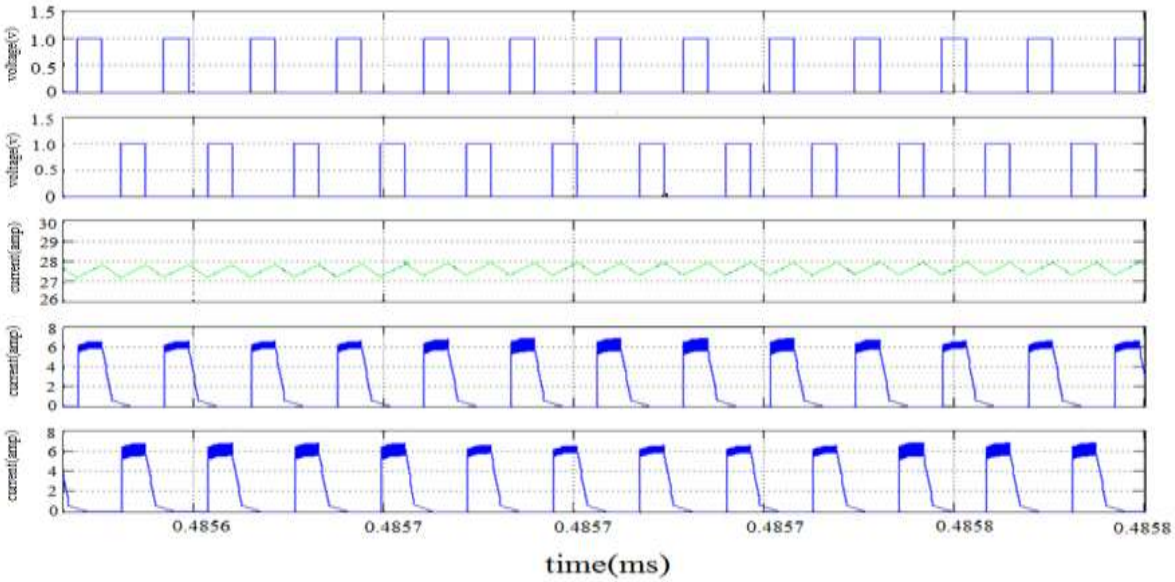

Fig.9.Gate pulses V_{Gsa} &V_{Gsb} , Inductor currents I_{La} & I_{Lb} , Switches currents I_{Sa} &I_{Sb}

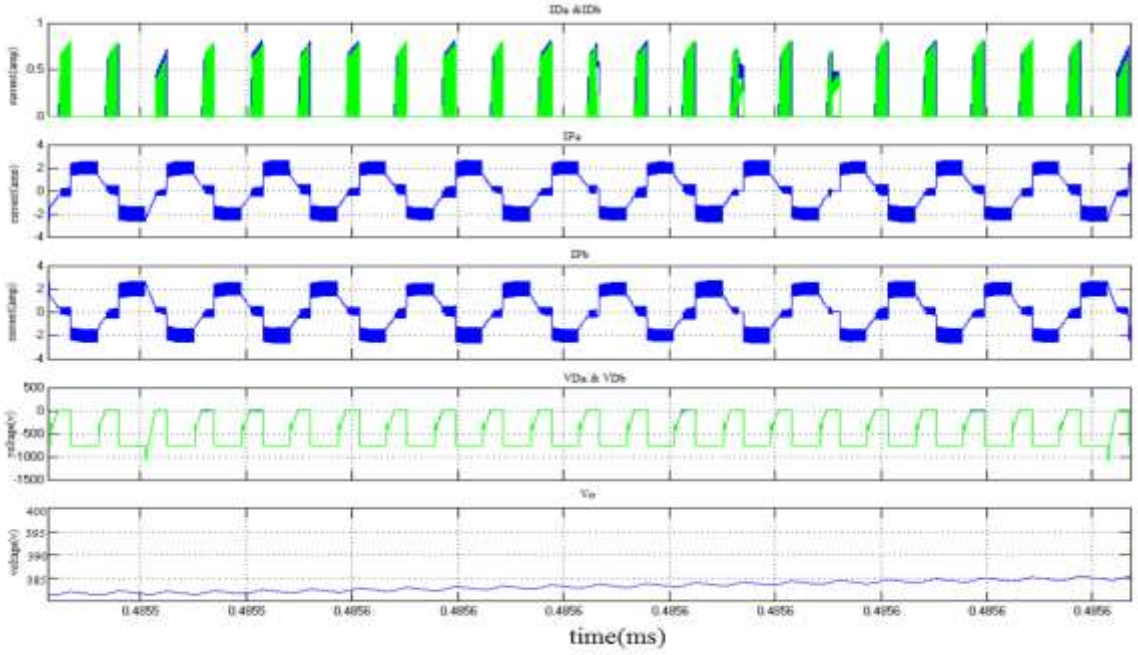

Fig.10. Diode currents I_{Da} & I_{Db}, Winding currents I_{Pa}&I_{Pb}, Voltage across switches V_{Da}&V_{Db}, Output voltage V_o

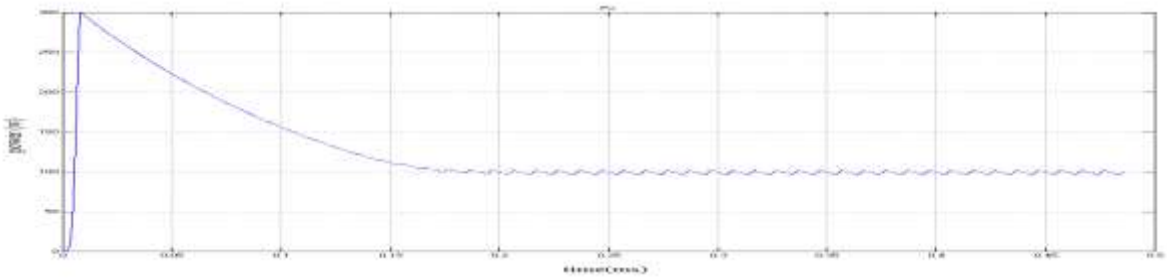

Fig.11.output power 100W

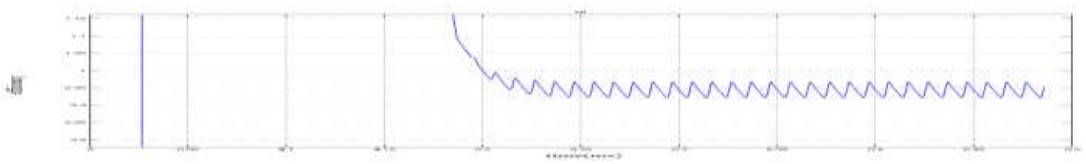

Fig.12. Efficiency of the converter

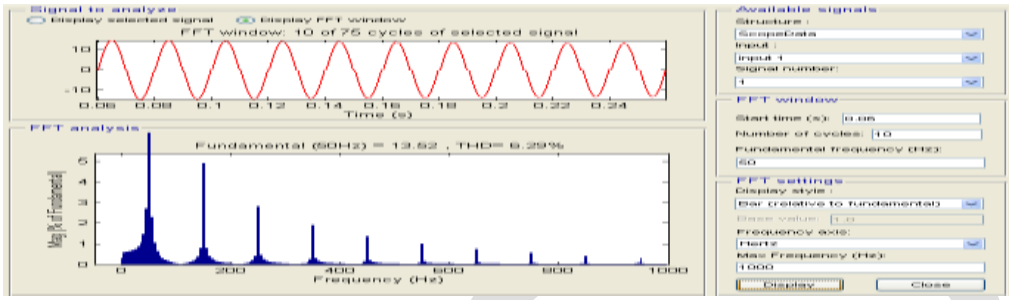

Fig.13. Input currents THD

LOAD	EFFICIENCY	THD	P.F
50	93.2%	7.01%	0.9
100	95.2%	6.24%	0.912
150	96.3%	4.63%	0.99
200	97.3%	3.22%	0.993

Table 1 : Efficiencies, P.F, and THD values at different load levels measured under 110 V_{ac}

LOAD	EFFICIENCY	THD	P.F
50	92.1%	1.12%	0.9224
100	96.2%	6.36%	0.95
150	98.1%	10.43%	0.98
200	98.2%	7.62%	0.995

Table 2 : Efficiencies, P.F, and THD values at different load levels measured under 220 V_{ac}

CONCLUSION

In this paper, a novel of push pull quasi resonant converter techniques for Boost PFC is simulated in order to boost up the voltage level and improve the power factor. Simulation has been done using MATLAB/SIMULINK for an input voltage of 110V AC and power output 100w for 380dc output voltage. In the systems we are gaining the power factor nearby unity

REFERENCES:

[1] K. Yao, X. Ruan, X. Mao, and Z. Ye, ―Reducing storage capacitor of a DCM boost PFC converter,‖ *IEEE Trans. Power Electron.*, vol. 27, no. 1, pp. 151–160, Jan. 2012.

[2] X. Zhang and J.W. Spencer, ―Analysis of boost PFC converters operating in the discontinuous conduction mode,‖ *IEEE Trans. Power Electron.*, vol. 26, no. 12, pp. 3621–3628, Dec. 2011.

[3] B. Su, J. Zhang, and Z. Lu, ―Totem-pole boost bridgeless PFC rectifier with simple zero-current detection and full-range ZVS operating at the boundary of DCM/CCM,‖ *IEEE Trans. Power Electron.*, vol. 26, no. 2, pp. 427–435, Feb. 2011.

[4] B. Akın and H. Bodur, ―A new single-phase soft-switching power factor correction converter,‖ *IEEE Trans. Power Electron.*, vol. 26, no. 2, pp. 436–443, Feb. 2011.

[5] Y.-S. Roh, Y.-J. Moon, J.-C. Gong, and C. Yoo, ―Active power factor correction (PFC) circuit with resistor free zero-current detection,‖ *IEEE Trans. Power Electron.*, vol. 26, no. 2, pp. 630–637, Feb. 2011.

[6] Y.-T. Chen, S. Shiu, and R. Liang, ―Analysis and design of a zero-voltage switching and zero-current-switching interleaved boost converter,‖ *IEEE Trans. Power Electron.*, vol. 27, no. 1, pp. 161–173, Jan. 2012.

[7] .-H. Hsia, H.-Y. Tsai, D. Chen, M. Lee, and C.-S. Huang, ―Interleaved active-clamping converter with ZVS/ZCS features,‖ *IEEE Trans. Power Electron.*, vol. 26, no. 1, pp. 29–37, Jan. 2011.

[8] S. Dwari and L. Parsa, ―An efficient high-step-up inter leaved DC–DC converter with a common active clamp,‖ *IEEE Trans. Power Electron.*, vol. 26, no. 1, pp. 66–78, Jan. 2011.

[9] Y.-C. Hsieh, M.-R. Chen, and H.-L. Cheng, ―An interleaved flyback converter featured with zero-voltage transition,‖ *IEEE Trans. Power Electron.*, vol. 26, no. 1, pp. 79–84, Jan. 2011.

[10] R.-L. Lin,C.-C. Hsu, and S.-K. Changchien, ―Interleaved four-phase buckbased current source with center-tapped energy-recovery scheme for electrical discharge machining,‖ *IEEE Trans. Power Electron.*, vol. 26, no. 1, pp. 110–118, Jan. 2011.

[11] W. Li and X. He, ―A family of isolated inter leaved boost and buck converters with winding-cross-coupled inductors,‖ *IEEE Trans. Power Electron.*, vol. 23, no. 6, pp. 3164–3173, Nov. 2008.

[12] L. Huber, B. T. Irving, andM.M. Jovanovic, ―Open-loop control methods for interleaved DCM/CCM boundary boost PFC converters,‖

[13] *IEEE Trans. Power Electron.*, vol. 23, no. 4, pp. 1649–1657, Jul. 2008

ISSN (Print) : 2320 – 3765
ISSN (Online): 2278 – 8875

International Journal of Advanced Research in Electrical, Electronics and Instrumentation Engineering

(An ISO 3297: 2007 Certified Organization)

Vol. 4, Issue 5, May 2015

Harmonic Analysis of Doubly Fed Induction Generator for Wind Energy Conversion Systems Using MATLAB/Simulink

Y.Mastanamma[1], S.Deepthi[2]

Associate Professor/HOD, EEE Department , Bhoj Reddy Engineering college for women, Saidabad, Hyderabad, Telangana, India

Asst. Professor, Department EEE, Bhoj Reddy Engineering college for women, Saidabad, Hyderabad, Telangana

ABSTRACT: In order to meet power needs, taking into account economical and environmental factors, wind energy conversion is gradually gaining interests as a suitable source of renewable energy. A Wind Energy Conversion System (WECS) differs from a conventional power system. The power output of a conventional power plant can be controlled whereas the power output of a WECS depends on the wind. In this paper the steady state characteristics of a WECS using doubly fed induction generator (DFIG) is proposed and simulated Wind Turbine and doubly-fed induction machine used in generating mode to produce electrical energy on a power network. Simulation analysis is performed to investigate harmonic analysis for DFIG based WECS.

KEYWORDS: Wind energy conversion system, doubly fed induction generator, simulation, MATLAB.

I.INTRODUCTION

Renewable energy sources currently supply about 10 % of the world energy demand. These energy sources will become increasingly important in the future. Wind energy is a form of solar energy produced by heating of the earth's surface. As a power source, wind power is less predictable than solar power, but it is also typically available for more hours in a given day. Wind resources are influence by the type of the land surface and the elevation of the land surface. Generally, if the land is in high elevation then it is good for wind energy conversion. Since the wind speed is extremely important for the amount of energy a wind turbine can convert it to electricity. The power in the wind can be defined as follows,

$$\mathbf{P_W} = \frac{1}{2}\rho A V^3$$

Where, **ρ**: Air density, kg/m3.

A*:* Cross sectional area of wind parcel,

V*:* The wind speed, m/sec.

It is clear that it is clear that the wind power is affected by the wind speed. The wind speed increases with the height most rapidly near the ground, increasing less rapidly with greater height.The wind speed at which electric power production starts called the cut-in wind speed. The turbine will developenough mechanical power to rotate itself at slightly lower speeds, but this wind speed will actually supply all the generator and transmission losses so that useful electric power cannot be produced. At rated wind speed the power input to the wind turbine will reach the limit for continuous operation (rated power). When the wind speed exceeds this level the excess power in the wind must be discarded by varying the pitch angle of the blades to prevent the turbine overloading. The power is maintained at its rated value until a maximum wind speed is reached the cut-off wind speed (Vcut-off) then the turbine will shut down.

ISSN (Print) : 2320 – 3765
ISSN (Online): 2278 – 8875

International Journal of Advanced Research in Electrical, Electronics and Instrumentation Engineering

(An ISO 3297: 2007 Certified Organization)

Vol. 4, Issue 5, May 2015

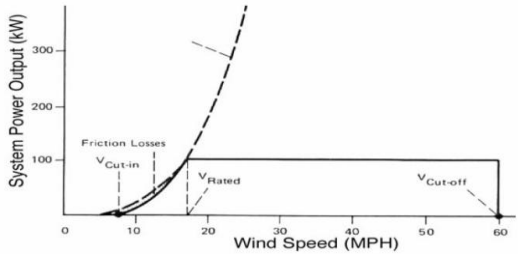

Fig.1. Actual WTG output power with the wind speed

II. GENERATOR SELECTION FOR WIND ENERGY

An important step for installation of wind energy system is to select the turbine rating, the generator and the distribution system. In general, the output characteristics of the wind turbine power do not follow exactly those of the generator power; so they have to be matched in the most reasonable way possible. Based on the maximum speed expected for the turbine and taking into account the cubic relationship between the wind speed and the generated power, the designer must select the generator and the gearbox so as to match these limits. The most sensitive point here is the correct selection of the rated speed for the generator. If it is too low, the high speed of the primary source wind will be wasted; if it is too high, the power factor will be harmed. The characteristics of the commercially available turbines and generators must be matched to the requirements of the project with regard to cost, efficiency, and maximum generated power is an iterative design process. Several types of generators can be coupled to the rotating wind power turbines: dc and ac types, parallel and compound dc generators, with permanent magnets or electrical field excitation, synchronous or non synchronous, and, especially, induction generators. The dc machines are not usually employed because of their high cost, bulky size, and maintenance needs. The right choice of generator depends on a wide range of factors related to the primary source, the type of load, and the speed of the turbine. Besides, systems differ with respect to their applications, whether they are stand-alone or connected to the grid, their degree of interruptibility, and the quality and cost of their output. Because of the way it works as a motor or generator, the possibility of variable speed operation, and its low cost compared to other generators, the induction machine offers advantages for rotating power plants, like the wind power, in both standalone and interconnected applications.

III. DOUBLY FED INDUCTION GENERATOR

A very important machine, typically used for high power applications, is the doubly fed induction generator (DFIG). The DFIG is a wound rotor machine where the rotor circuit is connected to an external variable voltage and frequency source via slip rings and the stator is connected to the grid network. There is also a possibility of altering the rotor reactance by effectively modulating some inductors in series with the original rotor reactance. Adjusting the frequency of the external rotor source of current controls the speed of the doubly fed induction generator, which is usually limited to a 2:1 range. Doubly fed machines were not very popular in the past due to the maintenance required for the slip rings. More recently, with the development of new materials, powerful digital controllers and power electronics, the doubly fed induction generator became a solution in power generation for up to several hundreds of kW ratings. Power converters usually make up the need for a variable frequency source for the rotor. As it is said above, the control of doubly fed induction generators can be exerted either through the stator or rotor variables. The controllable stator variables are number of poles, voltage and frequency. The rotor variables for squirrel cage rotors can be design resistance, design reactance and speed. The doubly fed induction generator is affected by the second power of the grid voltage and the controllable variables are current, voltage, frequency, and voltage phase shift with respect to the stator voltage angle. Obviously, in most applications, this setup can be simplified.

Wind turbines use DFIG consisting of a wound rotor induction generator and an AC/DC/AC IGBT-based PWM converter. The stator winding is connected directly to the 50 Hz grid while the rotor is fed at variable frequency through the AC/DC/AC converter. The DFIG technology allows extracting maximum energy from the wind for low wind speeds by optimizing the turbine speed, while minimizing mechanical stresses on the turbine during gusts of wind. The optimum turbine speed producing maximum mechanical energy for a given wind speed is proportional to the wind speed. Another advantage of the DFIG technology is the ability for power electronic converters to generate or

ISSN (Print) : 2320 – 3765
ISSN (Online): 2278 – 8875

International Journal of Advanced Research in Electrical, Electronics and Instrumentation Engineering

(An ISO 3297: 2007 Certified Organization)

Vol. 4, Issue 5, May 2015

absorb reactive power, thus eliminating the need for installing capacitor banks as in the case of squirrel-cage induction generator.The stator is directly connected to the AC mains, while the wound rotor is fed from the Power Electronics Converter via slip rings to allow DFIG to operate at a variety of speeds in response to changing wind speed. Indeed, the basic concept is to interpose a frequency converter between the variable frequency induction generator and fixed frequency grid. The DC capacitor linking stator- and rotor-side converters allows the storage of power from induction generator for further generation. To achieve full control of grid current, the DC-link voltage must be boosted to a level higher than the amplitude of grid line-to-line voltage. The slip power can flow in both directions, i.e. to the rotor from the supply and from supply to the rotor and hence the speed of the machine can be controlled from either rotor- or stator-side converter in both super and sub-synchronous speed ranges. As a result, the machine can be controlled as a generator or a motor in both super and sub-synchronous operating modes realizing four operating modes. Below the synchronous speed in the motoring mode and above the synchronous speed in the generating mode, rotor-side converter operates as a rectifier and stator-side converter as an inverter, where slip power is returned to the stator. Below the synchronous speed in the generating mode and above the synchronous speed in the motoring mode, rotor-side converter operates as an inverter and stator- side converter as a rectifier, where slip power is supplied to the rotor[3]. At the synchronous speed, slip power is taken from supply to excite the rotor windings and in this case machine behaves as a synchronous machine.

mechanical power and the stator electric power output are computed as follows

$$P_r = T_m * \omega_r$$

$$P_s = T_{em} * \omega_s$$

For loss less generator the mechanical equation is:

$$j\frac{d\omega r}{dt} = Tm - Tem$$

In steady state at fixed speed for a loss less generator $T_m = T_{em}$ *and*

$$P_m = P_s + P_r$$

$$P_r = P_m - P_s = T_{em}\,\omega_s = -sP_s$$

Where, $S = \frac{\omega r - \omega s}{\omega s}$ *is* defined as the slip of the generator. Generally the slip is much lower than 1 and consequently, P_r is only a fraction of P_s. Since Tm is positive for power generation and since ω_s is positive and constant for a constant frequency grid voltage, the sign of P_r is a function of the slip sign. P_r is positive for negative slip (speed greater than synchronous speed) and it is negative for positive slip (speed lower than synchronous speed). For super synchronous speed operation, P_r is transmitted to DC bus capacitor and tends to rise the DC voltage. For sub-synchronous speed operation, P_r is taken out of DC bus capacitor and tends to decrease the DC voltage. C_{load} is used to generate or absorb the power P_{gc} in order to keep the DC voltage constant. In steady-state for a lossless AC/DC/AC converter P_{gc} is equal to P_r and the speed of the wind turbine is determined by the power P_r absorbed or generated by C_{rotor}. The phase-sequence of the AC voltage generated by C_{rotor} is positive for sub-synchronous speed and negative for super synchronous speed. The frequency of this voltage is equal to the product of the grid frequency and the absolute value of the slip. C_{rotor} and C_{load} have the capability for generating or absorbing reactive power and could be used to control the reactive power or the voltage at the grid terminals.

The back to back PWM converter has two converters, one is connected to rotor side and another is connected to load side.

ISSN (Print) : 2320 – 3765
ISSN (Online): 2278 – 8875

International Journal of Advanced Research in Electrical, Electronics and Instrumentation Engineering

(An ISO 3297: 2007 Certified Organization)

Vol. 4, Issue 5, May 2015

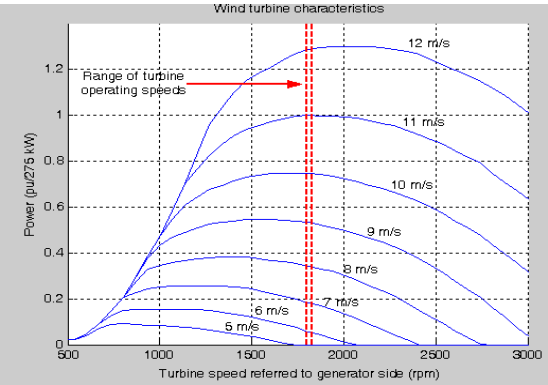

Fig. 4. Turbine power characteristics

The rotor-side converter is used to control the wind turbine output power and the voltage measured at the grid terminals.

IV. DOUBLY FED INDUCTIONGENERATOR FOR WIND TURBINES

Mainly due to the fact that the power electronic converter only has to handle a fraction (20–30%) of the total power[1].Therefore, the losses in the power electronic converter can be reduced, compared to a system where the converter has to handle the total power. In addition, the cost of the converter becomes lower. There exists a method that uses controllable external rotor resistances

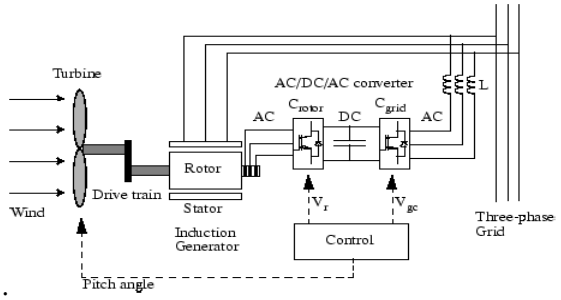

Fig.7. Variable-speed wind turbine with DFIG

Some of the drawbacks of this method are that energy is unnecessary dissipated in the external rotor resistances and that it is not possible to control the reactive power.

For variable-speed systems with limited variable-speed range, e.g.30% of synchronous speed, the DFIG can be an interesting solution. As mentioned earlier the reason for this is that power electronic converter only has to handle a fraction (20–30%) of the total power. This means that the losses in the power electronic converter can be reduced compared to a system where the converter has to handle the total power. In addition, the cost of the converter becomes lower. The stator circuit of the DFIG is connected to the load while the rotor circuit is connected to a converter via slip rings with a back to back converter [2].

The back-to-back converter consists oftwo converters, i.e., machine-side converter and load-side converter, that are connected “back-to-back”. Between the two converters a dc-link capacitor is placed, as energy storage, in order to keep the voltage variations (or ripple) in the dc-link voltage small. With the machine-side converter it is possible to control the torque or the speed of the DFIG and also the power factor at the stator terminals, while the main objective for the load-side converter is to keep the dc-link voltage constant [4].

ISSN (Print) : 2320 – 3765
ISSN (Online): 2278 – 8875

International Journal of Advanced Research in Electrical, Electronics and Instrumentation Engineering

(An ISO 3297: 2007 Certified Organization)

Vol. 4, Issue 5, May 2015

V. DFIG DRIVEN WIND TURBINE MODEL MULATION IN SIMULINK

The following is the simulink model of DFIG wind energy conversion system.

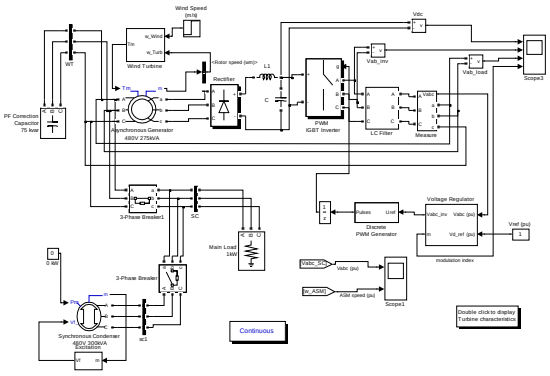

Fig.8. Simulink model of DFIG driven wind energy conversion systems

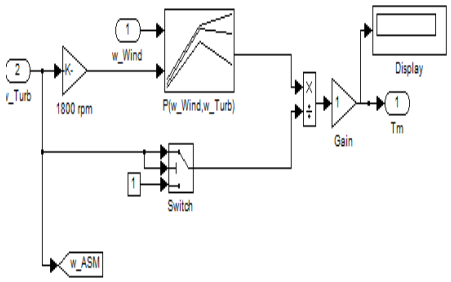

Fig.9. Wind turbine simulink block diagram

The above system is the subsystem of the wind turbine model where the wind velocity and reference speed of the turbine is given as the input.

VI. RESULTS

The wind turbine is assumed to be operated with variable speed *so* that it will operate in the peak power tracking mode. A varying wind speed profile is applied to the generator to investigate its performance. Due to variation of wind velocity power generated by the machine can also be changed.

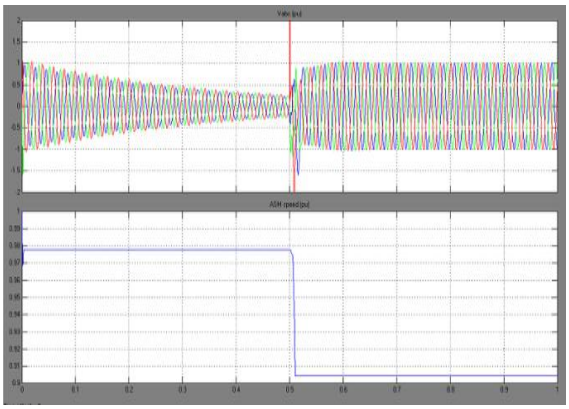

Fig.10.Waveforms of 3-phase voltages across load (above) and speed of generator (below)

ISSN (Print) : 2320 – 3765
ISSN (Online): 2278 – 8875

International Journal of Advanced Research in Electrical, Electronics and Instrumentation Engineering

(An ISO 3297: 2007 Certified Organization)

Vol. 4, Issue 5, May 2015

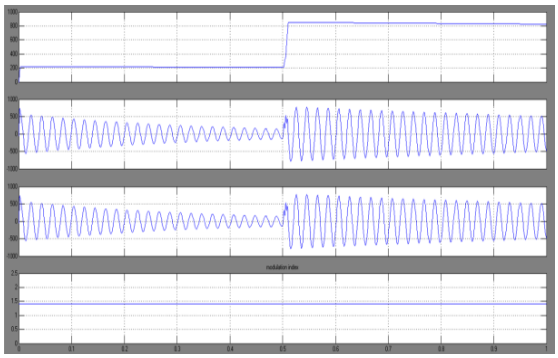

Fig.11.waveforms of Dc voltage, inverter output voltage, load voltage and Modulation index respectively with DFIGWEC supply and conventional power supply

The harmonic level in the three phase grid
Voltage wave forms are estimated by the concept of THD and it satisfies the IEEE 519-1992 standard. This is shown in the Fig. 12.

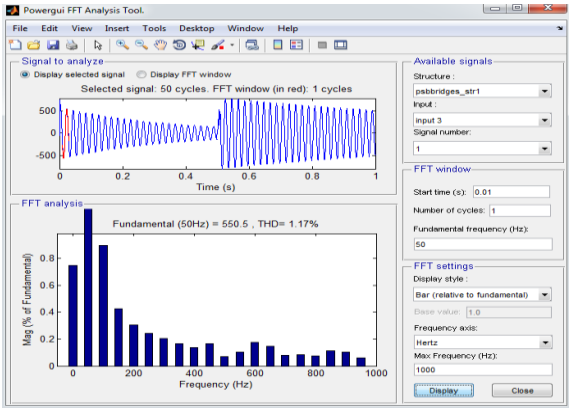

Fig.12. FFT analysis of the load voltage waveform

VII. CONCLUSIONS

The basic operation of DFIG and it's controls using AC/DC/AC converter is simulated using Matlab/Simulink. In total simulation time, half of the time operated with wind power and remaining with conventional supply and observed waveforms of load side and wind turbine side parameters. Here the is also connected to the load as backup. Considering the results it can be said that DFIG driven wind turbine proved to be more reliable and stable system with less total harmonic distortion(THD) and so gives stable and smooth performance.

REFERENCES

[1] Feng Wu, Xiao-Ping Zhang, Keith Godfrey, and Ping Ju, "Modeling and Control of Wind Turbine with Doubly Fed Induction Generator", *IEEE PES Conference on Power Systems Conference and Exposition*, pp. 1404-1409, 2006.
[2] Satish Choudhury, Kanungo Barada Mohanty, B. Chitti Babu, "Performance Analysis of Doubly fed Induction Generator For Wind Energy Conversion System" *The 5th PSU-UNS International Conference on Engineering and Technology (ICET-2011), Phuket*, pp. 532-536, 2-3 May 2011
[3] Huaqiang ZHANG, Zhixin WANG, "Study on Modeling and Simulation of Double-Fed Induction Wind Power Generator Control System", *International Conference on Sustainable Power Generation and Supply*, pp. 1-5, 6-7 April 2009.
[4] H. Sediki, Dj. Ould Abdeslam, T. Otmane-cherif, A. Bechouche, K. Mesbah, "Steady-State Analysis and Control of Double Feed Induction Motor", *World Academy of Science, Engineering and Technology* 61 2012.
[5] Zavadil, R.Miller, N.ellis, A.Muljadi, E. :Jeee power & energy magazine 3 no. 6 (nov 2005).
[6] PATEL, M. R. : Wind and Solar Power Systems, CRC Press,1999, pp. 82–83.